On the alert for pandemic flu—at the local pig show p. 347

Human gut commensals produce diverse genotoxins pp. 358 & 369

Martian meteorite impact pp. 360, 412, & 417

Science

$15
28 OCTOBER 2022
science.org

AAAS

BIG CHANGE

The shifting tempo of mammalian skull evolution

pp. 355 & 377

UT Southwestern Medical Center
Salutes Drs. Michael Brown and Joseph Goldstein

Celebrating 50 years of collaboration, discovery, and the science behind lifesaving statins.

UT Southwestern Medical Center is proud to honor Drs. Michael Brown and Joseph Goldstein as they celebrate 50 years of their collaborative research at UT Southwestern.

The duo launched their joint laboratory at UTSW in 1972 and were awarded the 1985 Nobel Prize in Physiology or Medicine for discovering the LDL ("bad cholesterol") receptor and its role in hypercholesterolemia. That discovery revealed the mechanism by which the blood LDL-cholesterol level is controlled and laid the foundation for the pharmaceutical development of lifesaving statin drugs for heart health, which today are used by more than 200 million people around the globe.

The Brown and Goldstein Nobel Prize was the first of six Nobels received by UT Southwestern faculty members in the past 40 years.

Brown and Goldstein's collaboration has been one of science's most successful partnerships over the past five decades – and it endures to this day. The two jointly have trained 175 young scientists and continue to work daily in their lab, sharing their work ethic and intellect with succeeding generations of scientists.

The Brown and Goldstein story is one of exceptional creativity, unwavering diligence, dogged persistence, unrelenting focus, and a remarkable partnership.

> "Joe and Mike's brilliant science seems to me to be vaguely magical, and, even in science, without enchantment there is nothing. Their science is an act of creation, and through their creativity they have constructed biological edifices that have profoundly enhanced our world."

– Richard Axel, M.D. | Nobel Laureate, 2004 | Co-Director of the Zuckerman Institute and University Professor | Columbia University

---

> "Mike and Joe are a duo whose discoveries have eased the burden of human disease while illuminating the processes that make life possible. They are truly biomedical superheroes."

– David Baltimore, Ph.D. | Nobel Laureate, 1975 | President Emeritus and Judge Shirley Hufstedler Professor of Biology | California Institute of Technology

UTSouthwestern
Medical Center

Federal research funding drives economic and public good

In August, in a major boon for the scientific research enterprise and for all Americans who benefit from the improvements in quality of life that science and technology advancements bring, President Biden signed into law the CHIPS and Science Act of 2022 (CHIPS stands for "Creating Helpful Incentives to Produce Semiconductors.") This historic legislation is designed to revitalize the American scientific research and technology development ecosystem and is the most significant piece of legislation in support of science seen in decades. Major scientific agencies, including the National Science Foundation, will greatly benefit from this bipartisan legislation. As the White House notes, "Public investments in R&D lay the foundation for the future breakthroughs that over time yield new businesses, new jobs, and more exports."

CHIPS and Science is one step, albeit a major one, in the right direction of supporting federal funding of research. But so much more is needed. "I am the staunchest supporter of doubling the budget for scientific research in this country," says **Gary K. Michelson**, an orthopedic surgeon whose patented inventions to improve spinal surgery outcomes enabled him to launch Michelson Philanthropies. A fierce advocate for federal research funding, Michelson has tirelessly endeavored to engender novel avenues to encourage public investment in science. He sees this need as an economic driver for the country. "It's quite clear that the United States is not going to outcompete the rest of the world on the cost of labor," he shares. "And it's certainly not going to outcompete the rest of the world on manufactured goods that depend on the cost of labor. Our only opportunity to thrive economically is technologically based."

Michelson and his foundations have been tracking the federal funding landscape: Ten years ago, he notes, the U.S. budget for research and development was $147 billion. In 2021, it was $156 billion. "In inflation-adjusted dollars, we're actually going in the wrong direction," he adds. Indeed, as Senator **Elizabeth Warren** (D-MA) writes in *CommonWealth* Magazine, "despite its critical importance and powerful economic impact, our nation has underinvested in basic research for so long that our base rate has fallen to appalling levels. Even with these new funding increases, federal investment in research remains only a tiny fraction of our GDP [gross domestic product]—far below where it stood decades earlier." In terms of its federal funding of research as a percentage of GDP, the United States has slipped to ninth place worldwide, down from fourth place only three decades ago.

We must encourage more federal funding of basic science, argues Michelson. "The best investment is the investment in technology, because that's the investment that has the potential to pay off in so many ways," he says. **Keith Yamamoto**, vice chancellor for science policy and strategy and professor of cellular and molecular pharmacology at the University of California, San Francisco, agrees. "Good science has proven over and over again to be economically rewarding," he says. "Federal investment in research needs to expand, not only across the basic sciences, but into development of applications of that knowledge." Yamamoto is heartened by the CHIPS and Science Act. "We saw the clear perception that in order to maintain economic strength in the U.S. and compete with other nations, public funds are justified."

While revving up the nation's economic engine is a critical motive for more robust federal funding mechanisms, there are other reasons to boost science. National security, public health, public safety, and technological improvements also propagate from public spending on science, as does

PHOTO: © GORODENKOFF/SHUTTERSTOCK.COM

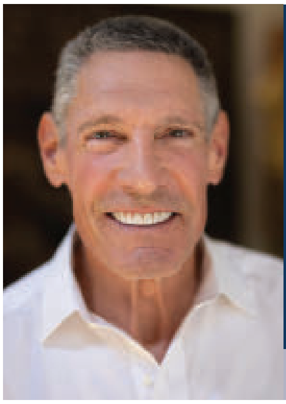

The Michelson Philanthropies & *Science* Prize for Immunology is a prestigious honor awarded annually to one early-career scientist based on research done in the past 3 years. The prize focuses on transformative research in human immunology, with trans-disease applications to accelerate vaccine and immunotherapeutic discovery. It is meant to encourage interdisciplinary approaches to grand challenges in immunology. As such, scientists in computer science, artificial intelligence/machine learning, protein engineering, nanotechnology, genomics, parasitology and tropical medicine, neurodegenerative diseases, gene editing, and many other fields are encouraged to apply. The winner receives USD 30,000 and the publication of their essay in *Science*. The next application window will open in May 2023.

MICHELSON
PHILANTHROPIES
& Science
PRIZE FOR
IMMUNOLOGY

For more information, go to science.org/michelson

something Yamamoto refers to as “public need.” This involves funds for research that industry might not undertake on their own because of their aversion to elevated financial risk or limited opportunity for financial gains—for example, pursuing pharmaceutical interventions for rare diseases. Federal funding encourages equity, says Yamamoto. “We really want to develop products that will benefit all people, not just those who are privileged,” he notes. The connection between investments in science and the goal of serving all is underscored by the fact that CHIPS and Science includes a distinct component designed to improve diversity, equity, and inclusion in the nation’s scientific workforce.

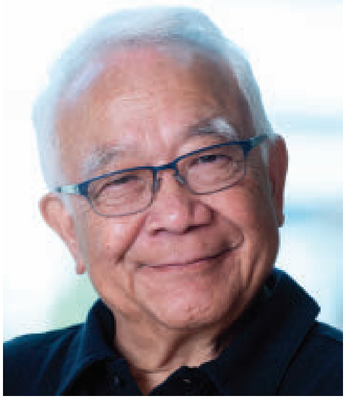

Part of the challenge funding champions face is a misperception and misaligned expectation that the private sector can or should be leading the charge in investing in basic research. “It’s no longer the case, if it ever was, that the profit motive for the private sector is sufficient to generate all of the applications from fundamental knowledge discovery that are needed,” says Yamamoto “It’s just open investigation into anything that raises the curiosity of scientists.”

While a helix of private and public support is helpful, it is proactive action from the government that is needed to spur innovations that have the potential to be game changers. We have seen this with the Advanced Research Projects Agency-Energy (ARPA-E) funding clever projects in green energy, and we can expect to see a similar outcome with the newly established Advanced Research Projects Agency for Health (ARPA-H).

“Bold research can reshape our understanding of the world and accelerate innovation,” said Senator **Alex Padilla** (D-CA), who holds a mechanical engineering degree from Massachusetts Institute of Technology, at the ceremony celebrating the 2022 winners of the Michelson Philanthropies & *Science* Prize for Immunology (see inset). “Our nation depends on scientists with big dreams and the perseverance to discover. As we reflect on the lessons of the [COVID-19] pandemic, we must renew our commitment to scientific research.”

This dedication through federal funding also ensures that the United States remains competitive on the global stage, something that many congressional representatives take seriously. “Maintaining America’s competitive edge against China is critical to our economic and national security,” said Senator **Roy Blunt** (R-MO), who as the chairman of the Senate Appropriations Subcommittee on Labor, Health and Human Services, Education, and Related Agencies secured seven consecutive funding increases for the U.S. National Institutes of Health. CHIPS and Science “includes targeted investments in technological development and manufacturing that will strengthen our position in the global economy,” states Blunt’s Senate website.

> **“We really want to develop products that will benefit all people, not just those who are privileged.”**
>
> **— Keith Yamamoto**

There is still more to do. In her *CommonWealth* op-ed, Senator Warren writes: “Amid the celebrations over increased support for the sciences, the years of neglect cannot be ignored. Now is the perfect time ... to make the case for continuing to increase the federal investments that will spur more innovation and power our economy into the future.”

PHOTOS: PROVIDED BY MICHELSON (TOP) AND UNIVERSITY OF CALIFORNIA, SAN FRANCISCO (BOTTOM)

Sponsored by

MICHELSON
PHILANTHROPIES

CONTENTS

28 OCTOBER 2022 • VOLUME 378 • ISSUE 6618

347
Flu risk by
the snoutful

NEWS

IN BRIEF

IN DEPTH

FEATURES

INSIGHTS

POLICY FORUM

PERSPECTIVES

Surface waves from a meteorite impact are detected on Mars.

CREDITS: (TOP TO BOTTOM) LORRIE CECIL/THISWEEK; DOYEON KIM, MARTIN VAN DRIEL, CHRISTIAN BÖHM

BOOKS *ET AL.*

LETTERS

RESEARCH

IN BRIEF

RESEARCH ARTICLES

REPORTS

DEPARTMENTS

ON THE COVER

The skeleton of Hope, a young female blue whale that beached in Ireland in 1891, is suspended from the ceiling of London's Natural History Museum, pictured here empty of visitors while the museum was closed during the COVID-19 pandemic. Hope's skull features in new research on mammals that shows how the ecology and life history of species shape the tempo of their evolution. See pages 355 and 377. *Photo: Jonathan Jackson; © The Trustees of the Natural History Museum, London*

PHOTO: RAUL ARBOLEDA/AFP/GETTY IMAGES

SCIENCE (ISSN 0036-8075) is published weekly on Friday, except last week in December, by the American Association for the Advancement of Science, 1200 New York Avenue, NW, Washington, DC 20005. Periodicals mail postage (publication No. 484460) paid at Washington, DC, and additional mailing offices. Copyright © 2022 by the American Association for the Advancement of Science. The title SCIENCE is a registered trademark of the AAAS. Domestic individual membership, including subscription (12 months): $165 ($74 allocated to subscription). Domestic institutional subscription (51 issues): $2212; Foreign postage extra: Air assist delivery: $98. First class, airmail, student, and emeritus rates on request. Canadian rates with GST available upon request, GST #125488122. Publications Mail Agreement Number 1069624. **Printed in the U.S.A.**
Change of address: Allow 4 weeks, giving old and new addresses and 8-digit account number. **Postmaster:** Send change of address to AAAS, P.O. Box 96178, Washington, DC 20090–6178. **Single-copy sales:** $15 each plus shipping and handling available from backissues.science.org; bulk rate on request. **Authorization to reproduce** material for internal or personal use under circumstances not falling within the fair use provisions of the Copyright Act can be obtained through the Copyright Clearance Center (CCC), www.copyright.com. The identification code for *Science* is 0036-8075. *Science* is indexed in the *Reader's Guide to Periodical Literature* and in several specialized indexes.

EDITORIAL

Credibility at stake in Sweden

Sweden's legacy as a global leader in the push to put climate and the environment at the heart of government decision-making may have come to an end on 18 October 2022. The first casualty of the country's new right-wing government was the Ministry of the Environment, eliminated on Day 1. A key question is the extent to which this change derails progress made toward building a sustainable nation and world.

Sweden has long been a leader in sustainability, both politically and scientifically. In 1972, Stockholm hosted the United Nations Conference on the Human Environment, the first meeting to place the environment on the international political agenda. Most recently, Sweden co-hosted the Nobel Prize Summit "Our Planet, Our Future" in 2021. Since helping to found the Intergovernmental Panel on Climate Change in 1988, Swedish scientists have led the development of concepts of resilience and planetary boundaries, the notion that a "safe zone" for humanity depends on remaining within a set of nine boundary conditions.

> "...shuttering the Ministry of Environment... is a painful symbolic blow."

Sweden also has brought together actors across science, policy, civil society, and business to engage with global challenges, as exemplified by the Stockholm World Water Week and the EAT Stockholm Food Forum. Without Sweden's long-standing reputation as a pioneer in environmental issues and sustainability, these collaborations would not have emerged.

But Sweden is in need of strong environmental policies and institutions, more today than at any time in the past 50 years. Indeed, science makes clear that no country is immune to the interconnected and increasingly evident global sustainability challenges. A healthy biosphere is a foundation for climate resilience and economic development, particularly during turbulent times.

Recent experiences in the United States, Norway, and Australia, for example, underscore how rapidly environmental policy can become eclipsed by short-sighted energy and economic policies, and by efforts to undermine established science. Although the move by the new Swedish government to absorb environmental issues into the Ministry of Enterprise and Innovation could indicate a strategic integration and mainstreaming of this area of politics, the expressed political priorities to date suggest the contrary. The new approach to climate is particularly troubling. A day after the environment ministry was eliminated, for instance, a representative of the far-right party, collaborating with the new government in parliament and with political officials in the government offices, claimed that there is insufficient scientific evidence of a climate crisis. And a previous national goal of 100% renewable energy has now morphed into a target of 100% "fossil free" energy, facilitated by construction of nuclear facilities and deregulation aimed at fast-tracking this shift.

But sustainability cannot be sidelined to prioritize a stable energy supply and low prices to consumers. Rather, sustainability should be central to all sectors, including transportation, the built environment, food systems, education, development aid, and more. Reduced political focus on a sustainability transition would not only be harmful to Sweden's capacity to innovate and accelerate toward a more sustainable future, it would also set back efforts of past generations who worked hard to elevate the environment to a policy priority. It also undermines Sweden's capacity to provide further leadership on sustainability issues internationally.

What ultimately matters is not how the country organizes its bureaucracy, but that its government gets things done. Although Sweden's level of ambition and engagement in sustainability has never been perfect, shuttering the Ministry of Environment 35 years after its establishment is a painful symbolic blow. The loss is further aggravated by the new government providing little indication that it understands sustainability as fundamentally dependent on the living biosphere, including land, forests, fresh water, and the ocean—issues hardly mentioned to date in existing policy priorities. Sweden's new government must accelerate and integrate sustainability efforts in line with the United Nations Sustainable Development Goals across society. The scientific community stands ready to help coproduce solutions and contribute its knowledge and networks to guide a transition to a low-carbon, equitable, and sustainable economy.

As Sweden takes on the European Union presidency in spring 2023, its international colleagues must help ensure that Sweden—like all countries—remains accountable to its international commitments and does its share to ensure a habitable planet for future generations. Scientists, civil society, and other governments must learn from Sweden's latest example: If Sweden abandons one of its proudest legacies, perhaps any country is at risk of doing so.

–Henrik Österblom and Robert Blasiak

Henrik Österblom is a professor of environmental science at the Stockholm Resilience Centre, Stockholm University, Stockholm, Sweden, and program director at The Beijer Institute of Ecological Economics, Royal Swedish Academy of Sciences, Stockholm, Sweden. henrik.osterblom@su.se

Robert Blasiak is a researcher at the Stockholm Resilience Centre, Stockholm University, Stockholm, Sweden, and a visiting researcher at the Graduate School of Agricultural and Life Sciences at the University of Tokyo, Tokyo, Japan. robert.blasiak@su.se

10.1126/science.adf4127

NEWS

> “Of course livelihoods matter, but so does life.”
>
> **University of Edinburgh public health researcher Devi Sridhar,** criticizing COVID-19 policies espoused by new U.K. Prime Minister Rishi Sunak during the pandemic as finance minister. Sunak opposed lockdowns for all but the most at-risk people, to avoid hurting the economy.

IN BRIEF

Edited by **Jeffrey Brainard**

#METOO

Ousted scientist sues U.S. academy

A prominent Peruvian archaeologist whom the U.S. National Academy of Sciences (NAS) ejected after he was investigated for sexual harassment sued the academy and its president this month for defamation. The plaintiff, Luis Jaime Castillo Butters, was ousted in 2021 in one of the first such actions by the academy since it updated bylaws in 2019 to permit expulsions for documented misconduct violations. Castillo Butters’s lawsuit, filed this month in a federal court in Washington, D.C., seeks $5 million in damages from the academy and NAS President Marcia McNutt. (McNutt served as editor-in-chief of *Science* from 2013 to 2016.) The filing does not specify what statements Castillo Butters views as defamatory. In 2020, his institution, the Pontifical Catholic University of Peru, concluded there was evidence he sexually harassed people. But it did not sanction him because the alleged harassment occurred before it adopted a policy authorizing such discipline. Castillo Butters, who denies the allegations, won a defamation lawsuit in Peru this year against one of his accusers, who has appealed.

WHO targets top fungal threats

BIOMEDICINE | Viruses and bacteria hog the limelight for public health threats, but last week the World Health Organization (WHO) published its first-ever list of “priority pathogens” that are fungi. Several of the 19 fungi species that present the greatest threats have developed resistance to treatments in the four classes of antifungal medications now available. As a result, treatment can require prolonged hospital stays and second-line drugs that are expensive and highly toxic. Diagnostics for these fungi must improve, too, the report says. The top four fungi threats are *Aspergillus fumigatus*, *Candida albicans*, *C. auris*, and *Cryptococcus neoformans*, according to a WHO survey of clinicians and researchers. They ranked the threats based on criteria including antifungal resistance, the role of infections in patient deaths, and available diagnostics. The report calls for more R&D funding and strengthening labs to do surveillance.

Bumble bees play with toys

ANIMAL BEHAVIOR | Researchers were training bumble bees to roll wooden balls to a goal when they observed a previously unknown behavior: Some bees spontaneously rolled the balls even without a reward. The scientists have now concluded in new experiments that the repeated manipulations of these balls for no apparent purpose is a form of play. The finding is a first for any insect species, although an earlier study observed wasps appearing to play fight with one another. As with mammals and birds, younger bees played more than older ones, the team reports this week in *Animal Behaviour*. Samadi Galpayage, a Ph.D. student at Queen Mary University of London who led the study, says the finding indicates a level of cognitive sophistication in bees that she hopes will encourage policies to protect them.

Bumble bees (*Bombus terrestris*) repeatedly manipulated wooden balls in a form of play.

PHOTO: RICHARD RICKITT

Indonesia wants fossils back

SCIENTIFIC COLLECTIONS | Indonesia has asked the Netherlands, its former colonizer, to return fossils of an original specimen dubbed Java Man, an early hominin unearthed in East Java in the 1890s and today named *Homo erectus erectus*. The remains, which include a skullcap, tooth, and thighbone, are the most famous items on a list of treasures Indonesia wants back. The inventory, sent to the Dutch government this summer and published by Dutch newspaper *Trouw* on 18 October, contains mostly cultural items, including a dagger used during a collective suicide in Bali. But Indonesia also seeks the return of 40,000 fossils dug up by paleoanthropologist Eugène Dubois, whose discovery of Java Man, one of the first “missing links” between apes and modern humans, caused a sensation at the time. The Dubois collection is owned by the Dutch government and managed by Naturalis Biodiversity Center, a museum in Leiden, where the fossils are still being studied by scientists from around the world, a museum spokesperson says. A commission will advise the government on whether to honor Indonesia’s request.

U.S. Ph.D. degrees fall off

HIGHER EDUCATION | The 2020–21 academic year saw 4% fewer science Ph.D.s awarded by U.S. universities compared with the preceding year, the largest annual drop since 1999, according to data released last week by the U.S. National Science Foundation. The decline was greatest in the physical and life sciences—8% and 6%, respectively. (Their decline was even greater—12% and 7%—when compared with 2018–19, the last full year before the pandemic began.) These fields largely require in-person work, and it's not clear how many students delayed graduation because of laboratory shutdowns, travel restrictions, and other pandemic-related challenges—and whether the easing of pandemic constraints will trigger a rebound.

Society bans James Webb name

EQUITY | The Royal Astronomical Society (RAS) said this week that papers in its journals must use the acronym JWST instead of the James Webb Space Telescope's full name because of concerns about the namesake's background and NASA's dismissal of calls to rename the telescope. Webb led the agency during the 1960s and the early years of the Apollo program. Evidence found since he died in 1992 suggests that while a Department of State employee during the 1950s, Webb helped start purges of gay men from the federal workforce. In 2021, months before NASA launched the telescope, its official historian and an outside expert reviewed archives regarding Webb's role. But NASA did not release the findings and later that year said it had found no evidence requiring a name change. In its 24 October statement about the acronym, RAS called "dismissing employees for their sexual orientation … entirely unacceptable." It also endorsed a request by the American Astronomical Society for NASA to open its archive to an independent historian with expertise in LGBTQ+ history to investigate Webb's role.

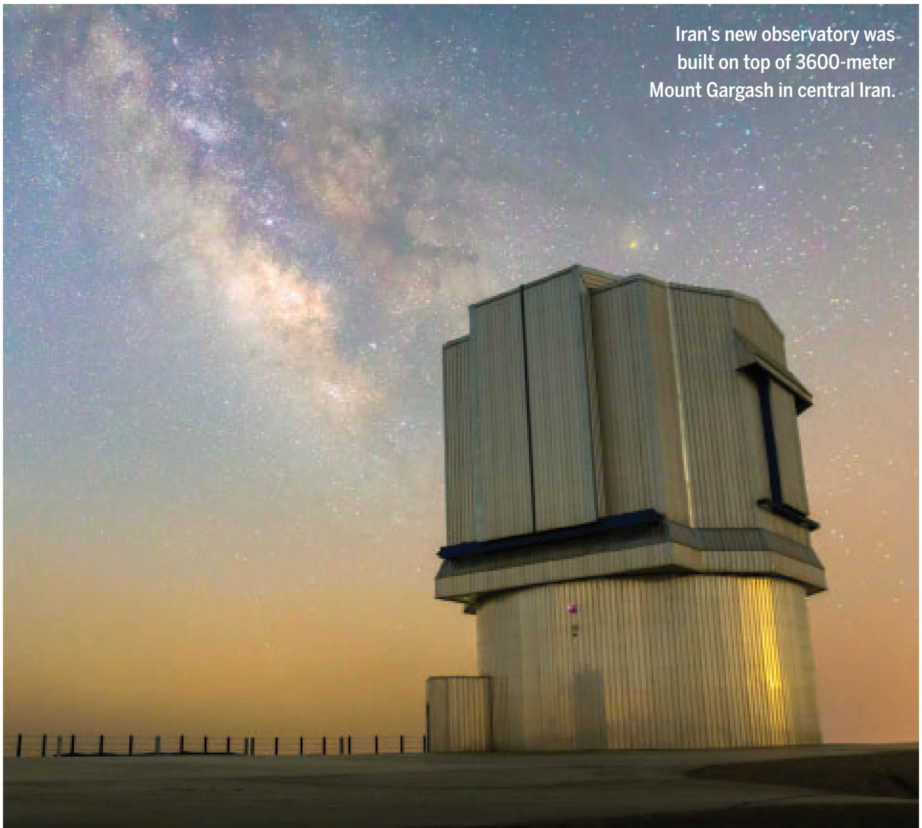

Iran's new observatory was built on top of 3600-meter Mount Gargash in central Iran.

ASTRONOMY

Iran's world-class telescope sees first light

In a major milestone for Iran's scientific community, astronomers announced last week that the $25 million Iranian National Observatory (INO) is operational. They said the resolution of the first images—showing Arp 282, a pair of galaxies some 319 million light-years from Earth—was better than expected. Iranian scientists first proposed building the INO 2 decades ago, and to complete it, they had to surmount hurdles that few colleagues elsewhere face: sanctions that curtail high-tech imports and visa restrictions limiting their travel abroad. Among other science goals, the 3.4-meter optical telescope on top of Mount Gargash will help fill a geographic gap in a global network that studies fleeting phenomena such as gamma ray bursts to try to pinpoint their locations and unravel their physics. Engineers have yet to install the first science instrument, a high-quality imaging camera. Operators hope to forge international collaborations to install additional instruments, assuming any sanctions restrictions can be resolved.

PHOTO: IRANIAN NATIONAL OBSERVATORY

U.K. eyes detecting disease early

BIOMEDICINE | A U.K. research organization began inviting participants this week for an ambitious, long-term health study that aims to enroll 5 million people by 2025 to improve the early detection of many common and rare diseases. The organization, Our Future Health, will partner with the National Health Service on the project, the largest of its kind globally. The venture has received £79 million in government research funding and aims to raise £160 million from charities and life science companies. Participants will provide blood samples and physical measurements, answer a questionnaire, and give consent for researchers to access their health records. The team expects that from 2023, it will be able to warn participants of early signs of disease and develop new diagnostic tools. The researchers hope these changes will help reduce health care costs and burdens on health care systems.

Fund backs ocean, carbon tech

ENTREPRENEURSHIP | A new venture capital fund is betting that a partnership with a leading marine research center will help create valuable new ocean technology companies that will fight climate change. Last week, Brian Halligan, who made a fortune in software, announced the launch of Propeller, a $100 million investment fund that is one of the first of its kind. The fund is partnering with the Woods Hole Oceanographic Institution in hopes of commercializing scientific discoveries and technological advances made by WHOI researchers. "We want to turn [WHOI] into an engine for creating startups," much like the Massachusetts Institute of Technology, Halligan told *The Boston Globe*. The partners released few financial details, but said potential commercialization targets for this "blue economy" include creating seaweed farms to remove carbon dioxide from seawater and finding environmentally sensitive ways to extract minerals from the sea floor.

Deaths from Uganda's Ebola outbreak have steadily increased since the burial on 13 October of a child who was a suspected case.

INFECTIOUS DISEASES

Forgotten Ebola vaccine could help in outbreak

Merck unearths a frozen batch of an experimental vaccine it made years ago

By **Jon Cohen**

In a revelation that may help Uganda combat its outbreak of Ebola, the pharmaceutical giant Merck has acknowledged it has up to 100,000 doses of an experimental vaccine for the deadly viral disease in its freezers. The company had previously told *Science* it had made the vaccine and destroyed tens of thousands of vialed doses after they expired, but failed to mention it still had a frozen bulk batch. The company now says it will donate the vaccine, and the World Health Organization (WHO) and the Ugandan government are discussing whether and how to incorporate the doses into one or more clinical trials of other candidate Ebola vaccines that could begin as soon as next month.

The Merck vaccine targets Sudan ebolavirus, the pathogen now circulating in Uganda, where, as of 23 October, it has sickened at least 90 people, killing 28 of them, and even reached the capital, Kampala, a bustling city of 1.5 million. Merck's disclosure "is amazingly good news," says Mark Feinberg, who led the company's program to develop a vaccine for a related killer, Zaire ebolavirus, that devastated West Africa between 2014 and 2016. "It allows this very promising vaccine to move forward quicker than would have otherwise been possible."

Feinberg left Merck in 2015 and now heads the nonprofit IAVI, which is developing its own vaccine for Sudan ebolavirus. But he and others think Merck's vaccine may be the best prospect, because it uses the same technology as Merck's successful Ebola Zaire vaccine.

It took repeated inquiries from *Science* before Merck revealed it still has Ebola Sudan vaccine. Merck quietly made the product in 2015 and 2016, soon after its landmark success with the Zaire Ebola vaccine, Ervebo, which has helped stem several outbreaks. The company froze the Sudan Ebola vaccine in vials and in bulk form and never tested it on people, though it protected monkeys when they were intentionally injected with Sudan ebolavirus.

Merck now says it plans to "fill and finish" the thawed bulk product, a process that puts it into vials; it expects that to take about 1 month, and the company will pay for it. "We're doing everything to move it as quickly as we possibly can," says Merck virologist Beth-Ann Coller, who has headed product development for the company's Ebola vaccines since May 2015.

Classic public health measures such as isolating patients and quarantining their contacts can bring Ebola outbreaks to an end, but Merck's unexpected announcement has buoyed hopes that a vaccine may help Uganda stop the outbreak more quickly. "The potential availability of large volumes of vaccine that can be tested sooner is potentially game changing," says Nicole Lurie, U.S. director for the Coalition for Epidemic Preparedness Innovations (CEPI), a nonprofit that funds vaccine development to prevent pandemics.

Merck's vaccine consists of the gene for the surface protein of the Sudan ebolavirus stitched into vesicular stomatitis virus (VSV), a livestock pathogen that rarely causes harm in humans. Two other developers of Sudan Ebola vaccines, the nonprofit Sabin Vaccine Institute and the University of Oxford, use chimpanzee adenoviruses to ferry the surface protein gene into the human body. Both are racing to produce enough doses to enter trials in Uganda. Sabin has 40,000 bulk doses and is working with CEPI to find a company that can do the fill and finish. Oxford has teamed up with the Serum Institute of India.

"Now there's this other wild card," Lurie says. Several vaccine scientists tell *Science* they are confident all three Sudan Ebola vaccines will protect people to varying degrees, but they consider Merck's vaccine the most promising candidate, in part because VSV—unlike the chimp adenoviruses—copies itself, leading to rapid immunity.

WHO was already collaborating with health officials in Uganda to design a protocol to test the Oxford and Sabin candidates with a strategy known as a "ring vaccination,"

PHOTO: LUKE DRAY/GETTY IMAGES

in which shots are offered to direct contacts of infected people (and possibly contacts of contacts). That approach was used in a 2015 trial of the Ebola Zaire version, in Guinea. An independent “expert group is currently reviewing the evidence and will advise on which vaccine(s) to test first,” a WHO spokesperson wrote to *Science*.

The ebolavirus-VSV platform used in Merck’s shots was developed nearly 20 years ago by virologists Heinz Feldmann, then with the Public Health Agency of Canada (PHAC), and Thomas Geisbert, then with the U.S. Army Medical Research Institute of Infectious Diseases. They showed a single dose of a VSV-based vaccine protected 100% of monkeys against an otherwise lethal dose of Zaire ebolavirus given 28 days later. Smaller animal studies showed the vaccine against the Sudan ebolavirus had promise as well.

In 2016, after the success of the Ebola Zaire vaccine, *Science* asked 50 leading vaccine researchers which other vaccines the world should develop to be ready for disease outbreaks. They ranked a Sudan ebolavirus vaccine as the No. 1 R&D priority based on feasibility and need (*Science*, 1 January 2016, p. 16). As it happens, Merck’s vaccine was in the works. Virologist Richard Peluso, who then ran vaccine bioprocessing for the company, says in 2015 he told his boss, Senior Vice President of R&D Joe Miletich, that if the Zaire Ebola vaccine was safe and effective, the company had “an obligation to the world” to use the VSV platform to also make a stock of Sudan Ebola vaccine. Merck proceeded to make the vaccine under strict “good manufacturing practices” and also produced a large batch of a VSV-based vaccine against Marburg disease, another rare but often lethal infection caused by an Ebola-like virus. (It ranked fifth in *Science*’s survey.)

“Fortuitously, it hadn’t yet been destroyed.”

Beth-Ann Coller, Merck

Outside vaccine experts *Science* contacted didn’t know about Merck’s batch of Sudan ebolavirus vaccine. In 2017, it gave the license for the vaccine back to PHAC, which subsequently cut a licensing deal with IAVI. In 2021, the U.S. government’s Biomedical Advanced Research and Development Authority (BARDA) awarded IAVI a grant worth up to $126 million to use upgraded technology to develop VSV-based vaccines for both Sudan ebolavirus and Marburg. (BARDA awarded a similar amount to Sabin to develop the same vaccines using its chimp adenovirus platform.)

Those vaccines are still at early stages of development, and when the Uganda outbreak began in September, Feldmann, who now works at the U.S. National Institute of Allergy and Infectious Diseases, was beside himself. “I sent an email to my boss and said, look, we are in the same situation as in 2014,” he says. “The VSV vaccine we know works in ring vaccination, and it would be perfect to stop this.” Feldmann also now has unpublished data that provide even more evidence of the VSV-based Ebola Sudan vaccine’s robust and durable ability to protect monkeys.

When and how Merck came to realize it has a big batch of the vaccine available and ready for clinical trials is not entirely clear. *Science* asked Merck on 13 October whether it had produced the Sudan Ebola vaccine and retained stocks of it. A spokesperson wrote back that although Merck had made approximately 70,000 vials of it in 2015–16, “the vials of Sudan ebolavirus (SUDV) vaccine candidate expired in 2021 and were destroyed.” (The email also said Merck had destroyed 96,000 filled vials of its Marburg vaccine.)

In response to follow-up questions, Merck acknowledged on 20 October that the company did retain bulk quantities of the frozen Ebola vaccine and arranged an interview with Coller. She says Merck destroyed the fill-and-finished doses of the Sudan Ebola vaccine because the single-dose vials had used rubber stoppers. “The stoppers become brittle when they’re stored frozen,” she explains.

The bulk product Merck has now disclosed had reached “the end of its shelf life” and was destined for destruction as well, but to the surprise of company scientists, it was still in the freezer. “Frankly, fortuitously, it hadn’t yet been destroyed,” Coller says. “We immediately looked at that and said, oh, my goodness, we can perhaps do something to help.” (Bulk Marburg vaccine, Coller says, was destroyed.)

Coller says she initiated a search to see whether any Sudan Ebola vaccine remained after attending a WHO meeting that ended on 6 October in which she learned Uganda’s outbreak was rapidly growing. Asked why the company did not mention the find in response to *Science*’s 13 October email, she says Merck was still conducting tests to assess whether the vaccine had remained free of contaminants. “We were not sure about whether or not we would be able to use that bulk material and didn’t want to speak out of turn until we knew that there was something that we could actually do with it.”

Merck never considered running human studies with the Sudan Ebola vaccine. “That was not something that was ever really put on the table,” Coller said, noting that there has not been an outbreak of this virus since 2012, when Uganda had a previous one. “With hindsight, perhaps it could have been done better.” ■

ANIMAL RESEARCH

Harvard studies on infant monkeys draw fire

Experiments involving eyelid suturing and maternal separation divide scientists

By **David Grimm**

Primatologists and animal rights activists are condemning monkey studies in the laboratory of Harvard University neuroscientist Margaret Livingstone. The work, which involves removing newborns from their mothers and, in two cases in 2016, suturing their eyelids shut to study how the primate brain processes faces, is cruel and unethical, they say. But some neuroscientists defend the studies as crucial for understanding human vision.

Livingstone says the eyelid suturing procedure she and colleagues utilized is similar to that used to treat children with eye tumors and invasive eye infections—and they have no plans to use it again. But some of her studies still involve separating infant monkeys from their mothers.

That’s shocking to Catherine Hobaiter, a primatologist at the University of St. Andrews who has studied primates in the wild for 17 years. “As a scientist, I question what we are learning that we couldn’t learn in another way,” she says. “As a human, I’m horrified.”

Last Monday, Hobaiter and her graduate student, Gal Badihi, sent a letter to the *Proceedings of the National Academy of Sciences* (*PNAS*) signed by more than 250 animal behavior researchers, grad students, and postdocs, asking it to retract Livingstone’s most recent publication. The animal rights group People for the Ethical Treatment of Animals (PETA) has done the same. It has also asked Harvard to terminate Livingstone’s studies, and the U.S. National Institutes of Health (NIH) to defund the work.

Such efforts could crush research “critical for human survival and empathy,” says

Bertha Madras, a neuroscientist at Harvard who has conducted brain imaging studies of monkeys for decades but doesn't work directly with Livingstone. "If we're going to understand how the brain functions, we're going to have to do experiments that generate visceral reactions," she says. "We have to be looking at the greater good."

Livingstone has spent 40 years studying vision in monkeys. To determine how the parts of the brain responsible for recognizing faces develop, her team sometimes removes rhesus macaques from their mothers after birth and hand-raises them for months, eventually housing them with other juveniles. In some experiments, the infants see no faces for a year, either because laboratory staff wear masks, or because the researchers effectively blind them. In 2016, the team sewed the eyelids shut in two monkeys; the sutures dissolved in a few days, but the eyes remained closed for a year. Since then, Livingstone says her team has used noninvasive approaches such as goggles.

A monkey mother whose infant was removed clutches a soft toy given to her by neuroscientist Margaret Livingstone.

PHOTO: MARGARET S. LIVINGSTONE/DEPARTMENT OF NEUROBIOLOGY/HARVARD MEDICAL SCHOOL

Few primatologists were aware of the experiments until Livingstone published an article in *PNAS* last month. The paper was not a standard research report; instead *PNAS* invited Livingstone to pen the piece as an "Inaugural Article" to highlight her contributions to the field as a newly elected member of the U.S. National Academy of Sciences.

Titled "Triggers for mother love," the piece recounts anecdotal observations Livingstone made in the course of her research—specifically after giving soft stuffed animals to monkey mothers whose infants her team had removed for vision experiments. The paper focused on maternal behavior, reporting that the toys often calmed the mothers down. But it also drew attention to the research on the infants, detailed in a 2020 *PNAS* research paper and other publications.

The fact that *PNAS* would highlight this work is deeply troubling to Hobaiter, who also serves as the vice president for communications for the International Primatological Society. Decades of research have shown how critical the mother-child bond is in nonhuman primates, she says. Orphaned animals "shut down socially. … In some cases, they never recover"—to say nothing of the impact on the mothers. Livingstone's recent paper, she says, adds nothing meaningful to our understanding of primate behavior. "It fails on every scientific and ethical level."

Hobaiter and Badihi sent a draft letter detailing their concerns to a few colleagues. "It snowballed," she says, eventually collecting 257 signatures from across the globe. The final letter asks *PNAS* to retract this year's paper, which Hobaiter says raises questions about all invasive research with primates. "We cannot ask monkeys for consent," it reads. "But we can stop using, publishing, and … actively promoting cruel methods that knowingly cause extreme distress."

A spokesperson says *PNAS* is aware of the concerns and is "evaluating formal criticism submitted to the journal," but declined to comment further.

Earlier this month, Katherine Roe, a former experimental psychologist who studied brain development in children and who now serves as the chief of science advancement and outreach at PETA, sent letters to Harvard and two NIH agencies. She called Livingstone's work inhumane and unscientific, and asked the institutions to end their support for it. "The long-term harms that these experiments are causing the mothers and the babies far outweigh any potential benefit to humans," Roe says. "The benefits are always 'potential.' The harms are definite."

Livingstone counters that her work builds on Nobel Prize–winning science that helped treat vision loss in children. Her research has provided insights into social deficits caused when autistic children look less at faces than neurotypical children do, she says, and has helped develop therapies for Alzheimer's disease and some brain cancers.

PETA has launched a public relations and social media campaign targeting both the maternal separation in Livingstone's work and the eyelid sewing, which it calls "straight out of a horror movie."

The social media storm is taking its toll, Livingstone says. "I've become the target of increasingly hostile harassment, and I am seriously fearful for my own and my family's safety." She says she has received "violent, threatening, and obscene" calls and emails. Harvard has released a statement condemning these "personal attacks." It has not responded to requests for further comment.

In its statement, Harvard says all of Livingstone's work rigorously follows federal guidelines for animal research, and it has been approved by the university's Institutional Animal Care and Use Committee, which is designed to ensure that animals are properly cared for and only necessary experiments take place.

That's a point echoed by Michael Goldberg, a neurologist at Columbia University who treats human patients and studies perception in monkeys. These committees don't take their jobs lightly, says Goldberg, who was one of the reviewers of this year's *PNAS* paper; they only approve experiments if there's no other way to answer the question. Livingstone's work is "ethical and justified," he says. "This isn't unnecessary cruelty to animals—it's critical research."

Hobaiter notes that ethics continue to evolve, especially when it comes to animal research. She hopes the current debate prompts more discussion about the issue. "Just because your university ethics committee sets minimal standards doesn't mean you can't do better," she says. "As scientists, we should hold ourselves to a higher standard." ■

INFECTIOUS DISEASES

Monkeypox outbreak is ebbing—but why exactly?

Models suggest rising immunity in a small group of people, not vaccination, is key

By **Kai Kupferschmidt**

When monkeypox cases in Europe began to decline this summer, researchers' first question was: Is it real? Some worried that people might not be getting tested because of receding fears of the virus, coupled with strict isolation requirements for patients. "They might be reluctant to be confirmed and be told not to go out at all," says Catherine Smallwood, monkeypox incident manager at the World Health Organization's (WHO's) Regional Office for Europe.

Passing waves

The two hardest hit World Health Organization regions—Europe and the Americas—are both seeing a steep decline in monkeypox cases.

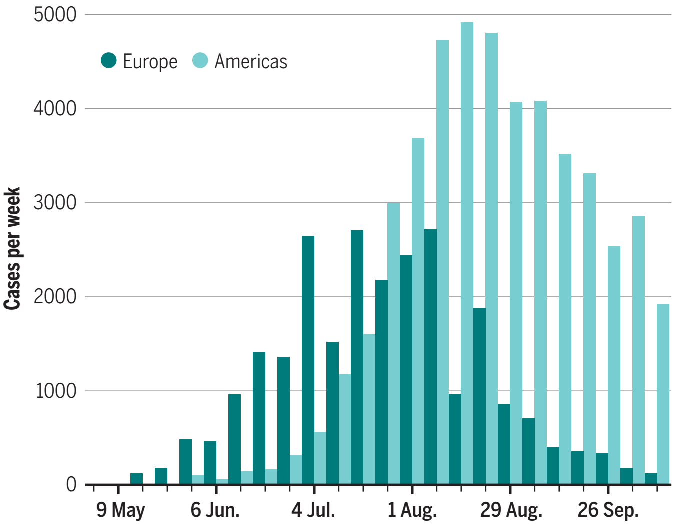

CREDITS: (GRAPHIC) K. FRANKLIN/*SCIENCE*; (DATA) WORLD HEALTH ORGANIZATION

But the decline is now unmistakable. WHO Europe, which reported more than 2000 cases per week during the peak in July, is now counting about 100 cases weekly. In the Americas, the other major epicenter of the outbreak, numbers have dropped by more than half (see graphic, right). "We're seeing a true decline," Smallwood says.

Vaccines, behavior change among the most affected group—men who have sex with men (MSM)—and immunity after natural infection are all playing a role in that decline, says Erik Volz, an infectious disease modeler at Imperial College London, but how much each factor has contributed is unclear. "This is something we've debated a lot internally."

The answer is important because it determines the likelihood of a resurgence of the virus. Knowing what has driven down cases so far will also help shape strategies to eliminate the virus outside endemic countries in Africa, a goal WHO Europe is already pushing for.

In the United Kingdom, at least, vaccination campaigns have played a minor role, according to a model published as a preprint this month by Samuel Brand, an infectious disease modeler at the University of Warwick. Monkeypox's reproductive number—the average number of new infections triggered by an infected person—began to drop by mid-June, even though campaigns only started in July, Brand notes. Several other European countries saw the same pattern.

That leaves behavior change and immunity from natural infections. A survey conducted by the U.S. Centers for Disease Control and Prevention among MSM in August found about half had reduced their number of sexual contacts. As awareness of the disease increased, people also became more likely to seek diagnosis and treatment early and to avoid sex while they were infectious. The UK Health Security Agency has presented data suggesting syphilis and other sexually transmitted infections declined as well—which would bolster the case for behavior change—although that signal is "suggestive but not conclusive," Volz says.

Immunity acquired through infections in the most sexually active men may be the biggest factor, however. Monkeypox has been affecting mostly MSM and their sexual networks because parts of those networks are densely connected, with some people having a large number of sexual contacts. Rising immunity in that group could limit the virus' ability to spread, says Jacco Wallinga, chief epidemic modeler at the Dutch National Institute for Public Health and the Environment. "Because the persons with a very high number of sexual contacts are also those at the highest risk of infection, the depletion of susceptibles due to natural infection is very rapid," he says. Brand agrees. His model suggests that among the estimated 1000 people in the United Kingdom who have 120 sexual partners per month or more, "maybe half got infected by the time of the peak." Still, Brand says his model suggests infections among this small part of the MSM population cannot explain the observed decline on their own. "I don't think it is as plausible" as behavior change playing a role as well, he says.

For Smallwood, that raises a concern: that MSM who feel reassured by the plummeting case numbers may revert to their past behavior. That's why vaccination of at-risk groups may now be more important than it was at the peak of the epidemic, she says. Brand agrees; in fact, his U.K. model suggests that although a slight uptick in cases in the coming months is likely, vaccinations should prevent a real resurgence. "I don't think there's room for complacency at this point," he says.

Eliminating the virus altogether from nonendemic countries may be difficult. "That last bit is always the hardest," Smallwood says. Among the reasons are stigma and discrimination. "In many countries, [infected people] will not be presenting purely because they're concerned about how they may be treated," she says. Besides, it has become clear that some people have asymptomatic infections and could pass on the virus unknowingly, says Boghuma Titanji, a virologist at Emory University.

Even if, say, Europe or the United States managed to eliminate the virus, reintroductions from sexual networks in countries where the virus is still circulating in humans would remain a threat, Smallwood says. And the ultimate source of the virus will remain untouched: the animal species in Africa where the virus circulates, occasionally spilling over to humans, as it has for decades. "This is not an outbreak that just needs to be fixed, and then the risk is gone," Smallwood says. ■

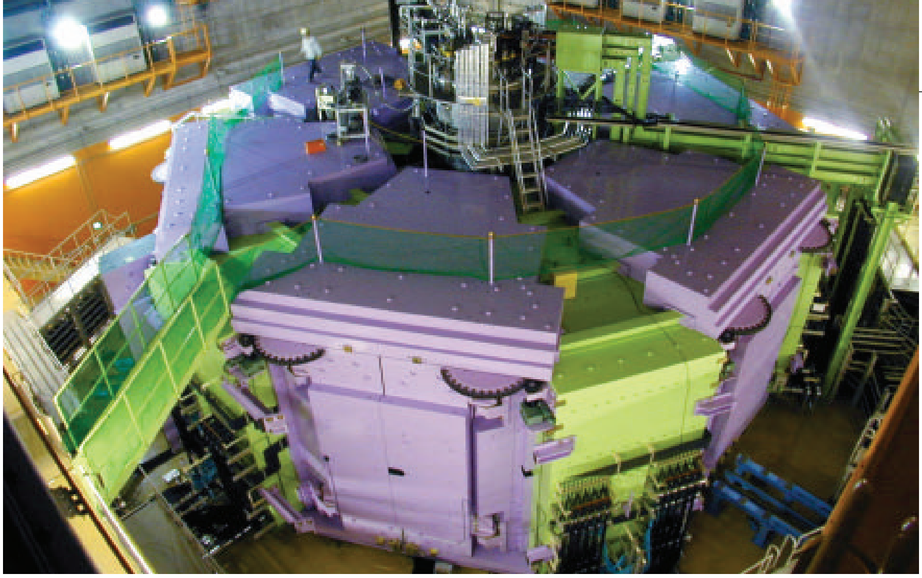

This cyclotron at a lab in Japan can accelerate beams of nuclei ranging from hydrogen to uranium.

NUCLEAR PHYSICS

New sodium isotope challenges theories of exotic atomic nuclei

How exploding stars forge elements could be harder to trace

By **Adrian Cho**

A new form of sodium—the element that combines with chlorine to make salt—packs a whacking 28 neutrons in its atomic nucleus, along with the 11 protons that define its chemical identity. With more than double the 13 neutrons in natural sodium, the neutron-rich isotope of the element is so extreme that few theoretical models predicted its existence. "It's a surprise that these neutrons keep on hanging on," says Katherine Grzywacz-Jones, a nuclear physicist at the University of Tennessee, Knoxville, who was not involved in the work.

Researchers at Japan's RIKEN Nishina Center for Accelerator-Based Science created just a handful of sodium-39 nuclei. But their mere existence challenges physicists' understanding of nuclear structure. It also suggests that tracing the process by which exploding stars forge many elements—a goal of a major new facility in the United States—may be more difficult than thought.

Three years ago, an experiment with the RIKEN center's particle accelerator, a superconducting cyclotron called the Radioactive Isotope Beam Factory, produced a tantalizing hint of a single sodium-39 nucleus. "Therefore, we repeated the experiment with much higher beam intensity and a longer beam time," says Toshiyuki Kubo, a RIKEN nuclear physicist.

Kubo's 26-member team shot a beam of calcium-48 nuclei through a beryllium target to shred them and funneled the fragments through a snaking chain of magnets called BigRIPS. Researchers tuned that chicane so only sodium-39 or a nucleus with a similar mass-to-charge ratio could slalom through. The energy a nucleus deposited in a detector at the end revealed its charge. From the charge and mass, Kubo and colleagues could easily tally a nucleus' protons and neutrons. Firing 500 quadrillion calcium-48 nuclei through the target, they spied nine sodium-39 nuclei, they report in a paper in press at *Physical Review Letters*.

Predicting which combinations of protons and neutrons will bind into a nucleus can be tricky. Protons and neutrons stick together by exchanging particles called pions, and a quantum mechanical effect favors nuclei with similar numbers of protons and neutrons. But the electrically charged protons repel one another, tilting the balance toward fewer protons. Nuclei also vary from a single proton to hundreds of protons and neutrons, and different theoretical approaches tend to work better in different mass ranges.

"By far most models did not predict that sodium-39 should be bound," says Brad Sherrill, a nuclear physicist at Michigan State University and an author on the paper. However, 2 years ago, Witold Nazarewicz, a nuclear theorist at Michigan State, and colleagues tried to predict all possible nuclei by averaging model predictions, each weighted by its uncertainty. That gave a 50% probability that sodium-39 would exist. "Is the [RIKEN] result surprising?" Nazarewicz says. "No. Is it important? Yes."

It adds an important detail to the nuclear landscape, he says. Physicists plot known and predicted nuclei on a checkerboard-like chart, with the number of protons climbing vertically and the number of neutrons increasing left to right. The nuclei form a wide swath diagonally across the chart, whose lower edge is called the neutron drip line. It marks the limit at which it becomes impossible to cram more neutrons into a nucleus with a given number of protons. And it's known only up to neon, element 10.

The neutron drip line has served up surprises before. For example, it leaps from 16 neutrons for oxygen (element 8) to 22 neutrons for fluorine (element 9). To explain that jump, theorists had to include forces not just among pairs of protons and neutrons in a nucleus, but also among trios, Sherrill says. Some other bit of overlooked physics may explain why the drip line appears to leap by four neutrons from neon-34 to sodium-39.

The results could complicate a goal for physicists. Half of all elements heavier than iron emerge from supernova explosions, as nuclei quickly absorb neutrons gushing from the explosion even as they repeatedly undergo radioactive beta decay—in which a neutron in a nucleus spits out an electron and morphs into a proton. Precisely identifying the nuclei in the process is a priority for a new $730 million linear accelerator called the Facility for Rare Isotope Beams (FRIB) at Michigan State. If the drip line lies farther out, those nuclei may contain more neutrons and be harder to make, Sherrill says.

The first results from FRIB, which turned on in May, examine nuclei near sodium-39. Researchers there also shredded a beam of calcium-48 to create neutron-rich isotopes of magnesium, aluminum, silicon, and phosphorus—the elements following sodium—and measured how quickly they beta decay, the team reports in a paper in press at *Physical Review Letters*. In another tidbit to inform models, the half-life of magnesium-38 was surprisingly short, says Heather Crawford, a nuclear physicist at Lawrence Berkeley National Laboratory and lead author.

For Crawford's experiment FRIB produced a beam one-twelfth as intense as the one in the RIKEN study. In a few years, FRIB should increase its beam intensity 400-fold, making it possible to trace the neutron drip line farther up the chart, Crawford notes. "As FRIB ramps up in power, that's one of the first things I expect will be pursued." ■

PHOTO: RIKEN NISHINA CENTER FOR ACCELERATOR-BASED SCIENCE

SYNTHETIC BIOLOGY

A big step toward mirror-image ribosomes

Synthetic protein factories could one day make durable drugs the body can't break down

By **Robert F. Service**

All of life exists on just one side of a mirror. To put it more technically, the biomolecules that comprise living things—DNA, RNA, and proteins—are all "chiral." Their building blocks have two possible mirror-image shapes, but in every case, life chooses just one. At least so far.

This week in *Science*, researchers report they've made strides toward exploring the other side of the mirror. They re-engineered a workhorse enzyme that synthesizes RNA so it makes the mirror-image form. They then used that enzyme to construct all the RNAs needed to make a ribosome, the cellular machine responsible for constructing proteins. Other components still need to be added, but once completed, a mirror-image ribosome might be able to churn out proteins that could serve as novel drugs and diagnostics and can't readily be broken down in the body. It also sets the stage for a grander goal: making mirror-image life, a prospect that has fired the imagination of scientists ever since Louis Pasteur discovered mirror-image compounds in 1848.

"This is a major step towards re-creating the central dogma of molecular biology in the mirror-image world," says Stephen Kent, a professor emeritus of chemistry at the University of Chicago who was not involved with the work.

That dogma refers to the standard operating procedure of life: The genetic code—usually DNA—is transcribed into a corresponding sequence of RNA, which is then translated into proteins that perform much of the essential chemistry in cells. Exquisitely complex molecular machines made of proteins or, in the case of the ribosome, a combination of proteins and RNA carry out each step. And every molecule involved churns out chiral products. Chemists have long been able to synthesize opposite-handed DNA, RNA, and proteins. But they've never been able to put all the pieces together to make mirror-image life, or even enough of them to see whether such a conceit is possible.

Ting Zhu, a synthetic biologist at Westlake University in Hangzhou, China, has been building toward this vision for years. Among the first steps, as Zhu sees it, is to make a mirror-image ribosome—the factory that can make so many other mirror-image parts. That's no small feat. The ribosome is a molecular behemoth, made up of three large RNA fragments, consisting of approximately 2900 nucleotide building blocks in total, along with 54 proteins.

"The most challenging part is making the long ribosomal RNAs," Zhu says. Chemists can synthesize fragments up to about 70 nucleotides long and stitch them together. But to make the three much longer ribosomal RNA fragments in mirror-image form they needed a molecular machine that could crank them out—a polymerase enzyme. In 2016, Zhu and his colleagues took a first stab at the task, synthesizing a mirror-image version of a polymerase from a virus. The polymerase made mirror-image RNA, but it was slow and prone to errors.

For the current study, Zhu and his graduate student Yuan Xu set out to synthesize a mirror-image version of a workhorse enzyme used in molecular biology labs worldwide to synthesize long RNA strands, the T7 RNA polymerase. A massive, 883 amino acid protein, it lay well beyond the limits of traditional chemical synthesis. But an analysis of T7's x-ray crystal structure showed the enzyme could likely be split into three sections, each stitched from short segments. So, they synthesized the three sections—one with 363 amino acids, a second with 238, and a third with 282. In solution, the fragments naturally folded into their proper 3D shapes and assembled themselves into a working T7. "It was a herculean effort to put together a protein of this size," says Jonathan Sczepanski, a chemist at Texas A&M University, College Station.

The researchers then put the polymerase to work. They assembled mirror-image genes encoding the three long RNA fragments the team hoped to make; then the mirror-image T7 RNA polymerase read the code and transcribed it into the ribosomal RNAs.

The result provided a tantalizing glimpse of the power of mirror-image molecules. The mirror-image RNAs fashioned by the polymerase were far more stable than the normal versions produced by a regular T7, the researchers showed, because they were untouched by the naturally occurring RNA chewing enzymes that almost unavoidably contaminate such experiments and quickly destroy normal RNAs.

This same resistance to degradation "could open the door to whole new types of diagnostics and other applications," including novel drugs, says Michael Jewett, a chemist and ribosome expert at Northwestern University. For example, Xu and

Re-engineering a workhorse enzyme

Many biomolecules come in mirror-image forms, much like gloves that fit a left or right hand. But life uses just one form. Now, synthetic biologists have made a mirror-image form of an enzyme that generates RNA components of the ribosome, a key step toward building a mirror-image protein factory.

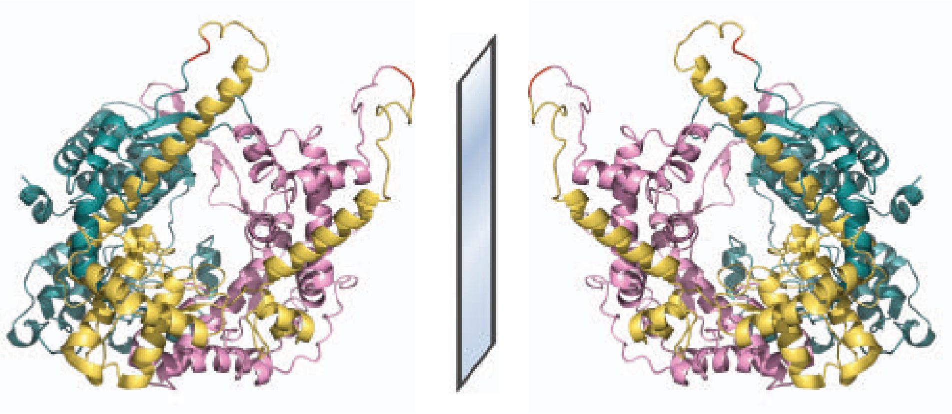

Natural-chirality T7 RNA polymerase

Mirror-image T7 RNA polymerase

GRAPHIC: YUAN XU AND TING ZHU

Zhu also used their mirror-image enzyme to make stable RNA sensors called riboswitches that could be used to detect molecules associated with diseases, as well as stable long RNAs that could be used to store digital data. Other researchers have shown that mirror-image versions of short strands of DNA and RNA called aptamers can serve as potent drug candidates that evade degrading enzymes and the immune system, which destroy most conventional aptamer drug candidates.

Exploiting this stability more broadly wouldn't be as simple as creating mirror-image copies of existing drugs, however, as such compounds, like wrong-handed gloves, would no longer match the chirality of their intended targets in the body. Instead, researchers would likely have to screen large numbers of mirror-image drug candidates to find ones that work.

But Jewett and others say the new work could aid that effort, because it sets the stage for making functional mirror-image ribosomes. Those could allow drug companies to more readily create mirror-image amino acid strings, or peptides, Jewett says. Because peptides draw from 20 amino acid building blocks, rather than just the four nucleic acids that make up aptamers, they offer greater chemical diversity and potentially more good drug candidates.

Now, Zhu and his team need to make the remaining components of a mirror-image ribosome. The three RNA fragments they synthesized make up about two-thirds of the total mass of a ribosome. What remains are the 54 ribosomal proteins and several proteins that work in concert with the ribosome, all of which are smaller and thus likely easier to synthesize. Then the question is whether the full parts kit will assemble into a ribosome.

Even if they do, the resulting molecular machines might still not be functional, cautions George Church, a synthetic biologist at Harvard University, who leads one of the few other groups around the world working on approaches to mirror-image life. In order to churn out proteins, ribosomes must work in conjunction with a suite of additional helper proteins. To make this work inside a living cell, Church thinks it will be necessary to rewrite an organism's genetic code so the engineered ribosome can recognize all those proteins, particularly the 20 that ferry amino acids for building new proteins. Church's group is working on this. "It's very challenging," he says.

But if everything comes together, researchers—and life—may finally be able to enter a looking glass world. ■

PUBLISHING

Journal declares an end to accepting or rejecting papers

Instead, *eLife* will offer to peer review selected submissions for $2000 fee, then make paper and critiques free to read

By **Jeffrey Brainard**

A publisher aiming to transform how scientists share research results has launched a new experiment. Last week, *eLife*—a nonprofit, selective, online-only journal that focuses on the life and medical sciences—announced it will cease accepting or rejecting manuscripts for publication, instead offering only peer reviews of manuscripts.

Until now, *eLife* has charged authors $3000 if it accepts their paper, which is free to read after publication. Under the new approach, *eLife* will charge authors $2000 if they accept the publisher's offer to have a submitted manuscript undergo peer review. Regardless of whether the critiques are positive or negative, the manuscript and its associated, unsigned peer-review statements will be posted online and be free to read. If the author revises the paper to address the comments, *eLife* will post the new version.

> **Critiques are "more useful to the community than our thumbs-up or thumbs-down publishing decision."**
>
> **Michael Eisen**, University of California, Berkeley

Since *eLife* was founded in 2012, it has tried other innovations. In 2020, for example, it started to require all submitted manuscripts be published as preprints. Abandoning the "accept" stamp is a logical next step, says *eLife*'s editor-in-chief, biologist Michael Eisen of the University of California, Berkeley.

Eisen, who co-founded the open-access Public Library of Science journals in 2003, says the detailed critiques written by reviewers that *eLife* recruits are its main contribution to the scientific process. The reviews, he says, are "more nuanced, more informative, and more useful to the community than our thumbs-up or thumbs-down publishing decision." He also argues that the new model will speed up a peer-review process that at other journals is often opaque and slow because it can involve multiple rounds.

Not everyone shares Eisen's vision. "I have zero interest in reading other people's peer reviews," tweeted Jason Pardo, a postdoctoral fellow at the Field Museum of Natural History. "Turning reviews into supplemental publications is silly." And the new model could struggle because in most fields, the majority of researchers do not post their manuscripts as preprints.

eLife's new approach, which takes full effect in January 2023, is not entirely original. The online platform F1000Research, for example, enables researchers to post manuscripts, which others can then review. Eisen hopes *eLife* will distinguish itself in this new marketplace by the quality of its critiques.

eLife is still finalizing details of its new model, including how editors will decide which papers to invite for review. They will likely ask prospective reviewers for their sense of which papers will be most "useful" to critique, Eisen says, perhaps because they present a valuable new method or, conversely, represent flawed science that requires correction. Like a handful of other journals, however, *eLife* will not consider the manuscript's perceived scientific importance, leaving that to readers to assess.

The publisher plans to enable authors to declare a reviewed manuscript the final "version of record." That will allow a key group of researchers—those funded by the National Institutes of Health—to meet NIH's requirement that their work be indexed by its PubMed search engine. Authors will also be able to submit an *eLife*-reviewed manuscript to a different journal for publication, but only if they and *eLife* have not declared it final.

Eisen says that, at $2000 per review, *eLife* should cover its costs without using the subsidies from donors that have backed the publisher since its founding. And he hopes the new policy will ultimately cause the publisher to fade into the background. "I would hope that we move pretty quickly to a world where … you won't be citing *eLife* at all, because you'll be citing the author's work" as it appears on a preprint server. ■

This girl at a Michigan county fair illustrates how children bond with their show pigs—and have close interactions with them that pose a flu risk.

PHOTO: MARK BUGNASKI/KALAMAZOO GAZETTE/AP PHOTO

FAIR WARNING

“Swientists” hunt for influenza virus at hog shows, hoping to cut off the next pandemic at the pen

By **Jon Cohen**, *in Des Moines, Iowa*

At 4:30 a.m. on 16 June, the last morning of the National Swine Registry’s Exposition, a weeklong hog show at the Iowa State Fairgrounds, Andrew Bowman and his team began winding through massive, open-air barns housing some 2000 pigs. Large fans blew across the pens to cool the pigs and ease the pungent ammonia stench of urine and feces. But Bowman, a swine veterinarian at Ohio State University (OSU), Columbus, and his group of nine vet students and research assistants were more interested in pig sounds than their smells.

“You hear the cougher?” asked Bowman, carrying a blue pail filled with supplies. “There’s somebody over in there that has the barking cough.”

When Bowman found the noisy culprit, he reached into his pail, opened a packet holding a fresh eight-ply gauze cloth, leaned over the rail of the pen, and wiped each nostril on the pig’s snout. As he likes to say, “I’m a professional pig nose picker.” He put the snot-filled rag into a test tube and sealed the cap.

Bowman and his team were hunting for a most unwelcome guest at the Exposition: influenza virus. Not all coughing pigs are infected, but Bowman’s work over the past decade has shown a “flu break” in even a few animals at a show like this can quickly spread the virus far and wide. As the best pigs fan out from the Exposition and other “jackpot shows" to competitions at the 2000 county and state fairs that take place across the United States through the early fall, they can carry flu with them. With about 150 million people visiting those events, the virus has plenty of opportunities to jump to humans, sickening people with flu outside its typical winter season.

Since 2010, the Centers for Disease Control and Prevention (CDC) has recorded nearly 500 human infections with those "variant viruses"—a term the pork industry prefers to the older, better known "swine flu." (Researchers say this surely undercounts the actual number because standard flu tests cannot detect an infection with a variant virus.) Most infections fizzle out without further person-to-person spread, possibly because humans have substantial immunity to similar flu viruses. But if a pig virus emerged that did spread readily in people, it could spark a pandemic. "It's about as real as any zoonotic threat," says Martha Nelson, an evolutionary biologist at the National Institutes of Health (NIH) who has collaborated with Bowman for 7 years.

It has happened before. Nelson, who works at NIH's National Center for Biotechnology Information and also studies highly lethal avian influenzas, was part of a team that found persuasive evidence that the 2009 flu pandemic, which infected hundreds of millions of people worldwide, began when a new flu virus jumped from commercial pigs on farms in central Mexico. Although many epidemiologists think viruses from birds touched off the 20th century's three influenza pandemics—including the infamous one that began in 1918 and killed about 50 million people—some argue pigs could have been a key intermediary between birds and humans in each one. "While people want to downplay it, I think the risk is much greater for swine-to-human influenza pandemics than it is for avian," says Gregory Gray, an epidemiologist at the University of Texas Medical Branch.

Fears about the next flu pandemic usually focus on Asia, where markets sell live poultry and exotic animals such as palm civets, raccoon dogs, and bamboo rats. "If we sit here and talk about the live-animal markets in China or East Asia, you say, 'Oh we'd never do that in the U.S.,'" Bowman notes. But U.S. hog shows, where handlers—often children—tend, groom, and even sleep with their charges pose a similar risk, he says. "I mean, is it really that different?"

Andrew Bowman (top) shows colleague Martha Nelson his pig snout swabbing prowess as they gather samples to test for flu at the Exposition, a show in Des Moines, Iowa.

To assess that risk, Bowman and his coworkers have become regulars at shows and fairs across the country. Winning the trust of sometimes-wary organizers and contestants, the researchers have visited about 1000 events and collected samples from some 40,000 pigs, analyzing them for clues to how novel flu viruses spread through the show circuit and shuttle between pigs and people. From their two dozen studies, "We've learned a lot about how swine influenza circulates in that particular niche," says virologist Richard Webby of St. Jude Children's Research Hospital.

Bowman and Nelson are also devising simple steps that could protect both pigs and people, including testing show entrants and limiting contact between swine and people. "Our goal is to try and figure out how we can make small tweaks in the whole system that will have outsized, downstream effects," Nelson says.

PIGS HAVE A SPECIAL PLACE in the ecology of influenza. Two types of influenza virus, A and B, sicken humans, killing up to 650,000 people worldwide in a bad year. Influenza B viruses only circulate in people, but type A can infect many species. Waterfowl harbor the most diversity, with 16 varieties of one surface protein, hemagglutinin, and nine of another, neuraminidase, leading researchers to conclude waterfowl are the main influenza A reservoir. The seasonal influenza A viruses that routinely infect humans today are restricted to variations of the H1N1 and H3N2 subtypes. But other type A viruses regularly spread to poultry, horses, dogs—and pigs.

As the virus circulates, it changes, constantly presenting new challenges to the immune system. One source of change is its highly mutable RNA genome, allowing "drifts" during each round of viral replication. But flu has another maneuver that speeds its own evolution. The viral RNA is broken into eight segments that can be swapped between related subtypes. So if one type A virus finds its way into a human cell already infected with another, their two genomes can mix when they replicate. This reassortment, or "shift," creates viral progeny with RNA segments from both strains.

Drift forces vaccine developers to roll out a new vaccine each year to combat the spread of seasonal flu. When shifted viruses emerge from an animal reservoir, the changes sometimes greatly enhance transmission and increase immune evasion—and can even spark a pandemic. "Flu is an acrobat," Nelson says. "You have to think in eight dimensions."

Pigs are a major venue for those acrobatics. When infecting pigs, avian viruses can reassort with viruses already in the swine that more readily infect people. The result can be a novel strain, foreign to the human immune system, that is more apt to spread in people than the original bird virus.

Just such a cascade of trouble began in 1979, when an avian H1N1 virus journeyed from wild ducks to pigs in Europe. Decades later, some of its genes were found in the H1N1 that triggered the 2009 pandemic after jumping from Mexican pigs to humans around March 2009.

Just 5 months after what was dubbed pH1N1 surfaced, nasal swabs of show pigs

PHOTO: J. COHEN/*SCIENCE*

Despite studying the evolution of influenza viruses from pigs and other animals for many years, Martha Nelson hadn't attended a pig show until this year.

at the Minnesota State Fair underscored the threat of cross-species transmission by showing 12% of the animals had the virus: This time, humans had infected the pigs. When then–Secretary of Agriculture Tom Vilsack reported the infection of pigs at the show, pork prices plummeted. "The industry was very angry at us," says Gray, who then was with the University of Florida and led the study. "We were just doing science, but it got political real fast."

The risk that a flu virus with pandemic potential finds its way to humans via pigs infected by birds remains as real as ever. But massive commercial farms raising hogs by the thousands may not be the biggest threat. On large farms in the United States and many other countries, biocontainment measures limit contact between people and pigs, says James Lowe, a swine vet at the University of Illinois, Urbana-Champaign, who studies influenza in commercial pig herds. Instead he worries about shows like the Exposition, where young handlers compete for belt buckles, banners, and ribbons for having raised the best-looking Duroc, Hampshire, Landrace, Berkshire, or crossbred hog. "The show pig population is the one that's got all this interaction with people." But it's a risk, he says, that "everybody kind of ignored."

IN 2009, BOWMAN WAS 2 years into his career as a practicing swine vet in Ohio, like his father before him. A professor from OSU, where Bowman went to vet school, contacted him, asking whether he'd consider coming back to do a Ph.D. focusing on testing show pigs at fairs for influenza. Bowman hesitated to return to academia, but the challenge enticed him. "We had no idea what was happening with flu and these pigs," he says.

Initially, his requests to take nasal swabs at pig shows were met with much suspicion. "The fear was that we would use the information and shut them down," Bowman says. Other people worried swabbing would somehow harm the pigs and lead judges to "show them the gate"—show lingo for being eliminated from the competition. "We've certainly had, 'My pig was going to win right up until you swabbed its nose,'" Bowman says. Early on, he did the sampling in the middle of the night to avoid confrontations.

But the scientific value of the work couldn't be disputed. In 2012, CDC documented 307 cases of humans infected with variant influenza strains, the highest number ever in a single year, with most connected to agricultural fairs. "Suddenly, I'm holding all of these samples from county fair pigs, and we've got all these kids breaking with swine lineage influenza at the same fairs we were at," Bowman says. "It was a case of me being at the right place at the right time."

Many human cases in 2012 were in Indiana, and the next year, organizers of

PHOTO: J. COHEN/*SCIENCE*

When pigs flu

The U.S. tradition of livestock shows allows influenza viruses to move between humans, commercial hogs, and show pigs in an annual cycle. Outside the normal human flu season, people may contract novel viral variants from show pigs. Those infections usually burn out. But each year a pandemic variant could emerge.

Winter
Flu moves from infected humans to commercial swine. Show pigs are born.

Spring
Viruses move between commercial pigs, which can mix viral genes from different subtypes. Infections jump to show pigs late in the season.

Summer
National and regional "jackpots" draw show pigs from many states; infected swine fan out to state and county fairs, where some people become infected.

Fall
Seasonal human infections begin, spreading virus to commercial pigs.

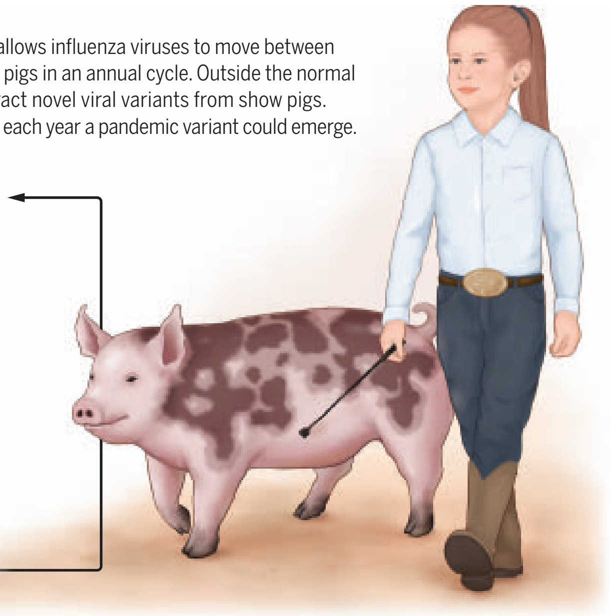

Showtime for viruses

In 2018, testing of pigs at 113 exhibitions in nine states found flu at all national "jackpot" shows that mixed pigs from several states. Relatively few pigs were infected, but they carried influenza virus to regional jackpot shows, as well as state and county fairs around the country. In any fairs it reached, the virus had a chance to spread widely because fairs typically last longer than other shows, and it sometimes jumped from pigs to people, causing at least 10 human cases in 2018.

Commercial pig
Farmers breed hogs for size and fat content; these are slaughtered at about 6 months. Larger farms have herds with thousands of hogs.

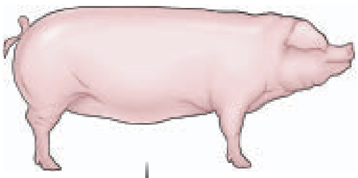

Transmission of flu viruses

Show pig
Bred to be lean and muscular, show pigs are mainly raised on small farms. They ideally show at about 6 months of age.

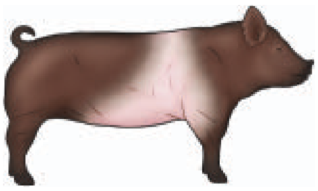

National/regional jackpot shows
All six shows tested had infected animals, with 12.9% of 594 pigs sampled being positive.

● Healthy pig ● Infected pig

County fairs (with infected pigs)
At the 42 fairs that had infections, 42.9% of the 1194 pigs tested carried flu viruses; another 56 fairs had no infections.

that state's fair asked Bowman to swab noses of incoming pigs to get a better understanding of how many were infected at the outset. The organizers also measured pigs' rectal temperatures, slowing entry to the fairgrounds and infuriating exhibitors, who wrongly blamed Bowman. Complaints reached the Indiana governor and the National Pork Board. Still, Bowman slowly convinced more and more fair organizers and exhibitors that there wasn't a great distance between their love of showing pigs and his studies, which aim to educate people and reduce disease in animals, handlers, and fairgoers. "They've been a blessing," says Kelly Morgan, a teacher in Columbus who organizes jackpot shows and, with her family, raises about three dozen show pigs.

Bowman is "a solid veterinarian, a solid scientist, and a pig guy, and so he's been able to bridge that gap," Lowe says. "What he's accomplished, building the relationships with that crowd that lets him get access to sites and do these data collections, is nothing short of a miracle."

BOWMAN AND NELSON FIRST SPOKE with each other at a 2015 meeting of an influenza research network organized by NIH's National Institute of Allergy and Infectious Diseases (NIAID). "In the first few minutes, we realized our interests fit like a glove," Nelson recalls. She had been studying the evolutionary origin of the variant viruses that caused the major human outbreak in fairs in 2012, but she only had samples from commercial swine. "I was salivating when I found someone actually sampling the show pigs themselves," she says.

Since then, Bowman's hands-on expertise with sampling pigs has combined with Nelson's hard-core focus on the evolutionary biology of the viruses they find. As Lowe puts it, "Martha can't do what Andy does, and Andy can't do what Martha does." The resulting studies of transmission between humans and pigs are "a whole other level," says Elodie Ghedin, who does genomic studies of parasites at NIAID. "These are really important studies to understand the dynamics and to see what is going on from year to year."

Bowman's and Nelson's first study, published in January 2016 in *The Journal of Infectious Diseases*, used ornate family trees that Nelson created from Bowman's virus samples to trace a four-season cycle of viral movement between pigs and people (see graphic, right). It starts in the winter, when seasonal flu viruses spread through the human population and occasionally infect pigs. On small farms, human-to-pig infections quickly burn out. But when humans infect commercial herds, which happens despite biocontainment efforts, the viruses move between the animals throughout the spring and reassort. They can then spread to show pigs that live in separate barns on the same property or even, through the wind, to neighboring farms. By summertime, when show pigs congregate at exhibitions, flu season for humans is over. But the pigs readily infect one another, leading to new reassortment viruses and occasional infections of humans with variant influenza viruses.

"If there were no commercial swine, there'd be no flu viruses in show pigs," Nelson says. Bowman's vast sequence library also allowed them to see that jumps

CREDITS: (GRAPHIC) A. MASTIN/*SCIENCE*; (DATA) M. I. NELSON *ET AL.*, *J. VIROL.* **90** 23 (2014) 10.1128/JVI.01457-16; M. I. NELSON *ET AL.*, *J. VIROL.* **94** 24 (2020) 10.1128/JVI.01453-20

from commercial to show swine likely occur many times each year. “There was a surprising amount of genetic diversity of flu viruses in show pigs, given that they’re such a small population and only convene in large numbers for a short summer show season,” Nelson says.

At the same time, as Nelson and Bowman reported in December 2016 in the *Journal of Virology*, animals at shows in counties and states distant from one another sometimes had identical viruses. “This was the head-scratching moment when we realized there must be something else helping to spread these viruses so quickly over long distances between fairs,” Nelson says.

Jackpot shows like the Exposition are key to dispersing those viruses, Nelson and Bowman realized. Hogs at a county fair must come from that county, and the same geographic restriction applies at state fairs. But jackpot shows draw contestants from far and wide. To understand how they affect viral traffic, the researchers went to an early-season show in Iowa that hosted exhibitors from 17 states. (They won’t name the show to avoid shaming it.) Four distinct influenza viruses spread at that show, one of which accounted for 80% of pig infections. When pigs from the show dispersed to their home states, they carried the virus with them. Through later sampling, researchers found influenza in hogs at 38 county and state fairs, and 94% had the variant dominant at the jackpot show. That variant was also responsible for 90% of that year’s show-linked flu cases in people.

The fairs, not the jackpot shows, are where the pig variants are most likely to jump to humans. Although the Bowman team’s sampling over the years has detected influenza in only about 30% of the fairs, compared with 80% of the jackpot shows, fairs often last longer. So fairs that start with infected pigs wind up with as many as 80% of hogs infected by the end, a far higher prevalence than at jackpot shows. And fairs have far more humans interacting with pigs, increasing the risk of zoonotic jumps. “You see the human cases show up usually in association with the end of the fair because if you’ve got 250 pigs shedding the virus, it’s going be just a cloud of flu virus in there,” Bowman says.

TO REDUCE THE RISK to people, say Bowman, Nelson, and others, regular testing of exhibition hogs, which make up a mere 1.5% of the U.S. swine herd, should be standard practice. But no such “active surveillance” program exists. Instead, the United States has a passive system that relies on farms to sample sick pigs and then voluntarily report what they find to the Department of Agriculture.

Bowman has already persuaded several pig show organizers to stop children from sleeping near their animals. At one show, kids hung hammocks over their prized pigs. “I’m like, *guys*,” Bowman says. The hammocks are gone now, as are pen cots—at least at shows his crew attends. “This is moving the needle,” Nelson says.

In the vendor hall at this year’s Exposition, Bowman’s team set up a station to educate kids directly about reducing the spread of influenza. The project, started 7 years ago by his collaborator Jacqueline Nolting—who has a Ph.D. in agricultural education—encourages the kids to join the OSU “swientist” program, offering free popsicles and stickers featuring a pig in a lab coat. A “pathogen shootout” has the kids kill influenza with squirt guns, knocking plastic viruses off pedestals. And they can pick up biosecurity buckets that hold soap, a scrub brush, disinfectant, gloves, and other essentials. “I’m not going to convince the parents to do things differently, but I think I can get the kid,” Bowman says. “So it’s really the long game. In a decade, I think I can change some behaviors.”


Ohio State University’s “swientist” program recruits children into their studies, educating them about measures to reduce flu virus transmission.

PHOTO: J. COHEN/*SCIENCE*

Bowman’s team also enrolls people between 5 and 21 years old in a long-term study to track any flu infections they pick up, which requires an immediate blood sample. (Bandages that look like bacon strips are on offer.) “I’m interested in seeing what they find in my blood,” says new recruit Sam Fox, 18, who lives in Indiana and has shown hogs most of his childhood. “I’d bet there are only a handful of weeks I haven’t been around hogs in the last 8 years.”

Morgan says the education program has helped calm initial concerns about their pig sampling. “Andy and Jacqueline are not there to do anything but better the health of the swine and kids,” says Morgan, whose son showed pigs and took part in the swientist program.

More ambitious ideas from Bowman and Nelson include requiring that all animals receive a flu vaccine, which, if matched to variants in circulation, could reduce transmissions. The researchers have even proposed that hogs attending national or regional jackpot shows not show again for 2 weeks: Hitting the pause button would allow enough time for any virus in infected pigs to burn out before they have a chance to spread it. But Bowman says the idea has had zero traction, in part because people who have winning pigs at jackpots understandably want to exhibit over the next few weeks at state and county fairs. “It’s hard,” he says. “We are making changes and it is pandemic prevention. But how do you even quantify the impact of those changes?”

Bowman says for now, the most urgent need is to gather enough data to properly assess the risks of this cherished U.S. tradition. “Is it going to be this show that kicks off something?” he asks about the Exposition held in June. “I don’t know, because we’ve had our thumb on the pulse of this one for quite a while. But what else is out there?” ■

This story was supported by a grant from the NIHCM Foundation.

INSIGHTS

POLICY FORUM

PHOTO: SETH WENIG/AP PHOTO

CLIMATE CHANGE

Mandatory disclosure is key to address climate risks

Financial regulations would help signal risks to investors

By **Stefano Carattini**[1], **Edgar Hertwich**[2], **Givi Melkadze**[1], **Jeffrey G. Shrader**[3]

Investors have known about climate change for decades. Yet it is only recently that several countries—including France, Japan, New Zealand, and the United Kingdom—have developed policies requiring large public companies to regularly disclose information about climate-related financial risks. In March 2022, the US Securities and Exchange Commission (SEC) proposed a climate disclosure rule that, distinctively, would affect all firms publicly traded in the United States regardless of their size or country of incorporation. With the policy's broad scope, the large size and exceptional liquidity of the US financial market, and the SEC's influence on securities regulations worldwide, this presents a major opportunity to standardize the way that public firms measure, report, and address climate risks. As the SEC digests a substantial number of public comments on their draft rule ahead of a planned October release of the final rule, we discuss their rationale and consider implications and opportunities for research and policy.

Not until the financial sector can access and respond to signals about climate risks can we hope to move the economy on a more sustainable and stable trajectory. In 2015, the then governor of the Bank of England, Mark Carney, highlighted three major climate-related risks to the financial system: physical risks, transition risks, and liability risks (*1*). The taxonomy introduced by Carney has been the reference for the scientific community, including the Intergovernmental Panel on Climate Change (*2*), and financial regulators (*3*). Physical risks are the risks that arise from damage to physical assets resulting from sea level rise or more extreme weather events, including droughts and storms, or other consequences of climate change. Liability risks are the risks to companies and insurers from litigation for compensatory damages by parties that suffer damage because of climate change.

At present, transition risks are the main focus of both the academic literature and the policy debate, including the proposal by the SEC as well as related efforts by the Office of the Comptroller of the Currency (OCC) and the Federal Deposit Insurance Corporation (FDIC). Transition risks are the risks to the value of existing assets from a transition away from fossil fuels. This describes the potential for climate policy, technological change, or investor and consumer preferences to sharply reduce future revenue streams of current assets. Transition risks highlight the tension between the need to decarbonize as fast as possible to meet climate goals, rather than gradually, and the potential financially damaging consequences that abrupt climate policy tightening may have. Given that the carbon contained in existing fossil fuel reserves exceeds the amount that can be burned before breaching the target of the Paris Agreement, scientists have described part of these reserves and the associated production, transport, and refining infrastructure as "stranded assets" (*4*). Hence, either humanity will emit more than the "carbon budget" allows and face more severe

---

[1]Department of Economics, Andrew Young School of Policy Studies, Georgia State University, Atlanta, GA, USA. [2]Department of Energy and Process Engineering, Faculty of Engineering, Norwegian University of Science and Technology, Trondheim, Norway. [3]School of International and Public Affairs, Columbia University, New York, NY, USA. Email: scarattini@gsu.edu

Companies whose shares are traded in the United States, such as at the New York Stock Exchange, may be required to disclose climate-related financial risks.

climate damages or a substantial portion of such reserves would have to remain in the ground ("stranded"), essentially losing their entire value.

As of now, public firms in the United States insufficiently report climate-related financial risks to the public. The current regulations from 2010 allow for some ambiguity on what risks are "material," a term that refers to the extent to which they may potentially compromise an investor's return, or what risks have "systemic implications," which means that they may affect the stability of the entire financial system (*5*).

Companies that do not disclose climate risks when material may be akin to misleading investors, calling for policy intervention. Further, widespread losses in stock valuations due to emissions externalities being finally internalized may represent a risk for the entire financial system, if the latter is substantially exposed to the assets being stranded and the reassessment happens abruptly. About 50% of the standard portfolio of an average European financial institution is exposed to transition risks, once one considers not only fossil fuel companies but also carbon-intensive sectors such as agriculture, aluminum, or steel as at-risk. Feedback effects within the banking system that occur because financial institutions own shares of, and lend to, other financial institutions can further increase systemic risk (*6, 7*). As we learned with the Great Recession, the realization of systemic risk can lead to a painful recession and high unemployment levels.

KEY RATIONALES

The SEC's proposal would require new climate disclosure from all firms publicly traded in the United States, both US-based companies and international companies that trade in the United States, to gain access to more-liquid and better-protected markets. In their periodic financial statements, firms would need to disclose current emissions, emissions targets, and plans to achieve them, as well as assessments of climate-related risks under transparent scenarios and corresponding management strategies, including internal carbon prices, whereby firms prepare for the implementation of ambitious nationwide climate policy by already accounting for a higher cost of carbon in their operations. Reported emissions should include scopes 1 and 2 and, starting from large firms in 2025, scope 3. Scope 1 refers to emissions that occur directly within the company; scope 2 refers to indirect emissions from acquired electricity, steam, heat, or cooling; and scope 3 refers to emissions associated with the value chain, including suppliers, workers' commutes, and customers' use of the product. To address concerns about potential "greenwashing" in the presence of information asymmetries, disclosures may be audited.

The key rationale for mandating the disclosure of climate risks is threefold. First, the proposal by the SEC would standardize the reporting of transition risks, addressing the issue of selection into reporting and nonreporting as well as into how much to report. These two aspects are intrinsically intertwined. If companies are free to report only if they want, and what they want, as is the case with voluntary disclosure, the danger is that only a subset of companies will do so and in a very selected fashion, possibly providing a misleading picture of their risk exposure (*8*). Addressing this selection issue ensures that material risks are properly disclosed so that investors and lenders can make informed decisions, including financial institutions with systemic roles.

Second, over the past few years, many central banks and financial regulators have started engaging in so-called "climate stress tests." Stress tests of financial institutions were initially introduced in the 1990s, with the Basel Capital Accord requiring banks to provide an internal assessment of their ability to sustain an important, negative market event. In practice, they consist of scenario analyses aimed at predicting how a bank's capital would be affected under hypothetical adverse macroeconomic conditions and use financial valuation models plus statistics on asset performance during similar historical periods. After the Great Recession, financial regulators started running stress tests themselves to prevent future financial crises, assessing the exposure of the financial institutions under their control to potential large market shocks. Only more recently have regulators started considering climate policy as a market event that is potentially able to trigger a financial crisis.

More than 100 central banks and financial supervisors make up the Network for Greening the Financial System, whose goal is to provide recommendations related to climate change to central banks, including on climate stress tests. To date, several institutions such as the Bank of France, the Bank of England, the European Central Bank, and the Dutch Central Bank have already completed their first round of climate stress testing. The Board of Governors of the US Federal Reserve Bank also recently announced that they will conduct a pilot of climate scenario analysis—a potential prelude to future, more systematic climate stress testing. The more information the regulator has about risk exposure, the more accurate a stress test can be, hence the need for mandated disclosure to compel companies to provide sufficient information so that regulators can reliably assess systemic risks from climate change.

Third, climate stress tests can highlight the potential for systemic risk, but "macroprudential" policy, aimed at mitigating risk to the financial system as a whole, might be necessary to address it, unless one can count on financial institutions to do so themselves. A common tool is minimum capital requirements. To ensure financial sector stability, banks are asked to provide sufficient equity in proportion to size and riskiness of the bank's assets. However, current regulatory frameworks do not directly consider climate-related risks when setting capital requirements. Thus, one policy that would be effective in tackling transition risk is to set differentiated capital requirements depending on a bank's exposure to climate risks. In essence, this policy would ask financial institutions that are largely exposed to transition risks to keep additional capital as a buffer (*9*).

Such differentiated capital requirements have been considered by financial regulators in several countries but have not yet been implemented. To do so, financial regulators would need to know how exposed financial institutions are to transition risks. Once more, mandatory disclosure would be crucial. It is important to keep in mind that addressing systemic risk is part of the financial regulators' mandate. Macroprudential policy would be used to prevent systemic risk and pave the way for ambitious climate policy, which is highly necessary. It would also protect the economy from the impact that disruptive technologies or behavioral changes could have, shifting demand away from fossil fuels. Although gradual changes may give financial institutions some time to adapt, both technological and behavioral changes can take place in unexpected ways.

GLOBAL LANDSCAPE

Mandatory disclosure already exists in some contexts. Large carbon emitters, for instance, may need to report their emissions to environmental regulators. For example, in the United States, some 8000 high-emitting facilities have reported since 2011 to the Environmental Protection Agency under the Greenhouse Gas Reporting Program. The stated goal of the program is to allow firms and the public to track and compare emissions and identify opportunities to reduce them.

Most of the climate-related financial risk disclosure policies and proposals emerging around the globe follow recommendations from the Task Force on Climate-related Financial Disclosures (TCFD) (*10*), an initiative by G20 countries with the goal of monitoring the global financial system. Additional standards were proposed this year by the International Sustainability Standards Board (ISSB) to foster consistent disclosure (*11*). The United States does not have a policy requiring public firms to homogeneously report their emissions for reasons related to transition risk, hence the proposal by the SEC.

With its proposal, the SEC would have the United States join other pioneers of mandatory disclosure, bringing its policy into close alignment with the latest international guidelines and standards, while also pushing ahead on issues, including scope 3 emissions reporting and coverage of regulated firms regardless of size and location. Given the large US market and the influence of the SEC, this effort would likely have considerable global influence, helping to bring greater consistency to how mandatory disclosure takes place. The insufficient, incomplete, and inconsistent information about climate risks is indeed largely a global issue, as are financial markets (*12*). Further, the proposal by the SEC would complement efforts by other regulators that are targeted, in particular, at large banks. These include the Federal Reserve as well as the OCC and the FDIC, whose draft proposals aim at providing general principles to manage banks' climate risks (*13*), after the recent release of similar principles by the Basel Committee on Banking Supervision, the main global standard setter for the prudential regulation of banks. Hence, the SEC's proposal could be part of a distinctively comprehensive approach that includes climate-stress tests and internal tests by banks, which both benefit from the SEC's driven disclosure efforts.

IMPLICATIONS FOR POLICY AND RESEARCH

Several avenues for future research are paramount in this context, including in response to issues raised during the comment period, which led to a total of more than 14,000 comments—far more than are received for a typical SEC rule. The vast majority of comments seemed supportive. Almost all highlighted several areas where future research is urgently needed.

First, industrial ecologists are called into action. Scope 3 reporting requirements received substantial attention and pushback during the public comment period. Many commenters highlighted the critical importance of disclosing scope 3 emissions, because outsourcing can substantially reduce scope 1 and 2 emissions without a material change in emissions or risks. For fossil fuel producers, much of transition risk is associated with scope 3 emissions. However, scope 3 reporting, including the Greenhouse Gas Protocol, was developed to measure potential responsibility for emissions (backward looking) rather than risk exposure (forward looking). Mandated release of scope 1 and 2 emissions data can improve the modeling of scope 3 emissions. The experience with environmental product declarations and organizational environmental footprints shows that comparable quantifications require industry-specific calculation rules. These efforts provide templates that can be further adapted for the purpose of financial risk modeling to focus on emissions that actually drive material risk. Inputs with carbon-intensive substitutes or those instrumental for decarbonization, such as clean electricity or battery materials, may be exposed to sudden price rises when transition becomes a priority. Input-output models can be used to screen supply chain risk exposure and flag inputs with material emissions. Scenario-based and consequential life cycle assessment can inform climate risk scenarios. These initiatives and sectorial specificities can facilitate the reporting effort not only for regulated but also for unregulated firms when the latter engage in reporting as well. Firms outside the SEC's jurisdiction also provided comments on the proposal.

Second, many comments emphasized the need to quickly improve our understanding of company-specific physical risks. Economists have the task of improving downscaled climate damage models that are appropriate for use by companies that link firm-level data to climate exposure. Economists can also draw out the implications of transition risks, including understanding the effects of timing of regulation and changes in market beliefs, by adapting macro–finance models that include realistic financial market frictions and rely on data that precisely point to risk exposure to measure its heterogeneity across banks. Loan data, for instance, could specify the "greenness" of the investment for which a firm is borrowing. Models could also feature information asymmetries, so to explicitly account for degrees of disclosure. This research should build on a growing literature in climate finance, which should also expand to better measure the extent to which investors may be willing to align with long-term climate goals and how they may react to climate policy uncertainty.

Third, researchers that engage in policy evaluation should start assessing the policies that are already in place to address comments raised about compliance costs and policy effectiveness. Research can leverage arbitrary company size thresholds and exemptions for causal purposes to better understand the gains from mandatory versus voluntary disclosure and assess the impact on actual disclosure, carbon emissions, stock market reactions, firms' investments, and potential attempts to avoid regulation by going private or being listed on unregulated markets. Disclosure requirements may also have beneficial cross-country spillovers, leading unregulated firms to disclose if multinational firms do. Rating agencies may also respond, improving the methodologies used to rank firms in terms of environmental, social, and governance criteria, which would allay criticisms of potential greenwashing. Further, mandatory disclosure may also increase market liquidity and efficiency and lead to lower capital costs to firms by addressing information asymmetries, potentially paving the way for more disclosure in search of its optimal level (*14*).

Fourth, economic and managerial sciences can improve our understanding of how investors and firms can reduce carbon footprints. For instance, although internal carbon pricing has expanded rapidly over the past few years, little is known about its medium-term impact on energy decisions in the many large companies that use it. Finally, there is growing interest in disclosure policies that account for broader sustainability issues, including biodiversity losses (*15*). Policy-making in this area can also build on research developments in effective measurement and disclosure metrics as well as on the interaction of biodiversity and climate risks. ■

REFERENCES AND NOTES

1. M. Carney, "Breaking the tragedy of the horizon—climate change and financial stability," speech given at Lloyd's of London, 29 September 2015.
2. Intergovernmental Panel on Climate Change (IPCC), "Climate change 2022: Mitigation of climate change" (IPCC, 2022).
3. P. Bolton, M. Despres, L. A. Pereira da Silva, F. Samama, R. Svartzman, "The green swan: Central banking and financial stability in the age of climate change" (Bank for International Settlements, 2020).
4. C. McGlade, P. Ekins, *Nature* **517**, 187 (2015).
5. Climate-Related Market Risk Subcommittee, "Managing climate risk in the U.S. financial system" (Market Risk Advisory Committee, 2020).
6. S. Battiston, A. Mandel, I. Monasterolo, F. Schütze, G. Visentin, *Nat. Clim. Chang*. **7**, 283 (2017).
7. S. Alogoskoufis *et al*., "ECB economy-wide climate stress test: Methodology and results" (ECB Occasional Paper No. 281, European Central Bank, 2021).
8. E.-H. Kim, T. P. Lyon, *J. Environ. Econ. Manage*. **61**, 311 (2011).
9. B. Annicchiarico, S. Carattini, C. Fischer, G. Heutel, *Environ. Energy Policy Econ*. **3**, 221 (2022).
10. Task Force on Climate-related Financial Disclosures (TCFD), "Task Force on Climate-related Financial Disclosures: 2021 status report" (TCFD, 2021).
11. International Sustainability Standards Board (ISSB), "Exposure draft: IFRS S2 climate-related disclosures" (ISSB, 2022).
12. European Systemic Risk Board (ESRB), "Positively green: Measuring climate change risks to financial stability" (ESRB, 2020).
13. A. Perrault, G. Giraud, *Science* **377**, 1021 (2022).
14. I. Goldstein, L. Yang, *Annu. Rev. Financ. Econ*. **9**, 101 (2017).
15. ISSB, "Exposure draft: IFRS S1 general requirements for disclosure of sustainability-related financial information" (ISSB, 2022).

10.1126/science.add0206

PERSPECTIVES

EVOLUTION

Bursts in skull evolution weakened with time

The skull shapes of mammals diversified more rapidly early in their history

By **Sharlene E. Santana**[1,2] *and*
David M. Grossnickle[1]

Evolutionary biologists generally agree that placental mammals began as small-sized animals that ate insects, and later evolved to become more varied in size and morphology. Today, the morphologies of placental mammals are incredibly diverse, ranging from the bumblebee bat to the blue whale (*1*–*3*). There is considerable debate over how the small, insect-eating ancestors of placental mammals gave rise to such incredibly divergent lineages. Among the competing hypotheses are varying opinions on the timing and pace of early placental mammal evolution, especially in the context of major environmental changes such as the Cretaceous-Paleogene (K-Pg) mass extinction event 66 million years ago and the Paleocene-Eocene Thermal Maximum (PETM) 56 million years ago. On page 377 of this issue, Goswami *et al.* (*4*) contribute to this discussion by reconstructing the patterns and possible drivers of placental mammal morphological diversification with a quantitative analysis of skull shape spanning over 70 million years of evolution.

Different traits tell different evolutionary stories about how mammals diversified (*3*). The skull is an informative structure for studying mammal evolution because of the multiple functions it serves that are critical to survival, such as feeding, protecting the brain, and supporting various sensory organs. For example, the shape of the skull can reflect dietary adaptations (consider the long snouts of anteaters) and thus inform how skull shape evolved across lineages with different diets. Despite these advantages, whole skulls are rarely used to study diversification in mammal evolution. This is partly because of their exceptional variation, which ranges from the elongated skulls in dolphins to the round skulls in primates, making direct and quantitative comparison difficult (*5*). In addition, well-preserved skull fossils are rare for extinct mammal species, which makes them less ideal for comprehensive studies.

Goswami *et al.* used geometric morphometrics, a method based on the placement of marks on specific anatomical features, and a library of hundreds of three-dimensional models of skulls to quantify and compare the skull shape of placental mammals (see the figure). To account for uncertainties in the evolutionary relationships among extinct placental mammal lineages, the authors also simulated the evolution of skull shape across nearly 2000 evolutionary trees relating the 322 mammal species analyzed in the study.

Tracking mammalian evolution with skulls

Placental mammal skulls can be compared to examine rates and patterns of anatomical diversification over evolutionary time.

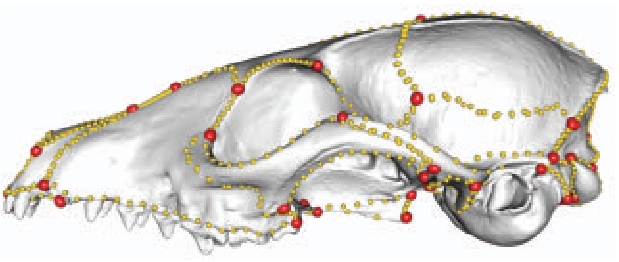

The skulls are digitally mapped in three dimensions and analyzed by using markers (shown here in red and gold) that track the shape of various anatomical features.

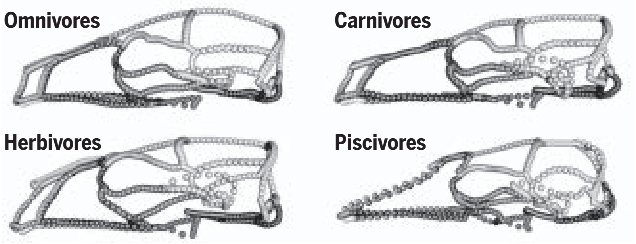

Because mammalian skull shape is influenced by many important functions, such as dietary preference, the analysis of skull shapes is informative for examining the environmental changes that could have affected the evolution of diverse mammalian lineages.

GRAPHIC: BASED ON GOSWAMI *ET AL.* (4)

Without the possibility of directly studying the behavior and physiology of extinct species, evolutionary biologists often use the geologic timing and pace of anatomical changes to identify major factors or events that influenced the diversification of a lineage. According to their data, Goswami *et al.* find that the ancestors of major placental mammal lineages likely had nonspecialized skull shapes and habits until shortly before or after the K-Pg mass extinction, when their skull shapes changed and diversified at a fast rate. After this initial phase of rapid change, skull shape evolved much more slowly within most lineages, albeit with occasional smaller bursts in evolution potentially related to climate changes, such as during the PETM, when the global temperature increased considerably in a relatively short amount of time. Their results are consistent with previous hypotheses that placental mammals began to ecologically diversify shortly before or at the K-Pg boundary, taking advantage of ecological opportunities in the wake of the mass extinction event (*3*). Goswami *et al.* also found that placental mammals that are aquatic, herbivorous, precocial, or social showed the fastest evolutionary rates. For example, skull shape evolved quickly for whales and dolphins as they adapted to a fully aquatic lifestyle.

The authors overcame many of the challenges faced by other similar studies. For instance, discrepancies in the patterns recovered from fossil versus molecular data are a common point of controversy in studies of early mammal evolution (*6*). They solved this problem by sampling both fossil and modern placental mammals to provide a comprehensive dataset. Many studies on the diversification of early mammals also tend to rely on single traits, such as body size or a specific ecological trait (e.g., nocturnal versus diurnal behavior). By exam-

---

[1]Department of Biology, University of Washington, Seattle, WA, USA. [2]Burke Museum of Natural History and Culture, University of Washington, Seattle, WA, USA.
Email: ssantana@uw.edu

ining the skull shape, which encompasses many anatomical traits, the study simultaneously examined a multitude of ecological and functional drivers of diversification. The breadth of the sample size analyzed by Goswami *et al.* is also impressive, containing species across all of Placentalia, rather than more restricted taxonomic groups, as is often the case for most studies of mammalian morphological evolution.

Despite the many insights provided by their extensive data and analyses, Goswami *et al.* cannot quantifiably verify if placental mammals experienced a diversification burst in the immediate wake of the K-Pg mass extinction. Similar to other studies (*7*), the authors are uncertain about the exact timing of placental mammal origins. When basing their analysis on evolutionary trees with relatively early origins of placental mammals (about 100 to 80 million years ago), the authors find evidence of rapid diversification before the K-Pg boundary. This could be interpreted as a refutation of the assumption that these mammals diversified rapidly after the K-Pg boundary and supports an earlier estimated date for when they first diversified (*3*). However, analyses using evolutionary trees with a more recent divergence time (about 80 to 70 million years ago) produce a pattern of rapid diversification at or immediately after the K-Pg boundary. The contradictory conclusions because of the different assumed timing of placental mammal origins highlight the need for a better understanding of early mammal evolution.

Elucidating how, when, and why mammals diversified will continue to require integrative and multidisciplinary approaches. Goswami *et al.* advance the understanding of placental mammal diversification and set a foundation for future work to examine the lineages of other modern and extinct groups and the evolution of other anatomical systems. In the context of pronounced ecological changes, including those induced by humans in recent history, the fossil record can provide clues about the functional mechanisms that could facilitate or constrain the evolution of animals. ■

REFERENCES AND NOTES

1. M. A. O'Leary *et al.*, *Science* **339**, 662 (2013).
2. J. Wu, T. Yonezawa, H. Kishino, *Curr. Biol.* **27**, 3025 (2017).
3. D. M. Grossnickle, S. M. Smith, G. P. Wilson, *Trends Ecol. Evol.* **11**, 1 (2019).
4. A. Goswami *et al.*, *Science* **378**, 377 (2022).
5. A. Goswami *et al.*, *Integr. Comp. Biol.* **59**, 669 (2019).
6. N. S. Upham, J. A. Esselstyn, W. Jetz, *Curr. Biol.* **31**, 4195 (2021).
7. N. S. Upham, J. A. Esselstyn, W. Jetz, *PLOS Biol.* **17**, e3000494 (2019).

10.1126/science.add8460

GENETICS

Stealing genes and facing consequences

The human genome contains a domesticated viral envelope gene with antiviral activity

By **Ricky Padilla Del Valle** and **Richard N. McLaughlin Jr.**

Sequencing the human genome delivered the surprising finding that endogenous retroviruses (ERVs) and other genomic parasites dominate the genetic code. Perhaps more surprising was the discovery that this "junk" DNA does not merely contain the scars from millions of years of (ongoing) coevolution of genomes and transposable elements. Instead, the human genome contains numerous genes and regulatory sequences that were once part of replicating transposable elements, particularly ERVs, but have been "domesticated" by the host genome—once viral, now human (*1, 2*). Less is known about the cost of using part of a virus's genome to execute critical organismal functions. On page 422 of this issue, Frank *et al.* (*3*) uncover hundreds of transcribed retroviral envelope genes that are primed for co-option. They demonstrate that a domesticated envelope gene called *Suppressyn* restricts viral infections when expressed in trophoblasts of the human placenta, a tissue where another domesticated envelope gene promotes the fusion of cells required for placental function.

> **"…domestication will happen, but… it comes with trade-offs that impose additional constraints in the future."**

Transposable elements are DNA sequences that encode all the information they need to replicate themselves within the environment of their host's genome. One class of transposable elements, the ERVs, come from retroviruses that infected germline cells and became "trapped" within the host's genome. These genome-bound parasites encode a few proteins but must steal cellular resources to complete their replication within the germline and their passage to the offspring of their host. Replicating ERVs impose a burden on the host genome because they can be potent mutagens. However, these parasites bring both challenges and opportunities. ERV replication creates abundant new DNA sequences—a pool of raw materials that could, by chance, benefit the afflicted host. Indeed, domestications of these sequences have contributed to fundamental aspects of organismal biology. For example, V(D)J recombination of immunoglobulin genes in jawed vertebrates is carried out by recombination-activating gene 1 (RAG1) and RAG2, which were domesticated from a RAG-like transposon (*4*). Additionally, the coordinated expression of immune genes in primates uses interferon-responsive enhancers that were domesticated from the MER41 family of ERVs (*5*). Even programmed genome rearrangement in ciliates requires transposase genes that are domesticated from piggyBac transposons (*6*).

In a key innovation within mammals, domestication of a viral envelope gene over 100 million years ago created the *Syncytin* gene, which became an essential part of the emergence of the placenta (*7, 8*). The first *Syncytin* gene was likely domesticated in the last common ancestor of placental mammals from an ERV that used the encoded envelope protein for fusion and entry into host cells. Now co-opted, this fusogenic activity mediates the formation of the multinucleate syncytium of the placenta (the syncytiotrophoblast), an essential barrier that enables transfer of nutrients from maternal blood to fetal blood while preventing passage of viruses to the fetus (*7, 8*). This evolutionary innovation may have been key to the emergence, diversification, and success of placental mammals. However, domestication of tools created by viral pathogens comes with an unavoidable cost.

The study of Frank *et al.* tackles the consequences of this co-option. The alanine, serine, cysteine-preferring transporter 2 (ASCT2) receptor, which binds primate Syncytin-1, must be expressed by trophoblasts to allow cellular fusion and formation of the syncytiotrophoblast. However, viruses that use Syncytin-1–like envelope genes can still recognize and bind ASCT2. Thus, Syncytin-1–mediated cell

---

Pacific Northwest Research Institute, Seattle, WA, USA. Email: rmclaughlin@pnri.org

Domestication of endogenous retrovirus genes

The placental syncytiotrophoblast is an important barrier between maternal and fetal blood that is formed by cell-cell fusion. The fusogenic property of trophoblasts derives from domestication of ERV genes, but this came at a cost that prompted further selection for ERV gene domestication.

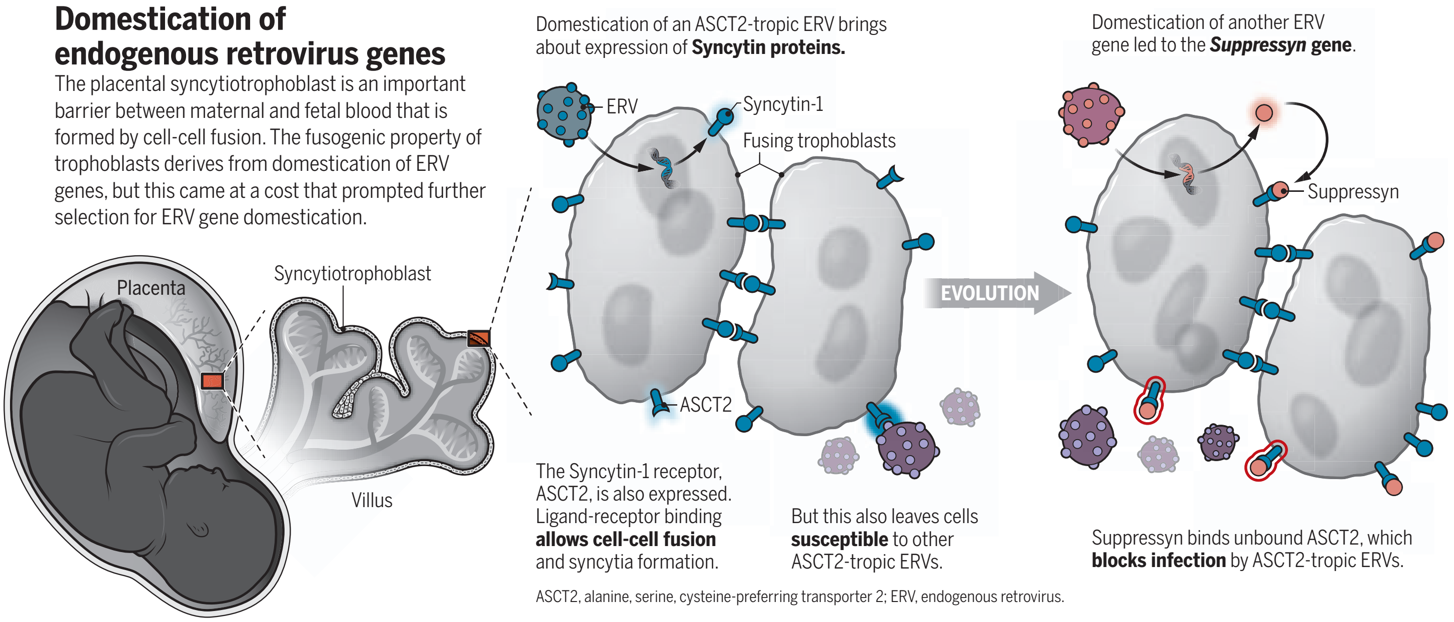

Domestication of an ASCT2-tropic ERV brings about expression of **Syncytin proteins.**

The Syncytin-1 receptor, ASCT2, is also expressed. Ligand-receptor binding **allows cell-cell fusion** and syncytia formation.

But this also leaves cells **susceptible** to other ASCT2-tropic ERVs.

Domestication of another ERV gene led to the ***Suppressyn* gene**.

Suppressyn binds unbound ASCT2, which **blocks infection** by ASCT2-tropic ERVs.

ASCT2, alanine, serine, cysteine-preferring transporter 2; ERV, endogenous retrovirus.

GRAPHIC: V. ALTOUNIAN/*SCIENCE*

fusion creates an inescapable vulnerability of the cells of the placental syncytiotrophoblast to ASCT2-tropic viruses, such as simian retrovirus and other RDR (RD114/simian type D) retroviruses. These viruses have diverse evolutionary origins but are united by their homologous ASCT2-binding envelope genes.

In several nonhuman mammalian species, domesticated viral envelope genes restrict virus binding and entry by occupying host proteins that act as viral receptors (*9*). This precedent suggested that a protein occupying ASCT2 could similarly block virus entry by interfering with envelope proteins expressed by RDR retroviruses. Frank *et al.* computationally screened the human genome to identify over 1500 open reading frames (ORFs, which are stretches of DNA sequence bound by a start and stop codon) that could encode viral envelope proteins—far more than previously appreciated. Surprisingly, many of these putative virus-derived envelope genes exhibit tissue-specific transcription. One ORF from their screen is a domesticated retroviral envelope gene called *Suppressyn*. The encoded protein lacks a transmembrane domain and regulates the fusion activity of Syncytin-1 in syncytiotrophoblasts by occupying the ASCT2 receptor (*10*). Frank *et al.* show that *Suppressyn* is expressed throughout human embryonic development, in contrast to many embryonic genes that are transcribed in specific windows of development. This regulation suggests that Syncytin-1 plays a vital role in a cellular function that is distinct from development per se but essential in developing embryos—antiviral defense.

Subsequent experiments in a human trophoblast cell line suggest that Suppressyn is a restriction factor that is required for complete resistance to infection by RD114 retroviruses and that resistance is specific to viruses with RDR envelopes. Seeking to place the origins of this antiviral activity, Frank *et al.* show that Suppressyn antiviral activity was likely born over 60 million years ago in the common ancestor of hominoids and Old World monkeys. Overall, this work demonstrates an endogenously expressed viral envelope gene that restricts viral replication in humans (see the figure).

The study of Frank *et al.* exposes the random and sometimes limited nature of natural selection in the complex interaction of genomes with viruses and transposable elements. Inevitably, domestication will happen, but (like most things in life) it comes with trade-offs that impose additional constraints in the future. These new pressures may select for even more layers of genomic complexity. Domesticating Syncytin to allow syncytiotrophoblast formation locks the need for expression of its receptor by trophoblasts and creates a susceptibility to viruses that use ASCT2 to infect cells. The consequences of this ratchet trap of obligatory expression of ASCT2 could be dealt with by adding more components to the system. For example, throughout mammalian evolution, new viral envelope genes have been domesticated numerous times to duplicate or even replace a genome's fusogenic *Syncytin*-like genes (*11*). In some cases, the new Syncytin uses a new receptor, perhaps gaining resistance to viruses that bind the older Syncytin's receptor (*12*). The data from this study suggest that mammals have also employed a revolving door of Suppressyn-like envelope proteins to block viruses from binding to ASCT2, expanding the list of ways mammalian genomes deal with the consequences of using stolen viral genes to carry out essential developmental functions.

Almost all mammals retain at least one copy of *Syncytin* (*11*, *13*). Therefore, most mammalian genomes would be predicted to encode inhibitors of viruses that use ASCT2 for cell entry; these antiviral genes could be hidden among the slew of domesticated viral envelope genes in each genome. Even within humans, *Suppressyn* was one of many ORF-containing and transcribed viral envelope genes identified by Frank *et al.* Additional restriction factors, regulators, and raw materials primed for domestication may yet be hiding among the numerous unexplored viral envelope sequences in mammalian genomes. ■

REFERENCES AND NOTES

1. A. Beauregard, M. J. Curcio, M. Belfort, *Annu. Rev. Genet.* **42**, 587 (2008).
2. R. Cordaux, M. A. Batzer, *Nat. Rev. Genet.* **10**, 691 (2009).
3. J. A. Frank, M. Singh, C. Feschotte, *Science* **378**, 422 (2022).
4. S. Huang *et al.*, *Cell* **166**, 102 (2016).
5. E. B. Chuong, N. C. Elde, C. Feschotte, *Science* **351**, 1083 (2016).
6. C. Baudry *et al.*, *Genes Dev.* **23**, 2478 (2009).
7. J.-L. Blond *et al.*, *J. Virol.* **74**, 3321 (2000).
8. S. Mi *et al.*, *Nature* **403**, 785 (2000).
9. R. M. Alfavon-Borja, C. Feschotte, *J. Virol.* **89**, 4047 (2015).
10. J. Sugimoto *et al.*, *Sci. Rep.* **3**, 1462 (2013).
11. C. Lavialle *et al.*, *Philos. Trans. R. Soc. Lond. B Biol. Sci.* **368**, 20120507 (2013).
12. A. Dupressoir *et al.*, *Proc. Natl. Acad. Sci. U.S.A.* **102**, 725 (2005).
13. K. Imakawa, S. Nakagawa, T. Miyazawa, *Genes Cells* **20**, 771 (2015).

ACKNOWLEDGMENTS

R.N.M. is supported by National Institutes of Health grant R35-GM142773.

10.1126/science.ade4942

CANCER

Microbial metabolites damage DNA

Unexpected members of the gut microbiota produce diverse host cell genotoxins

By **Jens Puschhof**[1] *and* **Cynthia L. Sears**[2,3]

Studies over the past two decades indicate that genotoxic gut bacteria, which damage or mutate DNA, are critical drivers of colorectal cancer (CRC) pathogenesis (*1*). Moreover, the notable increase in early-onset CRC incidence highlights the urgency to discover responsible exogenous factors that are amenable to therapeutic intervention. On page 369 of this issue, Cao *et al.* (*2*) report that individuals with inflammatory bowel disease (IBD), a common CRC precursor state, display diverse gut bacterial strains that potentially exert genotoxic activity. Pursuing *Morganella morganii*, a Gram-negative bacterium enriched in the gut microbiota of people with IBD and CRC, the authors identify a class of bacterial genotoxins called indolimines. They find evidence that indolimines promote tumor development in mice, thereby expanding the role of bacterial genotoxic metabolites in colorectal carcinogenesis.

Microbial genotoxins

Aspartate aminotransferase (*aat*)–positive *Morganella morganii* produce newly identified genotoxic metabolites. These indolimines may generate double-stranded DNA breaks that could lead to mutagenesis. The production of indolimines is required to promote colonic tumorigenesis when these bacteria are transplanted into a susceptible mouse model.

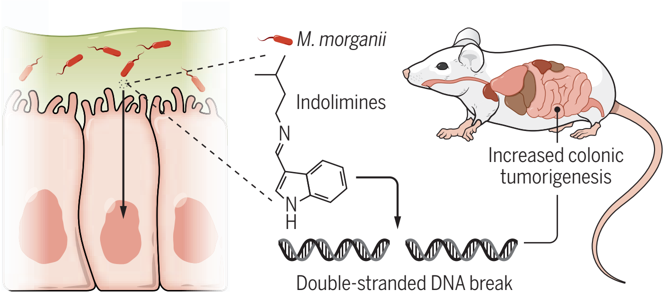

A. FISHER/*SCIENCE*

Among the most well-described genotoxic bacteria are enterotoxigenic *Bacteroides fragilis* (ETBF) (*3*) that produce *Bacteroides fragilis* toxin (BFT), strains of *Escherichia coli* or other bacteria that produce colibactin (*4*), and *Campylobacter jejuni* strains that express cytolethal distending toxin (CDT) (*5*). The DNA-damaging properties of these strains and their toxins vary considerably, ranging from alkylating DNA interstrand cross-links for colibactin to deoxyribonuclease (DNase) activity for CDT (*1*, *4*, *5*). Intriguingly, ETBF and *E. coli* producing colibactin have been linked to IBD and CRC development using in vitro and in vivo models.

The study of Cao *et al.* substantially increases the predicted number and diversity of colon microbiota strains with putative genotoxic activity. By screening 122 bacterial isolates from IBD patients in a cell-free DNA assay, the authors identify 18 strains with different types of DNA-damaging activity, including suspected DNA alkylation and DNase-like digestion of a linearized plasmid. They found that *M. morganii* strains are devoid of previously known genotoxicity-linked biosynthetic gene clusters but harbor the production machinery for genotoxic indolimines. The authors determine that synthesis of indolimines is mediated by enzymes belonging to the aspartate aminotransferase (AAT) family of pyridoxal-dependent decarboxylases. Because the amino acids leucine, valine, and phenylalanine provide the starting point for indolimine synthesis, whether diet and further amino acid metabolism affect indolimine production is a fascinating avenue for future research. Another intriguing question is whether related decarboxylases in other bacterial strains could catalyze the production of similar genotoxins.

Transferring leads from in vitro DNA damage carcinogenesis assays to in vivo systems is a formidable challenge. This is because functional effects can be modulated by bacterial mucosal adherence, bacterial community interactions, and a precancerous microenvironment. Pioneering work on interactions between an inflammatory microenvironment and colibactin in mice revealed a causative role for colibactin-mediated DNA damage in CRC (*6*). Cao *et al.* demonstrate that a community of seven nongenotoxic bacterial strains and *M. morganii* increase tumor formation in a mouse model of CRC (see the figure). This phenotype is lost upon deletion of the *aat* gene in *M. morganii*, which ablates indolimine production. This provides a key indication of a functional role of indolimines in CRC development. Double-stranded DNA breaks may mediate indolimine genotoxicity. Validation of *M. morganii* adherence to the mucus layer lining the colonic epithelium, mucosal delivery of indolimines by measuring tissue and stool, and assessing the impact of indolimines on colonic epithelial cells exposed to a complex microbial community will be essential to determine the mechanism in vivo. Beyond *M. morganii*, putatively genotoxic strains belonging to the *Firmicutes* and *Actinobacteria* phyla discovered by Cao *et al.* offer a starting point to identify potentially different genotoxicity mechanisms.

As the number of known CRC-associated bacteria rises, it is essential to identify human-relevant causal links. Indeed, a critical task is to understand the role of interbacterial or even intermicrobial interactions in driving cancer development. Previous work demonstrated colibactin-positive *E. coli* and ETBF drive genotoxicity through activation of interleukin-17 (IL-17)–producing immune cells, leading to inflammation and carcinogenesis. This example showcases the importance of considering multistrain interactions in the context of a complex microenvironment (*7*). Understanding the interactions of *M. morganii* and other putative genotoxic and cancer-linked bacteria will be essential to define bacterial consortia that underpin CRC development.

Assessing the clinical relevance of *M. morganii* and indolimines in CRC development will benefit from deeper insight in several areas. Although *M. morganii* DNA reads are enriched in a subset of CRC tumors in publicly available cancer whole-genome sequences (*8*), much remains unknown about the differential abundance and localization of this species in precancerous and cancerous states. Analyzing the impact of

---

[1] Microbiome and Cancer Division, German Cancer Research Center, Heidelberg, Germany. [2] Departments of Medicine and Oncology, Johns Hopkins University School of Medicine, Baltimore, MD, USA. [3] The Bloomberg~Kimmel Institute for Cancer Immunotherapy, Johns Hopkins University School of Medicine, Baltimore, MD, USA.
Email: csears@jhmi.edu

genotoxic bacteria on cancer genomes has become feasible (*9*–*11*). Mutagens yield different insults to DNA, the improper repair of which results in mutations ranging from single-base substitutions to large structural genomic rearrangements (*12*). By identifying the specific mutational footprints caused by bacterial genotoxins, they can be quantified and linked to functional and genomic features of human tumors. The diverse nature of bacteria-induced DNA damage indicated by the study of Cao *et al.* provides tantalizing leads that can be assessed using mutational signature analysis. Recent molecular studies have highlighted that colibactin causes DNA alkylation and attendant interstrand cross-links that lead to mutagenesis when improperly repaired (*13*, *14*). Unlike colibactin, indolimines appear to be more stable and abundant, and they can be chemically synthesized, which should facilitate studies of their molecular mechanisms.

The study of Cao *et al.* reveals that the human colon microbiota—already highly implicated in CRC pathogenesis—has a broad-ranging, previously unimagined capacity to produce genotoxins with colon disease–inducing potential. Numerous extracolonic tumors also possess distinct microbiota (*8*, *15*). Thus, the hypothesis that the tumor microbiome yields biologically relevant damage to human DNA, potentially contributing to pathogenic mutations, is plausible. Understanding microbial co-occurrence with tumors beyond the colon, the temporal relationship to cancer development, the relative genotoxicity, and the functional impact will help to identify the prime candidates for preventive interventions that target cancer-promoting microbes. ■

REFERENCES AND NOTES

1. A. Gagnaire, B. Nadel, D. Raoult, J. Neefjes, J.-P. Gorvel, *Nat. Rev. Microbiol.* **15**, 109 (2017).
2. Y. Cao *et al.*, *Science* **378**, eabm3233 (2022).
3. S. Wu *et al.*, *Nat. Med.* **15**, 1016 (2009).
4. J.-P. Nougayrède *et al.*, *Science* **313**, 848 (2006).
5. M. Lara-Tejero, J. E. Galán, *Science* **290**, 354 (2000).
6. J. C. Arthur *et al.*, *Science* **338**, 120 (2012).
7. C. M. Dejea *et al.*, *Science* **359**, 592 (2018).
8. G. D. Poore *et al.*, *Nature* **579**, 567 (2020).
9. C. Pleguezuelos-Manzano *et al.*, *Nature* **580**, 269 (2020).
10. P. J. Dziubańska-Kusibab *et al.*, *Nat. Med.* **26**, 1063 (2020).
11. J. Allen *et al.*, *Microbiol. Spectr.* **10**, e01055-22 (2022).
12. L. B. Alexandrov *et al.*, *Nature* **578**, 94 (2020).
13. M. R. Wilson *et al.*, *Science* **363**, eaar7785 (2019).
14. M. Xue *et al.*, *Science* **365**, eaax2685 (2019).
15. D. Nejman *et al.*, *Science* **368**, 973 (2020).

ACKNOWLEDGMENTS

The authors are supported by the Helmholtz Association (J.P.), the Bloomberg Philanthropies (C.L.S.), and the Cancer Grand Challenges OPTIMISTICC team grant (A27140) funded by Cancer Research UK (C.L.S.). J.P. receives support from Emulate. C.L.S. receives support from Janssen and Bristol Myers Squibb.

10.1126/science.ade6952

CERAMICS

A ceramic that bends instead of shattering

The microstructure of the ceramic silicon nitride can be tuned to create plasticity

By **Erkka J. Frankberg**

Ceramic materials are, at least in principle, capable of plastic deformation at room temperature (*1*). If ceramics can be shaped by hammering, bending, or pulling without fracturing, this will vastly expand the range of applications for these materials. For example, the strong ionic and covalent bonding in ceramics, combined with this hypothetical plasticity, could lead to materials that are lighter and stronger than even the best metal alloys of today. On page 371 of this issue, Zhang *et al.* (*2*) present how silicon nitride (Si_3N_4), one of the most versatile engineering ceramic materials, can be made to exhibit plasticity at room temperature. Their proof-of-concept experiment and simulation results offer a potential route to realizing the dream of flexible ceramics.

Plasticity in ceramic materials is rarely observed in nature. Because of the complicated structure of ceramics (compared with metals, for example), plasticity from simple dislocation—that is, the slipping of atoms against each other—is mostly limited to single crystalline ceramic and only happens at very high temperatures. For example, sapphire can become somewhat ductile, but only when the temperature is >1000°C. Zhang *et al.* show that under compressive loading at room temperature, the crystalline fragments in Si_3N_4 can undergo transformations that allow them to rearrange atoms and tolerate macroscopic strain without fracture. Specifically, the β-type crystals can transform into α-type crystals when the material is mechanically stressed. They observed that this plasticity-inducing transformation tends to occur at the coherent crystal interfaces, where neighboring crystals with different structures are in contact with each other where their atomic arrangements are similar. The mechanism bears some resemblance to the transformation-induced plasticity mechanism in steel, by which metastable iron crystals can transform under stress, leading to enhanced ductility and strength (*3*).

Microstructural transformation can induce improvement of mechanical performance in crystalline materials, such as ceramics. Zirconium oxide (ZrO_2) is an example of a ceramic material that is used because of its strength, for example, in dental applications. ZrO_2 can withstand pressures upward of 1500 MPa before fracture (*4*) because of its ability to undergo microstructural transformations when mechanically stressed (*5*). These transformations have even been shown to induce minor plasticity in ZrO_2 at room temperature (*6*, *7*). To date, the microstructural transformation–induced mechanisms in ZrO_2 remain one of the most important areas of research in engineering ceramics (*8*). Unlike ZrO_2, Si_3N_4 is a nonoxide and covalently bonded material, in which plasticity was not expected to occur by a similar mechanism. Thus, the plasticity discovered in Si_3N_4 provides an opportunity to extend the understanding of how plasticity can occur in ceramics at low temperatures.

Zhang *et al.* were able to control the portion of coherent interfaces that occur between the two main types of crystals of Si_3N_4. When this portion reaches ~32%, the material can withstand up to ~11 GPa of pressure with a plastic strain of up to ~20% before fracture. The authors conclude that the ultimate strength and plastic strain are correlated to the abundance of coherent interfaces and could be enhanced further if the total amount of coherent interfaces were to increase. The microstructural transformations at the interfaces allow atoms to change their locations and spread out the mechanical stress, thus preventing cracks from emerging and propagating (see the figure). This is different from a typical brittle ceramic material in which atoms are rigidly held in place by their crystal structure and are forced to break their bonds with neighboring atoms when stressed, leading to macroscopic fracture. In addition to the correlation between coherent interfaces and plasticity, Zhang *et al.* also revealed that the transformation mechanism of β-type to α-type

---

Unit of Materials Science and Environmental Engineering, Tampere University, Tampere, Finland. Email: erkka.frankberg@tuni.fi

The stress-strain behavior of Si_3N_4 ceramics

The ceramic material silicon nitride (Si_3N_4) can be engineered to possess plasticity and strength comparable to that of high-strength steel. This surprising property can be attributed to how its two main types of crystals interact when the material is under mechanical stress.

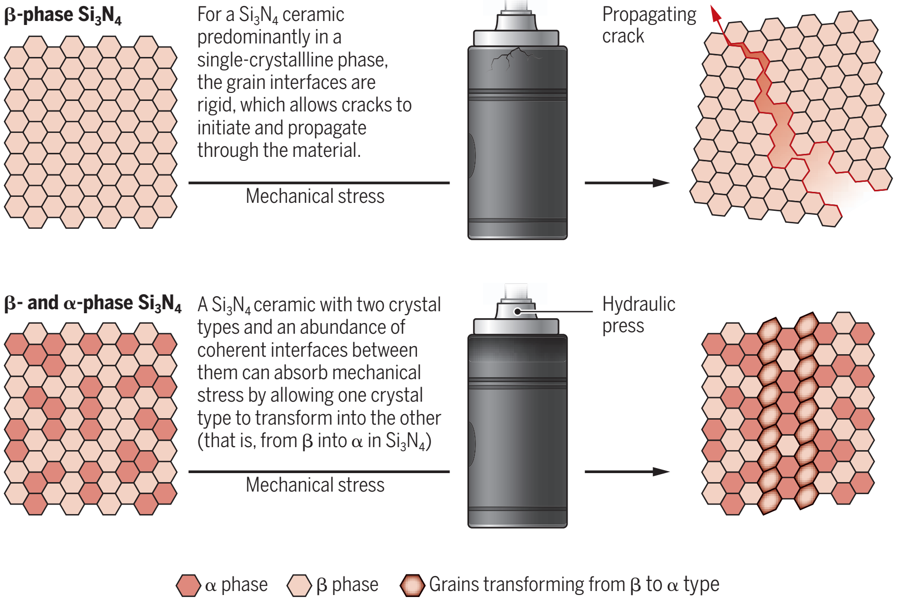

crystals only happens one way and not the other way around. These transformations allow changes to the macroscopic shape of the material without fracture.

Synthetic Si_3N_4 has been used in industrial and commercial applications for almost a century (*9*), for example, in cutting tools, bearings, and combustion engine components (*10*, *11*). One specific application of Si_3N_4 is the microshutters used by the near-infrared spectrometer instrument on board the James Webb Space Telescope (*12*). For these applications, Si_3N_4 is used primarily because of its balance of properties: It is lightweight, durable, and resistant to high temperatures. A ductile version of this already versatile material will usher in a host of new applications. However, it is worth noting that the samples tested by Zhang *et al.* are at the nanoscale and thus free of any macroscopic flaws. However, if the synthesis process is scaled up, the material may form pores and cracks that would make the material more susceptible to fracture initiation.

There is a long road ahead before the full potential of ductile ceramics is realized. However, considering the apparent scarcity of plastic ceramics at room temperature, each discovery of a plasticity mechanism should be regarded highly. A scaled-up, ductile ceramic material would offer a versatile and economically attractive alternative to metals in many applications, for example, by reducing the weight of machine components; increasing machinery uptime with higher wear, fatigue, and corrosion tolerance; and increasing the energy efficiency of thermal power engines by allowing them to run at higher temperatures. Future studies should investigate whether bulk Si_3N_4 gains similar benefits from the stress-induced microstructural transformations as ZrO_2 and whether the required coherent interfaces remain stable at temperatures and process conditions that are relevant for practical applications. How to control the number of coherent interfaces and process flaws in a bulkier material will also need to be clarified. Although ceramics are already a tremendously important group of functional materials, without plasticity, their full potential remains untapped. ■

REFERENCES AND NOTES

1. P. W. Bridgman, *Studies in Large Plastic Flow and Fracture* (Harvard Univ. Press, 1964).
2. J. Zhang *et al.*, *Science* **378**, 371 (2022).
3. M. Soleimani, A. Kalhor, H. Mirzadeh, *Mater. Sci. Eng. A* **795**, 140023 (2020).
4. B. D. Flinn, A. J. Raigrodski, L. A. Mancl, R. Toivola, T. Kuykendall, *J. Prosthet. Dent.* **117**, 303 (2017).
5. R. C. Garvie, R. H. J. Hannink, R. T. Pascoe, *Nature* **258**, 703 (1975).
6. G. A. Gogotsi, V. P. Zavada, M. V. Swain, *J. Eur. Ceram. Soc.* **15**, 1185 (1995).
7. A. Liens *et al.*, *Acta Mater.* **183**, 261 (2020).
8. J. Chevalier, L. Gremillard, A. V. Virkar, D. R. Clarke, *J. Am. Ceram. Soc.* **92**, 1901 (2009).
9. F. L. Riley, *J. Am. Ceram. Soc.* **83**, 245 (2000).
10. H. Klemm, *J. Am. Ceram. Soc.* **93**, 1501 (2010).
11. N. R. Katz, *Ceram. Ind.* **149**, 33 (1999).
12. M. J. Li *et al.*, in *Proceedings SPIE*, vol. 6687, H. A. MacEwen, J. B. Breckinridge, Eds. (Paper 668709, Society of Photo-Optical Instrumentation Engineers, 2007).

10.1126/science.ade7637

PLANETARY SCIENCE

A seismic meteor strike on Mars

A meteor impact and its subsequent seismic waves reveal the crustal structure of Mars

By **Yingjie Yang** and **Xiaofei Chen**

The crustal and mantle structures of a planet bear important information about its origin and evolution. Seismic waves propagating along the shallow surface of a planet, known as surface waves, can be used to map its crustal and upper mantle structures. However, no such waves have ever been detected on any planet besides Earth. On pages 412 and 417 of this issue, Posiolova *et al.* (*1*) and Kim *et al.* (*2*), respectively, report a large meteorite impact on Mars, as recorded by the National Aeronautics and Space Administration's (NASA's) InSight Mars lander and the Mars Reconnaissance Orbiter, and present analysis of the detected surface waves produced by the meteorite impact. Kim *et al.* also present an updated crustal model of Mars that provides a better understanding of the formation and composition of the martian crust and extends the current knowledge of the geodynamic evolution of Mars.

There are two types of seismic waves generated by quakes. Body waves travel into the deep interior of a planet and are useful for extracting information about the core and deep mantle. Then there are surface waves, which are most useful for mapping the shallower structures of a planet. The main task of the InSight lander (which stands for Interior Exploration using Seismic Investigation, Geodesy and Heat Transport) is to detect marsquakes and capture seismic data for studying the internal structure of Mars. Since February 2019, the seismometer deployed by InSight has recorded more than 1300 marsquakes, proving that Mars is a seismically active planet (*3*). The collected body wave data suggest that Mars has a layering structure similar to that of Earth, having a

---

Department of Earth and Space Sciences, Southern University of Science and Technology, Shenzhen, Guangdong, China. Email: yangyj@sustech.edu.cn

GRAPHIC: A. FISHER/*SCIENCE*

core radius of ~1830 km (*4*), a mantle thickness of ~1500 km (*5*), and a crust thickness of ~20 to 70 km (*6*).

Mars has a notable diversity of topographical features and crustal thicknesses (*7*). Better measuring of these variations is crucial to unravel the mysteries about the evolution of the martian crust and mantle. Because the InSight lander is the only seismometer on Mars, imaging the variations of the planet's internal structures based on body waves is limited. Because body waves from distant sources travel through paths deep inside the planet and arrive nearly vertically beneath the seismometer, it is difficult to infer the spatial variations of martian internal structure. By contrast, surface waves that travel through the planet's crust and upper mantle arrive at the seismometer horizontally, which makes it much easier to map the lateral variations of the martian crust and upper mantle.

Meteorite impacts on Mars are common, with ~200 impacts each year. On 24 December 2021, the InSight lander recorded a seismic event. By examining images of the martian surface from the Mars Color Imager onboard the Mars Reconnaissance Orbiter, Posiolova *et al.* identified a crater with a diameter of 150 ± 10 m that was created within a 24-hour window of the recorded seismic event (see the figure). They analyzed the data and confirmed that the recorded seismic event can be traced back to the location of this crater, thus concluding that the recorded seismic event was the result of a meteorite impact. This confirmation validates the method used to analyze the data from a single seismometer for locating the sources of marsquakes (*8*, *9*), which is a critical step in mapping the interior structure of Mars.

The meteorite impact on the surface of Mars generated both body and surface waves. Kim *et al.* analyzed the waveform features of the recorded body and surface waves on Mars on the basis of what is known about earthquakes. Surface waves generated by large earthquakes are observed at periods ranging from several seconds to minutes. Because of this broad range of surface wave periods, information about crustal and upper mantle structures can be extracted up to a few hundred kilometers deep. By comparison, the surface waves generated by the impact on Mars have a shorter and narrower period range because of the relatively weak force generated by the impact, which meant that the data could only reveal the structure of a shallower portion of the crust. Kim *et al.* measured the surface waves to have a period of 8 to 15 s, which translates to an imaging depth of ~30 km. Their result indicates that surface waves traveled faster between the impact crater and the InSight lander site than at the lander site. The speed difference means that the crust between the crater and the lander site is denser than that at the lander site itself and provides evidence for structural variations in the martian crust. Topography and gravity data of Mars are currently used to infer the large-scale crustal thickness of Mars. However, such an inference depends heavily on the presumption of a uniform crustal density (*10*). The seismic model reported by Kim *et al.* offers a more sophisticated way to understand the crustal structures of Mars, which should be considered in future topographical and gravitational analyses.

The north-south difference in the topography and morphology of Mars, with lowlands in the north and highly dense cratered highlands in the south, is the most pronounced geologic feature of the Red Planet. The reason behind this dichotomy is still under debate, with competing hypotheses including giant impact–related exogenic processes (*11*) and mantle convection–related endogenic models (*12*, *13*). A more granular understanding of deep crust and upper mantle structures would help discern the competing hypotheses on the geodynamic evolution of Mars. Recent development in seismic data processing suggests that long-period surface waves can be retrieved from single-station autocorrelation of seismic ambient noises (*14*, *15*), which are tiny ground vibrations excited by sources such as wind vortices and ocean waves on Earth. On Mars, seismic ambient noise excited by wind vortices may contain weak signals of long-period surface waves. The 3+ years of single-station seismic ambient noise data recorded by the Insight lander may be used to extract information about long-period surface waves on Mars. Additionally, surface waves excited by individual marsquakes may be too weak to be meaningfully analyzed, but the stacking of data collected from multiple marsquakes may enhance their statistics.

The InSight lander is expected to end its operation by December 2022 because of dust accumulation on its solar panels. However, continuing work on the already recorded seismic data should continue to deliver discoveries about the structure of Mars. Future exploration missions to Mars, such as ExoMars headed by the European Space Agency and Tianwen headed by the China National Space Administration, are expected to be launched with more advanced seismometers. With additional data from these missions, a more detailed map of crustal and upper mantle structure can be produced to paint a clearer picture of the crustal and mantle evolution of Mars. ■

Seismic waves on Mars

On 24 December 2021, the InSight Mars lander recorded, for the first time ever, a seismic surface wave on Mars generated by a meteor strike. The data revealed previously unknown structural details of the martian crust.

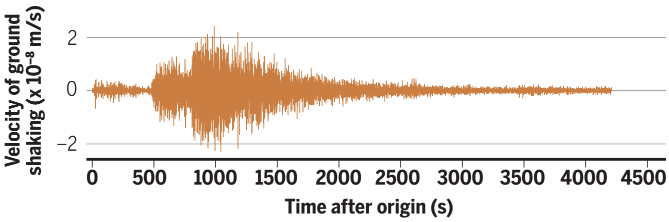

A Mars-shaking impact

A satellite image of the meteor impact site was captured by the Mars Reconnaissance Orbiter. The dark streaks radiating away from the crater were caused by the supersonic speed of the impact.

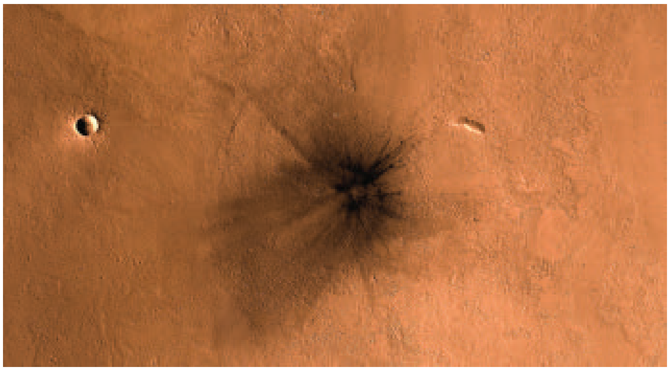

CREDITS: (GRAPHIC) K. HOLOSKI/*SCIENCE* BASED ON (*1*); (PHOTO) NASA/CALTECH-JPL/MSSS

REFERENCES AND NOTES

1. L. V. Posiolova *et al.*, *Science* **378**, 412 (2022).
2. D. Kim *et al.*, *Science* **378**, 417 (2022).
3. D. Giardini *et al.*, *Nat. Geosci.* **13**, 205 (2020).
4. S. C. Stähler *et al.*, *Science* **373**, 443 (2021).
5. A. Khan *et al.*, *Science* **373**, 434 (2021).
6. B. Knapmeyer-Endrun *et al.*, *Science* **373**, 438 (2021).
7. M. T. Zuber, *Nature* **412**, 220 (2001).
8. M. Böse *et al.*, *Phys. Earth Planet. Inter.* **262**, 48 (2017).
9. J. F. Clinton *et al.*, *Phys. Earth Planet. Inter.* **310**, 106595 (2021).
10. M. T. Zuber *et al.*, *Science* **287**, 1788 (2000).
11. M. M. Marinova, O. Aharonson, E. Asphaug, *Nature* **453**, 1216 (2008).
12. S. Zhong, M. T. Zuber, *Earth Planet. Sci. Lett.* **189**, 75 (2001).
13. J. H. Roberts, S. Zhong, *J. Geophys. Res.* **111**, E06013 (2006).
14. M. Schimmel, E. Stutzmann, S. Ventosa, *Seismol. Res. Lett.* **89**, 1488 (2018).
15. J. Xie, S. Ni, *Seismol. Res. Lett.* **90**, 708 (2019).

10.1126/science.add8574

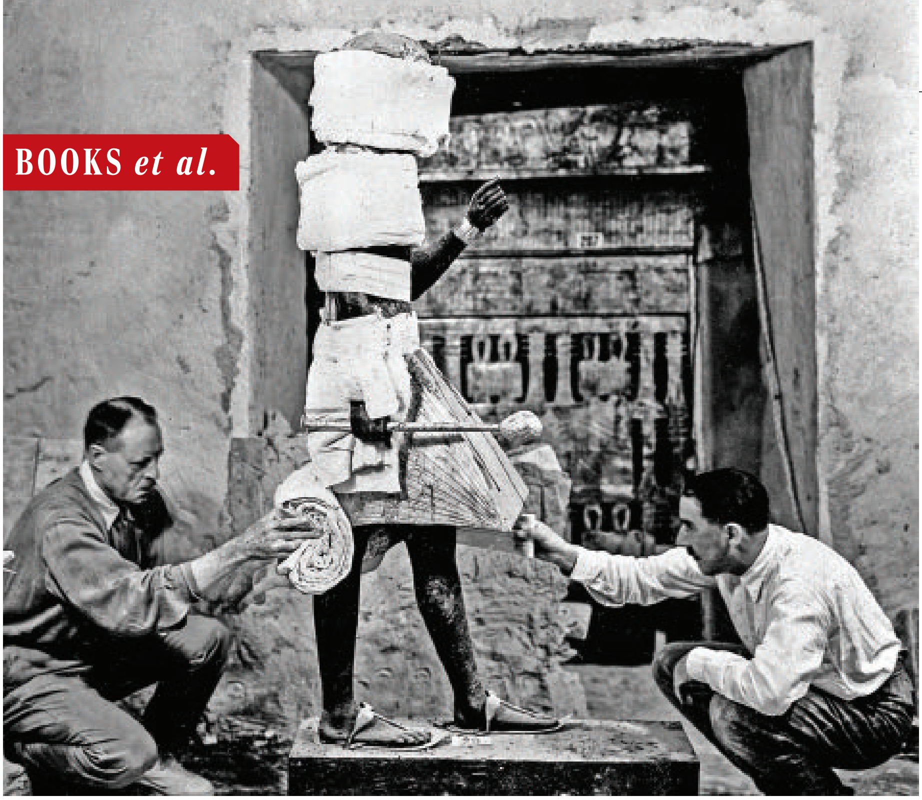

Howard Carter (right) and Arthur Callender (left) wrap a guardian statue from Tutankhamun's tomb.

ARCHAEOLOGY

Tales of Tutankhamun

A pair of authors set out to humanize the enigmatic pharaoh 100 years after his tomb's discovery

By **Andrew Robinson**

When the tomb of Tutankhamun—the pharaoh who died circa 1323 BCE at the age of 19 after a reign of about 9 years—was discovered by archaeologist Howard Carter in November 1922 in the Valley of the Kings near modern Luxor (ancient Thebes), the "boy king" was immediately identified from hieroglyphic inscriptions on seal impressions at its entrance and rapidly became world famous. Today, he is undoubtedly the most celebrated of ancient Egyptians, while at the same time remaining highly enigmatic.

As Carter warned in his three-volume work *The Tomb of Tut.ankh.Amen*, "The mystery of his life still eludes us—the shadows move but the dark is never quite dispersed" (*1*). There is no certainty about the identity of his mother, for example, or his health, or the cause of his death. Speculations about the latter include a chariot accident, a hippo attack, malaria, and even murder. CT scanning, MRI, and DNA analysis of his mummy, along with other techniques, have yet to yield an undisputed answer.

The two books about Tutankhamun reviewed here—both published to coincide with the centennial of the tomb's discovery (and the bicentennial of the hieroglyphic decipherment)—could scarcely be more different in appearance and approach. *The Story of Tutankhamun* is a relatively brief, decently illustrated, and widely appealing biography intended for nonexperts. It is written by author and journalist Garry Shaw, who has published several books on ancient Egyptian culture during the past decade. By contrast, *The Complete Tutankhamun* is a lengthy, multisectioned catalog of the contents of the tomb and related material with copious highly detailed and magnificently reproduced illustrations, aimed at specialists but also seductive for the dedicated general reader. Its compiler, Nicholas Reeves, is an Egyptologist who has excavated in the Valley of the Kings and a long-time Tutankhamun specialist. First published in 1990, the book has been extensively revised to include new discoveries and informed speculations, with a lovely redesigned cover featuring Tutankhamun's exquisite hieroglyphic cartouche in gold.

The Complete Tutankhamun
Nicholas Reeves
Thames & Hudson, 2023. 464 pp.

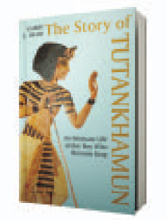

The Story of Tutankhamun
Garry J. Shaw
Yale University Press, 2023. 208 pp.

Naturally, both books set out to humanize the pharaoh. "My hope is that by the end of this book, you will see Tutankhamun in a new light," writes Shaw in his introduction. "Not just as a remote and ancient god king, who died young and was buried with fabulous treasures; not just as a symbol or celebrity; but as a real person, with loved ones, personal beliefs, responsibilities, hobbies and health problems." Likewise, Reeves, in his "Treasures" section, writes: "here, among the boy's treasures, are the materials to flesh out his bones, breathe air into his shrivelled lungs and glimpse something, perhaps, of personality, tastes and affections."

Note Reeves's cautionary "perhaps," plus the revealing fact that Shaw brings the story of Tutankhamun's life to an end halfway through his book. (The second half is devoted to the pharaoh's tomb; the history of its rediscovery; and "Tut-mania," the international fascination with the boy king since 1922.) For any Egyptologist, the chief difficulty in understanding Tutankhamun's life and mind, as opposed to his diverse and richly decorated possessions, is that no writing by Tutankhamun himself survives—only brief and insignificant inscriptions on some of the possessions found with his remains.

The tomb does contain multiple examples of scribal equipment, including two writing palettes bearing the pharaoh's name with evidence of their use. Such objects suggest that the teenager could write the cursive hieratic script and presumably read the more formal hieroglyphic script. But surprisingly, and to the disappointment of Egyptologists, no papyri—blank or inscribed—have been found, despite the discovery of a box probably used to store papyrus rolls. Reeves guesses that the tomb's papyri were stolen during two robberies within a few years of the burial.

Tutankhamun's sandals, walking sticks, tunics, wine jars, toys, heirlooms, and archetypal golden mask thus remain as intriguing as ever, but "the teenager behind the mask" (as Shaw refers to him) remains elusive. ■

The reviewer is the author of *Cracking the Egyptian Code: The Revolutionary Life of Jean-François Champollion* (Thames & Hudson, 2012). Email: andrew@andrew-robinson.org

REFERENCES AND NOTES

1. H. Carter, *The Tomb of Tut.ankh.Amen, Volumes I–III* (Cassell, 1923–1933).

10.1126/science.ade7192

PHOTO: DAVID COLE/ALAMY STOCK PHOTO

EDUCATION

What does a professor look like?

Scholars offer tips and advice for helping college students think beyond stereotypes

Picture a Professor: Interrupting Biases About Faculty and Increasing Student Learning
Jessamyn Neuhaus, Ed.
West Virginia University Press, 2022. 296 pp.

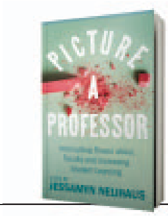

By **Ashley Huderson**

I began teaching as an adjunct professor at a local university in the fall of 2014. On my first day of class, I sat in the front row and waited for the 12 registered students to file in. As they arrived, whispers of "Where is the professor?" and "Does anyone know what he looks like?" began filling the air. After a few minutes, I stood up and introduced myself as the instructor and was met with apparent confusion. At the time, I was a 29-year-old Black woman with a recently minted PhD. Why, I asked, was everyone surprised to see me at the front of the class? "You don't look like any professor I've ever had, and honestly, I didn't think we did this type of work," admitted one brave student. In that moment, I knew exactly what she meant.

Almost 70% of college professors are white (*1*). Even if my student had encountered any of the 49.8% of female professors, it is possible that she may not have been taught by any Black professors (7.2%), let alone a Black female professor (2.1%), or a professor under the age of 30 (13%). In a new collected volume, *Picture a Professor*, edited by historian Jessamyn Neuhaus, a diverse group of scholars from a variety of disciplines offer advice for educators seeking to help students think beyond the stereotypical image of a college professor.

Picture a Professor showcases stories and personal anecdotes, as well as evidence-based insights and intersectional teaching strategies for navigating student preconceptions about identity and expertise. The volume goes beyond issues of gender and ethnicity, touching on age, ability and disability, and intersectional identities. In chapter 6, for example, dance professor Fen Kennedy draws on theories of queer pedagogy to cultivate trust in the classroom. The author describes using a collaboratively created rubric as one approach to facilitating authentic learning and creating a safe classroom environment for both students and faculty, queer and not. Meanwhile, in her chapter "Where's the Professor? First-Day Active Learning for Navigating Students' Perceptions of Young Professors," musicology professor Reba Wissner explores how facilitating active learning activities on the first day of class helps build trust and credulity with students, forcing them to look beyond their perceptions of "how old" a professor should be or look.

Each of the book's contributors recognizes the pervasiveness of racialized, gendered, and other biases and recommends specific ways to respond to and interrupt such preconceptions—helping students, teachers, and others reenvision what they think of when they picture a professor. In the chapter "Rippling the Patterns of Power: Enacting Anti-Racist Pedagogy with Students as Co-teachers," for example, Chanelle Wilson and Alison Cook-Sather recommend challenging assumptions and fostering critical analytical skills, developing students' awareness of their social positions, decentering authority in the classroom and making space for students to take responsibility for their learning, and empowering students to apply theory to practice. Meanwhile, in her chapter "Empowered Strategies for Women Faculty of Color Navigating Teaching Inequities in Higher Ed," sociologist Chavella Pittman encourages readers to know and internalize the research about the teaching efficacy of women faculty of color (WFOC), the broader benefits of WFOC's teaching, and the teaching inequalities faced by WFOC.

The book's chapters are organized into four sections: identifying strategies for starting the semester strong (part 1); making connections and building rapport with students (part 2); anti-racist pedagogies (part 3); and strategies for empowering professors to bring their whole selves to the classroom (part 4). Together, these sections cover every aspect of marginalized faculty life through anecdotal stories, lived experiences, and best practices.

Throughout the book, the contributors report being questioned, undermined, disempowered, and ignored as a result of various biases. Such stories and the strategies they inspire are unfortunately all too common, but they are not the only way forward. By shedding light on these harsh realities, *Picture a Professor* does a service to all who would prefer a different path, offering realistic strategies to engage students in undermining scholarly stereotypes with innovative course design, classroom activities, assessment techniques, and more. ■

REFERENCES AND NOTES

1. Zippia, College Professor Demographics and Statistics in the US; https://www.zippia.com/college-professor-jobs/demographics/.

10.1126/science.add9492

The reviewer is at the American Society of Mechanical Engineers, Washington, DC, USA; the Department of Biology, University of the District of Columbia, Washington, DC, USA; and STEM Innovation Consulting, Washington, DC, USA. Email: ahuderson@steminnovationconsulting.com

SCIENCE & FOOD

Commercially available bananas are just one of many varieties.

PHOTO: TON KOENE/ALAMY STOCK PHOTO

PODCAST

Eating to Extinction: The World's Rarest Foods and Why We Need to Save Them
Dan Saladino
Farrar, Straus and Giroux, 2022. 464 pp.

Through intensive agricultural techniques and technologies, we drastically increased food production in the 20th century, but the diversity of plant and animal species we regularly eat declined in the process. This week on the *Science* podcast, Dan Saladino describes the unusual species we stand to lose in a world of monoculture commercial crops and the importance of preserving the practices of those who cultivate rare foods.
https://bit.ly/3BULG3Z

10.1126/science.adf1091

LETTERS

Edited by **Jennifer Sills**

Sweden threatens European biodiversity

In June, the European Commission proposed a nature restoration law to repair Europe's damaged ecosystems (*1*). This regulation stands out by setting legally binding biodiversity targets for member states and has been well received by ecological scientists (*2*). However, the proposal faces an uphill battle to become European law. In January 2023, the rotating presidency of the European Union will be held by Sweden, whose parliament has already voted against the Commission proposal, arguing that its conservation measures were disproportionate (*3*). The newly appointed Swedish government terminated on its first day the 35-year-old standalone Ministry of Environment in charge of nature conservation (*4*). Given its political record of weakening biodiversity laws, Sweden is also likely to counter the proposed European law during its presidency.

Sweden has failed to align its wolf policy with European law for a decade (*5*) and has often undermined biodiversity conservation efforts when they affect extractive industries. A previous Swedish government instructed authorities to abuse exemptions allowed by the European Water Directive (*6*). Shortly after the UN environmental summit Stockholm+50 this spring, a majority in the Swedish parliament voted a motion to reopen an international convention on environmental democracy to introduce limits on litigation by environmental organizations (*7*). After the European Court of Justice ruled in 2021 on bird conservation and Swedish forestry, Sweden urgently amended its Species Protection Ordinance to remove alleged legal obstacles against forestry (*8*).

The political inbreeding between some authorities and forest industries is such that the latter has been able to overrule an independent scientific review when deciding to fund a large strategic research project by a public research foundation (*9*). On biodiversity issues, the Swedish state apparatus largely appears to have been captured by extractive industry lobbies (*10*).

Sweden faces hardly any backlash from its backward-looking biodiversity policies. Its administrative culture of consensus does not value dissent (*11*) and the country historically benefits from its reputation as a moral superpower (*12*). For example, the current Czech presidency of the EU has outsourced some environmental aspects to Sweden (*13*) because of its experience in international environmental relations. A 6-month presidency of the EU may not give Sweden the ability to irreversibly block the proposed nature restoration law, but it can provide enough political momentum for Sweden to substantially weaken or delay it. A likely outcome may be a law with added loopholes that allows Sweden to claim environmental leadership while safeguarding a status quo benefiting its environmentally damaging industries. European member states, institutions, and experts are therefore advised to handle biodiversity conservation policies made by Sweden with the highest level of skepticism and scrutiny.

Guillaume Chapron
Department of Ecology, Swedish University of Agricultural Sciences, 73993 Riddarhyttan, Sweden. Email: guillaume.chapron@slu.se

REFERENCES AND NOTES

1. N. Hoek, *Eur. Energ. Environ. Law Rev.* **31**, 320 (2022).
2. Society for Ecological Restoration (European Chapter), "Declaration on the European Commission proposal for a regulation on nature restoration" (2022).
3. Swedish Parliament, 2021/22:MJU32 (2022).
4. D. M. Dougall, "'Devastating consequences' as new Swedish government scraps environment ministry," *Euro News* (2022).
5. L. Laikre *et al.*, *Science* **377**, 162 (2022).
6. Swedish Government, 2017/18:243 (2018).
7. Swedish Parliament, 2021/22:MJU29 (2022).
8. Swedish Ministry of the Environment, "Ändringar av artskyddsförordningen ska skapa tydligare tillämpning" (2022) [in Swedish].
9. J. Andersson, E. Westholm, *Sci. Technol. Hum. Val.* **44**, 237 (2019).
10. L. Röstlund, *Skogslandet: En Granskning* (Forum, Stockholm, 2022) [in Swedish].
11. P. Hall, in *The Oxford Handbook of Swedish Politics* (2015), pp. 299–314.
12. A.-S. Dahl, *Int. J.* **61**, 15 (2022).
13. Council of the European Union, 10154/22 (2022); https://data.consilium.europa.eu/doc/document/ST-10154-2022-INIT/en/pdf.

10.1126/science.adf2714

PHOTO: RAUL ARBOLEDA/AFP/GETTY IMAGES

Vote against Amazon deforestation in Brazil

After Brazil's 2 October presidential elections, images showed that votes for the current administration corresponded with cities located in the Amazon's arc of deforestation (*1*). In these regions, where agribusiness is strong, forest clearing, criminal fires, illegal mining, and invasions of protected areas have proliferated under the management of the current government (*2*). The second round of the election on 30 October could put Brazil on a more environmentally responsible path.

Recently, there has been a rush of deforestation, land grabbing, and burning (*3*, *4*), perhaps due to the recognition that these could be the final months of a government lax on environmental crime. In September, with the electoral race underway, the deforested area in the Amazon was the largest since 2015. The 1455 km² lost was 48% higher than the area lost in September last year (*3*, *4*).

In a country with rain-fed agriculture, the current administration's management undermines the productivity of agribusiness (*5*). Fewer trees in the forest leads to less moisture in the air and less rainfall, putting crops at risk (*6*). Instead, Brazil should invest in a sustainable agribusiness, which preserves the forest and invests heavily in agricultural technologies to produce more in areas designated for cultivation (*7*).

Government policy that allows and encourages rapid deforestation jeopardizes Brazil's future (*8*). The choice of Brazilians in the second round of elections can prevent the collapse of the Amazon, the climate, and the country's agricultural productivity.

Cássio Cardoso Pereira
Departamento de Genética, Ecologia e Evolução, Centro de Síntese Ecológica e Conservação, Universidade Federal de Minas Gerais, Belo Horizonte, Minas Gerais 31270-910, Brazil. Email: cassiocardosopereira@gmail.com

REFERENCES AND NOTES

1. M. Couto, R. Galdo, B. Abbud, E. Gonçalves, "Bolsonaro venceu nas cidades mais desmatadas da Amazônia no primeiro turno; veja o mapa," *O Globo* (2022) [in Portuguese].
2. A. Pfaff, J. Robalino, C. Sandoval, D. Herrera, *Philos. Trans. R. Soc. B Biol. Sci.* **370**, 20140273 (2015).
3. P. Watanabe, "Amazônia tem recorde de desmate em setembro," *Folha de São Paulo* (2022) [in Portuguese].

Brazil's upcoming election could determine the degree of exploitation allowed in the Amazon going forward.

4. R. Peixoto, "Alertas de desmate na Amazônia têm pior setembro da série histórica, aponta Inpe," O Globo (2022); [in Portuguese].
5. L. J. C. Oliveira, M. H. Costa, B. S. Soares-Filho, M. T. Coe, *Environ. Res. Lett*. **8**, 024021 (2013).
6. D. Arruda, H. G. Cândido, R. Fonseca, *Science* **365**, 1387 (2019).
7. M. J. B. Silva, M. F. da Costa, S. A. de Farias, L. S. O. Wanderley, *Psychol. Market*. **37**, 1720 (2020).
8. T. O. Assis, A. P. D. C. V. Randow, C. A. Nobre, *Sci. Adv*. **8**, eabj3309 (2022).

10.1126/science.adf2475

Overfishing and warming put Persian Gulf at risk

The eight countries that border the Persian (or Arabian) Gulf, a critical marine ecosystem with the warmest water on Earth (*1*), share in the economic benefits produced by its fisheries. However, current harvest control rules for fisheries in the region are neither sufficiently strict nor sufficiently consistent across countries to protect Persian Gulf ecosystems, especially in the face of climate change. Rising temperatures affect the structure and function of marine food webs, exacerbating the vulnerabilities of marine species and the fisheries sector, as well as the challenges in accurately tracking ecosystem health. To prevent long-term harm to the Persian Gulf's ecosystems, fisheries management in the region must balance economic and environmental priorities.

Despite regulations, fishing activity is depleting most fish stocks in the Persian Gulf, and stock rebuilding and native fish restocking programs have been unable to substantially increase population numbers (*2*, *3*). Increased unsustainable harvesting of biomass at the top of the food chain, fisheries expansion, and pressure on the bottom of the food chain are evidence of ecosystem overfishing and ineffective management (*2*–*9*). In the past 70 years, the species composition of caught fish has changed and the mean trophic level of catch has declined, indicating that high–trophic-level species have collapsed and been replaced by low–trophic-level plankton feeders and invertebrates (*2*–*7*). Primary production (the energy transfer needed for each trophic level to support the one above it) has also decreased (*7*) which could reduce future catch potential. Although officially reported fisheries statistics are unreliable (*8*), it is clear that per capita fish supply is declining, as both local and foreign [e.g., (*9*)] fishing activities continue.

Monitoring the health of fish stocks in the Persian Gulf is complicated by environmental changes. Fish biomass has consistently declined over time, but climate ecological change impacts are amplified at higher trophic levels (*10*), confounding the effects of temperature changes on marine ecosystem functions and fisheries. Warm water temperatures can lead to faster fish growth but smaller fish size at a given age, decrease primary production by killing autotrophic microalga, and accelerate environmental degradation (*2*, *11*, *12*). Fisheries stock are also threatened by oil pollution, which is steadily increasing every year and currently exceeds the world average by 47 times (*12*).

All countries fishing in the Persian Gulf, in collaboration with global policymakers, must implement realistic and responsible fisheries management. Better monitoring should locate illegal offshore fishing. Fisheries regulatory regimes and climate resilience strategies should be modified, especially in very hot seasons. Safe catch limits should be decreased. Smaller fisheries, which operate more sustainably, should receive more support. More marine protected areas and endemic species protections should be established. Regional policies should put pressure on the countries with the highest percentage of food web destruction, and strict rules should provide additional protection for critical areas. The region should also ensure its own food security before providing international fisheries trade permits. Integrated science policy goals within and across the Persian Gulf's fisheries can manage sustainable fish supply while reversing biodiversity loss in the region.

Sakineh Mashjoor[1]*, Ehsan Kamrani[2], Rifaat Aziz[3]
[1]Department of Marine Biology, Faculty of Marine Science and Technology, University of Hormozgan, Bandar Abbas, Iran. [2]Fisheries Department, Faculty of Marine and Atmospheric Sciences, Hormozgan University, Iran. [3]Department of Conservation and Marine Sciences, Faculty of Applied Sciences, Cape Peninsula University of Technology, Cape Town, South Africa.
*Corresponding author.
Email: mashjoor.s@gmail.com

REFERENCES AND NOTES

1. N. Bayani, *Iran. Stud*. **49**, 1047 (2016).
2. L. A. Jawad, *The Arabian Seas: Biodiversity, Environmental Challenges, and Conservation Measures* (Springer Nature, 2021).
3. N. Al Wasmi, "Some 85% of key fish species in Arabian Gulf wiped out, UAE study finds," *The National News* (2019); www.thenationalnews.com/uae/environment/some-85-of-key-fish-species-in-arabian-gulf-wiped-out-uae-study-finds-1.818543.
4. L. Shannon, M. Coll, A. Bundy *et al.*, *Mar. Ecol. Prog. Ser.* **512**, 115 (2014).
5. M. Razzaghi, S. Mashjoor, E. Kamrani, *Chin. J. Oceanol. Limnol*. **35**, 528 (2017).
6. M. Daliri, E. Kamrani, A. Salarpouri, A. Ben-Hasan, *Ocean. Coast. Manag*. **199**, 105411 (2021).
7. S. Mashjoor, F. Heidary Jamebozorgi, E. Kamrani, *Ocean. Sci. J*. **53**, 655 (2018).
8. D. Al-Abdulrazzak, D. Pauly, *ICES J. Mar. Sci*. **71**, 450 (2014).
9. "How the Persian Gulf is being taken over By China's fishing trawlers," *Nspirement* (2020); www.nspirement.com/2020/10/14/how-the-persian-gulf-is-being-taken-over-by-chinas-fishing-trawlers.html.
10. H. K. Lotze *et al*., *Proc. Natl. Acad. Sci. U.S.A.* **116**, 12907 (2019).
11. M. Lindmark, A. Audzijonyte, J. Blanchard, A. Gårdmark, *Glob. Chang. Biol*. 10.1111/gcb.16341 (2022).
12. "Satellite monitoring of oil pollution in the Persian Gulf," Scanex (2018); www.scanex.ru/en/company/news/satellite-monitoring-of-oil-pollution-in-the-persian-gulf/.

10.1126/science.adf0216

RESEARCH

IN *SCIENCE* JOURNALS

Edited by
Michael Funk

CHEMISTRY

Making light work of nitrogen

Solar-driven synthesis of ammonia from atmospheric nitrogen offers an attractive approach to distributed fertilizer production and to a zero-carbon alternative fuel. Johansen *et al.* developed a photodriven transfer hydrogenation strategy in which blue-light irradiation activates Hantzsch ester, a dihydropyridine, to reduce nitrogen to ammonia (a net six-electron/six-proton reduction) in the presence of a molecular molybdenum catalyst. The net reaction is thermodynamically comparable to the industrial Haber-Bosch process, but light provides the energy that drives the reaction instead of high temperature and pressure. The oxidized pyridine by-product is potentially amenable to chemical (through hydrogenation) or electrochemical recycling. The addition of an iridium photoredox catalyst improves both the yield and rate of the process. —MRG *Sci. Adv.* 10.1126/sciadv.ade3510 (2022).

A newly developed process uses light energy to efficiently generate ammonia, which is commonly directly applied to fields as a fertilizer.

NEUROSCIENCE

A new class of antidepressant drugs

Presently available antidepressant drugs have unpleasant side effects, addictive properties, or can induce schizophrenia. Developing fast-onset antidepressants without these drawbacks is thus an important neuropharmacological goal. Sun *et al*. discovered that dissociating the serotonin transporter from nitric oxide synthase specifically reduced intercellular serotonin concentration in a brain region called the dorsal raphe nucleus. Disrupting this interaction enhanced serotonergic neuron activity in this area and dramatically promoted serotonin release into the medial prefrontal cortex, thereby producing a fast-onset antidepressant effect. A small-molecule blocker of the nitric oxide synthase–serotonin transporter interaction had a fast-onset antidepressant effect in an animal model. —PRS

Science, abo3566, this issue p. 390

MAMMALIAN EVOLUTION

Becoming diverse

Mammals have the greatest degree of morphological variation among vertebrate classes, ranging from giant whales to the tiny bumblebee bat. How they evolved this level of variation has been a persistent question, with much debate being centered around the timing and tempo of evolutionary change. Goswami *et al*. looked across a large dataset of extinct and extant mammalian skulls and found that the rate of evolutionary change peaked around the time of the Cretaceous-Paleogene boundary and has general tapered off since then (see the Perspective by Santana and Grossnickle). Certain lifestyles, such as aquatic habitats or herbivory, led to faster change, whereas in some species such as rodents, morphological change appeared to be decoupled from taxonomic diversification. —SNV

Science, abm7525, this issue p. 377;
see also add8460, p. 355

SYNTHETIC BIOLOGY

Writing genes in mirror image

Large mirror-image enzymes and RNAs are necessary to build mirror-image biology and related applications, but the synthesis of these components has remained challenging. Xu and Zhu chemically synthesized a 100-kilodalton mirror-image T7 RNA polymerase, which enabled efficient and faithful transcription of high-quality

PHOTO: DESIGN PICS INC/ALAMY STOCK PHOTO

L-RNAs as long as 2.9 kilobases. The realization of mirror-image T7 transcription is an important step in synthesizing the mirror-image ribosome toward creating functional in vitro mirror-image biomolecular systems and may provide new opportunities for practical applications in diagnostics and therapeutics. —DJ

Science, abm0646, this issue p. 405

ORGANIC CHEMISTRY

Better navigation in chemical space

Chemists typically discover reactions using a small set of relatively similar starting compounds. The conditions that work best for those compounds then get applied to numerous other, often dissimilar, compounds even if alternate conditions might improve outcomes. Angello *et al*. developed an iterative protocol of machine learning and automated synthesis to improve the baseline conditions for the venerable Suzuki-Miyaura carbon–carbon coupling reaction. Because this method sampled a broad region of chemical space and considered negative results that are rarely tracked in conventional studies, a substantial improvement in average yield was obtained. —JSY

Science, adc8743, this issue p. 399

CERAMICS

Phasing out fracture

Ceramics are not known for deforming in a plastic manner, instead tending to fracture as a response to loading. Zhang *et al*. found a method to avoid fracture and dramatically improve the ductility of silicon nitride (see the Perspective by Frankberg). The authors produced dual-phase silicon nitride samples that turned out to have coherent interfaces between the phases. This configuration allows for two sliding and two-phase transformation steps during loading that circumvent the traditional tendency of bonds to break and materials to fracture. If the mechanism works in other ceramics, then it may be a way to make them more plastic. —BG

Science, abq7490, this issue p. 371; see also ade7637, p. 359

AUTOIMMUNITY

A bacterial driver of arthritis

Autoantibodies can be detected in individuals at risk for developing rheumatoid arthritis (RA) before the development of clinical disease. The source of these autoantibodies, however, remains unclear. Chriswell *et al.* found that immunoglobulin G and A autoantibodies from individuals who are at risk for RA cross-react against gut bacteria in the Lachnospiraceae and Ruminococcaceae families. Further analysis identified a bacterial strain from the *Subdoligranulum* genus that was associated with autoantibody development. Mice colonized with this *Subdoligranulum* isolate developed arthritis with a pathology similar to human RA. These findings suggest that this *Subdoligranulum* strain may be a major contributor to RA autoantibody development. —CSM

Sci. Transl. Med. **14**, eabn5166 (2022).

CORONAVIRUS

Targeting the host instead of the virus

Despite the efficacy of vaccines against severe acute respiratory syndrome coronavirus 2 (SARS-CoV-2), there is a continuing need to develop new therapeutics to treat COVID-19. Yaron *et al*. identified multiple phosphorylation sites in a conserved region of the viral nucleocapsid (N) protein, which is critical for viral replication. Biochemical analyses identified the host kinases that sequentially phosphorylated distinct motifs in the N protein. A US Food & Drug Administration–approved drug that inhibits the first kinase in the phosphorylation sequence reduced N protein phosphorylation and blocked viral replication in vitro. —JFF

Sci. Signal. **15**, eabm0808 (2022).

IN OTHER JOURNALS

Edited by **Caroline Ash**
and **Jesse Smith**

PHOTO: IAN G DAGNALL/ALAMY STOCK PHOTO

CONSERVATION

Foraging matrix matters

Our planet has become a patchwork of landscapes made up of various types of land for humans surrounded by increasingly isolated protected areas considered land for everything else. In truth, however, nonhuman species will not stay in protected areas, nor do such areas always contain all of the habitat types required for all species. de la Torre et al. monitored over 100 Asian elephants in Peninsular Malaysia and Borneo and found that they preferred areas of secondary forest and other recently disturbed or transitional habitat types, consistent with their known foraging preferences. These regions are not well represented in protected areas, which are designed to protect the most intact forest, but they are essential for elephant survival. These results emphasize the importance of recognizing that wildlife will only persist if they are allowed to integrate into the broader landscape matrix and not be restricted to predesignated protected areas. —SNV

J. App. Ecol. 10.1111/1365-2664.14286 (2022).

Asian elephants prefer to forage in transitional habitats, but conservationists prefer to protect intact forest for elephants.

MEDICAL INFORMATICS

Digital masks for clinical records

For medical conditions associated with specific visible features, it can be helpful to keep photographs in patient records to track disease progression and aid communication among providers. Unfortunately, this can create privacy risks, and patients can be reluctant to allow uploading of photos to their medical records, especially for images of the eyes or other parts of the face. To assuage such

Deep learning can help improve the ability of autonomous vehicles (represented by the computer-rendered image shown) to navigate in adverse weather conditions.

MACHINE LEARNING

Toward all-weather autonomous driving

Adverse weather conditions such as snow, rain, or fog and driving scenarios with poor GPS signals are the main obstacles for safe and reliable positioning of autonomous vehicles and are major challenges for their practical realization. Using a geometry-aware learning technique that combines the complementary benefits of each on-board sensor (camera, lidar, and radar) under different weather conditions, Almalioglu *et al.* developed a self-supervised deep learning architecture for odometry (ego-motion estimation) that has demonstrated excellent all-weather performance and effective cross-domain generalization capabilities. This work is an important step toward safe and smooth all-weather autonomous driving. —YS

Nat. Mach. Intell. **4**, 749 (2022).

concerns, Yang *et al*. developed a "digital mask" approach to process videos of patients using a deep learning algorithm. This approach retains only disease-relevant features from the original video and irreversibly de-identifies the rest. The resulting videos cannot be de-anonymized even using machine learning, thus addressing privacy concerns while preserving their medical utility. —YN

Nat. Med. **28**, 1883 (2022).

CELL BIOLOGY

A close look at cell cycle arrest

Although the stages of the cell cycle are well understood at the molecular level, cell cycle arrest is not. A broad range of arrested cells, including senescent cells, are implicated in aging. Stallaert *et al.* used hyperplexed, single-cell imaging to follow 47 distinct cell cycle effectors in human retinal pigment epithelial cells in culture. The authors found stress-specific states of cell arrest and identified their mechanisms, but ultimately cells converged on a common molecular profile of senescence. Senescent cells had similarities to cells in G_1 phase but could escape from this state (which is sometimes thought of as irreversible) if the expression of G_1 cyclins was restored. —LBR

Mol. Syst. Biol. **18**, e11087 (2022).

STEM WORKFORCE

The tenure of stalled progress

As we enter into the academic hiring season, new data reveal stark inequalities in faculty production, retention, and gender. Wapman *et al.* examined the academic employment and doctoral education of faculty employed in the years 2011–2020 at 368 doctorate-granting universities in the United States, and found that a small number of schools were vastly overrepresented in terms of producing tenure track faculty. Network analysis further suggested that inequalities at the hiring stage are later magnified by differential rates of attrition, and that the hiring and, more importantly, the retention of women faculty has stalled. With regard to diversifying the professoriate, the data are bleak, and further reflection on these data by academic hiring committees and administrators is necessary to illuminate the opportunities for change found within. —MMc

Nature **610**, 120 (2022).

MEDICINE

Making ethanol in the gut

Nonalcoholic fatty liver disease (NAFLD) affects about one-fourth of the global population, and it has been proposed that microbially derived ethanol may be involved. Meijnikman *et al*. measured the amount of gut microbiota–derived ethanol in the portal vein and found that it was significantly higher in individuals with NAFLD who had undergone fasting. After eating, blood ethanol concentrations increased further and the liver appeared to metabolize much of it. Next, 20 individuals with NAFLD were given an alcohol dehydrogenase inhibitor, which resulted in even higher levels of ethanol in the peripheral blood. However, this response was ablated in individuals who were first treated with antibiotics, confirming a role for the gut microbiota. —GKA

Nat. Med. **28**, 2100 (2022).

FRAMEWORK MATERIALS

A soft, compacted honeycomb

Two-dimensional covalent organic frameworks (COFs) are usually assembled from rigid molecules to help ensure ordering, but "soft COFs" have been reported that have some linker flexibility. Liu *et al*. assembled a soft COF from a large amine linker bearing flexible alkyl side chains and a trigonal benzaldehyde node. Instead of forming a honeycomb lattice, the lattice formed was compacted and the hexagonal units flattened into a staircase structure through intramolecular π-stacking of aromatic rings. Rather than forming a porous material as most COFs do, imaging revealed compact layered structures containing helical structures. —PDS

J. Am. Chem. Soc. 10.1021/jacs.2c08468 (2022).

IMAGE: Y. ALMALIOGLU *ET AL.*, *NAT. MACH. INTELL.* **4**, 749 (2022).

ALSO IN *SCIENCE* JOURNALS

Edited by **Michael Funk**

CANCER MICROBIOME

A new class of bacterial genotoxins

Individuals with inflammatory bowel disease are at increased risk of developing colorectal cancer compared with the general population. The gut microbiome is among the many factors that can influence tumorigenesis, in part by modulating the immune system and producing microbial metabolites. Cao *et al*. developed a functional screen to test whether gut bacteria from patients with inflammatory bowel disease have genotoxic effects (see the Perspective by Puschhof and Sears). The authors discovered a family of DNA damage–inducing microbial metabolites called indolimines, which were produced by the Gram-negative bacteria *Morganella morganii*. In a mouse model of colon cancer, *M. morganii* exacerbated tumor burden, but a mutant form of the bacteria unable to produce indolimine did not. This diverse series of genotoxic small molecules from the human microbiome may play a role in intestinal tumorigenesis. —PNK

Science, abm3233, this issue p. 369;
see also ade6952, p. 358

AGING

Spermidine fights cancer in aging mice

Abundance of the polyamine spermidine decreases in aging mice, and supplementation can have restorative effects and extend life span. Al-Habsi *et al*. explored whether loss of spermidine might contribute to loss of antitumor immunity in aged mice. Restoration of spermidine concentrations enhanced antitumor responses stimulated by programmed death ligand-1 (PD-L1) monoclonal antibody therapy. Spermidine appeared to directly affect T cell function by increasing fatty acid oxidation. Tagged spermidine bound to components of the mitochondrial trifunctional protein complex, thus increasing fatty acid oxidation and the production of ATP. The authors propose that these effects may contribute to the effects of spermidine in promoting longevity. —LBR

Science, abj3510, this issue p. 370

ORGANIC CHEMISTRY

Light tweak to carbon–hydrogen configuration

The relative configuration of chemical bonds in a molecule often has great influence over its pharmaceutical properties. It therefore complicates drug synthesis that many readily available precursors, as well as many common reactions, can deliver one possible mutual configuration of carbon centers but not another. Zhang *et al*. report that a tungsten-based photocatalyst paired with a disulfide hydrogen transfer agent can efficiently modify the configuration of tertiary carbon–hydrogen bonds that are conventionally inert. This process, which generally, but not exclusively, favors the thermodynamic product, offers a convenient means of precisely toggling between diastereomers in complex molecules. —JSY

Science, add6852, this issue p. 383

PLANETARY SCIENCE

An insightful impact

On 24 December 2021, the seismometer for the InSight mission on Mars detected a large seismic event with a distinct signature. Posiolova *et al*. discovered that the event was caused by a meteor impact on the surface of Mars, which was confirmed by satellite observations of a newly formed 150-kilometer crater. The surface nature and size of the impact allowed Kim *et al*. to detect surface waves from the event, which have yet to be observed on Mars. These surface waves help to untangle the structure of the Martian crust, which has various amounts of volcanic and sedimentary rock, along with subsurface ice, in different regions of the planet (see the Perspective by Yang and Chen). The characteristics of the impact itself are important because they provide a seismic fingerprint of an impact event that is different from the marsquakes observed so far. —BG

Science, abq7704, abq7157,
this issue p. 412, p. 417;
see also add8574, p. 360

GENETICS

Retroviral origins of antiviral proteins

Sequences of retroviral origins are abundant in the human genome, but their functional significance remains poorly understood. Frank *et al*. identified a pool of sequences derived from retroviral envelopes (which normally facilitate viral entry into cells) that are expressed during human fetal development, viral infection, and immune stimulation (see the Perspective by Padilla Del Valle and McLaughlin). The authors hypothesized that some of these sequences encode proteins with antiviral activity by binding to and competing for cell surface receptors targeted by infectious viruses. Genetic manipulation in cell culture showed that one such protein, SUPYN, was capable of restricting infection by type D retroviruses circulating in several mammals. —DJ

Science, abq7871, this issue p. 422;
see also ade4942, p. 350

IMMUNE CELLS

Circulating iNKT cells protect

Invariant natural killer T cells (iNKTs) are tissue-resident, innate-like T cells that recognize lipid antigens and are involved in immune regulation. The heterogeneity and development of iNKT cell populations has not been well defined. Cui *et al.* used various mouse models, transcriptomics, flow cytometry, and histology to better understand iNKT subpopulations. The authors uncovered a circulating population of iNKT cells that expressed specific receptors and were distinct from conventional iNKT cells in mice and humans. This iNKT subset depended on interleukin-15–positive medullary thymic epithelial cells for development and maturation. The circulating iNKTs were highly cytotoxic and protected mice from melanoma metastasis and influenza infection. —DAE

Sci. Immunol. **7**, eabj8760 (2022).

VIROLOGY

Leukemia treatment risks viral resurgence

Cytomegalovirus (CMV) establishes a persistent, lifelong latent infection. However, various forms of immune dysregulation can result in the reactivation of CMV replication, posing a serious risk of morbidity and mortality. Wass *et al.* found that the CMV protein US28, in coordination with the host Ephrin receptor A2 (EphA2), controls Src-MAPK-c-Fos signaling, which in turn controls CMV latency. The authors show that an EphA2 inhibitor, dasatinib, results in CMV reactivation. This drug is clinically used to treat leukemia and may inadvertently reactivate CMV. Indeed, clinical data show that dasatinib treatment is associated with increased CMV-associated disease. —TGM

Sci. Adv. 10.1126/
sciadv.add1168 (2022).

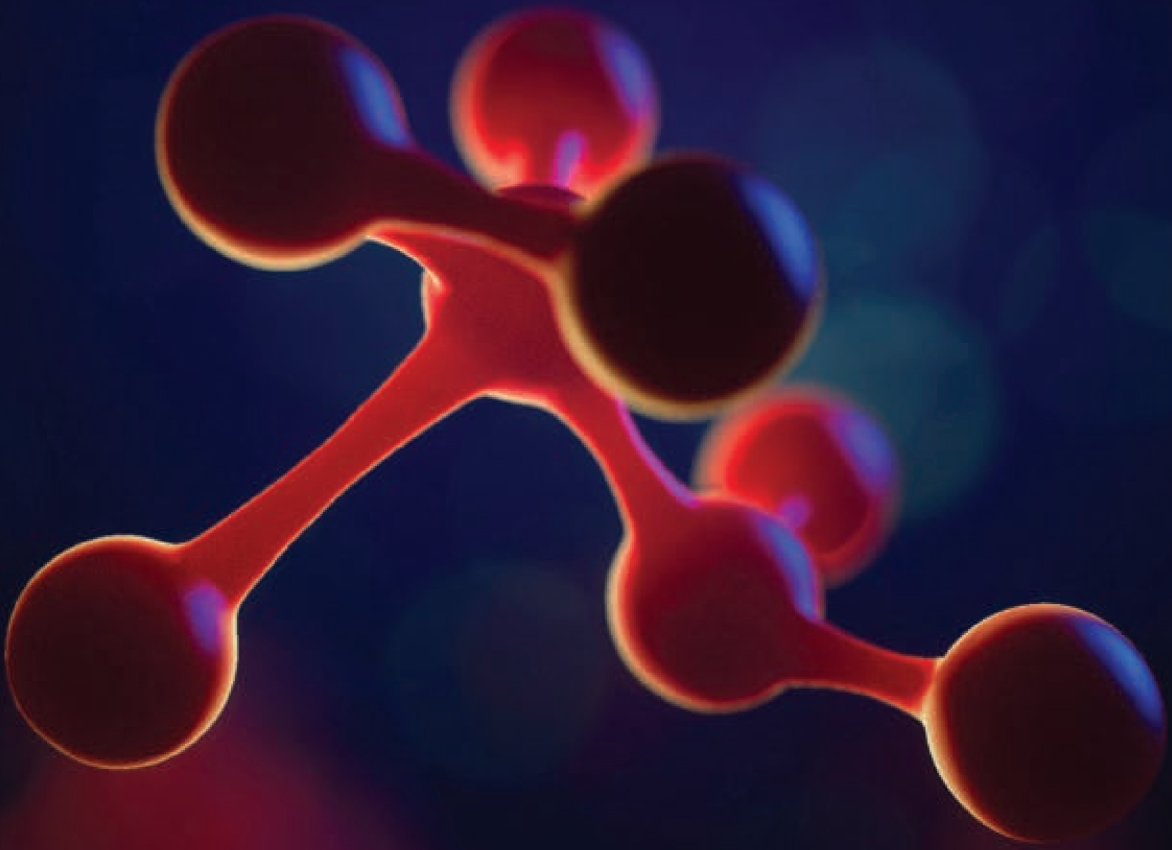

RESEARCH ARTICLE SUMMARY

CANCER MICROBIOME

Commensal microbiota from patients with inflammatory bowel disease produce genotoxic metabolites

Yiyun Cao, Joonseok Oh, Mengzhao Xue, Won Jae Huh, Jiawei Wang, Jaime A. Gonzalez-Hernandez, Tyler A. Rice, Anjelica L. Martin, Deguang Song, Jason M. Crawford, Seth B. Herzon, Noah W. Palm*

INTRODUCTION: Gut microbiota can potentially contribute to the development and progression of colorectal cancer (CRC) by producing small-molecule genotoxins. For example, select commensal *Escherichia coli* strains produce the canonical microbiota-derived genotoxin colibactin, which engenders the formation of DNA double-strand breaks (DSBs) in intestinal epithelial cells and exacerbates CRC in mouse models. Furthermore, human CRCs harbor colibactin-associated mutational signatures, implying a direct role for microbiota-induced DNA damage in CRC. However, the impacts of microbiota-derived genotoxins beyond colibactin remain largely unexplored.

RATIONALE: Given the extensive diversity of small-molecule metabolites produced by bacteria, we hypothesized that additional taxa from the human gut microbiome might produce previously undiscovered small molecules that cause DNA damage in host cells. Identifying and characterizing such genotoxins and their respective biosynthetic pathways may reveal causal roles of gut microbes in shaping host biology and disease susceptibility. Thus, we designed a large-scale electrophoresis-based DNA damage screening pipeline to evaluate the genotoxicity of a collection of more than 100 gut commensals isolated from patients with inflammatory bowel disease (IBD).

RESULTS: We identified diverse bacteria from the human microbiota whose small-molecule metabolites caused genotoxicity in both cell-free and cell-based DNA damage assays. For example, small-molecule metabolites from gram-positive bacteria (including *Clostridium perfringens* and *Clostridium ramosum* strains) and gram-negative bacteria (including multiple *Morganella morganii* strains) directly damaged DNA in cell-free assays and induced the expression of the DSB marker γ-H2AX and cell-cycle arrest in epithelial cells. However, the DNA damage patterns caused by these metabolites were distinct from colibactin-induced cross-links, and these isolates lacked the biosynthetic machinery to produce colibactin or other known genotoxins. These data thus implied the existence of previously unrecognized microbiota-derived genotoxins.

M. morganii is enriched in the gut microbiota of both IBD and CRC patients. Using a combination of comparative metabolomics and bioactivity-guided natural product-discovery techniques, we discovered a family of *M. morganii*–derived small-molecule genotoxins—termed the indolimines—that elicited DNA damage in cell-based and cell-free assays. Furthermore, we identified a previously uncharacterized bacterial decarboxylase (annotated as an aspartate aminotransferase encoded by the *aat* gene) that was essential for indolimine synthesis and constructed an isogenic *aat* mutant *M. morganii* that lacked genotoxicity in both cell-free and cell-based DNA damage assays.

Compared with the non–indolimine-producing mutant, wild-type *M. morganii* caused increased intestinal permeability and induced transcriptional signatures associated with abnormal DNA replication and intestinal epithelial cell proliferation in gnotobiotic mice. Furthermore, indolimine-producing *M. morganii* induced increased colonic tumor burden in the context of a mock microbial community in a mouse model of CRC.

CONCLUSION: By leveraging function-based assessments of the microbiome, we uncovered the existence of a broader universe of microbiota-derived small-molecule genotoxins. We found that diverse bacterial strains isolated from IBD patients exhibited DNA-damaging activities and discovered a previously undescribed family of genotoxins, termed the indolimines, produced by the IBD- and CRC-associated species *M. morganii*. Indolimine-producing *M. morganii* caused increased intestinal permeability and exacerbated colon tumorigenesis in gnotobiotic mice. Overall, these studies imply an expanded role for microbiota-derived genotoxins in shaping host biology and disease susceptibility. ■

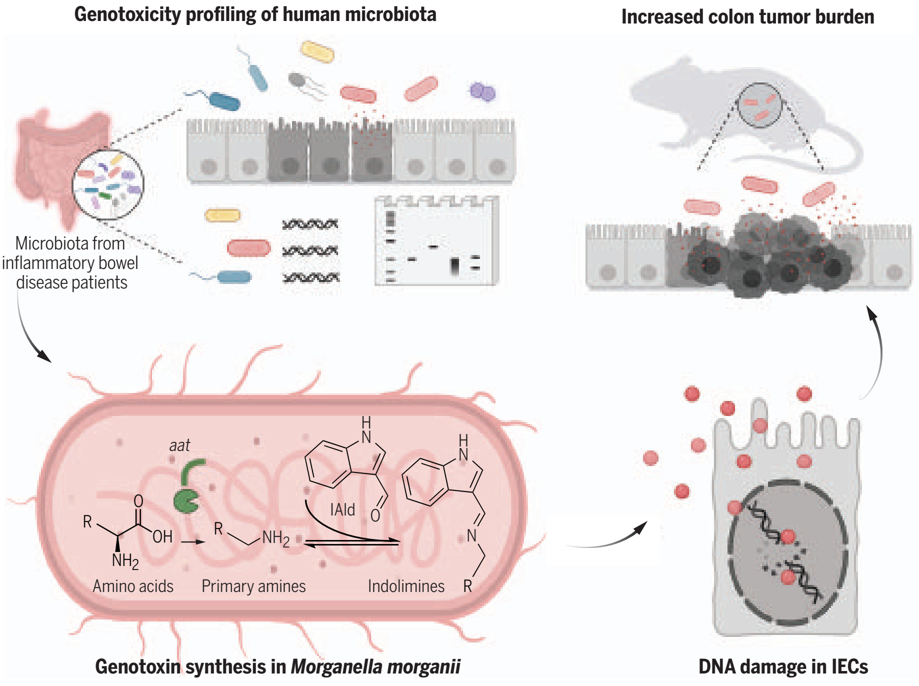

Human gut microbes isolated from IBD patients produce small-molecule genotoxins. Diverse gut microbes isolated from patients with IBD exhibit direct genotoxicity. *M. morganii* produces a family of genotoxic small molecule metabolites, termed the indolimines. Indolimine-producing *M. morganii* induces DNA damage in intestinal epithelial cells (IECs) and increased colon tumor burdens in gnotobiotic mouse models.

The list of author affiliations is available in the full article online.
*Corresponding author. Email: noah.palm@yale.edu
Cite this article as Y. Cao *et al.*, *Science* **378**, eabm3233 (2022). DOI: 10.1126/science.abm3233

S READ THE FULL ARTICLE AT
https://doi.org/10.1126/science.abm3233

RESEARCH ARTICLE

CANCER MICROBIOME

Commensal microbiota from patients with inflammatory bowel disease produce genotoxic metabolites

Yiyun Cao[1], Joonseok Oh[2,3], Mengzhao Xue[2]†, Won Jae Huh[4], Jiawei Wang[5], Jaime A. Gonzalez-Hernandez[1], Tyler A. Rice[1], Anjelica L. Martin[1], Deguang Song[1], Jason M. Crawford[2,3,6], Seth B. Herzon[2,7], Noah W. Palm[1]*

Microbiota-derived metabolites that elicit DNA damage can contribute to colorectal cancer (CRC). However, the full spectrum of genotoxic chemicals produced by indigenous gut microbes remains to be defined. We established a pipeline to systematically evaluate the genotoxicity of an extensive collection of gut commensals from inflammatory bowel disease patients. We identified isolates from divergent phylogenies whose metabolites caused DNA damage and discovered a distinctive family of genotoxins—termed the indolimines—produced by the CRC-associated species *Morganella morganii*. A non–indolimine-producing *M. morganii* mutant lacked genotoxicity and failed to exacerbate colon tumorigenesis in mice. These studies reveal the existence of a previously unexplored universe of genotoxic small molecules from the microbiome that may affect host biology in homeostasis and disease.

Colorectal cancer (CRC) is the third most common malignancy and the second leading cause of cancer deaths worldwide (*1*). Two thirds of all CRC cases occur in individuals without a family history of CRC or inherited genetic mutations predisposing an individual to CRC (*2*). Thus, environmental risk factors that promote the acquisition and accumulation of somatic-genetic and epigenetic aberrations are chief contributors to CRC development. The gut microbiome has been reported to modulate intestinal carcinogenesis through diverse mechanisms (*3*–*5*). Examples include short-chain fatty acid–producing *Clostridia* species [which induce regulatory T cells and temper inflammation–induced carcinogenesis (*6*)] and *Fusobacterium nucleatum* strains that enhance tumor growth by inducing epithelial proliferation through FadA-mediated engagement of E-cadherin and activation of Wnt/β-catenin signaling (*7*). Microbial products may also trigger DNA modifications in intestinal epithelial cells (*8*). For example, the 20-kDa *Bacteroides fragilis* toxin induces DNA damage through induction of reactive oxygen species (*9*) whereas cytolethal distending toxin from pathogenic gram-negative bacteria exhibits direct DNase activity (*10*).

Small-molecule metabolites from the microbiome may influence CRC risk by directly damaging DNA. Select *Escherichia coli* strains produce the reactive small-molecule genotoxin colibactin, which alkylates and crosslinks DNA, triggering double-strand DNA breaks (DSBs) that may facilitate intestinal carcinogenesis in mouse models (*11*–*14*). The colibactin biosynthetic machinery is encoded by a 54-kb hybrid polyketide synthase-nonribosomal peptide synthetase (PKS-NRPS) gene cluster referred to as the *pks* or *clb* locus (*11*), and the mature chemical structure of colibactin responsible for the pathway's DNA interstrand crosslinking activity was recently determined (*15*, *16*). Human CRCs also contain mutational signatures consistent with colibactin-induced DNA damage, implicating colibactin in human CRC (*17*, *18*).

The colibactin paradigm illustrates the importance of microbiota metabolite–induced DNA damage in human CRC. However, aside from colibactin the potential role of microbiota-derived small-molecule genotoxins in CRC initiation or progression remains mostly unexplored. Given the substantial complexity and diversity of metabolites produced by bacteria (*19*), we hypothesized that diverse taxa from the human gut microbiome may produce previously undiscovered small molecules that cause DNA damage in intestinal epithelial cells and contribute to the development of CRC. We established a pipeline to evaluate the genotoxicity of small-molecule metabolites derived from more than 100 phylogenetically diverse human gut microbes. We identified a diverse set of microbes that produced genotoxic small-molecule metabolites, including the gram-positive bacteria *Clostridium perfringens* and *Clostridium ramosum* and the gram-negative bacteria *Morganella morganii*. However, none of these isolates produced known genotoxins such as colibactin or encoded known genotoxin-producing biosynthetic gene clusters. We combined untargeted metabolomics and bioactivity-guided natural product discovery techniques to isolate and characterize a family of previously undescribed genotoxic metabolites—termed the indolimines—produced by CRC-associated *M. morganii.* Finally, we decoded the pathway for indolimine synthesis and constructed an isogenic non–indolimine-producing mutant of *M. morganii* that lacked genotoxicity in vitro and in vivo and failed to exacerbate colon tumorigenesis in a mouse model of CRC.

Results

Establishing a pipeline to identify genotoxic gut microbes from patients with inflammatory bowel disease

We established a pipeline to screen diverse human gut microbes based on their ability to directly damage DNA. We then applied this pipeline to a gut microbiota culture collection assembled by anaerobic culturomics of stool samples from 11 inflammatory bowel disease (IBD) patients (*20*), as IBD patients are at a considerably increased risk of developing CRC (*21*, *22*). This collection consists of 122 bacterial isolates that span 5 phyla, 9 classes, 10 orders, and 17 families, as well as multiple strains that were assigned to the same species (Fig. 1A).

To probe for genotoxicity, we evaluated the activity of each isolate in a plasmid DNA damage assay. As genotoxic metabolites such as colibactin can be recalcitrant to isolation (*15*), we focused our primary studies on co-incubation of individual bacterial isolates with linearized pUC19 plasmid DNA (Fig. 1A). This assay is based on the principle that the extent and modes of DNA damage can be assessed by electrophoresis under native and denaturing conditions (*23*): Double-stranded linearized pUC19 DNA migrates as a slow-moving band under native electrophoresis, whereas denaturing treatment separates double-stranded DNA into single-stranded DNA, leading to a band with higher mobility (Fig. 1A, L2). The formation of DNA interstrand cross-links—e.g., by colibactin—prevents unwinding under denaturing conditions, thereby resulting in a band with the same mobility as duplexed DNA (Fig. 1A, L3). Alkylation at many of the sites in DNA is known to decrease the stability of the glycoside bonds, resulting in deglycosylation and fragmentation. These damaged DNA products are detected as smaller fragments of higher mobility

---

[1]Department of Immunobiology, Yale University School of Medicine, New Haven, CT 06519, USA. [2]Department of Chemistry, Yale University, New Haven, CT 06520, USA. [3]Institute of Biomolecular Design and Discovery, Yale University, West Haven, CT 06516, USA. [4]Department of Pathology, Yale University School of Medicine, New Haven, CT 06510, USA. [5]Program of Computational Biology and Bioinformatics, Yale University, New Haven, CT 06510, USA. [6]Department of Microbial Pathogenesis, Yale University School of Medicine, New Haven, CT 06536, USA. [7]Department of Pharmacology, Yale University School of Medicine, New Haven, CT 06520, USA.
***Corresponding author. Email: noah.palm@yale.edu**
†Present address: Laboratory of Genetically Encoded Small Molecules, The Rockefeller University, New York, NY 10065, USA.

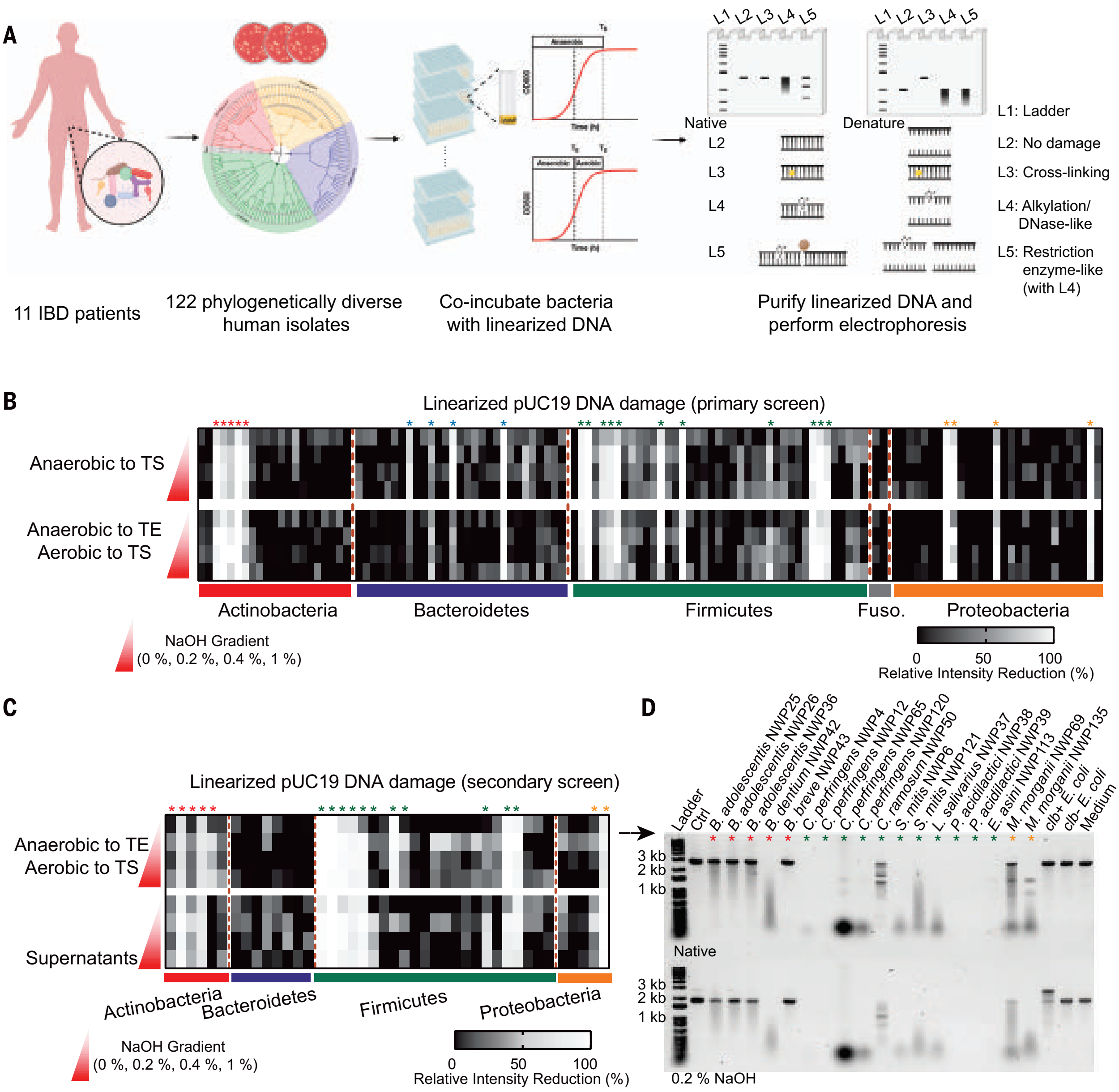

Fig. 1. Establishing a pipeline to identify genotoxic gut microbes from patients with IBD. (**A**) Overview of functional screening of gut microbes for direct genotoxicity; 122 phylogenetically diverse bacterial isolates from 11 IBD patients (shaded based on phylum: red, actinobacteria; blue, bacteroidetes; green, firmicutes; gray, fusobacteria; orange, proteobacteria) were evaluated for genotoxicity through co-incubation with plasmid DNA followed by gel electrophoresis. Bacterial growth curves for all isolates were determined through OD_{600} and individual isolates were cocultured with linearized pUC19 DNA under indicated conditions (T_E, time point of exponential phase; T_S time point of stationary phase). DNA damage was assessed with gel electrophoresis after native or denaturing treatment of purified plasmid DNA. (**B**) Diverse human gut microbes exhibited direct DNA-damaging activities ($N = 1$ independent experiments). Bacterial genotoxicity was determined by calculating the relative intensity reduction [(RIR) percent] of linearized pUC19 DNA bands after co-incubation with 122 diverse human gut bacteria [as outlined in (A)] under indicated conditions as compared with medium-only controls. Linearized pUC19 DNA was then purified through column purification and treated with or without gradient NaOH (0%, 0.2%, 0.4%, and 1%) before evaluating DNA integrity through gel electrophoresis. The 24 selected putative genotoxic isolates were labeled with asterisks and colors were assigned based on phylum: red, actinobacteria; blue, bacteroidetes; green, firmicutes; orange, proteobacteria. (**C**) Selected isolates consistently exhibited direct DNA-damaging activities under other culture conditions ($N = 1$). RIR percent of linearized pUC19 DNA bands after co-incubation with live bacteria or supernatants (SUP) of 42 isolates [24 genotoxic isolates selected from (B) and 18 phylogenetically related nongenotoxic isolates] under indicated conditions as compared with medium-only controls. Linearized pUC19 DNA was then purified through column purification and treated with or without gradient NaOH (0%, 0.2%, 0.4%, and 1%) before evaluating DNA integrity through gel electrophoresis. The 18 selected putative genotoxic isolates were labeled with asterisks and colors were assigned based on phylum: red, actinobacteria; green, firmicutes; orange, proteobacteria. (**D**) Representative image of gel electrophoresis for 18 selected genotoxic isolates ($N = 2$). Linearized pUC19 DNA damage was evaluated after co-incubation with 18 selected genotoxic isolates from (C). Column-purified DNA was treated with or without 0.2% NaOH before gel electrophoresis. Ctrl, nontreated linearized pUC19 DNA; *clb*+ *E. coli*, colibactin-producing *E. coli*; *clb*− *E. coli*, non–colibactin-producing *E. coli*; Medium, medium-alone treated linearized pUC19 DNA.

following electrophoresis (24) (Fig. 1A, L4). Extensive DNA damage, for example, by DNase-mediated degradation, results in a loss of DNA even under native conditions (Fig. 1A, L4). Finally, DNA damage induced by restriction enzyme–like molecules produces multiple bands under native conditions and even smaller fragments under denaturing conditions when combined with damage induced by alkylation or DNase-like molecules (Fig. 1A, L5).

We confirmed that plasmid DNA was stable under diverse anaerobic cultivation conditions including incubation in Gifu medium, which supports the growth of all isolates in our collections (fig. S1). To minimize the damage caused by bacterial DNases that are often produced in the stationary phase of bacterial growth, we measured growth curves for all 122 isolates in our collection and established a time point of exponential phase (T_E) and time point of stationary phase (T_S) (table S1). The isolates were then clustered into seven groups that exhibited similar growth dynamics (fig. S2). We selected two culture conditions for the initial screening: anaerobic co-incubation with DNA to T_S, or anaerobic co-incubation with DNA to T_E followed by aerobic co-incubation to T_S to approximate the oxygen stress encountered in an inflammatory gut environment. Finally, we purified the linearized pUC19 DNA from the bacterial cultures through column purification and performed gel electrophoresis under native and gradient denaturing conditions (0%, 0.2%, 0.4%, and 1% NaOH) (Fig. 1A and fig. S3, A to G).

We used the relative intensity reduction [(RIR), percent] of DNA after co-incubation with bacteria as a general measure of bacterially induced DNA damage (Fig. 1B and table S2). We found that diverse gut microbes exhibited DNA-damaging activities, which suggests that microbiota-mediated genotoxicity may be more widespread than previously acknowledged. Although previously described microbiota-derived genotoxins discovered in a case-by-case manner are primarily produced by gram-negative bacteria (e.g., *E. coli*, *B. fragilis*, *and Klebsiella oxytoca*) (25, 26), we observed that multiple gram-positive microbes from the phyla *Actinobacteria* and *Firmicutes* also caused substantial DNA damage. DNA-damaging activity was largely independent of culture conditions, although select microbes displayed varied genotoxicity in the presence versus absence of oxygen stress (Fig. 1B and table S2).

We selected 24 isolates that exhibited strong DNA-damaging activities in the primary screen and 18 phylogenetically related nongenotoxic isolates for evaluation in a secondary screening (Fig. 1C). We reestablished precise growth curves for each isolate (table S1) and rescreened all 42 isolates under four distinct culture conditions, including co-incubation of DNA with bacterial supernatants collected from anaerobic cultures at T_S (fig. S3, H to J, and table S2). Eighteen isolates that caused DNA damage in our primary screening also exhibited strong genotoxicity upon secondary screening (Fig. 1C and fig. S3, H to J). Moreover, supernatants from most of the selected genotoxic isolates also caused considerable RIR (percent) that were often comparable to co-incubation with live bacteria (Fig. 1C and fig. S3, H to J). Unlike the interstrand cross-links induced by a colibactin-producing *E. coli* strain (K-12 BW25113 containing the *clb* locus, designated as *clb*+ *E. coli*), these 18 isolates exhibited distinct DNA damage patterns after co-incubation with linearized pUC19 DNA. By contrast, a non–colibactin-producing *E. coli* strain (K-12 BW25113 with an empty bacterial artificial chromosome, designated as *clb*– *E. coli*) or medium alone did not induce substantial DNA damage (Fig. 1D and fig. S3K). Notably, most of the newly identified genotoxic isolates induced alkylation or DNase-like DNA damage patterns; we also observed evidence of DNA damage under native gel electrophoresis.

Gut microbes from patients with IBD produce small-molecule metabolites that can induce DNA damage

To determine whether the 18 putative genotoxic bacterial isolates we identified through electrophoresis-based screening (Fig. 1 and fig. S4A) produce genotoxic small molecules that cause DNA damage in human cells, we separated their supernatants (SUP) into small- and large-molecular weight fractions (<3 kDa SUP and >3 kDa SUP, respectively), and evaluated the genotoxicity of these fractions using HeLa cells. Small-molecule metabolites from most selected isolates, including multiple strains of *Bifidobacterium adolescentis* (three isolates), *C. perfringens* (four isolates), *C. ramosum* (phylogenetically related to *C. perfringens*), and *M. morganii* (two isolates), induced increased γ-H2AX, a marker of DNA double-strand breaks (DSBs) (27) (fig. S4B). As previously reported, supernatants from *clb*+ *E. coli* failed to induce γ-H2AX, which instead required live bacterial infection (11) (fig. S4B). Whereas both small and large molecules from *B. adolescentis* and *C. perfringens* induced increased γ-H2AX, only small-molecule metabolites from *C. ramosum* and *M. morganii* exhibited genotoxicity (fig. S4, B and C). Small-molecule metabolites from *B. adolescentis* and *B. dentium* induced increased apoptosis and necrosis, whereas small-molecule metabolites from all other isolates had minimal impacts on cell viability as measured by cell size and granularity (fig. S4D), Annexin V, or 7-AAD (fig. S4, E to G). Although large molecules from *C. perfringens* induced substantial cell death, likely a result of the effects of clostridial toxins (28), small-molecule metabolites from *C. perfringens* caused DNA damage without triggering substantial cell death (fig. S4, B to G). On the basis of these results, we selected *C. perfringens*, *C. ramosum*, and *M. morganii* for further study and confirmed that small-molecule metabolites from these strains induced γ-H2AX in HeLa cells, albeit at a reduced level compared with the well-known DNA-crosslinking chemical cisplatin (Fig. 2A). Small-molecule metabolites from *C. perfringens*, *C. ramosum*, and *M. morganii* also induced cell cycle arrest in HeLa cells (Fig. 2B), further implicating these taxa as potential genotoxin producers.

To enrich genotoxic small molecules, we performed ethyl acetate extractions using supernatants and found that extracts from *C. perfringens* (NWP4), *C. ramosum* (NWP50), *M. morganii* (NWP135), and *clb*+ *E. coli* cultures nicked circular pUC19 plasmid DNA, whereas extracts from *clb*– *E. coli* or medium alone had negligible impacts on DNA integrity (Fig. 2C). Similarly, ethyl acetate extracts from genotoxic species induced γ-H2AX expression in HeLa, HCT116, and MC38 cells (Fig. 2D and fig. S4H) and caused tailing in an alkaline comet unwinding assay (Fig. 2E).

Recent meta analyses have identified cross-cohort microbial signatures associated with CRC, including enrichment in *Clostridiaceae*, *Erysipelotrichaceae*, and *M. morganii* (29, 30). Notably, both *C. perfringens* and *M. morganii* were also increased in IBD patients (specifically in CD patients) compared with healthy controls in data from the Human Microbiome Project (Fig. 2F), suggesting potential roles in IBD patients who are at an increased risk of CRC diagnosis (21, 22). Overall, *M. morganii* is enriched in fecal samples from both IBD and CRC patients and the genotoxicity of this species is restricted to its small-molecule fractions. Therefore, we prioritized *M. morganii* for further genotoxin identification and characterization.

M. morganii *produces genotoxins that are distinct from colibactin*

The biosynthetic machinery involved in the production of microbial metabolites, including previously characterized small-molecule genotoxins, is often encoded by biosynthetic gene clusters (BGCs) (31). For example, colibactin production is encoded by a multimodular PKS-NRPS pathway in *E. coli* (11, 32) and tilimycin and tilivalline are encoded by an NRPS pathway in *K. oxytoca* (26). However, BGC analyses of genotoxic *C. perfringens*, C. *ramosum*, and *M. morganii* using antiSMASH (33) failed to detect any known genotoxin-encoding BGCs (fig. S5A and table S3). While *M. morganii* harbors one NRPS/PKS gene cluster, this BGC is entirely distinct from the *clb* genomic island and *M. morganii* lacks key genes involved in colibactin synthesis, such as *clbI* and *clbP* (fig. S5B) (34, 35). This is consistent with recent

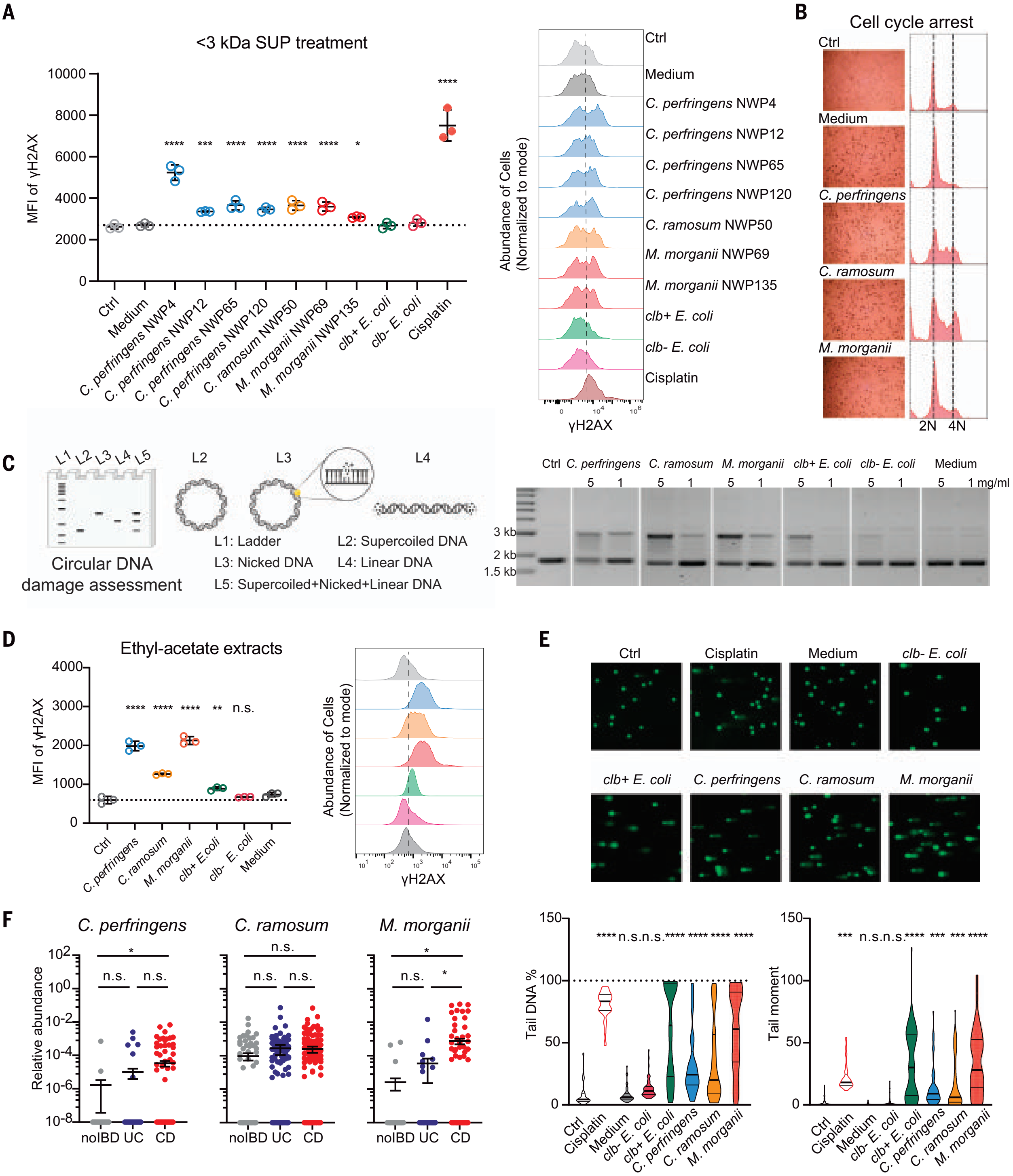

Fig. 2. Small-molecule metabolites produced by gut microbes induce DNA damage. (**A**) Geometric mean fluorescence intensity (MFI) and representative histograms of γ-H2AX staining of HeLa cells treated with 40% (v/v) PBS (ctrl), <3 kDa SUP (small-molecule supernatants) of medium, *C. perfringens*, *C. ramosum*, *M. morganii*, *clb*+ *E. coli*, *clb*− *E. coli* isolates, or cisplatin for 5 to 6 hours (n = 3 replicates, N = 3 independent experiments). *$P < 0.05$; ***$P < 0.001$; ****$P < 0.0001$, one-way analysis of variance (ANOVA). (**B**) Representative data of cell cycle arrest evaluated by propidium iodide (PI) staining (n = 3, N = 2). HeLa cells were treated with 40% (v/v) PBS or <3 kDa SUP of medium, *C. perfringens*, *C. ramosum*, or *M. morganii* isolates. (**C**) Assessment of circular pUC19 DNA damage after co-incubation with ethyl-acetate extracts of *C. perfringens*, *C. ramosum*, *M. morganii*, *clb*+ *E. coli*, *clb*− *E. coli* supernatants, or medium for 5 to 6 hours (N = 2). Ctrl, control pUC19 DNA in TE buffer. (**D**) MFI of γ-H2AX staining of HeLa cells treated with PBS (ctrl), 5 mg/ml bacterial or medium extracts for 5 to 6 hours (n = 3, N = 2). n.s., not significant; **$P < 0.01$; ****$P < 0.0001$, one-way ANOVA. (**E**) Comet assay for genomic DNA damage evaluation. Single-cell gel electrophoresis was performed after treating HeLa cells with PBS (ctrl), cisplatin, bacterial, or medium extracts for 5 to 6 hours (n = 49, N = 1). ***$P < 0.001$; ****$P < 0.0001$, one-way ANOVA. (**F**) Relative abundance of *C. perfringens*, *C. ramosum*, and *M. morganii* in data from the Human Microbiome Project. noIBD, healthy controls (n = 429); UC, ulcerative colitis patients (n = 459); CD, Crohn's disease patients (n = 750). *$P < 0.05$, one-way ANOVA. Data are means ± SEM.

analyses of 69 publicly available *Morganella* genomes, which suggest that *clb* genes are absent in *Morganella* genomes (*36*). The genotoxicity caused by *M. morganii* is also distinct from that caused by colibactin—whereas *clb+ E. coli* caused DNA crosslinking, DNA exposed to *M. morganii* displayed a smearing pattern under both native and denaturing conditions (fig. S5C). Finally, as previously reported, colibactin-induced γ-H2AX required live bacterial infection, and supernatants from *clb+ E. coli* failed to induce substantial increases in γ-H2AX in cell lines, likely as a result of documented colibactin instability (*11*, *37*). By contrast, *M. morganii* supernatants and small-molecule metabolites elicited substantial increases in γ-H2AX (Fig. 2 and fig. S4). Together, these data suggest that *M. morganii* produces previously undescribed genotoxins that are distinct from colibactin and are readily diffusible.

Isolation and identification of a family of genotoxins derived from M. morganii

To identify specific genotoxins produced by *M. morganii*, we employed a combination of ultraperformance liquid chromatography quadrupole time-of-flight mass spectrometry (UPLC-QTOF-MS)-based untargeted metabolomics, and bioactivity-guided fractionation using small-scale cultures, followed by large-scale cultivation and isolation for unambiguous structure elucidation and genotoxicity analyses (Fig. 3A). We generated an initial candidate ion list of the most abundant *M. morganii*-derived metabolites relative to Gifu medium control (~100 ion features; table S4) through comparative metabolomics. We then performed two rounds of activity-guided fractionation using preparative high-performance liquid chromatography (HPLC) and a circular pUC19 plasmid-based genotoxicity assay, then profiled the resulting fractions and subfractions using UPLC-QTOF-MS-based metabolomics (fig. S6, A and B). To identify potential genotoxins, we excluded ions present in inactive fractions from the initial ion list and ultimately identified four ion features (I to IV) as potential genotoxic hits (Fig. 3B and table S4). To enable structural elucidation and genotoxic activity assessment for these compounds, we performed large-scale cultivation (18 liters) and ethyl acetate extraction of *M. morganii* supernatant based on previously observed retention times that imply relatively low polarity of the compounds of interest. The crude extract was subjected to two rounds of HPLC to generate four semipure fractions enriched in the four target ion features (F1 to F4 enriched in I to IV, respectively). One of these fractions (F2) exhibited dose-dependent genotoxicity in a circular pUC19 plasmid-based genotoxicity assay (Fig. 3C). Based on UPLC-QTOF-MS analyses, F2 was primarily comprised of two metabolites with mass/charge ratio (*m/z*) values of 215.1543 (compound **1**, target ion feature II) and 234.1852 (compound **2**, a metabolite that was absent from the initial ion list but was co-enriched during extraction and fractionation) at a ratio of 4:6 (fig. S6C). This fraction was recalcitrant to further purification by preparative HPLC using diverse combinations of stationary and mobile phases. Thus, the chemical structures of the two components were characterized as a mixture using one- and two-dimensional nuclear magnetic resonance (NMR) spectroscopy analyses (Fig. 3D and fig. S7). Compound **1** consists of a conjugation of indole-3-aldehyde (IAld) and the primary amine isoamylamine, forming a functional imine group. Thus, we termed this previously undescribed metabolite indolimine-214.

To confirm which compound exerted the observed genotoxicity, we synthesized both indolimine-214 (**1**) and compound **2**. Formation of the reversible imine functional group in compounds such as indolimine-214 (**1**) varies depending on the chemical environment (e.g., pH, temperature, solvent, and solutes). Therefore, we fractionated fresh synthetic material and assessed the purity of **1** in each fraction using ^{1}H NMR for genotoxicity analysis (fig. S6D). Nonetheless, neither synthetic indolimine-214 (**1**) nor compound **2** alone (up to 1 mg/ml) induced DNA damage in the circular pUC19 plasmid-based genotoxicity assay. However, the mixture of indolimine-214 (**1**) and compound **2** elicited dose-dependent DNA damage (fig. S6D), suggesting that the presence of compound **2** may serve as an adjuvant for indolimine-214 (**1**) (target ion feature II) in the cell-free assay. In a more biologically relevant context, we assessed the genotoxicity of pure synthetic compounds in HeLa cells and found that indolimine-214 (**1**) alone—but not compound **2**—triggered increased γ-H2AX in a dose-dependent manner (Fig. 3E) and induced tailing in an alkaline comet unwinding assay (Fig. 3F). Furthermore, the genotoxicity of synthetic indolimine-214 (**1**) correlated directly with its purity (i.e., in relation to its hydrolytic degradation products; fig. S6E).

Using UPLC-QTOF-MS–based quantification, we found that *M. morganii* produces a high level of indolimine-214 (**1**) in vitro (~40 μg/ml; fig. S8A), which is comparable to the concentrations of the synthetic compound that induced genotoxicity in HeLa cells (Fig. 3, E to F). By contrast, indolimine-214 (**1**) was undetectable in supernatants from wild-type (WT) colibactin-producing (*clbP*+) or isogenic *clbP* mutant non–colibactin-producing (*clbP*−) *E. coli* NC101 strains (*38*) (fig. S8A). This is consistent with the observation that *M. morganii*-induced DNA damage was distinct from the damage caused by colibactin-producing *E. coli* (fig. S5). Cecal contents from mice colonized with *M. morganii*—but not those colonized by *clbP*− *E. coli* NC101—also contained high levels of indolimine-214 (**1**) (fig. S8B). Moreover, in the process of quantifying cecal indolimine-214 (**1**), we observed the presence of two additional new indolimines with similar structures in *M. morganii*-colonized mice: conjugates of IAld with either isobutylamine (indolimine-200, compound **3**, *m/z* 201.1386) or phenethylamine (indolimine-248, compound **4**, *m/z* 249.1386) (Fig. 3G, fig. S8C, and fig. S9). These additional indolimines were also detected within in vitro *M. morganii* bacterial cultures, but not *clbP*− *E. coli* NC101 cultures, as confirmed by synthetic standards (fig. S8D). Finally, synthetic indolimine-200 (**3**) and indolimine-248 (**4**) also triggered increased γ-H2AX in HeLa cells in a dose-dependent manner (Fig. 3H). Taken together, these data show that *M. morganii* produces a family of genotoxic indolimines both in vitro and in vivo.

A previously uncharacterized bacterial decarboxylase is necessary for indolimine synthesis

All *M. morganii*-derived indolimines contain a functional imine group, which is likely derived from the spontaneous condensation of a primary amine (isoamylamine, isobutylamine, and phenethylamine) and the aldehyde of indole-3-aldehyde (IAld) (Fig. 4A). Primary amines are microbial metabolites that can be synthesized from amino acids through a one-step reaction mediated by bacterial decarboxylases (*39*). Based on whole-genome sequencing, *M. morganii* NWP135 encoded 18 predicted decarboxylases, including three decarboxylases (Peg1085, Peg1320, and Peg3098) that were partially homologous to a previously characterized valine decarboxylase from *Streptomyces viridifaciens* (*39*) (Fig. 4B and table S5). We transformed codon-optimized DNA sequences of these three candidate decarboxylases into *E. coli*, induced protein expression with IPTG, and fed each culture with IAld and the relevant amino acid precursors (leucine, valine, or phenylalanine). Peg1085—annotated as pyridoxal-dependent decarboxylase or aspartate aminotransferase (AAT) superfamily (fold type I) in NCBI (Fig. 4B and table S5)—expression in *E. coli* enabled robust production of indolimine-214 (**1**), indolimine-200 (**3**), and indolimine-248 (**4**) based on QTOF-MS identification (Fig. 4C). Therefore, the *aat* gene encoding AAT_I (Peg1085) enables indolimine synthesis.

To evaluate whether the *aat* gene is necessary for indolimine synthesis in *M. morganii*, we constructed a random mutagenesis library of *M. morganii* NWP135 using EZ-Tn5 transposomes and isolated an isogenic *aat* mutant (*40*) (Fig. 5A). Briefly, after optimizing transposome electrotransformation, we picked ~16,000 colonies and mapped the transposon insertion sites by combining combinatorial

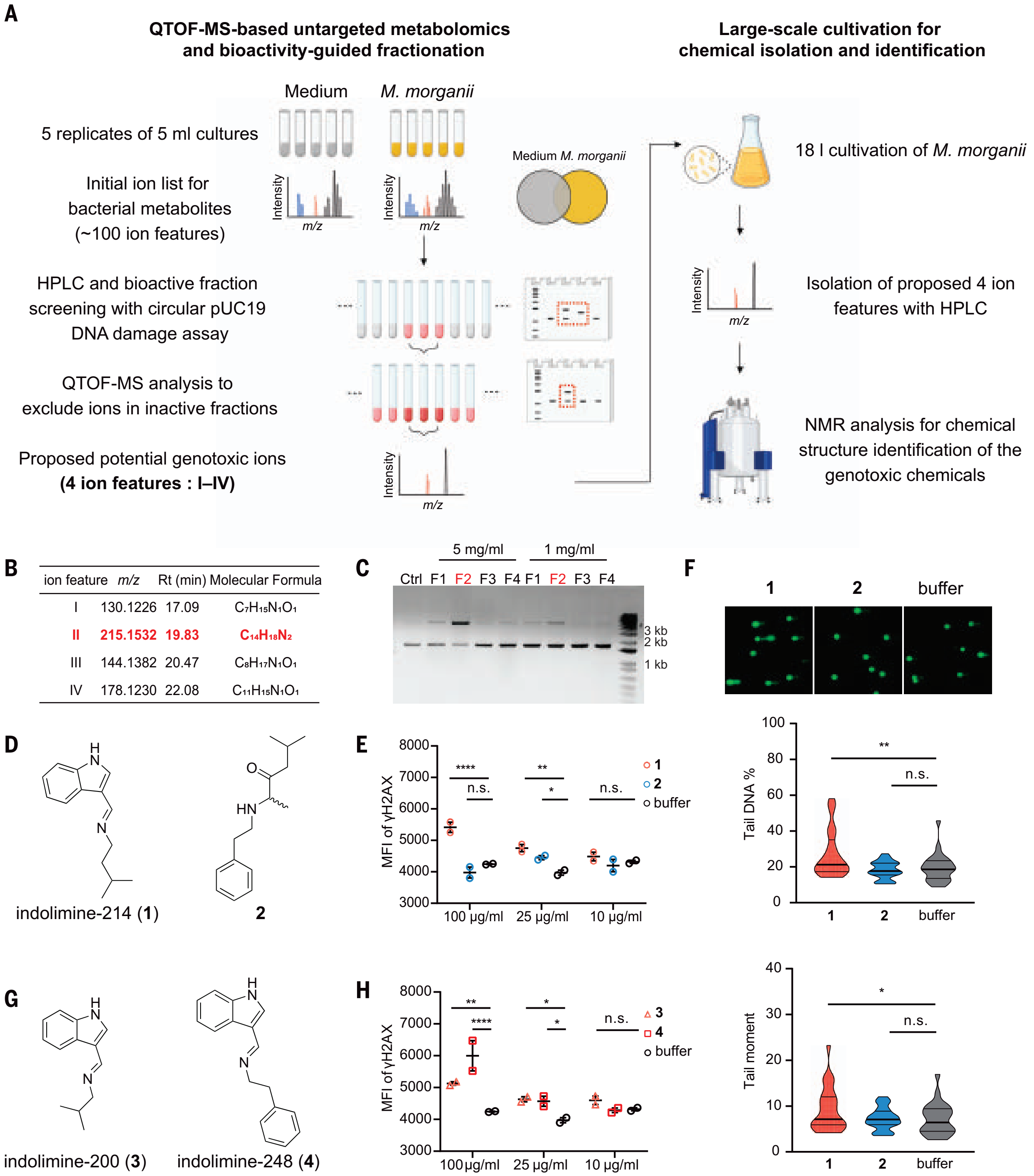

Fig. 3. Isolation and identification of a family of genotoxic metabolites derived from *M. morganii*. (**A**) Overview of isolation and identification of genotoxins derived from *M. morganii*. (**B**) Four proposed candidate ion features initially detected from *M. morganii* bacterial cultures. Rt, retention time. (**C**) Assessment of circular pUC19 DNA damage after co-incubation overnight with F1 to F4 fractions enriched with ion features I to IV, respectively ($N = 1$). Ctrl, control pUC19 DNA in TE buffer. (**D**) Chemical structures of compounds indolimine-214 (**1**) and **2**. (**E**) MFI of γ-H2AX staining of HeLa cells treated with synthetic compounds at indicated concentrations for 5 hours ($n = 2$, $N = 3$). n.s., not significant; $*P < 0.05$; $**P < 0.01$; $****P < 0.0001$, two-way ANOVA. (**F**) Single-cell genomic DNA comets in HeLa cells after treatment with 100 μg/ml synthetic compounds for 5 to 6 hours ($n = 25$, $N = 1$). $*P < 0.05$; $**P < 0.01$, one-way ANOVA. (**G**) Chemical structures of compounds indolimine-200 (**3**) and indolimine-248 (**4**). (**H**) MFI of γ-H2AX staining of HeLa cells treated with synthetic compounds at indicated concentrations for 5 hours ($n = 2$, $N = 2$). $*P < 0.05$; $**P < 0.01$; $****P < 0.0001$, two-way ANOVA. Data are means ± SEM.

pooling and transposon sequencing (Tn-Seq) using custom primers adapted from Knockout Sudoku (fig. S10A and table S6) (*41*, *42*). We identified one mutant strain (*aat*– *M. morganii*) with a transposon insertion 7 base pairs (bp) after the *aat* start codon (*aat*–; Fig. 5B and fig. S10B). As compared with WT (*aat*+) *M. morganii*, *aat*– *M. morganii* failed to produce indolimines (Fig. 5C) despite exhibiting normal growth dynamics (Fig. 5D). *aat*– *M. morganii* also failed to induce DNA damage in a cell-free linearized plasmid DNA electrophoresis assay (Fig. 5E) or cell-based γ-H2AX assay (Fig. 5F) as compared with *aat*+ *M. morganii*. Therefore, the *aat* gene is essential

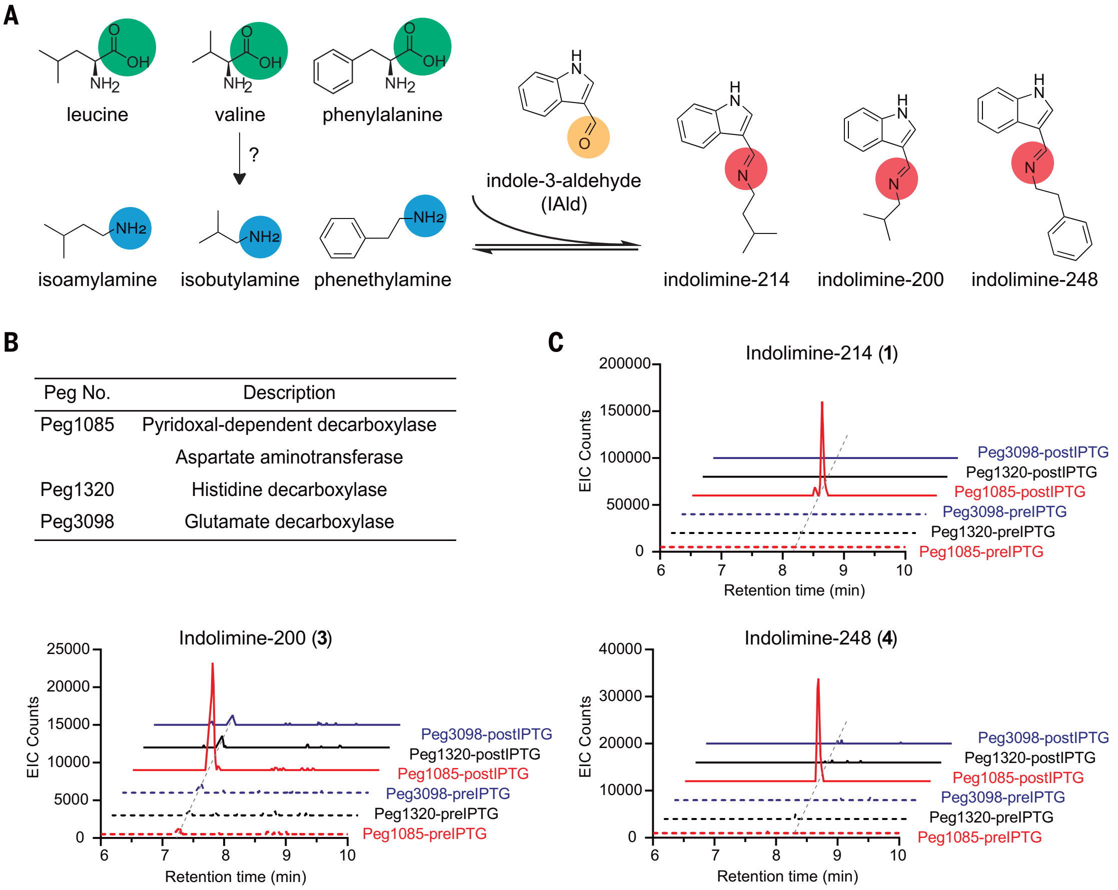

Peg No.	Description
Peg1085	Pyridoxal-dependent decarboxylase
	Aspartate aminotransferase
Peg1320	Histidine decarboxylase
Peg3098	Glutamate decarboxylase

Fig. 4. *M. morganii* decarboxylase encoded by the *aat* gene enables indolimine synthesis. (**A**) Proposed biosynthesis of indolimines in *M. morganii*. (**B**) Candidate proteins in *M. morganii* NWP135 with significant orthology to valine decarboxylase. Peg, protein encoding gene. (**C**) QTOF-MS identification of indolimine-214 (**1**), indolimine-200 (**3**), and indolimine-248 (**4**) in *E. coli* BL21(DE3) (*N* = 2). *E. coli* cells were separately transformed with the plasmid pET28-Peg harboring codon-optimized DNA sequences of Peg1085, Peg1320, or Peg3098. Indolimines were detected after IPTG induction and feeding with precursors (IAld and leucine, valine and phenylalanine, respectively). preIPTG, bacterial supernatants before IPTG induction; post-IPTG, bacterial supernatants after IPTG induction and precursor feeding.

for indolimine synthesis and *M. morganii*–induced genotoxicity.

Indolimine-producing M. morganii *induces increased gut permeability and exacerbates colon tumor burden in gnotobiotic mice*

To evaluate the impacts of *M. morganii*–derived indolimines in vivo, we first compared the effects of *aat*+ and *aat*– *M. morganii* strains on the intestinal epithelium using monocolonized mice. We found that mice colonized with *aat*+ *M. morganii* and fed IAld and leucine (precursors of indolimine-214) exhibited significantly increased intestinal permeability as compared with *aat*– *M. morganii*–colonized mice (Fig. 6A). Furthermore, RNA-seq of colonic intestinal epithelial cells and gene ontology analyses of differentially expressed genes revealed an increased expression of genes involved in cell cycle regulation, chromosome segregation, and DNA biosynthesis in mice colonized with *aat*+ *M. morganii* (Fig. 6B, fig. S10, C and D, and table S7). Together, these data suggest that the indolimines may cause abnormal DNA replication and IEC proliferation in vivo.

We next evaluated whether indolimine-producing *aat*+ and non–indolimine-producing *aat*– *M. morganii* strains induced differential inflammatory responses, with WT colibactin-producing *clbP*+ and non–colibactin-producing *clbP*– *E. coli* NC101 strains (*38*) as controls (fig. S11A). We found that all groups of monocolonized mice exhibited similar levels of bacterial colonization and roughly equivalent inflammatory responses after treatment with dextran sulfate sodium (DSS) (fig. S11, B to F), indicating that genotoxin production did not significantly alter bacterial colonization or gross inflammatory phenotypes in a model of acute colitis.

To test the potential effects of indolimine production on colon tumorigenesis, we colonized gnotobiotic mice with *aat*+ *M. morganii* or *aat*– *M. morganii* in the context of a mock community of human gut microbes, followed by treatment with azoxymethane (AOM) and three cycles of DSS (Fig. 6C). We selected seven nongenotoxic human gut isolates based on our prior in vitro cell-free genotoxicity screening (Fig. 1 and fig. S11G) to construct a mock community (Geno- community) and used WT colibactin-producing *clbP*+ or its isogenic mutant non–colibactin-producing *clbP*– *E. coli* NC101 strains (*38*) as genotoxin-producing or non–genotoxin-producing positive and negative controls (Fig. 6C). As expected, colonization with *clbP*+ *E. coli* NC101 induced increased colorectal tumor burden as compared with *clbP*– *E. coli* NC101; similarly, mice colonized with indolimine-producing *aat*+ *M. morganii* also exhibited an increased number of tumors and tumor scores (indicating overall tumor burden) as compared with mice colonized with non–indolimine-producing *aat*– *M. morganii* (Fig. 6D and fig. S11H). Moreover, mice colonized with *aat*+ *M. morganii* exhibited an increased ratio of adenomatous lesions with high-grade dysplasia (Fig. 6E). Nonetheless, mice colonized with *aat*+ or *aat*– *M. morganii* exhibited similar levels of *M. morganii* colonization (fig. S11I) and intestinal inflammation, as measured by colon length (fig. S11J), levels of fecal lipocalin 2 (fig. S11K) and histopathology (fig. S11L). These data suggest that genotoxic indolimine-producing *aat*+ *M. morganii* exacerbates colon tumorigenesis in this model, but does not elicit substantial

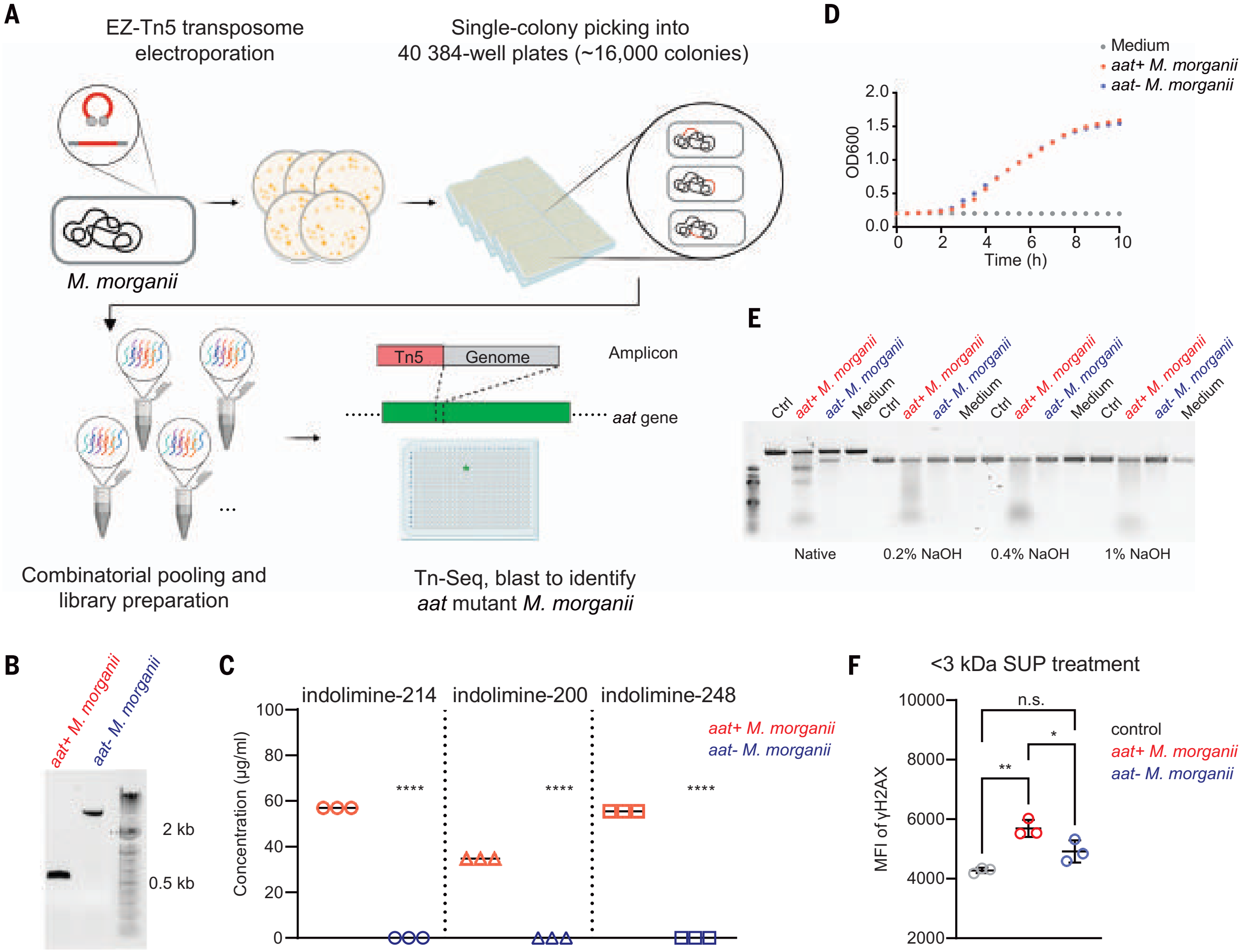

Fig. 5. An isogenic *M. morganii aat* mutant fails to produce indolimines and lacks genotoxicity in vitro. (**A**) Schematic pipeline of random mutagenesis library construction and mutant identification. (**B**) Gel result of PCR products of *aat* gene in *aat*– or *aat*+ *M. morganii* ($N = 2$). (**C**) QTOF-MS quantification of indolimine-214 (**1**), indolimine-200 (**3**), and indolimine-248 (**4**) in bacterial supernatants of *aat*+ *M. morganii* or *aat*– *M. morganii* ($n = 3$, $N = 2$). $^{****}P < 0.0001$, Student's t test. (**D**) Growth curves of *aat*+ *M. morganii* or *aat*– *M. morganii* ($n = 3$, $N = 1$). (**E**) Gel electrophoresis of cell-free DNA damage assay ($N = 2$). Linearized pUC19 DNA was co-incubated with medium, *aat*+ *M. morganii*, or *aat*– *M. morganii* for 7 to 8 hours, isolated through column purification and treated with or without NaOH (0%, 0.2%, 0.4%, and 1%) before evaluating DNA integrity through gel electrophoresis. (**F**) MFI of γ-H2AX in HeLa cells treated with 40% (v/v) <3 kDa SUP of *aat*+ *M. morganii*, or *aat*– *M. morganii* for 5 to 6 hours ($n = 3$, $N = 2$). n.s., not significant; $^{*}P < 0.05$; $^{**}P < 0.01$, one-way ANOVA. Data are means ± SEM.

increases in intestinal inflammation as compared with a nongenotoxic control.

Finally, we mined the Cancer Microbiome database (*43*) and found that *Morganella* exhibited increased prevalence or abundance in primary gastrointestinal (GI) tumors, including colon adenocarcinomas (TCGA-COAD), rectum adenocarcinomas (TCGA-READ), and stomach adenocarcinomas (TCGA-STAD), as compared with multiple non-GI tumors (fig. S12A). *Morganella* was also enriched in tumors from TCGA-READ and TCGA-STAD as compared with adjacent solid normal tissues (fig. S12B), consistent with a recent report that *Morganella* is enriched in cancerous tissues as compared with luminal contents (*44*). Notably, we also found that *aat* was conserved across nearly all *M. morganii* strains with full genome sequences in the NCBI database (51 of 52 genomes; fig. S12C), suggesting that indolimine production may be a conserved feature of *M. morganii*. Overall, our data—in combination with prior reports—suggest that genotoxic indolimines from *M. morganii* may serve as tumor-inducing factors in humans.

Discussion

Aside from a small number of case studies (*26*, *45*), the taxonomic distribution and repertoire of small-molecule genotoxins produced by microbiota remain mostly unexplored. We undertook a systematic evaluation of the genotoxicity of a diverse selection of human gut microbes based on prior evidence that colibactin-producing *E. coli* induces DNA damage and facilitates intestinal tumorigenesis (*14*). Through our investigation, we (i) found that diverse taxa from the human gut microbiota exhibited genotoxicity; (ii) identified and characterized a previously undescribed family of genotoxic *M. morganii*-derived small molecules termed the indolimines; (iii) decoded the indolimine production pathway in *M. morganii* and generated an isogenic non–indolimine-producing *M. morganii* mutant; and (iv) found that indolimine-producing *M. morganii* exacerbated colon tumorigenesis in gnotobiotic mice.

By revealing the existence of a previously uncharted universe of microbiota-derived genotoxins and defining the indolimines as a previously undescribed family of bioactive microbiota-derived small molecules, these studies imply an expanded role for genotoxic metabolites in CRC. We focused most of our studies on *M. morganii* as it is enriched in both CRC (*29*, *30*, *43*, *44*) and IBD patients, the latter of which are at increased risk of CRC diagnosis (*21*, *22*). However, additional genotoxic species identified in our initial screens may also contribute to CRC. Indeed, genotoxic *C. perfringens*

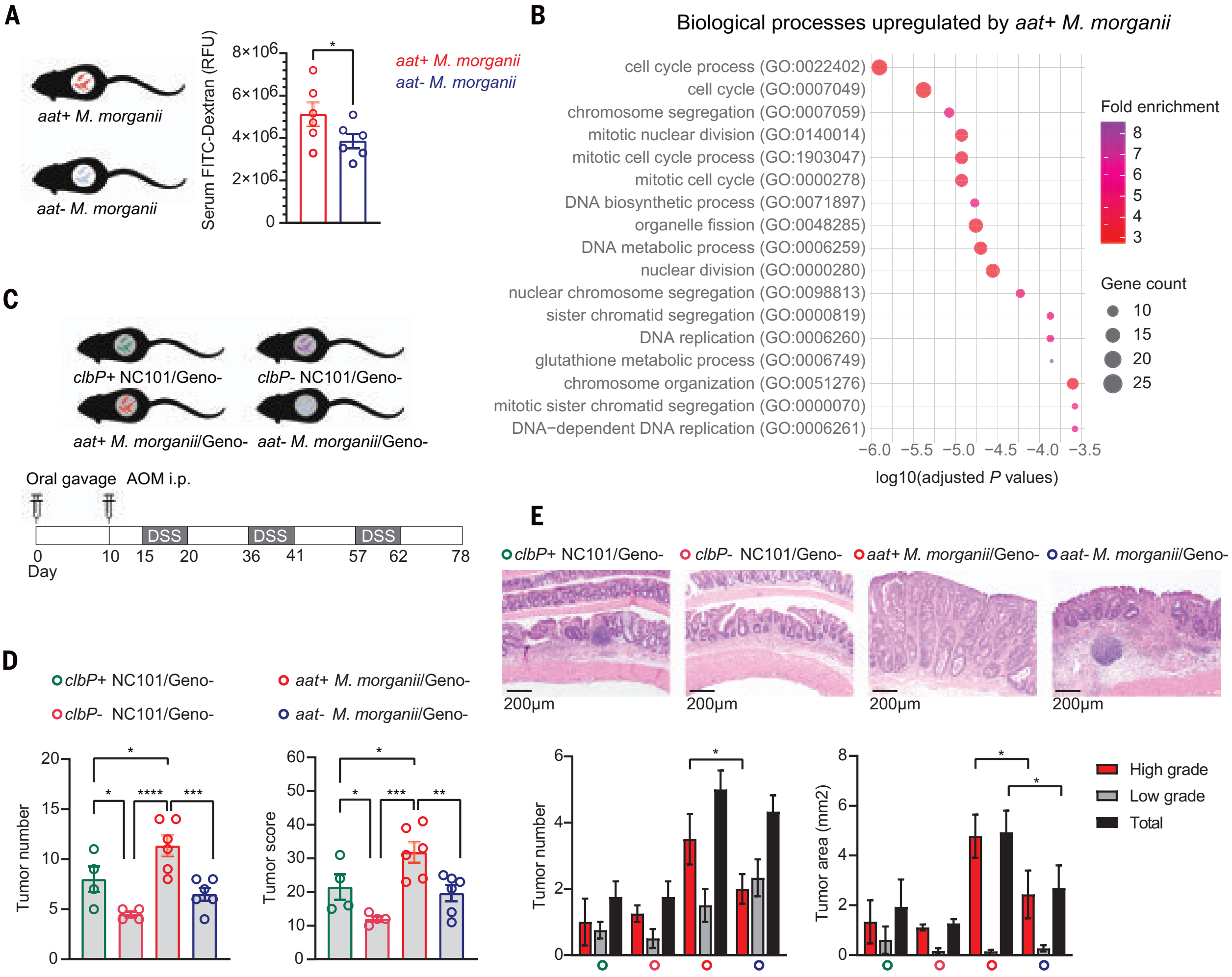

Fig. 6. Indolimine-producing *M. morganii* induces increased gut permeability and exacerbates colon tumor burden in gnotobiotic mice. (**A**) Evaluation of intestinal permeability of mice colonized with *aat*+ or *aat*− *M. morganii* based on serum FITC-Dextran RFU (relative fluorescence units) (n = 6). $^*P <$ 0.05, Student's t-test. (**B**) GO-Slim biological process analysis based on the gene ontology overrepresentation test for colonic epithelial cells from mice colonized with *aat*+ (n = 5) or *aat*− *M. morganii* (n = 6). Data are pooled from N = 1 experiment. (**C**) Schematic of experimental design for AOM/DSS model in age-matched gnotobiotic mice colonized with *clbP*+ *E. coli* NC101 (n = 4), *clbP*− *E. coli* NC101 (n = 4), *aat*+ *M. morganii* (n = 6) or *aat*− *M. morganii* (n = 6) with nongenotoxic mock community (Geno-, constructed with 7 nongenotoxic isolates) (N = 2). (**D** and **E**) Tumor number and tumor score (D), representative tumor histology images (scale bar = 200 μm) and tumor grade evaluation [(E) tumor number and tumor area per section of tissues], in gnotobiotic mice colonized with *clbP*+ *E. coli* NC101, *clbP*− *E. coli* NC101, *aat*+ *M. morganii* or *aat*− *M. morganii* with Geno- community. n.s., not significant; $^*P < 0.05$; $^{**}P < 0.01$; $^{***}P < 0.001$; $^{****}P < 0.0001$, one-way ANOVA. Data are means ± SEM.

and *C. ramosum* strains also promoted colorectal tumor burden in gnotobiotic mice as compared with a nongenotoxic mock community (fig. S12, D to G), but did not produce indolimines (fig. S12H), suggesting that additional microbiota-derived genotoxins remain to be characterized.

Notably, somatic mutations can be detected in human colonic epithelial cells even in early life, which suggests persistent mutagenesis throughout the lifespan of an individual (*46*, *47*), and colitis-related expansions of mutated clones may influence both IBD pathogenesis and CRC susceptibility (*48*). Furthermore, although CRC patients display increased carriage of *clb*+ *E. coli*, *clb*+ taxa (including *E. coli* relatives such as *Klebsiella* species) are also found in healthy individuals (*49*). Recent studies also revealed that increased epithelial oxygenation during colitis could drive *clb*+ *E. coli* expansion through aerobic respiration, increasing colibactin-mediated CRC-inducing activity (*50*). These observations support a model whereby genotoxic gut microbes contribute to CRC development by persistently inducing DNA damage in host epithelial cells, which synergizes with chronic inflammation in the gut microenvironment, along with additional environmental factors, and eventually facilitates the initiation and progression of CRC.

Microbiota-derived genotoxins may also affect diverse aspects of host biology beyond tumor initiation. Recent studies revealed that colibactin also influences gut microbiome composition (*51*), exacerbates lymphopenia and septicemia (*52*), triggers prophage induction through the bacterial SOS response (*53*), and restricts *Vibrio cholerae* colonization (*54*). Thus, commensal-derived genotoxins, including the indolimines, may also mediate diverse biological functions. Overall, our studies underscore the power of function-based assessments of the microbiome to provide new insights into the diverse impacts of indigenous microbes on host biology and disease susceptibility.

REFERENCES AND NOTES

1. N. Keum, E. Giovannucci, Global burden of colorectal cancer: Emerging trends, risk factors and prevention strategies. *Nat. Rev. Gastroenterol. Hepatol.* **16**, 713–732 (2019). doi: 10.1038/s41575-019-0189-8; pmid: 31455888
2. K. W. Jasperson, T. M. Tuohy, D. W. Neklason, R. W. Burt, Hereditary and familial colon cancer. *Gastroenterology* **138**,

2044–2058 (2010). doi: 10.1053/j.gastro.2010.01.054; pmid: 20420945

3. C. A. Brennan, W. S. Garrett, Gut Microbiota, Inflammation, and Colorectal Cancer. *Annu. Rev. Microbiol.* **70**, 395–411 (2016). doi: 10.1146/annurev-micro-102215-095513; pmid: 27607555
4. H. Tilg, T. E. Adolph, R. R. Gerner, A. R. Moschen, The Intestinal Microbiota in Colorectal Cancer. *Cancer Cell* **33**, 954–964 (2018). doi: 10.1016/j.ccell.2018.03.004; pmid: 29657127
5. W. S. Garrett, Cancer and the microbiota. *Science* **348**, 80–86 (2015). doi: 10.1126/science.aaa4972; pmid: 25838377
6. A. Koh, F. De Vadder, P. Kovatcheva-Datchary, F. Bäckhed, From Dietary Fiber to Host Physiology: Short-Chain Fatty Acids as Key Bacterial Metabolites. *Cell* **165**, 1332–1345 (2016). doi: 10.1016/j.cell.2016.05.041; pmid: 27259147
7. M. R. Rubinstein *et al*., Fusobacterium nucleatum promotes colorectal carcinogenesis by modulating E-cadherin/β-catenin signaling via its FadA adhesin. *Cell Host Microbe* **14**, 195–206 (2013). doi: 10.1016/j.chom.2013.07.012; pmid: 23954158
8. J. Allen, C. L. Sears, Impact of the gut microbiome on the genome and epigenome of colon epithelial cells: Contributions to colorectal cancer development. *Genome Med.* **11**, 11 (2019). doi: 10.1186/s13073-019-0621-2; pmid: 30803449
9. A. C. Goodwin *et al*., Polyamine catabolism contributes to enterotoxigenic *Bacteroides fragilis*-induced colon tumorigenesis. *Proc. Natl. Acad. Sci. U.S.A.* **108**, 15354–15359 (2011). doi: 10.1073/pnas.1010203108; pmid: 21876161
10. E. Buc *et al*., High prevalence of mucosa-associated *E. coli* producing cyclomodulin and genotoxin in colon cancer. *PLOS ONE* **8**, e56964 (2013). doi: 10.1371/journal.pone.0056964; pmid: 23457644
11. J.-P. Nougayrède *et al*., *Escherichia coli* induces DNA double-strand breaks in eukaryotic cells. *Science* **313**, 848–851 (2006). doi: 10.1126/science.1127059; pmid: 16902142
12. J. C. Arthur *et al*., Intestinal inflammation targets cancer-inducing activity of the microbiota. *Science* **338**, 120–123 (2012). doi: 10.1126/science.1224820; pmid: 22903521
13. A. Cougnoux *et al*., Bacterial genotoxin colibactin promotes colon tumour growth by inducing a senescence-associated secretory phenotype. *Gut* **63**, 1932–1942 (2014). doi: 10.1136/gutjnl-2013-305257; pmid: 24658599
14. G. Cuevas-Ramos *et al*., *Escherichia coli* induces DNA damage in vivo and triggers genomic instability in mammalian cells. *Proc. Natl. Acad. Sci. U.S.A.* **107**, 11537–11542 (2010). doi: 10.1073/pnas.1001261107; pmid: 20534522
15. M. Xue *et al*., Structure elucidation of colibactin and its DNA cross-links. *Science* **365**, eaax2685 (2019). doi: 10.1126/science.aax2685; pmid: 31395743
16. M. R. Wilson *et al*., The human gut bacterial genotoxin colibactin alkylates DNA. *Science* **363**, eaar7785 (2019). doi: 10.1126/science.aar7785; pmid: 30765538
17. C. Pleguezuelos-Manzano *et al*., Mutational signature in colorectal cancer caused by genotoxic pks$^+$ E. coli. *Nature* **580**, 269–273 (2020). doi: 10.1038/s41586-020-2080-8; pmid: 32106218
18. P. J. Dziubańska-Kusibab *et al*., Colibactin DNA-damage signature indicates mutational impact in colorectal cancer. *Nat. Med.* **26**, 1063–1069 (2020). doi: 10.1038/s41591-020-0908-2; pmid: 32483361
19. R. R. da Silva, P. C. Dorrestein, R. A. Quinn, Illuminating the dark matter in metabolomics. *Proc. Natl. Acad. Sci. U.S.A.* **112**, 12549–12550 (2015). doi: 10.1073/pnas.1516878112; pmid: 26430243
20. N. W. Palm *et al*., Immunoglobulin A coating identifies colitogenic bacteria in inflammatory bowel disease. *Cell* **158**, 1000–1010 (2014). doi: 10.1016/j.cell.2014.08.006; pmid: 25171403
21. O. Olén *et al*., Colorectal cancer in ulcerative colitis: A Scandinavian population-based cohort study. *Lancet* **395**, 123–131 (2020). doi: 10.1016/S0140-6736(19)32545-0; pmid: 31929014
22. O. Olén *et al*., Colorectal cancer in Crohn's disease: A Scandinavian population-based cohort study. *Lancet Gastroenterol. Hepatol.* **5**, 475–484 (2020). doi: 10.1016/S2468-1253(20)30005-4; pmid: 32066530
23. N. Bossuet-Greif *et al*., The Colibactin Genotoxin Generates DNA Interstrand Cross-Links in Infected Cells. *mBio* **9**, 02393-17 (2018). doi: 10.1128/mBio.02393-17; pmid: 29559578
24. K. S. Gates, An overview of chemical processes that damage cellular DNA: Spontaneous hydrolysis, alkylation, and reactions with radicals. *Chem. Res. Toxicol.* **22**, 1747–1760 (2009). doi: 10.1021/tx900242k; pmid: 19757819
25. C. M. Dejea *et al*., Patients with familial adenomatous polyposis harbor colonic biofilms containing tumorigenic bacteria. *Science* **359**, 592–597 (2018). doi: 10.1126/science.aah3648; pmid: 29420293
26. K. Unterhauser *et al*., *Klebsiella oxytoca* enterotoxins tilimycin and tilivalline have distinct host DNA-damaging and microtubule-stabilizing activities. *Proc. Natl. Acad. Sci. U.S.A.* **116**, 3774–3783 (2019). doi: 10.1073/pnas.1819154116; pmid: 30808763
27. L. J. Kuo, L. X. Yang, Gamma-H2AX - a novel biomarker for DNA double-strand breaks. *In Vivo* **22**, 305–309 (2008). pmid: 18610740
28. J. C. Freedman, A. Shrestha, B. A. McClane, Clostridium perfringens Enterotoxin: Action, Genetics, and Translational Applications. *Toxins* **8**, 73 (2016). doi: 10.3390/toxins8030073; pmid: 26999202
29. A. M. Thomas *et al*., Metagenomic analysis of colorectal cancer datasets identifies cross-cohort microbial diagnostic signatures and a link with choline degradation. *Nat. Med.* **25**, 667–678 (2019). doi: 10.1038/s41591-019-0405-7; pmid: 30936548
30. J. Wirbel *et al*., Meta-analysis of fecal metagenomes reveals global microbial signatures that are specific for colorectal cancer. *Nat. Med.* **25**, 679–689 (2019). doi: 10.1038/s41591-019-0406-6; pmid: 30936547
31. E. E. Shine, J. M. Crawford, Molecules from the Microbiome. *Annu. Rev. Biochem.* **90**, 789–815 (2021). doi: 10.1146/annurev-biochem-080320-115307; pmid: 33770448
32. G. Schneditz *et al*., Enterotoxicity of a nonribosomal peptide causes antibiotic-associated colitis. *Proc. Natl. Acad. Sci. U.S.A.* **111**, 13181–13186 (2014). doi: 10.1073/pnas.1403274111; pmid: 25157164
33. K. Blin *et al*., antiSMASH 5.0: Updates to the secondary metabolite genome mining pipeline. *Nucleic Acids Res.* **47** (W1), W81–W87 (2019). doi: 10.1093/nar/gkz310; pmid: 31032519
34. E. P. Trautman, A. R. Healy, E. E. Shine, S. B. Herzon, J. M. Crawford, Domain-Targeted Metabolomics Delineates the Heterocycle Assembly Steps of Colibactin Biosynthesis. *J. Am. Chem. Soc.* **139**, 4195–4201 (2017). doi: 10.1021/jacs.7b00659; pmid: 28240912
35. L. Zha *et al*., Colibactin assembly line enzymes use S-adenosylmethionine to build a cyclopropane ring. *Nat. Chem. Biol.* **13**, 1063–1065 (2017). doi: 10.1038/nchembio.2448; pmid: 28805802
36. H. Wami *et al*., Insights into evolution and coexistence of the colibactin- and yersiniabactin secondary metabolite determinants in enterobacterial populations. *Microb. Genom.* **7**, 000577 (2021). doi: 10.1099/mgen.0.000577; pmid: 34128785
37. E. E. Shine *et al*., Model Colibactins Exhibit Human Cell Genotoxicity in the Absence of Host Bacteria. *ACS Chem. Biol.* **13**, 3286–3293 (2018). doi: 10.1021/acschembio.8b00714; pmid: 30403848
38. S. Tomkovich *et al*., Locoregional Effects of Microbiota in a Preclinical Model of Colon Carcinogenesis. *Cancer Res.* **77**, 2620–2632 (2017). doi: 10.1158/0008-5472.CAN-16-3472; pmid: 28416491
39. D. I. Kim, T. U. Chae, H. U. Kim, W. D. Jang, S. Y. Lee, Microbial production of multiple short-chain primary amines via retrobiosynthesis. *Nat. Commun.* **12**, 173 (2021). doi: 10.1038/s41467-020-20423-6; pmid: 33420084
40. Y. Veeranagouda, F. Husain, H. M. Wexler, Transposon mutagenesis of the anaerobic commensal, Bacteroides fragilis, using the EZ:TN5 transposome. *FEMS Microbiol. Lett.* **333**, 94–100 (2012). doi: 10.1111/j.1574-6968.2012.02602.x; pmid: 22639975
41. I. A. Anzai, L. Shaket, O. Adesina, M. Baym, B. Barstow, Rapid curation of gene disruption collections using Knockout Sudoku. *Nat. Protoc.* **12**, 2110–2137 (2017). doi: 10.1038/nprot.2017.073; pmid: 28906493
42. P. J. Lariviere *et al*., An Essential Regulator of Bacterial Division Links FtsZ to Cell Wall Synthase Activation. *Curr. Biol.* **29**, 1460–1470 (2019). doi: 10.1016/j.cub.2019.03.066; pmid: 31031115
43. G. D. Poore *et al*., Microbiome analyses of blood and tissues suggest cancer diagnostic approach. *Nature* **579**, 567–574 (2020). doi: 10.1038/s41586-020-2095-1; pmid: 32214244
44. W. Chen, F. Liu, Z. Ling, X. Tong, C. Xiang, Human intestinal lumen and mucosa-associated microbiota in patients with colorectal cancer. *PLOS ONE* **7**, e39743 (2012). doi: 10.1371/journal.pone.0039743; pmid: 22761885
45. M. W. Dougherty, C. Jobin, Shining a Light on Colibactin Biology. *Toxins* **13**, 346 (2021). doi: 10.3390/toxins13050346; pmid: 34065799
46. I. Martincorena, P. J. Campbell, Somatic mutation in cancer and normal cells. *Science* **349**, 1483–1489 (2015). doi: 10.1126/science.aab4082; pmid: 26404825
47. H. Lee-Six *et al*., The landscape of somatic mutation in normal colorectal epithelial cells. *Nature* **574**, 532–537 (2019). doi: 10.1038/s41586-019-1672-7; pmid: 31645730
48. S. Olafsson *et al*., Somatic Evolution in Non-neoplastic IBD-Affected Colon. *Cell* **182**, 672–684.e11 (2020). doi: 10.1016/j.cell.2020.06.036; pmid: 32697969
49. J. Putze *et al*., Genetic structure and distribution of the colibactin genomic island among members of the family Enterobacteriaceae. *Infect. Immun.* **77**, 4696–4703 (2009). doi: 10.1128/IAI.00522-09; pmid: 19720753
50. S. A. Cevallos *et al*., Increased Epithelial Oxygenation Links Colitis to an Expansion of Tumorigenic Bacteria. *mBio* **10**, 02244-19 (2019). doi: 10.1128/mBio.02244-19; pmid: 31575772
51. S. Tronnet *et al*., The Genotoxin Colibactin Shapes Gut Microbiota in Mice. *MSphere* **5**, 00589-20 (2020). doi: 10.1128/mSphere.00589-20; pmid: 32611705
52. I. Marcq *et al*., The genotoxin colibactin exacerbates lymphopenia and decreases survival rate in mice infected with septicemic *Escherichia coli*. *J. Infect. Dis.* **210**, 285–294 (2014). doi: 10.1093/infdis/jiu071; pmid: 24489107
53. J. E. Silpe, J. W. H. Wong, S. V. Owen, M. Baym, E. P. Balskus, The bacterial toxin colibactin triggers prophage induction. *Nature* **603**, 315–320 (2022). doi: 10.1038/s41586-022-04444-3; pmid: 35197633
54. J. Chen *et al*., A commensal-encoded genotoxin drives restriction of *Vibrio cholerae* colonization and host gut microbiome remodeling. *Proc. Natl. Acad. Sci. U.S.A.* **119**, e2121180119 (2022). doi: 10.1073/pnas.2121180119; pmid: 35254905

ACKNOWLEDGMENTS

We thank A. L. Goodman, D. Bajic, B. Lim, Y. Surovtseva, and S. Umlauf, as well as the Yale Microbial Sciences Institute and Yale Center for Molecular Discovery for assistance with assembly of the transposon mutant libraries, the Yale Center for Genome Analysis for sequencing services, and the Yale Animal Resource Center for veterinary services. We also thank B. M. Barstow, P. Chien, and B. Aldikacti for technical advice on Knockout Sudoku and Tn-Seq. **Funding:** This work was supported by a Yale Cancer Center Team Challenge award funded by the National Cancer Institute of the National Institutes of Health under award 3P30CA016359 (to N.W.P., S.B.H., and J.M.C.) as well as R01CA215553 to S.B.H. and J.M.C. Approximately 35% of the funding for this research project (~$200,000) was financed with NIH funds; the remainder was financed by nongovernmental sources. N.W.P. also gratefully acknowledges support from the Common Fund of the National Institutes of Health (DP2DK125119), Leona M. and Harry B. Helmsley Charitable Trust (3083), Chan Zuckerberg Initiative, Michael J. Fox Foundation for Parkinson's Research, Ludwig Family, Mathers Foundation, Pew Charitable Trust, NIA, and NIGMS (R01AG068863 and RM1GM141649), and F. Hoffmann-La Roche Ltd. The funders of this work had no role in the study design, data collection and analysis, decision to publish, or preparation of the manuscript. The content is solely the responsibility of the authors and does not necessarily represent the official views of the National Institutes of Health. Yale Center for Molecular Discovery is supported in part by an NCI Cancer Center Support grant NIH P30 CA016359. Equipment and libraries were supported in part by the Program in Innovative Therapeutics for Connecticut's Health. **Author contributions:** Y.C. and N.W.P. designed the study and wrote the manuscript with input from all authors. Y.C., J.O., and M.X. designed and performed experiments and analysis. W.J.H. performed histopathological scoring. J.W., J.A.G.-H., T.A.R., A.L.M., and D.S. helped with experiments or contributed essential reagents. S.B.H., J.M.C., and N.W.P. participated in study design and supervised research. **Competing interests:** N.W.P. is a co-founder of Artizan Biosciences, Inc. and Design Pharmaceuticals, Inc. N.W.P. has received research funding for unrelated studies from Artizan Biosciences, Inc. and F. Hoffmann-La Roche AG. Y.C., J.O., J.M.C., M.X., S.B.H., and N.W.P. are inventors on a provisional patent application submitted by Yale University that covers the use of microbiome-targeted therapeutics to treat or prevent commensal genotoxin-induced disease. **Data and materials availability:** Bulk RNA-seq data, fecal 16S rRNA profiling of microbiota for AOM/DSS tumor experiments, and trimmed Tn-seq data for the *M. morganii* mutant library are available at NCBI Bioproject: PRJNA879774. Related analysis methods are available in the supplementary materials.

SUPPLEMENTARY MATERIALS

science.org/doi/10.1126/science.abm3233
Materials and Methods
Figs. S1 to S44
Tables S1 to S8
References (*55*–*62*)
MDAR Reproducibility Checklist

Submitted 9 September 2021; resubmitted 10 July 2022
Accepted 19 September 2022
10.1126/science.abm3233

RESEARCH ARTICLE SUMMARY

AGING

Spermidine activates mitochondrial trifunctional protein and improves antitumor immunity in mice

Muna Al-Habsi†, Kenji Chamoto†, Ken Matsumoto†, Norimichi Nomura†, Baihao Zhang, Yuki Sugiura, Kazuhiro Sonomura, Aprilia Maharani, Yuka Nakajima, Yibo Wu, Yayoi Nomura, Rosemary Menzies, Masaki Tajima, Koji Kitaoka, Yasuharu Haku, Sara Delghandi, Keiko Yurimoto, Fumihiko Matsuda, So Iwata, Toshihiko Ogura, Sidonia Fagarasan*, Tasuku Honjo*

INTRODUCTION: In mammals, the power of the immune system decreases with age. This is because of multiple factors, including a decrease in the output and diversity of the antigenic repertoire of T cells caused by thymus involution; changes in the cellular metabolism caused by inflammation; and defective proliferative, differentiation, or survival capacities of the immune cells. Aged individuals frequently suffer from severe infections and cancers, and often the therapies applied, including programmed cell death protein 1 (PD-1) blockade in cancer immunotherapy, are ineffective when compared with results in young patients. A biogenic polyamine, spermidine (SPD), decreases with age, and SPD supplementation was shown to improve or delay several age-related pathologies, including those of the immune system. Among the proposed mechanisms responsible for rejuvenation of the immune system by SPD were enhanced autophagy, translational activity, and mitochondrial metabolism. SPD supplementation has previously been shown to enhance the antitumor immunity in animal models. However, it remains largely unknown how SPD deficiency relates to the T cell immune suppression induced by aging.

RATIONALE: Because CD8$^+$ T cells are key players in tumor immunity, we investigated how aging would affect the metabolic and functional characteristics of CD8$^+$ T cells. We asked whether SPD insufficiency could be a factor contributing to nonresponsiveness to PD-1 antibody therapy in aged mice. We sought to characterize the CD8$^+$ T cell population changes induced by SPD supplementation in aged mice and to identify the molecular mechanisms for the SPD action.

RESULTS: We found that the total and free intracellular concentrations of SPD in CD8$^+$ T cells from aged mice were about half as much as the concentrations found in young mice. Bioenergetically, aged CD8$^+$ T cells showed impaired mitochondrial activity with lower oxygen consumption rate, adenosine 5′-triphosphate (ATP) production, and fatty acid oxidation (FAO) activity compared with young CD8$^+$ T cells.

We show that SPD supplementation enhanced the antitumor activity of PD-1 blockade immunotherapy in aged mice. SPD supplementation proved to also be effective in young mice with tumors unresponsive to single anti–programmed death-ligand 1 (PD-L1) antibody therapy. SPD and anti–PD-L1 antibody combination treatment enhanced the proliferation, cytokine production, and mitochondrial ATP production of CD8$^+$ T cells in vivo. In vitro, SPD effectively enhanced mitochondrial functions and metabolized palmitate into tricarboxylic acid cycle components within 1 hour, which suggests the possibility of direct SPD binding to mitochondria-related proteins. Biochemical analysis identified SPD binding to mitochondrial trifunctional protein (MTP), which is the central enzyme of fatty acid β-oxidation. MTP is composed of α and β subunits, both of which bind SPD. Several assays using the MTP synthesized and purified from *Escherichia coli* revealed that SPD bound with strong affinity [binding affinity (dissociation constant, K_d) = 0.1 μM] and allosterically enhanced their enzymatic FAO activities. Furthermore, we found that spermine, another polyamine derived from SPD with important cellular protective functions, also directly binds to MTP and competitively inhibits FAO activity of SPD, which suggests the importance of SPD and spermine balance for FAO evaluation in aged cells. T cell–specific deletion of the MTP α subunit abolished enhancement of PD-1 blockade immunotherapy by SPD, indicating that MTP is required for SPD-dependent T cell activation.

CONCLUSION: SPD enhances FAO by directly binding and activating the MTP. SPD supplementation enhances the FAO activity and boosts the mitochondrial activities and cytotoxic functions of CD8$^+$ T cells. We provide new insights into the properties of SPD that may facilitate the development of strategies to prevent and improve outcomes of age-related immune pathologies and combat unresponsiveness to PD-1 blockade therapy in cancers, regardless of age. ■

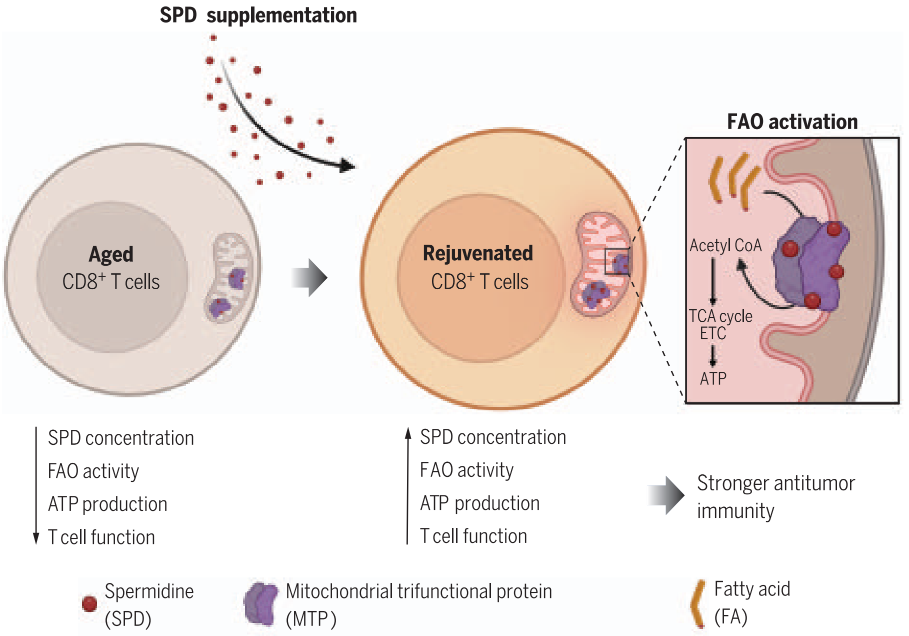

SPD binds to MTP and activates FAO in T cells. SPD directly activates MTP, which plays a central role in FAO. SPD concentration is decreased in aged T cells, leading to low FAO activity and ATP production compared with those in young T cells. SPD supplementation activates FAO in aged and young T cells, which enhances the efficacy of PD-1 blockade cancer immunotherapy. CoA, coenzyme A; TCA, tricarboxylic acid; ETC, electron transport chain. [Figure created by Biorender]

The list of author affiliations is available in the full article online.
*Corresponding author. Email: honjo@mfour.med.kyoto-u.ac.jp (T.H.); sidonia.fagarasan@riken.jp (S.F.)
†These authors contributed equally to this work.
Cite this article as M. Al-Habsi *et al*., *Science* 378, eabj3510 (2022). DOI: 10.1126/science.abj3510

READ THE FULL ARTICLE AT
https://doi.org/10.1126/science.abj3510

RESEARCH ARTICLE

AGING

Spermidine activates mitochondrial trifunctional protein and improves antitumor immunity in mice

Muna Al-Habsi[1,2,3]†, Kenji Chamoto[1]†, Ken Matsumoto[4]†, Norimichi Nomura[5]†, Baihao Zhang[6], Yuki Sugiura[7], Kazuhiro Sonomura[8,9], Aprilia Maharani[1], Yuka Nakajima[1], Yibo Wu[10,11], Yayoi Nomura[5], Rosemary Menzies[1], Masaki Tajima[3], Koji Kitaoka[1], Yasuharu Haku[1], Sara Delghandi[1], Keiko Yurimoto[1], Fumihiko Matsuda[8], So Iwata[5], Toshihiko Ogura[4], Sidonia Fagarasan[3,6]*, Tasuku Honjo[1]*

Spermidine (SPD) delays age-related pathologies in various organisms. SPD supplementation overcame the impaired immunotherapy against tumors in aged mice by increasing mitochondrial function and activating $CD8^+$ T cells. Treatment of naïve $CD8^+$ T cells with SPD acutely enhanced fatty acid oxidation. SPD conjugated to beads bound to the mitochondrial trifunctional protein (MTP). In the MTP complex, synthesized and purified from *Escherichia coli*, SPD bound to the α and β subunits of MTP with strong affinity and allosterically enhanced their enzymatic activities. T cell–specific deletion of the MTP α subunit abolished enhancement of programmed cell death protein 1 (PD-1) blockade immunotherapy by SPD, indicating that MTP is required for SPD-dependent T cell activation.

Aged animals undergo changes in metabolic pathways related to sugars, fatty acids, amino acids, and mitochondrial functions including redox homeostasis (*1*–*3*). For example, increased amounts of free fatty acids, decreased long-chain acylcarnitines, and decreased abundance of various amino acids such as proline and tyrosine occur in the plasma of aged mice (*1*). Abundance of spermidine (SPD), a natural polyamine, decreases with aging, and dietary supplementation of SPD not only prolongs the life span of diverse organisms, such as yeast, worms, flies, mice, and humans, but also improves age-related dysfunction of cardiac, nervous, hepatic, and immune systems (*4*). In mice, SPD administration induces metabolic changes in various tissues, including muscle and the liver, that resemble changes induced by fasting or the administration of caloric restriction mimetics, such as metformin (*4*). SPD induces autophagy in multiple cells and tissues (*4*, *5*). In the immune systems of aged mice, antitumor immunity is defective because of the impaired activation and differentiation of effector and memory ($CD44^{high}$ $CD62L^{low}$) T cells (*6*). SPD improves the generation and function of memory T lymphocytes, similarly to other autophagy inducers such as rapamycin or metformin (*7*, *8*). Because the generation and maintenance of memory T cells depend on fatty acid oxidation (FAO), we wondered whether SPD might also regulate FAO (*9*, *10*).

Biochemical mechanisms have been proposed by which SPD restores age-induced damage. SPD inhibits protein acetylation by direct inhibition of protein acetyl transferases, such as EP300, and may affect autophagy by epigenetic regulation (*11*). SPD is a substrate for the hypusination reaction of eukaryotic elongation factor 5A (elF5A), which is critical to cell proliferation because it activates protein synthesis and mitochondrial function (*12*, *13*). Epigenetic changes caused by SPD are also attributed to the SPD-hypusine axis (*14*). However, several SPD analogs that cannot provide the hypusine moiety also rescue acute growth arrest caused by SPD depletion, which suggests that there may be other mechanisms of SPD function (*15*).

SPD restores the efficacy of programmed cell death protein 1 (PD-1) blockade therapy in aged mice through the activation of effector and mitochondrial function in $CD8^+$ T cells

We confirmed that serum concentrations of SPD—but not those of other polyamines—were significantly decreased in aged mice (>12 months) (Fig. 1A) (*4*, *5*). Furthermore, intracellular total and free SPD concentrations in naïve $CD8^+$ T cells from old mice were about half as much as the concentrations found in young mice (Fig. 1B). We therefore wondered whether SPD insufficiency could be a factor contributing to nonresponsiveness to programmed death-ligand 1 (PD-L1) monoclonal antibody (mAb) therapy in aged mice (*6*). SPD supplementation significantly improved the antitumor effect of PD-L1 mAb treatment and prolonged the survival of aged mice (Fig. 1C). SPD alone had no antitumor effect (Fig. 1C). Flow cytometric analysis revealed that the frequency and numbers of $CD8^+$ T cells in tumor-infiltrating lymphocytes (TILs) were significantly increased in aged mice that received the combination therapy with PD-L1 mAb and SPD (Fig. 1, D and E). SPD combination therapy increased the abundance of $PD\text{-}1^-$ $Tim3^-$ nonexhausted effector $CD8^+$ T cells and increased the expression of cytotoxicity marker granzyme B (Fig. 1, F and G).

SPD supplementation also enhanced antitumor activity and prolonged survival in young mice, in which PD-L1 mAb treatment was partially effective and SPD alone was ineffective (fig. S1A). As in old mice, SPD combination therapy increased frequencies and numbers of $CD8^+$ T cells exhibiting a nonexhausted $PD\text{-}1^-$ $Tim3^-$ phenotype and producing more granzyme B (fig. S1, B to E). Treatment of young mice with SPD alone reportedly increased the abundance of regulatory T cells (T_{regs}) and inhibitory arginase-1 ($Arg1^+$) M2 macrophages (*16*, *17*). However, the abundance of $Foxp3^+$ regulatory cells and myeloid cells, including $Arg1^+$ macrophages (M2) or major histocompatibility complex (MHC) II^+ macrophage (M1), was not significantly changed by SPD treatment in our mice (fig. S1, F and G). This discrepancy might be related to the SPD amounts used, which were 15- to 25-fold higher than those that we used (30 mM in drinking water and 50 mg/kg for effects on T_{regs} and M2 macrophages, respectively, versus 200 μl of 1.4 mM intraperitoneal injection = 2 mg/kg in our case). The abundance of other cells with potential antitumor activity, such as natural killer (NK) cells, was not changed by the SPD treatment (fig. S1H). In other tumor models, SPD also enhanced the antitumor activity of PD-L1 mAb against unresponsive tumor cells, such as colorectal carcinoma (CT26) in BALB/c mice and Lewis lung carcinoma (LLC) in C57BL/6 mice (fig. S1I).

PD-1 blockade increases the number of activated effector T cells but reduces their longevity and promotes exhaustion through the glycolysis pathway (*18*–*20*). To know the effect of SPD on T cell differentiation in vivo, we assessed changes in subpopulations of $CD8^+$ T cells in draining lymph nodes (DLNs). SPD in combination with PD-1 blockade increased

---

[1] Division of Immunology and Genomic Medicine, Center for Cancer Immunotherapy and Immunobiology, Graduate School of Medicine, Kyoto University, Kyoto, Japan. [2] National Genetic Center, Ministry of Health, Muscat, Oman. [3] Division of Integrated High-Order Regulatory Systems, Center for Cancer Immunotherapy and Immunobiology, Graduate School of Medicine, Kyoto University, Kyoto, Japan. [4] Department of Developmental Neurobiology, Institute of Development, Aging and Cancer, Tohoku University, Miyagi, Japan. [5] Department of Cell Biology, Graduate School of Medicine, Kyoto University, Kyoto, Japan. [6] Laboratory for Mucosal Immunity, Center for Integrative Medical Sciences, RIKEN Yokohama Institute, Yokohama, Japan. [7] Department of Biochemistry, Keio University, Tokyo, Japan. [8] Center for Genomic Medicine, Graduate School of Medicine, Kyoto University, Kyoto, Japan. [9] Life Science Research Center, Technology Research Laboratory, Shimadzu Corporation, Kyoto, Japan. [10] YCI Laboratory for Next-Generation Proteomics, Center for Integrative Medical Sciences, RIKEN Yokohama Institute, Yokohama, Japan. [11] Chemical Biology Mass Spectrometry Platform, Faculty of Science, University of Geneva, Geneva, Switzerland.

***Corresponding author. Email: honjo@mfour.med.kyoto-u.ac.jp (T.H.); sidonia.fagarasan@riken.jp (S.F.)**

†These authors contributed equally to this work.

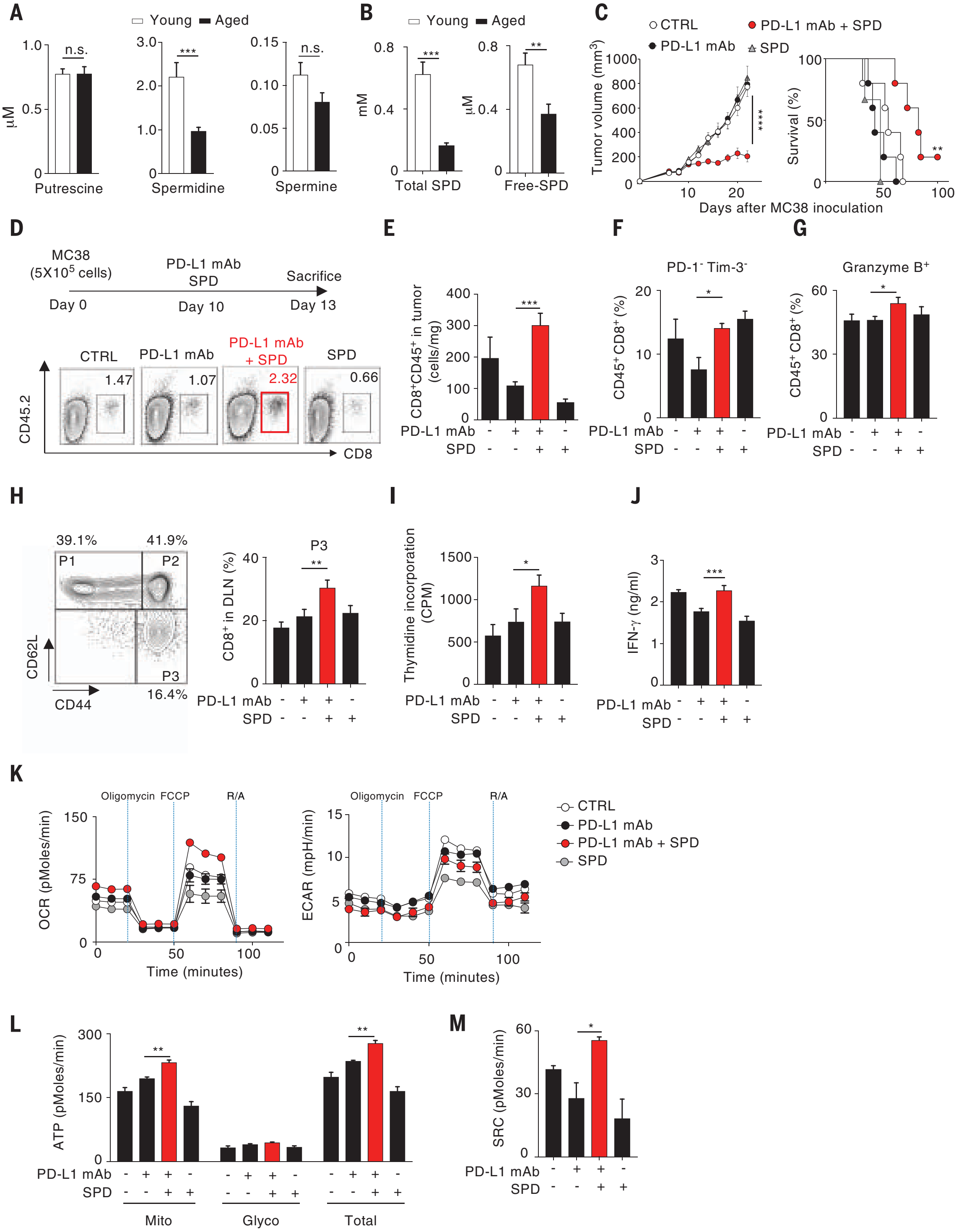

Fig. 1. SPD combination improves antitumor activity of PD-1 blockade therapy and enhances mitochondrial function of CD8⁺ T cells. (**A**) Quantification of polyamines in sera from young (1 to 3 months, *n* = 31 mice) and aged (>1 year, *n* = 30) mice using mass spectrometry. (**B**) Total and free SPD levels in naïve CD8⁺ T cells from young [*n* = 12 mice (total SPD) or 10 mice (free SPD)] and aged (*n* = 8) mice. (**C**) MC38 tumor–bearing aged mice were intraperitonially treated with PD-L1 mAb and/or SPD (2 mg/kg) every 5 days from day 10. Tumor growth and survival curve of mice are shown from pooled mice [*n* = 3 mice (SPD alone group) or 5 mice (the other groups)] (log-rank for survival curve). (D to G) Tumor-infiltrating CD8⁺ T cells were gated and analyzed on day 13 after MC38 inoculation. CTRL, control. (**D** and **E**) Flow cytometry frequencies and quantification (cells per milligram) of tumor-infiltrating CD8⁺ T cells (*n* = 6 mice). (**F**) Frequencies of PD-1⁻ Tim-3⁻ nonexhausted CD8⁺ T cells [*n* = 9 mice (control or SPD group) or 7 mice (the other groups)]. (**G**) Frequencies of granzyme B–producing CD8⁺ T cells in tumor without stimulation [*n* = 7 mice (control or SPD group) or 8 mice (the other groups)]. (**H**) A representative flow cytometry profile of CD8⁺ gated T cell subpopulations (P1 = naïve, P2 = memory, and P3 = effector) in the tumor DLNs (left) and frequencies of P3 cells (right) (*n* = 5 mice). (**I** and **J**) Thymidine incorporation (*n* = 5 technical replicates) (I) and IFN-γ production (*n* = 6 technical replicates) (J) of total DLN CD8⁺ T cells pooled from five mice, after restimulation with anti-CD3 and anti-CD28 coated beads. CPM, counts per minute. (**K**) Real-time OCR (left) and ECAR (right) of total DLN CD8⁺ T cells pooled from five mice per group, as assessed by Seahorse assay (*n* = 3 technical replicates). R/A, rotenone + antimycin A. (**L** and **M**) ATP production rate (L) and SRC (M) from data in (K), calculated as indicated in fig. S2, A and B. Data are the means ± SEMs [(C) and (K)] or + SEMs [(A), (B), (E) to (J), (L), and (M)]. *P* values were determined using unpaired two-tailed Student's *t* tests [(A) and (B)], two-way ANOVA [(C) on day 22], or one-way ANOVA [(E) to (J), (L), and (M)] with selected column comparison between PD-L1 mAb and SPD combination group. $^{*}P < 0.05$; $^{**}P < 0.01$; $^{***}P < 0.001$; n.s, not significant. All data are representative of three or more experiments.

the numbers of effector and memory (P3) CD8$^+$ T cells, whereas single treatment with PD-L1 mAb or SPD marginally increased the P3 CD8$^+$ T cells in the DLNs of aged mice (Fig. 1H). CD8$^+$ T cells isolated from the DLNs of tumor-bearing aged mice treated with the PD-L1 mAb and SPD combination showed higher proliferation capacity and augmented interferon-γ (IFN-γ) production compared with those treated with a single therapy or with control mice (Fig. 1, I and J). Because mitochondrial activity of T cells is associated with antitumor activity (*19*, *21*), we used the Seahorse assay system to assess the bioenergetics in the CD8$^+$ T cells in DLNs from tumor-bearing mice treated with or without SPD combination. We measured oxygen consumption rate (OCR) and extracellular acidification rate (ECAR)—which reflect oxidative phosphorylation (OXPHOS) and glycolysis, respectively—at the basal state and after sequential addition of oligomycin [blocking OXPHOS-dependent adenosine 5′-triphosphate (ATP) synthesis], carbonyl cyanide-4 (trifluoromethoxy) phenylhydrazone (FCCP) (uncoupling the ATP synthesis from the electron transport chain), and rotenone plus antimycin A (blocking electron transport complexes I and III, respectively) (Fig. 1K) (*22*). Mitochondria- and glycolysis-derived ATP production were calculated on the basis of the change in OCR and ECAR, respectively, caused by oligomycin injection (fig. S2, A and B). Compared with the CD8$^+$ T cells from mice receiving a single or no therapy, the CD8$^+$ T cells from the DLNs of aged mice receiving SPD combination therapy exhibited enhanced OXPHOS and mitochondrial ATP production (Fig. 1, K and L). SPD combination treatment also enhanced the spare respiratory capacity (SRC), which is represented by the OCR uncoupled from ATP production and reflects the mitochondrial metabolic potential linked to longevity and memory formation of T cells (fig. S2A and Fig. 1M) (*23*, *24*). Similar phenotypes and bioenergetic profiles were obtained with CD8$^+$ T cells isolated from the DLNs of MC38 tumor–bearing young mice (fig. S3, A to F). Further evidence of mitochondrial activation in vivo was obtained by proteomics analysis of sorted CD8$^+$ T cells from the DLNs of young mice, which showed a significant increase in abundance of many proteins by SPD combination treatment compared with treatment with PD-L1 mAb alone (fig. S3G). Among the 95 proteins that increased in abundance, 35 were related to OXPHOS, including the glycolysis-derived reduced form of nicotinamide adenine dinucleotide (NADH) dehydrogenase [ubiquinone] 1 α subunits (a component of complex-1), some cytochromes, and adenosine triphosphatases (ATPases) (fig. S3, H to J). These data indicate that SPD enhances the effectiveness of PD-1 blockade immunotherapy by preventing exhaustion and boosting the effector functions of CD8$^+$ T cells through the activation of mitochondrial metabolism.

SPD enhances mitochondrial FAO activity in CD8$^+$ T cells in 1 hour

Because SPD administration increased the SRC of CD8$^+$ T cells in vivo, which is associated with FAO activity (*10*, *23*, *24*), we next investigated the effect of SPD on FAO in vitro by using etomoxir, a specific inhibitor of carnitine palmitoyltransferase 1a (CPT1a) (*25*). To examine the effects of SPD on FAO activity, we measured bioenergetic states of naïve CD8$^+$ T cells from old mice after in vitro stimulation with anti-CD3 and -CD28 mAb-coated beads in the presence or absence of SPD and etomoxir. After 44 hours, SPD treatment increased ATP production and SRC by enhancing the mitochondrial and glycolytic activities (Fig. 2, A and B). SPD appeared to enhance OCR through FAO in stimulated CD8$^+$ T cells because SPD effects were inhibited by etomoxir (Fig. 2, A and B). FAO-dependent OCR coupled with ATP production (calculated as presented in fig. S2C) was increased by SPD (Fig. 2C). Mitochondrial bioenergetics, such as OCR, ATP production, and SRC, declined in aged CD8$^+$ T cells compared with CD8$^+$ T cells isolated from young mice (Fig. 2, D to F). In the absence of exogenous SPD, FAO activity in aged CD8$^+$ T cells was significantly decreased compared with that in young CD8$^+$ T cells, consistent with decreased SPD abundance in aged CD8$^+$ T cells (Fig. 2G and Fig. 1B). The addition of SPD restored proliferation in aged CD8$^+$ T cells (Fig. 2H). Because SPD combination treatment was effective not only in old but also in young mice (Fig. 1C and fig. S1A), we investigated whether SPD could boost the bioenergetics of CD8$^+$ T cells sorted from young mice. The addition of exogeneous SPD to CD8$^+$ T cell cultures from young mice also boosted the ATP production and FAO activity to a degree comparable to those changes observed in cultures with CD8$^+$ T cells isolated from old mice (fig. S4, A to C).

We examined the possibility that SPD directly stimulates FAO in mitochondria, which increases the SRC required for T cells' longevity and memory formation (*10*, *24*). Naïve CD8$^+$ T cells sorted from old mice and stimulated for only 1 hour with anti-CD3 and -CD28 mAb-coated beads in the presence of SPD showed enhanced mitochondrial and glycolytic activities and increased ATP production as well as SRC (Fig. 2, I to L). Similar results were obtained with naïve CD8$^+$ T cells isolated from young mice 1 hour after stimulation (fig. S4, D to G).

We further confirmed the immediate effect of SPD on FAO by several approaches using naïve CD8$^+$ T cells isolated from young mice. In the real-time Seahorse system in which SPD was injected in situ, SPD quickly increased the OCR of CD8$^+$ T cells stimulated with immobilized anti-CD3 and -CD28 mAb, and etomoxir cancelled enhancement of OCR (fig. S4H). SPD enhancement of OCR was observed in the media containing palmitate without glucose (fig. S4I). We further examined whether SPD directly facilitates FAO by analyzing the generation of energy metabolism–related compounds from ^{13}C-labeled palmitate in sorted naïve CD8$^+$ T cells, activated in vitro in the presence or absence of SPD. Just 1 hour after SPD stimulation, the incorporation of ^{13}C in tricarboxylic acid (TCA) cycle–associated metabolites, such as citrate, malate, isocitrate, and fumarate, was significantly enhanced by SPD (fig. S4, J and K). Although SPD exerted similar effects on effector and memory CD44$^+$ CD8$^+$ T cell populations at 44 hours, they were not as sizeable after 1 hour of stimulation (fig. S5, A and B). This suggests that the mechanism we describe is more prominent in naïve CD8$^+$ T cells.

SPD directly binds a central enzyme of FAO, mitochondrial trifunctional protein (MTP)

SPD enhances mitochondrial respiration through hypusination of translation factor eIF5A (*13*, *26*). Therefore, we tested whether a similar mechanism functions in boosting mitochondrial metabolism in CD8$^+$ T cells. GC7, a hypusination inhibitor that acts by blocking the deoxyhypusine synthase, the rate-limiting enzyme for eIF5A hypusination, did not inhibit acute (1 hour) mitochondrial activation of CD8$^+$ T cells by SPD (fig. S6A). In the later phase (44 hours), however, GC7 significantly decreased mitochondrial ATP production, as it dampened OXPHOS but not glycolytic activity (fig. S6B). Although SPD enhances autophagy and mitophagy activity, we did not observe changes in mitochondrial morphology or accumulation of autophagy-related proteins in 1 hour after stimulation (fig. S6, C and D). Thus, the synthesis of mitochondrial proteins and autophagic activity might be later effects of mitochondrial metabolism. Acute enhancement of mitochondrial respiration by SPD appears to be dependent on its direct activation of FAO.

To explore whether SPD directly activates FAO in mitochondria, we examined whether SPD bound to any mitochondrial components. We used nanomagnetic particles coated with SPD [SPD-coated ferrite-glycidyl methacrylate (FG) beads] to isolate SPD-binding proteins from the cell lysates of HeLa and eluted bound proteins in a high-salt buffer containing 2 or 4 mM SPD (Fig. 3A). We then separated the eluted proteins by electrophoresis and subjected the SPD-eluted bands A, B, and C to mass spectrometry (MS) (Fig. 3A). Among the proteins constantly detected in all three bands, we identified hydroxyl coenzyme A (CoA) dehydrogenase subunits α and β (HADHA and HADHB, respectively) that make up the MTP

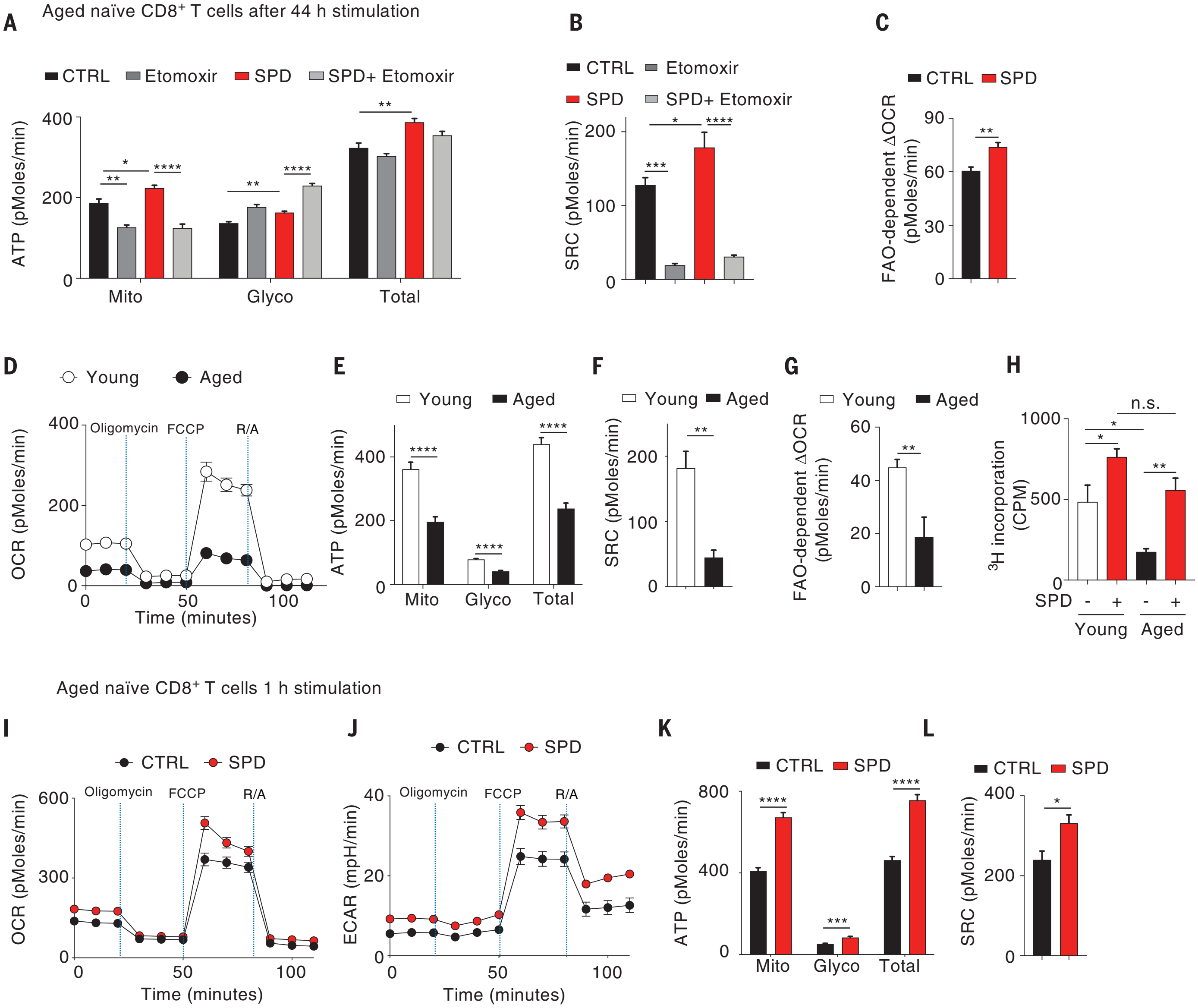

Fig. 2. SPD enhances mitochondrial respiration in a FAO-dependent manner. (**A** to **C**) Naïve CD8⁺ T cells from aged mice were stimulated for 44 hours with anti-CD3 and anti-CD28 coated beads in the presence or absence of SPD. Etomoxir was added 1 hour before the assay. ATP production (A), SRC (B), and FAO-dependent OCR (C) were calculated as indicated in fig. S2, A to C ($n = 4$ technical replicates pooled from 12 mice). (**D** to **G**) Mitochondrial bioenergetics in naïve CD8⁺ T cells isolated from young (white circle or bars) and aged mice (black circle or bars) ($n = 4$ to 5 technical replicates pooled from 4 young and 18 old mice). Real-time OCR (D), ATP production rate (E), SRC (F), and FAO-dependent coupled OCR (G) are shown. (**H**) Proliferation of naïve CD8⁺ T cells from young and aged mice after 20 hours stimulation with anti-CD3 and anti-CD28 coated beads with and without SPD ($n = 4$ to 5 technical replicates). (**I** to **L**) Naïve CD8⁺ T cells from aged mice were stimulated for 1 hour with anti-CD3 and anti-CD28 coated beads in the presence or absence of SPD (0.2 μM). OCR (I) and ECAR (J), ATP production rate (K), and SRC (L) are shown ($n = 5$ to 6 technical replicates). Data are the means ± SEMs [(D), (I), and (J)] or + SEMs [(A) to (C), (E) to (H), (K), and (L)]. *P* values were determined using unpaired two-tailed Student's *t* tests [(C), (E), (F), (G), (K), and (L)] or one-way ANOVA [(A), (B), and (H)]. $^{*}P < 0.05$; $^{**}P < 0.01$; $^{***}P < 0.001$; $^{****}P < 0.0001$; n.s, not significant. All data are representative of at least three independent experiments.

complex, responsible for β-oxidation of long-chain fatty acids (*27*, *28*). Western blotting experiments confirmed that the binding of HADHA and HADHB to SPD-coated FG beads was competitively decreased by the addition of 2 mM SPD to the mixing buffer (Fig. 3B). Similar binding of SPD to HADHA and HADHB was observed in mitochondrial lysates from Jurkat T cells (fig. S7A). We further confirmed the binding of SPD to HADHA and/or HADHB in situ by Duolink proximity ligation assay (PLA), in which the direct interactions between HADHA or HADHB proteins and SPD molecules were specifically detected as fluorescent spots by the interaction of two separate mAbs each to SPD or HADHA and HADHB (Fig. 3, C to E).

We expressed human HADHA and HADHB proteins in *E. coli* and purified the complex to homogeneity (Fig. 3, F and G). The purified protein complex with a single peak of 256 kDa in a gel filtration profile contained α and β subunits in an equal molar ratio, in agreement with the known $HADHA_2HADHB_2$ form (Fig. 3, H and I) (*27*, *28*). We confirmed that the antibody to SPD used in Duolink PLA recognized SPD bound to the purified $HADHA_2HADHB_2$ complex (fig. S7B). To test whether SPD binds to HADHA and HADHB independently, we also synthesized HADHA and HADHB separately in *E. coli*. Both HADHA and HADHB bound to

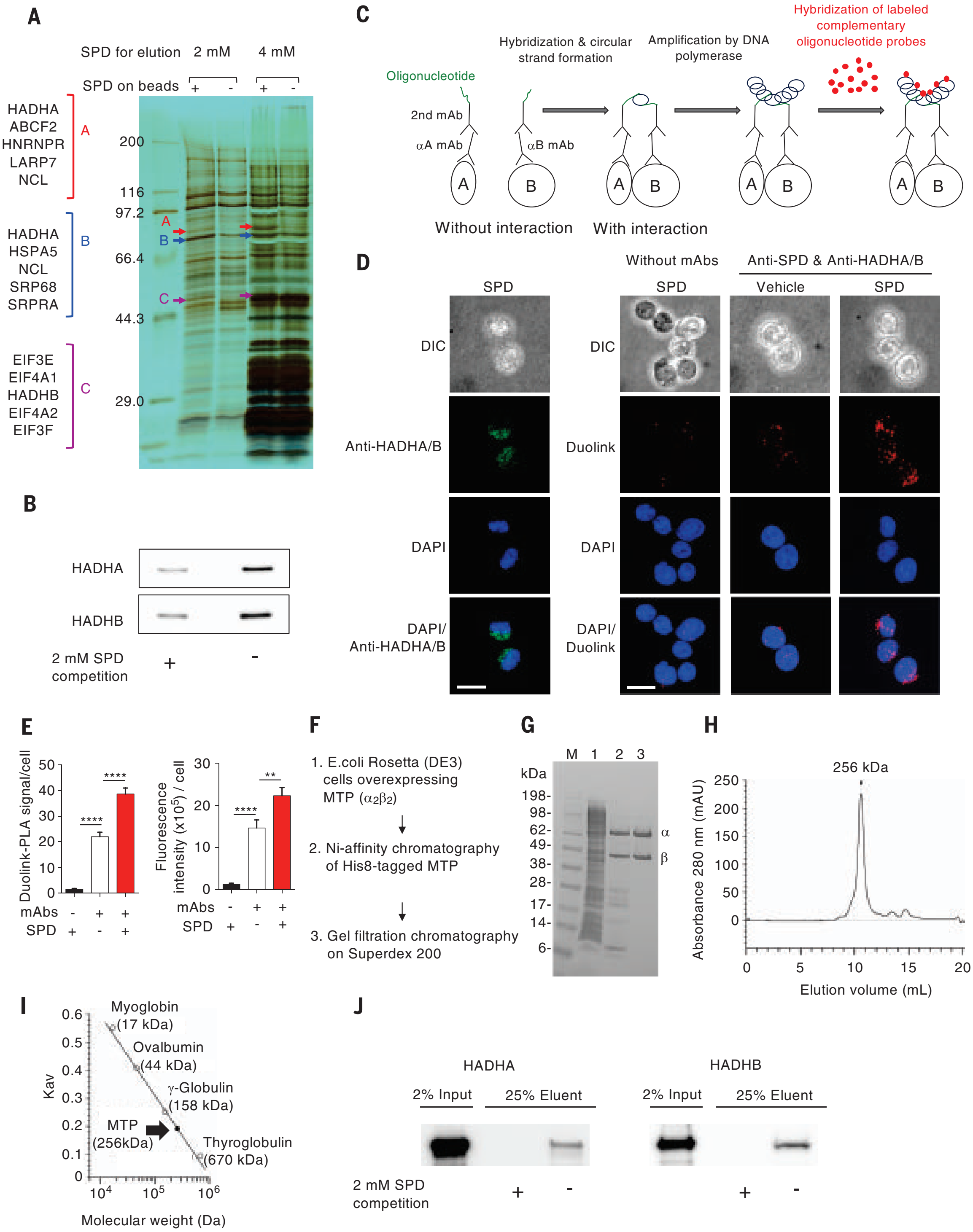

Fig. 3. SPD binds to HADHA and HADHB subunits of MTP. (**A**) Gel electrophoresis of HeLa cell lysate proteins captured by SPD-conjugated beads. Bands A, B, and C were eluted and subjected to mass spectrometry. The most abundant proteins in bands A, B, and C were listed on the left. (**B**) High concentration of SPD (2 mM) addition to HeLa cell lysate considerably decreased HADHA and HADHB proteins captured by SPD-conjugated beads. Bead-captured proteins were detected by HADHA- and HADHB-specific antibodies. (**C**) Illustrative figure of the principle of Duolink-PLA assay. (**D**) Molecular interaction between SPD and mitochondrial HADHA-HADHB (MTP) complex by in situ Duolink-PLA assay. Anti-SPD and anti-HADH antibodies were used for the assays. DIC, differential interference contrast; DAPI, 4′,6-diamidino-2-phenylindole. (**E**) The number and intensity of Duolink fluorescent dots (*n* = 19 to 25 cells). (**F**) Flow of human MTP purification steps. (**G**) Representative SDS-PAGE gel showing the purity of each step shown in (F). (**H**) Typical profile in gel filtration chromatography of the purified human MTP on a Superdex 200 Increase 10/300 GL column. mAU, milli–absorbance units (at the wavelength of 280 nm). (**I**) Calibration curve for the determination of the MTP molecular weight by gel filtration chromatography. (**J**) Separately produced HADHA and HADHB from *E. coli* were collected by SPD-conjugated beads. High dose of SPD addition to E. coli lysate decreased considerably, the HADHA or HADHB trapped by SPD-beads. Data are the means + SEMs (E). *P* values were determined using one-way ANOVA (E). $^{**}P < 0.01$; $^{****}P < 0.0001$. Data are representative of two to three independent experiments.

SPD beads, which was inhibited by the addition of free SPD (Fig. 3J).

SPD augments the PD-1 blockade efficacy by direct up-regulation of FAO enzymatic activity in T cells

During β-oxidation of long-chain fatty acids, the MTP complex catalyzes three out of four β-oxidation reactions—i.e., 2,3-enoyl-CoA hydrolase and 3-hydroxyl-CoA dehydrogenase (HAD) activities by HADHA and 3-ketothiolase (KT) activity by HADHB (Fig. 4A) (27–29). We thus examined the effect of SPD on the enzymatic kinetics of the purified $HADHA_2HADHB_2$ complex. SPD enhanced the HAD activity catalyzed by the HADHA subunit with a Michaelis constant (K_m) value of ~0.4 μM (Fig. 4B). SPD reduced the K_m value of NADH to the HAD enzyme and increased the maximum velocity of the enzymatic reaction (V_{max}). Thus, SPD may enhance the catalytic activity of HAD by allosteric binding to the HADHA subunit (Fig. 4C). SPD also activated the KT activity catalyzed by the HADHB subunit with a K_m value of ~0.7 μM (Fig. 4D). SPD also reduced the K_m value of acetoacetyl-CoA to the KT enzyme and appeared to shift the saturation curve of this substrate from the sigmoidal toward normal kinetics with apparently little change in V_{max}, supporting the allosteric effect of SPD on the MTP complex (Fig. 4E). We conclude that SPD interacts with both HADHA and HADHB subunits and allosterically activates their enzymatic activities.

To demonstrate physiochemical binding of SPD to the MTP complex in vitro, we used biolayer interferometry (BLI) (Octet). For this purpose, we expressed HADHA and HADHB separately in *E. coli*. We could purify $HADHA_2$ to homogeneity but failed to purify $HADHB_2$ as it showed heterogeneous peaks in a gel elution profile, suggestive of its hydrophobic properties (fig. S8). The biosensor tip, on the surface of which SPD was immobilized, was then immersed in a solution of purified $HADHA_2$ homodimer, and the difference in optical path length was traced in real time (Fig. 4F). Comparing two fitting model curves based on the binding molar ratio ($HADHA_2$:SPD = 1:1 or 1:2), we found that the 1:2 model, but not 1:1 model, fitted well, indicating that one purified $HADHA_2$ homodimer bound two SPD molecules with the binding affinity (dissociation constant, K_d) value of 0.10 μM. Because this method uses fixed SPD on the probe, the K_d value obtained tends to be much lower than the K_m value obtained by enzymatic kinetics (Fig. 4B).

Further depletion of CPT1a in a human T cell line (CPT1a knockdown Jurkat) abolished the acute enhancement effect of mitochondrial OCR by SPD (Fig. 4G and fig. S9A). To confirm that the SPD effect is mediated by MTP, we generated mice with specific deletion of HADHA in T cells (Fig. 4H). These mice showed frequencies of both $CD4^+$ and $CD8^+$ T cells, $CD44^{low}$ $CD8^+$ T cells, and $CD44^{high}$ $CD8^+$ T cells comparable to those in wild-type (WT) mice (fig. S9, B and C). The enhancement effects of SPD on OCR and tumor immunotherapy were not present in mice with T cell–specific deletion of HADHA (Fig. 4, I and J). Thus, we conclude that enhanced antitumor immunity by SPD supplementation depends in part on FAO activation through MTP, although we do not exclude other mechanisms.

Spermine competitively inhibits the FAO activity of SPD

FG beads coated with spermine, another natural polyamine derived from SPD, also bound to the $HADHA_2HADHB_2$ complex expressed in *E. coli* (fig. S10, A and B) and decreased SPD binding to the purified $HADHA_2HADHB_2$ complex (fig. S10B). Furthermore, spermine blocked SPD-induced activation of the HAD as well as KT activity of the purified MTP complex (fig. S10, C and D). Spermine decreased SPD-induced mitochondrial activation in a dose-dependent manner at both the early and late phases of $CD8^+$ T cell activation (fig. S10E). Additionally, norspermidine (norSPD), which does not have the moiety used for the hypusination reaction but shares the C_3-NH_2 structure with SPD and spermine, also increased mitochondrial ATP production in the later phase of activation (fig. S10, A and F). Within 20 hours, injected ^{13}C-labeled SPD was not metabolized into spermine, indicating that most injected SPD works directly as a positive regulator of FAO activity (fig. S11, A and B). Thus, it is likely that the late-phase mitochondrial activation by SPD may also be primarily a consequence of the activation of MTP.

Discussion

We showed that SPD acutely increased FAO and ATP production by direct activation of MTP in $CD8^+$ T cells, subsequently leading to de novo synthesis of proteins related to OXPHOS and translation. SPD binding and the activation of MTP may initiate a series of events, ultimately leading to enhanced mitochondrial metabolism. Hypusination of eIF5A may have critical roles in protein synthesis in a later phase of the SPD effect, although the relative contribution of these two mechanisms remains to be clarified. The K_m value (6.49 μM) of SPD to deoxyhypusine synthase is 10 times as high as that for MTP (0.4 to 0.7 μM in Fig. 4) (30). The inhibition of EP300 protein acetylase activity was demonstrated in vitro using 10 μM SPD, 50 times that required for MTP activation (31). These results support the possibility that MTP activation is the earliest and most efficient function of SPD. The current molecular mechanistic analysis of SPD function in $CD8^+$ T cells provides insight into the antiaging properties of SPD and may facilitate a better understanding of the strategies to prevent age-related immune diseases. SPD and caloric restriction mimetics induce drastic changes in the metabolome, resulting in autophagy. Also, starvation induces autophagy and promotes longevity, whereas exogenous lipid exposure inhibits autophagy (32, 33). Although lipid metabolism is closely linked to autophagy, its precise mechanism is still unknown (34). SPD administration has effects similar to those of starvation, preventing damage from exogenous lipid exposure and inducing autophagy within a few hours after administration (31, 35, 36). SPD is likely to induce a metabolic shift through FAO activation by allosteric binding to the MTP complex. Because the MTP complex also functions in energy production through FAO in other tissues, such as skeletal muscles and the heart, liver, and brain, in addition to the immune cells (19, 37–39), the current mechanism of FAO activation by SPD might be applicable to a whole-body antiaging effect of SPD. Although the FAO up-regulation by SPD demonstrated in this work may not represent its sole mechanism for longevity, it may be one of the critical pathways to maintain normal functions of various organs.

Materials and methods

Mice

Young C57BL/6N or BALB/c (1 to 3 months old) and aged C57BL/6N (>1 year old) mice were purchased from Charles River Laboratories Japan. C56BL/6N-background $HADHA^{flox}$ mice were purchased from Cyagen Biosciences. CD4 Cre were maintained at the Institute of Laboratory Animals, Graduate School of Medicine, Kyoto University (40). All mice were used under protocols approved by the respective institutional review board (IRB). All mice were maintained under specific pathogen–free (SPF) conditions.

Cell lines

Details of murine colon adenocarcinoma (MC38), Lewis lung carcinoma (LLC), and colon carcinoma (CT26) cell lines were described previously (41). MC38, CT26, and Jurkat cell lines were cultured in RPMI medium (Gibco) with 10% (v/v) heat-inactivated fetal calf serum (FCS) and 1% (v/v) penicillin–streptomycin mixed solution (Nacalai tesque). HeLa and LLC cells were cultured in DMEM medium (Gibco) with 10% (v/v) heat-inactivated fetal calf serum (FCS) and 1% (v/v) penicillin–streptomycin mixed solution (Nacalai tesque).

Chemical reagents

The following chemical reagents were used at the indicated concentrations for the combination therapy, mitochondrial activity assays, and MTP functional assays. SPD (Nacalai tesque) prepared in MiliQ as solvent (CTRL),

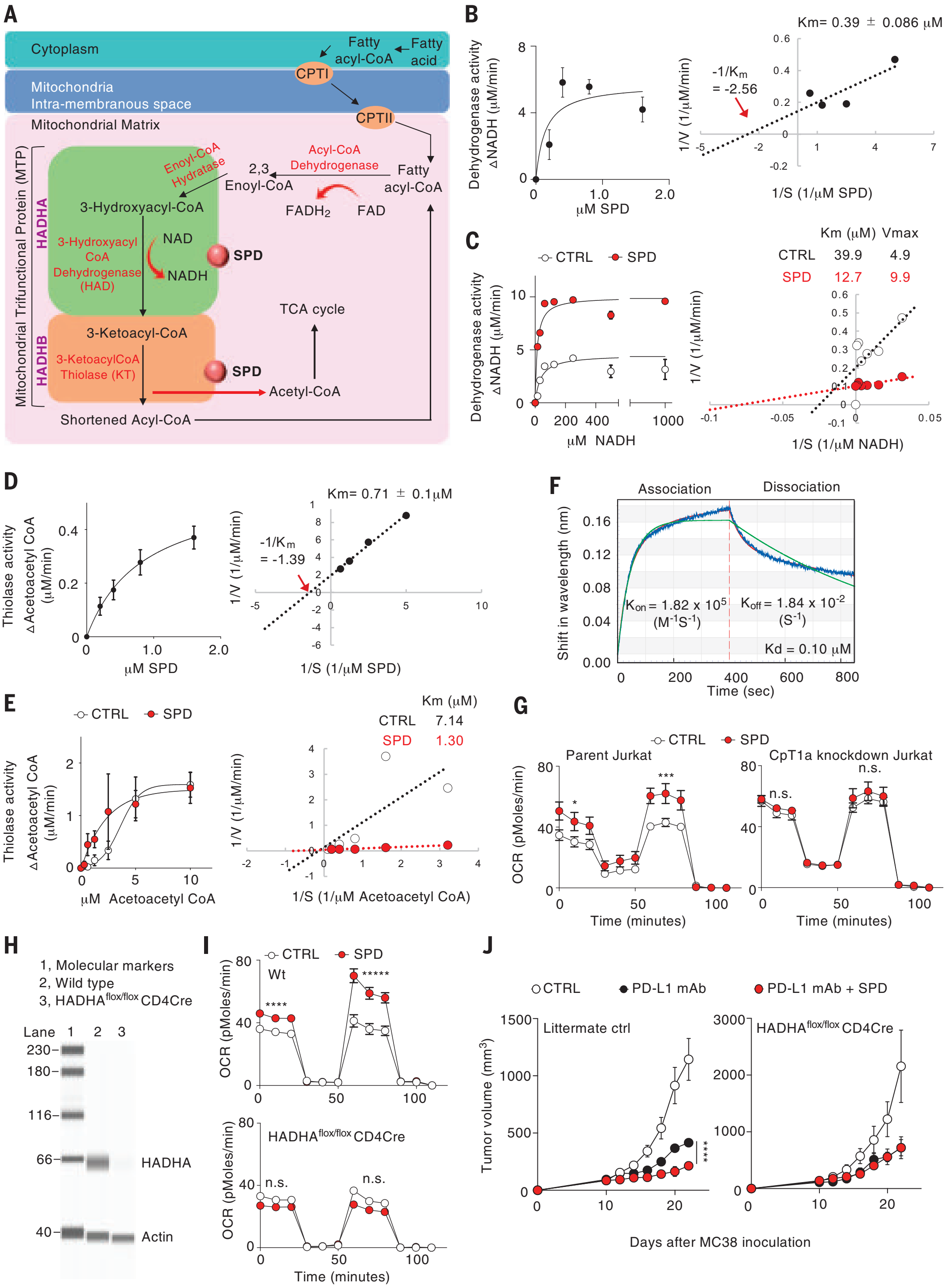

Fig. 4. SPD allosterically activates enzymatic activities of MTP. (**A**) A schematic diagram of the MTP complex and the enzymatic activities mediated by the HADHA and HADHB subunits. Long-chain fatty acids are transported into the mitochondria by carnitine and fatty acyl-CoA is catabolized by three steps of β-oxidation activity of MTP. (**B**) The effect of different doses of SPD on the dehydrogenase activity of the HADHA subunit in purified human MTP. The enzymatic activity was evaluated by the reduction of NADH in reverse reaction (left) (*n* = 4 technical replicates; HAD activity without SPD is used as a baseline to adjust the measurements in this graph). The best fit line of (1/V versus 1/SPD concentration) gave the K_m (K_d) value (right). (**C**) The effect of SPD on the NADH affinity in dehydrogenase activity of HADHA (left) (*n* = 5 technical replicates). The best fit line of (1/V versus 1/NADH concentration) gave the K_m and V_{max} value. (**D**) The effect of different doses of SPD on the 3-ketoacyl thiolase activity of HADHB subunit in purified human MTP. The enzymatic activity was evaluated by the reduction of acetoacetyl CoA in forward reaction (left) (*n* = 6 technical replicates; KT activity without SPD is used as a baseline to adjust the measurements in this graph). The best fit line of (1/V versus 1/SPD concentration) gave the K_m (K_d) value (right). (**E**) The effect of SPD on the acetoacetyl CoA affinity to HADHB in MTP (left) (*n* = 5 technical replicates). The best fit line of (1/V versus 1/ acetoacetyl CoA concentration) gave the K_m value (right). (**F**) Octet analysis of the molecular binding between SPD and the $HADHA_2$ homodimer. Green and red smooth lines represent models fitted by 1:1 and 1:2 binding stoichiometry, respectively. Actual binding data (blue wavy line) fit well to the 1:2 bivalent model, indicating that the $HADHA_2$ homodimer binds two SPD on the surface of the Octet probe. (**G**) CPT1a was knocked down by CRISPR interference system on human T cell line, Jurkat. In the medium with low glucose and high palmitate, the effect of SPD on the OCR of parent and CPT1a-knockdown Jurkat were evaluated (*n* = 3 to 5 technical replicates, unpaired two-tailed Student's *t* tests of the second point in each step of OCR assay). (**H**) Western blotting assay of protein levels of HADHA in $CD3^+$ T cells of T cell–specific HADHA knockout mice ($HADHA^{flox/flox}$ CD4Cre mice). (**I**) OCR of naïve $CD8^+$ T cells from $HADHA^{flox/flox}$ CD4 Cre or WT mice stimulated with anti-CD3 and anti-CD28 coated beads with or without SPD for 1 hour in the medium with low glucose and high palmitate (*n* = 6 technical replicates). (**J**) The effect of SPD combination on the MC38 growth in littermate control (ctrl) or $HADHA^{flox/flox}$ CD4Cre mice [*n* = 3 mice (PD-L1 mAb or PD-L1 mAb + SPD for control mice), 4 mice (PD-L1 mAb or PD-L1 mAb + SPD for $HADHA^{flox/flox}$ CD4Cre mice), or 5 mice (the other groups), with male and female mice distributed equally among the groups]. Data are the means ± SEMs [(B) to (E), (G), (I), and (J)]. *P* values were determined using multiple unpaired Student's *t* tests [(G) and (I) in the second point after each step of OCR assay] or two-way ANOVA [(J) on day 22]. $^{**}P < 0.01$; $^{***}P < 0.001$; $^{****}P < 0.0001$; n.s, not significant. Data are representative of two or more independent experiments.

spermine (Nacalai tesque), norSPD (Sigma-Aldrich), GC7 (EMD Milipore), etomoxir (Sigma-Aldrich), acetoacetylCoA (Cayman chemical company), NADH (Nacalai tesque), CoA (Sigma-Aldrich), and ^{3}H thymidine (PerkinElmer). Other chemical reagents used were equipped with the kits.

Mouse therapy model

MC38 (5×10^{5}), LLC (2×10^{6}), or CT26 (1×10^{6}) were intradermally (i.d.) injected on the right flank (day 0) into C57BL/6N or BALB/c mice. For treatment, the mice were intraperitoneally (i.p.) injected with 40 μg of anti–PD-L1 mAb (clone 1-111A, made in house) alone (*42*) or in combination with SPD 9 to 10 days after tumor inoculation. Anti–PD-L1 mAb and SPD were injected every 5 days until day 30. Tumor measurement was performed on each alternate day, and tumor volume was calculated using the formula for a typical ellipsoid: 3.14 × (length × breadth × height) / 6.

In vivo analysis

For in vivo analysis, MC38 tumor–bearing mice were treated with PD-L1mAb and SPD 10 days after tumor injection and euthanized on day 13. Cells from the DLNs [axillary, brachial, and inguinal lymph nodes (LNs)] on the right side of tumor-bearing mice were harvested. All LNs were homogenized and pooled. For TIL analysis, tumor samples were minced into 1- to 2-mm pieces with scissors and digested with collagenase type IV (Thermo Fisher Scientific) using a gentleMACS Dissociator (Miltenyi Biotec). The number of TILs per milligram was used to calculate absolute numbers. For peripheral blood mononuclear cells (PBMCs) analysis, 100 μl of blood was collected and then treated with ammonium-chloride-potassium lysing buffer to lyse red blood cells. To check the mitochondrial activity, total CD8^{+} T cells were sorted from pooled DLNs using autoMACS Pro Separator (Miltenyi Biotec, 130-1117-004) and used for Seahorse. The total CD8^{+} T cells were also stimulated with anti-CD3 and -CD28 mAb beads (Thermo Fisher Scientific) for 20 hours and used to measure the proliferation by thymidine incorporation assay (*41*). The supernatant after the stimulation was used to measure IFN-γ secretion by enzyme-linked immunosorbent assay (ELISA) (Biolegend, 430804) according to the manufacturer's instructions.

Absolute quantification of polyamines by liquid chromatography–mass spectrometry (LC-MS)

Sample preparation

For polyamine quantification in the serum of mice, whole blood was collected from the cranial vena cava and allowed to clot undisturbed at room temperature for 1 hour. The clot was then removed by sequential refrigerated centrifugation at 14,500 rpm for 15 min. Serum was collected to new tubes and then centrifuged for another 8 min. Serum was aliquoted and used for analysis.

For polyamine quantification in naïve CD8^{+} T cells, pooled peripheral LN (pLN) and spleen cells were used for sorting naïve CD8^{+} T cells by Mojosort system (BioLegend MojoSort: 480035). The cells were stained using CD8 (53-6.7) and CD44 (1M7) antibodies, and CD44^{-} cells (naïve fraction) were sorted using BD FACSAria (BD Biosciences). For total SPD concentrations, 1×10^{6} cells pellets were used for analysis. To measure free SPD concentrations, cells were homogenized in 150 μl of RNase-free, DNase-free, and protease-free water (Nacalai tesque) for 5 min on ice using Violamo Homogenizer Pestle. Then 150 μl of 70% alcohol was added, and RNAs were removed using RNA binding columns (Qiagen, 74104). The samples were subsequently filtered using DNA binding columns (Qiagen, 27106) to removed DNA and using Ultrafree-MC-PLHCC centrifugal filters (Milipore, UFC3LCCNB-HMT) to remove proteins. Filtered samples were used for analysis.

Quantification

Polyamine concentration in blood cells and serum was quantified by the internal standard method. To the filtered solution was added 200 μl of methanol containing isotopically labeled polyamines [0.01 μM, spermidine-(butyl-$^{13}C_4$) trihydrochloride, spermine-(butyl-d8) tetrahydrochloride, putrescine-15N2 dihydrochloride]. After centrifugation at 16,000 ×*g* for 30 min at 4°C, 250 μl of the supernatant was collected and dried using vacuum centrifugation. The dried sample was resuspended in 20 μl of 0.1% formic acid in water and then subjected to LC-MS analysis. Authentic standards of SPD (spermidine trihydrochloride) and spermine (spermine tetrahydrochloride) were purchased from SIGMA Aldrich. Putrescine was purchased from Tokyo Chemical Industry. Standard solutions were prepared at the concentration of 0.0002, 0.0004, 0.001, 0.002, 0.005, 0.01, 0.02, 0.05, and 0.1 and treated with the same procedure as the sample. The cellular concentration of polyamines was calculated, taking into account the mean cell volumes of each group (young = 302 fl; aged = 443 fl) estimated from measured cell diameter. The cell volume was significantly different between young and aged mouse ($P < 0.001$, Wilcoxon rank sum test). For serum samples, the protocol was slightly changed. Briefly, 50 μl of serum was treated with 250 μl of methanol for polyamine extraction, and the standard curve range was 0.01 to 4 μM. The correlation coefficient of standard curve was higher than 0.99. LC separation was conducted on a Shim-pack GIST C18-AQ column (3 μm, 150 mm × 2.1 mm id, Shimadzu GLC) with a Nexera UHPLC system (Shimadzu). The mobile phase consisted of 0.1% formic acid in water (A) and 0.1% formic acid in acetonitrile (B). The gradient program was as follows: 0 to 3 min, 0% B; 3 to 15 min, linear gradient to 60% B; 15 to 17.5 min, 95% B; 17.5 to 20.0 min, linear gradient to 0% B; hold for 4 min; flow rate, 0.2 ml/min. The column oven temperature was maintained at 40°C. The LC system was coupled with a triple-quadruple mass spectrometer LCMS-8060 (Shimadzu). LCMS-8060 was operated with the electrospray ionization and multiple reaction monitoring mode. The ion transitions (precursor–product ion) for SPD, spermidine $^{13}C_4$, spermine, spermine d8, putrescine, and putrescine 15N2 were *m*/*z* (mass/charge ratio) 146.2 to 72.1, 150.2 to 76.1, 203.2 to 112.1, 211.3 to 120.1, 89.1 to 72.1, and 91.1 to 73.0, respectively.

Cell preparation for in vitro analysis

For in vitro mitochondrial activity assays, cells from axillary, brachial, and inguinal pLNs on both sides of mice without tumor were harvested, homogenized, and pooled. Spleens were harvested and homogenized and then treated with ammonium-chloride-potassium (ACK) lysing buffer for 2 min to lyse red blood cells. After pooling the cells of pLNs and spleens, naïve (CD44^{low}) CD8^{+} T cells were purified using MojoSort system (BioLegend MojoSort: 480044) according to the manufacturer's instructions and used for Seahorse assays. For effector memory (CD44^{high}) CD8^{+} T cells in vitro experiments, total CD8^{+} T cell were first sorted from pooled LN and spleen cells using CD8^{+} T cell Mojosort system (BioLegend MojoSort: 480035). The cells were then stained using CD8 (53-6.7) and CD44 (1M7) antibodies, and CD44^{+} cells (effector memory fraction) were sorted using BD FACSAria (BD Biosciences). For Jurkat experiments, 24 hours before the seahorse assay, the cells were transfered to low-glucose (2.5 mM) RPMI medium.

Mitochondrial activity and ATP production rate measured by Seahorse

Isolated cells were seeded in an XFe96 plate (3 to 5×10^{5} and 8×10^{4} cells per well for the assays of primary cells and cell line, respectively), and their OCR and ECAR were measured by the XFe96 Extracellular Flux Analyzer (Seahorse Bioscience) as previously described (*21*). The three pharmaceutical modulators of mitochondrial OXPHOS, which were included in the XF Cell Mito Stress Test Kit (Seahorse Bioscience), were used for OCR and ECAR measurement (*22*). For these assays, XF DMEM Base Medium (Agilent, 103575-100) was used, supplemented with 1 mM HEPES (pH 7.4), 1 mM pyruvate (Nacalai Tesque), 2 mM glutamine (Nacalai Tesque), and 10 mM glucose (Nacalai Tesque). For the FAO measurement in CD8^{+} T cells isolated from in vivo treated mice, XF RPMI Base Medium (Agilent, 103576-100) was used, supplemented with 1 mM HEPES (pH 7.4), 2.5 mM glucose, and 0.75 mM carnitine (Sigma-Aldrich) on the day of the assay. Oligomycin (1.5 μM), carbonyl cyanide 4-(trifluoromethoxy) phenylhydrazone (FCCP) (1 μM), and rotenone/antimycin A (1 μM) were injected sequentially. Each parameter of mitochondrial activity was defined as follows (details in fig. S2, A and B). Basal OCR was defined as (the last rate measurement before oligomycin injection) – (nonmitochondrial respiration rate after rotenone/antimycin injection). Maximal OCR was defined as (the first rate-measurement after FCCP injection) – (nonmitochondrial respiration rate). OCR coupled with ATP production (coupled OCR) was defined as (basal OCR) – (the last rate-measurement before FCCP injection). OCR uncoupled with ATP production (uncoupled OCR or SRC) was defined as (maximal OCR) – (basal OCR). Mitochondrial and glycolytic ATP production rates were automatically calculated by the Seahorse machine operating software (Wave) based on the coupled OCR and the ECAR, the difference between measurements before and after oligomycin injection, respectively. FAO-dependent OCR (ΔOCR) was defined as the (OCR untreated with etomoxir) – (OCR treated with etomoxir) (details in fig. S2C). Etomoxir (5 μM) or dimethyl sulfoxide (DMSO) (as solvent control) were added 50 min before running the assay. Palmitate (100 to 200 μM) or bovine serum albumin (BSA) (as solvent control) were added to the correspondent groups 30 s before running the assay.

Mitochondrial activity in response to SPD and etomoxir in situ injection measured by Seahorse

Isolated cells (8×10^4 per well) were seeded in an XFe96 plate coated or uncoated with functional grade CD3/CD28 mAb. OCR was then measured by the XFe96 Extracellular Flux Analyzer (Seahorse Bioscience). The measurement protocol was modified so that the machine injects SPD (final concentration of 0.2 μM) from the first port and etomoxir (final concentration of 3 μM) from the second port. Oligomycin (final concentration of 1.5 μM) was injected from the thirst port and rotenone/antimycin A (final concentration of 1 μM) from the fourth port. For these assays, XF RPMI Base Medium (Agilent, 103576-100) was used, supplemented with 1 mM HEPES (pH 7.4), 2.5 mM glucose, 0.75 mM carnitine (Sigma-Aldrich) and 200 μM palmitate (Cayman) on the day of the assay

Proteomics

Preparation of unlabeled tryptic peptide samples for data-independent acquisition mass spectrometry (DIA-MS)

Tryptic peptide samples were prepared following the phase transfer surfactant method (*22*), with modifications described as follows: Protein extracts were prepared from 4×10^5 cells in 10 μl of lysis buffer containing 12 mM sodium deoxycholate, 12 mM sodium N-dodecanoylsarcosinate, and 100 mM Tris-HCl pH 9.0, with complete EDTA-free protease inhibitor cocktail (Roche). To reduce and alkylate the disulphide bonds, DL-dithiothreitol was added to 10 mM with incubation at 50°C for 30 min, followed by iodoacetamide added to 40 mM at room temperature for 30 min the dark, then cysteine was added to 55 mM for 10 min to quench the alkylation reactions. Samples were diluted 1:2.76 with 50 mM ammonium bicarbonate solution. Mass spectrometry–grade lysyl endopeptidase (FUJIFILM Wako Chemical Corporation) was added at 200 ng, after mixing, 200 ng sequencing grade modified trypsin (Promega) was added, followed by protein digestion at 37°C for 14 hours. Afterward, 1.83 volumes ethyl acetate was added together with trifluoroacetic acid (TFA) to 0.5% (v/v). Centrifugation at 12,000 ×*g* for 5 min produced an upper organic phase which was discarded and a lower aqueous phase containing digested tryptic peptides, which was dried using a centrifugal vacuum concentrator. Afterward, samples were desalted with ZipTip C18, 0.6 μl Pipette Tips (MilliporeSigma) and dried.

The protein concentration of protein extracts in lysis buffer was determined using a Pierce BCA Protein Assay Kit (ThermoFisher Scientific). From each sample, 5 μg protein at a concentration of 0.5 μg/μl was used to prepare digested tryptic peptide samples, as described above. Afterward, the tryptic peptide samples were desalted with MonoSpin C18 columns (GL Sciences Inc.) and dried using a vacuum centrifuge. To generate a spectral library, a combined sample containing tryptic peptides from each sample condition was fractionated using a Pierce High pH Reversed-Phase (HPRP) Fractionation Kit, according to the manufacturer's instructions (ThermoFisher Scientific).

Mass spectrometry measurement for proteomic analysis

For liquid chromatography with tandem mass spectrometry (LC-MS/MS), a Q-Exactive Plus Orbitrap mass spectrometer with an attached Nanospray Flex ion source connected to an EASY-nLC 1200 system was used (ThermoFisher Scientific). The peptides were separated using an analytical column with 3 μm C18 particles, an inner diameter of 75 μm and a length of 12.5 cm (Nikkyo Technos Co., Ltd.). Solvents were LC/MS grade. LC solvent A consisted of 0.1% (v/v) formic acid in water and LC solvent B consisted of 0.1% (v/v) formic acid in 80% (v/v) acetonitrile. The flow rate was 300 nl/min with a 2-hour gradient: 0 to 108 min (2% B to 34% B), 108 to 110 min (34% B to 95% B), and 110 to 120 min consisted of a final wash at 95% B. A 2.0-kV spray voltage was applied, and the ion transfer tube temperature was 250°C.

For data-dependent acquisition (DDA) measurement of the TMT-labeled peptide samples, the peptides were dissolved in 6.8 μl of 0.1% (v/v) formic acid, 3% (v/v) acetonitrile in water, and 5 μl was measured. The full MS spectra were acquired from 380 to 1400 *m/z* at a resolution of 70,000, the automatic gain control (AGC) target was 3×10^6, with a maximum injection time (IT) of 50 ms. MS^2 scans were recorded for the top 15 precursors at 17,500 resolution with an AGC target of 2×10^5 and a maximum IT of 100 ms. The isolation window was set at 0.7 *m/z* with a fixed first mass of 105.0 *m/z*. The default charge state was 2. HCD fragmentation was set to normalized collision energy of 32%. The intensity threshold was 8.0×10^3, charge states 2 to 5 were included, and the dynamic exclusion was set to 20 s.

For data-independent acquisition (DIA), the peptide samples were dissolved in 10 μl of 0.1% (v/v) formic acid, 3% (v/v) acetonitrile in water, and 3 μl was loaded. Data were acquired with 1 full MS and 32 overlapping isolation windows constructed covering the precursor mass range of 400 to 1200 *m/z*. For full MS, resolution was set to 70,000, AGC target was 5×10^6, and the IT was 120 ms. DIA segments were acquired at 35,000 resolution with an AGC target of 3×10^6 and an automatic maximum IT. The first mass was fixed at 200 *m/z*. HCD fragmentation was set to normalized collision energy of 27%.

For data-dependent acquisition (DDA) of unlabeled HPRP-fractionated peptide samples, each fraction was dissolved in 6.5 μl of 0.1% (v/v) formic acid, 3% (v/v) acetonitrile in water, and 5.0 μl was loaded. The full MS spectra were acquired from 380 to 1500 *m/z* at a resolution of 70,000, the AGC target was 3×10^6 and a maximum IT of 100 ms. The MS^2 scans were recorded for the top 20 precursors at 17,500 resolution with an AGC target of 1×10^5 and a maximum IT of 60 ms. The isolation window was 2.2 *m/z*. The default charge state was 2. HCD fragmentation was set to normalized collision energy of 27%. The intensity threshold was set to 1.3×10^4, charge states 2 to 5 were included, and the dynamic exclusion was set to 20 s.

Protein identification and quantification in proteomic analysis

For analysis of the DIA data, a spectral library was first generated from the eight raw data files obtained from DDA measurement of the HPRP-fractionated unlabeled samples using Proteome Discoverer version 2.4 with the Uniprot reviewed *Mus musculus* (taxon 10090) database. The filtered output from Proteome Discoverer was used to generate a sample-specific spectral library using Spectronaut software (Biognosys). Raw data files from DIA measurement were used for extraction of peptide quantities with the generated spectral library and integration of these quantities into protein abundances. False discovery rate (FDR) was estimated with the mProphet approach and set to 0.01 at both peptide precursor level and protein level (43, 44). Data filtering parameters for quantification were Q-value percentile fraction 0.5 with global imputing, and cross run normalization with global normalization on the median.

In vitro metabolic trace analysis of ^{13}C-labeled palmitate and SPD

For palmitate-$^{13}C_{16}$ tracing, naïve CD8$^+$ T cells were sorted from LNs and spleens of 3-month-old mice and cultured in glutamine/glucose/FBS-free RPMI-1640 medium (Wako) supplemented with 1× MEM NEAA, 10 mM HEPES, 50 μM 2-mercaptoethanol, 100 U/ml penicillin, 100 U/ml streptomycin, 500 μM L-carnitine hydrochloride (Sigma), and 200 μM BSA-conjugated palmitate-$^{13}C_{16}$ (Isotec). Cells were stimulated for 1 hour in the presence of anti-CD3 and -CD28 mAb beads (Thermo Fisher Scientific) with and without 0.2 μM SPD (Nacalai).

For SPD-(butyl-$^{13}C_4$) tracing, naïve CD8$^+$ T cells were cultured in RPMI-1640 medium (Wako) with glutamine/glucose supplemented with 10% (v/v) dialyzed FBS (Thermo Fisher Scientific), 1× MEM NEAA, 10 mM HEPES, 50 μM 2-mercaptoethanol, 100 U/ml penicillin, 100 U/ml streptomycin, and 1 mM sodium pyruvate. Cells were stimulated as described above for 1 and 20 hours with and without 0.2 μM spermidine-(butyl-$^{13}C_4$) (Sigma).

Metabolite extraction from cultured cells for metabolome analyses was performed as described previously (45). Briefly, cells were washed twice with cold phosphate-buffered saline (PBS), and residual wash solvent was carefully removed. Cells were then immediately frozen into liquid nitrogen and stored at −80°C until assayed. The frozen cultured cells were scraped with methanol containing internal standards (450 μl) followed by the addition of 500 μl of chloroform and 250 μl of ultrapure water. After centrifugation, the aqueous phase was ultrafiltered using an ultrafiltration tube (Ultrafree MC-PLHCC; Human Metabolome Technologies, Inc., Yamagata, Japan). Then, the filtrate was concentrated with a vacuum concentrator. The concentrated filtrate was dissolved in 50 μl of ultrapure water and used for LC-MS/MS and IC-MS analyses.

Mass spectrometry analysis to detect ^{13}C-labeled metabolites

For metabolome analysis focused on glycolytic metabolites, TCA cycle intermediates as well as ketone bodies, anionic metabolites were measured using an orbitrap-type MS (Q-Exactive focus; Thermo Fisher Scientific) connected to a high-performance ion chromatography (IC) system (ICS-5000+, Thermo Fisher Scientific) that enabled us to perform highly selective and sensitive metabolite quantifications owing to the IC-separation and Fourier Transfer MS principle. The IC was equipped with an anion electrolytic suppressor (Thermo Scientific Dionex AERS 500) to convert the potassium hydroxide gradient into pure water before the sample entered the mass spectrometer. The separation was performed using a Thermo Scientific Dionex IonPac AS11-HC, 4-μm particle size column. The IC flow rate was 0.25 ml/min supplemented post-column with 0.18 ml/min makeup flow of MeOH. The potassium hydroxide gradient conditions for IC separation were as follows: from 1 mM to 100 mM (0 to 40 min), 100 mM (40 to 50 min), and 1 mM (50.1 to 60 min), at a column temperature of 30°C. The Q Exactive focus mass spectrometer was operated under an ESI negative mode for all detections. Full mass scan (m/z 70 to 900) was performed at a resolution of 70,000. The automatic gain control target was set at 3×10^6 ions, and the maximum ion injection time was 100 ms. Source ionization parameters were optimized with the spray voltage at 3 kV, and other parameters were as follows: transfer temperature = 320°C, S-Lens level = 50, heater temperature = 300°C, Sheath gas = 36, and Aux gas = 10. The amount of cat ionic metabolites including amino acids were quantified using LC-MS/MS (45). Briefly, a triple-quadrupole mass spectrometer equipped with an electrospray ionization (ESI) ion source (LCMS-8060, Shimadzu Corporation) was used in the positive and negative-ESI and multiple reaction monitoring (MRM) modes. The samples were resolved on the Discovery HS F5-3 column (2.1 mmI.D. x 150 mmL, 3 μm particle, Sigma), using a step gradient with mobile phase A (0.1% formate) and mobile phase B (0.1% acetonitrile) at ratios of 100:0 (0 to 5 min), 75:25 (5 to 11 min), 65:35 (11 to 15 min), 5:95 (15 to 20 min), and 100:0 (20 to 25 min), at a flow rate of 0.25 ml/min and a column temperature of 40°C.

Preparation of SPD FG beads

Immorbilization of SPD on NHS FG magnetic beads (TAS8848 N1141, Tamagawa Seiki) was carried out according to the manufacturer's instruction. Briefly, 2.5 mg of NHS beads, which have a binding capacity for ~600 nmol of SPD, were washed twice with DMF (N,N-dimethylformamide, Nacalai Tesque) and then mixed with 5 mM SPD (Nacalai Tesque) dissolved in DMF. After dispersion by sonication, beads were incubated for 70 min at room temperature on a micro tube mixer. Then, beads were centrifuged at 15,000 rpm for 5 min to remove supernatant. 500 μl of 1M aminoethanol (Nacalai Tesque) in DMF was added to the beads, followed by dispersion by sonication. Beads were incubated further for 1 hour at room temperature. After being washed three times by 50% methanol, beads were stored in 150 μl of 50% methanol at 4°C.

Affinity purification with SPD FG beads

Cytoplasmic lysates of HeLa cells were dialyzed against KCl binding buffer [20 mM Hepes (pH 7.9), 100 mM KCl, 1 mM $MgCl_2$, 0.2 mM $CaCl_2$, 0.2 mM EDTA, 0.1 mM DTT, 0.1% NP-40, 10% (v/v) glycerol, supplemented with 1x protease inhibitor cocktail (Nacalai Tesque)]. For affinity purification, 50 μl of SPD FG beads were washed three times with the KCl binding buffer by sonication and centrifugation and then mixed with 500 μl of cell cytoplasmic lysates (~2 mg/ml of protein). As a negative control, SPD was added to the lysate to 2 mM for 1 hour competition at 4°C before mixing with the SPD beads. After being incubated for 4 hours at 4°C on a rotator, SPD beads were isolated by magnetic separation, and then suspended in the KCl binding buffer by sonication. Magnetic separation and sonication were repeated twice. After the final wash, elution buffers [20 mM Hepes (pH 7.9), 100 mM NaCl, 1 mM MgCl2, 0.2 mM CaCl2, 0.2 mM EDTA, 0.1 mM DTT, 0.1% NP-40, 10% (v/v) glycerol] containing 2 and 4 mM of SPD were mixed thoroughly with the beads by sonication, followed by 1 hour incubation at 4°C on a micro tube mixer for elution. Beads were separated magnetically, and eluates were subjected to SDS–polyacrylamide gel electrophoresis (SDS-PAGE). Gels were stained by EzStain Silver (ATTO), and protein bands were excised for mass spectrometric analysis. Affinity purification with spermine FG beads were conducted in the same way.

For the affinity purification from the lysate of Jurkat mitochondria, mitochondria were isolated using the EzSubcell Farction kit (WSE-7422, ATTO) according to the manufacturer instructions. They were then lysed in 2 volumes of lysis buffer [10 mM HEPES-NaOH (pH 7.9), 10 mM KCl, 1% NP40, 0.1 mM EDTA, 1 mM DTT, 0.5 mM PMSF] and then centrifuged at 13,500 ×g for 2 min. The supernatants were collected and diluted 10 times with pull-down buffer [820 mM HEPES (pH7.9), 100 mM KCl, 0.1% NP-40, 1 mM $MgCl_2$, 0.2 mM $CaCl_2$, 0.2 mM EDTA, 10% (v/v) glycerol, 1 mM DTT, 0.2 mM PMSF]. Affinity purification using SPD-immorbilized beads was performed as described above.

Western blotting

For HADHA and HADHB detection in the FG bead experiments, pull-downed samples were subjected to SDS-PAGE and transferred to TransBlot Turbo PVDF membranes (Bio-Rad). The following antibodies were used for detection: HADHA and HADHB (1/300, HPA015536, HPA066099, Atlas Antibodies, respectively) and rabbit immunoglobulin G (IgG) HRP (1/20000, no. 7074, Cell Signaling Technology).

Membrane was blocked with 5% (w/v) nonfat dry milk (Nacalai Tesque) for 1 hour at room temperature and then incubated with primary antibodies at 4°C overnight. The following day, secondary antibodies conjugated to horseradish peroxidase (HRP) were incubated for 1 hour at room temperature. Proteins were detected by Chemi-lumi One Ultra ECL Western Blotting Substrate (WAKO).

For the detection of HADHA protein from the T cells of HADHA$^{flox/flox}$ CD4 Cre mice and CPT1a knockdown Jurkat, T cell lysates were run through the automated Simple Western system, Jess according to the instructions (ProteinSimple Japan K.K.). The following antibody was used for detection; HADHA (1/100, 60250-1-Ig, Proteintech), CPT1a (1/250, ab128568, abcam) and beta-actin (1/250, no. 1978, Sigma), anti-Mouse Detection Module (MD-002A, biotechne). Mitochondrial morphology- and autophagy-related proteins Mitofusin (1/250, no. 9482, CST), Atg5 (1/250, no. 12994, CST), and Atg7 (1/50, no. 8558, CST) in stimulated T cells were detected in the similar way.

BLI experiment

Measurement of binding kinetics was performed by the BLI method using the Octet K2 system (Fortebio), according to the manufacturer's protocols. 10 mM SPD in PBS (pH7.4) was immobilized on an Amine Reactive 2nd Generation (AR2G) sensor (Fortebio). Purified HADHA$_2$ protein was diluted in PBS (pH 7.4) / 0.04% Tween / 0.01% BSA (kinetics buffer) to a concentration of 15 nM. The kinetics buffer was used as a running buffer in all data acquisition steps. Actual binding to SPD was obtained by subtracting nonspecific binding to a reference sensor (no SPD immobilized) from total binding to the SPD sensor. K_D, k_{on}, and k_{off} values were calculated and fitted by the Octet Data Analysis 8.1 Software (Fortebio). 1:2 bivalent binding model gave the best fit between the theoretical values and the actual measurement. Kinetic constants were determined by integrating the experimental data using the differential rate equation $dR / dt = k_{on} \cdot C \cdot (Rmax - R) - k_{dis} \cdot R$ to obtain k_{on} and k_{off} values simultaneously (R = observed response, Rmax = maximum response upon saturation, C = analyte concentration, k_{on} = association rate constant, k_{off} = dissociation rate constant). Then, the ratio between k_{dis} and k_{off} gives the reported dissociation constants (K_D). The goodness of fit was evaluated by the reduced chi-square (χ2) and the R2 value.

Immunofluorescent staining of HDAHA and HADHB

For immunostaining of HDAHA and HADHB, Jurkat cells were fixed with 4% paraformaldehyde in phosphate buffer solution (09154-85, Nacalai Tesque) for 15 min and washed three times with fluorescence-activated cell sorting (FACS) buffer. Briefly, cells were permeabilized using 0.5% TritonX-100 buffer (10 mM Tris HCl, 50 mM NaCl, 5 mM EDTA, 0.02% NaN_3, and 0.5% TrotonX-100) for 10 min and washed three times with FACS buffer (10% FCS in PBS). Cells were then incubated with anti-HADHA/HADHB antibody (1:100 dilution in FACS buffer, ab110302, abcam). One hour after the primary antibody incubation, cells were washed three times with FACS buffer and incubated with FITC conjugated anti-mouse IgG antibody (1:100 dilution in FACS buffer, 103002, SouthernBiotech) for 1.5 hours at room temperature in the dark. After washing with FACS buffer, immunofluorescence images were collected using Olympus SpinSR10 spining disk confocal super-resolution microscope high-sensitivity model (×100 magnification).

Duolink in situ PLA

Jurkat cells were cultured with or without SPD (0.2 μM) for 2 days. To detect interaction between SPD and HADHA/HADHB by Duolink analysis (*46*), fixation and permiabilization were performed as described in immunofluorescent part. Cells were then subjected to anti-HADHA/HADHB antibody (1:100; ab110302, abcam) and rabbit anti-SPD antibody (1:300; abcam, ab7318). According to manufacturer's instructions, the hybridization reaction between oligonucleotide conjugated to 2nd mAb (Sigma-Aldaich, anti-mouse DUO92001 for HADHA/HADHB and anti-rabbit DUO92006 for SPD) and PLA probes were amplified with DNA polymerase. The signals were detected by Duolink in situ detection reagent orange (Sigma-Aldaich, DUO92007). Cells were mounted onto slides using Vactashield mounting medium with DAPI (Vector laboratories, Inc.) and images were taken using Olympus SpinSR10 confocal microscope (×100 magnification).

Recombinant MTP protein expression and purification

Construction of the expression plasmid for human HADHA (also known as MTPα subunit) and human HADHB (MTPβ subunit) was based on the backbone of the *E. coli* plasmid pET-21b (+) and pET-28a (+), respectively. For expression of the MTP in the $\alpha_2\beta_2$-heterotetrameric form, the tag-free HADHA (UniProt ID: P40939, residues 37 to 763) was inserted downstream of the T7 promoter of pET-21b (+). The HADHB (UniProt ID: P55084, residues 34 to 474) was fused with a His_8 tag at the N terminus and inserted downstream of the T7 promoter of pET-28a (+). *E. coli* Rosetta (DE3) cells (Novagen) were transformed with the resulting two plasmids. The transformants were selected on LB plates supplemented with 100 mg/liter ampicillin and 50 mg/liter kanamycin. For purification of HADHA alone in the α_2 form, the HADHA was fused with a His_8 tag at the N terminus and inserted downstream of the T7 promoter of pET-21b (+). This was followed by *E. coli* Rosetta (DE3) transformation and selection on LB plates supplemented with 100 mg/liter ampicillin. All of the cloned inserts were verified by sequencing both strands.

E. coli Rosetta (DE3) cells harboring the two expression plasmids for MTP were grown overnight at 37°C and 250 rpm in LB supplemented with 100 mg/liter ampicillin and 50 mg/liter kanamycin. The culture was diluted 1:100 into the same medium and grown at 37°C to an OD_{600} of 0.7 followed by overnight incubation at 23°C with 0.1 mM IPTG. The cells were harvested by centrifugation at 6000 g for 15 min and re-suspended in buffer A (100 mM Tris-HCl, pH 8.0, 200 mM NaCl, Roche EDTA-free protease inhibitor tablet). Cells were disrupted by several cycles of sonication on ice for 10 min. The membranes were isolated by ultracentrifugation at 45,000 rpm for 30 min, homogenized in buffer A supplemented with 40% glycerol, frozen in liquid nitrogen and stored at −80°C. For MTP purification, membrane extraction from 16 liters of culture was used for each batch of preparation. Membranes were solubilized with 1% DDM in buffer B (50 mM HEPES-NaOH, pH 7.5, 150 mM NaCl, 20 mM imidazole, 1 mM EDTA, 10% glycerol). After ultracentrifugation for 30 min at 45,000 rpm, the supernatant was loaded onto a 5-ml HisTrap Crude column (Cytiva) equilibrated with buffer C (100 mM Tris-HCl, pH 8.0, 200 mM NaCl, 0.02% DDM, 20 mM imidazole). A linear gradient of 20 to 500 mM imidazole was used for elution. The MTP fractions were collected, concentrated and loaded onto a Superdex 200 Increase 10/300 GL gel filtration column (Cytiva) equilibrated with buffer D (20 mM potassium phosphate buffer, pH 7.7, 100 mM NaCl, 0.02% DDM). The peak fractions were pooled, concentrated using an Amicon Ultra-4 spin filter (MWCO 50 K; Millipore) and used for enzymological and ligand-binding studies without freezing. The same purification method was used for the HADHA alone in the α_2 form.

Coimmunoprecipitation of SPD-conjugated MTP by anti-SPD antibody

Purified MTP was incubated with or without SPD (5 mM) and then immunoprecipitated with anti-SPD antibody (abcam, ab7318)–coated Dynabeads Protein G (Invitrogen). After incubation for overnight at 4°C on a rotator, the beads were washed three times using 10 times diluted buffer D (20 mM potassium phosphate buffer, pH 7.7, 100 mM NaCl, 0.02% DDM) in 100 mM Tris-HCl (pH 7.5). To elute precipitated proteins, the beads were incubated for 1 hour at 4°C with 5 mM SPD in the same buffer as described above except containing 0.1% NP-40. The eluted proteins were separated in

4 to 20% Mini-PROTEAN TGX Precast gels (Bio-Rad) for SDS-PAGE and transferred to Immobilon-P membranes (Millipore). For the detection of HADHA and HADHB bands, the anti-HADHA/HADHB (1/500, ab110302, abcam) mAb used in PLA assays and mouse IgG HRP (1/20000,18-8817-33, Rockland) were used. Membranes were blocked with 4% (w/v) nonfat dry milk for 30 min at room temperature and then incubated with primary antibodies for 3 hours at room temperature. Then, secondary antibodies conjugated to horseradish peroxidase (HRP) were incubated for 1 hour at room temperature. Proteins were detected by Chemilumi One Super (Nacalai Tesque).

MTP enzyme activities

3-hydroxyacyl-CoA dehydrogenase assay

The activity of HADHA subunit of MTP was evaluated as a measurement of change in the concentration of NADH. The assay buffer is composed of 50 mM of Tris-HCl (pH 7.5), 1 mM of EDTA (pH 7.5), 250 μM (or as specified) of NADH, and 100 μM of acetoacetyl CoA. In 180 μl of assay buffer, 10 μl of MTP enzyme (containing 0.5 to 0.7 μg) and 10 μl of SPD were added, and the change in NADH concentration was monitored by the absorbance decrease at 340 nm at room temperature (24° to 25°C) every 1 min for 20 min. To obtain the enzymatic activity graphs and K_m values, the data after 10 min were used. The value at each point was adjusted so that the value of the respective controls comes to 0. The control in SPD affinity to MTP experiments is 0 μM SPD and in NADH affinity experiments is 0 μM MTP.

3-ketoacyl-CoA thiolase assay

The activity of the HADHB subunit of MTP was evaluated as a measurement of change in the concentration of acetoacetyl CoA. The assay buffer is composed of 100 mM of Tris-HCl (pH 7.5), 25 mM of $MgCl_2$, and 100 μM (or as specified) of acetoacetyl CoA. In 180 μl of assay buffer, 10 μl of MTP enzyme (containing 1 to 2 μg) and 10 μl of SPD were added. The change in acetoacetyl CoA concentration was monitored by the absorbance decrease at 303 nm at 30°C every 1 min for 20 min. To obtain the enzymatic activity graphs and K_m values, the data after 10 min were used. The value at each point was adjusted so that the value of respective experimental controls comes to 0. The control in SPD affinity to MTP experiments is 0 μM SPD and in acetoacetyl CoA affinity experiments is 0 μM MTP.

Flow cytometry analysis

The following monoclonal antibodies recognizing the indicated antigens were used: CD8 (53-6.7), CD45.2 (104), CD44 (1M7), CD62L (MEL14), CD4 (RM4-5), Foxp3 (FJK-16s), F4/80 (BM8), and Arg1 (A1exF5) from eBioscience; PD-1 (RMP1-30), Tim-3 (RMT3-23), granzyme b (QA16A02), CD49b (DX5), and CD11b (M1/70) from Biolegend; and MHCII (M5/114.15.2) and MHCI (AF6-88.5) from BD bioscience. For cell surface staining, 2×10^5 cell pellets were stained with appropriately diluted antibodies for 12 min in 4°C. Cells were washed by 10% FCS PBS and run. To measure intracellular granzyme B production, cells were stimulated with PMA and ionomycin (Sigma-Aldrich) in the presence of GolgiStop (BD Biosciences) for 4 hours. Intracellular staining was performed using Fixation/Permeabilization Solution Kit (BD Biosciences). All flow cytometry experiments were performed on a FACSCanto II (BD Biosciences) or LSR Fortessa X-20 (BD Bioscences) and analyzed using FlowJo software.

Transmission electron microscopy (TEM)

For TEM observation, treated cells were embedded in iPGell (GenoStaff) according to the manufacturer's instructions. The cell blocks were fixed with 4% formaldehyde and 2% glutaraldehyde in 0.1 M phosphate buffer (PB) (pH 7.4) overnight at 4°C, then postfixed with 1% O_SO_4 in 0.1M PB for 2 hours. After dehydration in a series of graded concentrations of ethanol, the fixed cell blocks were embedded in epoxy resin (Luveak 812; Nacalai Tesque). Ultrathin sections (70-nm thickness) were prepared on an ultramicrotome (EM UC6; Leica). The sections were then stained with uranyl acetate and lead citrate and finally examined with an electron microscope (H-7650 Hitachi Tokyo). TEM was performed at the Division of Electron Microscopic Study, Center for Anatomical Studies, Graduate School of Medicine, Kyoto University.

CPT1a knock down by CRISPR interference system in Jurkat

Jurkat cells were transfected with pLKO5d.SFFV.dCas9-KRAB.P2A.BSD using FuGENE 6 (E2691, Promega) and selected with blasticidin (*47*). The PB-Human CPT1a oligo#1-Puro was transfected by electroporation with Cell Line NucleofectorTM Kit V (Lonza VCA-1003). The guide RNA sequence of human CPT1a oligo#1 was as follows

Human CPT1a -1F: 5′- CACC AGGCC-GAGCGCACCCGACGC - 3′

Human CPT1a -1R: 5′- AAAC GCGTCGGGTGCGCTCGGCCT - 3′

Statistical analysis

Statistical analysis was performed using Prism 8 (GraphPad Software). For multiple-group analysis, one- or two-way analysis of variance (ANOVA) followed by Sidak's multiple comparisons test or column factor comparison were used to analyze, focusing on the main groups. To compare two groups, the two-tailed unpaired Student's *t* test or unpaired multiple *t* test were used. To assess the statistical significance in survival curves, we used the Mantel-Cox test. All statistical tests were two-tailed, assume parametric data accordingly, and a *P* value of ≦0.05 was considered significant. The variations of data were evaluated as the means, standard errors of the mean (SEMs), or standard deviations (SDs). Three or more samples were thought to be appropriate for the sample size estimate in this study. In some cases, cells were pooled from multiple mice in one experiment. Samples and animals were randomly chosen from the pool and treated. No blinding method was used for the treatment of samples and animals.

REFERENCES AND NOTES

1. R. H. Houtkooper *et al.*, The metabolic footprint of aging in mice. *Sci. Rep.* **1**, 134 (2011). doi: 10.1038/srep00134; pmid: 22355651
2. R. Sharma, A. Ramanathan, The Aging Metabolome—Biomarkers to Hub Metabolites. *Proteomics* **20**, 1800407 (2020). doi: 10.1002/pmic.201800407; pmid: 32068959
3. V. Azzu, T. G. Valencak, Energy Metabolism and Ageing in the Mouse: A Mini-Review. *Gerontology* **63**, 327–336 (2017). doi: 10.1159/000454924; pmid: 28118636
4. F. Madeo, T. Eisenberg, F. Pietrocola, G. Kroemer, Spermidine in health and disease. *Science* **359**, eaan2788 (2018). doi: 10.1126/science.aan2788; pmid: 29371440
5. T. Eisenberg *et al.*, Induction of autophagy by spermidine promotes longevity. *Nat. Cell Biol.* **11**, 1305–1314 (2009). doi: 10.1038/ncb1975; pmid: 19801973
6. Y. Nakajima, K. Chamoto, T. Oura, T. Honjo, Critical role of the $CD44^{low}CD62L^{low}$ $CD8^+$ T cell subset in restoring antitumor immunity in aged mice. *Proc. Natl. Acad. Sci. U.S.A.* **118**, e2103730118 (2021). doi: 10.1073/pnas.2103730118; pmid: 34088845
7. G. Alsaleh *et al.*, Autophagy in T cells from aged donors is maintained by spermidine and correlates with function and vaccine responses. *eLife* **9**, e57950 (2020). doi: 10.7554/eLife.57950; pmid: 33317695
8. K. Araki *et al.*, mTOR regulates memory CD8 T-cell differentiation. *Nature* **460**, 108–112 (2009). doi: 10.1038/nature08155; pmid: 19543266
9. E. L. Pearce *et al.*, Enhancing CD8 T-cell memory by modulating fatty acid metabolism. *Nature* **460**, 103–107 (2009). doi: 10.1038/nature08097; pmid: 19494812
10. M. D. Buck, D. O'Sullivan, E. L. Pearce, T cell metabolism drives immunity. *J. Exp. Med.* **212**, 1345–1360 (2015). doi: 10.1084/jem.20151159; pmid: 26261266
11. E. Morselli *et al.*, Spermidine and resveratrol induce autophagy by distinct pathways converging on the acetylproteome. *J. Cell Biol.* **192**, 615–629 (2011). doi: 10.1083/jcb.201008167; pmid: 21339330
12. M. H. Park, E. C. Wolff, Hypusine, a polyamine-derived amino acid critical for eukaryotic translation. *J. Biol. Chem.* **293**, 18710–18718 (2018). doi: 10.1074/jbc.TM118.003341; pmid: 30257869
13. Y. Liang *et al.*, eIF5A hypusination, boosted by dietary spermidine, protects from premature brain aging and mitochondrial dysfunction. *Cell Rep.* **35**, 108941 (2021). doi: 10.1016/j.celrep.2021.108941; pmid: 33852845
14. D. J. Puleston *et al.*, Polyamine metabolism is a central determinant of helper T cell lineage fidelity. *Cell* **184**, 4186–4202.e20 (2021). doi: 10.1016/j.cell.2021.06.007; pmid: 34216540
15. M. T. Hyvönen *et al.*, Role of hypusinated eukaryotic translation initiation factor 5A in polyamine depletion-induced cytostasis. *J. Biol. Chem.* **282**, 34700–34706 (2007). doi: 10.1074/jbc.M704282200; pmid: 17901051
16. G. M. Carriche *et al.*, Regulating T-cell differentiation through the polyamine spermidine. *J. Allergy Clin. Immunol.* **147**, 335–348.e11 (2021). doi: 10.1016/j.jaci.2020.04.037; pmid: 32407834
17. Q. Yang *et al.*, Spermidine alleviates experimental autoimmune encephalomyelitis through inducing inhibitory macrophages. *Cell Death Differ.* **23**, 1850–1861 (2016). doi: 10.1038/cdd.2016.71; pmid: 27447115

18. N. Patsoukis *et al*., PD-1 alters T-cell metabolic reprogramming by inhibiting glycolysis and promoting lipolysis and fatty acid oxidation. *Nat. Commun.* **6**, 6692 (2015). doi: 10.1038/ncomms7692; pmid: 25809635
19. P. S. Chowdhury, K. Chamoto, A. Kumar, T. Honjo, PPAR-Induced Fatty Acid Oxidation in T Cells Increases the Number of Tumor-Reactive CD8$^+$ T Cells and Facilitates Anti–PD-1 Therapy. *Cancer Immunol. Res.* **6**, 1375–1387 (2018). doi: 10.1158/2326-6066.CIR-18-0095; pmid: 30143538
20. V. Kalia *et al*., Metabolic regulation by PD-1 signaling promotes long-lived quiescent CD8 T cell memory in mice. *Sci. Transl. Med.* **13**, eaba6006 (2021). doi: 10.1126/scitranslmed.aba6006; pmid: 34644150
21. K. Chamoto *et al*., Mitochondrial activation chemicals synergize with surface receptor PD-1 blockade for T cell-dependent antitumor activity. *Proc. Natl. Acad. Sci. U.S.A.* **114**, E761–E770 (2017). doi: 10.1073/pnas.1620433114; pmid: 28096382
22. D. A. Ferrick, A. Neilson, C. Beeson, Advances in measuring cellular bioenergetics using extracellular flux. *Drug Discov. Today* **13**, 268–274 (2008). doi: 10.1016/j.drudis.2007.12.008; pmid: 18342804
23. P. Marchetti, Q. Fovez, N. Germain, R. Khamari, J. Kluza, Mitochondrial spare respiratory capacity: Mechanisms, regulation, and significance in non-transformed and cancer cells. *FASEB J.* **34**, 13106–13124 (2020). doi: 10.1096/fj.202000767R; pmid: 32808332
24. G. J. van der Windt *et al*., Mitochondrial respiratory capacity is a critical regulator of CD8$^+$ T cell memory development. *Immunity* **36**, 68–78 (2012). doi: 10.1016/j.immuni.2011.12.007; pmid: 22206904
25. B. Raud *et al*., Etomoxir Actions on Regulatory and Memory T Cells Are Independent of Cpt1a-Mediated Fatty Acid Oxidation. *Cell Metab.* **28**, 504–515.e7 (2018). doi: 10.1016/j.cmet.2018.06.002; pmid: 30043753
26. D. J. Puleston *et al*., Polyamines and eIF5A Hypusination Modulate Mitochondrial Respiration and Macrophage Activation. *Cell Metab.* **30**, 352–363.e8 (2019). doi: 10.1016/j.cmet.2019.05.003; pmid: 31130465
27. K. Liang *et al*., Cryo-EM structure of human mitochondrial trifunctional protein. *Proc. Natl. Acad. Sci. U.S.A.* **115**, 7039–7044 (2018). doi: 10.1073/pnas.1801252115; pmid: 29915090
28. C. Xia, Z. Fu, K. P. Battaile, J. P. Kim, Crystal structure of human mitochondrial trifunctional protein, a fatty acid β-oxidation metabolon. *Proc. Natl. Acad. Sci. U.S.A.* **116**, 6069–6074 (2019). doi: 10.1073/pnas.1816317116; pmid: 30850536
29. M. M. Adeva-Andany, N. Carneiro-Freire, M. Seco-Filgueira, C. Fernández-Fernández, D. Mouriño-Bayolo, Mitochondrial β-oxidation of saturated fatty acids in humans. *Mitochondrion* **46**, 73–90 (2019). doi: 10.1016/j.mito.2018.02.009; pmid: 29551309
30. A. M. Rahul, K. Sasaki, K. Titani, M. Miyazaki, Biochemical and immunological characterization of deoxyhypusine synthase purified from the yeast *Saccharomyces carlsbergensis*. *J. Biochem.* **121**, 769–778 (1997). doi: 10.1093/oxfordjournals.jbchem.a021652; pmid: 9163530
31. F. Pietrocola *et al*., Spermidine induces autophagy by inhibiting the acetyltransferase EP300. *Cell Death Differ.* **22**, 509–516 (2015). doi: 10.1038/cdd.2014.215; pmid: 25526088
32. M. Bagherniya, A. E. Butler, G. E. Barreto, A. Sahebkar, The effect of fasting or calorie restriction on autophagy induction: A review of the literature. *Ageing Res. Rev.* **47**, 183–197 (2018). doi: 10.1016/j.arr.2018.08.004; pmid: 30172870
33. I. Guerrero-Ros *et al*., The negative effect of lipid challenge on autophagy inhibits T cell responses. *Autophagy* **16**, 223–238 (2020). doi: 10.1080/15548627.2019.1606635; pmid: 30982401
34. Y. Xie, J. Li, R. Kang, D. Tang, Interplay Between Lipid Metabolism and Autophagy. *Front. Cell Dev. Biol.* **8**, 431 (2020). doi: 10.3389/fcell.2020.00431; pmid: 32582708
35. F. Pietrocola *et al*., Caloric Restriction Mimetics Enhance Anticancer Immunosurveillance. *Cancer Cell* **30**, 147–160 (2016). doi: 10.1016/j.ccell.2016.05.016; pmid: 27411589
36. L. Ma *et al*., Spermidine ameliorates high-fat diet-induced hepatic steatosis and adipose tissue inflammation in preexisting obese mice. *Life Sci.* **265**, 118739 (2021). doi: 10.1016/j.lfs.2020.118739; pmid: 33186567
37. M. Hargreaves, L. L. Spriet, Skeletal muscle energy metabolism during exercise. *Nat. Metab.* **2**, 817–828 (2020). doi: 10.1038/s42255-020-0251-4; pmid: 32747792
38. M. Knobloch *et al*., A Fatty Acid Oxidation-Dependent Metabolic Shift Regulates Adult Neural Stem Cell Activity. *Cell Rep.* **20**, 2144–2155 (2017). doi: 10.1016/j.celrep.2017.08.029; pmid: 28854364
39. D. Shao *et al*., Increasing Fatty Acid Oxidation Prevents High-Fat Diet-Induced Cardiomyopathy Through Regulating Parkin-Mediated Mitophagy. *Circulation* **142**, 983–997 (2020). doi: 10.1161/CIRCULATIONAHA.119.043319; pmid: 32597196
40. K. Tanigaki *et al*., Regulation of αβ/γδ T cell lineage commitment and peripheral T cell responses by Notch/RBP-J signaling. *Immunity* **20**, 611–622 (2004). doi: 10.1016/S1074-7613(04)00109-8; pmid: 15142529
41. A. Kumar, K. Chamoto, P. S. Chowdhury, T. Honjo, Tumors attenuating the mitochondrial activity in T cells escape from PD-1 blockade therapy. *eLife* **9**, e52330 (2020). doi: 10.7554/eLife.52330; pmid: 32122466
42. M. Ishida *et al*., Differential expression of PD-L1 and PD-L2, ligands for an inhibitory receptor PD-1, in the cells of lymphohematopoietic tissues. *Immunol. Lett.* **84**, 57–62 (2002). doi: 10.1016/S0165-2478(02)00142-6; pmid: 12161284
43. L. Reiter *et al*., mProphet: Automated data processing and statistical validation for large-scale SRM experiments. *Nat. Methods* **8**, 430–435 (2011). doi: 10.1038/nmeth.1584; pmid: 21423193
44. G. Rosenberger *et al*., Statistical control of peptide and protein error rates in large-scale targeted data-independent acquisition analyses. *Nat. Methods* **14**, 921–927 (2017). doi: 10.1038/nmeth.4398; pmid: 28825704
45. M. Miyajima *et al*., Metabolic shift induced by systemic activation of T cells in PD-1-deficient mice perturbs brain monoamines and emotional behavior. *Nat. Immunol.* **18**, 1342–1352 (2017). doi: 10.1038/ni.3867; pmid: 29058703
46. M. S. Alam, Proximity Ligation Assay (PLA). *Curr. Protoc. Immunol.* **123**, e58 (2018). doi: 10.1002/cpim.58; pmid: 30238640
47. A. Schwarzer *et al*., The non-coding RNA landscape of human hematopoiesis and leukemia. *Nat. Commun.* **8**, 218 (2017). doi: 10.1038/s41467-017-00212-4; pmid: 28794406

ACKNOWLEDGMENTS

We sincerely thank Y. Kitawaki, A. Kumar, M. Akrami, R. Hatae, P. Chowdhury, M. Demir, T. Hirano, Y. Zou, K. Yamasaki, E. Mohemad, W. Yu, K. Ito, J. Wang, T. Oura, and M. Hajime-Sumikawa for assistance with sample preparation and useful discussion. **Funding:** This work was supported by the Japan Agency for Medical Research and Development (AMED) under grant nos. 20cm0106302 (T.H.), 19gm0710012 (S.F.), 19gm0810001 (T.O.), and JP21zf0127004 and 22ama221305 (K.C.); the Ministry of Education, Culture, Sports, Science and Technology–Japan (MEXT) under grant no. 150709 (M.A.-H.); Grant-in-aid Scientific Research (B) under grant nos. 21H03087 (K.C.) and 18H02425 (Y.W.); the Tang Prize Foundation (T.H.); the Yanai Fund (T.H.); 2019 Bristol-Myers Squibb Research Grants (K.C.); the RIKEN Aging Project grant (S.F.); Meiji Holdings Co., Ltd. (T.H.); Meiji Seika Pharma Co., Ltd. (T.H.); and the Bristol-Myers Squibb Company (T.H.). **Author contributions:** M.A.-H., K.C., T.O., S.F., and T.H. designed the research; M.A.-H., K.C., T.O., K.S., N.N., A.M., Y.W., R.M., B.Z., Y.Na., K.M., Y.S., T.M., K.K., Y.H., S.D., K.Y., and Y.No. performed research; M.A.-H., K.C., T.O., N.N., F.M., and S.I. analyzed data; and M.A.-H., K.C., S.F., and T.H. wrote the paper. **Competing interests:** T.H. received research grants from Meiji Holdings Co., Ltd., Meiji Seika Pharma, and Bristol-Myers Squibb Company for this study. T.H., K.C., and S.F. are inventors on a patent (PCT/JP2020/041190) submitted by Kyoto University and RIKEN that covers combination therapy of PD-1 blockade therapy and SPD. The authors declare no other competing interests. **Data and materials availability:** All of the proteomics data (protein expression data) generated in this study have been deposited in Proteomexchange database (http://www.proteomexchange.org/) with accession no. PXD036425. All other data are available in the manuscript or the supplementary materials.

SUPPLEMENTARY MATERIALS

science.org/doi/10.1126/science.abj3510
Figs. S1 to S11
MDAR Reproducibility Checklist

Submitted 7 May 2021; resubmitted 21 February 2022
Accepted 29 September 2022
10.1126/science.abj3510

Your Legacy to Science

AN ESTATE GIFT TO THE
AMERICAN ASSOCIATION FOR THE ADVANCEMENT OF SCIENCE

Since 1848, our founding year, the American Association for the Advancement of Science (AAAS) has been deeply committed to advancing science, engineering and innovation around the world for the benefit of all people.

By making AAAS a beneficiary of your will, trust, retirement plan or life insurance policy, you become a member of our 1848 Society, joining Thomas Edison, Alexander Graham Bell and the many distinguished individuals whose vision led to the creation of AAAS and our world-renowned journal, *Science*, so many years ago.

Unlike many of its peers, *Science* is not for-profit. Your estate gift would provide long-term financial stability and durable annual income that will support operations and competitive innovation for years to come. **This support is vital.**

> ***"As a teacher and instructor, I bear responsibility for the younger generations. If you have extra resources, concentrate them on organizations, like AAAS, that are doing work for all."***
>
> **—Prof. Elisabeth Ervin-Blankenheim, 1848 Society member**

If you intend to include AAAS in your estate plans, provide this information to your lawyer or financial adviser:

Legal Name: American Association for the Advancement of Science
Federal Tax ID Number: 53-0196568
Address: 1200 New York Avenue, NW, Washington, DC 20005

If you would like more information on making an estate gift to AAAS, cut out and return the form below or send an email to philanthropy@aaas.org. Additional details are also available online at **www.aaas.org/1848Society**.

1848
SOCIETY
AAAS

cut here ✂

Yes, I would like more information about joining the AAAS 1848 Society.

PLEASE CONTACT ME AT:

Name: ____________________

Address: ____________________

City: ____________ State: ______ Zip code: ____________ Country: ________

Email: ____________________ Phone: ____________

RETURN THIS FORM TO:
AAAS Office of Philanthropy and Strategic Partnerships • 1200 New York Avenue, NW • Washington, DC 20005 USA

RESEARCH ARTICLES

CERAMICS

Plastic deformation in silicon nitride ceramics via bond switching at coherent interfaces

Jie Zhang[1]†, Guanghua Liu[1]†, Wei Cui[1]†, Yiyao Ge[1], Songmo Du[1], Yixuan Gao[2], Yuyang Zhang[2], Fei Li[1], Zhanglin Chen[1], Shixuan Du[2], Kexin Chen[3]*

Covalently bonded ceramics exhibit preeminent properties—including hardness, strength, chemical inertness, and resistance against heat and corrosion—yet their wider application is challenging because of their room-temperature brittleness. In contrast to the atoms in metals that can slide along slip planes to accommodate strains, the atoms in covalently bonded ceramics require bond breaking because of the strong and directional characteristics of covalent bonds. This eventually leads to catastrophic failure on loading. We present an approach for designing deformable covalently bonded silicon nitride (Si_3N_4) ceramics that feature a dual-phase structure with coherent interfaces. Successive bond switching is realized at the coherent interfaces, which facilitates a stress-induced phase transformation and, eventually, generates plastic deformability.

Covalently bonded ceramics such as silicon nitride (Si_3N_4) have attractive mechanical, chemical, and physical properties that feature high-temperature tolerance, superior hardness, excellent wear and corrosion resistance, relatively high thermal conductivity, and electrical insulation. These properties make the ceramics suitable for applications such as high-temperature structural materials, cutting tools, bearings, and substrates in electronic packaging (*1*–*5*). For example, metal components in gas turbine engines are replaced with covalently bonded ceramics to improve efficiency (*6*–*8*). However, ceramics tend to be brittle, such that even a tiny crack can lead to catastrophic failures without observable plastic deformation. This problem severely restricts the applicability of ceramics. Mechanistically, because of the strong and directional characteristic of covalent bonds, local plastic deformation in covalently bonded ceramics is normally initiated via the bond-breaking mechanism (*9*). Unfortunately, this process induces nucleation, growth, and coalescence of nanopores, eventually leading to brittle fracture (*10*). Although numerous efforts have been devoted to toughening covalently bonded ceramics by interlocking the microstructures with elongated grains or designing laminated structures (*11*–*21*), and certain deformability of amorphous ceramics has been observed (*22*–*24*), covalently bonded crystalline deformable ceramics have yet to be achieved as a result of the intrinsic strong and directional characteristics of covalent bonds. As such,

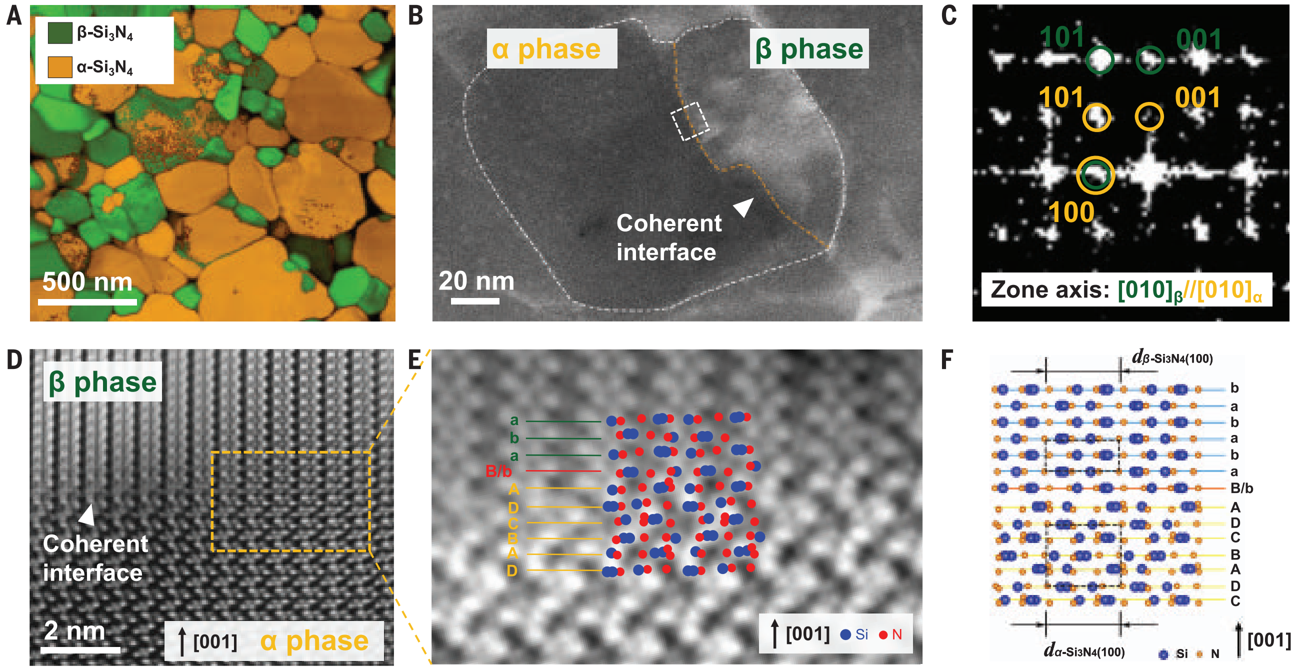

Fig. 1. Microstructure of dual-phase α/β-Si_3N_4 ceramics with coherent interfaces. (**A**) Phase map of the α/β-Si_3N_4 sample with precession electron diffraction. (**B**) TEM image of an α/β coherent interface (highlighted by the orange dashed line). The white dashed line indicates the outline of the Si_3N_4 grain. The area enclosed by the white dashed square is discussed in (D). (**C**) Fast Fourier transform at the interface shows that the α and β subgrains have a specific orientation relationship of $[010]_\alpha//[010]_\beta$, $[001]_\alpha//[001]_\beta$, and $(100)_\alpha//(100)_\beta$. (**D**) HAADF-STEM image showing the α and β phase atomically matched along the [001] direction at the interface. The image corresponds to the area marked by the white dashed square in (B) and is rotated here to make the coherent interface horizontal. (**E**) Close-up iDPC-STEM image [corresponding to the area marked by the orange dashed square in (D)] showing the atomic stacking order at the coherent interface; the B-layer atoms of the α phase are shared with the β phase to form the interface atomic layer. (**F**) Atomic model corresponding to the observation; Si and N atoms are represented as blue and orange spheres, respectively. *d*, *d*-spacing in the crystal.

---

[1] State Key Laboratory of New Ceramics and Fine Processing, School of Materials Science and Engineering, Tsinghua University, Beijing 100084, P.R. China. [2] University of Chinese Academy of Sciences, Chinese Academy of Sciences, Beijing 100190, P.R. China. [3] Department of Engineering and Material Sciences, National Natural Science Foundation of China (NSFC), Beijing 100085, P.R. China.
***Corresponding author. Email: kxchen@mail.tsinghua.edu.cn**
†These authors contributed equally to this work.

realizing the plastic deformability of covalently bonded crystalline ceramics has been a long-standing and critical challenge.

Macroscopic plastic deformation in response to external loading is often an accumulative result of successive multiple atomic displacements. In alloys with metallic bonds, plastic deformation is realized by local atomic displacements that proceed through switching one or a few interatomic bonds at a time along the lattice planes, also known as dislocation motion (*25*, *26*). Stress-induced phase transformation and the consequent plasticity have been realized in metallic materials and even in ionically bonded ceramics such as ZrO_2 (*27*–*32*) with nondirectional bonding. Although this mechanism has enabled plastic deformation in other materials, it has remained elusive in covalently bonded ceramics (*33*), mainly because of the directionality of covalent bonds.

Theoretically, it could be possible to achieve macroscopic plastic deformation in covalently bonded ceramics provided that bond breaking in covalent bonds occurs in a very small volume together with immediate healing by new bond formations, which we define as bond switching in this text. In this sense, the energy barrier needs to be lower for local atomic rearrangement to enable a relatively easy transition of one bonding configuration to another, and simultaneously, the lattices on both sides of the slip plane must have roughly the same unit atomic distance to ensure successive atomic translation in crystalline ceramics (*34*).

Accordingly, a dual-phase structure with a coherent interface may meet these requirements and serve as a good candidate to realize phase transformation–mediated plastic deformation via bond switching in covalently bonded crystalline ceramics. Here, we demonstrate this design strategy in Si_3N_4, a typical covalently bonded crystalline ceramic of wide interest (*35*–*40*). Under normal conditions, Si_3N_4 has two polymorphs, the α and β phases. These two polymorphs have similar hexagonal lattice structures composed of corner-shared [SiN_4] tetrahedra, that is, their lattice constant is almost the same along the *a* direction but differs along the *c* direction, with the lattice constant of α being twice that of β (*41*, *42*). Such a crystallographic configuration allows Si_3N_4 to potentially possess coherent phase interfaces in the crystals. Given this, we designed a dual-phase α/β-Si_3N_4 ceramic with coherent interfaces and observed substantial plastic deformation in the ceramic.

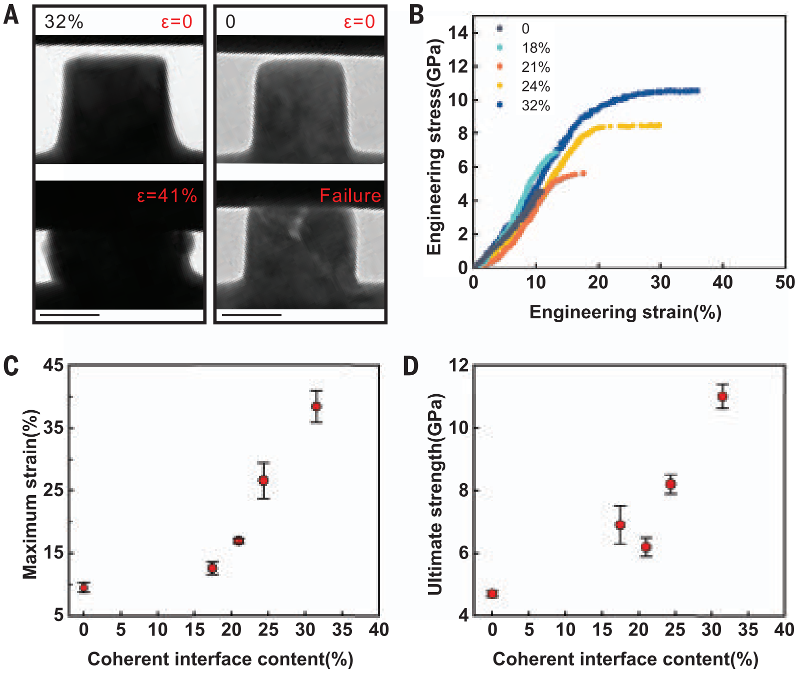

Fig. 2. Mechanical behaviors of polycrystalline Si_3N_4 nanopillars with different proportions of coherent interfaces (proportion of the total length of the interfaces). (**A**) A series of TEM images of α/β-Si_3N_4 (coherent interface content is 32%) and β-Si_3N_4 (coherent interface content is 0) nanopillars recorded during the in situ test; the coherent interface content was tested by transmission Kikuchi diffraction (fig. S4). The scale bars are 200 nm, and both the nanopillars have a diameter of about 350 nm. ε, compression strain. (**B**) Nanopillars with a richer coherent interface showing higher engineering stress-strain. (**C** and **D**) The measured maximum strain (C) and ultimate strength (D) versus coherent interface content showing that both the maximum strain and ultimate strength simultaneously increase with the proportion of coherent interface ($N = 5$, where N is the number of samples used to calculate the average value and the error of each data point). Error bars represent SD.

Microstructure characterization of α/β-Si_3N_4 with coherent interfaces

Bulk Si_3N_4 ceramics are usually prepared by liquid-phase sintering from α-Si_3N_4 powder, in which the α→β phase transformation occurs via the dissolution-reprecipitation mechanism (*43*, *44*), and consequently, the sintered dense Si_3N_4 ceramics are mostly single-phase β-Si_3N_4. Using a method that largely differs from the conventional process, we prepared the dual-phase α/β-Si_3N_4 ceramics (hereafter referred to as α/β-Si_3N_4) with a varying fraction of coherent α/β phase interfaces through precise control of the sintering parameters to quench the α→β transformation (*45*). During this process, the α- and β-Si_3N_4 grains with a specific orientation relationship were directly integrated (Fig. 1).

We examined the microstructure of α/β-Si_3N_4 using high-angle annular dark-field scanning transmission electron microscopy (HAADF-STEM). The sample showed a dual-phase grain structure, where each grain consists of both α- and β-Si_3N_4 with a coherent interface between the two phases (Fig. 1, A and B). Further analysis at the interfaces shows that the α and β subgrains have a specific orientation relationship of $[001]_\alpha//[001]_\beta$ and $(100)_\alpha//(100)_\beta$ (Fig. 1C and fig. S1), where the angle mismatch between the α and β subgrains is less than 1.8° (Fig. S2). We did not observe sharp interfaces, indicating a high degree of lattice matching between the α- and β-Si_3N_4 (Fig. 1D). The integrated differential phase contrast (iDPC)–STEM image of the interface (Fig. 1E) along the [010] direction shows the atomic columns with periodically strong and weak intensities, corresponding to the atomic stacking sequence of ···ABCDABababab··· along the [001] direction. Based on the iDPC-STEM images, we established a structure model (Fig. 1F) to schematically reveal the highly coherent interface at the atomic scale. To achieve atomic-scale matching in α/β-Si_3N_4, a small lattice distortion caused by a slight difference in the interplanar spacings of (100) planes of the α and β phases still exists in the β grain, which agrees with the result of strain field analysis (fig. S3). Clearly, the coherent α/β interface is largely distinguished from the conventional grain interfaces in Si_3N_4 ceramics, where two randomly oriented grains are separated by an intergranular glassy film (*38*, *39*).

Mechanical properties of α/β-Si_3N_4 by nanopillar compression

We evaluated the mechanical properties of the α/β-Si_3N_4 samples by nanopillar compression

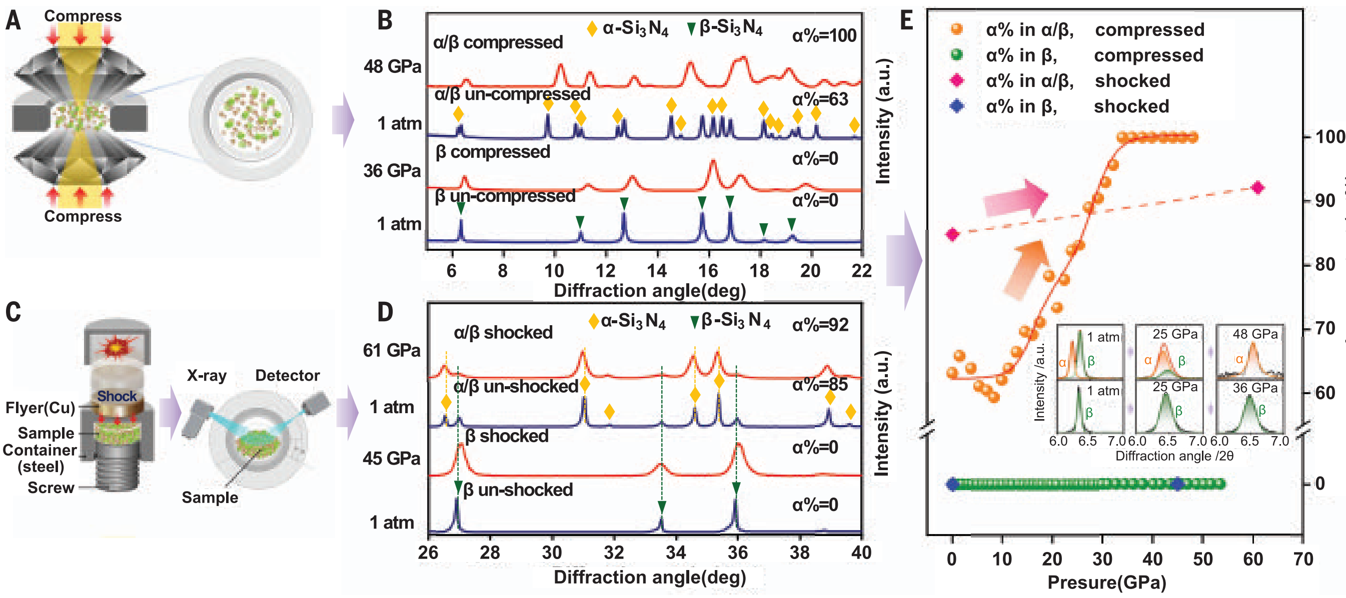

Fig. 3. Phase-content change of Si_3N_4 samples during compression under high pressure. (**A**) Schematic diagram of the ADXRD test under uniaxial pressure; the wavelength of the monochromatic x-ray beam was 0.7293 Å. (**B**) Selected x-ray diffraction (XRD) spectra of β-Si_3N_4 and α/β-Si_3N_4. The diffraction peak shifted to the right for pure β-Si_3N_4, the α phase never appeared, and the β phase remained stable up to 36 GPa; by contrast, the β phase gradually decreased until it could not be detected up to 48 GPa in α/β-Si_3N_4. a.u., arbitrary units. (**C**) Schematic diagram of the shock experiment; the sample was shocked through high-speed flyer (Cu) and then the phase content was detected by XRD. The monochromatic x-ray beam had a wavelength of 1.54178 Å. (**D**) XRD spectra of β-Si_3N_4 and α/β-Si_3N_4 before and after shocking. The β phase remained stable after shocking by ~45 GPa in pure β-Si_3N_4, and no α phase was observed even though obvious lattice distortion of the β phase was induced, as indicated by the peak shift. By contrast, the diffraction intensity of the β phase decreased in α/β-Si_3N_4 after shocking; thus, the content of the α phase increased by ~7%. (**E**) Variation in the α phase content under pressure. The α phase content in α/β-Si_3N_4 gradually increased as the pressure increased; under static pressure, the β phase gradually transformed to the α phase and almost completely transformed at ~34 GPa in α/β-Si_3N_4. Under shock load, the β→α transformation could still occur, but the amount of phase transformation was less than that under static pressure because the duration of the peak pressure was extremely short. In pure β-Si_3N_4, the β→α transformation could not happen, irrespective of the type of stress stimulus. The insets show the (110) diffraction peaks of the α and β phases in α/β-Si_3N_4 (top) and β-Si_3N_4 (bottom) after compression under different pressures.

tests. During the sintering of Si_3N_4 ceramics, densification usually occurs along with the α→β phase transformation; both densification and phase transformation are thermally activated and achieved by the dissolution-reprecipitation mechanism (*43*, *44*). To prepare our α/β-Si_3N_4 samples containing coherent α/β interfaces, both lowering the sintering temperature and shortening the holding time are required to limit the α→β phase transformation and hamper the densification process. As a result, the prepared α/β-Si_3N_4 samples are not fully dense and are prone to contain defects such as pores. The mechanical properties of covalently bonded ceramics are sensitive to these defects, which affect crack generation and propagation and, consequently, may cause a deterioration of mechanical behavior (*9*). To minimize the ambiguities caused by the structural defects and reveal the intrinsic properties of the prepared α/β-Si_3N_4 samples, we therefore used nanopillar-shaped samples (rectangular nanopillars of about 350 nm by 350 nm by 250 nm) to evaluate the mechanical properties (*45*).

The α/β-Si_3N_4 nanopillars exhibited higher strength and plastic deformation compared with conventional β-Si_3N_4 fractured just in the elastic deformation stage (Fig. 2, A and B, and figs. S5 to S9). The α/β-Si_3N_4 nanopillar (coherent interface proportion of ~32%) showed a fracture strength of 11.0 ± 0.4 GPa and a plastic strain of about 20% (Fig. 2, C and D, and movie S1). For comparison, a conventional β-Si_3N_4 nanopillar of almost the same size showed a fracture strength of 4.7 ± 0.1 GPa with no plastic deformation (Fig. 2, C and D, and movie S2). The plastic deformation of α/β-Si_3N_4 under uniaxial compression is quite different from the localized deformation under confined compression that is observed in nanoindentation tests (*46*). The Si_3N_4 nanopillars exhibited an elastic strain of ~10%, which is considerably larger than those observed in bulk Si_3N_4 samples mainly because of the small sample size. Similar results have been reported for other ceramics; for instance, an elastic strain of ~8% was observed during the compression of $MgAl_2O_4$ micropillars with a diameter of 2.5 μm at room temperature, which is much larger than that of the bulk samples (<1%) (*47*). Furthermore, the strength and plasticity of the α/β-Si_3N_4 samples showed a strong dependence on the proportion of α/β coherent interfaces in all the interfaces. By increasing the proportion of coherent interfaces, we simultaneously enhanced the plasticity and strength considerably (Fig. 2, C and D). The effect of electron beam irradiation on the plasticity of the α/β-Si_3N_4 nanopillars was negligible, which we confirmed by nanopillar compression tests with the electron beam switched off (fig. S10).

Stress-induced β→α phase transformation in α/β-Si_3N_4

To investigate the structural evolution upon external loading, we performed in situ static compression under angle dispersive x-ray diffraction (ADXRD) on the α/β-Si_3N_4 and β-Si_3N_4 samples (Fig. 3A). The β→α phase transformation began at a pressure of ~10 GPa and completed at ~35 GPa during the compression

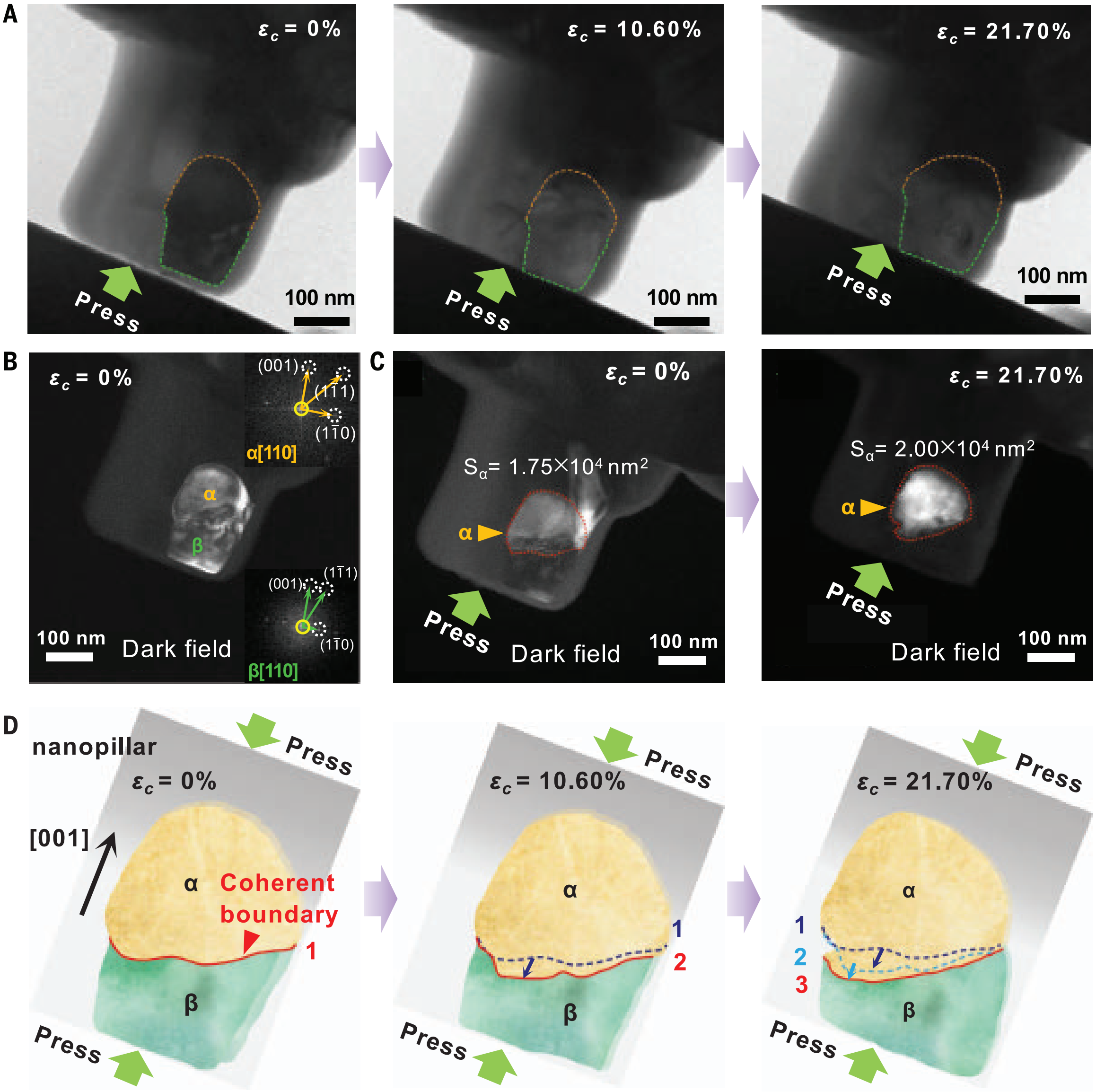

Fig. 4. A representative β→α phase transformation event revealed by in situ TEM. (**A**) Bright-field images of a nanopillar at different compression strains (ε_c = 0, 10.60, and 21.70%); the orange and green dashed lines show the outlines of the α and β grains, respectively, with coherent interfaces; outside of the dashed lines in the nanopillar are the Si_3N_4 grains bonded by the glass phase. The nanopillar was compressed by the diamond flat indenter shown in the bottom-left corner of the image. (**B**) Coherent structure caused the diffraction patterns of $(1\text{-}10)_\alpha$ and $(1\text{-}10)_\beta$ to overlap; hence, the dark-field image [diffraction beam of (1-10) was captured] reveals the outlines of the α and β grains. (**C**) When the diffraction beam of the $(001)_\alpha$ was captured, only the α grain appeared bright in the dark-field image; the projected area of the α grain along the electron beam (S_α) is ~1.75×10^4 nm^2, and the bottom of the α grain is the coherent interface with the β grain. After compression, the coherent interface extended into the β grain, and S_α increased to ~$2.00{\times}10^4$ nm^2. The image drift during in situ compression was negligible, which was confirmed by comparing the contours of the grains in dark-field images before and after compression. (**D**) Sketch maps of this nanopillar at three compression stages show the movement of the coherent interface more clearly during the compression process. The coherent interface that separates the grains is denoted by the red line and is labeled 1, 2, and 3.

of the α/β-Si_3N_4 sample (Fig. 3, B and E, and fig. S11). The onset pressure for the β→α phase transformation here is higher than the yield stress of α/β-Si_3N_4 nanopillars that we observed in the uniaxial compression tests (Fig. 2B), mostly because the sample here is compressed under a constrained condition (*48*). After unloading to 0.1 MPa, only the α phase existed and no β phase was detected (fig. S12). During the compression of the single-phase β-Si_3N_4 sample, however, we did not observe any β→α phase transformation, even under the maximum pressure of 54 GPa (Fig. 3B and fig. S13) and unloading to 0.1 MPa (fig. S14). Furthermore, we performed dynamic compression experiments for the α/β-Si_3N_4 and β-Si_3N_4 samples (Fig. 3C). We used explosion shock to generate a pulse of pressure on the sample with a peak stress of ~61 GPa. We observed the β→α phase transformation during compression of the α/β-Si_3N_4 sample (which was incomplete due to the extremely short time duration of high pressure) (Fig. 3D). The transformation was absent in the conventional β-Si_3N_4 sample.

The structural evolution that we observed during both static and dynamic compression

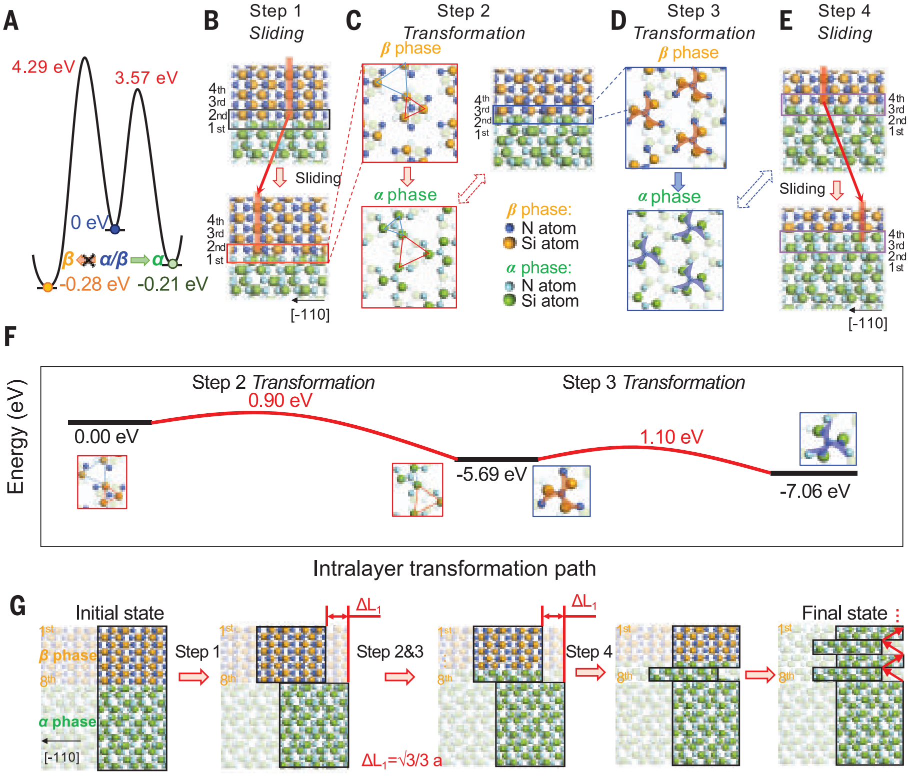

Fig. 5. Density functional theory calculations showing the pathway of the β→α phase transformation. (**A**) Energy landscape of α, β, and α/β dual-phase with coherent interface. The energy barrier for the transformation of the α/β dual-phase structure to α is much lower than that of the transformation to β. (**B**) Side view of an β(001)/α(001) interface before (top) and after (bottom) sliding along the [–110] direction by $\frac{\sqrt{3}}{3}a$, in which a is the lattice constant of the supercell. In step 1, the β phase slides along the [–110] direction with respect to the α phase. The orange vertical lines and the red arrow are used to highlight the sliding direction. (**C**) Shown are the top views of the first and second layers in the bottom panel of (B) (top left) and the final state after the second layer transforms to the β phase (bottom left). The side view of the supercell after the phase transformation is shown at the top right. In step 2, the second layer of the β phase transformed to the α phase after the breaking and rebonding of the Si-N bonds. (**D**) The top view of the second and third layers in the top right panel of (C) (top) and the final state after the third layer transformed to the β phase (bottom). In step 3, the Si atoms in the third layer of the β phase rotate around the central N atoms, as indicated by the windmills, resulting in the third layer of the β phase transforming to the α phase. (**E**) The side views of the structure in the bottom panel of (D) (top) and the structure after sliding (bottom). In step 4, after the whole β phase slides along the [1-10] direction by $\frac{\sqrt{3}}{3}a$, the stacking sequence of the fourth layer of the β phase changes to the α phase naturally. (**F**) Density functional theory–calculated energy profile of the interface transformation steps shown in (C) and (D). (**G**) The shearing of original β atom layers with respect to the α phase during the β→α phase transformation. Atoms in the same supercell are highlighted to track the corresponding atoms in each step. The orange and blue spheres represent Si and N atoms in the β phase, whereas the green and light blue spheres represent those in the α phase, respectively.

confirmed the occurrence of a stress-induced β→α phase transformation in Si_3N_4. In the past few decades, only the α→β phase transformation was recognized to take place, whereas the β→α transformation has been strictly limited because of the higher stability of β compared with α. The β→α phase transformation has not been observed at any temperature and pressure (including at tens of GPa) (*49–51*). The β→α transformation that we observed is intrinsically different from the well-known α→β transformation, which is a thermally induced dissolution-reprecipitation process with the presence of a liquid phase and strongly relies on its diffusion property. It appears that the β→α transformation is a stress-induced, diffusionless solid-state phase transformation with no liquid participation. We also found that the stress-induced β→α phase transformation only occurred in the α/β-Si_3N_4 sample but not in the β-Si_3N_4 sample, indicating a close relation to the dual-phase structure, especially with the coherent interface of our α/β-Si_3N_4 sample.

We used in situ transmission electron microscopy (TEM) to reveal the role of the coherent α/β interface during the stress-induced β→α phase transformation. We compressed an α/β-Si_3N_4 nanopillar approximately along the [001] direction of the highlighted grains of the α and β phases with a coherent interface (Fig. 4A) and monitored the movement of the coherent α/β interface in a dual-phase grain. In the nanopillar, the orange and green dashed lines in Fig. 4A indicate the boundaries of the α and β subgrains, respectively, with the same orientation in the dark-field image (Fig. 4B). During compression (movie S3), the coherent α/β interface moved to the β subgrain and the [001]-projected area of the α subgrain (S_α) increased from 1.75×10^4 to 2.00×10^4 nm^2 (Fig. 4C). Figure 4D illustrates that the stress-induced β→α phase transformation is related to the movement of the coherent interface during compression.

Mechanism of the β→α phase transformation in α/β-Si_3N_4

We simulated the detailed atomic movement on the coherent interface using first-principle calculations based on a supercell with a coherent α/β interface. The supercell contains 8 atomic layers of the β phase and 12 atomic layers of the α phase, as shown in the top panel of Fig. 5B and fig. S16. The transformation energy barrier from α/β-Si_3N_4 to β phase is higher than that from α/β-Si_3N_4 to α phase (Fig. 5A), which makes the transformation to α phase more energetically favorable. By comparing all possible pathways of the β→α phase transformation (see figs. S15 and S16), we rationalized the following pathway for the β→α phase transformation. The pathway contains four steps: The first step involves sliding at the β/α interface, followed by two steps of intralayer transformation, and a final step of sliding at the newly formed β/α interface (Fig. 5, B to E). In the first step, an energy minimum occurs at a displacement of $\frac{\sqrt{3}}{3}a$ (where a is the lattice constant of the supercell) when the β phase layers slide along the [–110] direction (Fig. 5C and fig. S15A). In the second step (Fig. 5C), the second layer (marked in Fig. 5B), which belongs to the β phase, transforms to the α phase via a bond breaking and rebonding process (marked by the blue and red triangles in Fig. 5C) with an energy barrier of 0.90 eV (Fig. 5F). The bond breaking and rebonding process is also observed in our ab initio molecular dynamics simulations (fig. S17 and movie S4). In the third step, the Si atoms in the third layer rotate around the central N atoms, leading to the transformation from β phase to α phase (highlighted by orange and blue windmills in Fig. 5D) with an energy barrier of 1.10 eV. In the final step (purple rectangles in Fig. 5E), the β phase layers slide along the [1-10] direction by $\frac{\sqrt{3}}{3}a$, resulting in a stacking layer of α phase (see fig. S15B for the energy profile). Therefore, the three neighboring layers in the β phase are all transformed to the α phase during this process. Because the atomic structure of the first layer in the α phase is the same as that of the fifth layer in the β phase and the periodicity in the α phase along the [001] direction is four layers, the remaining β phase could eventually transform to the α phase by continuing this process.

The pathways are characteristic of bond switching of Si-N bonds, $[NSi_3]$ unit rotation, and structure distortion at the interface (figs. S17 to S21 and movie S4). One crucial process is the sliding along the [–110] direction, which is involved in both the first and fourth steps (figs. S18 and S21) and leads to a shearing between the two subgrains. Bond breaking and rebonding of Si atoms with N (or Si) atoms participate in the process, where the rebonding between the Si atom and another N atom occurs immediately after the preceding Si-N breaking, resulting in bond switching. Such a bond switching mechanism fundamentally differs from the conventional bond-breaking mechanism that leads to crack formation.

As elaborated on earlier, the coherent interfaces between α- and β-Si_3N_4 facilitate the rebonding of atoms after bond breaking, giving rise to a bond-switching process without initiating a crack, which always occurs in a conventional bond breaking process. The atomic-scale sliding leads to a displacement between the α and β subgrains and subsequently the $[NSi_3]$ unit rotation, as well as structure distortion, at the interface (Fig. 5G and figs. S17 to S21). The accumulation of successive atomic reshufflings from bond switching results in the stress-induced $\beta \rightarrow \alpha$ phase transformation and the subsequent macroscopic deformability. However, the $\beta \rightarrow \alpha$ phase transformation dissipates energy to release the strain, which helps to avoid fracturing failure and thus increase the strength. Consequently, the internal stress in the α/β-Si_3N_4 sample was lower than that in the single-phase β-Si_3N_4 after dynamic compression (fig. S22 and table S1).

The stress-induced $\beta \rightarrow \alpha$ phase transformation of Si_3N_4 is different from the martensitic $t \rightarrow m$ phase transformation of ZrO_2, despite their similarities of being diffusionless and leading to plastic deformation. ZrO_2 is composed of ionic bonds, in which the $t \rightarrow m$ phase transformation is displacive and realized by a lattice shearing. By contrast, Si_3N_4 consists of directional covalent bonds, and the $\beta \rightarrow \alpha$ transformation cannot be achieved by a lattice shearing but instead involves an extra rotation of $[NSi_3]$ units, which makes the $\beta \rightarrow \alpha$ phase transformation reconstructive rather than displacive.

We found that bond switching, which is a prerequisite for the dislocation motion and phase transformation in metals, can also be realized in covalently bonded ceramics through the design of coherent interfaces. However, other factors that contribute to the increased strain and strength of α/β-Si_3N_4 cannot be excluded, requiring even better illumination of the interactions between the $\beta \rightarrow \alpha$ phase transformation and stress-strain behaviors. The absolute values of the strain and strength from the compression of nanopillar samples usually differ from those of bulk samples, requiring better fabrication methods to obtain bulk-scale deformable Si_3N_4 ceramics with dual-phase grand structure and coherent interfaces.

Polymorphism has also been found in other covalent ceramics, which makes it possible to tailor the dual-phase structure with coherent interfaces, especially in those with correlated crystalline structures and atomic distances (e.g., the cubic and hexagonal phases of silicon carbide). In this sense, we anticipate that the approach of our present work can be extended to develop more deformable ceramics.

REFERENCES AND NOTES

1. W. D. Kingery, H. K. Bowen, D. R. Uhlmann, *Introduction to Ceramics* (Wiley, ed. 2, 1976).
2. R. N. Katz, *Science* **208**, 841–847 (1980).
3. R. Riedel *et al.*, *Nature* **382**, 796–798 (1996).
4. T. Ohji, M. Singh, Eds., *Engineered Ceramics: Current Status and Future Prospects* (Wiley, 2016).
5. B. R. Golla, A. Mukhopadhyay, B. Basu, S. K. Thimmappa, *Prog. Mater. Sci.* **111**, 100651 (2020).
6. P. Baldus, M. Jansen, D. Sporn, *Science* **285**, 699–703 (1999).
7. H. A. Bale *et al.*, *Nat. Mater.* **12**, 40–46 (2013).
8. N. P. Padture, *Nat. Mater.* **15**, 804–809 (2016).
9. B. Lawn, *Fracture of Brittle Solids* (Cambridge Univ. Press, ed. 2, 1993).
10. Y.-C. Chen *et al.*, *Phys. Rev. Lett.* **99**, 155506 (2007).
11. M. Rühle, A. G. Evans, *Prog. Mater. Sci.* **33**, 85–167 (1989).
12. F. Wakai *et al.*, *Nature* **344**, 421–423 (1990).
13. P. F. Becher, *J. Am. Ceram. Soc.* **74**, 255–269 (1991).
14. B. R. Lawn, N. P. Padture, H. Cait, F. Guiberteau, *Science* **263**, 1114–1116 (1994).
15. I. W. Chen, A. Rosenflanz, *Nature* **389**, 701–704 (1997).
16. C. A. Wood, H. Zhao, Y. B. Cheng, *J. Am. Ceram. Soc.* **82**, 421–428 (1999).
17. Z. Shen, Z. Zhao, H. Peng, M. Nygren, *Nature* **417**, 266–269 (2002).
18. W. Clegg, K. Kendall, N. M. N. Alford, T. W. Button, J. D. Birchall, *Nature* **347**, 455–457 (1990).
19. M. P. Rao, A. J. Sánchez-Herencia, G. E. Beltz, R. M. McMeeking, F. F. Lange, *Science* **286**, 102–105 (1999).
20. E. Munch *et al.*, *Science* **322**, 1516–1520 (2008).
21. F. Bouville *et al.*, *Nat. Mater.* **13**, 508–514 (2014).
22. K. Zheng *et al.*, *Nat. Commun.* **1**, 24 (2010).
23. R. Ramachandramoorthy *et al.*, *Nano Lett.* **19**, 2350–2359 (2019).
24. E. J. Frankberg *et al.*, *Science* **366**, 864–869 (2019).
25. W. Cai, V. V. Bulatov, J. Chang, J. Li, S. Yip, in vol. 12 of *Dislocations in Solids*, F. R. N. Nabarro, J. P. Hirth, Eds. (Elsevier, 2004), chap. 64.
26. J. Li, K. J. Van Vliet, T. Zhu, S. Yip, S. Suresh, *Nature* **418**, 307–310 (2002).
27. D. A. Porter, K. E. Easterling, *Phase Transformations in Metals and Alloys* (CRC Press, 2009).
28. R. C. Garvie, R. Hannink, R. Pascoe, *Nature* **258**, 703–704 (1975).
29. M. Swain, *Nature* **322**, 234–236 (1986).
30. R. H. Hannink, P. M. Kelly, B. C. Muddle, *J. Am. Ceram. Soc.* **83**, 461–487 (2000).
31. A. Lai, Z. Du, C. L. Gan, C. A. Schuh, *Science* **341**, 1505–1508 (2013).
32. A. Liens *et al.*, *Acta Mater.* **183**, 261–273 (2020).
33. D. J. Green, R. H. J. Hannink, M. V. Swain, *Transformation Toughening of Ceramics* (CRC Press, 1989).
34. J. B. Bilde-Sørensen *et al.*, *Acta Mater.* **44**, 2145–2152 (1996).
35. M. W. Lindley, D. J. Godfrey, *Nature* **229**, 192–193 (1971).
36. F. L. Riley, *J. Am. Ceram. Soc.* **83**, 245–265 (2000).
37. J. Meléndez-Martínez, A. Domınguez-Rodrıguez, *Prog. Mater. Sci.* **49**, 19–107 (2004).
38. A. Ziegler *et al.*, *Science* **306**, 1768–1770 (2004).
39. N. Shibata *et al.*, *Nature* **428**, 730–733 (2004).
40. Y. Zhou, H. Hyuga, D. Kusano, Y. Yoshizawa, K. Hirao, *Adv. Mater.* **23**, 4563–4567 (2011).
41. D. Hardie, K. Jack, *Nature* **180**, 332–333 (1957).
42. C.-M. Wang, X. Pan, M. Rühle, F. L. Riley, M. Mitomo, *J. Mater. Sci.* **31**, 5281–5298 (1996).
43. P. Drew, M. Lewis, *J. Mater. Sci.* **9**, 261–269 (1974).
44. D. R. Messier, F. Riley, R. Brook, *J. Mater. Sci.* **13**, 1199–1205 (1978).
45. Materials and methods are available as supplementary materials.
46. T. Csanádi, D. Németh, J. Dusza, Z. Lenčéš, P. Šajgalík, *J. Eur. Ceram. Soc.* **36**, 3059–3066 (2016).
47. S. Korte, W. Clegg, *Scr. Mater.* **60**, 807–810 (2009).
48. Y. Wu *et al.*, *Acta Mater.* **124**, 478–488 (2017).
49. A. Zerr *et al.*, *Nature* **400**, 340–342 (1999).
50. P. Kroll, *J. Solid State Chem.* **176**, 530–537 (2003).
51. B. Xu, J. Dong, P. F. McMillan, O. Shebanova, A. Salamat, *Phys. Rev. B* **84**, 014113 (2011).

ACKNOWLEDGMENTS

We thank A. Nie (Yanshan University) and Z. Shan, Y. Wang, and W. Xu (Xi'an Jiaotong University) for assistance with the in situ TEM compression characterizations; Z. Quan, Q. Li, and J. Han (Southern University of Science and Technology) for assistance with ADXRD; and Z. Gao (China Academy of Engineering Physics) for providing additional shock experiment support. High-pressure ADXRD experiments were carried out at the beamline 15U1, Shanghai Synchrotron Radiation Facility (SSRF). We also thank L. Zhao (Beihang University) for many discussions and helpful suggestions on both data interpretation and manuscript preparation. **Funding:** This work was supported by the National Key R&D Program of China (no. 2021YFB3702300) and the Strategic Priority Research Program of the Chinese Academy of Sciences (no. XDB30000000). **Author contributions:** K.C. conceived the idea, designed the experiments, and guided the whole project. J.Z., SM.D., and YY.G. synthesized the samples. J.Z., W.C., F.L., and Z.C. performed the corresponding measurements. SX.D., Y.Z., and YX.G. performed the computational studies. G.L., J.Z., and K.C. wrote the manuscript. All authors contributed to data interpretation and discussed the results. **Competing interests:** The authors declare that they have no competing interests. **Data and materials availability:** All data are available in the manuscript or the supplementary materials.

SUPPLEMENTARY MATERIALS

science.org/doi/10.1126/science.abq7490
Materials and Methods
Figs. S1 to S22
Table S1
References (*52–56*)
Movies S1 to S4

Submitted 14 May 2022; accepted 14 September 2022
10.1126/science.abq7490

MAMMALIAN EVOLUTION

Attenuated evolution of mammals through the Cenozoic

Anjali Goswami[1,2]*, Eve Noirault[1], Ellen J. Coombs[1,2,3], Julien Clavel[4], Anne-Claire Fabre [1,5,6], Thomas J. D. Halliday[1,7], Morgan Churchill[8], Abigail Curtis[9], Akinobu Watanabe[1,10,11], Nancy B. Simmons[12], Brian L. Beatty[10,13], Jonathan H. Geisler[10,13], David L. Fox[14], Ryan N. Felice[1,2,15]

The Cenozoic diversification of placental mammals is the archetypal adaptive radiation. Yet, discrepancies between molecular divergence estimates and the fossil record fuel ongoing debate around the timing, tempo, and drivers of this radiation. Analysis of a three-dimensional skull dataset for living and extinct placental mammals demonstrates that evolutionary rates peak early and attenuate quickly. This long-term decline in tempo is punctuated by bursts of innovation that decreased in amplitude over the past 66 million years. Social, precocial, aquatic, and herbivorous species evolve fastest, especially whales, elephants, sirenians, and extinct ungulates. Slow rates in rodents and bats indicate dissociation of taxonomic and morphological diversification. Frustratingly, highly similar ancestral shape estimates for placental mammal superorders suggest that their earliest representatives may continue to elude unequivocal identification.

Placental mammals make up 94% of extant mammalian diversity, with more than 6100 recognized extant species (*1*). This richness in species numbers is paired with an immense variation in ecology and morphology, with fully volant to fully aquatic forms spanning six orders of magnitude in size. Much diversification of placental mammals is thought to have been achieved quickly in the early Cenozoic, in the aftermath of the Cretaceous-Paleogene (K/Pg) mass extinction that removed nonavian dinosaurs from global ecosystems (*2*). However, despite a wealth of data from extant and fossil species, the timing, tempo, and drivers of the placental mammal morphological radiation have remained contentious. Studies of body size evolution variably support an early burst (*3*), accelerating rates linked to climate (*4*), or stable rates after the initial superordinal divergences. These studies often suggest that the K/Pg event had little impact on placental mammal evolution (*5*). By contrast, studies of tooth morphology or discrete character data suggest that either morphological diversification postdated the K/Pg extinction (*6*, *7*) or that rates of evolution increased rapidly at K/Pg boundary (*8*). Some of this uncertainty is due to the ongoing debate on the timing of origin of Placentalia and its proximity to the K/Pg mass extinction (*9*–*16*). Two additional critical factors contribute to this uncertainty: (i) the exclusion of fossils from most studies, despite wholly extinct lineages dominating the initial post-K/Pg fauna (*17*); and (ii) the limited phenotypic data that are used in most analyses of the morphological diversification of placentals. Phenotype is the object of natural selection, as the interface between organisms and their environment, but most studies reduce complex morphologies to highly simplified metrics such as body size (*11*, *12*) or discrete binary characters (*9*, *13*), hindering robust understanding of the influence of social, ecological, and developmental factors on morphological evolution.

Here, we reconstruct the pattern and drivers of the morphological diversification of Placentalia with a quantitative analysis of cranial evolution that samples the full breadth of living and extinct placental mammal diversity. Our dense three-dimensional (3D) morphometric dataset (757 landmarks and sliding semilandmarks) for 322 species spans the Cenozoic Era and represents every extant family and a majority of extinct orders (Figs. 1 and 2, fig. S1, table S1, and data S1). We focus on the cranium because it is a feature-rich structure that performs several critical functions implicated in placental mammal success, from feeding, fighting, and communication to housing and protecting sensory structures and the brain. Given the ongoing debate on the timing of placental mammal diversification and the phylogenetic positions of some extinct clades, we perform these analyses across 1800 evolutionary trees, using multiple topologies and divergence estimates spanning from 100 to 70 million years ago (Ma), and thereby incorporate the impact of this chronological and phylogenetic uncertainty on our understanding of placental mammal evolution. We summarized our results by binning these phylogenetic frameworks into a total of 18 sets, which are divided by tree topology and 5-million–year intervals for the placental mammal root age; for example, 100 trees use tree topology 2 and a divergence estimate for Placentalia ranging between 80 and 85 Ma. With these analyses, we reconstructed the tempo and mode of evolution of the placental mammal skull to robustly test the hypothesis that placental mammals radiated quickly in the aftermath of the K/Pg mass extinction and to assess the primary social, developmental, and ecological factors associated with their morphological diversification.

Results

Cranial variation across placental mammals

Despite the vast ecological range of placental mammals, skull variation is overwhelmingly concentrated into a single region of morphospace, suggesting extensive conservation or convergence of cranial form across all placental mammal superorders (Fig. 1 and fig. S2). There are two other clusters observed, but each is populated by single clades, specifically whales and rodents. The first principal component (PC1) (34.1% of the total variation) is dominated by shifts associated with the land-to-water transition of whales, with two distinct concentrations that represent "terrestrial" and "aquatic" adaptive peaks. Extreme elongation of the premaxilla and maxilla and retraction of the nasals in Cetacea drives change along this axis, with early whales overlapping substantially with terrestrial Laurasian "ungulates" that include Litopterna, Perissodactyla, and Artiodactyla. Several other lineages converge on aspects of this morphology, particularly the retraction of the nasals, including Sirenia, Desmostylia, Proboscidea, and Embrithopoda. The opposite extreme of PC1 is dominated by short-faced, globular euarchontaglirans, particularly Rodentia and Primates. Whales span the full breadth of PC2 (14.9% of the total variation), with the unusual extinct walrus-like whale *Odobenocetops* defining the maximum end of the axis and the early archaeocete *Pakicetus* at the opposite extreme. Many placental mammal lineages are better discriminated along this axis, with extremely dolicocephalic armadillos occupying lower PC2 values and brachycephalic primates, bats, and elephants at the positive end. Rodents are further distinguished on PC3, on which they form a distinct concentration of

---

[1]Department of Life Sciences, Natural History Museum, London, UK. [2]Department of Genetics, Evolution, and Environment, University College London, London, UK. [3]Department of Vertebrate Zoology, National Museum of Natural History, Smithsonian Institution, Washington, DC, USA. [4]Université Lyon, Université Claude Bernard Lyon 1, CNRS, ENTPE, UMR 5023 LEHNA, Villeurbanne, France. [5]Naturhistorisches Museum Bern, Bern, Switzerland. [6]Institute of Ecology and Evolution, University of Bern, Bern, Switzerland. [7]School of Geography, Earth and Environmental Sciences, University of Birmingham, Birmingham, UK. [8]Department of Biology, University of Wisconsin Oshkosh, Oshkosh, WI, USA. [9]Department of Biology, University of Washington, Seattle, WA, USA. [10]Department of Anatomy, New York Institute of Technology College of Osteopathic Medicine, Old Westbury, New York, NY, USA. [11]Division of Paleontology, American Museum of Natural History, New York, NY, USA. [12]Department of Mammalogy, Division of Vertebrate Zoology, American Museum of Natural History, New York, NY, USA. [13]Department of Paleobiology, National Museum of Natural History, Smithsonian Institution, Washington, DC, USA. [14]Department of Earth and Environmental Sciences, University of Minnesota, Minneapolis, MN, USA. [15]Centre for Integrative Anatomy, Department of Cell and Developmental Biology, University College London, London, UK.
***Corresponding author. Email: a.goswami@nhm.ac.uk**

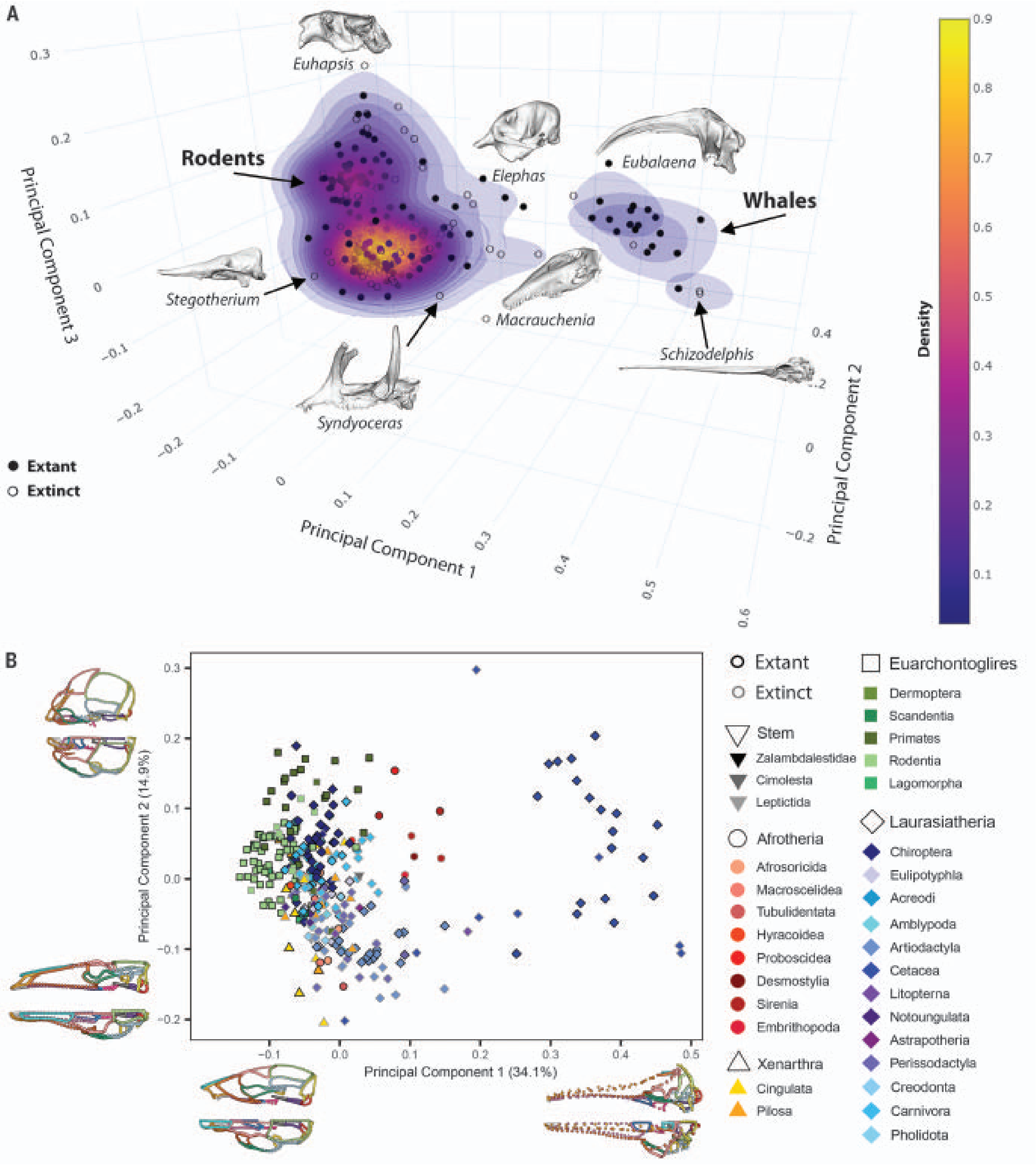

Fig. 1. Cranial variation across placental mammals is highly concentrated. (**A**) Cranial morphospace for placental mammals showing PC1 to 3, with density contours that reflect three concentrations of placental mammal skull shapes (two dominated by single clades) and highlighting specimens along the edges of each of the high-density regions. (**B**) Detailed morphospace of PC1 and 2, showing superordinal and ordinal affiliations of specimens and wireframe models of the variation along each axis. Symbols and colors in the morphospace indicate clade affiliation, as described on the legend (version with color-blind palette provided in fig. S2). Colors on skull wireframes denote different cranial elements (see table S1 for details).

variation that is separate from other terrestrial placental mammals (Fig. 1 and fig. S2) and is driven largely by the height of the facial region, the size of the nasals, and the orientation of the occipital region. Extant and extinct taxa largely overlap in cranial morphospace, with Paleogene to Recent taxa occupying similar positions on the principal axes. Fossil forms fill the gap between the terrestrial and aquatic clusters on PC1, but they also define the extremes of most principal axes, demonstrating the exceptional extinct diversity of placentals. By contrast, the pale fox

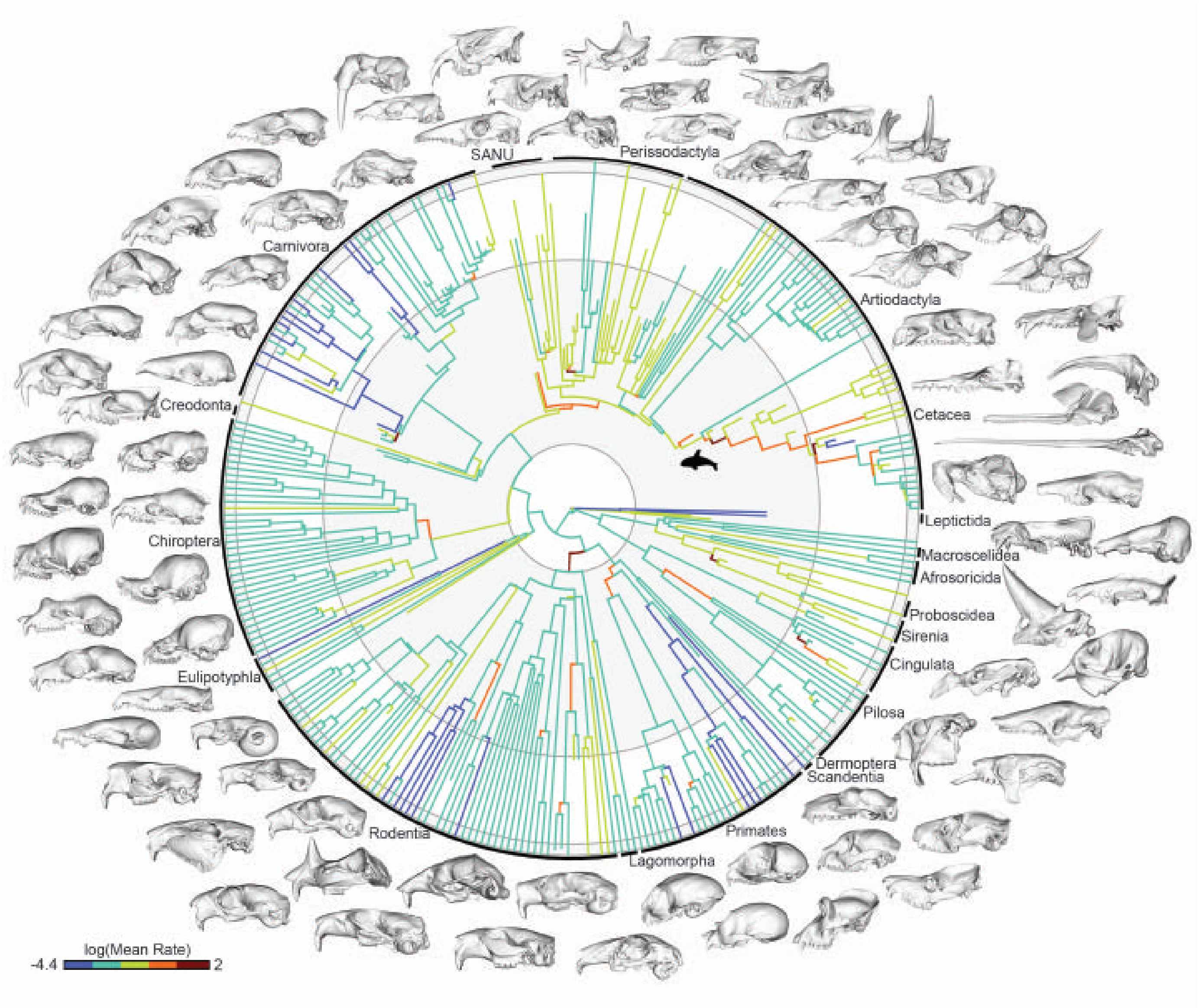

Fig. 2. Rapid evolutionary rates are observed near the base of several placental mammal clades. Estimated branch-specific rates of cranial evolution by using a variable-rates Brownian motion model with a lambda tree transformation, shown here for one example tree (topology 2, root age 80 to 85 Ma, tree 85 of 100). Warmer and cooler colors indicate faster and slower rates of evolution, respectively, with yellow indicating moderate rates. SANU refers to South American native ungulates. Fast branches are concentrated within Cetacea, indicated with a whale icon, as well as more basal branches for several orders. A subset of the sampled skulls is positioned proximal to their terminal branches to demonstrate the immense cranial diversity of living and extinct placentals. Geological age is indicated with alternating shading of circles, from innermost outwards: Cretaceous, Paleogene, Neogene, Quaternary.

(*Vulpes pallida*) is closest to the average cranial shape of extant placental mammals, with an extinct confamilial, the borophagine dog *Desmocyon matthewsi*, possessing a skull most similar to the average shape among the sampled living and extinct mammals.

Tempo of cranial evolution across placental mammals

Bayesian analysis using a reversible-jump Markov chain Monte Carlo (MCMC) algorithm supported variable-rates Brownian motion with a lambda tree transformation (λ = 0.629 to 0.741) as the best supported model of evolution across every phylogenetic topology and divergence time bin sampled in this study (fig. S3). Despite vast differences in the estimated root age for placentals, which ranges from 100 to 70 million years in the phylogenetic hypotheses included here, the results are notably consistent, with little to no difference in positions of rate shifts or relative rates of evolution across the placental mammal tree (Fig. 2 and fig. S4). Rate shifts are clustered at the base of Placentalia, varying slightly in whether they occur at the basal nodes for each superorder or more inclusive nodes (e.g., Boreoeutheria and Atlantogenata) and demonstrating an increase in rate from stem to crown Placentalia (fig. S4). High rates are also concentrated at the base of many orders, reflecting the rapid accumulation of ecological and morphological diversity early in the placental mammal radiation. Multiple rate increases occur along the stem of Cetacea, with particularly fast rates of evolution on the branches leading to fully aquatic whales (basilosaurid archaeocetes plus crown cetaceans), as well as to odontocetes. High rates of evolution are also observed at or near the base of Paenungulata (and/or Sirenia, depending on phylogenetic tree), Cingulata, Primates (and/or Catarrhini), Rodentia, and

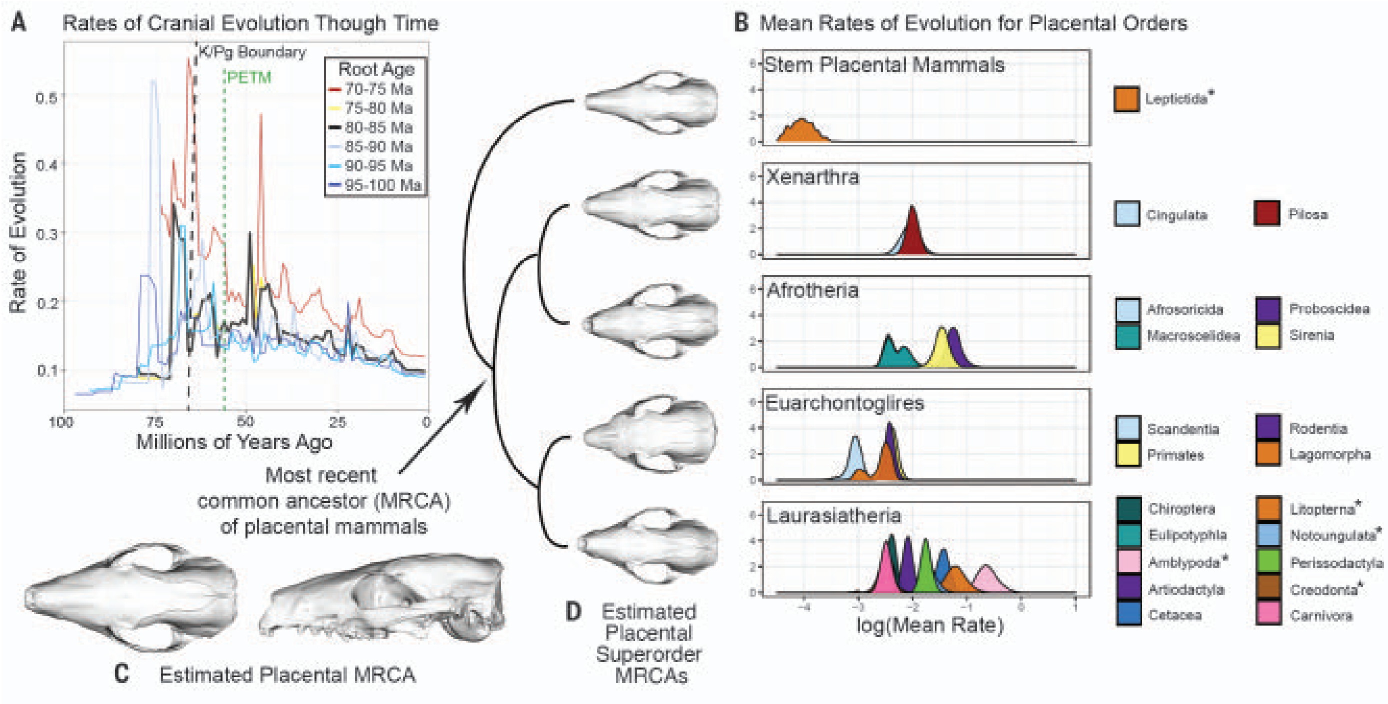

Fig. 3. Rates of evolution peak early in placental mammal evolution and attenuate through time. (**A**) Rates of evolution through time are shown for one sample tree per root age for topology 2, colored by root age, and clade-specific tip rates and ancestral estimates are shown for topology 2, root age 80 to 85, tree 85, as in Fig. 2. The K/Pg boundary and the PETM are indicated with red and green lines, respectively. (**B**) Subsetting terminal branch rates by each order demonstrates the slow pace of evolution in stem placental mammals and euarchontoglirans, in contrast to Afrotheria and several laurasiatherian clades. Asterisk indicates wholly extinct orders. (**C** and **D**) Estimated ancestral cranial shapes (excluding teeth and bullae) for (C) Placentalia and (D) each superorder, by using *Vulpes pallida* for the reference mesh, suggest a marked similarity among the estimated MRCAs for placental mammal superorders.

Chiroptera. There are relatively fewer high rates of evolution observed in less-inclusive clades, but high rates are observed on the branches leading to hominids, saber-toothed cats, pinnipeds, beavers, camels, yangochiropteran bats, and the extinct large-bodied brontothere perissodactyls (Fig. 2 and fig. S4).

Placing evolutionary rates in temporal context necessarily depends heavily on the divergence estimates of the phylogenetic framework. Nonetheless, the distribution of evolutionary rates across a range of phylogenetic hypotheses is strongly indicative that the tempo of cranial evolution increased rapidly early in placental mammal evolution, proximal to the end-Cretaceous mass extinction, and fell equally rapidly, in contrast to studies of body size evolution in extant taxa (*4*, *5*). This initial burst is followed by long-term decline, but this decline is punctuated by multiple smaller peaks throughout the Cenozoic, a pattern that we describe as "attenuated evolution," indicating the decreasing amplitude of peaks in evolutionary rate along a backdrop of declining rates. The initial radiation and declining rates are consistent with an early burst model (*18*), but the presence of numerous intermediate peaks in evolutionary rates distinguishes this pattern from a standard early burst. The declining size of those peaks likely reflects increasingly limited niche space with distance from the K/Pg mass extinction, whereas their timing, allowing for the aforementioned uncertainties, likely reflects subsequent bursts of diversification that are associated with major climatic and geologic events. Several scenarios reconstruct a large peak in rates in the early to middle Eocene and smaller peaks near the Eocene-Oligocene and Oligocene-Miocene boundaries, all of which are associated with transitions between warmer and cooler climates (Fig. 3). By contrast, the impact of the rapid warming event at the Paleocene-Eocene boundary, the Paleocene-Eocene Thermal Maximum (PETM), on evolutionary rates is ambiguous, with sharp declines, small increases, or little change in rate during this interval, depending on the estimated root age of Placentalia.

Both the slowest and the fastest evolving clades in this study are wholly extinct lineages that straddle the end-Cretaceous mass extinction (Fig. 3 and fig. S5). Stem placental mammals with unambiguous Late Cretaceous origins and a rich fossil record evolved much more slowly than all crown placental mammals in every phylogenetic framework. "Archaic" and South American native ungulates (SANU), both of which first appear in the fossil record in the Paleocene in the aftermath of the mass extinction, display the fastest rates of evolution in every scenario. Comparing the overall rates of cranial evolution across orders also demonstrates a clear dissociation of taxonomic diversification and morphological evolution in the crown placental mammal radiation. Irrespective of topology and divergence estimates, laurasiatherian and afrotherian clades display the fastest rates of cranial evolution (Fig. 3 and fig. S5), whereas the most speciose placental mammal orders, Rodentia and Chiroptera, show some of the lowest evolutionary rates for cranial shape. The relative ranking among the five orders with the fastest rates of cranial evolution varies depending on topology and divergence time bin but always includes Cetacea, Proboscidea, Sirenia, and the extinct orders Litopterna and "Amblypoda" (a likely paraphyletic grouping of early Cenozoic large-bodied ungulates). Notably, members of the defunct, paraphyletic "Insectivora," including Afrosoricida, Macroscelidea, Scandentia, and Eulipotyphla, consistently show some of the slowest rates of evolution, which may have contributed to the long-standing difficulties with ascertaining their phylogenetic relationships on the basis of morphology alone.

Among extant superorders, Euarchontoglires is consistently the slowest evolving, with all clades, including rodents and primates, exhibiting some of the slowest evolutionary rates among placentals. The xenarthran clades all consistently

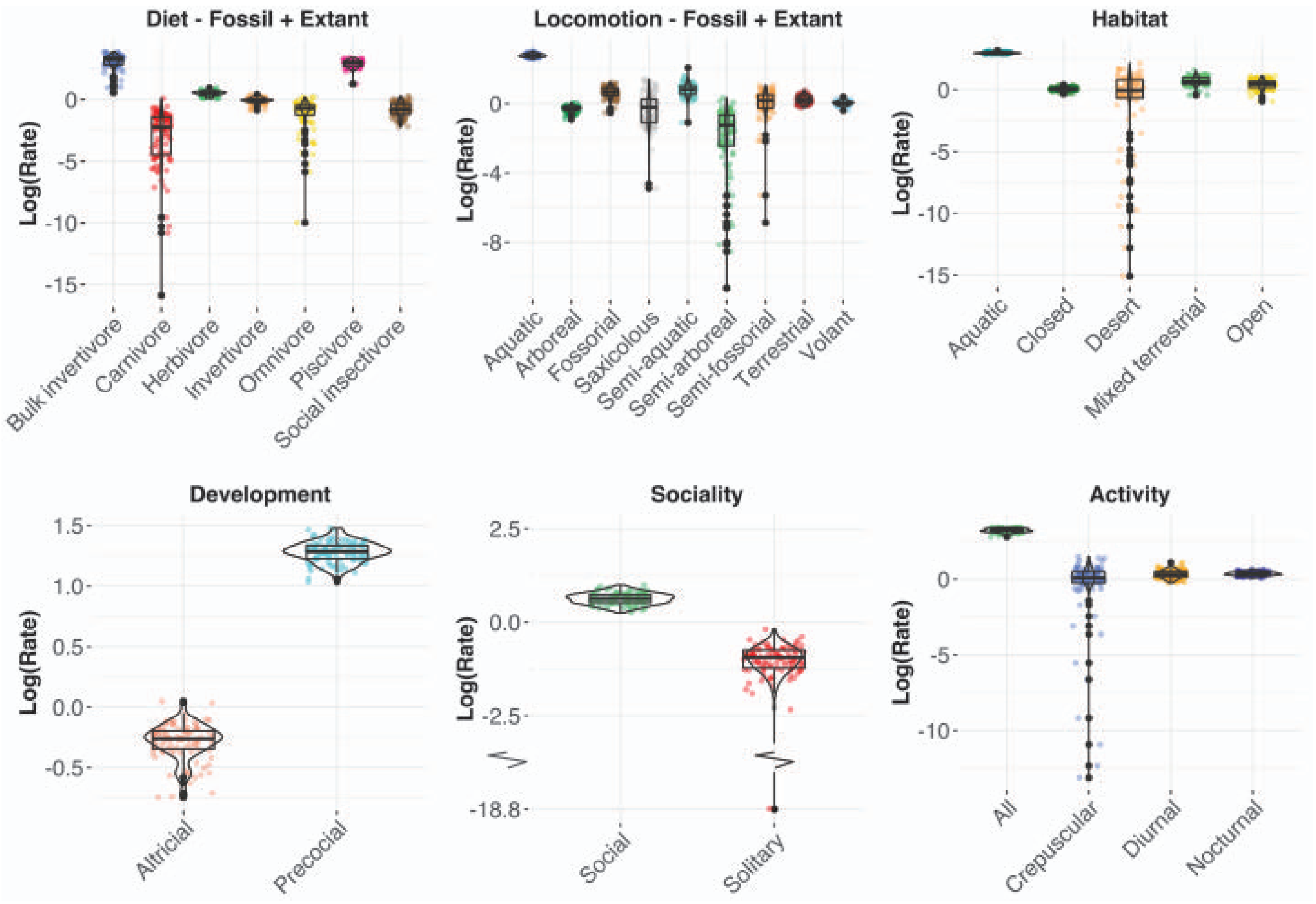

Fig. 4. Aquatic, herbivorous, precocial, and social placental mammals evolve at the fastest rates. Rates of evolution on the basis of ecological and life-history traits for placentals, with diet and locomotion estimated for all living and extinct taxa sampled, whereas the other four categories are limited to extant taxa. Distributions represent results from 100 sampled trees for topology 2, root age 80 to 85.

display an intermediate rate of evolution relative to other placentals, whereas laurasiatherians show the broadest range of evolutionary rates across orders. Other than the fast-evolving aquatic or extinct ungulates and slow-evolving bats noted above, the other laurasiatherians show a division between herbivorous ungulate orders (Artiodactyla, Perissodactyla, and Notoungulata) that evolve at moderate rates, whereas carnivorous laurasiatherians, including Carnivora and the extinct creodonts, display relatively slow rates of evolution. Although we do not quantify taxonomic diversification in this study, our results do suggest that the expected close association of rates of speciation and rates of phenotypic evolution may not extend cleanly to the placental mammal skull. This expectation stems from hypotheses of positive coupling between lineage splitting and adaptation to new niches via phenotypic evolution (*19*). By contrast, numerous examples exist of taxonomic diversification occurring in the absence of ecological or morphological divergence (*20*). Recent study of rates of body size evolution and speciation in several vertebrate clades identified a general relationship between these two rates within each vertebrate class but noted that the strength of this association varied widely in subclades within each class. Moreover, some smaller clades displayed a negative relationship between rate of speciation and that of body size evolution (*20*). Similarly, the lack of a clear association between taxonomic diversity and rate of cranial evolution across placental mammals does not preclude a stronger association existing within placental mammal clades. A focused analysis of this relationship, taking into account the ongoing debate on the ability to accurately estimate rates of taxonomic diversification (*21*), is needed, but it is worth considering whether the likely drivers of nonadaptive radiations, such as geographic isolation, may be more pronounced in smaller taxa, such as those that dominate the two most speciose placental mammal clades, Rodentia and Chiroptera.

Drivers of cranial evolution in placental mammals

We further examined the influences of size, diet, and locomotion on skull shape and rate of cranial evolution using multivariate phylogenetic linear models fitted by penalized likelihood, across the same distribution of phylogenetic tree topologies and divergence time bins that we described above. The additional factors of habitat, development (altricial or precocial), diel activity pattern, and social structure (social or solitary) were further examined for the 207 extant species (data S1). When limited to extant taxa, size and diet were the only factors consistently supported as significantly influencing cranial shape and significantly interacting with each other across all phylogenetic frameworks and time bins ($p <$ 0.05; table S2). Locomotion has a significant, albeit weaker, effect on skull shape in all but the youngest divergence time bin (70 to 75 Ma), whereas habitat type was supported as a significant factor in a minority of analyses. Analyses that include extinct taxa are congruent with these results, with diet and size showing the strongest and most consistent influence on cranial shape, as well as having a significant interaction (table S2). Shape changes associated with increased size are concentrated in the elongation of the rostral region (fig. S6), as suggested by previous studies (*22*). Large size is additionally associated with retraction of the nasals, which is noted in numerous lineages as described above. Variation associated with dietary categories also reflects traits long identified as informative for ecomorphological analyses, including a larger sagittal crest in carnivores, reduced zygomatics in social insectivores, and rostrum elongation and cranial telescoping in bulk invertivores (a category that is composed entirely of cetaceans).

Although most of the factors that we examined are not significantly associated with cranial shape, there are substantial differences in the rate of cranial evolution associated with these factors, which could be informative for modeling species response to environmental change. In particular, diet, locomotion, social structure, and development show significant differences in cranial rate among character states (Fig. 4 and fig. S7). Dietary categories dominated by aquatic taxa, specifically bulk invertivores and piscivores, evolve the fastest, followed by herbivores. Aquatic and semiaquatic mammals evolve the fastest among locomotor categories, with arboreal and semiarboreal showing comparatively slow evolution. Aquatic mammals similarly dominated among habitat categories, whereas desert taxa exhibit a broad range of rates. Notably, social animals evolve significantly faster than solitary animals, which is potentially due to pressure for elaborate cranial ornamentation in many social species. Precocial species also evolve at a markedly faster rate than altricial mammals, suggesting that extended parental care of young may result in overall slower rates of evolution. Placental mammals without a fixed period of activity, a category that is dominated by fast-evolving whales and proboscideans, evolve more rapidly than diurnal, nocturnal, or crepuscular species, but there are no significant differences among taxa that display these latter three activity patterns. Some of these patterns, such as fast rates in bulk invertivores, are clearly driven by cetaceans. However, several of the character states exhibited by some or most cetaceans are shared with other placentals, and these noncetacean taxa also display higher rates of evolution. For example, aquatic mammals in this dataset include cetaceans, pinnipeds, sirenians, and desmostylians, all of which display elevated rates of skull evolution. Other character states associated with higher rates of evolution, such as precociality, sociality, and cathemeral activity pattern, are observed across placentals. In particular, these states are exhibited by many terrestrial herbivores (another fast-evolving ecological group), as well as cetaceans (fig. S8), demonstrating that these results are not solely driven by a single, fast-evolving clade.

Although not considered explicitly here, we may expect postcranial systems to diverge from the patterns observed here, particularly in terms of the differences across clades. Specifically, we may expect higher rates of postcranial evolution in bats and euarchontans, as well as in arboreal and semiarboreal taxa more generally, in contrast to the low rates of cranial evolution that we observed for these groups. More similarity in temporal pattern of cranial and postcranial evolution is likely, because those are likely driven by extrinsic phenomenon, such as mass extinctions or large-scale environmental change. However, some of the most extreme postcranial transitions, which are associated with the appearance of fully aquatic or fully volant mammals, occur during the Eocene. Quantifying postcranial evolution would thus likely increase the amplitude of evolutionary rates during that interval, but further work along these lines is needed to test this hypothesis.

Ancestral estimations of the earliest placental mammals and implications for resolving their origins

We used our extensive sample of living and extinct placental mammals to estimate cranial shapes for the most recent common ancestor (MRCA) of placental mammals and of each of the four placental mammal superorders (Fig. 3). Regardless of the starting 3D mesh used (which is shown here for *V. pallida*, the most average extant placental mammal in this sample), ancestral estimates for the four superorders are very similar, with only the euarchontogliran MRCA distinguished by a broader vault and a shorter and narrower rostrum. Subtle differences among all superordinal MRCAs exist, largely in the breadth and tapering of the rostrum. However, the similarities in these ancestral reconstructions may explain the persistent difficulties with identifying unambiguous Cretaceous crown placentals, despite the near certain divergence of the superorders in advance of the end-Cretaceous mass extinction. Rather than reflecting shortcomings of the fossil record or phylogenetic methodologies, this uncertainty may be due to the lack of clear morphological differences among the earliest representatives of the placental mammal superorders (*7*). This more pernicious source of uncertainty may be unresolvable, but fortunately, our results demonstrate that reconstructions of the tempo and drivers of the exceptional morphological diversification of placental mammals are robust to considerable uncertainty in both phylogenetic topology and the timing of their initial radiation.

Materials and methods

Our dataset samples 322 crown and stem placental mammals, including 207 extant and 115 extinct species. Sixty-six 3D landmarks and 69 semilandmark curves were collected for the left side of the skull by using Stratovan Checkpoint (Stratovan, Davis, CA, USA). Landmarks and semilandmarks were imported into R for analysis, in which curves were resampled to a common number of semilandmarks, slid to minimize bending energy, and registered with generalized Procrustes analysis, which resulted in a total of 757 3D landmarks and sliding semilandmarks. Data on diet, locomotion, habitat, development, social structure, and activity pattern were collected from the published literature.

In the absence of a well-resolved phylogenetic hypothesis that samples all living and extinct taxa in our dataset, we constructed an extensive range of alternative phylogenies. Starting with a set of node-dated trees from the posterior distribution of a recent species-level molecular analysis of placental mammal relationships (*14*), we binned these trees into six 5-million–year bins (70 to 75 Ma, 75 to 80 Ma, 80 to 85 Ma, 85 to 90 Ma, 90 to 95 Ma, and 95 to 100 Ma). We then grafted in fossil taxa on the basis of a suite of recent morphological phylogenetic analyses (see supplementary materials), resulting in three alternative topologies that capture the major points of uncertainty, and generated 419,400 alternative trees to capture uncertainty in divergence estimates. Lastly, we subsampled this set to 1800 trees, 100 for each of the six 5-million–year root-age bins for each of the three topologies, which was used in subsequent analyses.

Macroevolutionary analyses

To examine the overall pattern of cranial variation across placentals, we conducted a principal components analysis using Procrustes-aligned 3D data and reconstructed wireframe models for the minimum and maximum shapes on the primary axes of variation. We further estimated the ancestral shape for the placental MRCA and each superordinal MRCA by maximum likelihood and warping of a reference shape to the ancestral estimates.

We assessed 10 alternative evolutionary models (variable- and single-rate models for Brownian motion [BM], Ornstein-Uhlenbeck, and BM with lambda, kappa, or delta tree transformations) for cranial evolution using phylogenetic PC scores that represented 95% of the total variation in the dataset and a reversible-jump MCMC algorithm implemented in BayesTraits v. 3 (*5*). For the best supported model, we binned rates by geological time and plotted their pattern through time for one randomly selected tree from 18 alternative tree topologies and divergence estimate bins. We further extracted rates for the terminal branches and plotted them by clade to assess differences in mean rate across clades.

We assessed the association of life-history and ecological traits on cranial variation and evolutionary rates using Type II phylogenetic multivariate analyses of variance (phylogenetic regressions) on the Procrustes coordinates with log centroid size and each of the six factors as predictors across the same 18 trees. We conducted one analysis of size, diet, and locomotion for the full dataset of living and extinct species (n = 322) and a second one of all six factors for just the extant taxa (n = 207). Subsequently, we used a state-specific Brownian motion model to estimate rates of evolution for each ecological and life-history state across the full suite of 1800 trees. Further details of all materials and methods are provided in the supplementary materials.

REFERENCES AND NOTES

1. C. J. Burgin, J. P. Colella, P. L. Kahn, N. S. Upham, *J. Mammal.* **99**, 1–14 (2018).
2. G. G. Simpson, *Biol. Rev. Camb. Philos. Soc.* **12**, 1–46 (1937).
3. N. Cooper, A. Purvis, *Am. Nat.* **175**, 727–738 (2010).
4. J. Clavel, H. Morlon, *Proc. Natl. Acad. Sci. U.S.A.* **114**, 4183–4188 (2017).
5. C. Venditti, A. Meade, M. Pagel, *Nature* **479**, 393–396 (2011).
6. D. M. Grossnickle, E. Newham, *Proc. Biol. Sci.* **283**, 20160256 (2016).
7. N. Brocklehurst, E. Panciroli, G. L. Benevento, R. B. J. Benson, *Curr. Biol.* **31**, 2955–2963.e4 (2021).
8. T. J. D. Halliday, P. Upchurch, A. Goswami, *Proc. Biol. Sci.* **283**, 20153026 (2016).
9. R. M. D. Beck, M. S. Y. Lee, *Proc. Biol. Sci.* **281**, 20141278 (2014).
10. M. S. Springer *et al.*, *Mol. Phylogenet. Evol.* **106**, 86–102 (2017).
11. R. W. Meredith *et al.*, *Science* **334**, 521–524 (2011).
12. S. Álvarez-Carretero *et al.*, *Nature* **602**, 263–267 (2022).
13. M. A. O'Leary *et al.*, *Science* **339**, 662–667 (2013).
14. T. J. D. Halliday *et al.*, *Proc. Biol. Sci.* **286**, 20182418 (2019).
15. N. S. Upham, J. A. Esselstyn, W. Jetz, *PLOS Biol.* **17**, e3000494 (2019).
16. N. M. Foley, M. S. Springer, E. C. Teeling, *Philos. Trans. R. Soc. Lond. B Biol. Sci.* **371**, 20150140 (2016).
17. T. R. Lyson *et al.*, *Science* **366**, 977–983 (2019).
18. L. J. Harmon *et al.*, *Evolution* **64**, 2385–2396 (2010).
19. G. G. Simpson, *The Major Features of Evolution* (Columbia Univ. Press, 1953).
20. C. R. Cooney, G. H. Thomas, *Nat. Ecol. Evol.* **5**, 101–110 (2021).
21. S. Louca, M. W. Pennell, *Nature* **580**, 502–505 (2020).
22. A. Cardini, P. D. Polly, *Nat. Commun.* **4**, 2458 (2013).

ACKNOWLEDGMENTS

We are indebted to the numerous colleagues, curators, and collections staff at international museums that provided access to specimens for this project, in particular R. Portela Miguez, R. Pappa, P. Brewer, R. Sabin, and L. Tomsett (NHM); P.-H. Fabre (Université de Montpellier); J. Galkin, R. O'Leary, and A. Gishlick (AMNH); G. Rößner (BSP); S. and R. Boessenecker (CCNHM); B. Simpson (FMNH); D. Miao (KU); J. Chupasko (MCZ); S. McLeod, X. Wang, and J. Velez-Juarbe (LACM); J. Ashby and P. Viscardi (LDUCZ); M. Reguero (MLP); G. Billet, J. Cuisin, and G. Veron (MNHN); P. Holroyd, M. Goodwin, and J. Tseng (UCMP); B. Sanders (UMMP); A. Millhouse and S. Peurach (USNM); C. Norris and D. Brinkman (YPM); R. Secord and G. Carter (UNSM); and L. Costeur (NMB). We are grateful to V. Fernandez and B. Clark (NHM) and J. Keller (UMN) for support in microCT scanning and to the "plate-forme de morphometrie" of the UMS 2700 (CNRS, MNHN) for access to the surface scanner. We thank E. Watt (NHM/UCL) for uploading scans to online repositories. We are grateful to the two anonymous reviewers and the editor for their thoughtful comments. We thank V. Herridge for putting a name to this phenomenon. **Funding:** European Research Council grant STG-2014-637171 (to A.G.), National Science Foundation SF-EAR 1349607 (to J.H.G., B.L.B., A.G., and M.C.), Gerstner Scholar Postdoctoral Research Fellowship (to A.C. and N.B.S.), Natural Environment Research Council Doctoral Training Partnership training grant NE/L002485/1 (to E.J.C.), Horizon 2020 MCSA Fellowship IF 797373-EVOTOOLS (to J.C.), National Science Foundation EAR 1338262 (to D.L.F.), and Labex BCDiv 10-LABX-0003 (to A.C.F.). **Author contributions:** Conceptualization: A.G.; Methodology: A.G., R.N.F., J.C., A.C.F., and A.W.; Software: A.G., R.N.F., J.C., A.W., and A.C.F.; Investigation: A.G., R.N.F., E.N., J.C., E.J.C., A.C.F., T.J.D.H., A.C., M.C., B.L.B., J.H.G., N.B.S., and D.L.F.; Visualization: A.G. and R.N.F.; Funding acquisition: A.G., E.C., J.H.G., B.L.B., A.C., and N.B.S.; Writing—original draft: A.G.; Writing—review and editing: A.G., R.N.F., E.N., J.C., E.J.C., A.C.F., T.J.D.H., A.C., M.C., B.L.B., J.H.G., N.B.S., D.L.F., and A.W. **Competing interests:** The authors declare that they have no competing interests. **Data and materials availability:** Morphometric data and novel code are provided on Github (https://github.com/anjgoswami/Goswami_et_al_Placental_evolution_2022). 3D meshes for all specimens are available for free download on phenome10k.org or morphosource.org, as detailed in data S1, unless specifically restricted by specimen repositories. All specimen and species details, including physical and online repository information and trait data, are provided in data S1.

SUPPLEMENTARY MATERIALS

science.org/doi/10.1126/science.abm7525
Materials and Methods
Figs. S1 to S8
Tables S1 and S2
References (*23*–*97*)
Data S1

Submitted 8 October 2021; accepted 20 September 2022
10.1126/science.abm7525

ORGANIC CHEMISTRY

Stereochemical editing logic powered by the epimerization of unactivated tertiary stereocenters

Yu-An Zhang†, Vignesh Palani†, Alexander E. Seim, Yong Wang, Kathleen J. Wang, Alison E. Wendlandt*

The stereoselective synthesis of complex targets requires the precise orchestration of chemical transformations that simultaneously establish the connectivity and spatial orientation of desired bonds. In this work, we describe a complementary paradigm for the synthesis of chiral molecules and their isomers, which tunes the three-dimensional structure of a molecule at a late stage. Key to the success of this strategy is the development of a mild and highly general photocatalytic method composed of decatungstate polyanion and disulfide cocatalysts, which enable the interconversion of unactivated tertiary stereogenic centers that were previously configurationally fixed. We showcase the versatility of this method—and the implementation of stereoediting logic—by the rapid construction of chiral scaffolds that would be challenging to access using existing tools and by the late-stage stereoediting of complex targets.

Stereochemistry plays a defining role in the chemical and physical properties of chiral molecules (*1*). Specific stereoisomers (enantiomers and diastereomers) frequently exhibit distinct interactions with chiral receptors (e.g., enzymes and proteins), giving rise to critical pharmacokinetic and pharmacodynamic differences (Fig. 1A) (*2*–*4*). Equally notable changes in the chemical and physical characteristics of diastereomers have been leveraged in the design of catalysts and functional materials (*5*, *6*). However, because the influences of altering a single stereocenter within a complex molecule (and within bimolecular interactions) are rarely intuitive, such isomer effects are typically discovered empirically. Comprehensive synthetic access to the full complement of stereoisomers is thus essential for structure-function studies seeking to assess desirable properties of chiral organic molecules.

The construction of stereochemically well-defined complex organic molecules remains a central challenge in organic synthesis and catalysis. Stereoselective synthetic sequences often revolve around a small number of highly general and highly selective chemical reactions or seek to leverage enantiopure, chiral pool–derived starting materials to reliably establish the desired stereocenter(s). Consequently, selective access to some stereocenters and stereochemical patterns remains more challenging than access to others, and access to distinct stereoisomers frequently requires de novo synthesis of each target—often from specific starting materials or through complementary synthetic strategies. For example, a highly selective reduction of drimene (**1**) to 8α(H)-drimane (**2a**) was achieved using conventional hydrogenation conditions, whereas access to the 8β(H) epimer (**2b**) from the same intermediate required route redesign through an alternative, multistep sequence (Fig. 1B) (*7*).

A deceptively simple alternative would be the direct editing of chiral products to adjust their relative stereochemistry in a late-stage setting. In contrast to conventional stereoselective synthetic strategies, this stereochemical editing approach would enable a fundamentally different synthetic logic, allowing bond connectivity to be decoupled from the intrinsic stereoselectivity of the bond formation step(s). In principle, stereoediting logic would do several things: (i) enable challenging chiral target molecules to be prepared through unconventional and/or unselective retrons, (ii) provide a strategy to override strong substrate control

---

Department of Chemistry, Massachusetts Institute of Technology, Cambridge, MA 02139, USA.
*Corresponding author. Email: awendlan@mit.edu
†These authors contributed equally to this work.

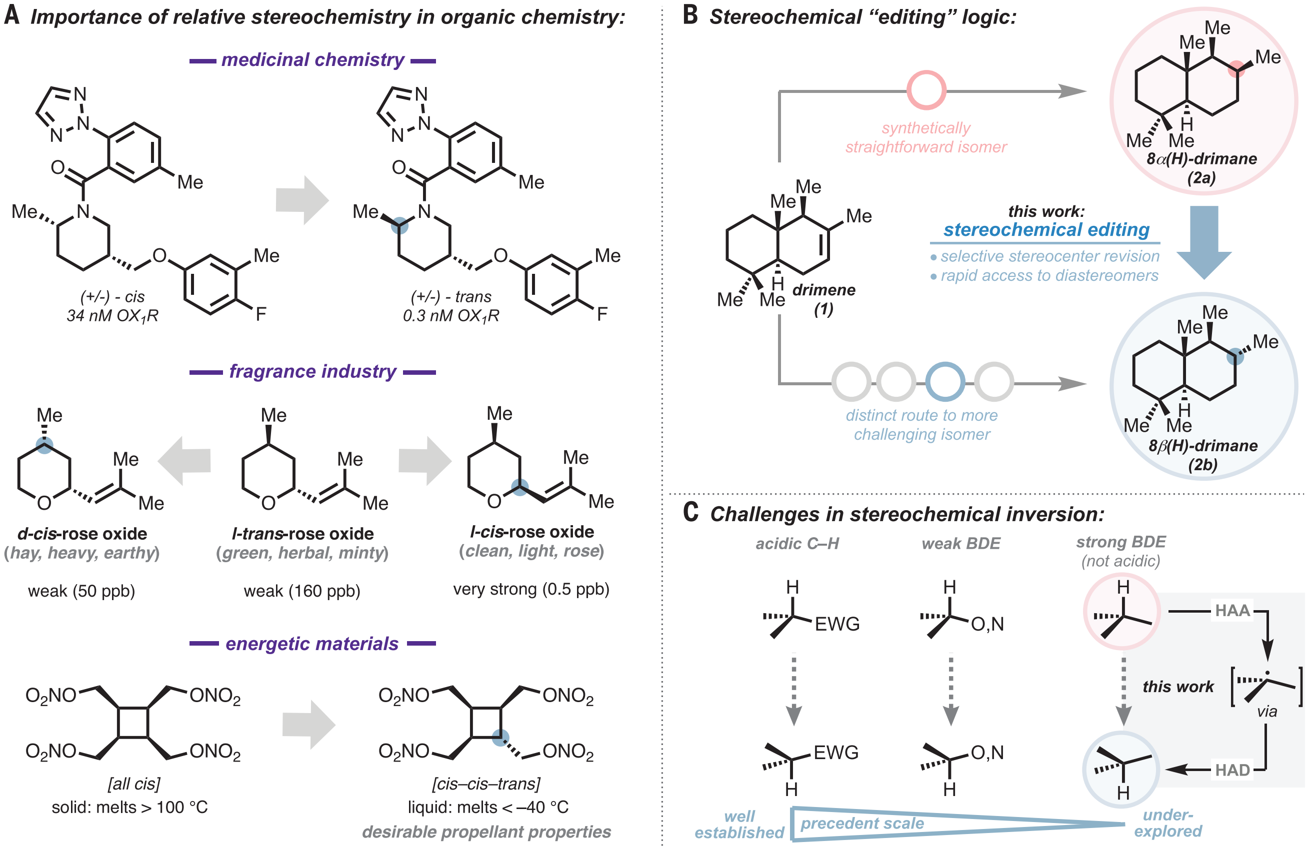

Fig. 1. Overview of stereochemical editing logic. (**A**) Diastereomers have distinct chemical and physical properties. ppb, parts per billion. (**B**) Illustration of a stereochemical inversion strategy in multistep synthesis. (**C**) Established and underexplored areas for stereoediting tools (*3*, *4*, *5*). BDE, bond-dissociation energy; EWG, electron withdrawing group; HAA, H atom abstraction; HAD, H atom donation.

effects within complex settings, and (iii) present new opportunities for late-stage diversification. Here, we report the realization of these goals, enabled by the identification of a highly general, broadly functional group–tolerant catalytic method to interconvert unactivated methine stereogenic centers.

The revision of stereogenic centers is routinely integrated into synthetic design but frequently requires multiple chemical steps and the use of stoichiometric redox or acid-base pairs. The direct, catalytic interconversion of stereocenters featuring acidic C–H bonds (e.g., α-carbonyl) is well established, and recent efforts have identified innovative strategies to control isomer distributions (*8*, *9*). We and others have sought to expand the scope of stereoediting tools to allow for the revision of conventionally static stereocenters, leveraging radical reactions that selectively target homolytically weak C–H bonds adjacent to secondary alcohols (*10*–*14*) or other heteroatoms (*15*–*18*) and transiently electronically activated positions (*19*, *20*). In spite of these substantial advances, the selective interconversion of stereocenters having strong, hydridic C–H bonds—such as unactivated tertiary methines—remains an unsolved problem. Limited reaction scope, poor functional group compatibility, long reaction times, use of super-stoichiometric reagent, and/or complex side-product profiles limit the application of existing tools using photoexcited ketone (*21*), $HgBr_2$ (*22*), azidyl radical (*23*), and transition metal–based (*24*, *25*) reagents. The lack of general and efficient methods targeting unactivated tertiary stereocenters has limited the broad exploration of stereoediting logic in organic synthesis (Fig. 1C).

We selected *cis*-cyclobutane **3a**, which does not undergo efficient isomerization to the trans isomer using established conditions, as a model substrate to explore the epimerization of unactivated methine stereocenters. Combs-Walker and Hill have previously reported the epimerization of *cis*-decalin to *trans*-decalin using a decatungstate (DT) polyanion photocatalyst; however, the formation of **3b** was prohibitively slow using these conditions (Fig. 2B, black trace) (*26*). On the basis of our experience with cocatalytic systems composed of distinct H atom acceptor and donor reagents, we examined the effect of thiol and disulfide additives on isomerization efficiency (see the supplementary materials for full optimization details). Enhanced reaction rate was observed in the presence of latent H atom donors, such as bis(4-chlorophenyl) disulfide (Fig. 2B, red trace) (*12*, *13*, *27*, *28*). Optimal reaction conditions using catalytic quantities of DT, disulfide, and base in $MeCN/H_2O$ reached a final equilibrium after 4 hours at room temperature under 390-nm light-emitting diode (LED) irradiation (Fig. 2B, blue trace), allowing for the isolation of **3b** in 82% yield.

We applied these conditions to a suite of substrates featuring representative tertiary stereogenic centers to systematically assess the reactivity and selectivity of the method across diverse synthetic settings. In addition to 1,2-disubstituted cyclobutane **3a**, cyclopentane and cyclohexane congeners also react to form trans isomers **4b** and **5b**. We evaluated the effect of substitution pattern using a series of dimethylcyclohexanes (**6a** to **8a**) as substrates: *cis*-1,2- and *cis*-1,4-dimethylcyclohexanes reacted to form the corresponding trans isomers, whereas *trans*-1,3-dimethylcyclohexane reacted to preferentially form the cis isomer.

We next assessed substituent effects using a series of 1-methylcyclohexanols bearing 4-methyl- (**9a**), 4-*n*-pentyl- (**10a**), 4-isopropyl- (**11a**), 4-phenyl- (**12a**), and 4-*tert*-butyl- (**13a**) substituents. This series revealed the feasibility

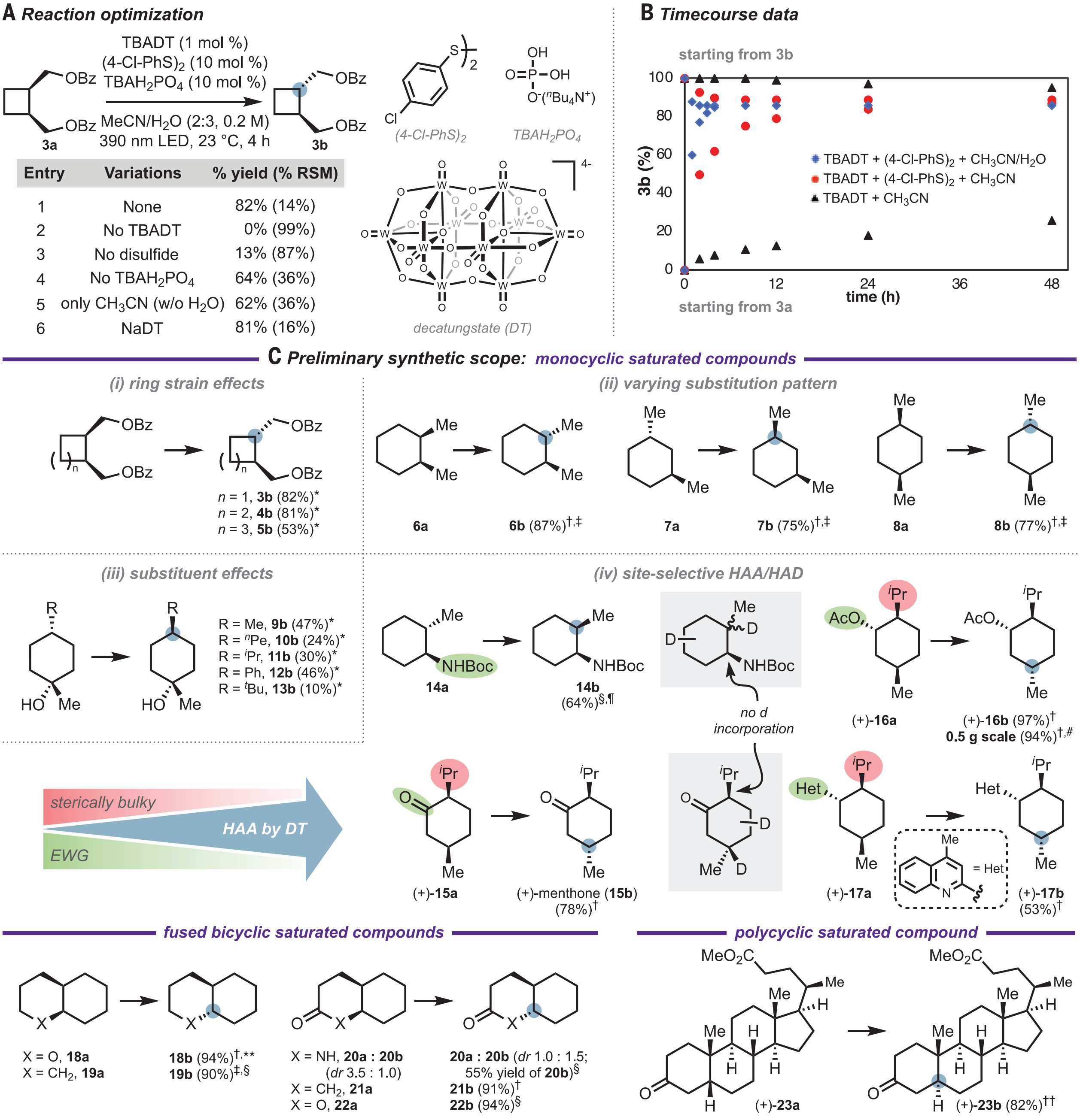

Entry	Variations	% yield (% RSM)
1	None	82% (14%)
2	No TBADT	0% (99%)
3	No disulfide	13% (87%)
4	No $TBAH_2PO_4$	64% (36%)
5	only CH_3CN (w/o H_2O)	62% (36%)
6	NaDT	81% (16%)

Fig. 2. Reaction optimization and preliminary substrate scope. (**A**) Reaction optimization. RSM, recovered starting material; dr, diastereomeric ratio. (**B**) Timecourse data highlighting difference in rate of the reaction. (**C**) Preliminary synthetic scope. Reactions were performed on 0.1- to 0.5-mmol scale with 1 mol % DT with either $N(^nBu)_4^+$ counterions (TBADT) or Na^+ counterions (NaDT), 10 mol % $(4\text{-ClPhS})_2$, and 10 mol % $TBAH_2PO_4$ or $NaH_2PO_4{\bullet}H_2O$ under 390-nm LED irradiation at 23°C in MeCN (0.2 M) or $MeCN/H_2O$ (v/v 4:1 or 2:3, 0.2 M) for 24 hours. Isolated yields are the average of two runs. *Reaction was performed with 1 mol % TBADT, 10 mol % $(4\text{-ClPhS})_2$, and 10 mol % $TBAH_2PO_4$ in $MeCN/H_2O$ (v/v 2:3). †Reaction was performed with 1 mol % TBADT, 10 mol % $(4\text{-ClPhS})_2$, and 10 mol % $TBAH_2PO_4$ in $MeCN/H_2O$ (v/v 4:1). ‡Yield was determined by gas chromatography (GC) analysis with nitrobenzene as an external standard. §Reaction was performed with 1 mol % TBADT, 10 mol % $(4\text{-ClPhS})_2$, and 10 mol % $TBAH_2PO_4$ in MeCN. ¶No D incorporation was observed adjacent to the carbamate group. See the supplementary materials for full experimental details. #Reaction was performed on 2.5-mmol scale (single run). **Given yield is the proton nuclear magnetic resonance (^1H NMR) yield determined with nitrobenzene as an external standard. The isolated yield was 54% because of the volatility of **18b**. ††Reaction was performed with 1 mol % NaDT, 10 mol % $(4\text{-ClPhS})_2$, and 10 mol % $NaH_2PO_4{\bullet}H_2O$ in MeCN.

of isomerizing methine stereocenters bearing larger substituents, such as phenyl and isopropyl groups, although the reaction of **13a** (bearing a *tert*-butyl substituent) was prohibitively slow (10% yield after 24 hours). Based on the preferential isomerization of substrates **3a** to **8a** to form lower-energy isomers, we initially anticipated this series to strongly favor formation of the corresponding trans isomers. However, final equilibrium product ratios up to 1:1 trans:cis were obtained starting from either cis- or trans-configured isomers, allowing for the isolation of higher-energy cis isomers **9b** to **12b** in 24 to 47% yields starting from the corresponding trans starting materials

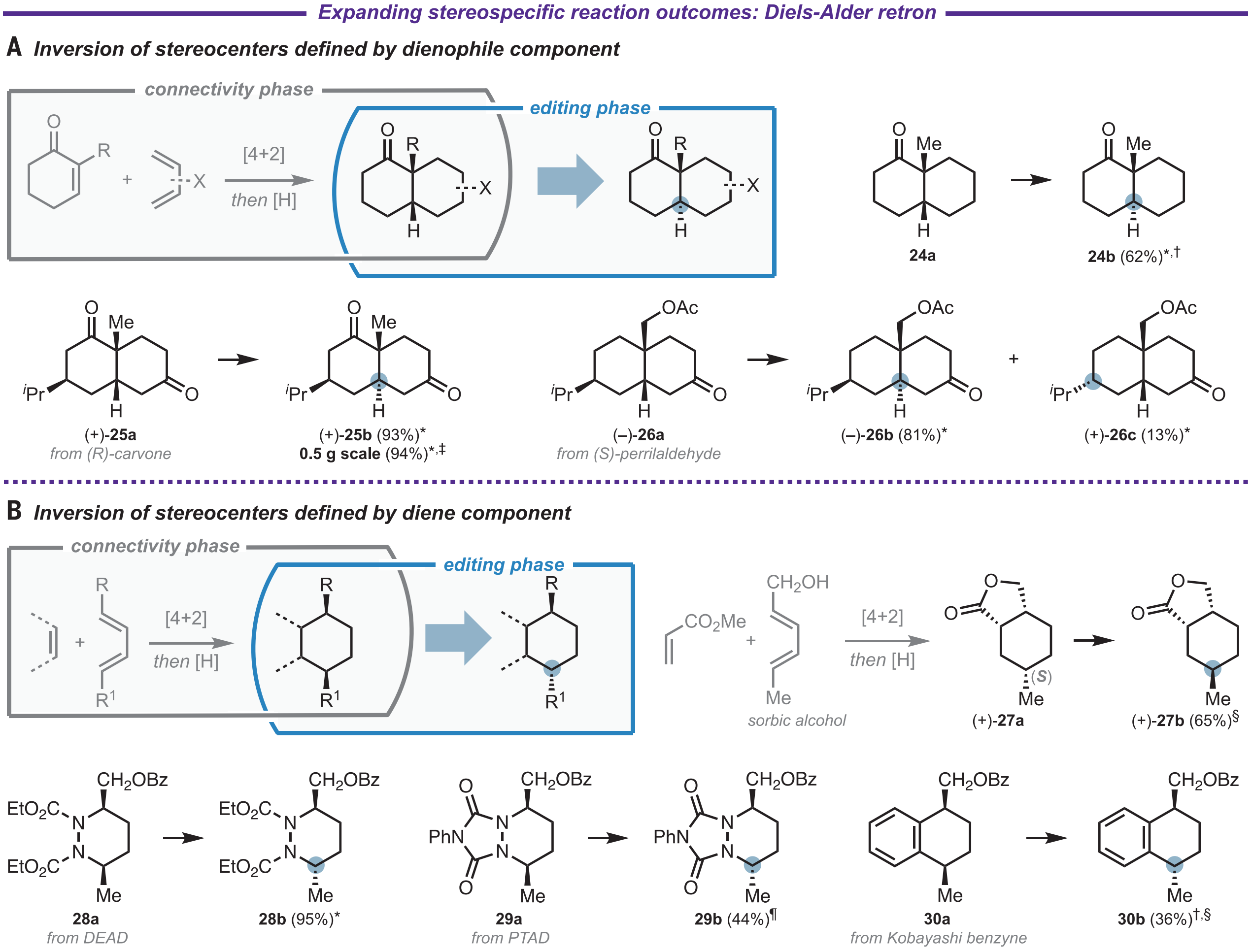

Fig. 3. Strategic application of stereocenter editing to DA cycloadducts. (**A**) Stereochemical configuration dictated by the parent dienophile conformer. (**B**) Stereochemical configuration dictated by the parent diene conformer. Reactions were performed on 0.1- to 0.5-mmol scale with 1 mol % DT with either $N(^{n}Bu)_4^+$ counterions (TBADT) or Na^+ counterions (NaDT), 10 mol % $(4\text{-ClPhS})_2$, and 10 mol % $TBAH_2PO_4$ or $NaH_2PO_4 \cdot H_2O$ under 390-nm LED irradiation at 23°C in MeCN (0.2 M) or $MeCN/H_2O$ (v/v 4:1 or 2:3, 0.2 M) for 24 hours. Isolated yields are the average of two runs. See the supplementary materials for full experimental details. *Reaction was performed with 1 mol % TBADT, 10 mol % $(4\text{-ClPhS})_2$, and 10 mol % $TBAH_2PO_4$ in $MeCN/H_2O$ (v/v 2:3). †Number in parentheses denotes ^1H NMR yield with nitrobenzene as an external standard. ‡Reaction was performed on 2.3-mmol scale (single run). §Reaction was performed with 1 mol % TBADT, 10 mol % $(4\text{-ClPhS})_2$, and 10 mol % $TBAH_2PO_4$ in $MeCN/H_2O$ (v/v 4:1). ¶Reaction was performed with 1 mol % TBADT, 10 mol % $(4\text{-ClPhS})_2$, and 10 mol % $TBAH_2PO_4$ in MeCN.

9a to **12a**. A similarly contra-thermodynamic final product ratio was obtained from the reaction of *trans*-1,2-methylaminocyclohexane **14a**, which equilibrated to a 2:1 cis:trans mixture, despite a 2.1 kcal/mol calculated thermochemical bias favoring the trans isomer (see the supplementary materials). Collectively, these data support the formation of a stereochemical photostationary state distinct from the thermodynamic product ratio, although the lower-energy isomer is frequently preferentially formed.

The reaction of **14a** was also carried out under deuterium isotope exchange conditions to identify the position(s) of C–H bond scission. No D incorporation was detected adjacent to the –NHBoc group (see the supplementary materials), implicating selective epimerization of the electron-rich α-methyl C–H bond, where D incorporation was observed. Similarly, the reaction of isomethone (+)-**15a** led to the formation of (+)-menthone **15b** in 78% yield; again, no D incorporation was detected at the electronically deactivated α-carbonyl methine. The selective isomerization of electron-rich C–H bonds in the presence of electronically deactivated and/or more sterically encumbered positions also allows the isomerization of (+)-isomenthol derivatives **16a** and **17a** to react to form (+)-menthyl acetate congeners (**16b** and **17b**) without racemization. Finally, cis-fused bicyclic substrates, including decalin (**18a** and **19a**) and lactam and lactone congeners (**20a** to **22a**) reacted to form the corresponding trans-fused rings. These findings were readily translated into more complex polycyclic systems, allowing for the conversion of cis-fused AB ring of steroid (+)-**23a** to trans-fused (+)-**23b**.

We next sought to explore the strategic implications of this DT-mediated stereochemical editing method in more challenging synthetic settings. We focused our efforts on a series of retron-based strategies to explore the integration of this method into (retro)synthetic logic.

Expanding stereochemical outcomes accessible using versatile stereospecific reactions

Pericyclic reactions—such as the Diels-Alder (DA) reaction—are powerful complexity-generating transformations that have been broadly implemented in the synthesis of polysubstituted cyclic small molecule and natural product targets. Like all stereospecific reactions, the DA reaction offers fixed stereochemical outcomes

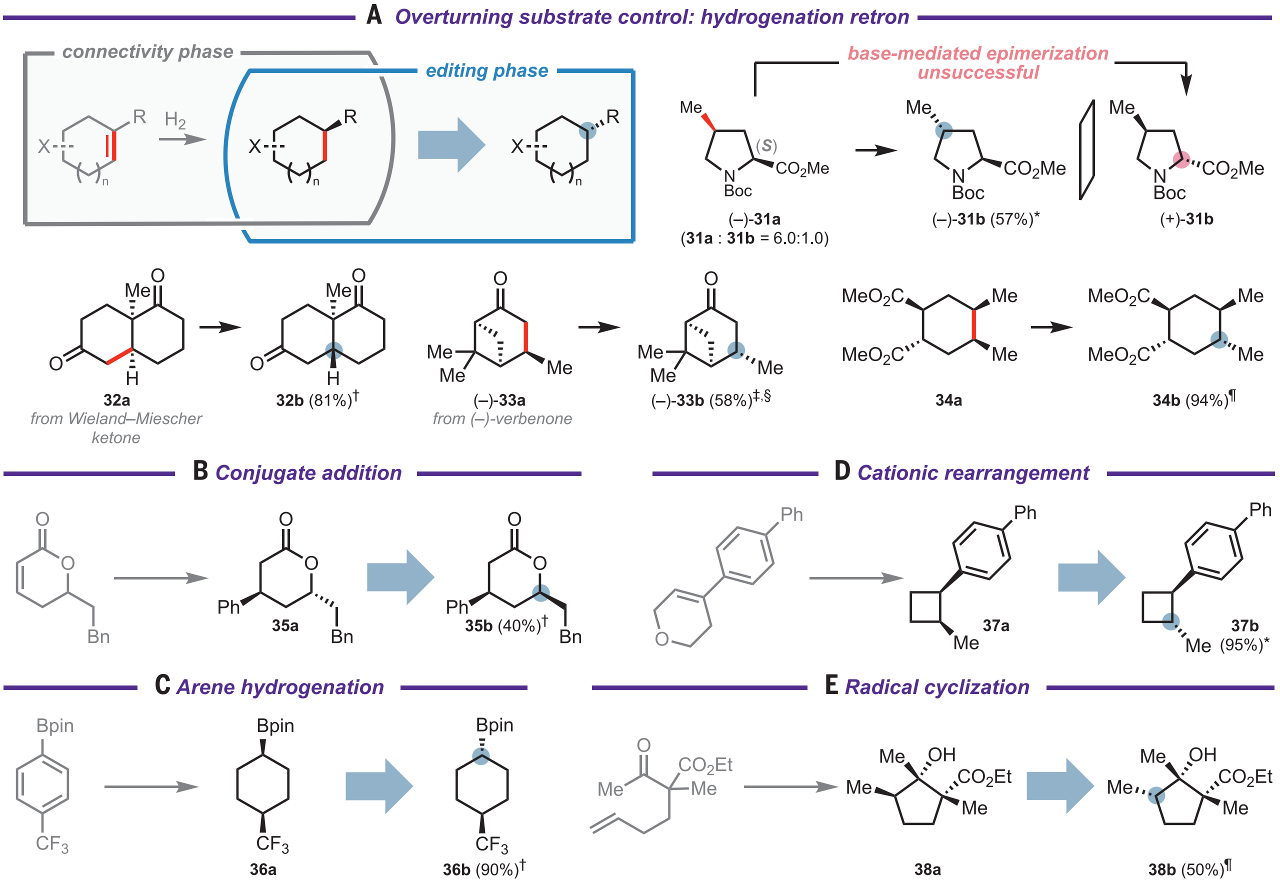

Fig. 4. Strategic application of stereocenter editing in diverse synthetic settings. (**A** to **E**) Stereoediting of hydrogenation (A), conjugate addition (B), arene hydrogenation (C), cationic rearrangement (D), and radical cyclization products (E). Reactions were performed on 0.2- to 0.5-mmol scale with 1 mol % DT with either $N(^nBu)_4^+$ counterions (TBADT) or Na^+ counterions (NaDT), 10 mol % $(4\text{-ClPhS})_2$, and 10 mol % $TBAH_2PO_4$ or $NaH_2PO_4{\bullet}H_2O$ under 390-nm LED irradiation at 23°C in MeCN (0.2 M) or $MeCN/H_2O$ (v/v 4:1 or 2:3, 0.2 M) for 24 hours. Isolated yields are the average of two runs. See the supplementary materials for full experimental details. *Reaction was performed with 1 mol % TBADT, 10 mol % $(4\text{-ClPhS})_2$, and 10 mol % $TBAH_2PO_4$ in MeCN. †Reaction was performed with 1 mol % NaDT, 10 mol % $(4\text{-ClPhS})_2$, and 10 mol % $NaH_2PO_4{\bullet}H_2O$ in MeCN. ‡Reaction was performed with 1 mol % TBADT, 10 mol % $(4\text{-ClPhS})_2$, and 10 mol % $TBAH_2PO_4$ in $MeCN/H_2O$ (v/v 2:3). §Number in parentheses denotes ^1H NMR yield with nitrobenzene as an external standard. ¶Reaction was performed with 1 mol % TBADT, 10 mol % $(4\text{-ClPhS})_2$, and 10 mol % $TBAH_2PO_4$ in $MeCN/H_2O$ (v/v 4:1).

dictated by the configuration of the starting diene and dienophile isomers. In cases where the desired product configuration is mismatched with the intrinsic reaction specificity—or where the requisite well-defined diene or dienophile isomers are challenging to access—these intrinsic features of the DA reaction restrict its implementation.

We envisioned that the combination of DA and stereoediting reactions might expand the scope of stereochemical outcomes accessible using DA logic to provide rapid access to otherwise challenging scaffolds (Fig. 3). We first examined a series of DA reactions between cyclohexenones and 1,3-butadiene derivatives, which conventionally exclusively afford products with *cis*-decalin skeletons (Fig. 3A). Efforts to construct α-substituted *trans*-decalin products through a similar DA retron have met with limited success, requiring prefunctionalized dienophiles and multiple posttransformation steps (*29*). By contrast, our stereoediting method transforms the cis-configured adducts to trans isomers in a single step. For example, bicyclic ketone **24a**, which was prepared readily from 2-methyl cyclohexanone and 1,3-butadiene, was isomerized into *trans*-decalin **24b** in 62% yield along with 14% recovered **24a** after 24 hours. (After 48 hours, no remaining **24a** was detected; however, the yield of desired **24b** was reduced slightly to 57%. See the supplementary materials.) Dione (+)-**25a**—derived from (*R*)-carvone—reacted to form (+)-**25b** in >90% yield on a 0.5-g scale. (*S*)-Perrilaldehyde–derived ketone (−)-**26a** was converted to (−)-**26b** in 81% yield along with the minor epimer (+)-**26c** in 13% yield. These examples showcase the utility of stereoediting methods in bridging DA logic to access *trans*-decalin synthons and further provide a strategy for efficient entry into a previously undisclosed array of chiral building blocks.

We next applied this logic to a different type of DA scaffold accessed using 1,4-disubstituted dienes (Fig. 3B). These cycloadditions produce two exocyclic stereogenic centers with configurations defined by the geometry of the diene component. For example, the reaction of sorbic alcohol [(2*E*,4*E*)-hexa-2,4-dien-1-ol] with methyl acrylate forms 1,4-*cis* lactone (+)-**27a** selectively. When (+)-**27a** was subjected to stereoediting conditions, methyl epimer (+)-**27b** was obtained in 65% yield. A direct DA approach to form 1,4-*trans* adducts, such as (+)-**27b**, would require the use of the corresponding (E,Z) dienes, which are generally regarded as poorer substrates for DA reaction; in this specific case, [(2*E*,4*Z*)-hexa-2,4-dien-1-ol] is also substantially less accessible than the sorbate-derived alcohol. Notably, enantioenriched (+)-**27a** was converted into (+)-**27b** without racemization, revealing that no epimerization occurred at the bicyclic juncture. DA adducts (**28a** to **30a**) that arose from various dienophiles, such as azodicarboxylate, triazoledione, and benzyne, all reacted to give the

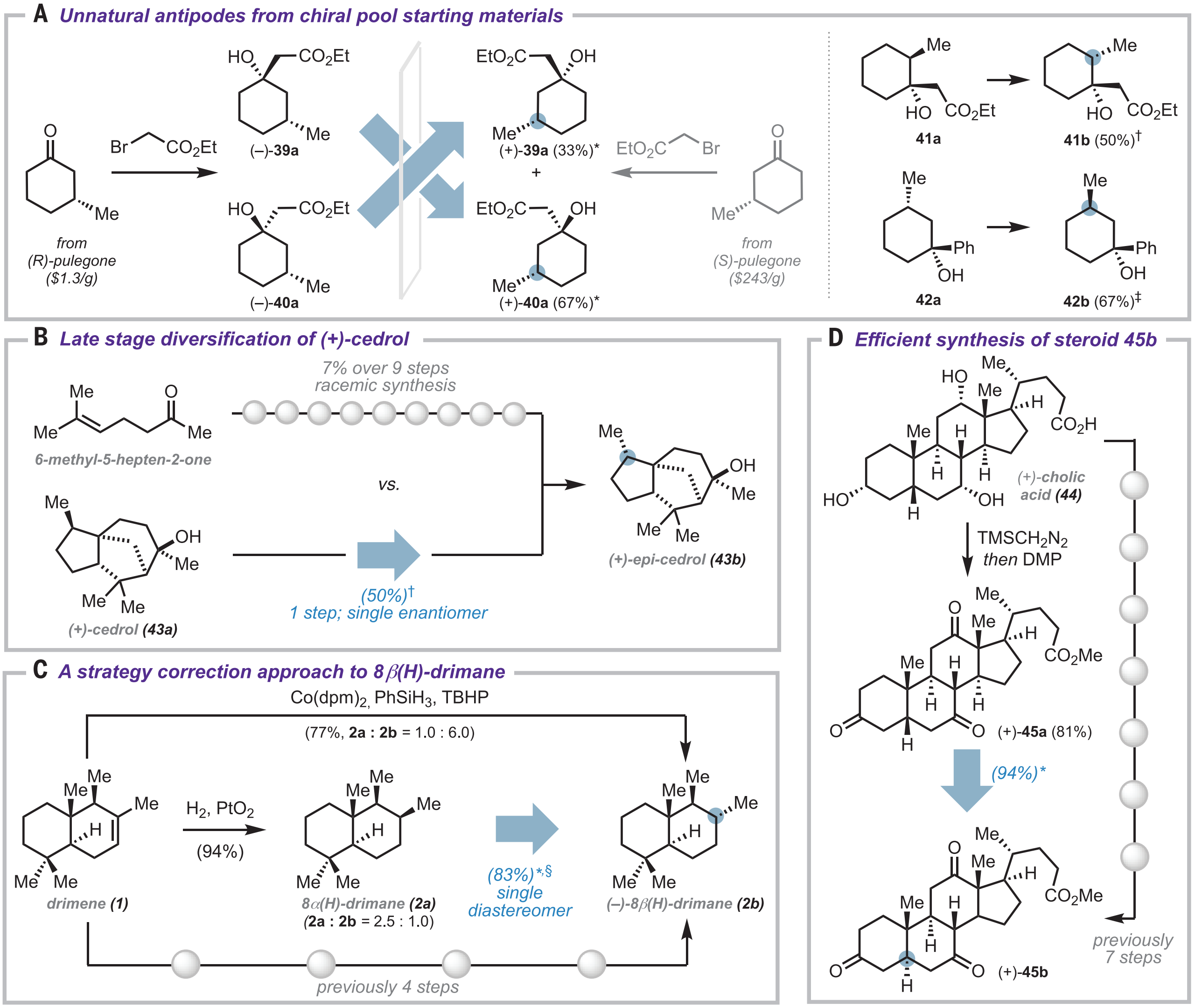

Fig. 5. Integration of stereocenter editing tools in late-stage and total synthesis applications. (**A**) Access to unnatural antipodes from chiral pool starting materials. (**B**) Semisynthetic approach to access (+)-*epi*-cedrol. (**C**) A strategy correction approach to 8β(H)-drimane. (**D**) Synthesis of steroid **45b**. Reactions were performed on 0.2- to 0.5-mmol scale with 1 mol % DT with either $N(^{n}Bu)_4^+$ counterions (TBADT) or Na^+ counterions (NaDT), 10 mol % $(4\text{-ClPhS})_2$, and 10 mol % $TBAH_2PO_4$ or $NaH_2PO_4•H_2O$ under 390-nm LED irradiation at 23°C in MeCN (0.2 M) or $MeCN/H_2O$ (v/v 4:1 or 2:3, 0.2 M) for 24 hours. Isolated yields are the average of two runs. See the supplementary materials for full experimental details. *Reaction was performed with 1 mol % NaDT, 10 mol % $(4\text{-ClPhS})_2$, and 10 mol % $NaH_2PO_4•H_2O$ in MeCN. †Reaction was performed with 1 mol % TBADT, 10 mol % $(4\text{-ClPhS})_2$, and 10 mol % $TBAH_2PO_4$ in $MeCN/H_2O$ (v/v 4:1). ‡Reaction was performed with 1 mol % TBADT, 10 mol % $(4\text{-ClPhS})_2$, and 10 mol % $TBAH_2PO_4$ in $MeCN/H_2O$ (v/v 2:3). §Reaction was performed in acetone instead of MeCN as the solvent.

corresponding epimerized products (**28b** to **30b**) in synthetically useful yields, illustrating the broad functional group compatibility of the method and the broad applicability of this approach.

Overturning substrate-controlled selectivities

The presence of an existing stereogenic center can present substantial challenges for the selective formation of additional stereocenters in a molecule. In cases strongly governed by so-called substrate control, efforts to achieve complementary stereochemical outcomes through tuning the reagent or catalyst may meet with limited success. We explored opportunities to use stereoediting to upgrade or overturn substrate-controlled selectivities, using representative examples obtained through the hydrogenation retron (Fig. 4A). For example, *cis*-methylproline (–)-**31a** is obtained selectively (6:1 **31a**:**31b**) from the corresponding precursor *exo*-methylene using a conventional hydrogenation protocol. The reaction of this mixture under epimerization conditions resulted in the isolation of *cis*-epimer (–)-**31b** in 57% yield, with no detectable erosion of enantiomeric excess (see the supplementary materials). Treatment of (–)-**31a** under base-mediated epimerization conditions would, in principle, afford (+)-**31b**; however, our efforts to promote this isomerization were unsuccessful, illustrating the difficulty of obtaining the trans isomer in this system while also showcasing the complementary chemoselectivity preferences of the DT-based conditions. Likewise, hydrogenation of Wieland-Miescher ketone and (–)-verbenone followed by epimerization afford the corresponding trans isomers **32b** and (–)-**33b** in 81 and 58% yields, respectively. Diester **34a**—obtained from syn-selective hydrogenation of the precursor alkene—also reacted under DT conditions to form trans isomer **34b** in 94% yield.

This stereoediting approach was also applied to a suite of other (retro)synthetic scenarios. A 1,4-conjugate addition forms trans-configured lactone **35a**, which reacted under epimerization conditions to form cis isomer **35b** in 40%

yield (Fig. 4B). Exhaustive reduction of 1,4-subsituted arene formed *cis*-boronate ester **36a**; reaction of this substrate under standard conditions resulted in 90% yield of trans isomer **36b** (Fig. 4C). Cationic ring contraction to form **37a** (Fig. 4D) and radical cyclization to form **38a** (Fig. 4E) both occurred with excellent levels of diastereoselectivity. In both cases, epimerization under standard conditions resulted in the formation of the more synthetically intractable trans diastereomers **37b** (90% yield) and **38b** (50% yield). The latter two examples illustrate the potential application of epimerization for the revision of stereocenters generated in reactions that proceed through highly reactive intermediates that are intrinsically challenging to control.

Tools for late-stage diversification and to expand the chiral pool

In most synthetic applications, high yields and selectivities for a single reaction product are desired. However, in some cases, access to several different isomers may be advantageous—for example, when the starting materials are abundantly available and where both products are potentially useful. Likewise, in other contexts, the formation of even small quantities of an isomer may be valuable, such as to access—and validate—a diastereomer that is extremely challenging to make so as to justify a targeted synthesis campaign.

We thus sought to explore whether a stereoediting approach could be leveraged to provide access to unnatural antipodes of a desired target starting from abundant, but incorrectly configured, chiral pool precursors. We obtained enantiopure 3-methylcyclohexanone from the naturally occurring (*R*)-pulegone through a retro-aldol reaction (Fig. 5A). A subsequent Reformatsky reaction resulted in the formation of a 1.3:1 mixture of diastereomers (−)-**39a** and (−)-**40a** as single enantiomers, respectively, which were readily separated by routine silica gel chromatography. Each diastereomer was then independently subjected to the epimerization conditions, which allowed for the isolation of another diastereomer having the opposite absolute stereochemistry [i.e., (−)-**39a** converted to (+)-**40a**, and (−)-**40a** converted to (+)-**39a**]. Overall, this strategy enables access to enantiopure diastereomers corresponding to the unnatural enantiomer of (*S*)-pulegone, which is more challenging to obtain, and illustrates the potential to use selective isomerization tools to expand the scope of chiral building blocks that can be obtained from the chiral pool. In principle, this strategy can extend to other 1,2-addition products with varying substitution patterns when commenced from enantiomerically pure starting materials (see also **41a** and **42a**).

We next examined the application of stereoediting as a late-stage diversification strategy. Cedrol is an important fragrance compound, and molecules that contain the cedrane scaffold have shown activity in diverse biological settings (*30*, *31*). Studies of structurally related C-7 cedrane epimers have not yet been reported. One factor that may have constrained advancement in this direction is the difficulty in accessing cedrane analogs: To date, the only reported synthesis of C-7-*epi*-cedrol (**43b**) was completed in a racemic form, in 7% yield over nine steps (*32*). Using stereoediting conditions, enantiopure (+)-**43b** was obtained from commercially available (+)-cedrol (**43a**) in a single step in 50% yield (Fig. 5B).

Integrating stereoediting into the logic of multistep synthesis

Finally, we sought to integrate this stereocenter editing tool within the logic of multistep organic synthesis (*33*). The efficient assembly of complex organic molecules requires the precise orchestration of connectivity- and selectivity-generating bond formation steps; unexpected selectivity outcomes encountered along the way can require the global revision or iteration of the overall synthetic design. For example, in the total synthesis of petroleum biomarker (−)-8β(H)-drimane (**2b**) by González-Sierra *et al.*, hydrogenation of drimene (**1**) with Adam's catalyst afforded the undesired isomer **2a** as the major product; a four-step workaround was devised to obtain pure (−)-**2b** (*7*). This case represents a typical dilemma encountered by synthetic chemists: Strategic innovation was required because of undesired diastereoselective outcomes. This limitation was later addressed by Iwasaki and co-workers, who developed an elegant, mechanistically distinct Co-mediated radical reduction method to provide access to the desired trans isomer (−)-**2b** (6:1 diastereomeric ratio) (*34*). In our study, the stereoediting method offers a complementary approach to resolving this situation without requiring (i) revision of the optimal route or (ii) the development of novel chemical methods to achieve the desired transformation by direct revision of the undesired chiral center. This strategy correction approach upgrades the mixture of drimane (**2a** and **2b**) resulting from the original hydrogenation directly to (−)-8β(H)-drimane (**2b**) in 83% yield with no remaining **2a** detected (Fig. 5C).

The same logic can be applied in the synthesis of allocholate derivative (+)-**45b**, which shares a common scaffold with various bioactive compounds and has found application in supramolecular systems (*35*, *36*). Starting from (+)-cholic acid (**44**), a one-pot esterification-oxidation sequence afforded trione (+)-**45a** in 81% yield. The ensuing stereoediting step converted the cis-fused AB ring junction of (+)-**45a** to trans-fused (+)-**45b** in 94% yield (Fig. 5D). Overall, this route reflects an efficient two-step synthesis of (+)-**45b** from (+)-**44**, where previously reported efforts for the same purpose have required seven steps (*37*).

The stereoediting method reported here enables the selective isomerization of completely unactivated tertiary stereocenters, providing efficient one-step access to distinct stereoisomers in diverse synthetic settings. This tool adds to a growing suite of stereoediting methods capable of independently tuning the three-dimensional structure of complex chiral molecules and unlocks a fundamentally distinct (retro)synthetic strategy. We further illustrate how stereoediting logic can be used to amplify the versatility of powerful existing transformations, streamline the synthesis of complex chiral targets, and expand access to previously undiscovered chiral pool building blocks and natural product analogs.

REFERENCES AND NOTES

1. E. L. Eliel, S. H. Wilen, *Stereochemistry of Organic Compounds* (Wiley, 1994).
2. J.-K. Jiang, M. Shen, C. J. Thomas, M. B. Boxer, *Curr. Top. Med. Chem.* **11**, 800–809 (2011).
3. P. J. Coleman *et al.*, *ChemMedChem* **7**, 415–424 (2012).
4. T. Yamamoto, H. Matsuda, Y. Utsumi, T. Hagiwara, T. Kanisawa, *Tetrahedron Lett.* **43**, 9077–9080 (2002).
5. L. M. Barton *et al.*, *J. Am. Chem. Soc.* **141**, 12531–12535 (2019).
6. G. W. Coates, *Chem. Rev.* **100**, 1223–1252 (2000).
7. M. González-Sierra, M. de los Angeles Laborde, E. A. Rúveda, *Synth. Commun.* **17**, 431–441 (1987).
8. C. Zhang *et al.*, *J. Am. Chem. Soc.* **143**, 13393–13400 (2021).
9. M. Huang, L. Zhang, T. Pan, S. Luo, *Science* **375**, 869–874 (2022).
10. Y. Wang, H. M. Carder, A. E. Wendlandt, *Nature* **578**, 403–408 (2020).
11. Y.-A. Zhang, X. Gu, A. E. Wendlandt, *J. Am. Chem. Soc.* **144**, 599–605 (2022).
12. C. J. Oswood, D. W. C. MacMillan, *J. Am. Chem. Soc.* **144**, 93–98 (2022).
13. H. M. Carder, Y. Wang, A. E. Wendlandt, *J. Am. Chem. Soc.* **144**, 11870–11877 (2022).
14. H.-S. Dang, B. P. Roberts, *Tetrahedron Lett.* **41**, 8595–8599 (2000).
15. N. Y. Shin, J. M. Ryss, X. Zhang, S. J. Miller, R. R. Knowles, *Science* **366**, 364–369 (2019).
16. J. Großkopf *et al.*, *J. Am. Chem. Soc.* **143**, 21241–21245 (2021).
17. M. M. Walker *et al.*, *J. Am. Chem. Soc.* **142**, 8194–8202 (2020).
18. A. M. Kazerouni *et al.*, *ACS Catal.* **12**, 7798–7803 (2022).
19. J. S. DeHovitz *et al.*, *Science* **369**, 1113–1118 (2020).
20. L. Saudan, J. Quintaine, "Isomerization Reactions," US Patent Application 20220041536A1 (2022).
21. R. G. Salomon, J. K. Kochi, *Tetrahedron Lett.* **14**, 4387–4390 (1973).
22. M. Gorodetsky, Y. Mazur, *J. Am. Chem. Soc.* **90**, 6540–6541 (1968).
23. Y. Wang *et al.*, *J. Am. Chem. Soc.* **140**, 9678–9684 (2018).
24. X. Zeng *et al.*, *J. Org. Chem.* **71**, 8864–8875 (2006).
25. R. L. Augustine, J. A. Caputo, *J. Am. Chem. Soc.* **86**, 2751–2752 (1964).
26. L. A. Combs-Walker, C. L. Hill, *J. Am. Chem. Soc.* **114**, 938–946 (1992).
27. J. Dong *et al.*, *Chem. Sci.* **11**, 1026–1031 (2019).
28. Y. Kuang *et al.*, *Chem. Sci.* **11**, 8912–8918 (2020).
29. J. H. Lee, Y. Zhang, S. J. Danishefsky, *J. Am. Chem. Soc.* **132**, 14330–14333 (2010).
30. K.-F. Chang *et al.*, *J. Nat. Prod.* **83**, 3021–3029 (2020).
31. Y.-M. Zhang *et al.*, *J. Agric. Food Chem.* **69**, 5332–5343 (2021).
32. E. G. Breitholle, A. G. Fallis, *J. Org. Chem.* **43**, 1964–1968 (1978).

33. J. F. Hoskin, E. J. Sorensen, *J. Am. Chem. Soc.* **144**, 14042–14046 (2022).
34. K. Iwasaki, K. K. Wan, A. Oppedisano, S. W. M. Crossley, R. A. Shenvi, *J. Am. Chem. Soc.* **136**, 1300–1303 (2014).
35. J. C. Judkins *et al.*, *Angew. Chem. Int. Ed.* **53**, 2110–2113 (2014).
36. V. Mancino *et al.*, *Org. Biomol. Chem.* **19**, 5403–5412 (2021).
37. K. M. Bhattarai *et al.*, *Chem. Commun.* **2006**, 2335–2337 (2006).

ACKNOWLEDGMENTS

The authors thank S. McMinn (Merck) for separation of cedrol epimers, X. Gu (MIT) for preliminary computational data, S. Feng (MIT) and J. L. Knippel (MIT) for supercritical fluid chromatography data collection, T. Pinto (MIT) for chiral high-performance liquid chromatography, and Z. Wickens (University of Wisconsin–Madison) for helpful discussions. **Funding:** Support for this work was provided by the National Institutes of Health (GM146248). **Author contributions:** All authors contributed to the design of the project. Y.-A.Z. and V.P. carried out the main experimental work, mechanistic studies, and data analysis. A.E.S., Y.W., and K.J.W. conducted preliminary studies. A.E.W. directed the research. A.E.W., V.P., and Y.-A.Z. drafted the manuscript, which was approved by all authors. **Competing interests:** The authors declare no competing interests. **Data and materials availability:** All data are available in the manuscript or the supplementary materials.

SUPPLEMENTARY MATERIALS

science.org/doi/10.1126/science.add6852
Materials and Methods
Figs. S1 to S44
Tables S1 to S5
NMR Spectra
References (*38*–*90*)

Submitted 30 June 2022; accepted 30 September 2022
10.1126/science.add6852

NEUROSCIENCE

Design of fast-onset antidepressant by dissociating SERT from nNOS in the DRN

Nan Sun[1,2]†, Ya-Juan Qin[3]†, Chu Xu[1,4]†, Tian Xia[1]†, Zi-Wei Du[1], Li-Ping Zheng[3], An-an Li[5], Fan Meng[1], Yu Zhang[1], Jing Zhang[1], Xiao Liu[6], Ting-You Li[3,*], Dong-Ya Zhu[1,7*], Qi-Gang Zhou[1,7,8*]

Major depressive disorder (MDD) is one of the most common mental disorders. We designed a fast-onset antidepressant that works by disrupting the interaction between the serotonin transporter (SERT) and neuronal nitric oxide synthase (nNOS) in the dorsal raphe nucleus (DRN). Chronic unpredictable mild stress (CMS) selectively increased the SERT-nNOS complex in the DRN in mice. Augmentation of SERT-nNOS interactions in the DRN caused a depression-like phenotype and accounted for the CMS-induced depressive behaviors. Disrupting the SERT-nNOS interaction produced a fast-onset antidepressant effect by enhancing serotonin signaling in forebrain circuits. We discovered a small-molecule compound, ZZL-7, that elicited an antidepressant effect 2 hours after treatment without undesirable side effects. This compound, or analogous reagents, may serve as a new, rapidly acting treatment for MDD.

Major depressive disorder (MDD) is one of the most common mental disorders (*1*). The serotonin transporter (SERT) is presently the primary target for antidepressants (*2*). However, SERT inhibitors have serious limitations: (i) they take at least 3 to 4 weeks to take effect, (ii) only a portion of patients recover after treatment, and (iii) they have extensive side effects, including suicide in some patients (*3*–*5*). Rapid elicitation of an antidepressant response by ketamine has been reported (*6*, *7*). A low dose of ketamine effectively inhibited the suicidal tendency of patients and was effective in >70% of patients with refractory depression within hours of administration (*8*, *9*). However, potential addictive properties and the risk for schizophrenia have raised concerns. Therefore, scientists are still searching for new, fast-acting antidepressant targets and compounds (*10*–*13*).

The dorsal raphe nucleus (DRN) is a main source of 5-hydroxytryptamine (5-HT) in the brain. It projects to the cortex and limbic system and plays a major role in modulating depressive mood (*14*, *15*). The effect of the 5-HT/5-HT$_{1A}$ autoreceptor (5-HT$_{1A}$R$_{\text{auto}}$) in the DRN is completely opposite to that of 5-HT/postsynaptic 5-HT$_{1A}$ heteroreceptor (5-HT$_{1A}$R$_{\text{heter}}$) in the cortex and hippocampus (HPC) (*14*, *16*, *17*). Under physiological conditions, the activation of somatodendritic 5-HT$_{1A}$R$_{\text{auto}}$ in the DRN represses neural firing of serotonergic neurons, leading to decreased 5-HT release in the cortex, HPC, and other parts of the brain (*14*). Under depressive status, somatodendritic 5-HT$_{1A}$R$_{\text{auto}}$s in the DRN are hyperactive, causing a reduced firing frequency of 5-HT neurons, a low 5-HT level in the synaptic cleft, and deactivation of postsynaptic 5-HT$_{1A}$R$_{\text{heter}}$s (*18*, *19*). SERT inhibitors activate both somatodendritic 5-HT$_{1A}$R$_{\text{auto}}$s and postsynaptic 5-HT$_{1A}$R$_{\text{heter}}$s. Desensitization of 5-HT$_{1A}$R$_{\text{auto}}$s breaks the balance between 5-HT$_{1A}$R$_{\text{auto}}$s and 5-HT$_{1A}$R$_{\text{heter}}$s within weeks after treatment and induces antidepressant effects through postsynaptic 5-HT$_{1A}$R$_{\text{heter}}$s (*14*, *20*, *21*), indicating that enhanced DRN 5-HT/5-HT$_{1A}$R$_{\text{auto}}$ signaling is the primary reason for the delayed onset of SERT inhibitors.

Neuronal nitric oxide synthase (nNOS) controls the cell surface localization of SERT through physical interaction between nNOS and SERT in the DRN (*22*). The cell surface localization of SERT determines the intercellular 5-HT concentration in the DRN and thus the function of DRN 5-HT$_{1A}$R$_{\text{auto}}$s (*2*). We hypothesized that dissociating SERT from nNOS may diminish DRN 5-HT/5-HT$_{1A}$R$_{\text{auto}}$ signaling by enhancing SERT function, thereby enhancing the firing of DRN serotonergic neurons. If this is indeed the case, then SERT-nNOS interaction blockers (SNIBs) may produce a fast-onset antidepressant effect without the drawbacks of current monoamine antidepressants.

Results

DRN SERT-nNOS coupling is implicated in the modulation of depressive behaviors

SERT interacts with nNOS through the binding of its C-tail motif to the atypical disk large/ZO-1 (PDZ) domain of nNOS in the DRN (*22*). We observed ~90% co-localization of nNOS and SERT immunoreactivities in the mouse DRN (fig. S1A). Coimmunoprecipitation and Western blot revealed that the levels of SERT, the SERT-nNOS complex, and the complex as fraction of total SERT protein in the DRN were much higher than in other depression-associated brain regions, including the HPC, prefrontal cortex (PFC), nucleus accumbens, hypothalamus, and corpus striatum, suggesting a selective enrichment of the complex as a fraction of total SERT protein in the DRN (fig. S1B). The selective enrichment of SERT-nNOS complex is possibly due to the lack of nNOS in the presynaptic part in the terminal regions of serotonergic neurons such as those in the PFC and HPC (fig. S1C). CMS is a classic model of depression in rodents. Four-week CMS exposure caused a significantly increased SERT-nNOS complex in the DRN of mice but

---

[1]State Key Laboratory of Reproductive Medicine, Department of Clinic Pharmacology, School of Pharmacy, Nanjing Medical University, Nanjing 211166, China. [2]Jiangsu Province Key Laboratory of Anesthesiology, Jiangsu Province Key Laboratory of Anesthesia and Analgesia Application, NMPA Key Laboratory for Research and Evaluation of Narcotic and Psychotropic Drugs, Xuzhou Medical University, Xuzhou 221004, China. [3]Department of Pharmacochemistry, School of Pharmacy, Nanjing Medical University, Nanjing 211166, China. [4]Institute of Dermatology, Chinese Academy of Medical Science and Peking Union Medical College, Nanjing 210042, China. [5]Jiangsu Key Laboratory of Brain Disease and Bioinformation, Research Center for Biochemistry and Molecular Biology, Xuzhou Medical University, Xu Zhou 221004, China. [6]College of Pharmacy, Nanjing University of Chinese Medicine, Nanjing 210023, China. [7]The Key Center of Gene Technology Drugs of Jiangsu Province, Nanjing Medical University, Nanjing 211166, China. [8]Department of Clinic Pharmacology, Sir runrun Hospital, Nanjing Medical University, Nanjing 211167, China.

***Corresponding author. Email: dyzhu@njmu.edu.cn (D.-Y.Z.); l_tingyou@njmu.edu.cn (T.-Y.L.); qigangzhou@njmu.edu.cn (Q.-G.Z.)**

†These authors contributed equally to this work.

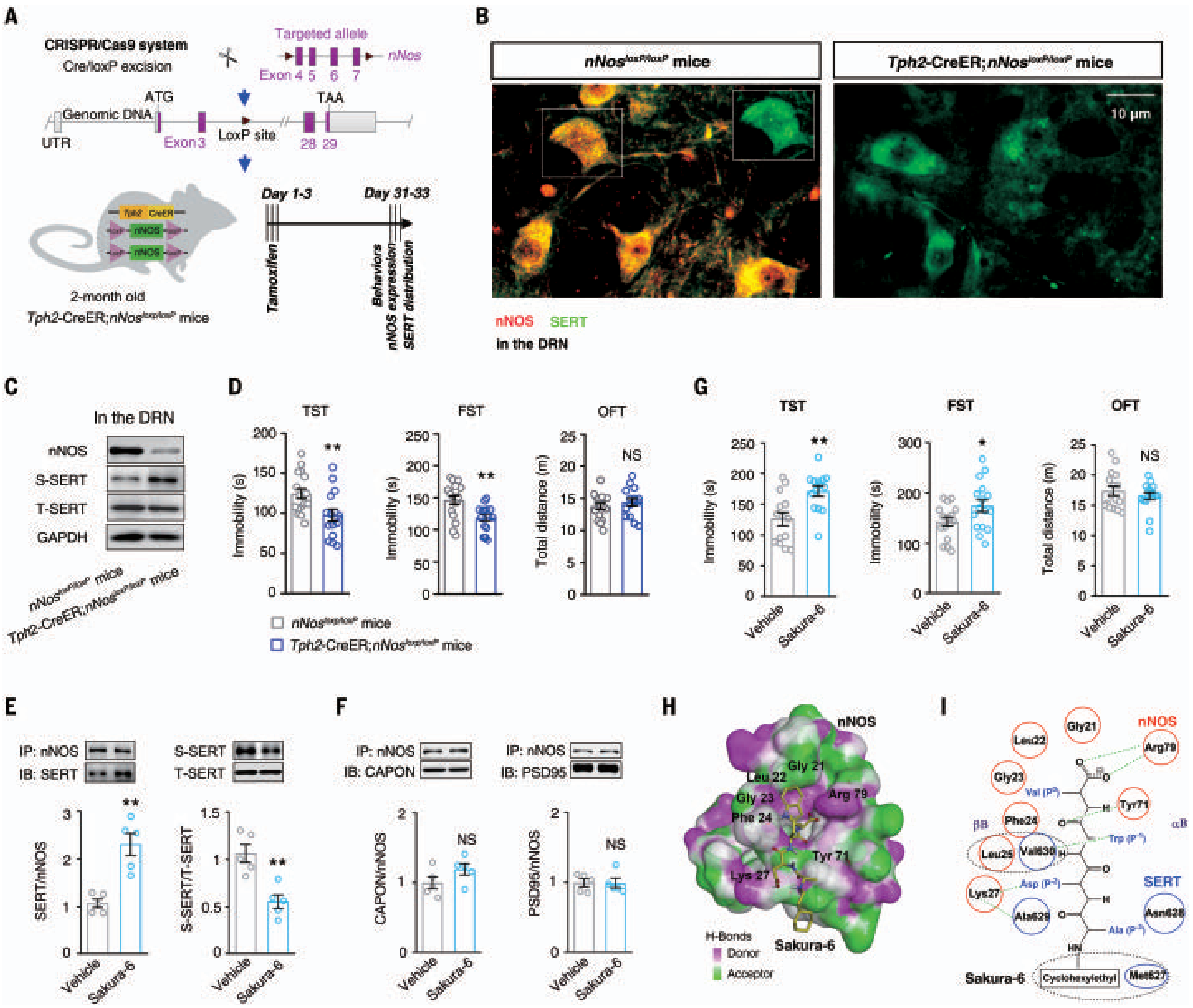

Fig. 1. Depression-like phenotype induced by promoting the level of SERT-nNOS coupling in the DRN. (**A**) Schematic of construction of *nNos*$^{\text{loxP/loxP}}$ mice using the CRISPR-Cas9 technique. (**B**) Expression level of SERT and nNOS in serotonergic neurons 1 min after conditional knockout of *nNos* as shown by immunofluorescence ($n = 5$ mice). (**C**) Expression of nNOS and SERT in the DRN after conditional deletion of nNOS in the serotonergic neurons ($n = 5$ mice). (**D**) Animal behavior in the TST, FST, and open-field test (OFT) 1 min after tamoxifen administration ($n = 15$ to 18 mice; data were analyzed with Student's t test). (**E**) SERT-nNOS coupling level and membrane expression of SERT in the DRN 2 hours after infusion of Sakura (3 μg, 200 nl) into the DRN ($n = 5$ mice; data were analyzed with Student's t test). (**F**) nNOS-CAPON and nNOS-PSD95 coupling level and membrane expression of SERT in the DRN 2 hours after infusion of Sakura (1 μg) into the DRN ($n = 5$ mice; data were analyzed with Student's t test). (**G**) Depression-related behavior change measured by the FST, TST, and OFT 2 hours after infusion of Sakura (1 μg) into the DRN ($n = 14$ to 16 mice; data were analyzed with Student's t test). (**H**) Soft hydrogen bond donor/acceptor surface of the binding pocket of nNOS PDZ with Sakura. (**I**) Proposed interactions among SERT, Sakura-6, and the nNOS PDZ domain. Val^{630}, Ala^{629}, Asn^{628}, and Met^{627} are the C-terminal tetrapeptide of SERT. Gly^{21}, Leu^{22}, Gly^{23}, Phe^{24}, Lys^{27}, Tyr^{71}, and Arg^{79} are part of nNOS PDZ domain. *$P < 0.05$; **$P < 0.01$; NS, not significant. Error bars indicate SEM. S-SERT, cell membrane surface SERT; T-SERT, total SERT of the whole cell; IB, immunoblotting; IP, immunoprecipitation; Co-IP, coimmunoprecipitation analysis; WB, Western blot analysis.

not in other brain regions (fig. S1, D and E). However, CMS did not affect mRNA and protein levels of nNOS, nitric oxide production, and protein nitrosylation in the DRN (fig. S1, F to I).

To selectively disrupt the SERT-nNOS interaction in DRN serotonergic neurons, we conditionally knocked out *nNos* in TPH2-positive neurons (Fig. 1A). In *Tph2*-CreER; *nNos*$^{\text{loxp/loxp}}$ mice, no nNOS was detected in the DRN serotonergic neurons (Fig. 1B and fig. S1J), and the nNOS level in the DRN was much lower than that in *nNos*$^{\text{loxp/loxp}}$ mice (Fig. 1C). *Tph2*-CreER;*nNos*$^{\text{loxp/loxp}}$ mice showed significantly increased SERT on the cell membrane surface in the DRN (Fig. 1C and fig. S1, K and L) and displayed antidepressant-like behaviors as shown by the tail suspension test (TST) and forced swimming test (FST) 4 weeks after tamoxifen administration (Fig. 1D). No abnormal phenotype was observed in *nNos*$^{\text{loxp/loxp}}$ mice compared with wild-type (WT) mice (fig. S1, M to P).

To further examine the role of SERT-nNOS coupling in the DRN as it relates to depression, we screened our compound library previously established on the basis of nNOS-mediated protein-protein interactions, some of which has been published previously (*23–26*). Unexpectedly, we found that two compounds of the Sakura series (fig. S2A), Sakura-6 (*N*-cyclohexylethyl-Ala-Asp-Trp-Val-OH) and Sakura-8 (*N*-cyclohexylethyl-Ala-Asp-Ala-Val-OH), significantly increased the SERT-nNOS complex but decreased the cell surface SERT level, thus working as SERT-nNOS interaction promotors (Fig. 1, E and F, and fig. S2, B and C). Microinjection of Sakura-6 into the DRN acutely (2 hours after injection) caused depression-like behaviors in mice, as indicated by enhanced immobility time in the TST and FST (Fig. 1G). This treatment did not change the total content of nNOS and SERT (fig. S2D) and had no impact on nNOS–C-terminal PDZ ligand of nNOS (CAPON) coupling and nNOS-postsynaptic density protein-95 (PSD95) coupling in the DRN (Fig. 1F). Pretreatment with intra-DRN Way-100635, a 5-HT$_{1A}$R antagonist, blocked the effect of Sakura-6 (fig. S2E), implicating the DRN 5-HT$_{1A}$R in the effect. In addition, microinjecting Sakura-6 into the medial PFC (mPFC) or the ventral HPC (vHPC), the two brain regions that receive serotonergic projections and are closely related to depression (*27*, *28*), did not induce depression-like behavior (fig. S2, F and G), and microinjection of Sakura-8 into the DRN, the other screened SERT-nNOS interaction promotor, also induced depression-like behavior (fig. S2H), further confirming an important role of DRN SERT-nNOS in the modulation of depression. Through molecular docking and chemical calculations, we speculated that Sakura may act as linker between the nNOS PDZ domain and SERT to facilitate the association of nNOS and SERT (Fig. 1, H and I).

Next, we constructed a recombinant lentiviral vector carrying full-length cDNA of nNOS with or without a mutated nucleotide critical for the catalytic activity (*29*) (LV-nNOS-GFP and LV-nNOSΔ-GFP) (fig. S3, A and B). We infused LV-nNOS-GFP, LV-nNOSΔ-GFP, or LV-GFP into the DRN of mice. Overexpression of nNOSΔ lacking catalytic activity resulted in a significantly increased SERT-nNOSΔ complex and a decreased cell surface SERT level (fig. S3, C and D), and caused depression-like behaviors, as shown by TST and FST, 28 d after virus infection (fig. S3E). However, overexpression of nNOS did not have this effect (fig. S3, F and G), possibly because of the unexpected effects of forced overproduction of nitric oxide (*22*).

Dissociating SERT from nNOS in the DRN produces a fast-onset antidepressant effect

Serotonergic neuronal activity is essential for the regulation of emotion and DRN somatodendritic 5-HT$_{1A}$R$_{auto}$s, which is crucial for the self-inhibitory mechanism of serotonergic neuronal activity (*14*, *30*). A PDZ-binding motif of nNOS, the 15 C-terminal amino acids (TPTEIPCGDIRMNAV) of SERT (SERT-15C), is sufficient for the interaction between SERT and nNOS, and the SERT-nNOS association diminishes the cell surface localization of SERT in the brain and thereby reduces 5-HT reuptake of serotonergic neurons in the DRN (*22*). On the basis of these previous results and our present data (Fig. 1), we hypothesized that emotional stress may reduce the cell surface localization of SERT by promoting a SERT-nNOS association, thereby facilitating the activation of DRN 5-HT$_{1A}$R$_{auto}$ and causing depression. Therefore, dissociating SERT from nNOS may reverse this pathological process (Fig. 2A). We synthesized a peptide named TAT-SERT-15C, in which the SERT-15C was N-terminally fused to the transduction domain of the Tat protein from the HIV type 1 (YGRKKRRQRRR) to permit its intracellular delivery. We incubated the 293T cell line transfected by the full length of cDNA encoding SERT and nNOS with Tat-SERT-15C and found that Tat-SERT-15C decreased the SERT-nNOS complex and increased SERT in the cell surface dose dependently (fig. S4A). Microinjection of Tat-SERT-15C into the DRN of mice caused a reduction in the SERT-nNOS complex as a fraction of total SERT protein, a significant increase in the SERT level in the cell surface 2 hours after the microinjection (fig. S4B), and a significant decrease in the intercellular 5-HT concentration in the DRN measured in vivo (fig. S4C), and produced an antidepressant-like effect (fig. S4D). Moreover, the treatment did not change nNOS-PSD95 and nNOS-CAPON complex levels in the DRN (fig. S4E). Microinjection of a modified peptide with 15 random amino acids (KKADNHSMGAYAGHK) fused to Tat (Tat-Control-15A), which is not capable of disrupting the SERT-nNOS interaction, into the DRN did not cause a depression-like behavior change (fig. S4F). Additionally, microinjecting Tat-SERT-15C into the DRN of *nNos*$^{-/-}$ mice did not affect depression-related behaviors (fig. S4G).

Next, we microinjected Tat-SERT-15C, fluoxetine, or vehicle into the DRN of mice at 29 d after CMS exposure for 28 d (28d-CMS). We measured SERT expression, SERT-nNOS complex and intercellular 5-HT in the DRN, and depression behaviors using the TST, FST, and sucrose preference test 2 hours after microinjection. CMS significantly increased the intercellular 5-HT concentration (Fig. 2B) and SERT-nNOS complex and decreased the cell surface SERT level in the DRN (Fig. 2C). Tat-SERT-15C reversed the CMS-induced changes (Fig. 2, B and C). However, fluoxetine, a classical SERT inhibitor, amplified the CMS-induced elevation in intercellular 5-HT in the DRN (Fig. 2B). CMS-caused depression behaviors were reversed by Tat-SERT-15C acutely (Fig. 2D). Systematic treatment of Tat-SERT-15C in mice subjected to 28d-CMS produced similar effects (fig. S4, H and I). Moreover, we microinjected 8-OH-DPAT, a selective agonist of 5-HT$_{1A}$R, into the DRN through a previously implanted cannula and then administered mice with Tat-SERT-15C intraperitoneally. Behavior tests 2 hours after treatment showed that 8-OH-DPAT significantly blocked the induction of antidepressant-like behaviors by Tat-SERT-15C (Fig. 2E). Moreover, activating DRN somatodendritic 5-HT$_{1A}$R$_{auto}$s by 8-OH-DPAT or deactivating 5-HT$_{1A}$R$_{auto}$s by Way-100635 was sufficient to induce a depression-like or an antidepressant-like effect (Fig. 2, F and G). Together, these data suggest that the SERT-nNOS interaction modulates depression through DRN somatodendritic 5-HT$_{1A}$R$_{auto}$s (Fig. 2A).

Activating the serotonergic circuit is crucial for the action of SERT-nNOS in the DRN

The activity of DRN serotonergic neurons is regulated by negative feedback from intercellular 5-HT acting through somatodendritic 5-HT$_{1A}$R$_{auto}$s (*16*, *31*). We thus investigated whether the fast-onset antidepressant effect of Tat-SERT-15C was due to the enhancement of firing activity of DRN serotonergic neurons (Fig. 3A). To test this, we optogenetically stimulated DRN neurons and recorded neural firing 28 d after AAV infection (Fig. 3, B and C). Tat-SERT-15C was given 2 hours before in vivo electrophysiology recording (Fig. 3B). Tat-SERT-15C increased the neural firing rate of serotonergic neurons significantly compared with vehicle (Fig. 3C). To determine whether the enhanced firing activity of serotonergic neurons is necessary for the effect of Tat-SERT-15C on behaviors, we silenced DRN neurons expressing SERT in the presence of the designer receptors exclusively activated by designer drugs (DREADDs) agonist clozepine-*N*-oxide (CNO) (Fig. 3D). Four weeks after AAV infection, we injected Tat-SERT-15C or vehicle with or without CNO to these mice 2 hours before performing behavioral tests. Although the mice treated with Tat-SERT-15C without CNO displayed marked antidepressant-like behaviors, the mice treated with Tat-SERT-15C plus CNO did not (Fig. 3E). Moreover, these treatments did not affect locomotor activity of mice in the open-field test (Fig. 3E).

Terminal serotonin release into the mPFC and vHPC is strictly controlled by firing activity of serotonergic neurons in the DRN, and the firing activity is negatively regulated by DRN 5-HT$_{1A}$R$_{auto}$s (*14*). We thus hypothesized that the CMS-induced increase in intercellular 5-HT in the DRN (Fig. 2B) may activate 5-HT$_{1A}$R$_{auto}$s and weaken the activity of serotonergic neurons, resulting in reduced 5-HT release into the mPFC and vHPC. If this is the case, then dissociating SERT-nNOS may

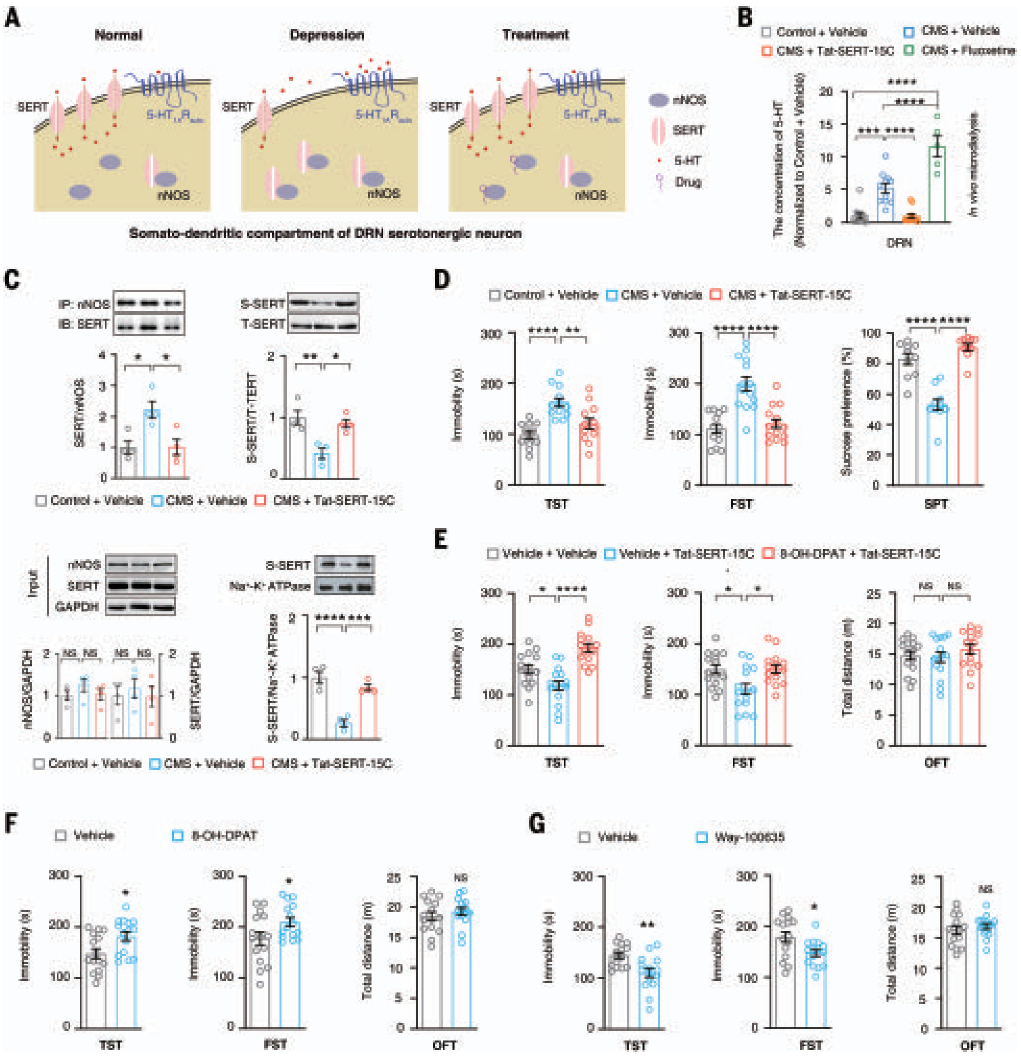

Fig. 2. Dissociating SERT from nNOS in the DRN reverses CMS-induced depressive behaviors. (**A**) Sketch describing our hypothesis: chronic stressors reduce the cell surface translocation of SERT by promoting a SERT-nNOS association, thereby increasing intercellular 5-HT concentration, facilitating the activation of DRN somatodendritic $5\text{-HT}_{1A}R_{auto}$s, and causing depression. Dissociating SERT from nNOS may reverse this pathological process. (**B**) Microinjection of Tat-SERT-15C (1.6 μg) but not fluoxetine (2 μg) into the DRN reversed CMS-induced elevated intercellular 5-HT in the DRN at 2 hours as measured by in vivo microdialysis (n = 5 to 13 mice; data were analyzed with one-way ANOVA). (**C**) Microinjection of Tat-SERT-15C (1.6 μg) into the DRN reversed 28d-CMS–induced SERT-nNOS overcoupling and reduced translocation on the cellular membrane in the DRN at 2 hours. The expression of nNOS and SERT in the DRN were not affected (n = 4 mice; data were analyzed by one-way ANOVA). (**D**) Microinjection of Tat-SERT-15C (1.6 μg) into the DRN rescued depressive behaviors of CMS-exposed mice in TST, FST, and sucrose preference test at 2 hours. n = 10 to 14 mice; data were analyzed by one-way ANOVA). (**E**) Microinjecting 8-OH-DPAT (1 μg) into the DRN through a previously implanted cannula, followed by Tat-SERT-15C treatment (5 mg/kg, intraperitoneally) at 5 min. TST, FST, and OFT were performed 2 hours later (n = 15 mice; data were analyzed by one-way ANOVA). (**F**) TST, FST, and OFT 2 hours after microinjecting 8-OH-DPAT (1 μg) or vehicle into the DRN (n = 15 mice; data were analyzed by Student's t test). (**G**) TST, FST, and OFT 2 hours after microinjecting Way-100635 (3 μg) or vehicle into the DRN (n = 15 mice; data were analyzed using Student's t test). $^*P < 0.05$; $^{**}P < 0.01$; $^{***}P < 0.001$; $^{****}P < 0.0001$; NS, not significant. Error bars indicate SEM.

reverse the CMS-induced changes (Fig. 3A). We therefore measured concentrations of 5-HT in the DRN, mPFC, and vHPC 24 hours after microinjection of Tat-SERT-15C and fluoxetine into the DRN. Tat-SERT-15C decreased intercellular 5-HT in the DRN and increased intercellular 5-HT in the mPFC and vHPC significantly, whereas fluoxetine had the completely opposite effect (fig. S5, A and B). Although chronic administration of fluoxetine has antidepressant activity, acute microinjection of fluoxetine into the DRN induced depressive-like behavior (fig. S5C). Neither treatment affected intercellular NA and DA concentrations in any of the regions (fig. S5D). 28d-CMS exposure caused significantly reduced intercellular 5-HT in the mPFC and vHPC. Microinjecting Tat-SERT-15C, but not fluoxetine, into the DRN reversed the CMS-induced decrease in intercellular 5-HT in the mPFC and vHPC 2 hours after treatment (Fig. 3F).

Next, we microinjected AAV9-DIO-hM4Di-GFP virus into the DRN of SERT-Cre mice and implanted a cannula in the mPFC or vHPC. Four weeks later, we treated the mice with Tat-SERT-15C intraperitoneally and infused CNO into the mPFC or vHPC through a cannula 2 hours before the behavioral tests (Fig. 3G). GFP-labeled projection fibers observation showed DRN-mPFC ($\text{5-HT}^{\text{DRN-mPFC}}$) and DRN-vHPC ($\text{5-HT}^{\text{DRN-vHPC}}$) serotonergic circuits (Fig. 3H). Silencing the $\text{5-HT}^{\text{DRN-mPFC}}$ circuit by CNO abolished the antidepressant-like effect of Tat-SERT-15C, but silencing the $\text{5-HT}^{\text{DRN-vHPC}}$ circuit did not (Fig. 3I). Microinjection of either CNO or Tat-SERT-15C into the mPFC of WT

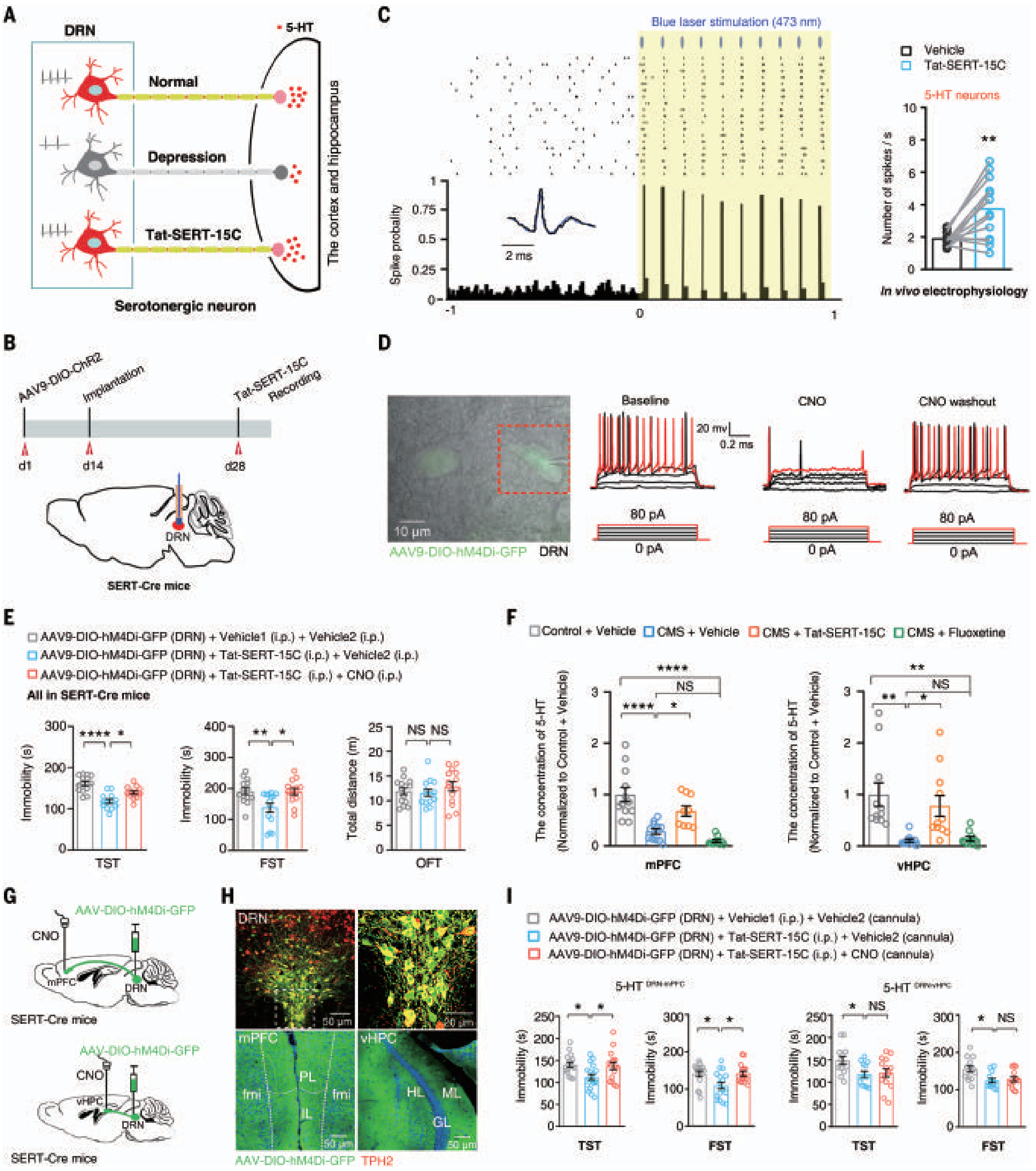

Fig. 3. Circuit mechanism mediates the antidepressant effect produced by dissociating SERT-nNOS. (**A**) Diagrammatic sketch of our hypothesis. (**B**) A volume of 0.5 μl of AAV9-DIO-ChR2 was microinjected into the DRN of 2-month-old SERT-Cre mice, followed by implantation of a photogenetic lens and an in vivo electrophysiological recording electrode 14 d later. Two weeks later, Tat-SERT-15C (5 mg/kg, intraperitoneally) was administered 2 hours before recording. (**C**) The recording of neural firing of serotonergic neurons was validated by blue laser (473 nm) stimulation (n = 14 neurons from n = 3 mice; data were analyzed by paired Student's t test). (**D**) A volume of 0.5 μl of AAV9-DIO-hM4Di-GFP was microinjected into the DRN of 2-month-old SERT-Cre mice. One month later, mice were treated with Tat-SERT-15C (5 mg/kg, intraperitoneally) or vehicle1 (saline) with or without CNO (5 mg/kg, intraperitoneally) or vehicle2. Brain slices were prepared 2 hours after treatment for in vitro electrophysiology recording. Data are representative of 10 individual neurons. (**E**) Mice behavior in the TST, FST, and OFT 2 h after treatments (n = 13 to 14 mice; data were analyzed by one-way ANOVA). (**F**) Microinjection of Tat-SERT-15C (1.6 μg) but not fluoxetine (2 μg) reversed the CMS-induced decrease of intercellular 5-HT in the mPFC and vHPC at 2 hours, as measured by in vivo microdialysis (n = 9 to 12 mice; data were analyzed by one-way ANOVA). (**G**) Design of the selective deactivation of the 5-HT$^{\text{DRN-mPFC}}$ or 5-HT$^{\text{DRN-vHPC}}$

circuit. (**H**) Infection status 1 min after injection of AAV9-DIO-hM4Di-GFP into the DRN of SERT-Cre mice. Note the projected GFP^{+} serotonergic fibers in the mPFC and vHPC (n = 5 mice). (**I**) Behavior in the TST and FST 2 hours after CNO (2 μg) infusion into the mPFC or vHPC through a previously implanted cannula in SERT-Cre mice (n = 13 to 18 mice; data were analyzed by one-way ANOVA). $*P < 0.05$; $**P < 0.01$; $***P < 0.001$; $****P < 0.0001$; NS, not significant. Error bars indicate SEM. PL/IL, prelimbic/infralimbic area of the mPFC; fmi, forceps minor of the corpus callosum; HL, hilus; ML, molecular layer; GL, granule layer.

mice did not induce a depression-associated behavior change at 2 hours (fig. S5C). Additionally, neither ketamine nor fluoxetine treatment altered SERT-nNOS coupling in the DRN (fig. S6, A and B). RNA-sequencing data showed that microinjection of Tat-SERT-15C into the DRN and intraperitoneal injection of ketamine or fluoxetine affected different profiles of gene expression in the mPFC (fig. S6, C and D), suggesting that they have different underlying mechanisms.

Small-molecule fast-onset antidepressant drug designed by dissociating SERT from nNOS

To find small molecules that selectively dissociate SERT from nNOS, we analyzed the chemical mechanism of binding the C-tail of SERT to the PDZ of nNOS in the DRN and, based on this, designed a common chemical structure (Fig. 4A). Using cultured 293T cells transfected with plasmids encoding nNOS and SERT, we detected the effects of a series of compounds on the SERT-nNOS interaction (fig. S7). The quantitative structure-activity relationship indicated that the chemical structure of Ac-Ala-Val-OH, tightly bound into the groove between the αB helix and βB folding of the nNOS PDZ domain and the L configuration of Val, was crucial for blocking SERT-nNOS. Steric hindrance caused by large groups on the ester may be disadvantageous for binding into nNOS PDZ domain, and the chirality of Ala did not affect the binding activity (Fig. 4, B and C, and fig. S7A). Of these compounds, ZZL-7 had advantageous structural characteristics: The acetylated amino of Ala of ZZL-7 formed an H-bond with Phe^{24} of nNOS with a 2.11-Å bond distance; the carbonyl of Val of ZZL-7 made two H-bonds with the guanidino of Arg^{79} of nNOS with 1.96-Å, 2.18-Å, respectively; and there was a hydrophobic interaction between the methyl of acetyl and the benzene ring of Phe^{24} of nNOS (Fig. 4, A to C, and fig. S7B).

Incubation of the cultured 293T cells transfected with nNOS and SERT with ZZL-7 for 2 h significantly decreased the SERT-nNOS complex level (Fig. 4D). In vivo electrophysiology in SERT-Cre mice showed that ZZL-7 caused significantly increased firing frequency of serotonergic neurons 2 hours after treatment (Fig. 4E). In WT mice, ZZL-7 reduced immobility time as shown by TST and FST 2 hours after systematic administration, suggesting a fast antidepressant-like effect. In *nNos*$^{-/-}$ mice, however, the treatment did not affect immobility time in the TST and FST (fig. S7C). Treatment with ZZL-7 caused a significantly decreased SERT-nNOS complex level and an increased cell surface SERT level in the DRN in WT but not in *nNos*$^{-/-}$ mice (fig. S7D). Intragastric administration of ZZL-7 produced antidepressant-like behaviors dose dependently 2 hours after treatment (Fig. 4F). To investigate whether ZZL-7 could elicit a fast-onset antidepressant effect in depressed mice, we injected ZZL-7 intravenously to 28d-CMS–experienced mice. As expected, ZZL-7 reversed the CMS-induced increase in the SERT-nNOS complex in the DRN (Fig. 4G) and reversed CMS-induced depressions behaviors 2 hours after treatment (Fig. 4H). The fast-onset antidepressant effect persisted at least for 24 hours (fig. S8A). At 30 min after administration of ZZL-7, ZZL-7 was detected in the DRN tissue, indicating that it crossed the blood–brain barrier readily (fig. S8B). We incubated 293T cells with ZZL-7 and washed out the culture medium 30, 60, 90, and 120 min later. Liquid chromatography–mass spectrometry analysis of compound composition in the cytoplasm demonstrated that ZZL-7 also penetrated the cellular membrane (fig. S8, C and D).

ZZL-7 had no effect on general activity or locomotor activity, memory, or cognition (fig. S9, A to F) and did not induce aggressive behavior, addiction, or abnormal brain waves (fig. S9, G to I). Our results suggest that ZZL-7 should be developed as a new, fast-onset antidepressant candidate. All of the uncropped Western blots are shown in fig. S10.

Discussion

Significantly increased 5-HT concentration, somatodendritic 5-HT$_{1A}$R$_{\text{auto}}$ level, and 5-HT$_{1A}$R$_{\text{auto}}$ binding rate in the DRN are related to MDD and suicide attempts (*19*). Suppression of 5-HT$_{1A}$R$_{\text{auto}}$s evokes strong and rapid antidepressant-like effects (*21*). Rapid DRN 5-HT$_{1A}$R$_{\text{auto}}$ desensitization or knockdown can accelerate the onset of the therapeutic effects of antidepressants (*32*, *33*). Therefore, selectively blocking DRN 5-HT$_{1A}$R$_{\text{auto}}$s could be a strategy for discovering fast-onset antidepressants. However, how to selectively manipulate DRN 5-HT$_{1A}$R$_{\text{auto}}$s without affecting postsynaptic 5-HT$_{1A}$R$_{\text{heter}}$s remains unresolved. If intercellular 5-HT in the DRN could be selectively reduced, then DRN 5-HT$_{1A}$R$_{\text{auto}}$ function could be selectively suppressed. We discovered that dissociating SERT from nNOS specifically reduces intercellular 5-HT concentration in the DRN by facilitating the cell surface translocation of SERT, enhances DRN serotonergic neurons activity, and substantially promotes 5-HT release into the mPFC, thereby producing a fast-onset antidepressant effect. Further, the small molecule SNIB ZZL-7 that we designed had a fast-onset antidepressant effect in our mouse depression model.

Current antidepressants such as fluoxetine, which work as selective serotonin reuptake inhibitors (SSRIs), have no selectivity in inhibiting somatodendritic SERT in the DRN or presynaptic SERT in nerve terminals. They also have no preference in enhancing the functions of DRN 5-HT$_{1A}$R$_{\text{auto}}$s and postsynaptic 5-HT$_{1A}$R$_{\text{heter}}$s in the cortex and HPC (*34*). Because of the enhancement of DRN 5-HT$_{1A}$R$_{\text{auto}}$ function caused by inhibiting somatodendritic SERT, SSRIs suppress neural firing and 5-HT release of serotonergic neurons (*16*, *35*). The effects of SSRIs depend on the desensitization of DRN 5-HT$_{1A}$R$_{\text{auto}}$s (*16*, *21*, *36*). The desensitization of 5-HT$_{1A}$R$_{\text{auto}}$s explains the drawbacks of SSRIs, including third delayed onset, unstable effectiveness, individual differences, and even aggravating symptoms (*19*, *33*, *34*). By contrast, SNIBs work by reducing intercellular 5-HT and thereby deactivating DRN 5-HT$_{1A}$R$_{\text{auto}}$s without the requirement for desensitization, thus potentially avoiding the deficits of SSRIs.

The concentration of intercellular 5-HT in the DRN is critically regulated by SERT on the cell surface. SERT is a natural ligand of the nNOS PDZ domain and can bind to the pocket constituted by the αB helix and βB fold of this domain through its C-terminal peptides (*22*). The binding site on the nNOS PDZ domain is a shallow and long groove containing the binding pocket of the conserved sequence GLGF (Gly^{21}, Leu^{22}, Gly^{23}, Phe^{24}) (*37*). The C-terminal residue of SERT also binds transport molecules Sec23A and Sec24C, two subunits of coat complex II, which is critical for the trafficking of SERT to the plasma membrane, and nNOS may compete with Sec23-Sec24 for binding to the SERT C terminus (*22*). Therefore, the fast-onset antidepressant effect of SNIBs may be explained by the fact that the dissociation of SERT-nNOS facilitates Sec23-Sec24–mediated trafficking of SERT to the cell surface, thereby reducing intercellular 5-HT and in turn downregulating 5-HT$_{1A}$R$_{\text{auto}}$ activity.

The limitations of ketamine, including neurotoxicity, cognitive dysfunction, abnormal mental status, and psychotomimetic effects, have been reported (*38*). Although ketamine is a noncompetitive antagonist of the *N*-methyl-D-aspartate receptor, it also binds on many other receptors, with potentially extensive pharmacological effects and side effects (*39*). Our data showed that ketamine had no effect

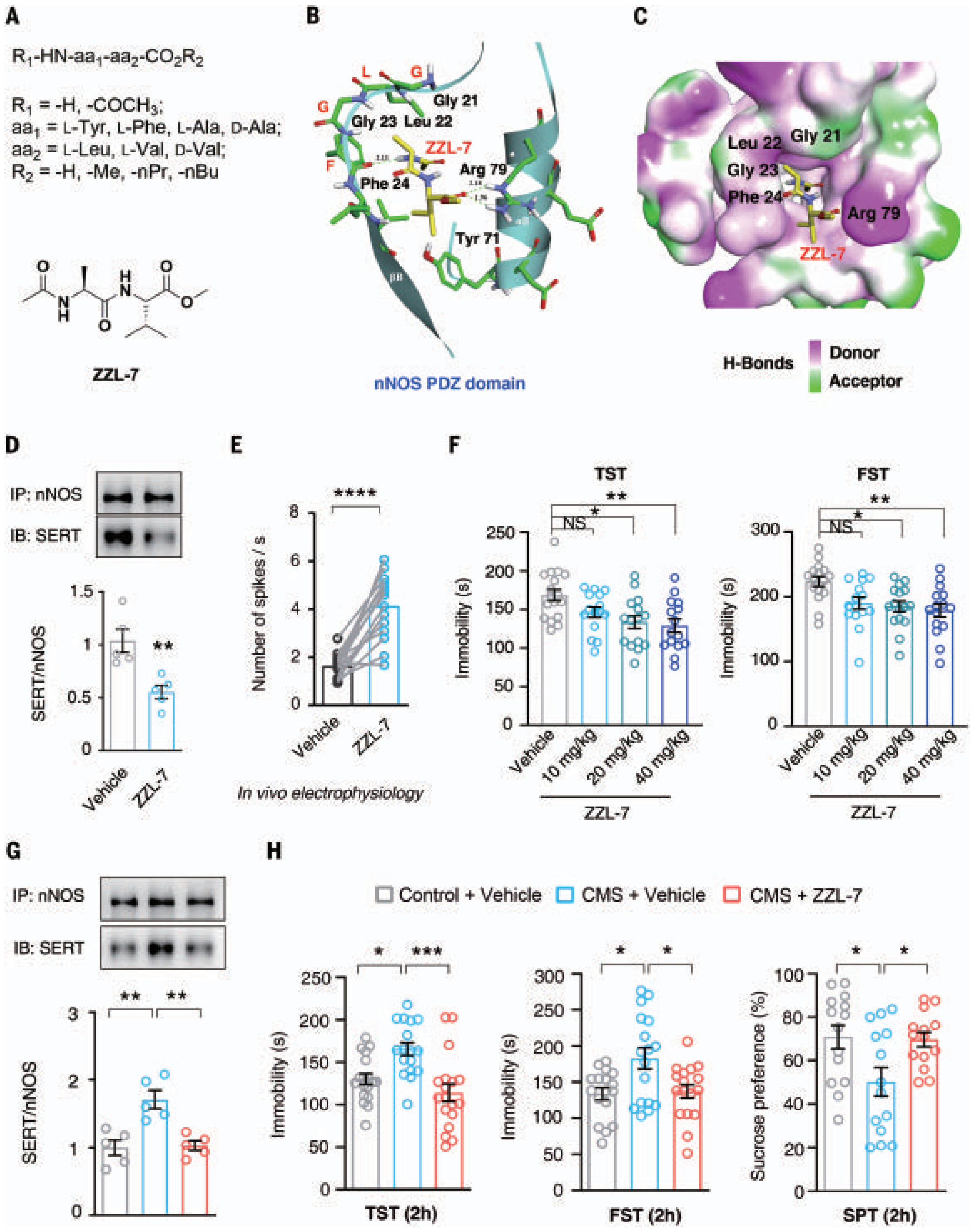

Fig. 4. Development of a small-molecule drug eliciting rapid-onset antidepressant effect. (**A**) Top: general structure with potential bioactivity to uncouple nNOS and SERT. Bottom: structure of ZZL-7. (**B** and **C**) ZZL-7 (Ac-Ala-Val-OCH_3) was tightly bound into the groove between the αB helix and βB folding of the nNOS PDZ domain. In the ZZL-7-nNOS PDZ domain complex, there was a hydrogen bonding interaction between the ZZL-7 and GLGF loop (Gly^{21}-Leu^{22}-Gly^{23}-Phe^{24}) of the nNOS PDZ domain. The acetylated amino of Ala (ZZL-7) formed a H-bond with Phe^{24}; the H-bond distance was 2.11 Å. The –carbonyl of Val made two H-bonds with the guanidino of Arg^{79} and H-bond distances were 1.96 Å, 2.41 Å. (**D**) Co-IP showing SERT-nNOS complex levels in 293T cells incubated with 1.0 μM ZZL-7 for 2 hours (*n* = 5 mice; data were analyzed by Student's *t* test). (**E**) Enhanced firing frequency of serotonergic neurons 2 hours after ZZL-7 administration (10 mg/kg, intraperitoneally) in SERT-Cre mice detected by in vivo electrophysiology (*n* = 15 neurons measured from *n* = 3 individual mice; data were analyzed by paired Student's *t* test). (**F**) Mouse behavior in the TST and FST 2 hours after intragastric administration of ZZL-7 (10, 20, and 40 mg/kg). (**G**) SERT-nNOS complex level in the DRN of 28d-CMS–exposed or control mice 2 hours after intraperitoneal administration of ZZL-7 (10 mg/kg) (*n* = 5 mice; data were analyzed by one-way ANOVA). (**H**) TST, FST, and sucrose preference test in 28d-CMS–exposed or control mice 2 hours after intraperitoneal administration of ZZL-7 (10 mg/kg) (*n* = 14 to 18 mice; data were analyzed by one-way ANOVA). $^*P < 0.05$; $^{**}P < 0.01$; $^{***}P < 0.001$; NS, not significant. Error bars indicate SEM.

on SERT-nNOS association, and the gene expression profile was differently regulated by ketamine and SNIB. Therefore, SNIBs may produce a fast-onset antidepressant effect without the drawbacks of ketamine.

The mPFC is closely related to rapid antidepressant responses (*40*–*43*). The activity of mPFC is significantly elevated during periods of struggling in depression-related behavior tests including TST and FST (*44*). Ketamine acutely increases the activity of mPFC pyramidal neurons (*45*). Neuronal vascular endothelial growth factor (VEGF) and mammalian target of rapamycin (mTOR) signaling in the mFPC are the mediators of ketamine's rapid antidepressant effects (*46*, *47*). Intra-mPFC infusion of 8-OH-DPAT induces rapid and long-lasting antidepressant-like effects (*48*). We found that the activity of the 5-HT$^{\text{DRN-mPFC}}$ circuit contributes to the fast-onset antidepressant effect of SNIBs. Consistent with previous reports (*49*, *50*), our data suggest that the 5-HT$^{\text{DRN-vHPC}}$ circuit may be implicated in the chronic antidepressant effect of SNIBs.

The level of SERT as part of the SERT-nNOS complex and the fraction of total SERT protein in the DRN are much higher than in other depression-associated brain regions. The selective existence and formation of SERT-nNOS are possibly due to the predominant and intensive expression of SERT in the DRN and the selective postsynaptic location of nNOS in the synaptic terminal regions of serotonergic neurons (*51*, *52*). In these regions, presynaptic membrane SERT is the target of SSRIs, and no nNOS is found (*51–53*). Although a few SERT-nNOS complexes are detected in the fibers of serotonergic neurons, such as those in the mPFC, the interaction is predominantly located in the cell body (*54*, *55*), and our results suggest that the SERT-nNOS complex in the mPFC is not implicated in depression. Moreover, there was no evidence for the existence of SERT-nNOS complexes outside of the brain, such as in the gut, platelets, and the immune system. Therefore, SNIBs may selectively target the DRN, thus avoiding undesirable pharmacological effects.

Furthermore, although a large number of protein-protein interaction inhibitors have been reported, compounds that promote protein-protein interactions are rare. We found here that Sakura can promote the SERT-nNOS association. We deduce that Sakura may act as a linker of the nNOS PDZ domain and SERT and thereby facilitate the SERT-nNOS interaction, because it not only forms several H-bonds with Lys^{27}, Tyr^{71}, and Arg^{79} on the nNOS PDZ domain, but also binds to SERT through H-bond and hydrophobic interactions. For example, there is a hydrophobic interaction between the side chain of Met^{627} in SERT and the cyclohexylethyl of Sakura, the carbonyl of Ala^{629} in SERT forms an H-bond with Lys^{27} of nNOS PDZ, the side chain of Val^{630} in SERT has a hydrophobic interaction with Leu^{25} of the nNOS PDZ, and the carboxyl of Val^{630} in SERT can form an H-bond with indole of Trp on Sakura.

In sum, we show here that dissociating SERT-nNOS can rapidly reverse the depressive behaviors caused by CMS in mice, opening a new avenue for developing therapeutics for mood disorders, which should now be tested in humans.

Methods summary

Mice

Male C57BL/6J (8 to 12 weeks old, 20 to 25 g, stock no. 000664), *Tph2*-CreER (stock no. 016584), *nNos*$^{-/-}$ (stock no. 002986), and SERT-Cre (stock no. 014554) mice were purchased from the Jackson Laboratory (Bar Harbor, ME, USA) and maintained at the Model Animal Research Center of Nanjing Medical University (Nanjing, China). The *nNos*$^{\text{flox/flox}}$ mice (C57BL/6J background), exons 4 to 7 with loxP recombination sites, were generated by CRISPR genome editing technology (CRISPR-Cas9 system) and maintained at the Model Animal Research Center of Nanjing University (Nanjing, China). Conditional knockout of *nNos* in serotonergic neurons (*nNos* CKO) was established by crossing *Tph2*-CreER mice with *nNos*$^{\text{flox/flox}}$ mice to generate *Tph2*-CreER; *nNos*$^{\text{flox/flox}}$ mice, treated with tamoxifen (150 mg/kg subcutaneously for 3 days) when mice were 2 months old. Behavior tests and immunofluorescence were performed 1 month later. Every effort was made to minimize pain and suffering, and we reduced the number of animals used in the experiments. Mice were housed five per cage under standard laboratory conditions (22 ± 1°C, 60% humidity, 12 h light-dark cycle with lights on at 7:00 a.m., food and water ad libitum) for 1 week before starting experiments. All procedures concerning animal care and treatment were performed in accordance with the protocols approved by the ethical committee of Nanjing Medical University (protocol no. IACUC-1704010-1).

Drugs and polypeptides

ZZL molecules and Sakura were designed and synthesized by the Ting-You Li laboratory at the Department of Pharmacochemistry, Nanjing Medical University (Nanjing, China). CNO, Way-100635, and 8-OH-DPAT were purchased from Sigma-Aldrich (St. Louis, MO, USA) and introperitoneally injected (10 mg/kg) or locally microinjected into the mPFC or vHPC to activate hM4Di DREADD receptors. Dimethyl sulfoxide (0.5%) in saline was used as a vehicle (referred to as "vehicle2" in Fig. 3) (*56*). To selectively knock out the *nNos* gene in serotonergic neurons in *Tph2*-CreER;*nNos*$^{\text{flox/flox}}$ mice, tamoxifen (150 mg/kg, intraperitoneally, dissolved in a 1:10 mixture of ethanol and sunflower oil, Sigma-Aldrich) was administered daily for 3 days when the mice were 2 months old (*56*). Fluoxetine and (2R,6R)-hydroxynorketamine hydrochloride were purchased from Sigma-Aldrich and Jiangsu Pharmaceutical Co., Ltd. (Jiangsu, China), dissolved in saline, and administered as approved by the Food and Drug Administration of Jiangsu Province (2018). A cannula was implanted into the DRN, mPFC, or vHPC and used for microinjection of drugs or peptides 3 d later. During microinjection, mice were anesthetized temporarily for 5 min by isoflurane (induction 3%, 0.8 liters/min O_2; maintenance 1 to 1.5%, 0.5 liters/min O_2).

Microdialysis

The microdialysis methods used in the construction of guide cannula and probes have been previously described (*57*). Under isoflurane anesthesia, all animals underwent a stereotactic surgical procedure for placement of a polysulfone recording chamber (Crist Instruments, Damascus, MD), in the DRN, mPFC, or vHPC, which directs the insertion of the microdialysis probes. Microdialysis probes were placed in sites that had not been previously sampled the day before the experiment. After lowering the probe, a protective cap was used to cover the chamber overnight. The following day, the cap was removed, and inlet and outlet lines were attached to the probe for microdialysis. Probes were held in place snugly and were prevented from rotating by using a tab. The solution used to perfuse the probe at 1.0 μl/min contained the following (in mM): KCl 2.4, NaCl 137, $CaCl_2$ 1.2, $MgCl_2$ 1.2, and NaH_2PO_4 0.9, pH 7.4, ascorbate 0.2. The levels of serotonin, noradrenalin, and dopamine in the perfusates were then determined using liquid chromatography–mass spectrometry. Using these procedures, dialysate transmitters were sampled every 10 min from the regions of interest at baseline and after treatments.

Coimmunoprecipitation and pull-down analysis

Procedures for coimmunoprecipitation and pull-down analysis were previously described (*24*). The DRN or cultured 293T cells were lysed and centrifuged. The supernatant was preincubated with protein G–Sepharose beads (Sigma-Aldrich) and then centrifuged to obtain the target supernatant. Antibody-conjugated protein G–Sepharose beads were incubated with the target supernatant, centrifuged, washed, and heated to elute bound proteins, and proteins were analyzed by immunoblotting. For more details, see the supplementary materials.

Stereotaxic injection

The surgical procedure was performed as described previously (*58*), with additional changes to the injection coordinates. Under isoflurane anesthesia, stereotactic surgery was performed to deliver virus or solution into the DRN and to implant cannulas into the DRN, mPFC, or vHPC using the following coordinates: DRN, AP = 0 mm, ML = 0 mm, DV = 3.0 mm, from lambda; mPFC, AP = +1.8 mm, ML = ± 0.3 mm, DV = 2.1 mm; vHPC, AP = −2.9 mm, ML = ± 2.8 mm, DV = −3.6 mm, from bregma. A volume of 200 nl of drugs or 500 nl of viruses was microinjected into brain regions. A motorized stereotaxic injector (Stoelting, model no. 53311) was used to infuse virus at a rate of 0.2 μl/min.

Design and synthesis of ZZL-7

H-Ala-Val-OH was the C-terminal dipeptide of SERT, which was potential as a small-molecule blocker of SERT/nNOS interaction. In view of the poor stability of enzymatic hydrolysis and the blood–brain barrier permeability of H-Ala-Val-OH, acetylated alanine and esterified Val were used to form ZZL-7 (Ac-Ala-Val-OMe).

ZZL-7 has the advantages of small molecular weight and being easy to synthesize. ZZL-7 was obtained by following the next synthetic steps. To a solution of Boc-Ala-OH (4 g, 21.1 mmol) and H-Val-OMe·HCl (3.9 g, 23.3 mmol) in anhydrous DMF (50 ml), DIPEA (9.3 ml, 53.3 mmol) and PyBOP (12 g, 23.3 mmol) were added at 0°C. The mixture was stirred overnight at room temperature. The solvent was removed in vacuo. The residue was dissolved in EA (100 ml), washed with 10% critic acid (3 × 40 ml), 5% $NaHCO_3$ (3 × 40 ml), and brine (2 × 40 ml), dried over Na_2SO_4, and concentrated in vacuo. The crude product was purified by silica gel chromatography (PE: EA=2:1) to give Boc-Ala-Val-OMe (6.07 g, 95%) as a white solid. ^{1}H nuclear magnetic resonance (^{1}H NMR) imaging (400 MHz, $CDCl_3$): δ 6.96 (d, J = 8.0 Hz, 1H), 5.40 (d, J = 6.7 Hz, 1H), 4.54 (q, J = 8.9 Hz, 1H), 4.34 – 4.16 (m, 1H), 3.74 (s, 3H), 2.14-2.22 (m, 1H), 1.45 (s, 9H), 1.36 (d, J = 7.0 Hz, 3H), and 0.92 (dd, J = 10.9, 6.9 Hz, 6H). A solution of Boc-Ala-Val-OMe (6 g, 19.8 mmol) in 80.6 ml (386.9 mmol) of hydrochloride dioxane (4.8 mol/L) was stirred at room temperature for 2 hours. After completion of the reaction, the solution was concentrated in vacuo to obtain the crude H-Ala-Val-OMe·HCl.

DIPEA (6.9 ml, 39.7 mmol) was added to a solution of H-Ala-Val-OMe·HCl and Ac_2O (2.8 ml, 29.8 mmol) in THF at 0°C. The mixture was stirred for 10 min and then warmed to room temperature to stir for 2 hours. The solvent was concentrated in vacuo. The residue was dissolved in EA and washed with 10% critic acid, 5% $NaHCO_3$, and brine, dried over Na_2SO_4, and concentrated in vacuo. The crude product was purified by silica gel chromatography (CH_2Cl_2: MeOH = 30:1) to give ZZL-7 (Ac-Ala-Val-OMe, 3.6 g, 74%) as a white solid. ^{1}H NMR (400 MHz, $CDCl_3$): δ 6.77 (d, J = 8.4 Hz, 1H), 6.30 (d, J = 6.9 Hz, 1H), 4.59 (p, J = 7.0 Hz, 1H), 4.50 (dd, J = 8.7, 5.0 Hz, 1H), 3.75 (s, 3H), 2.24 – 2.13 (m, 1H), 2.00 (s, 3H), 1.38 (d, J = 6.9 Hz, 3H), 0.92 (dd, J = 9.4, 6.9 Hz, 6H). ^{13}C NMR (101 MHz, $CDCl_3$) δ 172.43, 172.19, 170.03, 57.39, 52.24, 48.90, 31.11, 23.17, 19.01, 18.32, 17.74. MS (ESI) calculated for $C_{11}H_{19}N_2O_4$ $[M-H]^-$ was 243.13; found: m/z 243.2.

Statistics

All data were analyzed using Prism 8 software (GraphPad Software, Cary, NC, USA). After a homogeneity test of variance, when equal variances were assumed, unpaired or paired Student's t test was used to estimate the differences between two groups, one-way ANOVA was used for comparison among three or four groups, and two-way ANOVA with Bonferroni's multiple-comparisons corrections was used to compare the effect of two factors with respect to a numeric outcome. The results were considered significant at $P <$ 0.05. All experimental results are shown as mean ± SEM. Sample sizes were based on previous studies in this field. Outliers were excluded according to the analysis of identify outliers using Prism software. Animals were randomly assigned to experimental groups. The investigator was blinded to the group allocation during the experiment and/or when assessing the outcome. Statistical parameters, including n, t, and F values and P values, and the analytical method used for each experiment, are listed in the supplementary materials.

Additional methods

Detailed methodology, including electrophysiological recordings, viral production, behavioral testing, CMS model, Western blot analysis, and drug concentration determination are described in the supplementary materials.

REFERENCES AND NOTES

1. H. Herrman *et al*., *Lancet* **399**, 957–1022 (2022).
2. D. L. Murphy, K. P. Lesch, *Nat. Rev. Neurosci.* **9**, 85–96 (2008).
3. D. Chancellor, *Nat. Rev. Drug Discov.* **10**, 809–810 (2011).
4. J. Licinio, M. L. Wong, *Nat. Rev. Drug Discov.* **4**, 165–171 (2005).
5. I. Maany, *JAMA* **292**, 2833, author reply 2833 (2004).
6. E. T. Kavalali, L. M. Monteggia, *Curr. Opin. Pharmacol.* **20**, 35–39 (2015).
7. K. M. Bozymski *et al*., *Ann. Pharmacother.* **54**, 567–576 (2020).
8. R. B. Price, M. K. Nock, D. S. Charney, S. J. Mathew, *Biol. Psychiatry* **66**, 522–526 (2009).
9. C. G. Abdallah, G. Sanacora, R. S. Duman, J. H. Krystal, *Annu. Rev. Med.* **66**, 509–523 (2015).
10. E. J. Daly *et al*., *JAMA Psychiatry* **75**, 139–148 (2018).
11. A. C. Hayley, C. Stough, J. C. Verster, A. J. van de Loo, L. A. Downey, *Curr. Drug Abuse Rev.* **8**, 1–2 (2015).
12. O. Lipsitz *et al*., *Am. J. Geriatr. Psychiatry* **29**, 899–913 (2021).
13. K. A. Trujillo, S. D. Iñiguez, *Behav. Brain Res.* **394**, 112841 (2020).
14. P. R. Albert, B. Le François, A. M. Millar, *Mol. Brain* **4**, 21 (2011).
15. B. W. Okaty, K. G. Commons, S. M. Dymecki, *Nat. Rev. Neurosci.* **20**, 397–424 (2019).
16. J. W. Richardson-Jones *et al*., *Neuron* **65**, 40–52 (2010).
17. H. Gozlan, S. El Mestikawy, L. Pichat, J. Glowinski, M. Hamon, *Nature* **305**, 140–142 (1983).
18. J. D. Coplan, S. Gopinath, C. G. Abdallah, B. R. Berry, *Front. Behav. Neurosci.* **8**, 189 (2014).
19. C. A. Stockmeier *et al*., *J. Neurosci.* **18**, 7394–7401 (1998).
20. M. L. Wong, J. Licinio, *Nat. Rev. Drug Discov.* **3**, 136–151 (2004).
21. A. Bortolozzi *et al*., *Mol. Psychiatry* **17**, 612–623 (2012).
22. B. Chanrion *et al*., *Proc. Natl. Acad. Sci. U.S.A.* **104**, 8119–8124 (2007).
23. L. J. Zhu *et al*., *Nat. Med.* **20**, 1050–1054 (2014).
24. L. Zhou *et al*., *Nat. Med.* **16**, 1439–1443 (2010).
25. C. Qin *et al*., *Mol. Psychiatry* **26**, 6506–6519 (2021).
26. Y. Qin *et al*., *ACS Chem. Neurosci.* **12**, 244–255 (2021).
27. K. A. Michelsen, J. Prickaerts, H. W. M. Steinbusch, *Prog. Brain Res.* **172**, 233–264 (2008).
28. P. E. Lutz, *J. Neurophysiol.* **109**, 2245–2249 (2013).
29. Y. Sato, I. Sagami, T. Shimizu, *J. Inorg. Biochem.* **87**, 261–266 (2001).
30. P. Blier, G. Piñeyro, M. el Mansari, R. Bergeron, C. de Montigny, *Ann. N. Y. Acad. Sci.* **861** (1 ADVANCES IN S), 204–216 (1998).
31. G. Piñeyro, P. Blier, *Pharmacol. Rev.* **51**, 533–591 (1999).
32. A. Ferrés-Coy *et al*., *Psychopharmacology* **225**, 61–74 (2013).
33. J. M. Watson, L. A. Dawson, *CNS Drug Rev.* **13**, 206–223 (2007).
34. N. A. Gray *et al*., *Biol. Psychiatry* **74**, 26–31 (2013).
35. J. A. Stamford, C. Davidson, D. P. McLaughlin, S. E. Hopwood, *Trends Neurosci.* **23**, 459–465 (2000).
36. E. Quentin, A. Belmer, L. Maroteaux, *Front. Neurosci.* **12**, 982 (2018).
37. H. Tochio, Q. Zhang, P. Mandal, M. Li, M. Zhang, *Nat. Struct. Biol.* **6**, 417–421 (1999).
38. B. Short, J. Fong, V. Galvez, W. Shelker, C. K. Loo, *Lancet Psychiatry* **5**, 65–78 (2018).
39. P. Zanos *et al*., *Pharmacol. Rev.* **70**, 621–660 (2018).
40. M. V. Fogaça *et al*., *Mol. Psychiatry* **26**, 3277–3291 (2021).
41. E. S. Wohleb *et al*., *J. Clin. Invest.* **126**, 2482–2494 (2016).
42. T. Kato *et al*., *J. Clin. Invest.* **129**, 2542–2554 (2019).
43. B. D. Hare *et al*., *Nat. Commun.* **10**, 223 (2019).
44. R. N. Moda-Sava *et al*., *Science* **364**, eaat8078 (2019).
45. B. D. Hare, S. Pothula, R. J. DiLeone, R. S. Duman, *Neuropharmacology* **166**, 107947 (2020).
46. S. Deyama *et al*., *Am. J. Psychiatry* **176**, 388–400 (2019).
47. F. Guo *et al*., *Eur. Neuropsychopharmacol.* **26**, 1087–1098 (2016).
48. K. Fukumoto *et al*., *Neuropsychopharmacology* **45**, 1725–1734 (2020).
49. C. Anacker *et al*., *Nature* **559**, 98–102 (2018).
50. B. A. Strange, M. P. Witter, E. S. Lein, E. I. Moser, *Nat. Rev. Neurosci.* **15**, 655–669 (2014).
51. A. Burette, U. Zabel, R. J. Weinberg, H. H. H. W. Schmidt, J. G. Valtschanoff, *J. Neurosci.* **22**, 8961–8970 (2002).
52. C. Cserép *et al*., *Cereb. Cortex* **21**, 2065–2074 (2011).
53. G. E. Torres, R. R. Gainetdinov, M. G. Caron, *Nat. Rev. Neurosci.* **4**, 13–25 (2003).
54. L. Léger *et al*., *Histochem. Cell Biol.* **110**, 517–525 (1998).
55. K. L. Simpson, B. D. Waterhouse, R. C. Lin, *J. Comp. Neurol.* **466**, 495–512 (2003).
56. Q. G. Zhou *et al*., *J. Clin. Invest.* **129**, 310–323 (2019).
57. R. T. Kennedy, *Curr. Opin. Chem. Biol.* **17**, 860–867 (2013).
58. Q. G. Zhou *et al*., *Stem Cell Reports* **9**, 543–556 (2017).

ACKNOWLEDGMENTS

We thank J. L. Chen., L. D. Li., Y. P. Zhou., M. Y. Zhu., and H. Y. Wu. for assistance with techniques and M. Naveed for editing the revised manuscript. **Funding:** This research was supported by the Brain Research Plan of China (grant 2022ZD0211700) and of Guangdong Province (grant 2018B030334001), the National Natural Science Foundation of China (grants 82071525, 81871065, and 82090042), the Jiangsu Province Natural Science Foundation for Distinguished Young Scientists (grant SBK2019010180), the Key Lab of Cardiovascular and Cerebrovascular Drugs of Jiangsu Province, and the Collaborative Innovation Center for Cardiovascular Disease Translational Medicine for data collection, analysis, and interpretation. **Author contributions:** Q.G.Z., and D.Y.Z. conceived the ideas and prepared the manuscript. T.Y.L. designed the compounds. N.S., Y.J.Q., C.X., T.X., Z.W.D., and L.P.Z. performed experiments and acquired the data. A.-A.L. assisted with in vivo electrophysiology. Y.Z. assisted with cloning. X.L. assisted with measurement of neural transmitters. F.M. and J.Z. supported techniques. D.Y.Z. gave advice for the project and provided part materials for the experiments. **Competing interests:** The authors declare no competing interests. **Data and materials availability:** Plasmids and *nNos*$^{flox/flox}$ mice are available upon request from Q.G.Z. (qigangzhou@njmu.edu.cn) under a material transfer agreement with the University of Nanjing Medical University. All data needed to evaluate the conclusions in this study are present in main text or the supplementary materials.

SUPPLEMENTARY MATERIALS

science.org/doi/10.1126/science.abo3566
Materials and Methods
Figs. S1 to S10
References (*59*–*73*)
MDAR Reproducibility Checklist

Submitted 28 January 2022; accepted 28 September 2022
10.1126/science.abo3566

ORGANIC CHEMISTRY

Closed-loop optimization of general reaction conditions for heteroaryl Suzuki-Miyaura coupling

Nicholas H. Angello[1,2]†, Vandana Rathore[1,2]†, Wiktor Beker[3], Agnieszka Wołos[3,4], Edward R. Jira[2,5], Rafał Roszak[3,4], Tony C. Wu[6,7], Charles M. Schroeder[1,2,5,8], Alán Aspuru-Guzik[6,7,9,10,11,12], Bartosz A. Grzybowski[3,4,13,14]*, Martin D. Burke[1,2,15,16,17]*

General conditions for organic reactions are important but rare, and efforts to identify them usually consider only narrow regions of chemical space. Discovering more general reaction conditions requires considering vast regions of chemical space derived from a large matrix of substrates crossed with a high-dimensional matrix of reaction conditions, rendering exhaustive experimentation impractical. Here, we report a simple closed-loop workflow that leverages data-guided matrix down-selection, uncertainty-minimizing machine learning, and robotic experimentation to discover general reaction conditions. Application to the challenging and consequential problem of heteroaryl Suzuki-Miyaura cross-coupling identified conditions that double the average yield relative to a widely used benchmark that was previously developed using traditional approaches. This study provides a practical road map for solving multidimensional chemical optimization problems with large search spaces.

The development of automated synthesis methods for peptides (*1*), nucleic acids (*2*), and polysaccharides (*3*) required discovery of highly general reaction conditions applicable to a wide range of building block combinations. In contrast, in the synthesis of small organic molecules, bespoke reaction conditions are usually developed to maximize the yield of each target molecule, minimize side products, and/or minimize the cost of the corresponding process. Reaction optimization per target is often necessary because synthetic methods are typically optimized on only one or a few pairs of substrates and then applied to a wider range of substrate combinations with the rarely fulfilled hope that the same conditions will generally lead to high yields (*4*). Even the application of machine learning to optimization protocols (*5*–*9*) does not ensure generality, which is critical for automating, accelerating, and ultimately democratizing the small molecule–making process. Identification of such general conditions is difficult because the search space—spanning all possible combinations of substrates multiplied by all possible combinations of reaction conditions—is enormous and thus impractical to navigate using standard approaches.

Heteroaryl molecular fragments are ubiquitous in many industrially relevant functional molecules, including pharmaceuticals, materials, catalysts, dyes, and natural products. In all of these spaces, synthesis remains a key bottleneck. Finding general conditions for (hetero)aryl Suzuki-Miyaura cross-coupling (SMC) is therefore an important problem. It is also a challenging and largely unsolved problem, primarily owing to variable degrees of both desired and undesired reactivities across the very large and diverse range of potential heteroaryl and aryl substrates (*10*–*12*). We recently attempted, but failed, to use machine learning (ML) to discover general reaction conditions by mining the extensive chemical literature on (hetero)aryl SMC (*13*). This is mainly because the choices of conditions reported in the literature lacked causal links to the substrates' structures, and because of a lack of published (or otherwise accessibly archived) negative results.

Here, we report a simple closed-loop workflow that can efficiently navigate vast substrate-condition space to discover general reaction conditions. The approach leverages: (i) data-guided matrix down-selection to render the vast search space tractable while retaining validity to the whole; (ii) uncertainty-minimizing ML to efficiently drive prediction optimization; and (iii) robotic experimentation to increase throughput, precision, and reproducibility of datasets recursively generated on demand (Fig. 1). We demonstrate that this workflow succeeds in identifying general reaction conditions for the (hetero)aryl SMC reaction. The optimized solution doubled the average yield compared with benchmark general conditions that had previously been developed through traditional human-guided experimentation (hereafter referred to as *JACS* 2009) (*14*) and that have since been used extensively in academic and industrial laboratories worldwide (cited in >590 papers and patent applications). This approach can thus find powerful

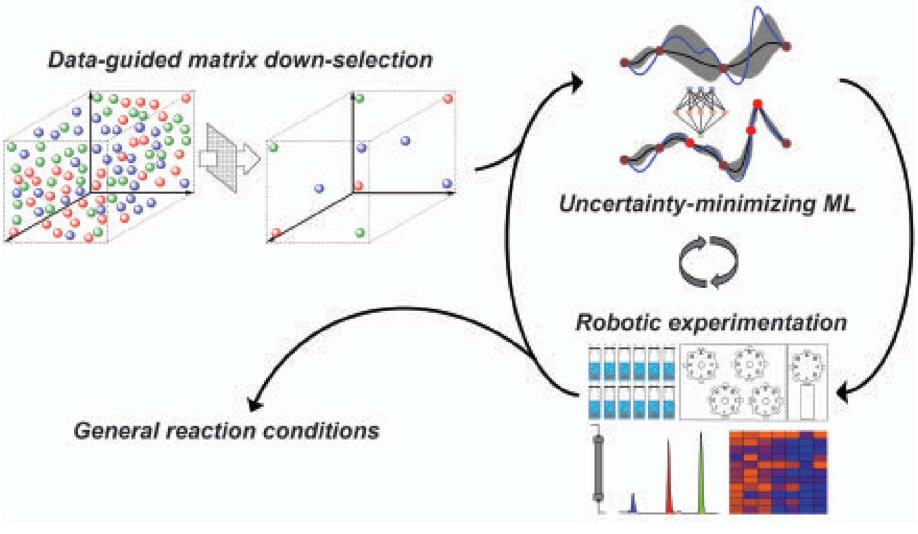

Fig. 1. Problem definition and substrate scope for generalized heterocyclic cross-coupling. Workflow developed in this work for the discovery of general reaction conditions.

---

[1]Department of Chemistry, University of Illinois at Urbana-Champaign, Urbana, IL, USA. [2]Beckman Institute for Advanced Science and Technology, University of Illinois at Urbana-Champaign, Urbana, IL, USA. [3]Allchemy, Inc., Highland, IN, USA. [4]Institute of Organic Chemistry, Polish Academy of Sciences, Warsaw, Poland. [5]Department of Chemical and Biomolecular Engineering, University of Illinois at Urbana-Champaign, Urbana, IL, USA. [6]Department of Chemistry, University of Toronto, Toronto, ON, Canada. [7]Department of Computer Science, University of Toronto, Toronto, ON, Canada. [8]Department of Materials Science and Engineering, University of Illinois at Urbana-Champaign, Urbana, IL, USA. [9]Vector Institute for Artificial Intelligence, Toronto, ON, Canada. [10]Canadian Institute for Advanced Research, Toronto, ON, Canada. [11]Department of Chemical Engineering and Applied Chemistry, University of Toronto, Toronto, ON, Canada. [12]Department of Materials Science and Engineering, University of Toronto, Toronto, ON, Canada. [13]Center for Soft and Living Matter, Institute for Basic Science, Ulsan, Republic of Korea. [14]Department of Chemistry, Ulsan Institute of Science and Technology, Ulsan, Republic of Korea. [15]Carl R. Woese Institute for Genomic Biology, University of Illinois at Urbana-Champaign, Urbana, IL, USA. [16]Cancer Center at Illinois, University of Illinois at Urbana-Champaign, Urbana, IL, USA. [17]Carle Illinois College of Medicine, University of Illinois at Urbana-Champaign, Urbana, IL, USA.

***Corresponding author. Email: mdburke@illinois.edu (M.D.B.); nanogrzybowski@gmail.com (B.A.G.)**

†These authors contributed equally to this work.

solutions that lie in vast multidimensional search spaces and stands to accelerate the field of organic chemistry's march toward automated and democratized small molecule synthesis (*15*–*28*), which critically requires more general reaction conditions.

Data-guided down-selection of substrates

To enable practical pursuit of general hetero(aryl) SMC reaction conditions, we first strategically down-selected both the matrix of possible building block combinations and the matrix of possible reaction conditions in a way that preserved relevance of the subsets to their wholes (Fig. 1). Specifically, we first data mined the inventories of common fine chemical suppliers and assembled a list of ~5400 (hetero)aryl halide building blocks that were practically purchasable and therefore accessible for study [supplementary materials (SM) section 4]. To define a representative subset of this chemical space, we applied a stratified clusterization strategy (fig. S21) to algorithmically cluster the building blocks by their common (hetero)aromatic ring substructures and pendant functionalities, down-selecting 54 "centroid" molecules most representative of each section of the available chemical space. Combining these molecules with a selection of 54 commercially available (hetero)aryl *N*-methyliminodiacetic acid (MIDA) boronates defined a down-selected substrate scope composed of 2688 representative cross-coupling products (figs. S22 and S23). Mapping this potential product space and comparing it to all previously reported heteroaryl products in the literature revealed substantial overlap between both sets, suggesting that it is representative of heteroaryl chemical space as a whole (Fig. 2A). However, testing even this initially down-selected collection of cross-coupling products against many possible reaction conditions is technically unfeasible. Accordingly, we pursued a second layer of down-selection. Specifically, we used a greedy algorithm based on the Tanimoto similarity (*29*) to identify from this larger collection a set of 11 representative substrate pairs that maximize mutual dissimilarity of the resulting products (Fig. 2B). For all of these products, we determined liquid chromatography–mass

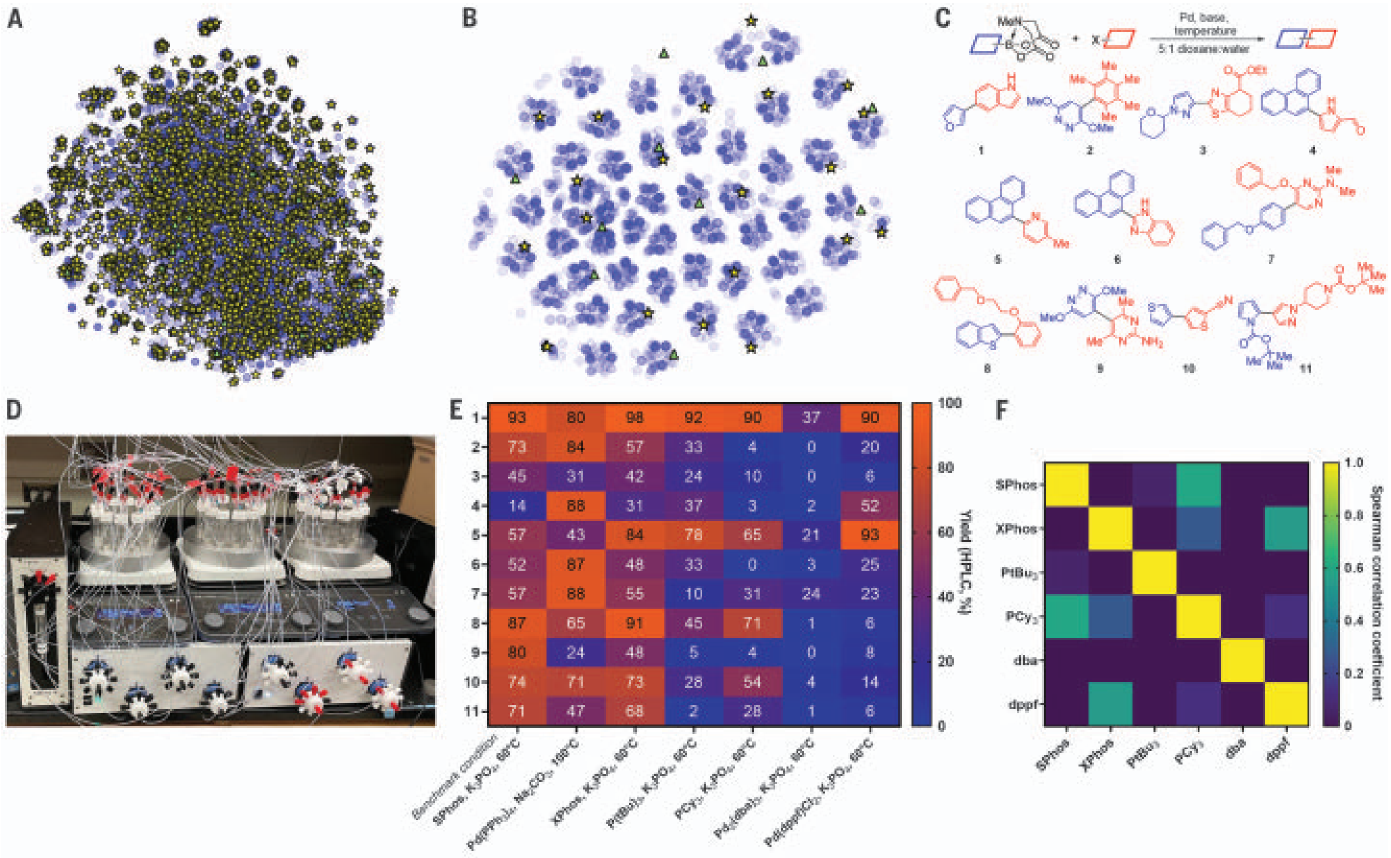

	Benchmark condition SPhos, K_3PO_4, 60°C	$Pd(PPh_3)_4$, Na_2CO_3, 100°C	XPhos, K_3PO_4, 60°C	$P(tBu)_3$, K_3PO_4, 60°C	PCy_3, K_3PO_4, 60°C	$Pd_2(dba)_3$, K_3PO_4, 60°C	$Pd(dppf)Cl_2$, K_3PO_4, 60°C
1	93	80	98	92	90	37	90
2	73	84	57	33	4	0	20
3	45	31	42	24	10	0	6
4	14	88	31	37	3	2	52
5	57	43	84	78	65	21	93
6	52	87	48	33	0	3	25
7	57	88	55	10	31	24	23
8	87	65	91	45	71	1	6
9	80	24	48	5	4	0	8
10	74	71	73	28	54	4	14
11	71	47	68	2	28	1	6

Fig. 2. Automated synthesis of the initial training set. (**A**) T-distributed stochastic neighbor embedding (t-SNE) mapping of the substrate combinations (2688 heteroaryl products) examined in this work versus all (hetero)aryl products previously reported in the literature. Blue circles represent literature-reported products, yellow stars represent products exclusively belonging in this reported search space, and green triangles represent products present in both sets. (**B**) t-SNE mapping of the product space synthesized during the training and test sets versus the overall reaction space. Blue circles represent products belonging to the reported search space, green triangles represent products belonging to the training set, and yellow stars represent products belonging to the test set. (**C**) Reaction scheme and chemical structures of the initial training set. Me, methyl; Et, ethyl. (**D**) Photo of the automated synthesis instrument used in this work. (**E**) Initial training set with the benchmark condition; all other common palladium catalysts reported in the literature; and a condition with the most common catalyst [$Pd(PPh_3)_4$], base (Na_2CO_3), temperature (100°C), and solvent (dioxane:water) used in the literature. Yields are the average of two automated repetitions (±2% deviation), measured by LCMS-UV/Vis with an authentic product standard (response factor to phenanthrene; SM section 9). HPLC, high-performance liquid chromatography. (**F**) Yield-based similarity between Pd-based catalysts differing only in organic ligands. Each square quantifies the Spearman rank correlation coefficient between yields obtained for each of the 11 substrate pairs. Two pairs of ligands (XPhos and dppf, and SPhos and PCy_3) were highly correlated and redundant. $PtBu_3$, tri-tert-butylphosphine; PCy_3, tricyclohexylphosphine; dba, dibenzylideneacetone; dppf, 1,1′-bis(diphenylphosphino)ferrocene.

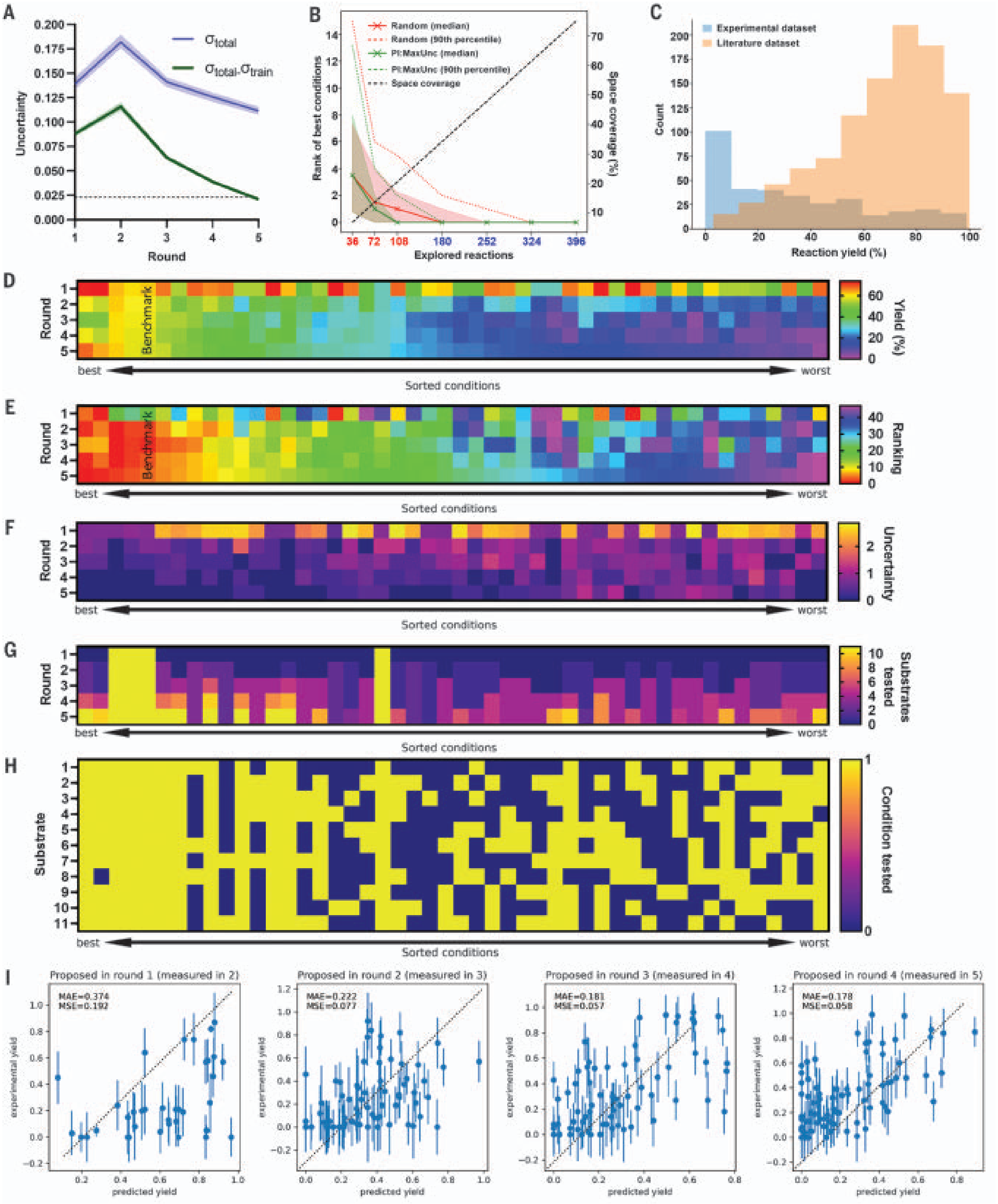

Fig. 3. Closed-loop experimentation and analysis. (**A**) Convergence of the model's uncertainty. Dashed horizontal line depicts threshold for $\bar{\sigma}_{total} - \bar{\sigma}_{train}$ obtained in calibration simulations. The shaded areas correspond to 95% confidence interval computed by repeatedly training the model 10 times. (**B**) Comparison of ML-guided searches versus random searches for general conditions. Simulations with both model selection policy [probability of improvement (PI) in conditions space and maximum uncertainty (MaxUnc) in substrate space for given conditions; abbreviated as PI:MaxUnc and corresponding to green lines] and random selection of the next reactions (red lines) were repeated 100 times to evaluate the random factor in the algorithm (random initialization of neural network weights as well as selection of the next step in the random baseline). The shaded areas mark the

interquartile range. (**C**) Comparison of yield distribution between literature-reported reactions and those explored in this work. (**D**) Color scale indicates the percent yield per general condition as perceived by the ML model at the conclusion of a given optimization round, 1 to 5. Along the horizontal axis, the conditions are ranked according to the ML prediction after round 5. (**E**) Ranking per general condition per round as perceived by the ML model. (**F**) Uncertainty per general condition per round as perceived by the ML model (computed from 10 repetitions). (**G**) Number of substrates tested per general condition per round of closed-loop optimization. (**H**) Coverage of reaction space tested by round 5 of closed-loop experimentation. A value of 1 indicates that the condition was tested, and a value of 0 indicates that the condition was not tested. (**I**) Distributions of yields measured and predicted prior to the measurement for each round of closed-loop optimization. MAE, mean absolute error; MSE, mean squared error.

spectrometry ultraviolet/visible spectroscopy (LCMS-UV/Vis) response factor curves, which enabled us to automatically measure the yields of automated reactions (SM sections 8 and 9).

Data-guided down-selection of conditions

We considered four condition variables—solvent, base, catalyst and ligand, and temperature. As our aim was to test a broad range of conditions, we initially down-selected representatives of condition classes on the basis of not only their extent of prior use from our earlier comprehensive literature analysis (*13*) but also structural and functional diversity. For instance, whereas the two most commonly used solvents in the literature are dioxane and dimethoxyethane, they both belong to the same solvent class of ethers, and so we selected only one of them (dioxane). Similar reasoning led us to keep only one carbonate base [in (*13*), we showed that the nature of the cation did not alter the yields]. We selected 100°C as the most frequently used temperature in the literature, as well as 60°C, which was used in the previously developed benchmark protocol (*14*). In the end, we selected three solvents (dioxane, toluene, and dimethylformamide, all used in 5:1 mixture with water), two bases (sodium carbonate and potassium phosphate), two temperatures (60° and 100°C), and seven catalysts [Pd SPhos G4, Pd(PPh$_3$)$_4$, Pd XPhos G4, Pd P(tBu)$_3$ G4, Pd PCy$_3$ G4, Pd$_2$(dba)$_3$, and Pd(dppf)Cl$_2$; G4 refers to the fourth-generation Buchwald precatalyst] to evaluate. The down-selected 11 building block combinations described above were tested under an initial set of conditions to "seed" the ML optimization (Fig. 2C) and then tested iteratively under a much broader set of conditions during the ML-guided optimization phase.

Seeding experiments, reaction standardization, and conditions space

All reactions were performed automatically on the robotic system shown in Fig. 2D. Before solvent addition, heating, and stirring, reaction mixtures were purged with 10 automated vacuum and argon cycles, which led to highly reproducible reaction yields (fig. S11). This automated Schlenk process was necessary—even when using air-stable precatalysts and building blocks—for reproducibility. To "seed" the optimization procedure, we performed all couplings between the aforementioned 11 pairs of substrates, each under seven different conditions: those corresponding to the *JACS* 2009 benchmark (5:1 dioxane:water, 60°C, K$_3$PO$_4$, Pd SPhos G4); same base and solvents but with the other selected palladium catalysts [Pd XPhos G4, Pd P(tBu)$_3$ G4, Pd PCy$_3$ G4, Pd$_2$(dba)$_3$, and Pd(dppf)Cl$_2$]; and a condition with the most common catalyst [Pd(PPh$_3$)$_4$], base (Na$_2$CO$_3$), temperature (100°C), and solvent (dioxane:water) used in the literature (Fig. 2E). When each reaction was repeated twice, the yields exhibited only ±2% deviation, underscoring one of the key advantages of automated experimentation [indeed, it has previously been reported (*30*) that repetition of the same reaction even by the same human experts entails variability of ~10 to 15%].

This initial round of experiments also allowed us to identify catalysts that, for different substrate pairs, systematically gave similar yields and could thus be redundant. Such functional rather than structural similarity is quantified by the Spearman rank matrix shown in Fig. 2F and correlating yields obtained for all 11 substrate pairs using two different catalyst ligands—in this representation, redundant catalysts correspond to high-correlation, off-diagonal elements (e.g., XPhos and dppf, or PCy$_3$ and SPhos). On the basis of this analysis, we eliminated PCy$_3$ and dppf from our pool of ligands to decrease redundancy, and we eliminated Pd$_2$(dba)$_3$ because of poor performance (<5% yield for 8 of 11 substrates), yielding a full space to be explored of 528 reactions (11 substrates × 2 temperatures × 2 bases × 3 solvents × 4 catalysts).

Uncertainty-minimizing ML for generality

A reaction condition can be considered maximally general when it provides the highest average yield across the widest range of chemical space. Optimization for generality is an unsolved and underexplored challenge in the evolving field of ML. We thus considered an alternative de novo approach, where small sets of highly reproducible data are generated on demand during ML-guided closed-loop optimization, including negative data vastly underrepresented in existing datasets. We also decided to strategically focus the ML algorithm on decreasing model uncertainty and thereby maximize the efficiency of the learning process.

Denoting the set of possible reaction conditions as $C = \{c\}$, a set of substrate pairs as $S = \{s\}$, and reaction yield as $y(s,c)$, our aim is to maximize the objective function given by

$$f(c) = \frac{1}{|S|}\sum\nolimits_{s \in S} y(s, c) \tag{1}$$

Then, the general conditions c_{general} are given as

$$c_{\text{general}} = \arg\max_{c \in C} f(c) \tag{2}$$

At first glance, the problem of identifying c_{general} in the least number of experiments resembles standard Bayesian optimization (BO). However, there is a substantial difference: In all BO algorithms, each experiment or measurement performed immediately provides information about the objective function desired for optimization. In contrast, experimental evaluation of $f(c)$ in our problem requires multiple experiments (because summation in Eq. 1 runs over the entire set S)—that is, determination of $f(c)$ for given conditions requires experiments with every pair of substrates in the S set. To address this problem, we modified the standard BO approach by constructing a surrogate model for predicting reaction yields, $\hat{y}(s, c)$. We then used its predictions to estimate $\hat{f}(c)$ according to Eq. 1 and using the model's prediction for the yet-unperformed reactions. Note that in standard BO, we would have observed $f(c)$ for the "seen" conditions and estimated for the "unseen" ones; in our case, $f(c)$ was estimated even for the already-tested conditions, unless the entire substrate space S had already been tested. On the basis of these considerations, the optimization over C (selection of the next conditions to examine) is performed with standard BO techniques, whereas sampling of S is achieved using an active learning approach—each of these techniques is known on its own (*8*, *31*), but the combination of the two (where the observation of the BO objective can be incomplete) seems to be unknown. In particular, we decided to choose substrate pairs on the basis of the model's prediction of uncertainty for given substrates under given reaction conditions: the highly uncertain (low-confidence) predictions indicate missing information, and providing the model with the corresponding experimental data should decrease its uncertainty the most.

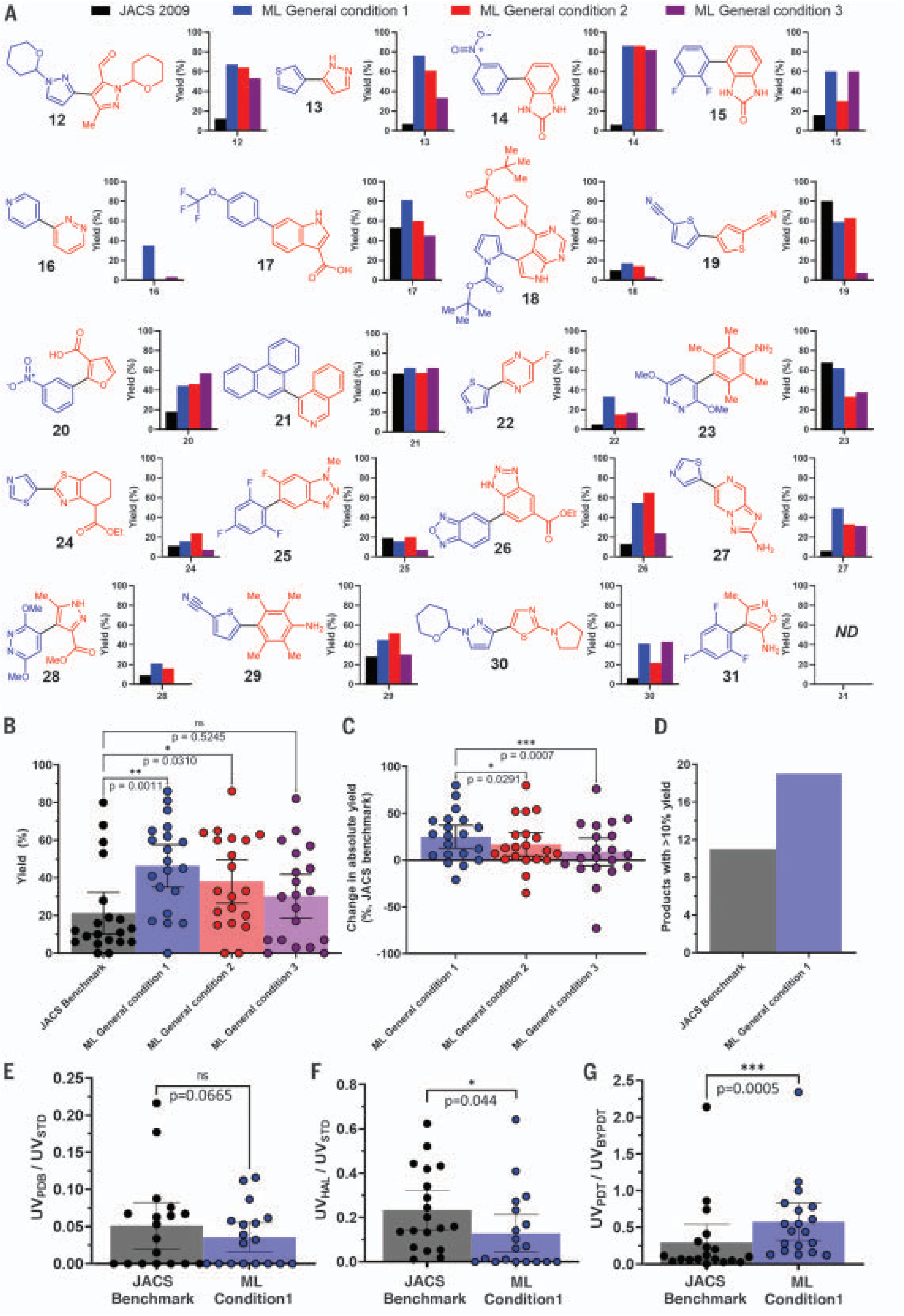

Fig. 4. Test set for ML-discovered reaction conditions. (**A**) Set of 20 diverse compounds from outside the training set selected to test whether the discovered general reaction conditions translate to other diverse heteroaryl product classes. *JACS* 2009 condition: 5:1 dioxane:water, 60°C, K_3PO_4, Pd SPhos G4. ML General condition 1: 5:1 dioxane:water, 100°C, Na_2CO_3, Pd XPhos G4. ML General condition 2: 5:1 dioxane:water, 100°C, Na_2CO_3, Pd SPhos G4. ML general condition 3: 5:1 dioxane:water, 100°C, Na_2CO_3, $Pd(PPh_3)_4$. ND, not detected. (**B**) Jitter plot showing the performance of the top ML conditions versus the benchmark. Brackets indicate 95% confidence interval. (**C**) Jitter plot showing the relative performance in change of yield of the top ML conditions versus the benchmark. Brackets indicate 95% confidence interval. (**D**) The number of products per general condition with >10% yield measured. (**E**) Relative protodeboronation per condition, as measured by integrated UV peak area (UV_{PDB}) standardized to the internal standard (UV_{STD}). (**F**) Relative remaining halide per condition, as measured by integrated UV peak area (UV_{HAL}) standardized to the internal standard (UV_{STD}). (**G**) Relative product formation per condition (UV_{PDT}) relative to by-product formation (UV_{BYPDT}).

For uncertainty estimation, we sought a model offering prediction uncertainty commensurate with prediction error—for instance, highly confident predictions with high error are undesirable. Per the analyses of numerous neural-network (NN) and Gaussian process (GP) models (SM section 3), we ultimately selected an ensemble of GP supplemented with a NN kernel component [GPE(NN)]; similar approaches were recently used in BO (*32*) and interactive learning (*33*). Such a model is particularly appealing because of its flexibility (the similarity metric between different conditions will be learned from the data) and the reliability of the prediction uncertainties (e.g., it is guaranteed that the prediction of a test sample will not be more confident than a training sample). For the selection of conditions to be tested, we chose as an acquisition function the probability of improvement (PI).

Closed-loop, ML-driven optimization with robotic experimentation

The GPE(NN)/PI model guided the automated experiments over the down-selected search space. We worked in experimental batches, meaning that multiple experiments were performed before the theoretical model was updated. Within each batch, the algorithm formed a "priority queue" of unexplored reactions by sorting and selecting conditions according to the computed PI and substrate pairs according to the prediction uncertainty. The batch size for rounds 1 and 2 of optimization was 36 duplicated reactions, followed by 72 and 84 unduplicated reactions for rounds 3 and 4 and round 5, respectively.

Over the closed-loop rounds, the model's uncertainty decreased and converged at the fifth round to the threshold obtained during calibration simulations (Fig. 3A and fig. S20), suggesting that the model gained sufficient knowledge about the whole space, at which point the optimization was terminated. This strategy converges to this optimum in about half as many reactions as does random sampling (Fig. 3B) and with a higher likelihood of success compared with typical BO strategies (fig. S30). As the algorithm explored the reaction-condition space, reaction yields for our dataset were distributed more or less uniformly over the range of possible values (Fig. 3C). In other words, our protocol learned by probing both low- and high-yielding conditions. This contrasts with the distribution of yields in published reaction sets—such yields are heavily skewed toward positive outcomes, which, as we discussed in many of our previous works on computerized synthesis (*34*–*36*), limits the usefulness of approaches aiming to learn from published datasets.

In this dataset, the discovered top-1 condition conferred 72% average yield across all 11 substrates, whereas the benchmark condition [found to also be the top-5 (i.e., fifth best) condition] conferred 64% average yield. To understand how the model arrived at this optimum, we examined the model's perception of the average yield and ranking of each general condition per round (Fig. 3, D and E). Within the first two rounds, the model gains the ability to accurately categorize these conditions into high, medium, and low overall average yield and, in the subsequent rounds, establishes the correct ranking within these categories. The increasing accuracy of the model over the course of the experiment is recapitulated in Fig. 3F, which shows the model's ranking uncertainty decreasing between rounds and is especially apparent for the top conditions. The model chose to test a few substrates per round across many conditions for the first three rounds, followed by primarily filling in the top conditions in the latter rounds (Fig. 3G). By the fifth round, the model explored nearly all of the top-7 conditions, which corresponds to every condition with >50% overall average yield, as estimated by the model (Fig. 3H).

Finally, we analyzed the yields of reactions the model requested in order to gain more information about the reaction-condition space (Fig. 3I). These values are not expected to increase as the optimization progresses, because the yield of a single experiment is not our objective. Given the uncertainty-guided selection of substrates, one could even expect the opposite: Once a set of suitable conditions is identified, further exploitation should involve lower-yielding reactions to verify that the found candidate conditions are indeed better, as well as to increase confidence of the estimate of $f(c)$. The results shown in Fig. 3I indicate that after exploring good reactions in the second iteration, the model gradually shifted its attention toward the parts of the reaction-condition space that can be considered as "negative examples" (and, in doing so, improved its prediction accuracy). From these results, it appears that (i) relatively good candidate solutions were identified early, (ii) the model initially tried to look for better-yielding reactions (to find better candidates), and (iii) more and more attention was dedicated to decreasing the uncertainty of its estimates as the "loop" progressed.

Quantifying generality

After the discovery of higher-yielding general conditions in the training set, we next sought to determine whether the learning would transfer to substrates outside of the optimization—specifically, over 20 substrate pairs chosen [by the Butina algorithm (*37*)] to maximize dissimilarity to the training set while ensuring coverage of the heterocyclic substructure and functional group space (Fig. 2B). We then set out to synthesize and purify all of the computer's suggestions and test them against the benchmark condition and the top-3 highest yielding general reaction conditions discovered during the closed-loop optimization (Fig. 4A), as ranked by the model after the completion of round 5. Despite including some very challenging building block combinations, this process was 95% successful, with only one product having no measurable yield under all four conditions.

The ML-discovered general reaction conditions performed substantially better than the previously reported and widely used benchmark condition (*14*). The top-2 conditions provided statistically significant increases in average yield compared with the benchmark, with the top condition doubling the overall average yield from 21% to 46% (Fig. 4B). Comparing the relative increase in yield reveals statistically significant differences between the top-1 and both the top-2 and top-3 conditions (Fig. 4C). Notably, the experimental yields correlate with the predicted ranking of the conditions such that the yield for the top-1 is higher than that for the top-2, which, in turn, is higher than that for the top-3. In the context of functional discovery efforts, the binary capacity to isolate or not isolate testable quantities of purified targeted compounds is arguably even more important than the specific percent yield. We estimate that the practical limit for isolating purified products is 10% yield. For the benchmark condition, only 11/20 targeted products cleared this bar, whereas this fraction rose to 19/20 for the top-1 condition (Fig. 4D).

Extending the reaction times for couplings that were low yielding under the benchmark conditions did not increase yields (fig. S33). Comprehensive analysis of by-products and product formation for all 20 reactions (SM section 10) demonstrated that a favorable shift from the former to the latter accompanies the shift from the benchmark to the ML-discovered reaction conditions. Specifically, the ML-discovered conditions were associated with a trend toward decreased protodeboronation (Fig. 4E), increased halide conversion (Fig. 4F), and an overall statistically significant increase in the ratio of product to total by-products formation (Fig. 4G) (0.30 ± 0.12 for *JACS* 2009 versus 0.58 ± 0.12 for ML conditions; $P = 0.0005$).

Outlook

The straightforward workflow developed here has enabled the accelerated discovery of improved general reaction conditions for difficult C–C bond forming reactions, representing a key step toward increasing the efficiency, generality, and accessibility of small molecule synthesis. This result also highlights the power of down-selection as an entry point into large multidimensional search spaces, the distinct advantages of a de novo ML approach for navigating such spaces by generating datasets that evenly reflect the reality of positive and negative data during optimization, and the particular suitability of robotized chemistry for generating high-quality, reproducible data. Future studies will incorporate next-generation ligands and reagents to yield further improved general reaction conditions, creating an actionable path for automated small molecule synthesis to achieve reaction efficiencies approaching that of automated peptide synthesis. This general workflow should be applicable to the optimization of reactions beyond SMC, as it did not require extensive prior literature data to be successful.

REFERENCES AND NOTES

1. R. B. Merrifield, *Science* **150**, 178–185 (1965).
2. M. H. Caruthers, *Science* **230**, 281–285 (1985).
3. O. J. Plante, E. R. Palmacci, P. H. Seeberger, *Science* **291**, 1523–1527 (2001).
4. I. W. Davies, *Nature* **570**, 175–181 (2019).
5. D. T. Ahneman, J. G. Estrada, S. Lin, S. D. Dreher, A. G. Doyle, *Science* **360**, 186–190 (2018).
6. C. W. Coley *et al.*, *Science* **365**, eaax1566 (2019).
7. M. Christensen *et al.*, *Commun. Chem.* **4**, 112 (2021).
8. B. J. Shields *et al.*, *Nature* **590**, 89–96 (2021).
9. A. B. Clayton *et al.*, *React. Chem. Eng.* **4**, 1545–1554 (2019).
10. P. A. Cox, A. G. Leach, A. D. Campbell, G. C. Lloyd-Jones, *J. Am. Chem. Soc.* **138**, 9145–9157 (2016).
11. P. A. Cox *et al.*, *J. Am. Chem. Soc.* **139**, 13156–13165 (2017).
12. H. L. D. Hayes *et al.*, *J. Am. Chem. Soc.* **143**, 14814–14826 (2021).
13. W. Beker *et al.*, *J. Am. Chem. Soc.* **144**, 4819–4827 (2022).
14. D. M. Knapp, E. P. Gillis, M. D. Burke, *J. Am. Chem. Soc.* **131**, 6961–6963 (2009).
15. J. Li *et al.*, *Science* **347**, 1221–1226 (2015).
16. A. Buitrago Santanilla *et al.*, *Science* **347**, 49–53 (2015).
17. A.-C. Bédard *et al.*, *Science* **361**, 1220–1225 (2018).
18. J. M. Granda, L. Donina, V. Dragone, D.-L. Long, L. Cronin, *Nature* **559**, 377–381 (2018).
19. S. Lin *et al.*, *Science* **361**, eaar6236 (2018).
20. D. Perera *et al.*, *Science* **359**, 429–434 (2018).
21. M. Trobe, M. D. Burke, *Angew. Chem. Int. Ed.* **57**, 4192–4214 (2018).
22. S. Steiner *et al.*, *Science* **363**, eaav2211 (2019).
23. S. Chatterjee, M. Guidi, P. H. Seeberger, K. Gilmore, *Nature* **579**, 379–384 (2020).
24. S. H. M. Mehr, M. Craven, A. I. Leonov, G. Keenan, L. Cronin, *Science* **370**, 101–108 (2020).
25. C. Liu *et al.*, *Nat. Chem.* **13**, 451–457 (2021).
26. D. J. Blair *et al.*, *Nature* **604**, 92–97 (2022).
27. V. Fasano *et al.*, ChemRxiv [Preprint] (2020). https://doi.org/10.26434/chemrxiv-2022-zwctv-v2.
28. A. Bender *et al.*, *Nat. Rev. Chem.* **6**, 428–442 (2022).
29. D. Bajusz, A. Rácz, K. Héberger, *J. Cheminform.* **7**, 20 (2015).
30. F. S. Emami *et al.*, *Angew. Chem. Int. Ed.* **54**, 10797–10801 (2015).
31. Y. Gong, D. Xue, G. Chuai, J. Yu, Q. Liu, *Chem. Sci.* **12**, 14459–14472 (2021).
32. M. Wistuba, J. Grabocka, arXiv:2101.07667 [cs.LG] (2021).
33. J. Bowden, J. Song, Y. Chen, Y. Yue, T. A. Desautels, "Deep kernel Bayesian optimization," 37th Conference on Uncertainty in Artificial Intelligence (UAI 2021), 27 to 30 July 2021.
34. T. Klucznik *et al.*, *Chem* **4**, 522–532 (2018).
35. B. Mikulak-Klucznik *et al.*, *Nature* **588**, 83–88 (2020).
36. F. Strieth-Kalthoff *et al.*, *Angew. Chem. Int. Ed.* **61**, e202204647 (2022).
37. D. Butina, *J. Chem. Inf. Comput. Sci.* **39**, 747–750 (1999).
38. N. H. Angello *et al.*, Closed-loop optimization of general conditions for heteroaryl Suzuki coupling, version 0.1.2, Zenodo (2022); https://doi.org/10.5281/zenodo.7099435.
39. N. H. Angello *et al.*, Closed-loop optimization of general conditions for heteroaryl Suzuki coupling, version 2, Zenodo (2022); https://doi.org/10.5281/zenodo.7106075.
40. verysure, P. Schleich, aspuru-guzik-group/b3: Release for Science Publication, version 1.0, Zenodo (2022); https://doi.org/10.5281/zenodo.7094835.
41. N. H. Angello *et al.*, Closed-loop optimization of general conditions for heteroaryl Suzuki coupling, version 1.0, Zenodo (2022); https://doi.org/10.5281/zenodo.6517012.

ACKNOWLEDGMENTS

Funding: This work was supported by the Defense Advanced Research Projects Agency under the Accelerated Molecular Discovery Program (cooperative agreement no. HR00111920027 dated 1 August 2019) to M.D.B., B.A.G., and A.A.-G. The content of the information presented in this work does not necessarily reflect the position or the policy of the US government. This work was also supported by funding from the Molecule Maker Lab Institute: An AI Research Institutes program supported by NSF under award no. 2019897 to C.M.S. Any opinions, findings, and conclusions or recommendations expressed in this material are those of the author(s) and do not necessarily reflect those of the National Science Foundation. N.H.A. was supported by the Department of Defense (DoD) through the National Defense Science and Engineering Graduate (NDSEG) Fellowship Program. B.A.G. was supported by the Institute for Basic Science, Korea (project code IBS-R020-D1). **Author contributions:** N.H.A., V.R., W.B., A.W., R.R., B.A.G., and M.D.B. conceived of the study. N.H.A. and E.R.J. developed and validated the automated synthesizer. V.R. and N.H.A. performed the automated synthesis experiments. V.R. and N.H.A. purified, characterized, and generated response factor curves for new compounds. W.B., A.W., R.R., and B.A.G developed the closed-loop machine-learning strategy, building block clustering, and chemical space quantifications. N.H.A. and T.C.W. data mined the substrate scope building block set. M.D.B., B.A.G., A.A.-G., and C.M.S. supervised the research. The manuscript was written by N.H.A., V.R., W.B., A.W., R.R., B.A.G., and M.D.B., with contributions from all other authors. **Competing interests:** The University of Illinois has filed patent applications related to MIDA boronates (US20170002026A1, US9845317B2, WO2011103435A3, and US20160207943A1 with M.D.B. as inventor). A.A.-G. is chief visionary officer and board member of Kebotix, Inc., a company that carries out closed-loop molecular materials discovery. **Data and materials availability:** All data and code generated as part of this study are freely accessible either in the supplementary materials or in open repositories. Code for the simulation example, model selection, and substrates clusterization as well machine- and human-readable versions of the reaction data are freely accessible at Zenodo (*38*). The automated synthesis code, machine parts list and build guide, datamined commercially available building block set, checklist for reporting and evaluating machine learning models, and tabulated numerical data underlying Figs. 2 to 4 are deposited at Zenodo (*39*). The code used in the building block selection process is available at Zenodo (*40*). All code related to the closed-loop optimization is freely available at Zenodo (*41*). **License information:**

SUPPLEMENTARY MATERIALS

science.org/doi/10.1126/science.adc8743
Materials and Methods
Supplementary Text
Figs. S1 to S56
Tables S1 to S3
References (*42–50*)

Submitted 5 May 2022; resubmitted 23 August 2022
Accepted 29 September 2022
10.1126/science.adc8743

SYNTHETIC BIOLOGY

Mirror-image T7 transcription of chirally inverted ribosomal and functional RNAs

Yuan Xu[1,2,3] and Ting F. Zhu[2,3]*

To synthesize a chirally inverted ribosome with the goal of building mirror-image biology systems requires the preparation of kilobase-long mirror-image ribosomal RNAs that make up the structural and catalytic core and about two-thirds of the molecular mass of the mirror-image ribosome. Here, we chemically synthesized a 100-kilodalton mirror-image T7 RNA polymerase, which enabled efficient and faithful transcription of the full-length mirror-image 5*S*, 16*S*, and 23*S* ribosomal RNAs from enzymatically assembled long mirror-image genes. We further exploited the versatile mirror-image T7 transcription system for practical applications such as biostable mirror-image riboswitch sensor, long-term storage of unprotected kilobase-long L-RNA in water, and L-ribozyme–catalyzed L-RNA polymerization to serve as a model system for basic RNA research.

More than 160 years after Louis Pasteur's discovery of molecular chirality and proposal of a chirally inverted form of life (*1*), mirror-image life has not been discovered in nature. The laboratory realization of in vitro mirror-image biology systems with D-amino acids and L-nucleic acids as the building blocks (as opposed to the natural-chirality L-amino acids and D-nucleic acids) presents unique opportunities but remains challenging. An important part of this effort is establishing a mirror-image version of the central dogma of molecular biology (*2*, *3*). After mirror-image DNA replication, transcription, and reverse transcription (*2*, *4–8*), the next step is to realize mirror-image translation (Fig. 1A) (*3*, *9*, *10*). This requires high-quality long L-RNAs such as the kilobase-long mirror-image ribosomal RNAs (rRNAs), which make up the structural and catalytic core of the >2-MDa mirror-image ribosome.

The chemical synthesis of high-quality long L-RNAs remains difficult because traditional phosphoramidite chemistry only allows efficient RNA synthesis of up to 60 to 70 nucleotides (nt) (*11*). One way to overcome this limitation is through enzymatic transcription by mirror-image polymerases. We previously used a Y12S mutant of the mirror-image *Sulfolobus solfataricus* P2 DNA polymerase IV (D-Dpo4-5m-Y12S) to transcribe a 120-nt mirror-image *Escherichia coli* (*E. coli*) 5*S* rRNA (*7*). Additionally, cross-chiral ribozymes have been developed to polymerize L-RNAs (*12*, *13*). However, both systems suffer from low efficiency and fidelity, and require single-stranded L-DNA or L-RNA templates, which are difficult to prepare and remove from the polymerized L-RNAs.

An alternative is to synthesize a mirror-image version of the bacteriophage T7 RNA polymerase, which is a widely used workhorse enzyme

---

[1] School of Life Sciences, Tsinghua-Peking Center for Life Sciences, Beijing Frontier Research Center for Biological Structure, Tsinghua University, Beijing, China. [2] School of Life Sciences, Research Center for Industries of the Future, Westlake University, Hangzhou, Zhejiang, China. [3] Westlake Laboratory of Life Sciences and Biomedicine, Hangzhou, Zhejiang, China.
*Corresponding author. Email: tzhu@westlake.edu.cn

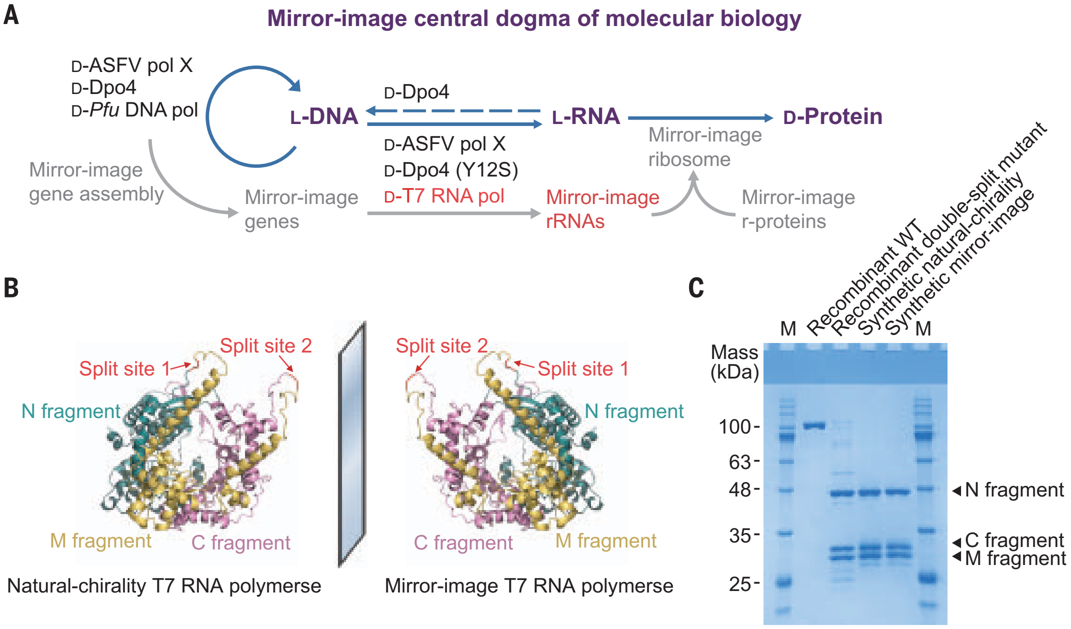

Fig. 1. Synthetic natural-chirality and synthetic mirror-image T7 RNA polymerases. (**A**) Mirror-image version of the central dogma of molecular biology, including mirror-image DNA replication, transcription, reversetranscription, and translation (blue arrows), and the role of the synthetic mirror-image T7 RNA polymerase in transcribing the mirror-image rRNAs (shown in red) to be assembled with the mirror-image ribosomal proteins (r-proteins) into a mirror-image ribosome. (**B**) Structure of the WT T7 RNA polymerase (Protein Data Bank ID: 1CEZ) in natural-chirality and mirror-image forms. The N fragment is shown in green, the M fragment in yellow, and the C fragment in pink, with the amino acids at the two split sites (K363 and P364, N601 and T602) shown in red. (**C**) Recombinant WT, recombinant double-split mutant, synthetic natural-chirality, and synthetic mirror-image T7 RNA polymerases analyzed by SDS-PAGE and stained by Coomassie brilliant blue. M, protein marker.

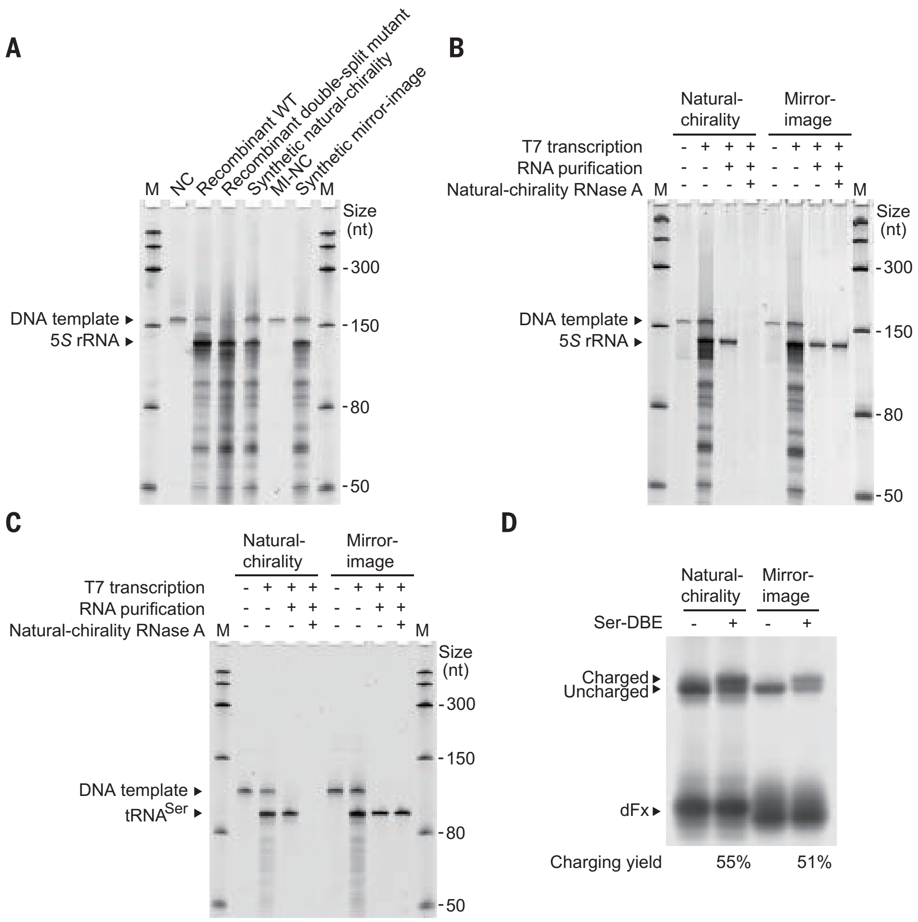

Fig. 2. Mirror-image T7 transcription of short L-RNAs. (**A**) Transcription of the natural-chirality and mirror-image 122-nt 5*S* rRNAs from the double-stranded D- or L-DNA template by the recombinant WT, recombinant double-split mutant, synthetic natural-chirality, and synthetic mirror-image T7 RNA polymerases, respectively, analyzed by denaturing PAGE and stained by SYBR green II. NC and MI-NC, negative controls without natural-chirality or mirror-image T7 RNA polymerase, respectively; M, Low Range ssRNA ladder. (**B** and **C**) Transcription of the natural-chirality and mirror-image 122-nt 5*S* rRNAs (B) and 90-nt $\text{tRNAs}^{\text{Ser}}$ (C) from the double-stranded D- or L-DNA template by the synthetic natural-chirality and synthetic mirror-image T7 RNA polymerases, respectively, purified by denaturing PAGE, treated by natural-chirality RNase A, analyzed by denaturing PAGE, and stained by SYBR green II. M, Low Range ssRNA ladder. (**D**) Natural-chirality and mirror-image dFx charging of L- or D-serine onto the natural-chirality and mirror-image $\text{tRNAs}^{\text{Ser}}$ with L- or D-Ser-DBE, respectively, analyzed by acid PAGE and stained by SYBR green II.

for both in vitro and in vivo transcription in the laboratory because of its excellent efficiency, fidelity, and promoter specificity (*14*). The T7 RNA polymerase uses double-stranded DNA templates for transcription, the mirror-image version of which can be readily assembled by mirror-image polymerase chain reaction (PCR) (*4*–*6*, *8*). However, the full-length T7 RNA polymerase contains 883 amino acids, beyond the general size limit for chemical protein synthesis that combines solid-phase peptide synthesis (SPPS) (*15*) with native chemical

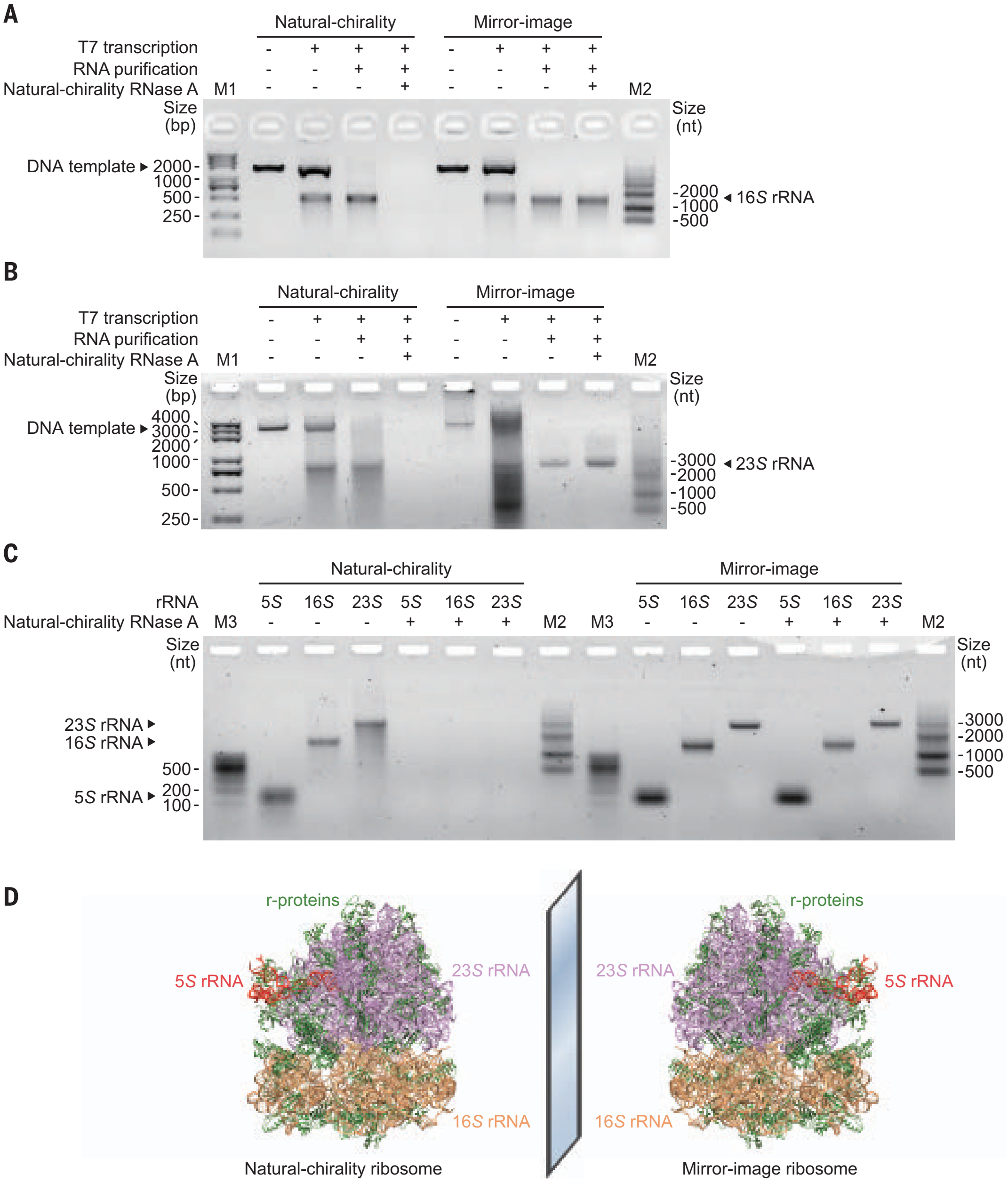

Fig. 3. Mirror-image T7 transcription and purification of kilobase-long mirror-image rRNAs. (**A** and **B**) Transcription of the natural-chirality and mirror-image 1.5-kb 16*S* (A) and 2.9-kb 23*S* (B) rRNAs from the double-stranded D- or L-DNA template by the synthetic natural-chirality and synthetic mirror-image T7 RNA polymerases, respectively, purified by low-melting-point agarose gel electrophoresis and β-agarase I digestion, treated by natural-chirality RNase A, analyzed by agarose gel electrophoresis, and stained by ExRed. M1, Trans2K Plus DNA marker; M2, RNA marker RL6,000. (**C**) Gel-purified natural-chirality and mirror-image 122-nt 5*S*, 1.5-kb 16*S*, and 2.9-kb 23*S* rRNAs treated by natural-chirality RNase A, analyzed by agarose gel electrophoresis, and stained by ExRed. M2, RNA marker RL6,000; M3, RNA marker RL1,000. (**D**) Structure of the *T. thermophilus* ribosome (Protein Data Bank ID: 4V4P) in natural-chirality and mirror-image forms, showing the 5S rRNA in red, 16S rRNA in gold, 23S rRNA in pink, and r-proteins in green.

ligation (NCL) (*16*), enabling the synthesis of various mirror-image enzymes (*2*, *5*, *6*, *17*–*21*) typically smaller than ~400 amino acids, or ~45 kDa. Recently, we applied split-protein design and systematic isoleucine substitution to facilitate the total chemical synthesis of a 90-kDa high-fidelity mirror-image *Pfu* DNA polymerase, which enabled the accurate assembly of a 1.5-kb mirror-image 16*S* rRNA gene (*8*). Although we also developed a mutant *Pfu* DNA polymerase for transcribing RNA, the suboptimal transcription efficiency and difficulty in preparing long single-stranded L-DNA templates will likely make this approach impractical (*8*). Here, we set out to synthesize a 100-kDa mirror-image T7 RNA polymerase using split-protein design and systematic isoleucine substitution and test its ability to efficiently and faithfully transcribe high-quality long L-RNAs such as the mirror-image 5*S*, 16*S*, and 23*S* rRNAs and various functional L-RNAs.

Results

Design and synthesis of a 100-kDa mirror-image T7 RNA polymerase

Split-protein design divides a large (natural-chirality or mirror-image) protein into two or more smaller split-protein fragments that can co-fold in vitro into a functionally intact enzyme (*8*). Many enzymes have naturally occurring or engineered split versions, including the T7 RNA polymerase (*22*, *23*). However, some of the previously reported split sites alter its transcription efficiency (*22*) or are near the N or C terminus of the polymerase (*22*, *23*), resulting in split-protein fragments larger than 400 amino acids, which are difficult to chemically synthesize. We designed a double-split version of the T7 RNA polymerase with a previously reported split site between N601 and T602 (*23*) and a newly discovered split site between K363 and P364 in a solvent-exposed loop, dividing the 883–amino acid polymerase into three split-protein fragments: the 363–amino acid N fragment, the 238–amino acid M fragment, and the 282–amino acid C fragment (Fig. 1B). Additionally, we substituted 14 of the 51 isoleucines in the polymerase with valine, leucine, and methionine (fig. S1 and table S1) to facilitate the chemical protein synthesis and to reduce the D-amino acid costs (*8*).

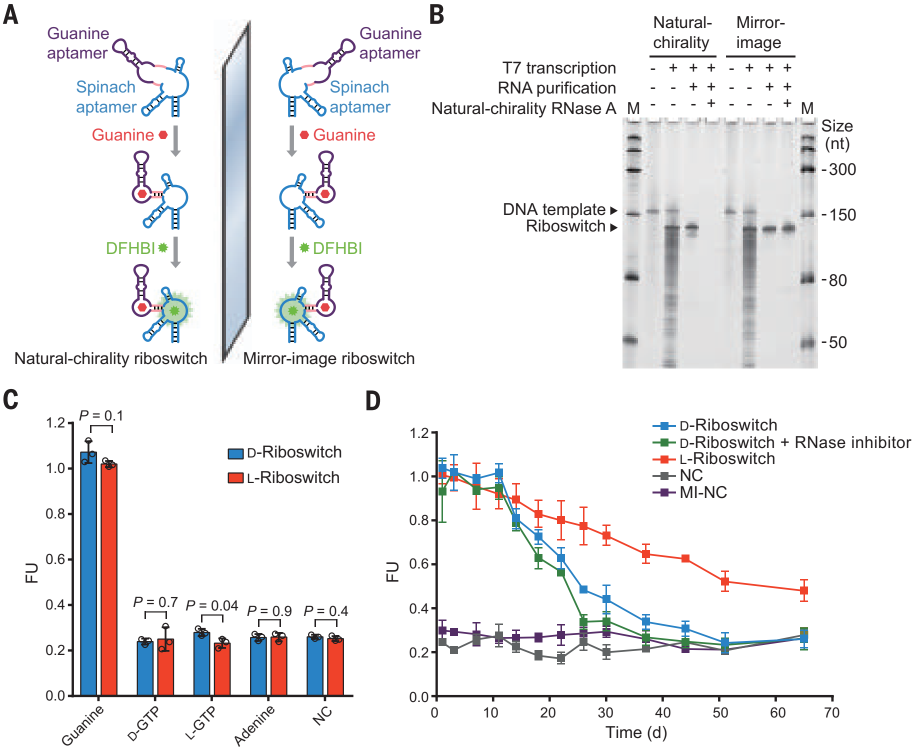

Fig. 4. Mirror-image riboswitch sensor. (**A**) Schematic overview of the natural-chirality and mirror-image riboswitch sensors by fusing a guanine aptamer (purple) with a Spinach aptamer (blue) through a "transducer" stem sequence (pink). (**B**) Transcription of the natural-chirality and mirror-image 130-nt riboswitch sensors from the double-stranded D- or L-DNA template by the synthetic natural-chirality and synthetic mirror-image T7 RNA polymerases, respectively, purified by denaturing PAGE, treated by natural-chirality RNase A, analyzed by denaturing PAGE, and stained by SYBR green II. M, Low Range ssRNA ladder. (**C**) Fluorescence intensities measured at 500 nm of the natural-chirality and mirror-image riboswitch sensors incubated with DFHBI and guanine, D-GTP, L-GTP, and adenine in a buffer prepared with DEPC-treated water and RNase-free reagents at 37°C for 30 min. NC, negative control with the natural-chirality or mirror-image riboswitch sensor but without guanine; FU, fluorescence unit. Data are presented as mean ± SD ($n = 3$) with individual data points. *P* values were calculated by the Student's two-tailed *t* test. (**D**) Fluorescence intensities measured at 500 nm of the natural-chirality riboswitch sensor without or with RNase inhibitor and of the mirror-image riboswitch sensor without RNase inhibitor incubated with DFHBI and guanine in a buffer prepared with DEPC-treated water and RNase-free reagents at 37°C for up to 65 days and longitudinally measured at selected time points. NC and MI-NC, negative controls with the natural-chirality or mirror-image riboswitch sensor but without guanine, respectively; FU, fluorescence unit. Data are presented as mean ± SD ($n = 3$).

We next biochemically validated the design by comparing the transcription efficiencies of the recombinant wild-type (WT) and recombinant double-split mutant (containing 14 isoleucine substitutions) T7 RNA polymerases at various enzyme concentrations with a double-stranded D-DNA template, and observed similar transcription efficiencies between them (fig. S2).

We then performed total chemical synthesis of the double-split mutant version of both the natural-chirality and mirror-image T7 RNA polymerases (hereafter referred to as the synthetic natural-chirality and synthetic mirror-image T7 RNA polymerases, respectively). The N, M, and C fragments of the natural-chirality and mirror-image polymerases were each divided into five to eight peptide segments ranging from 20 to 76 amino acids in length (figs. S3 to S6 and table S2). All of the peptide segments were prepared by 9-fluorenylmethoxycarbonyl (Fmoc)-SPPS, purified by reversed-phase high-performance liquid chromatography (RP-HPLC), and assembled by hydrazide-based NCL (*24*), followed by metal-free radical-based desulfurization (*25*) to convert unprotected cysteine to alanine (*26*). After the synthesis, ligation, purification, and lyophilization (figs. S7 to S55), the N, M, and C fragments of the natural-chirality and mirror-image polymerases were obtained at milligram scales with the expected molecular masses of 41.4, 26.8, and 31.5 kDa, respectively, totaling ~100 kDa (table S2). Both the synthetic natural-chirality and synthetic mirror-image T7 RNA polymerases were folded in vitro by dialysis, as validated by 8-anilino-1-naphthalene sulfonate (ANS) fluorescence (fig. S56), and analyzed by SDS-polyacrylamide gel electrophoresis (SDS-PAGE) (Fig. 1C).

Mirror-image T7 transcription of short L-RNAs

We tested the transcription activity of the synthetic mirror-image T7 RNA polymerase with a double-stranded L-DNA template coding for the *Thermus thermophilus* (*T. thermophilus*) *5S* rRNA (tables S5 to S7) assembled by mirror-image PCR (*5*), and found that it was capable of transcribing the full-length 122-nt mirror-image *5S* rRNA (Fig. 2A) despite having lower efficiency than the recombinant WT, recombinant double-split mutant, and synthetic natural-chirality polymerases (fig. S57). The gel-purified 122-nt mirror-image *5S* rRNA was resistant to natural-chirality ribonuclease A (RNase A) digestion (Fig. 2B). Because of the lack of high-fidelity mirror-image reverse transcriptase and Sanger sequencing tools, we were unable to evaluate the transcription fidelity of the synthetic mirror-image T7 RNA polymerase directly, and thus we examined the transcription fidelity of the synthetic natural-chirality T7 RNA polymerase as an estimate for the mirror-image version. We reverse-transcribed the DNase-treated transcription product of the synthetic natural-chirality T7 RNA polymerase by a high-fidelity reverse transcriptase, followed by high-fidelity PCR and Sanger sequencing (fig. S58). We measured the error rate of the synthetic natural-chirality T7 RNA polymerase on the order of 10^{-4}, consistent with those of the recombinant WT and recombinant double-split mutant polymerases, as well as the WT polymerase reported in previous studies (table S3) (*27*).

Toward realizing mirror-image translation, we previously used a mirror-image version of the 46-nt dinitro-flexizyme (dFx) (*28*) to charge three D-amino acids (D-lysine, D-alanine, and D-phenylalanine) and the achiral glycine onto the corresponding mirror-image transfer RNAs (tRNAs) transcribed by D-Dpo4-5m-Y12S (*10*). However, D-Dpo4-5m-Y12S was unable to transcribe certain mirror-image tRNA sequences, such as the 90-nt mirror-image serine tRNA (tRNA^{Ser}) (fig. S59), likely because of the length and extensive secondary structure of the single-stranded L-DNA template. We addressed this issue by mirror-image T7 transcription with a double-stranded L-DNA template coding for tRNA^{Ser} (tables S5 to S7) assembled by mirror-image PCR (*5*). We found that the transcription efficiency of the 90-nt mirror-image tRNA^{Ser} by the synthetic mirror-image T7 RNA polymerase was substantially higher than that by D-Dpo4-5m-Y12S (fig. S59). The gel-purified 90-nt mirror-image tRNA^{Ser} was resistant to natural-chirality RNase A digestion (Fig. 2C). Furthermore, we charged D-serine onto the mirror-image tRNA^{Ser} using the mirror-image

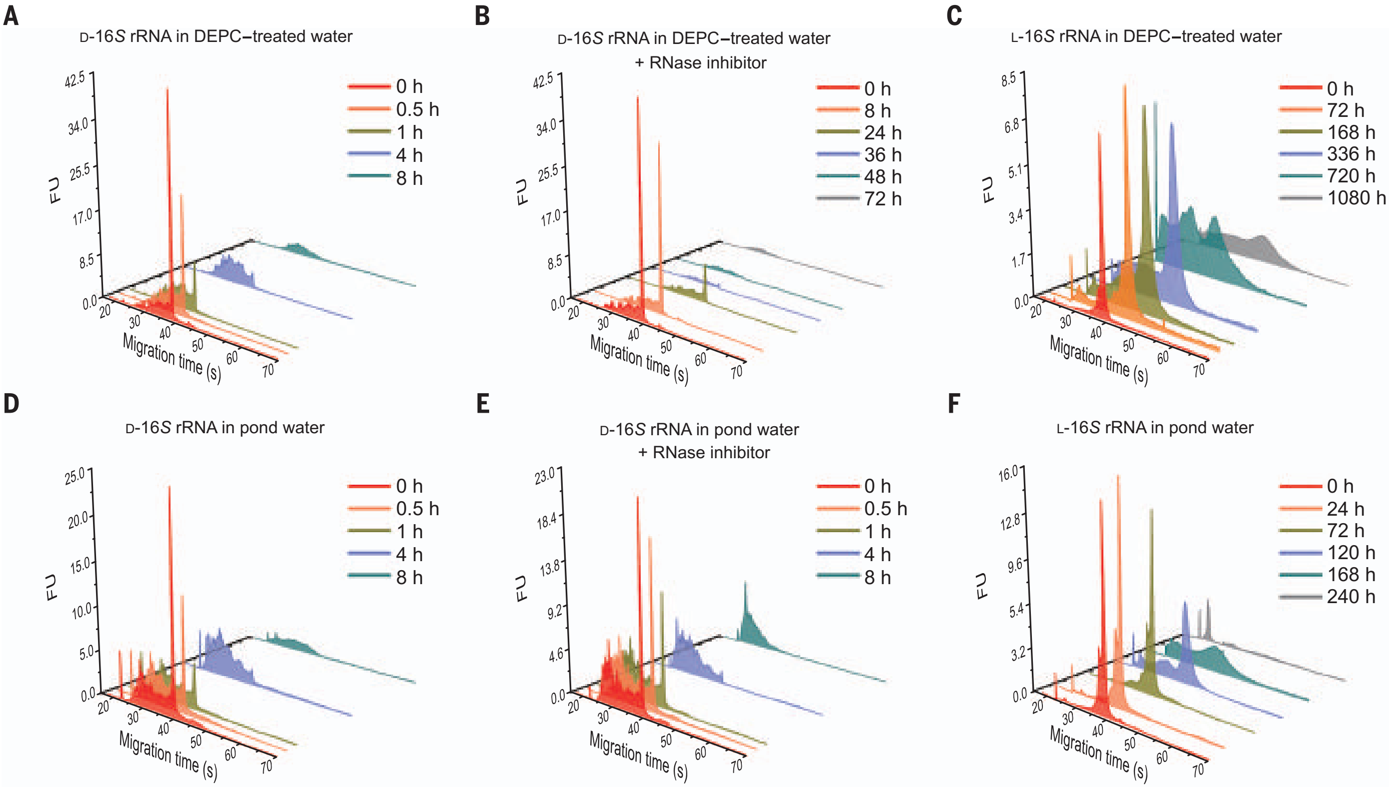

Fig. 5. Stability of kilobase-long L-RNA. (**A** and **B**) Electropherograms of the 1.5-kb natural-chirality 16*S* rRNA incubated in DEPC-treated water at 37°C without (A) or with (B) RNase inhibitor for up to 8 or 72 hours, respectively, and longitudinally measured at selected time points. (**C**) Electropherograms of the 1.5-kb mirror-image 16*S* rRNA incubated in DEPC-treated water at 37°C without RNase inhibitor for up to 1080 hours and longitudinally measured at selected time points. (**D** and **E**) Electropherograms of the 1.5-kb natural-chirality 16*S* rRNA incubated in pond water at 37°C without (D) or with (E) RNase inhibitor for up to 8 hours and longitudinally measured at selected time points. (**F**) Electropherograms of the 1.5-kb mirror-image 16*S* rRNA incubated in pond water at 37°C without RNase inhibitor for up to 240 hours and longitudinally measured at selected time points. FU, fluorescence unit. The corresponding data are also shown in figs. S65 and S67, with the full-length RNA peaks appearing within the migration time of 35 to 45 s.

dFx and D-Ser-3,5-dinitrobenzyl ester (Ser-DBE), with a charging yield similar to that of the natural-chirality version (Fig. 2D).

Mirror-image T7 transcription and purification of kilobase-long mirror-image rRNAs

Encouraged by the results of the transcription and purification of short L-RNAs, we performed the mirror-image T7 transcription of the kilobase-long mirror-image rRNAs. Using double-stranded L-DNA templates coding for the *T. thermophilus* 16*S* and 23*S* rRNAs (tables S5 to S7) assembled by mirror-image PCR (fig. S60) (*5*, *8*) and through further optimizing the transcription conditions, particularly for 23*S* rRNA (figs. S61 and S62), we transcribed the full-length mirror-image 1.5-kb 16*S* and 2.9-kb 23*S* rRNAs by the synthetic mirror-image T7 RNA polymerase (Fig. 3, A and B). Meanwhile, we also transcribed the natural-chirality rRNAs by the synthetic natural-chirality T7 RNA polymerase (Fig. 3, A and B).

Because a mirror-image DNase to digest L-DNA templates is unavailable, we purified the kilobase-long mirror-image 16*S* and 23*S* rRNAs from the double-stranded L-DNA templates by low-melting-point agarose gel electrophoresis and β-agarase I digestion (Fig. 3, A and B). The kilobase-long natural-chirality rRNAs and RNA markers were partially degraded despite our best effort to avoid natural-chirality RNase contamination and use of RNase inhibitor in conjunction, whereas the mirror-image 5*S*, 16*S*, and 23*S* rRNAs were stable (Fig. 3C), suggesting that the assembly of the mirror-image ribosome (Fig. 3D) could be more experimentally convenient to perform than the natural-chirality version because of the stability of the mirror-image rRNAs. We further evaluated the transcription fidelity of the synthetic natural-chirality T7 RNA polymerase (again, as an estimate for the mirror-image version) with double-stranded D-DNA templates coding for the 5*S*, 16*S*, and 23*S* rRNAs, and measured error rates on the order of 10^{-4}, consistent with that of the WT polymerase reported in previous studies (table S4) (*27*).

Mirror-image riboswitch sensor

Inspired by the broad utility of T7 transcription in the laboratory, we explored the practical applications of the mirror-image T7 transcription system through developing a 130-nt mirror-image riboswitch sensor by fusing a mirror-image guanine aptamer with a mirror-image Spinach aptamer according to the previously reported design (Fig. 4A) (*29*). Because both guanine and 3,5-difluoro-4-hydroxybenzylidene imidazolinone [DFHBI, the small-molecule fluorophore of the Spinach aptamer (*30*)] are achiral, the natural-chirality and mirror-image riboswitch sensors would be expected to exhibit identical binding characteristics. We transcribed the mirror-image riboswitch sensor by the synthetic mirror-image T7 RNA polymerase with a double-stranded L-DNA template (tables S5 to S7) assembled by mirror-image PCR (*5*). The gel-purified 130-nt mirror-image riboswitch sensor was resistant to natural-chirality RNase A digestion (Fig. 4B). We found that the natural-chirality and mirror-image riboswitch sensors exhibited nearly identical fluorescence intensities when incubated with the same concentration of guanine, whereas no apparent binding was detected between the natural-chirality and mirror-image riboswitch sensors with D- or L-guanosine triphosphate (GTP) and adenine at the same concentration (Fig. 4C).

When we performed long-term incubation of both the natural-chirality and mirror-image riboswitch sensors under presumed "RNase-free" conditions in a buffer prepared with diethylpyrocarbonate (DEPC)–treated water and RNase-free reagents at 37°C, we observed that the mirror-image riboswitch sensor exhibited a longer estimated half-life than the natural-chirality version without or with RNase inhibitor (Fig. 4D and fig. S63). We validated this result by denaturing PAGE analysis of the natural-chirality and mirror-image riboswitch sensors incubated under the same conditions for up to 65 days, and found that the relative full-length band intensities correlated well with relative fluorescence intensities (fig. S64). We attribute the difference in the stability of the natural-chirality and mirror-image riboswitch sensors to the extraordinary efficiency, stability, and pervasiveness of natural-chirality RNase in the environment (*31*), to which the natural-chirality riboswitch is highly sensitive and the mirror-image riboswitch is resistant.

Stability of kilobase-long L*-RNA*

We then tested the stability of the unprotected kilobase-long L-RNA in various environments. We incubated the gel-purified natural-chirality and mirror-image 1.5-kb 16*S* rRNAs under presumed RNase-free conditions in DEPC-treated water at 37°C. The natural-chirality 16*S* rRNA, in the absence of RNase inhibitor, was partially degraded after 1 hour and completely degraded after 4 hours (Fig. 5A and figs. S65A and S68). Despite the use of RNase

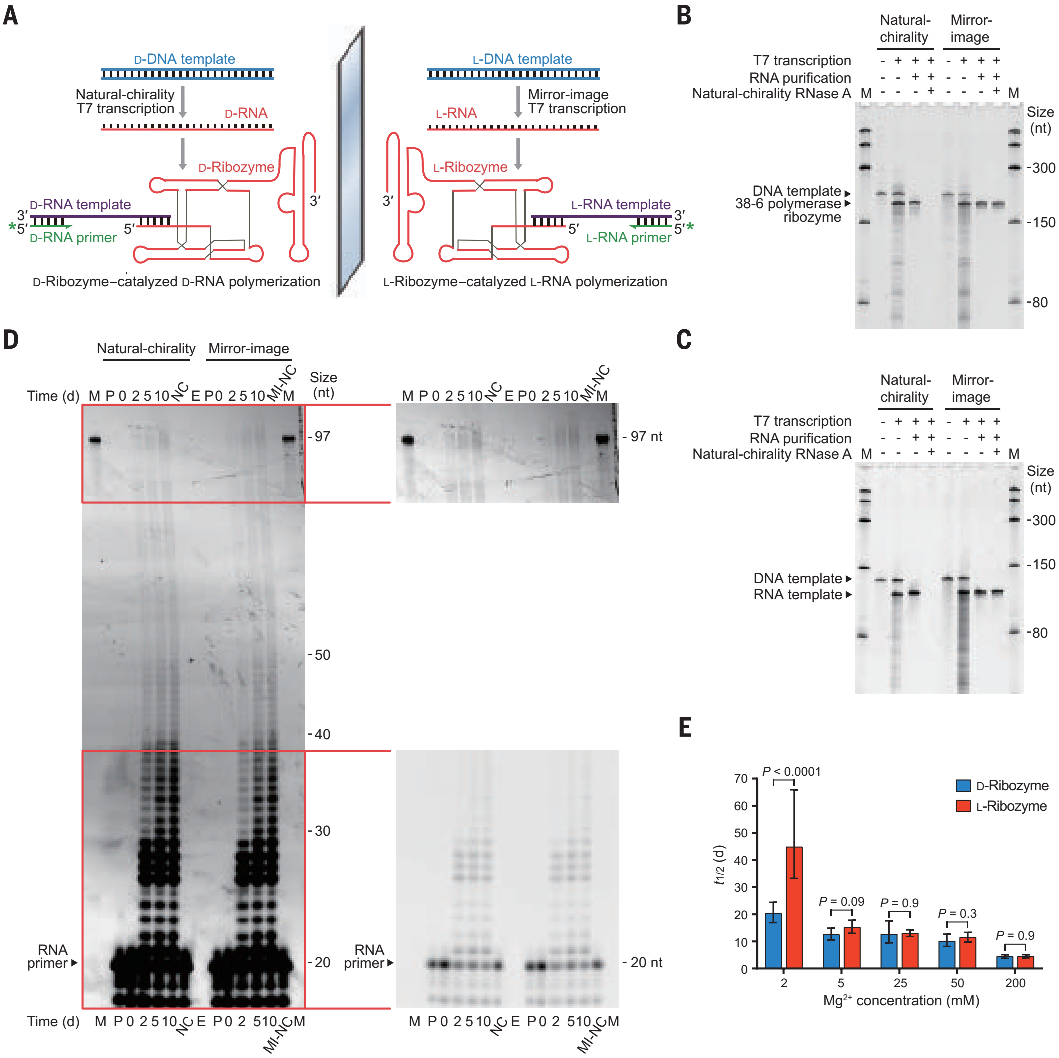

Fig. 6. L-Ribozyme–catalyzed L-RNA polymerization. (**A**) Schematic overview of the natural-chirality and mirror-image ribozyme–catalyzed RNA polymerization using the natural-chirality or mirror-image 38-6 polymerase ribozyme (red) on D- or L-RNA template (purple), prepared by natural-chirality or mirror-image T7 transcription from the double-stranded D- or L-DNA template (blue), respectively, with D- or L-RNA primer (green). (**B** and **C**) Transcription of the natural-chirality and mirror-image 182-nt 38-6 polymerase ribozymes (B) and 112-nt RNA templates (C) from the double-stranded D- or L-DNA template by the synthetic natural-chirality and synthetic mirror-image T7 RNA polymerases, respectively, purified by denaturing PAGE, treated by natural-chirality RNase A, analyzed by denaturing PAGE, and stained by SYBR green II. M, Low Range ssRNA ladder. (**D**) Natural-chirality and mirror-image ribozyme–catalyzed RNA polymerization of the 97-nt class I ligase ribozyme with the natural-chirality or mirror-image 38-6 polymerase ribozyme, RNA template, and 5′-FAM-biotin–labeled D- or L-RNA primer incubated with D- or L-NTPs in 200 mM $MgCl_2$, pH 8.3, at 17°C for up to 10 days and analyzed by denaturing PAGE. Contrast-adjusted images are shown on the right to more clearly show the RNA primers and full-length polymerization products, respectively. NC and MI-NC, negative controls without natural-chirality or mirror-image 38-6 polymerase ribozyme, respectively; E, two empty lanes; P, 20-nt 5′-FAM-biotin–labeled D- or L-RNA primer; M, 97-nt 5′-FAM–labeled D-RNA marker. (**E**) Comparison of estimated half-lives ($t_{1/2}$) of the natural-chirality and mirror-image 38-6 polymerase ribozymes at various Mg^{2+} concentrations. Data are presented as best-fit values and 95% confidence intervals, and the corresponding data for curve fitting are also shown in fig. S73. *P* values were calculated by the extra sum-of-squares *F* test.

inhibitor, it was partially degraded after 24 hours and completely degraded after 48 hours (Fig. 5B and figs. S65B and S68). By contrast, no substantial degradation of the mirror-image 16*S* rRNA was observed after 72 hours, with partial degradation observed after 336 hours and complete degradation observed after 720 hours (Fig. 5C and figs. S65C and S68).

Next, we incubated the natural-chirality and mirror-image 16*S* rRNAs in pond water at 37°C, and observed that regardless of the use of RNase inhibitor, the natural-chirality 16*S* rRNA was partially degraded after 1 hour and completely degraded after 4 hours (Fig. 5, D and E, and figs. S67, A and B, and S68). By contrast, no substantial degradation of the mirror-image 16*S* rRNA was observed after 72 hours, with partial degradation observed after 120 hours and complete degradation observed after 168 hours (Fig. 5F and figs. S67C and S68). The degradation pattern of the mirror-image 16*S* rRNA in both DEPC-treated water and pond water was different from that of the natural-chirality 16*S* rRNA (Fig. 5 and figs. S65 to S67) in that the full-length L-RNA peak widened before partial and complete degradation took place. This may provide opportunities for future research to reveal the kinetics and underlying mechanisms for the spontaneous hydrolysis of RNA with different lengths and sequences at various pH values, Mg^{2+} concentrations, and temperatures (*32*) without the interference of natural-chirality RNase–catalyzed degradation.

L-Ribozyme–catalyzed L-RNA polymerization

The biostable L-RNA model system may facilitate in vitro studies on ribozymes, particularly for investigating the origins of life, during which most of the modern RNA-processing machinery such as RNase would be presumably absent. Key to the "RNA world" hypothesis is ribozyme-catalyzed RNA polymerization (*33*). The directed evolution of RNA sequences in vitro has revealed various polymerase ribozymes, including the ~180-nt "24-3" and "38-6" polymerase ribozymes, which are capable of amplifying short RNA sequences and polymerizing a 97-nt class I ligase ribozyme, respectively (*34*, *35*). We transcribed the mirror-image 38-6 polymerase ribozyme and single-stranded L-RNA template coding for the class I ligase ribozyme (hereafter referred to as the L-RNA template) by the synthetic mirror-image T7 RNA polymerase (Fig. 6, A to C) with double-stranded L-DNA templates (tables S5 to S7) assembled by mirror-image PCR (*8*). The gel-purified 182-nt L-ribozyme and 112-nt L-RNA template were both resistant to natural-chirality RNase A digestion (Fig. 6, B and C).

We next used the gel-purified mirror-image 38-6 polymerase ribozyme to polymerize the mirror-image class I ligase ribozyme with a 5′-FAM-biotin–labeled L-RNA primer annealed to the gel-purified L-RNA template (Fig. 6A), incubated with L-nucleoside triphosphates (L-NTPs) in 200 mM $MgCl_2$, pH 8.3, at 17°C for up to 10 days. Compared with the D-ribozyme [which exhibited a polymerization efficiency similar to that reported in previous studies (*35*)], the L-ribozyme was almost equally efficient in extending the L-RNA primer to the full length (Fig. 6D), illustrating the high quality of the mirror-image T7–transcribed L-RNAs. Moreover, we evaluated the stability of the natural-chirality and mirror-image 38-6 polymerase ribozymes, RNA templates, and RNA primers (figs. S69 to S72), and estimated the half-lives of the natural-chirality and mirror-image 38-6 polymerase ribozymes incubated at various Mg^{2+} concentrations. We found that the L-ribozyme exhibited a longer estimated half-life than the natural-chirality version at 2 mM Mg^{2+} concentration (Fig. 6E and fig. S73). With future efforts to discover polymerase ribozymes with lower Mg^{2+} concentration requirements (*36*–*38*), the mirror-image T7–transcribed biostable L-ribozymes may be incubated and evolved in the laboratory for longer periods of time, potentially outperforming their natural-chirality counterparts.

Discussion

The realization of mirror-image T7 transcription may enable a variety of practical applications of high-quality long L-RNAs in diagnostics and therapeutics (*39*–*43*), information storage, computation, imaging, and basic RNA research. Furthermore, the ensemble of efficient mirror-image DNA polymerase, RNA polymerase, reverse transcriptase, and sequencing tools may lead to the realization of a mirror-image selection scheme for the directed evolution and selection of L-RNA aptamers targeting biologically important molecules as potential clinical and research tools (*44*).

Traditional laboratory studies of RNA have been hindered by its rapid degradation resulting from spontaneous hydrolysis and predominantly natural-chirality RNase–catalyzed degradation (*31*), with longer RNAs typically being more vulnerable (Fig. 5 and figs. S65 to S68). Without the interference of natural-chirality RNase–catalyzed degradation, which is virtually unavoidable in laboratory experiments, L-RNAs may serve as an alternative model system for studying RNA spontaneous hydrolysis (*32*). Furthermore, because mirror-image biomolecules behave in a reciprocal manner to their natural-chirality twins, the biostable L-RNA model system may also be applied to a variety of biochemical and biophysical studies in basic RNA research.

To build a mirror-image ribosome that translates D-proteins requires mirror-image rRNAs, tRNAs, mRNAs, r-proteins, and translation factors, the synthesis and in vitro assembly of which can be tested and optimized in the natural-chirality version first, after which the mirror-image version can be synthesized and assembled following the same methodology. Because the mirror-image T7–transcribed L-RNAs contain no RNA modification, the translationally essential modifications of the 16*S* and 23*S* rRNAs (the 5*S* rRNA is known to contain no modifications) (*45*, *46*) can also be validated in the natural-chirality version and may be added either chemically or enzymatically (*11*) to the mirror-image T7–transcribed L-RNAs. Moreover, although the efficiency and fidelity of the synthetic mirror-image T7 RNA polymerase appear sufficient for transcribing the mirror-image rRNAs, tRNAs, and mRNAs for mirror-image translation, the accuracy of mirror-image gene assembly remains to be further improved for preparing high-quality long mirror-image genes (*8*). The realization of mirror-image translation will complete the mirror-image central dogma of molecular biology (Fig. 1A), translating D-proteins and enabling various practical applications such as the directed evolution and selection of biostable D-peptide drugs with a mirror-image version of ribosome or mRNA display (*47*, *48*).

REFERENCES AND NOTES

1. L. Pasteur, *Researches on the Molecular Asymmetry of Natural Organic Products (1860). Alembic Club Reprint No. 14: Edinburgh* (1905).
2. Z. Wang, W. Xu, L. Liu, T. F. Zhu, *Nat. Chem.* **8**, 698–704 (2016).
3. M. Peplow, *ACS Cent. Sci.* **4**, 783–784 (2018).
4. W. Xu *et al*., *Cell Discov.* **3**, 17008 (2017).
5. W. Jiang *et al*., *Cell Discov.* **3**, 17037 (2017).
6. A. Pech *et al*., *Nucleic Acids Res.* **45**, 3997–4005 (2017).
7. M. Wang *et al*., *Chem* **5**, 848–857 (2019).
8. C. Fan, Q. Deng, T. F. Zhu, *Nat. Biotechnol.* **39**, 1548–1555 (2021).
9. J.-J. Ling *et al*., *Angew. Chem. Int. Ed.* **59**, 3724–3731 (2020).
10. J. Chen, M. Chen, T. F. Zhu, *Chem* **7**, 786–798 (2021).
11. Y. Liu *et al*., *Nature* **522**, 368–372 (2015).
12. J. T. Sczepanski, G. F. Joyce, *Nature* **515**, 440–442 (2014).
13. G. A. L. Bare, G. F. Joyce, *J. Am. Chem. Soc.* **143**, 19160–19166 (2021).
14. R. Sousa, S. Mukherjee, *Prog. Nucleic Acid Res. Mol. Biol.* **73**, 1–41 (2003).
15. R. B. Merrifield, *J. Am. Chem. Soc.* **85**, 2149–2154 (1963).
16. P. E. Dawson, T. W. Muir, I. Clark-Lewis, S. B. Kent, *Science* **266**, 776–779 (1994).
17. R. C. Milton, S. C. Milton, S. B. Kent, *Science* **256**, 1445–1448 (1992).
18. L. E. Zawadzke, J. M. Berg, *J. Am. Chem. Soc.* **114**, 4002–4003 (1992).
19. M. T. Weinstock, M. T. Jacobsen, M. S. Kay, *Proc. Natl. Acad. Sci. U.S.A.* **111**, 11679–11684 (2014).
20. A. A. Vinogradov, E. D. Evans, B. L. Pentelute, *Chem. Sci.* **6**, 2997–3002 (2015).
21. J. Weidmann, M. Schnölzer, P. E. Dawson, J. D. Hoheisel, *Cell Chem. Biol.* **26**, 645–651.e3 (2019).
22. R. A. Ikeda, C. C. Richardson, *J. Biol. Chem.* **262**, 3790–3799 (1987).
23. T. H. Segall-Shapiro, A. J. Meyer, A. D. Ellington, E. D. Sontag, C. A. Voigt, *Mol. Syst. Biol.* **10**, 742 (2014).
24. G.-M. Fang *et al*., *Angew. Chem. Int. Ed.* **50**, 7645–7649 (2011).
25. Q. Wan, S. J. Danishefsky, *Angew. Chem. Int. Ed.* **46**, 9248–9252 (2007).
26. L. Z. Yan, P. E. Dawson, *J. Am. Chem. Soc.* **123**, 526–533 (2001).
27. J. Huang, L. G. Brieba, R. Sousa, *Biochemistry* **39**, 11571–11580 (2000).
28. H. Murakami, A. Ohta, H. Ashigai, H. Suga, *Nat. Methods* **3**, 357–359 (2006).
29. J. S. Paige, T. Nguyen-Duc, W. Song, S. R. Jaffrey, *Science* **335**, 1194 (2012).
30. J. S. Paige, K. Y. Wu, S. R. Jaffrey, *Science* **333**, 642–646 (2011).

31. M. R. Green, J. Sambrook, *Cold Spring Harb. Protoc.* **2019**, pdb.top101857 (2019).
32. Y. Li, R. R. Breaker, *J. Am. Chem. Soc.* **121**, 5364–5372 (1999).
33. G. F. Joyce, J. W. Szostak, *Cold Spring Harb. Perspect. Biol.* **10**, a034801 (2018).
34. D. P. Horning, G. F. Joyce, *Proc. Natl. Acad. Sci. U.S.A.* **113**, 9786–9791 (2016).
35. K. F. Tjhung, M. N. Shokhirev, D. P. Horning, G. F. Joyce, *Proc. Natl. Acad. Sci. U.S.A.* **117**, 2906–2913 (2020).
36. J. Attwater, A. Wochner, P. Holliger, *Nat. Chem.* **5**, 1011–1018 (2013).
37. F. Wachowius, P. Holliger, *ChemSystemsChem* **1**, 1–4 (2019).
38. X. Portillo, Y. T. Huang, R. R. Breaker, D. P. Horning, G. F. Joyce, *eLife* **10**, e71557 (2021).
39. J. T. Sczepanski, G. F. Joyce, *J. Am. Chem. Soc.* **135**, 13290–13293 (2013).
40. J. T. Sczepanski, G. F. Joyce, *J. Am. Chem. Soc.* **137**, 16032–16037 (2015).
41. L. Yatime *et al.*, *Nat. Commun.* **6**, 6481 (2015).
42. D. Oberthür *et al.*, *Nat. Commun.* **6**, 6923 (2015).
43. D. Ji, K. Lyu, H. Zhao, C. K. Kwok, *Nucleic Acids Res.* **49**, 7280–7291 (2021).
44. J. Chen, M. Chen, T. F. Zhu, *Nat. Biotechnol.* (2022).
45. R. Guymon, S. C. Pomerantz, P. F. Crain, J. A. McCloskey, *Biochemistry* **45**, 4888–4899 (2006).
46. J. Mengel-Jørgensen *et al.*, *J. Biol. Chem.* **281**, 22108–22117 (2006).
47. L. C. Mattheakis, R. R. Bhatt, W. J. Dower, *Proc. Natl. Acad. Sci. U.S.A.* **91**, 9022–9026 (1994).
48. R. W. Roberts, J. W. Szostak, *Proc. Natl. Acad. Sci. U.S.A.* **94**, 12297–12302 (1997).

ACKNOWLEDGMENTS

We thank J. Chen, M. Chen, Q. Deng, C. Fan, G. Wang, J. Xu, G. Zhang, and R. Zhao for assistance with the experiments. **Funding:** The work was supported by the National Natural Science Foundation of China (grants 21925702 and 32050178), the Research Center for Industries of the Future (RCIF) at Westlake University, the Westlake Education Foundation, the Tencent Foundation, the Tsinghua-Peking Center for Life Sciences (CLS), and the Beijing Frontier Research Center for Biological Structure. **Author contributions:** Y.X. performed the experiments. Both authors analyzed and discussed the results. T.F.Z. designed and supervised the study and wrote the paper. **Competing interests:** A patent application has been filed relating to this work. The authors declare no other competing interests. **Data and materials availability:** All data are available in the main text or the supplementary materials.

SUPPLEMENTARY MATERIALS

science.org/doi/10.1126/science.abm0646
Materials and Methods
Figs. S1 to S73
Tables S1 to S7
References (*49*–*57*)
MDAR Reproducibility Checklist

Submitted 23 August 2021; resubmitted 22 March 2022
Accepted 28 September 2022
10.1126/science.abm0646

REPORTS

PLANETARY SCIENCE

Largest recent impact craters on Mars: Orbital imaging and surface seismic co-investigation

L. V. Posiolova[1]*, P. Lognonné[2], W. B. Banerdt[3], J. Clinton[4], G. S. Collins[5], T. Kawamura[2], S. Ceylan[6], I. J. Daubar[7], B. Fernando[8], M. Froment[2,9], D. Giardini[6], M. C. Malin[1], K. Miljković[10], S. C. Stähler[6], Z. Xu[2], M. E. Banks[11], É. Beucler[12], B. A. Cantor[1], C. Charalambous[13], N. Dahmen[6], P. Davis[14], M. Drilleau[15], C. M. Dundas[16], C. Durán[6], F. Euchner[6], R. F. Garcia[15], M. Golombek[3], A. Horleston[17], C. Keegan[1], A. Khan[6,18], D. Kim[6,19], C. Larmat[9], R. Lorenz[20], L. Margerin[21], S. Menina[2], M. Panning[3], C. Pardo[2], C. Perrin[12], W. T. Pike[13], M. Plasman[2], A. Rajšić[10]†, L. Rolland[22], E. Rougier[9], G. Speth[1], A. Spiga[23], A. Stott[15], D. Susko[1], N. A. Teanby[17], A. Valeh[1], A. Werynski[1], N. Wójcicka[5], G. Zenhäusern[6]

Two >130-meter-diameter impact craters formed on Mars during the later half of 2021. These are the two largest fresh impact craters discovered by the Mars Reconnaissance Orbiter since operations started 16 years ago. The impacts created two of the largest seismic events (magnitudes greater than 4) recorded by InSight during its 3-year mission. The combination of orbital imagery and seismic ground motion enables the investigation of subsurface and atmospheric energy partitioning of the impact process on a planet with a thin atmosphere and the first direct test of martian deep-interior seismic models with known event distances. The impact at 35°N excavated blocks of water ice, which is the lowest latitude at which ice has been directly observed on Mars.

Seismic recordings of hypervelocity impacts (>3 km/s) are rare despite being the most common terrain modification process in the Solar System. Earth is shielded by its atmosphere, consequently there are few seismically recorded ground impacts, and meteoroids that do reach the ground usually travel at terminal subsonic velocity and only form small craters (*1*–*3*). The Apollo Passive Seismic Experiments on the Moon recorded ground motions from artificial impacts, but these had slow relative velocities (<2.6 km/s), with respect to typical impact velocities of comets or asteroids colliding with the Moon, and formed craters smaller than 30 m in diameter (*4*). Larger natural impacts on the Moon were detected but have not been associated with imaged craters (*4*, *5*), and all are expected to be smaller than 100 m in diameter (*6*). On Earth, a multitude of seismic events with known source locations, for example, explosion sources, have been used extensively for evaluating seismic velocity models, even down to the Earth's core (*7*). In contrast, there have been only a few confirmed seismic source locations on Mars (all impacts), but these were small (<12 m in diameter) and near InSight (<300 km away), so the seismic paths only sampled the shallow crust (*8*). The two newly formed impact craters reported here allow for an evaluation of deep interior Mars global velocity models and observations of the dynamics of the hypervelocity impact process.

The notable impacts (Fig. 1) were discovered using the Mars Reconnaissance Orbiter (MRO) Context Camera (CTX) (*9*) and the Seismic Experiment for Interior Structure (SEIS) (*10*) of the Interior Exploration using Seismic Investigations, Geodesy and Heat Transport (InSight) mission (*11*). Our CTX team independently discovered the Amazonis crater that we associated with the S1094b event. The earlier S1000a event, given its similar seismic signature, was then used to direct a search with MRO cameras to find the Tempe impact crater site. Both impacts generated craters >130 m in diameter,

---

[1]Malin Space Science Systems, San Diego, CA, USA. [2]Université Paris Cité, Institut de Physique du Globe de Paris, CNRS, Paris, France. [3]Jet Propulsion Laboratory, California Institute of Technology, Pasadena, CA, USA. [4]Swiss Seismological Service, ETH Zurich, Zurich, Switzerland. [5]Department of Earth Science and Engineering, Imperial College London, London, UK. [6]Institute of Geophysics, ETH Zurich, Zurich, Switzerland. [7]Department of Earth, Environmental, and Planetary Sciences, Brown University, Providence, RI, USA. [8]Department of Earth Sciences, University of Oxford, Oxford, UK. [9]Earth and Environmental Sciences Division, Los Alamos National Laboratory, Los Alamos, NM, USA. [10]Space Science and Technology Centre, School of Earth and Planetary Sciences, Curtin University, Perth, WA, Australia. [11]NASA Goddard Space Flight Center, Greenbelt, MD, USA. [12]Nantes Université, Université Angers, Le Mans Université, CNRS, UMR 6112, Laboratoire de Planétologie et Géosciences, Nantes, France. [13]Department of Electrical and Electronic Engineering, Imperial College London, London, UK. [14]Department of Earth, Planetary, and Space Sciences, University of California, Los Angeles, CA, USA. [15]Institut Supérieur de l'Aéronautique et de l'Espace ISAE-SUPAERO, Toulouse, France. [16]U.S. Geological Survey, Astrogeology Science Center, Flagstaff, AZ, USA. [17]School of Earth Sciences, University of Bristol, Bristol, UK. [18]Physik-Institut, University of Zurich, Zurich, Switzerland. [19]Department of Geology, University of Maryland, College Park, MD, USA. [20]Johns Hopkins Applied Physics Laboratory, Laurel, MD, USA. [21]Institut de Recherche en Astrophysique et Planétologie, Université Toulouse III Paul Sabatier, CNRS, CNES, Toulouse, France. [22]Université Côte d'Azur, Observatoire de la Côte d'Azur, CNRS, IRD, Géoazur, Valbonne, France. [23]Laboratoire de Météorologie Dynamique/IPSL, Sorbonne Université, CNRS, Ecole Normale Supérieure, PSL Research University, Ecole Polytechnique, Paris, France.
***Corresponding author. Email: posiolov@msss.com**
†Present address: Department of Earth, Atmospheric, and Planetary Sciences, Purdue University, West Lafayette, IN, USA.

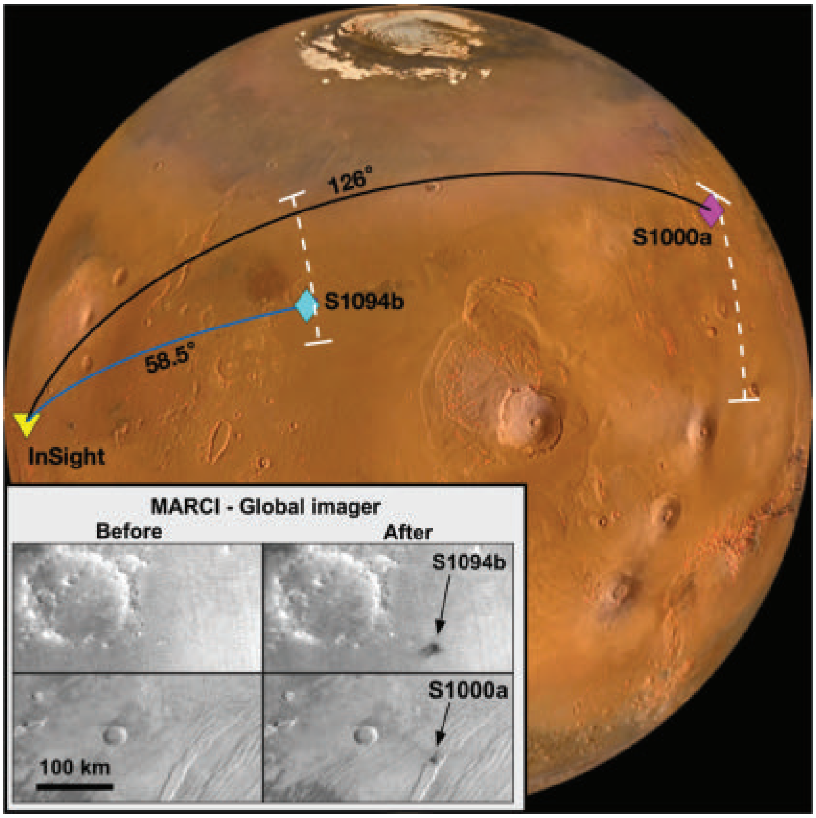

Fig. 1. Impact event location map. The location of the impact craters (diamonds) and the InSight lander (yellow triangle) are shown. The S1094b crater is located at 34.80°N, 189.92°E in Amazonis Planitia. The S1000a crater is located at 38.11°N, 280.12°E in Tempe Terra. The great-circle paths between the new craters and InSight are superimposed onto the underlying globe image derived from MARCI (*13*), Mars Orbiter Camera (*49*), and Mars Orbiter Laser Altimeter (MOLA) data (*50*). The seismic epicentral distance estimates are indicated by the dashed white lines that extend over the azimuthal uncertainty estimate. The inset shows MARCI images from before and after the impacts. The MARCI images have ~2 km per pixel resolution at nadir.

Fig. 2. Orbital images of the impact crater and surrounding area. CTX image (main panel; image ID U05_073077_2154_XI_35N170W): The hypervelocity impactor traveled from southwest to northeast at an inferred azimuth of ~60° (fig. S3), creating a Mach cone shock wave that altered the surface albedo up-range of the impact, region labeled A in the figure. The inner dark ring, near B, is interpreted to be the result of blast wave mobilization of surface fines, impact-derived material directly deposited on the surface, or by ejecta-induced disturbances of the surface dust. The absence of up-range ejecta disturbances indicates an oblique (~30° elevation) impact (*15*). Faint arcuate rays, labeled C, emanating cross-track of the impactor were likely caused by the superposition of the Mach cone and the atmospheric blast (*17*), indicating that both blast waves propagated out at least 18 km. The long-range ejecta–induced disturbances are concentrated in the down-range direction, region D, extending to at least 37 km. HiRISE image (inset; image ID ESP_073077_2155): The crater has a rim-to-rim diameter of ~150 m. The crater floor has an irregular shape, with a depth of roughly 21 m. The light-toned material, for example, areas indicated by arrows labeled E, around the crater is inferred to be water ice ejected during the impact.

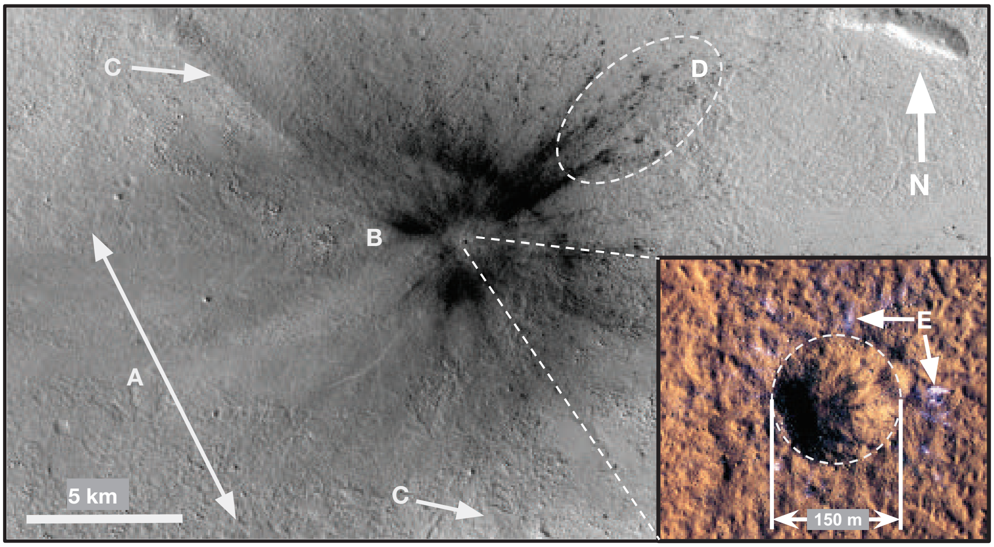

CREDIT: (CTX IMAGE) NASA/JPL-CALTECH/MSSS; (HIRISE IMAGE) NASA/JPL-CALTECH/UNIVERSITY OF ARIZONA

making them the largest fresh craters identified since the beginning of the MRO mission 16 years ago. The seismic events have identifiable surface waves, distinguishing them from other recorded and analyzed events on Mars and indicating shallow sources (*12*). Before these events, surface waves had not been unambiguously identified on any terrestrial planet other than Earth. The closer impact (S1094b) occurred at a distance of 58.5° (3460 km) from the InSight lander on 24 December 2021 and formed the larger of the two craters (150 ± 10 m in diameter). The other impact (S1000a) occurred at a distance of 126° (7455 km) from the InSight lander on 18 September 2021 and formed a cluster of craters (the largest being 130 ± 12 m in diameter). The formation of the craters was time-constrained using the MRO

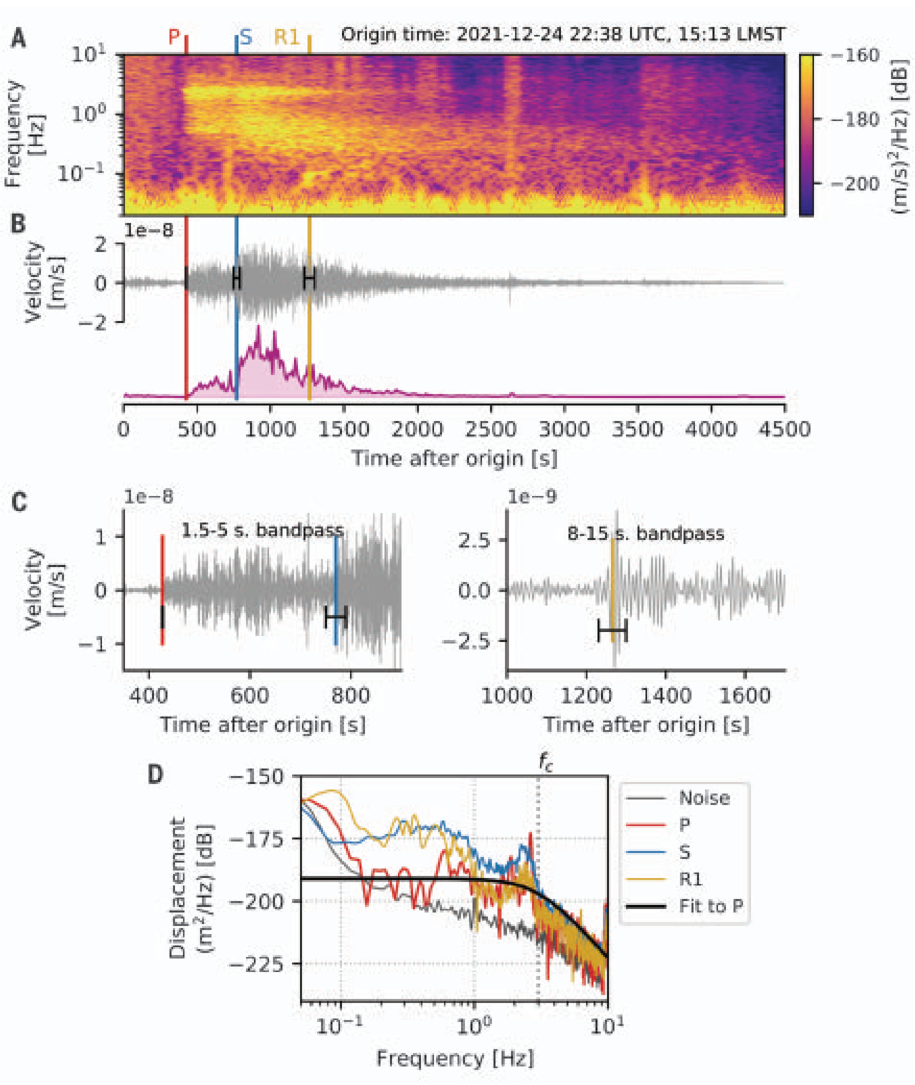

Fig. 3. Seismic observation of S1094b, using de-glitched broadband data. (**A**) Vertical component velocity spectrogram. The event occurred at the end of a noisy period typical of martian afternoons. (**B**) Vertical component velocity time series bandpassed between 1 and 10 s and the derived spectral envelope. Phase picks for *P*, *S*, and Rayleigh (R1) wave arrivals are indicated with pick uncertainty indicated by black bars in the time series. (**C**) Waveform details of the *P* and *S* body waves (left) and Rayleigh wave (right). (**D**) Displacement spectra for the *P*, *S*, and Rayleigh waves and pre-event noise. See fig. S1 for a similar analysis of S1000a.

Mars Color Imager (MARCI) (*13*) to within a day (table S1), making the association with the seismic events highly probable. The seismic events associated with the impacts have similar characteristics, both with ~4.0 magnitudes (tables S1 and S2). Because the seismic waves traveled deep in the mantle, both events are critical for analysis of mantle velocity models. However, given the S1000a event's long distance from the lander, direct seismic waves are eclipsed by Mars' core (*14*) and more-complex bouncing seismic body wave phases (*PP* and *SS*) were detected (fig. S1). The additional attenuation and scattering experienced by these waves obscure the source characteristics, making source analysis much more challenging. In addition, the S1000a-associated crater is located on the side of a graben (fig. S2), which perturbed the blast pattern and prevented an easy identification of impactor parameters. In contrast, the closer impact (S1094b) occurred in a flat, dust-covered region. We first analyze the impact process for this closer impact before considering the implications for Mars interior models of both impacts.

Prominent surface albedo disturbances surrounding the S1094b impact allow for the estimation of ephemeral events that would otherwise be unknown, such as the impactor trajectory and the extent of atmospheric blast waves (Fig. 2 and fig. S3). The bearing of the bolide was estimated to be 60° ± 5° clockwise from north by measuring the up-range "forbidden zone" (*15*) in the albedo ray pattern and a down-range extended cluster of secondary impacts. We infer that the impactor approached the surface at an elevation angle of ~30° from horizontal. A steeper angle requires the asymmetric ejecta pattern to be muted, and a much shallower angle should have led to an elliptical crater planform (*15*, *16*). Two distinct arcuate rays ("scimitars") extending approximately northwest and south of the impact site likely formed from the superposition of two atmospheric blast waves disturbing surface dust: one generated by the passage of the meteoroid through the atmosphere (Mach cone) and the other by the ground impact (*17*), thus indicating that both blast waves extended to at least 18 km laterally. These arcuate rays provide an independent, albeit consistent, measure of the impactor trajectory (56°). The meteoroid struck the surface at 18:49 LMST (Local mean solar time, thus impacting on the orbital trailing side of Mars. We estimate the radial extent of surface dust disturbance from the crater to be 9 km (fig. S3). This limit is consistent with the atmospheric blast pressure produced by a 0.1 to 1 kiloton (4×10^{11} to 4×10^{12} J) surface explosive source (fig. S4). The size of the atmospheric blast allows us to evaluate its contribution to the seismic signal.

Crater size is an important quantity for estimating the kinetic energy and momentum of the impactor for use in numerical models. An image from another camera on MRO, the High Resolution Imaging Science Experiment (HiRISE) (*18*), revealed additional details of the crater and its immediate surroundings (Fig. 2). The crater is irregular in shape, with an estimated rim-to-rim diameter of 150 ± 10 m. Its depth, measured from crater floor to crater rim on the basis of photogrammetry results using HiRISE stereo images, is roughly 21 m. The abundant craters surrounding this impact are likely almost all secondaries generated by the primary impactor, as, in comparison, areas far (>10 to 20 km) from the new impact have few small craters. The bright patches and blocks surrounding the crater reveal that it excavated water ice from the subsurface at a lower latitude (35°N) than any prior ice-exposing crater (39°N) (*19*).

The geological context from orbital imagery aids in determining the appropriate physical models to use in numerical calculations. The S1094b crater is in the Amazonis Planitia region in an area of rugged volcanic plains (*20*), with CTX images showing lava-flow morphologies mantled by a modest cover of debris. The lava flow indicates that a target ground with properties of porous fractured basalt is appropriate for modeling the surface impact. To account for a harder rock site at the crater compared with the region around InSight, we use a local subsurface velocity model based on

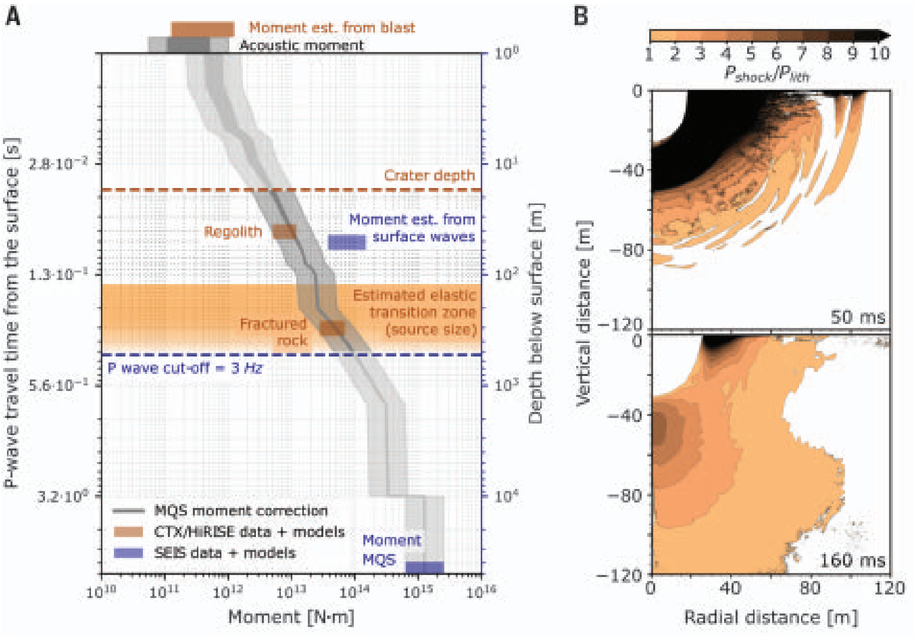

Fig. 4. Seismic source analysis for impact S1094b. (**A**) Seismic moment extrapolated to different source depths and in the air (gray). The blue bars are MQS moment and moment from surface wave amplitude. For more details on the moment/depth relation and modeling methodology see figs. S5 and S6. The brown bars show three moment calculations: two seismic moments estimated from crater size assuming different target materials (*29*, *30*) and one acoustic moment at the surface. Note the overlap between the predicted moment from the atmospheric blast and the estimated acoustic moment (brown and gray bars, respectively). The orange-shaded region indicates the estimated depth range for the transition from shock to elastic waves (*29*). (**B**) iSALE-2D hydrocode simulation of shock wave caused by a vertical impact at 12 km/s of a 5-m-diameter (180 ton) meteoroid into fractured basalt. Two snapshots, at 50 and 160 ms, show the zone of seismic wave generation where the shock pressure (P_{shock}) is substantially higher than the lithostatic pressure (P_{lith}).

terrestrial lava flows (*21*) extrapolated to Mars surface conditions (*22*, *23*) (figs. S5 and S6) for seismic modeling.

The seismic source duration for an impact of this size is expected to be shorter than the crater formation time scale and limited to the duration of the nonlinear shock wave propagation regime (*6*). The seismic event S1094b had a very broad frequency content and relatively flat spectra, from 0.1 Hz to 3 Hz (Fig. 3), with a signal lasting >100 min (*24*) owing to propagation coda (*25*). The event had an impulsive first-arrival *P* wave (1-s uncertainty), followed by an emergent strong *S* wave 6 min later (20-s uncertainty). The third wave observed, arriving 8 min later, was a Rayleigh surface wave, expressed as a long-period dispersed pulse with an 8- to 15-s period (*12*). All body wave phases are characterized by a long coda, indicative of strong scattering due to a near-surface source. The spectra display unusually high corner frequencies (3 Hz) compared with most other seismic events recorded on Mars. Shock physics modeling of the impact in a porous fractured basalt target (Fig. 4) indicates that most of the seismic moment was contained within a few hundred meters of the impact (Fig. 4A, orange bar). The moment release occurred over a short time period consistent with the cutoff frequency of 3 Hz identified in the *P*-wave displacement spectrum (Fig. 3D). Above the cutoff frequency, the amplitude shows a cubed frequency drop-off, as also observed for closer, smaller impacts on Mars (*8*) and for shallow explosions on Earth (*26*, *27*).

Seismic moment (M_0) is the key quantity that links the orbital observations of the impact and the impactor parameters to the seismic observations. For S1094b, the seismic moment estimate from *S* body waves was originally calculated assuming a marsquake at 50 ± 30 km depth to be 1.3×10^{15} N·m (*28*). However, the impact seismic source deposits its energy at much shallower depths, in the strongly shocked region, estimated by impact modeling to be at a depth of between 17 and 120 m, or ~50 m (Fig. 4B). We use our lava-flow seismic velocity model to conclude that the moment of a source at this depth is ~100 times smaller than a corresponding deep-crustal source for the same observed amplitude (Fig. 4A and fig. S5). This is comparable to the seismic moment estimated from surface wave spectra, $M_0 = 7.5 \times 10^{13}$ N·m, at the same source depth (fig. S7).

Empirical and numerical models were used to compute seismic moments for S1094b on the basis of the observed crater size. The imaged crater diameter of 150 ± 10 m corresponds to a vertical impactor momentum of $3.3 \pm 1.4 \times 10^9$ N·s according to empirical crater-scaling relationships and impactor mass, angle, and velocity probability distributions (figs. S8 and S9). For these values, numerical simulations predict seismic moments of 0.5×10^{13} to 1.2×10^{13} N·m for impacts in regolith and 2.8×10^{13} to 7×10^{13} N·m for fractured rock conditions (*29*, *30*). These estimates are consistent with the observed seismic moment corrected for relevant depths in our subsurface model (Fig. 4A). The seismic efficiency was estimated to be 10^{-5} on the basis of scaling relations between seismic moment and crater diameter (*31*) with an order of magnitude uncertainty. This is lower than values estimated for lunar and Earth analogs (*32*) but larger than that previously modeled for small martian impact craters (*29*).

The extensive blast pattern around the S1094b crater suggests that some of the seismic energy may have also originated from energy released in the atmosphere and then coupled to the ground. Numerical impact simulations suggest that up to 10% of the impact energy was partitioned into kinetic energy on the planetary surface, primarily in the ejecta (*33*). For impact scenarios on Mars similar to S1094b, simulations with an atmosphere further suggest that ~5% of the impact energy is partitioned into the blast wave (*34*). An estimated impact energy of between 1×10^{13} and 8×10^{13} J (fig. S4) could produce an atmospheric blast comparable to a 0.1 to 1 kiloton (4×10^{11} to 4×10^{12} J) surface explosion. Therefore, both seismic and image observations are consistent with such a blast and provide coherent constraints in time and space, respectively. Semiempirical airblast theory (*35*) extrapolated to Mars suggests that such a blast would transition from the strong shock regime after 0.2 to 0.4 s, which is consistent with the observed ~3 Hz *P*-wave cut-off frequency. The induced blast pressure is sufficient to mobilize surface dust to a radius of ~10 km, which is consistent with the observed disturbed dust pattern (Fig. 1 and figs. S3 and S4). The estimated blast energy translates to an atmospheric moment $M_0 \approx (\gamma - 1)E = 0.1 \times 10^{12}$ to 1.3×10^{12} N·m, where γ is the adiabatic index (1.33 for Mars), and E is the blast energy (*36*). This is remarkably consistent with the moment-depth model when extrapolated to the surface (Fig. 4A), implying that a moment of only 10^{12} N·m released in the atmosphere could explain a substantial part of the seismic body wave signal, with the remaining part coming from direct coupling of the impactor with the ground.

On Earth, atmospheric explosions easily excite surface waves (*37*) and are highly sensitive to burst altitude (*38*). Solid Mars Rayleigh modes with atmospheric coupling (*14*, *39*) are predicted to have excitation coefficients up to 10 times larger for a near-surface atmospheric source compared with one that is 50 m below the subsurface (fig. S7). Surface waves are expected to have an increase in the excitation coefficients between 0.1 and 0.15 Hz for sources above 50 m altitude. The increase is not observed in the estimated S1094b spectra and may be due to attenuation and scattering, which is not unexpected given that scattering effects are predicted to generate increasing attenuation of surface waves with frequency on the Moon and Mars (*40*). Comparison of S1094b surface wave spectra with near-surface excitation coefficients (fig. S7) suggests that a portion of the surface wave signal could have originated from the blast just above the surface.

The Marsquake Service (MQS) (*41*) using SEIS data (*24*) estimated the seismic locations for both events (S1094b and S1000a). The distance to the events is determined using *S*-minus-*P* arrival times (*SS*-minus-*PP* for S1000a) (*42*, *43*) and polarization measurements of *P* and Rayleigh waves (*PP* for S1000a) (*12*). For the closer event, S1094b, the epicentral distance from the InSight lander was estimated to be 59.7° ± 6.1° (3530 ± 360 km), as compared with the actual distance of 58.5° (3460 km), a difference of only 70 km. For the second impact S1000a, the distance was estimated at 128.3° ± 19° (7591 ± 1240 km), as compared with the actual distance of 126.1°, a difference of 130 km. Additional source parameters for these events are detailed in tables S1 and S2.

The close agreement between distance estimates and the imaged locations increases our confidence in the martian seismic velocity models (*44*–*48*) for the regions sampled by the direct body waves (fig. S10). In particular, the models indicate the absence of mantle discontinuities in the 600 to 700 km depth range, which is the depth at which the *P*, *S*, *PP*, and *SS* waves turn (*44*). For the S1000a event, the P_{diff} phase, the *P* wave that diffracts along the core mantle boundary (CMB), has been tentatively identified (*14*). The PP-P_{diff} travel time difference is sensitive to lower mantle *P* velocities below 800 km. Current models at these depths are constrained by core-reflected *S* phases and the mineral physics–based V_P/V_S ratio (fig. S10). The observed PP-P_{diff} does not match the predicted values given by these models. This mismatch implies that either the *P* velocities at the CMB need adjustment, or the V_P/V_S ratio in the lower mantle is different from current predictions. These two events act as calibrated measurements and help select among various martian interior seismic velocity models (*44*–*48*); they corroborate Mars mantle velocity models to 800 km depth and will help to improve future models down to the CMB.

The first two recorded teleseismic events on Mars with orbital ground-truth observations have been used to constrain martian interior seismic velocity models and infer dynamic impact processes including seismic moment release, impact source duration, and atmosphere-subsurface energy partitioning. The success in observing the formation of impact craters on Mars using instruments on several missions opens up a more detailed understanding of impact dynamics, atmospheric physics, and the exploration of planetary interiors.

REFERENCES AND NOTES

1. W. N. Edwards, D. W. Eaton, P. G. Brown, *Rev. Geophys.* **46**, RG4007 (2008).
2. P. Brown *et al.*, *J. Geophys. Res. Planets* **113**, E09007 (2008).
3. E. Gnos *et al.*, *Meteorit. Planet. Sci.* **48**, 2000–2014 (2013).
4. Y. Nakamura, G. V. Latham, H. J. Dorman, *J. Geophys. Res.* **87**, A117–A123 (1982).
5. P. Lognonné, C. L. Johnson, in vol. 10 of *Treatise on Geophysics: Second Edition*, G. Schubert, Ed. (Elsevier, 2015), pp. 65–120.
6. T. V. Gudkova, Ph. Lognonné, J. Gagnepain-Beyneix, *Icarus* **211**, 1049–1065 (2011).
7. W. Wang, J. E. Vidale, *Sci. Adv.* **8**, eabm9916 (2022).
8. R. F. Garcia *et al.*, *Nat. Geosci.* (2022).
9. M. C. Malin *et al.*, *J. Geophys. Res. Planets* **112**, E05S04 (2007).
10. P. Lognonné *et al.*, *Space Sci. Rev.* **215**, 12 (2019).
11. W. B. Banerdt *et al.*, *Nat. Geosci.* **13**, 183–189 (2020).
12. D. Kim *et al.*, *Science* **378**, 417–421 (2022).
13. J. F. Bell *et al.*, *J. Geophys. Res. Planets* **114**, E08S92 (2009).
14. A. C. Horleston *et al.*, *Seism. Rec.* **2**, 88–99 (2022).
15. D. E. Gault, J. A. Wedekind, *Lunar Planet. Sci. Conf. Proc.* **3**, 3843–3875 (1978).
16. D. Elbeshausen, K. Wünnemann, G. S. Collins, *J. Geophys. Res. Planets* **118**, 2295–2309 (2013).
17. B. Ivanov *et al.*, "New craters on Mars: Air shock wave traces," EGU General Assembly 2020, 4 to 8 May 2020, EGU2020-4212 (2020).
18. A. S. McEwen *et al.*, *J. Geophys. Res. Planets* **112**, E05S02 (2007).
19. C. M. Dundas *et al.*, *J. Geophys. Res. Planets* **126**, e2020JE006617 (2021).
20. K. L. Tanaka *et al.*, Geologic Map of Mars: U.S. Geological Survey Scientific Investigations Map 3292 (USGS, 2014); https://doi.org/10.3133/sim3292.
21. P. Lesage, M. J. Heap, A. Kushnir, *J. Volcanol. Geotherm. Res.* **356**, 114–126 (2018).
22. C. Larmat, K. Onodera, R. Maguire, P. Lognonné, Modelling to resolve whether SEIS, the seismometer of the NASA Insight lander, has detected the formation of a 1.5m diameter crater which occurred about 40km away, Institut de Physique du Globe de Paris (IPGP) (2020); https://doi.org/10.18715/jgr_newcratermod_2020.
23. I. J. Daubar *et al.*, *J. Geophys. Res. Planets* **125**, e2020JE006382 (2020).
24. InSight Mars SEIS Data Service, SEIS raw data, Insight Mission, IPGP, JPL, CNES, ETHZ, ICL, MPS, ISAE-Supaero, LPG, MFSC (2019); https://doi.org/10.18715/SEIS.INSIGHT.XB_2016.
25. P. Lognonné *et al.*, *Nat. Geosci.* **13**, 213–220 (2020).
26. W. R. Walter, K. F. Priestley, in *Explosion Source Phenomenology*, S. R. Taylor, H. J. Patton, P. G. Richards, Eds. (American Geophysical Union, 1991), pp. 219–228.
27. S. R. Ford *et al.*, "Toward an empirically-based parametric explosion spectral model," accession no. ADA568895 (Lawrence Livermore National Lab, 2011); https://apps.dtic.mil/sti/citations/ADA568895.
28. M. Böse *et al.*, *Bull. Seismol. Soc. Am.* **111**, 3003–3015 (2021).
29. N. Wójcicka *et al.*, *J. Geophys. Res. Planets* **125**, e2020JE006540 (2020).
30. A. Rajšić *et al.*, *J. Geophys. Res. Planets* **126**, e2020JE006662 (2021).
31. N. A. Teanby, J. Wookey, *Phys. Earth Planet. Inter.* **186**, 70–80 (2011).
32. I. Daubar *et al.*, *Space Sci. Rev.* **214**, 132 (2018).
33. J. D. Okeefe, T. J. Ahrens, *Lunar Planet. Sci. Conf. Proc.* **3**, 3357–3374 (1977).
34. I. V. Nemtchinov, V. V. Shuvalov, R. Greeley, *J. Geophys. Res.* **107**, 17-1–17-8 (2002).
35. S. Glasstone, P. J. Dolan, "The effects of nuclear weapons," ed. 3 (Tech. Rep. TID-28061, U.S. Department of Defense, U.S. Department of Energy, 1977); https://doi.org/10.2172/6852629.
36. P. Lognonné, B. Mosser, F. A. Dahlen, *Icarus* **110**, 180–195 (1994).
37. M. N. Toksöz, A. Ben-Menahem, *J. Geophys. Res.* **69**, 1639–1648 (1964).
38. D. G. Harkrider, C. A. Newton, E. A. Flinn, *Geophys. J. Int.* **36**, 191–225 (1974).
39. P. Lognonné, F. Karakostas, L. Rolland, Y. Nishikawa, *J. Acoust. Soc. Am.* **140**, 1447–1468 (2016).
40. K. Onodera, T. Kawamura, S. Tanaka, Y. Ishihara, T. Maeda, *J. Geophys. Res. Planets* **126**, e2020JE006406 (2021).
41. InSight Marsquake Service, Mars Seismic Catalogue, InSight Mission; V11 2022-07-01, ETHZ, IPGP, JPL, ICL, Univ. Bristol (2022); https://doi.org/10.12686/a17.
42. M. Böse *et al.*, *Phys. Earth Planet. Inter.* **262**, 48–65 (2017).
43. J. F. Clinton *et al.*, *Phys. Earth Planet. Inter.* **310**, 106595 (2021).
44. C. Durán *et al.*, *Phys. Earth Planet. Inter.* **325**, 106851 (2022).
45. S. C. Stähler *et al.*, *Science* **373**, 443–448 (2021).
46. A. Khan *et al.*, *Science* **373**, 434–438 (2021).
47. A. Khan, P. A. Sossi, C. Liebske, A. Rivoldini, D. Giardini, *Earth Planet. Sci. Lett.* **578**, 117330 (2022).
48. M. Drilleau *et al.*, *J. Geophys. Res. Planets* **127**, e2021JE007067 (2022).
49. M. C. Malin, K. S. Edgett, *J. Geophys. Res.* **106**, 23429–23570 (2001).
50. D. E. Smith *et al.*, *J. Geophys. Res.* **106**, 23689–23722 (2001).

ACKNOWLEDGMENTS

Any use of trade, firm, or product names is for descriptive purposes only and does not imply endorsement by the U.S. Government. This is InSight contribution 221 and LA-UR-22-27122. We acknowledge NASA, CNES, partner agencies and institutions (UKSA, SSO, DLR, JPL, IPGP-CNRS, ETHZ, ICL, and MPS-MPG), and the operators of JPL, SISMOC, MSDS, IRIS-DMC, and PDS for providing SEED SEIS data. This research was carried out in part at the Jet Propulsion Laboratory, California Institute of Technology, under a contract with NASA. **Funding:** This work was funded by NASA-NNN12AA01C with subcontract JPL-1515835 (L.V.P., M.C.M., B.A.C., C.K., G.S., D.S., A.V., and A.W.); NASA-80NM0018D0004 (W.B.B., M.G., and M.Pa.) InSight PSP grant 80NSSC20K0971 (I.J.D.) and 80NSSC18K1626 (R.L); the MRO HiRISE project (C.M.D.); ETH Zurich through the ETH+ funding scheme (ETH+02 19-1: "Planet Mars") (J.C., D.G., S.C., S.C.S., C.D., N.D., A.K., D.K., and G.Z.); ETH research grant ETH-10 17-3 (S.C.S.); UK Space Agency grants ST/R002096/1, ST/V00638X/1, ST/T002026/1, ST/S001514/1, and ST/W002523/1 (A.H., C.C., N.A.T., G.S.C., N.W., and W.T.P.); the Australian Research Council (DP180100661 and FT210100063) (K.M. and A.R.); the French Space Agency CNES and ANR fund (ANR-19-CE31-0008-08) (P.L., T.K., M.F., Z.X., É.B., R.F.G., L.M., S.M., C.Pa., C.Pe., M.Pl., L.R., A.Sp., A.St., and M.D.); and the Center for Space and Earth Science of LANL (Student Fellow Project) (M.F., C.L., and E.R.). This study contributes to IdEx Université Paris Cite ANR-18-IDEX-0001 (P.L., T.K., M.F., Z.X., S.M., C.Pa., M.Pl., and M.D.). **Author contributions:** Lead of the CTX/imaging interpretation: L.V.P. Lead of the SEIS interpretation: P.L. Text contributions: B.F., I.J.D., G.S.C., J.C., L.V.P., P.L., S.C.S., T.K., and Z.X. Edits to the main text and supplementary materials: B.F., I.J.D., M.E.B., R.L., S.C., K.M., and S.C.S. Figure contributions: A.V., B.A.C., C.K., G.S., J.C., L.V.P., M.C.M., P.L., S.C., T.K., K.M., and M.F. Data services: C.Pa., C.Pe., and F.E. Geological interpretation: M.E.B., M.G., and M.C.M. Seismic analysis: A.H., C.C., C.D., C.Pe., D.K., É.B., G.Z., J.C., M.D., M.Pa., M.Pl., N.D., P.D., S.C., S.C.S., T.K., and W.T.P. Seismic interpretation: A.H., A.K., D.G., D.K., J.C., L.M., M.F., P.D., S.M., S.C.S., T.K., W.T.P., and Z.X. Image analysis: A.W., B.A.C., C.M.D., C.K., D.S., G.S., I.J.D., L.V.P., and M.C.M. Targeting orbital assets: A.W., C.D., D.S., G.S., I.J.D., and L.V.P.

Seismic moment analysis: P.L., T.K., and Z.X. Impact model contribution and/or simulations: A.R., C.L., G.S.C., K.M., N.W., and R.L. Seismo-atmosphere coupling work: A.Sp., L.R., M.F., P.L., T.K., and Z.X. Seismic source modeling discussion: C.L., E.R., M.F., N.A.T., and P.L. Seismic efficiency analysis: A.St. and N.A.T. Search for atmospheric signals: A.St., P.L., and R.F.G. InSight mission management: W.B.B. and M.Pa. SEIS instrument development and management: P.L., D.G., W.T.P., and W.B.B. CTX/MARCI development: M.C.M. CTX/MARCI management: L.V.P. **Competing interests:** The authors declare that they have no competing interests. **Data and materials availability:** MRO data are available from the NASA-PDS repository. The InSight event catalog and waveform data are available from the IRIS-DMC, NASA-PDS, SEIS-InSight data portal, and IPGP data center.

SUPPLEMENTARY MATERIALS
science.org/doi/10.1126/science.abq7704
Materials and Methods
Figs. S1 to S10
Tables S1 and S2
References (*51*–*73*)

Submitted 29 April 2022; accepted 22 September 2022
10.1126/science.abq7704

PLANETARY SCIENCE

Surface waves and crustal structure on Mars

D. Kim[1,3]*, W. B. Banerdt[2], S. Ceylan[1], D. Giardini[1], V. Lekić[3], P. Lognonné[4], C. Beghein[5], É. Beucler[6], S. Carrasco[7], C. Charalambous[8], J. Clinton[9], M. Drilleau[10], C. Durán[1], M. Golombek[2], R. Joshi[11], A. Khan[1,12], B. Knapmeyer-Endrun[7], J. Li[5], R. Maguire[13], W. T. Pike[7], H. Samuel[4], M. Schimmel[14], N. C. Schmerr[3], S. C. Stähler[1], E. Stutzmann[4], M. Wieczorek[15], Z. Xu[4], A. Batov[16], E. Bozdag[17], N. Dahmen[1], P. Davis[5], T. Gudkova[16], A. Horleston[18], Q. Huang[17], T. Kawamura[4], S. D. King[19], S. M. McLennan[20], F. Nimmo[21], M. Plasman[4], A. C. Plesa[22], I. E. Stepanova[16], E. Weidner[5], G. Zenhäusern[1], I. J. Daubar[23], B. Fernando[24], R. F. Garcia[10], L. V. Posiolova[25], M. P. Panning[2]

We detected surface waves from two meteorite impacts on Mars. By measuring group velocity dispersion along the impact-lander path, we obtained a direct constraint on crustal structure away from the InSight lander. The crust north of the equatorial dichotomy had a shear wave velocity of approximately 3.2 kilometers per second in the 5- to 30-kilometer depth range, with little depth variation. This implies a higher crustal density than inferred beneath the lander, suggesting either compositional differences or reduced porosity in the volcanic areas traversed by the surface waves. The lower velocities and the crustal layering observed beneath the landing site down to a 10-kilometer depth are not a global feature. Structural variations revealed by surface waves hold implications for models of the formation and thickness of the martian crust.

The martian crust exhibits substantial variations in topography, inferred thickness, age, cratering, resurfacing, and volcanism (*1*). Constraining the variation of the crust's properties and composition with depth is crucial for understanding its origin and evolution (*2*). Inferences of crustal thickness and density variations, which are derived from joint analysis of topography and gravity data, suffer from substantial trade-offs (*3*). For example, the ~5-km topographic difference between the highly cratered southern highlands and the low-lying, less-cratered northern plains can be explained by differences in crustal thickness, by large variations in crustal density (*4*), or by a combination thereof.

The InSight mission to Mars (*5*) has provided direct constraints on the layering of the crust at the landing site (*6*). Analyses of body wave conversions and ambient noise wave field have constrained the crustal thickness beneath the InSight lander in Elysium Planitia as being 39 ± 8 km (*7*–*9*), providing a key anchoring point for global models of crustal thickness and density variations. Looking deeper, travel times of body waves from several marsquakes have enabled the determination of seismic velocity profiles of the upper mantle (*10*), core radius (*8*, *11*), and mean density (*12*). Despite these achievements, the competing effects of epicentral distance, source depth, and radial structure on body wave travel times (*13*) have stymied efforts to constrain lateral variations in structure using a single seismometer on Mars.

The velocity of surface waves, unlike that of body waves, depends on frequency, with lower-frequency waves sensitive to greater depths. The measurement of surface wave dispersion therefore provides a direct observation of the depth-dependent variation of seismic velocities averaged along the path from source to receiver (*14*). Until now, surface waves had not been observed on any marsquake records. Their absence could be due to the relatively small magnitude of the recorded seismic events (*15*), large source depths (*8*), and/or contamination of seismic data by long-period wind noise and atmospheric pressure waves (*16*). Strong crustal scattering on Mars (*6*, *17*) can also impede the propagation and affect the visibility of surface waves, as was the case on the Moon (*18*).

We report here the first detection of surface waves on Mars in the seismic waveforms of events S1094b and S1000a. S1094b, which occurred on 24 December 2021, is the fourth largest seismic event [moment magnitude ($M_{\mathrm{w}}^{\mathrm{Ma}}$) = 4.0 ± 0.2] and has one of the longest-duration seismic signals recorded to date by InSight (*19*), with coda energy persisting for >135 min. On the basis of the differential travel time of the direct P- and S-wave arrivals and the measured P-wave polarization, the initial distance and back azimuth estimates provided by the Marsquake Service were 59.7 ± 6° and 40° (–9°, +18°), corresponding to a source region in Amazonis Planitia ~3460 km northeast from InSight (Fig. 1). The Mars Reconnaissance Orbiter (MRO) images taken between 24 and 25 December 2021 revealed a large impact crater in Amazonis Planitia 3532 km away from the lander and consistent with the source location estimated for S1094b (*20*). With broad frequency content and M_{W} similar to those of S1094b, event S1000a has also been identified as atypical on the basis of its seismic characteristics (*19*), and it was recently associated with an impact crater near the Tharsis province ~7460 km away from the InSight lander (*20*). The ground-truth identification of the two events as impacts removes all uncertainties related to hypocentral depth.

---

[1]Institute of Geophysics, ETH Zürich, Zürich, Switzerland. [2]Jet Propulsion Laboratory, California Institute of Technology, Pasadena, CA, USA. [3]Department of Geology, University of Maryland, College Park, MD, USA. [4]Université Paris Cité, Institut de physique du globe de Paris, CNRS, Paris, France. [5]Department of Earth, Planetary and Space Sciences, University of California, Los Angeles, CA, USA. [6]Nantes Université, Université Angers, Le Mans Université, CNRS, UMR 6112, Laboratoire de Planétologie et Géosciences, Nantes, France. [7]Bensberg Observatory, University of Cologne, Bergisch Gladbach, Germany. [8]Department of Electrical and Electronic Engineering, Imperial College London, London, UK. [9]Swiss Seismological Service, ETH Zürich, Zürich, Switzerland. [10]Institut Supérieur de l'Aéronautique et de l'Espace ISAE-SUPAERO, Toulouse, France. [11]Max Planck Institute for Solar System Research, Göttingen, Germany. [12]Physik-Institut, University of Zürich, Zürich, Switzerland. [13]Department of Geology, University of Illinois Urbana-Champaign, Champaign, IL, USA. [14]Geosciences Barcelona, CSIC, Barcelona, Spain. [15]Université Côte d'Azur, Observatoire de la Côte d'Azur, CNRS, Laboratoire Lagrange, Nice, France. [16]Schmidt Institute of Physics of the Earth, Russian Academy of Sciences, Moscow, Russia. [17]Department of Geophysics, Colorado School of Mines, Golden, CO, USA. [18]School of Earth Sciences, University of Bristol, Bristol, UK. [19]Department of Geosciences, Virginia Tech, Blacksburg, VA, USA. [20]Department of Geosciences, Stony Brook University, Stony Brook, NY, USA. [21]Department of Earth and Planetary Sciences, University of California Santa Cruz, Santa Cruz, CA, USA. [22]Institute of Planetary Research, German Aerospace Center (DLR), Berlin, Germany. [23]Department of Earth, Environmental, and Planetary Sciences, Brown University, Providence, RI, USA. [24]Department of Earth Sciences, University of Oxford, Oxford, UK. [25]Malin Space Science Systems, San Diego, CA, USA.
***Corresponding author. Doyeon Kim (doyeon.kim@erdw.ethz.ch)**

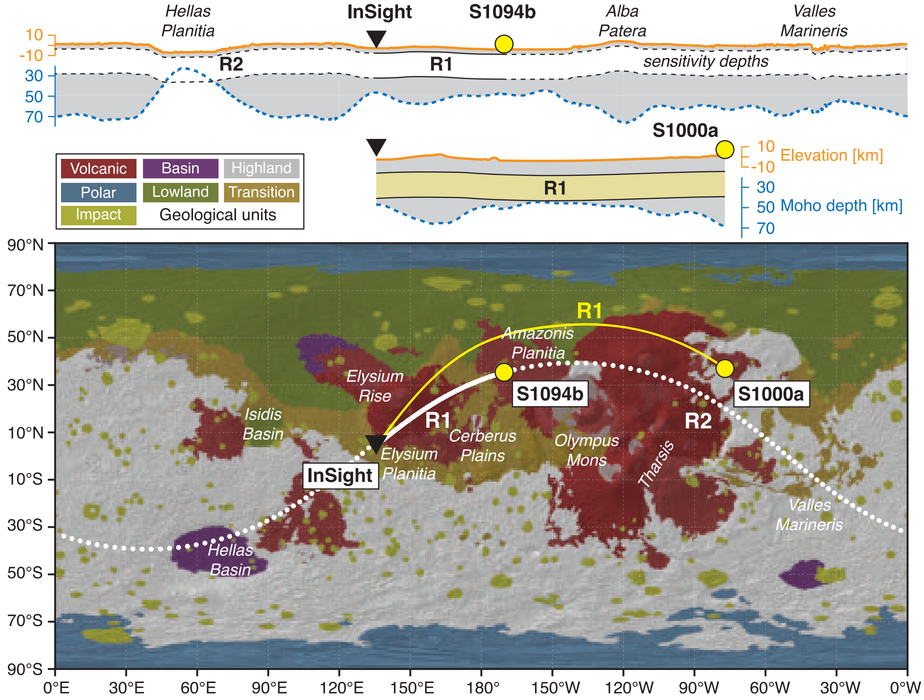

Fig. 1. Locations of two large meteorite impacts (yellow circles) identified in MRO images. The great circle paths for S1094b R1 (solid) and R2 (dashed) are shown in white, and the R1 path for S1000a is shown in yellow. Background topographic relief is from the Mars Orbiter Laser Altimeter (*47*). The distribution and sequence of major geological unit groups of Hesperian and Amazonian age (*32*) are overlaid. Global elevation (orange) and the crust-mantle boundary depth profiles (*25*) along the R1 and R2 paths (dashed blue) are shown at the top.

We applied standard marsquake data-processing methodologies (*19*) to the S1094b waveform data. An unusually large-amplitude seismic arrival was observed 800 s after the P-wave in the S-wave coda in the vertical component spectrogram (Fig. 2). The arrival's frequency content was considerably lower than typical P- and S-wave arrivals in the low-frequency family marsquakes (*8*, *10*). Narrowband filter banks of the raw vertical component data showed dispersion in the 6- to 18-s period range (Fig. 2). Frequency-dependent polarization analysis confirmed that particle motion was strongly elliptically polarized in the vertical plane (fig. S1E). The systematic phase shift between the vertical and horizontal components suggests that the arrival had a predominantly retrograde particle motion and arrived from 51° due northeast, consistent with the polarization of the direct P-wave (fig. S6).

Taken together, these characteristics allow the positive identification of this phase as the minor-arc Rayleigh wave (R1). Although strong elliptical polarization has been previously observed in the 3- to 30-s period range of the ambient seismic noise recordings, they were strictly polarized in the horizontal plane (*16*) and correlated with daytime wind direction on Mars. Despite heavy late afternoon winds, a comodulation analysis of the potential wind injection during the R1 arrival documented excess seismic energy over that generated by wind between 8 and 15 s at the time of the observation (fig. S3). Moreover, we confirmed that the seismic data recorded during the surface wave arrival were not contaminated by any known electromechanical artifacts associated with the seismic sensor or the InSight spacecraft system (*21*).

We found no evidence for Love waves in the S1094b records. This observation is consistent with an impact origin for S1094b, because an isotropic source would primarily excite Rayleigh waves. The detection of Rayleigh waves from this impact source, but not from other low-frequency marsquakes, supports the argument that the marsquakes recorded to date are generally too deep to effectively excite surface waves (*22*). Our waveform simulation confirms that surface waves from shallow seismic sources are far more likely to be detectable, given the diurnal ambient noise level on Mars (fig. S15).

We observed an additional anomalous seismic arrival ~75 min after the identified R1 (fig. S2). As for the R1 observation, the time of this arrival was far outside the time window for a potential direct or ground-coupled infrasound wave originating from the impact source region (*20*, *23*). However, the timing was consistent with that expected for the major-arc Rayleigh wave (R2) that propagated in the opposite direction around Mars. Dispersion and enhanced elliptical polarization in the vertical plane in the 6- to 11-s period range supports the R2 interpretation. Although the frequency content of this arrival was comparable to that of R1, broadband environmental injection in the analysis window was also evident (fig. S4). Because of the low signal-to-noise ratio, the direction of propagation and particle motion of this phase were unclear, and thus the identification of R2 is not definitive. We found no evidence for the arrival of surface wave overtones or multi-orbiting Rayleigh waves in the S1094b waveforms (*19*).

Surface wave data on Earth are typically interpreted assuming that propagation occurs along the great circle path from source to receiver and that it can be related to the average flat-layer structure along that path (*24*). Using a number of crustal thickness models constructed on the basis of gravimetric data and the extrapolated crustal thickness estimates from the InSight location (*25*), our kinematic ray tracing predicted negligible deviations from great circle paths for R1 and R2 that were <0.2% of the total travel time (*19*). We measured the group velocities of R1 and R2 and obtained average values of 2.77 and 3.14 km/s, respectively, which implies structural differences along their propagation paths (fig. S7). Indeed, whereas the R1 path traverses only the northern lowlands, a large fraction of the R2 path crosses the southern highlands, and between 12 and 17% of the path passes through the Hellas impact basin, where the crust has been largely removed and replaced by uplifted mantle (*26*). Therefore, the crustal thickness within the Hellas impact basin could be as low as a few kilometers (*25*), and R2 would travel at a seismic velocity of the uppermost mantle (corresponding to S-wave velocities, V_S = 4 to 4.5 km/s) at periods of 10 to 16 s. The observed higher value in the average group velocity of R2 with respect to R1 could then be accounted for by Hellas alone, and as a result the average crustal velocity of the southern and northern hemispheres would be very similar (fig. S19).

Both phases showed little dispersion in the observed frequency range, which is primarily sensitive to crustal structure between ~5- and 30-km depth (Fig. 2C). Path-averaged radial P- and S-wave velocity profiles were inverted using the R1 measurements with multiple approaches (Fig. 2C, and figs. S9 to S11), and regardless of the parameterization strategies considered (*19*), we obtained a uniform V_S of ~3.2 km/s, with a slight linear increase down to a 30-km depth. At greater depths, we lose sensitivity because of the lack of dispersion measurements at long periods (Fig. 2). At the shallowest

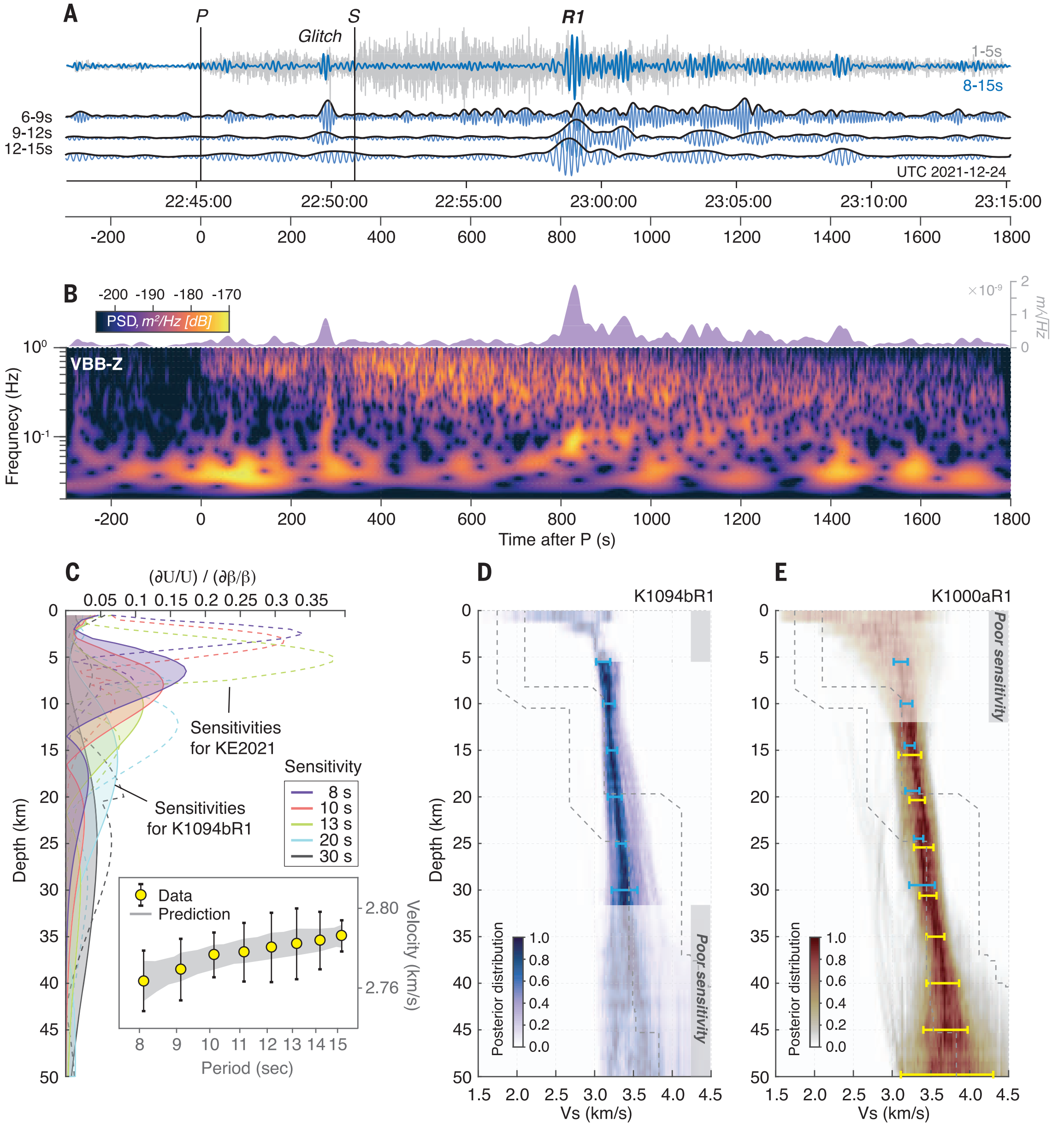

Fig. 2. Seismic waveforms and velocity profiles. (**A**) Vertical component seismogram of S1094b band-pass filtered between 1 and 5 s (gray) and between 8 and 15 s (blue) with P- and S-wave picks (black vertical lines). Narrow-band filter banks and envelopes show dispersed signals 800 s after the P-wave. (**B**) Vertical component S-transform showing a large-amplitude seismic arrival that exhibits dispersion [compare with (A)]. The frequency domain envelope averaged across the 8- to 15-s period range is plotted at the top of the spectrogram. Other characteristics enabling the identification of this dispersive arrival as R1 are described in the supplementary materials (*19*). (**C**) Depth sensitivity kernels and data misfit of R1 in S1094b (inset). The mean and SD are drawn from 10 pairs of dispersion measurements (fig. S7). Kernels in dashed lines were computed on the basis of the three-layer crustal model in (*7*) denoted as KE2021. Note the substantial differences between the kernels caused by the different velocity profiles. Shaded kernels and predictions are computed using the average model in (D). (**D**) Posterior distribution of V_S structure inverted from the group velocity measurements of S1094b R1 (K1094bR1). Posterior distribution and prediction are based on the best-fitting 10,000 models after one million iterations. Depths where sensitivity is inadequate (<40% in cumulative kernel strength) are muted. The range of V_S in the three-layer crustal models beneath the lander (*7*) are indicated by gray dashed lines. (**E**) Posterior distribution of the V_S structure inverted with the group velocity measurements of the S1000a R1 (K1000aR1) at ~20-s and ~30-s periods (fig. S13). Blue and yellow horizontal error bars denote the interquartile ranges of the posterior distributions in (D) and (E), respectively.

depths, we cannot rule out a thin slow layer; however, because of the nonlinear relationship between V_S profiles and surface wave sensitivity kernels (Fig. 2C), the greatest permissible thickness of such a layer depends on its V_S. The uniform V_S in the 5- to 30-km crustal depth range is different from the three-layer crustal structure observed beneath InSight (*7–9*). The obtained V_S was substantially higher in the upper 10 km and was similar to the average velocities of the second and third layers beneath the lander (Fig. 2D), but did not show the same velocity jump around the 20-km depth. From the comparison of the local and the R1 path-average velocity structures, we concluded that the low V_S observed down to the 8- to 10-km depth below the lander was a local feature, and if it is present in other parts along the path, it must be restricted to only few kilometers below the surface. We cannot exclude the presence of deeper layering in the crust, but this would have to occur at varying depths along the path to be averaged in the observed linear V_S increase with depth.

The high crustal seismic velocities inferred from the S1094b dispersion analysis were supported by S1000a data. Two distinct long-period arrivals, at the ~20-s and ~30-s periods, were visible in the vertical component spectrogram of S1000a in the R1 group arrival time range predicted on the basis of the posterior distribution of V_S (fig. S12). Although R1 in S1094b showed clear polarization, the comparative strength of the environmental injection during the expected R1 window of S1000a prevents a definitive identification. The inferred V_S structure using the S1000a group velocity measurements at the ~20-s and ~30-s periods (2.73 and 2.83 km/s, respectively) overlaps with our posterior V_S distribution for S1094b down to 30-km depth, and provides additional constraints to image a slowly increasing V_S in the lower crust down to 45-km depth (Fig. 2E). This agreement suggests a high degree of similarity in the average crustal structure along the two R1 paths.

Unlike dispersion, the frequency dependence of Rayleigh wave ellipticity, expressed as the ratio of horizontal-to-vertical amplitude (H/V), is strongly sensitive to the structure directly beneath InSight. We found that the H/V measurements made on R1 were consistent with previous models of crustal layering beneath the lander (figs. S16 and S17), as were P- to S-wave conversions in the P-wave coda of S1094b, which showed prominent arrivals at 2.4, 4.8, and 7.2 s after the direct P arrival (figs. S20 and S21). Even with a single event, we can confirm that the shallow crustal structure at the landing site down to 10-km depth was substantially slower than the average crustal velocity sampled by the R1 path.

The observed surface waves allowed us to expand the current understanding of crustal structure on Mars beyond the crustal layering inferred beneath the InSight landing site (*7*). We found that the low V_S layer extending down to 10-km depth in the shallow crust of Elysium Planitia does not exist globally on Mars. Instead, the average crustal velocities along the R1 paths of S1000a and S1094b (Fig. 3) were considerably faster and are likely to be more representative of the average crustal structure. Large geographic variations in upper crustal structure hold implications for interpreting waveforms of surface-bouncing seismic waves such as PP and SS and must be explicitly accounted for when constructing models of the spherically symmetrical structure of Mars. These structural variations hold clues for the deeper signature of surface geologic units and for interpretations of gravity data.

A large portion of the R1 paths between Elysium and Amazonis Planitiae passes through the Elysium rise, the largest volcanic province in the northern lowlands (Fig. 1). Its surface geology is characterized by lava flows of Hesperian to Amazonian age, reaching up to several kilometers of thickness and representing a history of major resurfacing (*27*). Beyond Elysium, the S1000a R1 path again encounters extensive regions covered by Hesperian and Amazonian volcanics in Amazonis Planitia and north of Alba Patera. By contrast, the plains around the InSight lander are composed of Early Hesperian and Early Amazonian lava flows (*28*, *29*), and their limited thickness is insufficient to affect R1 dispersion. Below ~200 m, weaker sedimentary material is suggested to extend in places at least to 5- to 6-km depth on the basis of the phyllosilicate signatures and layered sedimentary rocks brought up in the central peaks of large impact craters (*30*).

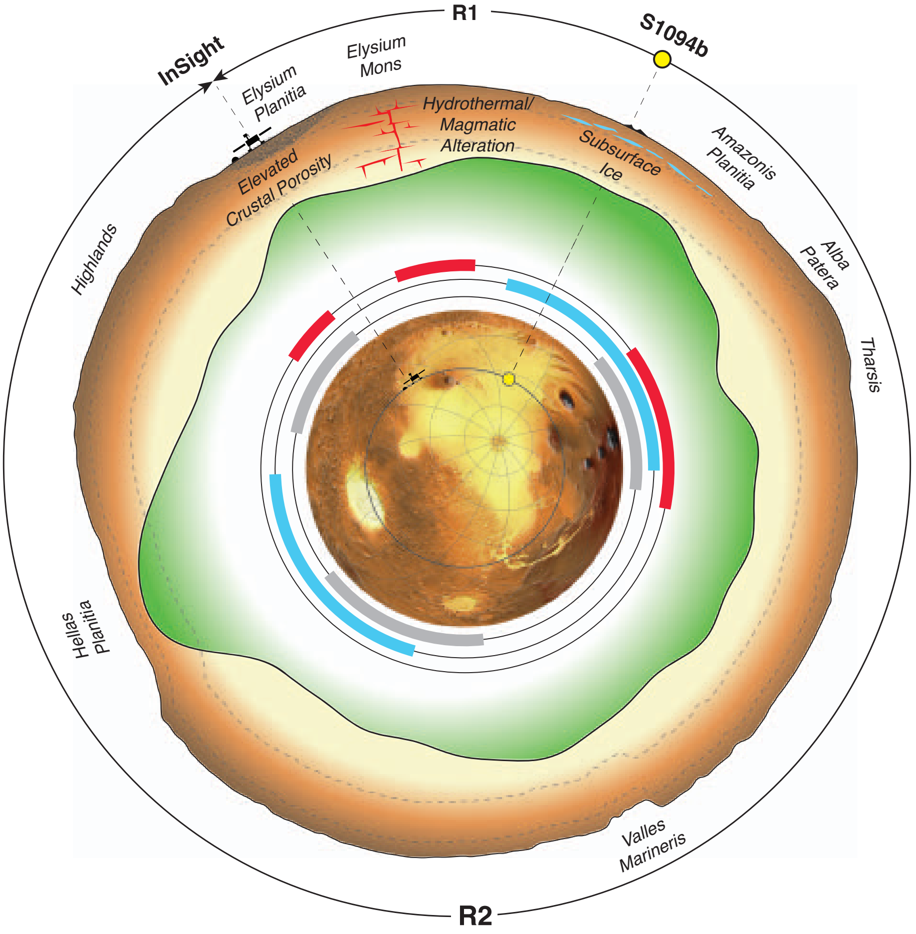

Fig. 3. Cross section of the S1094b surface wave path through Mars. Surface topography (*47*) and crustal thickness (*25*) with a 20× vertical exaggeration are shown along the path of R1 and R2, with major geological provinces labeled at the surface and potential subsurface structures that affect surface wave velocity. The approximate sampling depth of the observed surface waves is indicated by a gray dashed line. The inset context map shows the topography along the surface wave paths. The colored arcs indicate the path length(s) through provinces with surface volcanism (red), ice stability at latitudes >30° (cyan), and cratered highlands (gray).

Similar constraints are provided by density inferred from gravity data. The maximum permissible density of the overall crust on Mars (2850 to 3100 kg/m^3) is lower than the density of most martian basaltic materials found at the surface, as estimated by gamma-ray compositional mapping (*31*) and by mineralogical norms for SNC meteorites of predominantly Amazonian age [see summary in (*25*)]. The two factors contributing to a layered crustal density structure on a global scale could be of a less mafic (less dense) composition and/or an elevated porosity (*6*, *7*, *25*) (Fig. 3).

Most of the R1 paths pass through regions resurfaced by relatively young volcanic rocks, and this results in similar, higher densities of the upper and lower crust. Although Elysium volcanic cumulates are only a few kilometers thick (*32*), and thus within the uppermost zone of poor seismic sensitivity (Fig. 2), their magmatic history influenced the nature of the whole crust in this region (*33*, *34*). The average ratio of intrusive to extrusive magmatism on Mars (*35*, *36*) implies that intrusives account for >5 km of average crustal thickness integrated over the entire Elysium rise and even more near the volcanic centers traversed by R1 (Fig. 1). One proposal for Mars is that intrusive rocks (i.e., magma chamber centers) would concentrate at greater depths than on Earth (*33*). These intrusive magmas represent, at least in part, residues of the partial melting giving rise to surface lavas, and thus they are likely of greater density (*37*) and have elevated seismic wave speeds closer to values typical of basaltic volcanic rocks, consistent with the path-average velocity profiles that we observed below a 5-km depth (Fig. 2).

Substantial porosity is also likely to be present in the upper crustal layers beneath the lander

(*6*, *7*, *25*). Their low V_S is compatible with fractured basalt having, for example, 10% porosity, although the exact amount depends strongly on both the aspect ratio of the pore spaces and material contained therein (fig. S22). However, the higher path-averaged velocities that we observed in the upper 10 km would require lower porosity, which could result from viscous closure of pore spaces caused by the thermal annealing expected to accompany volcanic resurfacing processes (*25*, *38*), partial filling of pore spaces by the deposition of precipitated minerals from a briny ancient aquifer system (*39*), or the presence of a deep cryosphere or substantial water table beneath the thick Amazonian lava flows along the R1 path (*19*, *40*, *41*) (Fig. 3). Images from the High Resolution Imaging Science Experiment of the S1094b impact crater show large blocks of pure ice ejected from the shallower layers (*20*). This would not be expected to be the case near InSight, because the shallow crust with a V_S of 1.7 to 2.1 km/s in the upper 8 to 11 km (*7*) rules out an ice-saturated cryosphere (*39*).

Another possibility is that a low-density, high-porosity layer beneath InSight results from ejecta deposited by the Utopia impact (*25*). Because ejecta thickness is a strong function of radial distance, one would expect the ejecta thickness averaged along the R1 path to be much less than that beneath InSight, which is consistent with observations.

Regardless of the exact origin, composition, and/or porosity, the variations of the martian crustal seismic structure presented here are likely correlated with density variations, because both temperature and compositional variations increase density together with V_S. Therefore, our results imply greater crustal densities between Elysium and Amazonis Planitiae than directly beneath the lander. This result is consistent with previous estimates of higher crustal density beneath the Elysium rise of 3100 ± 100 kg m^{-3} (*42*) and lower density beneath the lander (*43*) from gravity topography measurements. Density variations would also affect inferences of crustal thickness from topographic and gravity signals associated with the crustal dichotomy (*4*, *25*). Currently, both exogenic processes [i.e., one or more large impacts (*44*)] and endogenic processes [i.e., mantle convection (*45*)], or a combination thereof (*46*), continue to be debated as the origin of the dichotomy. Both processes would be expected to generate a basaltic secondary crust in the northern lowlands, consistent with the R1 observations from the two recent impacts. However, if confirmed by further analyses or other events, the S1094b R2 observation of similar group velocities across the southern hemisphere (once corrected for the path in the Hellas impact basin) preliminarily indicates that the crustal structure at relevant depths could be substantially similar north and south of the dichotomy (Fig. 3).

REFERENCES AND NOTES

1. S. R. Taylor, S. M. McLennan, *Planetary Crusts: Their Composition, Origin, and Evolution* (Cambridge Univ. Press, 2009).
2. S. E. Smrekar *et al.*, *Space Sci. Rev.* **215**, 3 (2019).
3. M. T. Zuber, *Nature* **412**, 220–227 (2001).
4. V. Belleguic, P. Lognonné, M. Wieczorek, *J. Geophys. Res. Planets* **110**, E002437 (2005).
5. W. B. Banerdt *et al.*, *Nat. Geosci.* **13**, 183–189 (2020).
6. P. Lognonné *et al.*, *Nat. Geosci.* **13**, 213–220 (2020).
7. B. Knapmeyer-Endrun *et al.*, *Science* **373**, 438–443 (2021).
8. C. Durán *et al.*, *Phys. Earth Planet. Inter.* **325**, 106851 (2022).
9. D. Kim *et al.*, *J. Geophys. Res. Planets* **126**, JE006983 (2021).
10. A. Khan *et al.*, *Science* **373**, 434–438 (2021).
11. S. C. Stähler *et al.*, *Science* **373**, 443–448 (2021).
12. A. Khan, P. A. Sossi, C. Liebske, A. Rivoldini, D. Giardini, *Earth Planet. Sci. Lett.* **578**, 117330 (2022).
13. A. Khan *et al.*, *Phys. Earth Planet. Inter.* **258**, 28–42 (2016).
14. M. N. Toksöz, D. L. Anderson, *J. Geophys. Res.* **71**, 1649–1658 (1966).
15. M. Böse *et al.*, *Bull. Seismol. Soc. Am.* **111**, 3003–3015 (2021).
16. É. Stutzmann *et al.*, *J. Geophys. Res. Planets* **126**, e2020JE006545 (2021).
17. M. van Driel *et al.*, *J. Geophys. Res. Planets* **126**, e2020JE006670 (2021).
18. A. M. Dainty *et al.*, *Moon* **9**, 11–29 (1974).
19. Materials and methods are available as supplementary materials.
20. L. V. Posiolova *et al.*, *Science* **378**, 412–417 (2022).
21. D. Kim *et al.*, *Bull. Seismol. Soc. Am.* **111**, 2982–3002 (2021).
22. D. Giardini *et al.*, *Nat. Geosci.* **13**, 205–212 (2020).
23. R. F. Garcia *et al.*, *Nat. Geosci.* **15**, 774–780 (2022).
24. P. Moulik *et al.*, *Geophys. J. Int.* **228**, 1808–1849 (2022).
25. M. A. Wieczorek *et al.*, *J. Geophys. Res. Planets* **127**, e2022JE007298 (2022).
26. M. A. Wieczorek, R. J. Phillips, *Icarus* **139**, 246–259 (1999).
27. T. Platz, G. Michael, *Earth Planet. Sci. Lett.* **312**, 140–151 (2011).
28. M. Golombek *et al.*, *Space Sci. Rev.* **214**, 84 (2018).
29. M. Golombek *et al.*, *Nat. Commun.* **11**, 1014 (2020).
30. L. Pan *et al.*, *Icarus* **338**, 113511 (2020).
31. D. Baratoux *et al.*, *J. Geophys. Res. Planets* **119**, 1707–1727 (2014).
32. K. L. Tanaka, S. J. Robbins, C. M. Fortezzo, J. A. Skinner Jr., T. M. Hare, *Planet. Space Sci.* **95**, 11–24 (2014).
33. L. Wilson, J. W. Head III, *Rev. Geophys.* **32**, 221–263 (1994).
34. E. H. Christiansen, M. G. Best, J. Radebaugh, in *Planetary Volcanism Across the Solar System*, T. K. P. Gregg, R. M. C. Lopes, S. A. Fagents, Eds. (Elsevier, (2022); pp. 235–270.
35. G. J. Taylor, *Chem. Erde* **73**, 401–420 (2013).
36. B. A. Black, M. Manga, *J. Geophys. Res. Planets* **121**, 944–964 (2016).
37. F. M. McCubbin, H. Nekvasil, A. D. Harrington, S. M. Elardo, D. H. Lindsley, *J. Geophys. Res.* **113**, E11013 (2008).
38. S. Gyalay, F. Nimmo, A. C. Plesa, M. Wieczorek, *Geophys. Res. Lett.* **47**, e2020GL088653 (2020).
39. M. Manga, V. Wright, *Geophys. Res. Lett.* **48**, e2021GL093127 (2021).
40. S. M. Clifford *et al.*, *J. Geophys. Res. Planets* **115**, E003462 (2010).
41. B. De Toffoli, M. Massironi, F. Mazzarini, A. Bistacchi, *J. Geophys. Res. Planets* **126**, e2021JE007007 (2021).
42. A. Broquet, M. A. Wieczorek, *J. Geophys. Res. Planets* **124**, 2054–2086 (2019).
43. T. V. Gudkova, I. E. Stepanova, A. V. Batov, *Sol. Syst. Res.* **54**, 15–19 (2020).
44. J. C. Andrews-Hanna, M. T. Zuber, W. B. Banerdt, *Nature* **453**, 1212–1215 (2008).
45. F. Nimmo, K. Tanaka, *Annu. Rev. Earth Planet. Sci.* **33**, 133–161 (2005).
46. R. I. Citron, M. Manga, D. J. Hemingway, *Nature* **555**, 643–646 (2018).
47. D. E. Smith *et al.*, *Science* **284**, 1495–1503 (1999).
48. InSight Marsquake Service, "Mars Seismic Catalogue, InSight Mission; V11 2022-07-01" (ETHZ, IPGP, JPL, ICL, Univ. of Bristol, 2022); https://doi.org/10.12686/a18.
49. InSight Mars SEIS Data Service, "InSight SEIS Data Bundle" (PDS Geosciences, 2019); https://doi.org/10.17189/1517570.
50. InSight Mars SEIS Data Service, "SEIS raw data, Insight Mission (IPGP, JPL, CNES, ETHZ, ICL, MPS, ISAE-Supaero, LPG, MFSC, 2019); https://doi.org/10.18715/SEIS.INSIGHT.XB_2016.
51. P. Lognonné *et al.*, *Space Sci. Rev.* **215**, 12 (2019).

ACKNOWLEDGMENTS

This paper is InSight contribution number 266. The authors acknowledge the National Aeronautics and Space Administration (NASA), Centre National d'Études Spatiales (CNES), their partner agencies and institutions (UKSA, SSO, DLR, JPL, IPGP-CNRS, ETHZ, IC, and MPS-MPG), and the flight operations team at JPL, SISMOC, MSDS, IRIS-DMC, and PDS for providing the SEED SEIS data. We acknowledge the thorough and thoughtful reviews from the editor and from three anonymous reviewers that greatly improved the manuscript. **Funding:** D.K., S.C., D.G., J.C., C.D., A. K., S.C.S., N.D., and G.Z. were supported by the ETH+ funding scheme (ETH+02 19-1: "Planet Mars"). Marsquake Service operations at ETH Zürich were supported by ETH Research grant ETH-06 17-02. N.C.S. and V.L. were supported by NASA PSP grant no. 80NSSC18K1628. Q.H. and E.B. are funded by NASA grant 80NSSC18K1680. C.B. and J.L. were supported by NASA InSight PSP grant no. 80NSSC18K1679. S.D.K. was supported by NASA InSight PSP grant no. 80NSSC18K1623. P.L., E.B., M.D., H.S., E.S., M.W., Z.X., T.W., M.P., R.F.G. were supported by CNES and the Agence Nationale de la Recherche (ANR-19-CE31-0008-08 MAGIS) for SEIS operation and SEIS Science analysis. A.H., C.C. and W.T.P. were supported by the UKSA under grant nos. ST/R002096/1, ST/ W002523/1 and ST/V00638X/1. Numerical computations of McMC Approach 2 were performed on the S-CAPAD/DANTE platform (IPGP, France) and using the HPC resources of IDRIS under the allocation A0110413017 made by GENCI. A.H. was supported by the UKSA under grant nos. ST/R002096/1 and ST/W002523/1. F.N. was supported by InSight PSP 80NSSC18K1627. I.J.D. was supported by NASA InSight PSP grant no. 80NSSC20K0971. L.V.P. was funded by NASA-NNN12AA01C with subcontract JPL-1515835. The research was carried out in part by W.B.B., M.G. and M.P.P. at the Jet Propulsion Laboratory, California Institute of Technology, under a contract with the National Aeronautics and Space Administration (80NM0018D0004). **Author contributions:** D.K., S.C., D.G., V.L., P.L., C.B., E.B., J.C., A.K., B.K., J.L., M.S., S.C.S., and E.S. analyzed the seismic data and contributed to the detection and identification of the surface wave arrivals. D.K., V.L., C.B., M.D., R.J., B.K., J.L., R.M., H.S., and E.W. performed the inversions. C.C. and W.T.P. performed the comodulation analysis. S.C.S. performed the analysis on ray tracing. D.K. performed waveform simulations. S.C., B.K., and Z.X. performed the H/V analysis. D.K., C.D., and B.K. performed the receiver function analysis. D.K., S.C., C.C., J.C., C.D., S.C.S., N.D., A.H., T.K., M.P., and G.Z. reviewed the continuous data and detected seismic events. D.K., W.B.B., S.C., D.G., V.L., P.L., C.B., J.C., M.G., A.K., B.K., J.L., R.M., N.S., S.C.S., M.W., A.B., T.G., S.K., S.M.M., F.N., A.C.P., I.E.S., and M.P.P. contributed to the interpretation of the results. D.K. wrote the main paper with contribution from D.G. and V.L. D.K., W.B.B., S.C., V.L., C.B., C.C., J.C., M.G., A.K., B.K., J.L., W.T.P., R.M., N.S., S.C.S., M.S., E.S., M.W., E.B., P.D., Q.H., S.K., S.M.M., F.N., A.C.P., and R.F.G. edited the main text and supplementary materials. D.G., P.L., J.C., S.C.S., A.H., I.J.D., B.F., R.F.G., and L.V.P. performed S1094b and S1000a impact analysis and participated in discussions. W.B.B. and M.P.P. managed the InSight mission. P.L., D.G., W.T.P., and W.B.B. led the development of the SEIS instrument. **Competing interests:** The authors declare no competing interests. **Data and materials availability:** The InSight event catalog (*48*) and waveform data are available from the IRIS-DMC, NASA-PDS (*49*), and IPGP (*50*) data centers. Complete descriptions of the SEIS instrument and seismic channels are in (*51*). **License information:** Copyright © 2022 the authors, some rights reserved; exclusive licensee American Association for the Advancement of Science. No claim to original US government works. https://www.science.org/about/science-licenses-journal-article-reuse

SUPPLEMENTARY MATERIALS

science.org/doi/10.1126/science.abq7157
Materials and Methods
Supplementary Text
Figs. S1 to S22
References (*52*–*91*)

Submitted 28 April 2022; accepted 22 September 2022
10.1126/science.abq7157

GENETICS

Evolution and antiviral activity of a human protein of retroviral origin

John A. Frank[1], Manvendra Singh[1], Harrison B. Cullen[1], Raphael A. Kirou[1], Meriem Benkaddour-Boumzaouad[2], Jose L. Cortes[2,3], Jose Garcia Pérez[2,4], Carolyn B. Coyne[5], Cédric Feschotte[1]*

Endogenous retroviruses are abundant components of mammalian genomes descended from ancient germline infections. In several mammals, the envelope proteins encoded by these elements protect against exogenous viruses, but this activity has not been documented with endogenously expressed envelopes in humans. We report that the human genome harbors a large pool of envelope-derived sequences with the potential to restrict retroviral infection. To test this, we characterized an envelope-derived protein, Suppressyn. We found that *Suppressyn* is expressed in human preimplantation embryos and developing placenta using its ancestral retroviral promoter. Cell culture assays showed that *Suppressyn*, and its hominoid orthologs, could restrict infection by extant mammalian type D retroviruses. Our data support a generalizable model of retroviral envelope co-option for host immunity and genome defense.

Viruses pose a persistent threat to human health and may be potent evolutionary drivers of immune adaptation (*1*–*3*). It is therefore critical to identify host factors that protect against viral infection. Endogenous retroviruses (ERVs) are abundant components of mammalian genomes and are descended from ancient retroviral germline infections (*1*). ERV sequences are a source of novel genes in evolution (*2*). ERV-derived envelopes (env) are interesting because they can serve as antiviral factors by binding to and competing for target cell receptors of exogenous viruses (*1*). Env-derived proteins that restrict against contemporary infectious retroviruses have been documented in mouse (Fv4), cat (Refrex-1), and sheep (enJSS6A1) but not in humans (*1*, *2*, *4*). The receptor-binding surface domain of an env can be sufficient to restrict infection by this interference mechanism (*4*). Because the human genome contains thousands of remnant retroviral sequences with coding potential (*5*), we hypothesized that it includes envelope sequences with the capacity to restrict against modern viruses.

We scanned the human genome for potentially antiviral *env*-derived open reading frames (*envORFs*) that encode at least 70 amino acids and are predicted to include the receptor-binding surface (SU) domain (see methods). This search identified 1507 unique *envORF*s, including ~20 *env*-derived sequences presently annotated as human genes such as *Supppressyn* (*SUPYN*), *Syncytin-1*, and *Syncytin-2* (*6*, *7*). This number is consistent with a previous genome-wide scan for ERV-derived ORFs that predicted 1731 ORFs with homology to retroviral envelopes (*5*). Next, we mined transcriptome datasets generated from human embryos and various adult tissues (table S1) and observed that ~44% of *envORF*s (668 of 1507) showed evidence of RNA expression in at least one of the cell types surveyed (Fig. 1A). These analyses revealed three general trends about expressed *envORF*s: (i) like known *env*-derived genes, *envORF*s exhibit tissue-specific expression patterns, but some are widely expressed (HERVK13, ERV3; HERV, human endogenous retrovirus) (Fig. 1A and figs. S1 and S2); (ii) most *envORF*s are expressed during early human development, often in stem and primordial germ cells and/or in placenta (Fig. 1A and fig. S1); (iii) with the exception of brain, *envORF*s are rarely expressed in differentiated tissues under normal conditions (Fig. 1A and figs. S1 and S2). Because antiviral factors are generally expressed in immune cells and/or induced upon immune stimulation or infection, we also profiled *envORF* expression using transcriptome datasets generated from various immune cells, including resting, stimulated, and HIV-infected cells (table S1). These analyses revealed that a substantial fraction of *envORF*s (145 loci from multiple families) are expressed in immune cells and tend to be induced by immune stimulation (Fig. 1B and fig. S3). Consistent with previous reports (*8*), we observed that a subset of *envORF*s are induced upon HIV infection (Fig. 1C and fig. S4). These data suggest that the human genome harbors a vast reservoir of *env*-derived sequences that have coding potential for receptor-binding proteins. Many are expressed in a tissue-specific or infection-inducible fashion, suggesting that they may function as antiviral factors.

As a paradigm to test the antiviral activity of an envORF, we focused on SUPYN for two primary reasons. First, SUPYN was reported to be expressed in the developing placenta, as has been observed for many envORFs, a tissue that can be vulnerable to viral infection and a barrier against vertical transmission to the fetus (*9*). Second, SUPYN lacks a transmembrane domain but retains the ability to bind the amino acid transporter ASCT2 (also known as SLC1A5), which is the receptor for a diverse group of retroviruses, including endogenous (e.g., HERV-W) and exogenous viruses such as RD114 in cat and simian retrovirus (SRV) in Old World monkeys (OWMs) (*6*, *10*–*12*). These viruses are collectively referred to as RD114 and type D (RDR) retroviruses (*12*). We hypothesized that SUPYN might restrict RDR retroviruses by virtue of its binding to ASCT2.

To obtain a more detailed view of *SUPYN* expression and regulation in human development and tissues, we analyzed publicly available bulk and single-cell RNA-seq (RNA sequencing), ATAC-seq (assay for transposase-accessible chromatin with high-throughput sequencing), DNase-seq (DNase I hypersensitive sites sequencing), and ChIP-seq (chromatin immunoprecipitation sequencing) datasets generated from adult tissues, preimplantation embryos, human embryonic stem cell (hESC) lines, in vitro trophoblast (TB) differentiation models, and placenta explants isolated at multiple stages of pregnancy (table S1). Apart from testis and cerebellum, *SUPYN* expression is generally low [$<1 \log_2$ (TPM + 1), where TPM is transcripts per million] or absent in adult tissues (fig. S2). *SUPYN* is expressed at high levels in preimplantation embryos from the eight-cell stage of development (Fig. 2A). Accordingly, the *SUPYN* promoter region, which corresponds to the long terminal repeat (LTR) of the ancestral HERVH48 provirus, is marked by several peaks of accessible chromatin from the eight-cell to blastocyst stages (fig. S5, B and C). In hESCs, *SUPYN* RNA is abundant (Fig. 2A and fig. S5, A and C), and its promoter region is marked by histone modifications characteristic of transcriptionally active chromatin [monomethylated histone H3 lysine 4 (H3K4me1), trimethylated H3K4 (H3K4Me3), acetylated H3K27 (H3K27ac)] and bound by core pluripotency (OCT4, NANOG, KLF4, SMAD1) and self-renewal (SRF, OTX2) transcription factors (Fig. 2B and fig. S5C). During hESC-to-TB differentiation, pluripotency factors (NANOG, OCT4) that occupy the *SUPYN* promoter region are replaced by TB-specific transcription factors (TFAP2A, GATA3), and active chromatin marks (H3K27ac, H3K4me3, H3K9ac) are maintained across all analyzed TB lineages (Fig. 2B). These observations indicate that *SUPYN* expression persists through the TB differentiation process. We next mined single-cell RNA-seq data generated from placenta at multiple developmental stages. After classifying cell clusters based on known markers, we found that expression of *SUPYN* and *ASCT2* was relatively high in

---

[1] Department of Molecular Biology and Genetics, Cornell University, Ithaca, NY, USA. [2] GENYO Centre for Genomics and Oncological Research, Pfizer/University of Granada/Andalusian Regional Government, PTS Granada, Spain. [3] Eppendorf, Iberica, Spain. [4] MRC-Human Genetics Unit, Institute of Genetics and Molecular Medicine, University of Edinburgh, Western General Hospital, Edinburgh, UK. [5] Department of Molecular Genetics and Microbiology, Duke University School of Medicine, Durham, NC, USA.
***Corresponding author. Email: cf458@cornell.edu**

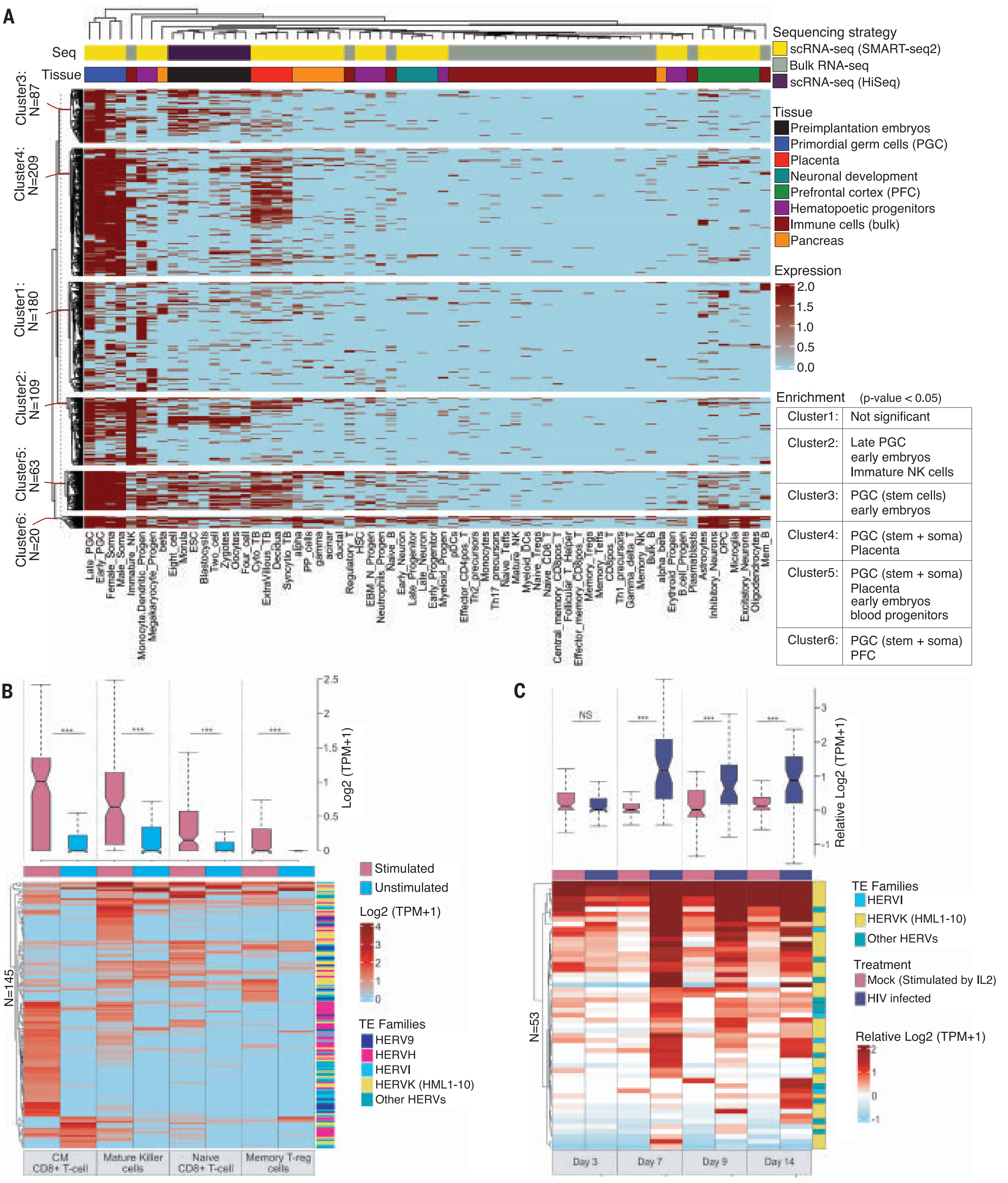

Cluster1:	Not significant
Cluster2:	Late PGC early embryos Immature NK cells
Cluster3:	PGC (stem cells) early embryos
Cluster4:	PGC (stem + soma) Placenta
Cluster5:	PGC (stem + soma) Placenta early embryos blood progenitors
Cluster6:	PGC (stem + soma) PFC

Fig. 1. Expression profile of env-derived transcripts over a subset of human cell types. (**A** to **C**) Heatmaps show *envORF* locus (rows) expression ($\log_2$ (TPM + 1) > 1) in tissues (columns) (A) and stimulated immune (B) or HIV-infected CD4$^+$ T cells (C). The bars above the heatmaps denote sequencing strategy (A) and tissue (A) or treatment [(B) and (C)] with the same color scheme that is used in figs. S1, S3, and S4. Rows and columns are ordered by hierarchical clustering of *envORF* expression. Significant *envORF* cluster enrichment was calculated by hypergeometric test. In (B) and (C), boxplots represent the distribution of envORF expression levels relative to unstimulated (B) and mock-infected cells (C). For (C), envORF expression is averaged across donors (n = 3) and normalized to the mean expression of unstimulated cells (n = 6) (see fig. S4). Boxes and whiskers represent the interquartile range and the minimum and maximum values, respectively. Data were analyzed by Wilcoxon rank-sum test; ***$p < 0.01$, and NS is not significant. NK, natural killer; scRNA-seq, single-cell RNA-seq; TE, transposable element.

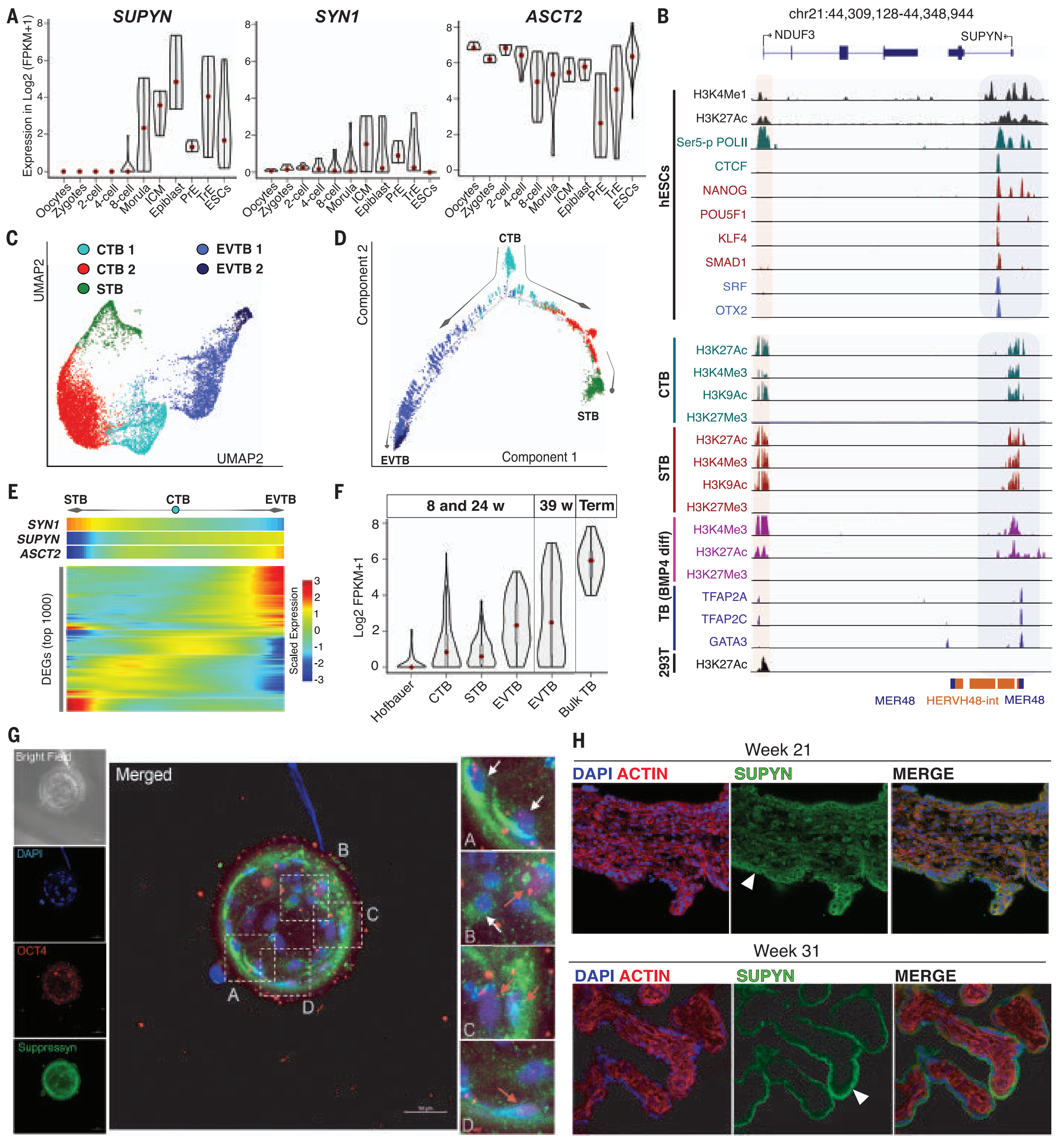

Fig. 2. Pluripotency and placentation regulatory factors drive SUPYN expression during fetal development. (**A**) Violin plots represent single-cell *SUPYN*, *SYN1*, and *ASCT2* expression in human preimplantation embryos and ESCs. ICM, inner cell mass; PrE, primitive endoderm; TrE, trophectoderm. (**B**) Genome browser view of regulatory elements surrounding the *SUPYN* locus in hESCs, CTBs, STBs, BMP4-differentiated TBs, and 293T cells. ChIP-seq profiles show the indicated transcription factors and histone modifications. The shaded area highlights regions of active chromatin. (**C**) Uniform manifold approximation and projection (UMAP) visualization of TB cell clusters (see fig. S6). (**D**) Monocle2 pseudotime analysis of cell clusters in (C) illustrates the developmental trajectory of CTBs to STBs and EVTBs. (**E**) Heatmap representing the top 1000 differentially expressed genes (DEGs) (row) of single cells (column). Cells are ordered according to pseudotime progression in (D). *SYN1*, *SUPYN*, and *ASCT2* were fetched from the heatmap. (**F**) Violin plots denote single-cell *SUPYN* expression in placental-cell lineages throughout the indicated pregnancy stages. (**G** and **H**) Confocal microscopy images of human preimplantation embryo (G) and placental villus explants (H) stained for SUPYN (green), OCT4 (red), ACTIN (red), and 4′,6-diamidino-2-phenylindole (DAPI) (blue). Trophectoderm cells (white arrows) and OCT4-expressing cells (red arrows) are highlighted in the subpanels of (G). STBs are marked by white arrowheads in (H). In the left and middle panels of (G), scale bars are 50 μm.

cytotrophoblasts (CTBs) and extravillous trophoblasts (EVTBs) but was also detectable in syncytiotrophoblasts (STBs) (Fig. 2, C to F, and fig. S6). To confirm these transcriptomic observations, we performed immunostaining of SUPYN in preimplantation embryos as well as second- and third-trimester placentas. In early embryos, SUPYN is primarily detectable in the trophectoderm, which will give rise to placenta, and in some OCT4-expressing cells, which mark pluripotent stem cells of blastocysts (Fig. 2G and figs. S7 and S8). In placenta,

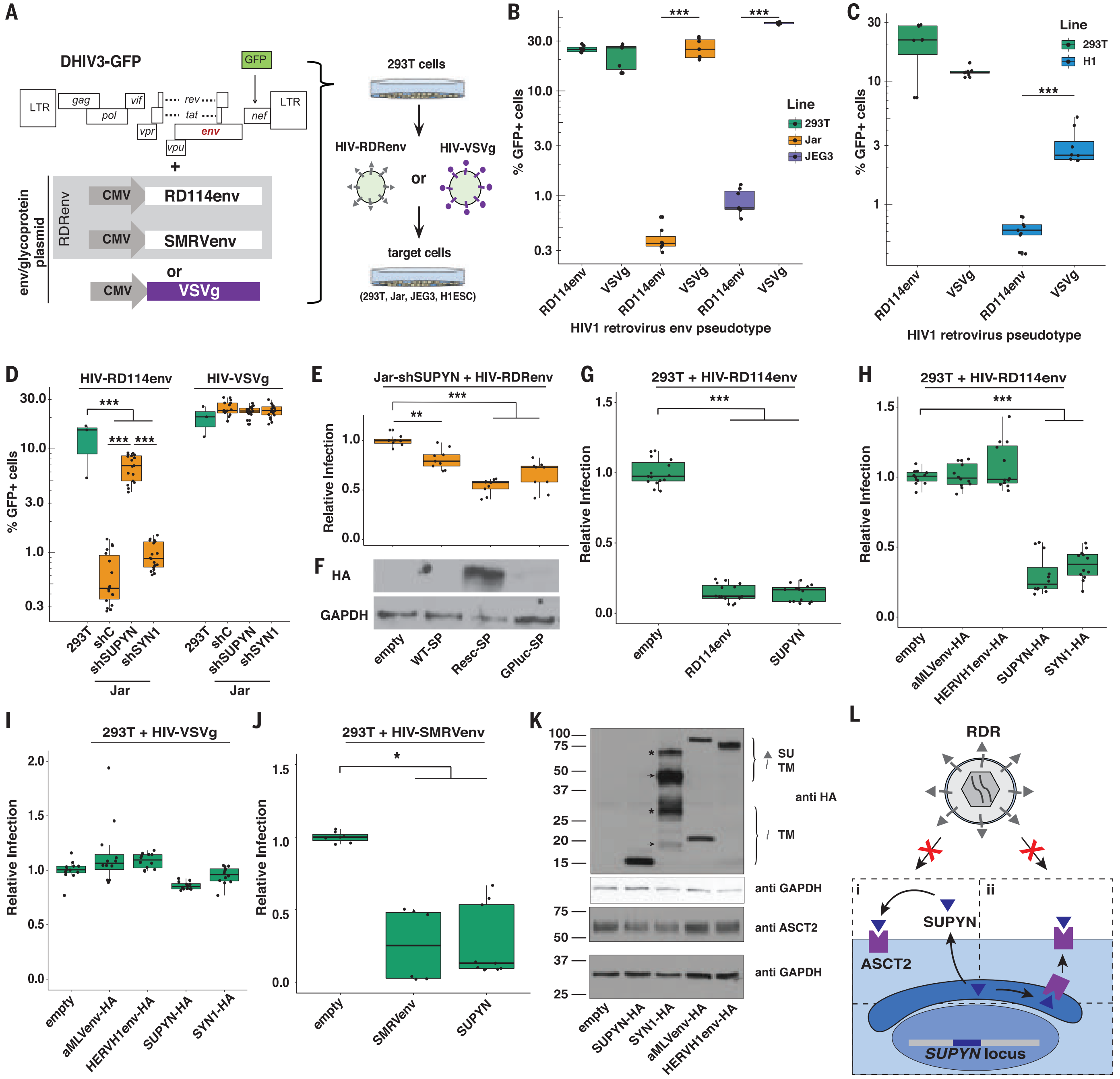

Fig. 3. SUPYN confers resistance to RD114env-mediated infection. (**A**) HIV-glycoprotein reporter virus production and infection assay approach (see methods). CMV, cytomegalovirus promoter. (**B** to **D**) Proportion of GFP$^+$ 293T, JEG3, and Jar cells (B); GFP$^+$ 293T cells and H1-ESCs (C), and GFP$^+$ 293T and shSUPYN-Jar cells (D) infected with the indicated reporter virus pseudotypes. (**E**) Relative infection rates of shSUPYN-Jar cells transfected with HA-tagged wild-type (WT-SP), rescue signal peptide (Resc-SP), or luciferase signal peptide (GPluc-SP) encoding SUPYN overexpression constructs. (**F**) Western blot analysis (αHA, αGAPDH; GAPDH, glyceraldehyde phosphate dehydrogenase) of Jar-shSUPYN cell lysates transfected with the indicated SUPYN overexpression constructs. (**G** to **J**) Relative infection rates of 293T cells transfected with unmodified RD114env (G), SUPYN [(G) and (J)], SMRVenv (J), or the indicated HA-tagged protein [(H) and (I)] overexpression plasmids and infected with the indicated reporter viruses (identified above each graph). (**K**) Representative Western blot analysis (αHA, αGAPDH, αASCT2) of 293T cell lysates after transfection with the indicated constructs. Arrowheads and asterisks denote unglycosylated and glycosylated protein fragments, respectively. SU, surface domain; TM, transmembrane domain. (**L**) Model of SUPYN-dependent RDR infection restriction. SUPYN likely binds ASCT2 after secretion (I) or within the secretory compartment (II). Boxes and whiskers represent the interquartile range and the minimum and maximum values, respectively. Data were analyzed by analysis of variance (ANOVA) with Tukey's honestly significant difference (HSD) test; $n \geq 3$ with ≥2 technical replicates; ***adjusted $p < 0.001$, **adjusted $p < 0.01$, and *adjusted $p < 0.05$.

SUPYN is widely expressed in STBs and potentially CTBs of second-trimester placental villi (Fig. 2H and fig. S9). The combined transcriptome, genome regulatory data, and immunohistochemical staining establish that *SUPYN* is expressed throughout human fetal development (Fig. 2 and figs. S5 to S9). These analyses also indicate that *SUPYN* transcription consistently initiates from its ancestral HERVH48 provirus (Fig. 2B and figs. S5, B and C, and S13).

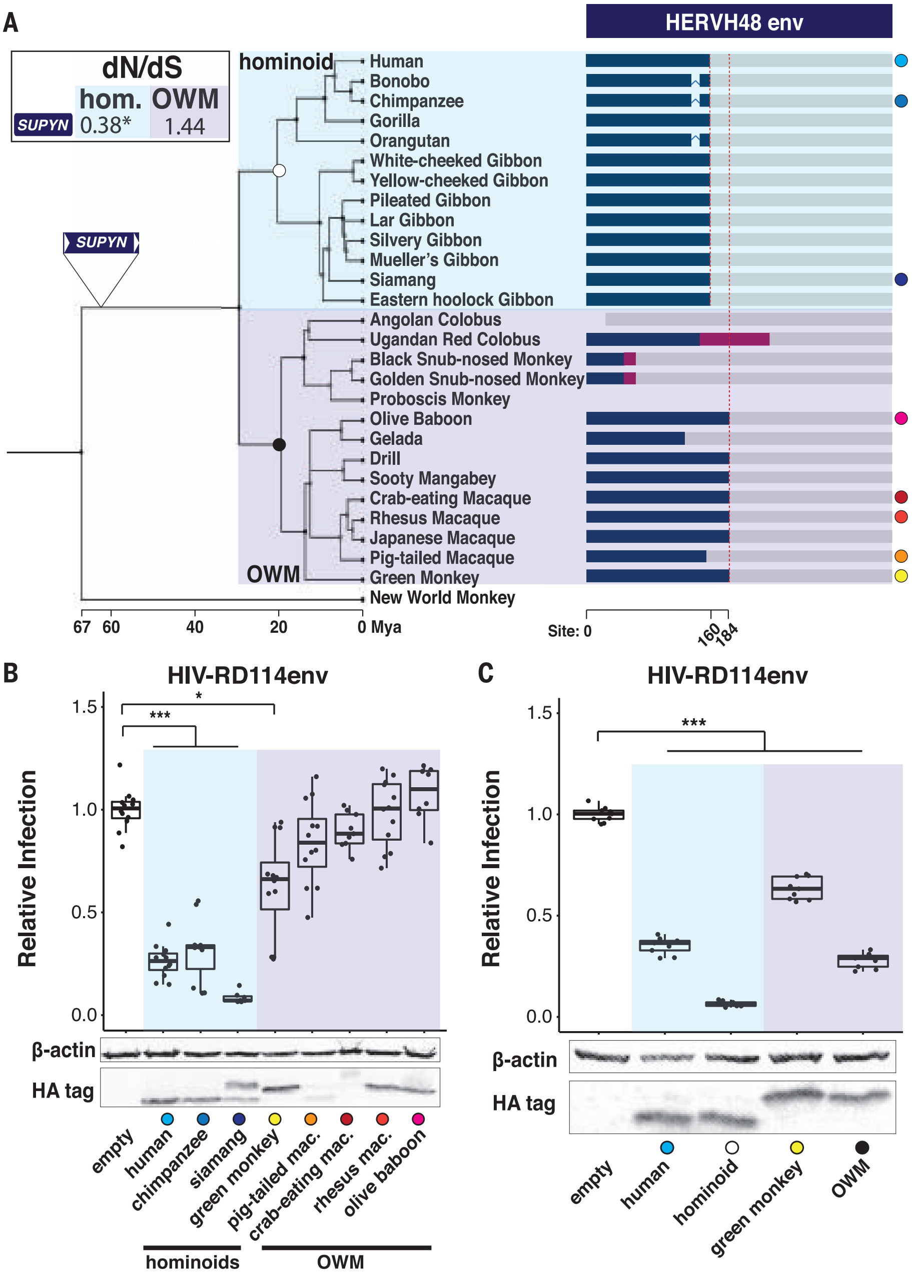

Fig. 4. SUPYN emerged in a Catarrhine ancestor and has conserved antiviral activity in hominoids. (**A**) Consensus primate phylogeny with cartoon representation of *SUPYN* ORFs (blue box). Magenta boxes represent *SUPYN* ORF frameshifts. Red dashed lines denote conserved premature stop codon positions. Gray bars represent degraded HERVH48env sequence. The labeled triangle denotes the ancestral lineage where HERVH48env was acquired. Colored circles indicate species used in (B) and (C). *SUPYN* dN/dS values are shown in the box. Data were analyzed by likelihood ratio test; $*p < 0.05$. Mya, million years ago. (**B** and **C**) Relative infection rates and Western blot of 293T cells transfected with primate (B) or ancestral (C) SUPYN-HA constructs and infected with HIV-RD114env. Relative infection rates were determined by normalizing GFP^+ counts to empty vector. Boxes and whiskers represent the interquartile range and the minimum and maximum values, respectively. Data were analyzed by ANOVA with Tukey's HSD test; $n \geq 3$ with ≥2 technical replicates; ***adjusted $p < 0.001$, and *adjusted $p < 0.05$. mac., macaque.

The expression profile of SUPYN is consistent with the hypothesis that it could protect the developing embryo and germline against RDR infection. We first examined whether human placenta–derived Jar and JEG3 cell lines and H1 hESCs, which robustly express SUPYN and ASCT2 (figs. S10 and 11A) (*10*), are resistant to RDR env-mediated infection. We generated HIV-EGFP viral particles pseudotyped with either RD114 env (HIV-RD114) or vesicular stomatitis virus glycoprotein G (HIV-VSVg), which uses the low-density lipoprotein receptor (*13*), to monitor the level of infection in cell culture based on enhanced green fluorescent protein (EGFP) expression (Fig. 3A and fig. S12). These experiments revealed that Jar, JEG3, and H1 cells were susceptible to HIV-VSVg, as previously reported (*14*, *15*), but resistant to HIV-RD114 infection (Fig. 3, B and C). By contrast, 293T cells, which do not express *SUPYN* (fig. S5A), were similarly susceptible to infection by HIV-RD114 and HIV-VSVg (Fig. 3, B and C). To test whether SUPYN contributes to the HIV-RD114 resistance phenotype, we repeated these infection experiments in Jar cells engineered to stably express short hairpin RNAs (shRNAs) that depleted ~80% of *SUPYN* mRNA (fig. S11A). Depletion of *SUPYN* in Jar cells resulted in a significant increase in susceptibility to HIV-RD114 infection but not HIV-VSVg infection (Fig. 3D). To confirm that SUPYN expression confers RD114 resistance and control for potential off-target effects of *SUPYN*-targeting shRNAs, we transfected Jar-shSUPYN cells with two shRNA-resistant, hemagglutinin (HA)–tagged SUPYN rescue constructs and examined their susceptibility to HIV-RD114 infection. The shRNA-targeted SUPYN signal peptide sequence was replaced with a luciferase (SUPYN-lucSP) or modified signal peptide sequence (SUPYN-rescSP) that disrupts shRNA-binding but retains codon identity (see methods). Transfection with either SUPYN-rescSP or SUPYN-lucSP restored a significant level of resistance to HIV-RD114 infection (Fig. 3E). Western blot analysis of transfected cell lysates showed that SUPYN-rescSP was more abundantly expressed than SUPYN-lucSP (Fig. 3F), which may account for the stronger HIV-RD114 resistance conferred by the former (Fig. 3E). These results suggest that SUPYN expression is at least partially responsible for preventing Jar cells from RD114env-mediated infection.

To test if SUPYN expression alone is sufficient to confer protection against RD114env-mediated infection, we transfected 293T cells with either an unmodified or HA-tagged SUPYN overexpression construct and subsequently infected both sets of cells with either HIV-RD114 or HIV-VSVg. As a positive control, we also transfected 293T cells with an unmodified RD114env overexpression construct, which is predicted to confer resistance to HIV-RD114. Expression of either SUPYN or RD114env resulted in an ~80% reduction in the level of HIV-RD114 infection (Fig. 3, G and H) but had no significant effect on HIV-VSVg infectivity (Fig. 3I). Taken together, our knockdown and overexpression experiments indicate that SUPYN expression is sufficient to confer resistance to RD114env-mediated infection.

Our RD114env-specific resistance phenotype (Fig. 3, G to I) suggests that SUPYN restricts viral entry through receptor interference. If so, this protective effect should extend to infection mediated by other RDRenv (*11*, *16*, *17*). To test this, we generated HIV-GFP reporter virions pseudotyped with squirrel monkey retrovirus env (HIV-SMRVenv) (*11*) (Fig. 3J) and infected 293T cells previously transfected with SUPYN, SMRVenv (as a positive control), or an empty vector. Cells expressing SUPYN or SMRVenv showed an ~80% reduction of HIV-SMRVenv infected cells (Fig. 3J), indicating that SUPYN can restrict infection mediated by multiple RDRenv.

Another prediction of RDR restriction through receptor interference is that resistance should be conferred by env that bind ASCT2, such as SUPYN, but not by those binding other cellular receptors. Consistent with this prediction and previous work with overexpressed SYN1 (*18*), expressing HA-tagged SUPYN and SYN1 strongly restricted HIV-RD114, whereas HA-tagged env from amphotrophic murine leukemia virus (aMLV) or human endogenous retrovirus H (HERVH), neither of which are expected to interact with ASCT2 (*19*–*21*), had no effect on HIV-RD114 or HIV-VSVg infection in 293T cells (Fig. 3, H and I). All tested env proteins were expressed at comparable levels (Fig. 3K). Furthermore, we observed that SUPYN overexpression led to a decrease in ASCT2 protein levels in 293T cells (Fig. 3K and fig. S11, E and F). This result suggests that if SUPYN acts by receptor interference, its interaction with ASCT2 leads to partial receptor degradation, which is consistent with some instances of receptor interference (*22*, *23*). In agreement with previous observations (*6*, *24*), we noted that *SUPYN* knockdown in Jar cells resulted in selective loss of a putative unglycosylated isoform of ASCT2 (fig. S11, B to D). We speculate that the presence of SUPYN-dependent unglycosylated ASCT2 may result from SUPYN sterically interfering with glycosylation machinery that is present within the secretory pathway. Collectively, these observations converge on the model that SUPYN restricts against RDR infection through receptor interference by two possible mechanisms that are not mutually exclusive: SUPYN may bind ASCT2 either within the secretory pathway or extracellularly after secretion (Fig. 3L).

To gain insights into the evolutionary emergence of *SUPYN* antiviral activity, we used comparative genomics to investigate the origin and functional constraint acting on *SUPYN*. We found that the HERVH48 provirus from which *SUPYN* is derived is present at an orthologous position across the genomes of all available hominoids and most OWMs but is absent in other primate lineages (Fig. 4A and fig. S13). Thus, the provirus that gave rise to *SUPYN* inserted in the genome of a catarrhine primate ancestor ~27 million to 38 million years ago (*25*) (Fig. 4A). We next examined whether *SUPYN* ORFs have evolved under functional constraint during primate evolution. The *SUPYN* ORF is almost perfectly conserved in length across hominoids but not in OWMs where the ORFs of some species display frameshifting and truncating mutations (Fig. 4A and figs. S14 and S15), suggesting that *SUPYN* evolved under different evolutionary regimes in hominoids and OWMs. To test this idea, we analyzed the ratio (ω) of nonsynonymous (dN) to synonymous (dS) substitution rates using codeml (*26*), which provides a measure of selective constraint acting on codons. Log-likelihood ratio tests that compare models of neutral evolution with selection indicate that *SUPYN* evolved under purifying selection in hominoids ($\omega = 0.38$; $p = 1.47 \times 10^{-2}$) but did not depart from neutral evolution in OWMs ($\omega = 1.44$; $p = 0.29$) (Fig. 4A). These results indicate that *SUPYN* antiviral activity may be conserved across hominoids but not in OWMs. To assess this, we transfected 293T cells with HA-tagged overexpression constructs for the orthologous *SUPYN* sequences of two hominoid species (chimpanzee and siamang) and five OWM species (African green monkey, pigtailed macaque, crab-eating macaque, rhesus macaque, and olive baboon) and challenged these cells with HIV-RD114. Both chimpanzee and siamang SUPYN proteins displayed antiviral activity with a potency comparable to or greater than that of human SUPYN, respectively (Fig. 4B). By contrast, of the five OWMs, only African green monkey SUPYN exhibited a modest but significant level of antiviral activity (Fig. 4, B and C). The lack of restriction activity for some OWM proteins may be attributed to their relatively low expression level in human 293T cells (Fig. 4B) and/or their inability to bind the human ASCT2 receptor because of SUPYN sequence divergence (figs. S14 and S15). To further trace the evolutionary origins of SUPYN antiviral activity, we expressed ancestral *SUPYN* sequences that were phylogenetically reconstructed for the hominoid and OWM ancestors (fig. S15) and assayed their antiviral activity in 293T cells. Both ancestral proteins were expressed at levels comparable to that of human and African green monkey SUPYN and exhibited strong restriction activity (Fig. 4C). These data indicate that SUPYN antiviral activity against RDRenv-mediated infection is an ancestral trait preserved over ~20 million years of hominoid evolution but apparently lost in several OWM lineages.

Because envORFs are predicted to encode proteins with the ability to bind receptors used by their ancestral retroviruses and possibly many contemporary exogenous viruses, we propose that they constitute a reservoir of potential antiviral factors. The prominent expression of envORFs, including SUPYN, in the developing germ line suggests that they may have repeatedly acted as a barrier against the vertical propagation of cognate endogenous retroviruses by reinfection (*27*). This may explain why most HERV families appear to have propagated in the genome primarily through retrotransposition rather than reinfection (*28*). Under this model, we predict the adaptive benefits of envORFs to be generally transient, unless they have broader antiviral activity or gain additional cellular function. This conjecture may explain why *SUPYN* has been preserved by natural selection throughout hominoid evolution; *SUPYN* may have shielded the early embryo and nascent germline not only from the persistent threat of RDRs but also against the adverse effects of SYN1-mediated infections and syncytalization of the developing placenta (*6*, *10*, *29*). The human genome may hold many other retrovirus-derived proteins with protective effects against viral infection.

REFERENCES AND NOTES

1. W. E. Johnson, *Nat. Rev. Microbiol.* **17**, 355–370 (2019).
2. J. A. Frank, C. Feschotte, *Curr. Opin. Virol.* **25**, 81–89 (2017).
3. H. W. Virgin, *Cell* **157**, 142–150 (2014).
4. R. Malfavon-Borja, C. Feschotte, *J. Virol.* **89**, 4047–4050 (2015).
5. S. Nakagawa, M. U. Takahashi, *Database* **2016**, baw087 (2016).
6. J. Sugimoto *et al.*, *Sci. Rep.* **9**, 19502–19512 (2019).
7. C. Lavialle *et al.*, *Philos. Trans. R. Soc. London Ser. B* **368**, 20120507 (2013).
8. A. C. van der Kuyl, *Retrovirology* **9**, 6 (2012).
9. N. Arora, Y. Sadovsky, T. S. Dermody, C. B. Coyne, *Cell Host Microbe* **21**, 561–567 (2017).
10. J. Sugimoto, M. Sugimoto, H. Bernstein, Y. Jinno, D. Schust, *Sci. Rep.* **3**, 1462–1468 (2013).
11. A. Sinha, W. E. Johnson, *Curr. Opin. Virol.* **25**, 105–112 (2017).
12. M. Scalise, L. Pochini, L. Console, M. A. Losso, C. Indiveri, *Front. Cell Dev. Biol.* **6**, 96 (2018).
13. D. Finkelshtein, A. Werman, D. Novick, S. Barak, M. Rubinstein, *Proc. Natl. Acad. Sci. U.S.A.* **110**, 7306–7311 (2013).
14. M. Dottori, C. Tay, S. M. Hughes, *J. Cell. Biochem.* **112**, 1955–1962 (2011).
15. M. Sakata *et al.*, *Sci. Rep.* **7**, 11607 (2017).
16. W. E. Johnson, *Annu. Rev. Virol.* **2**, 135–159 (2015).
17. M. A. Sommerfelt, R. A. Weiss, *Virology* **176**, 58–69 (1990).
18. V. G. Ponferrada, B. S. Mauck, D. P. Wooley, *Arch. Virol.* **148**, 659–675 (2003).
19. N. de Parseval, J. Casella, L. Gressin, T. Heidmann, *Virology* **279**, 558–569 (2001).
20. M. van Zeijl *et al.*, *Proc. Natl. Acad. Sci. U.S.A.* **91**, 1168–1172 (1994).
21. D. G. Miller, R. H. Edwards, A. D. Miller, *Proc. Natl. Acad. Sci. U.S.A.* **91**, 78–82 (1994).
22. Z. Jobbagy, S. Garfield, L. Baptiste, M. V. Eiden, W. B. Anderson, *J. Virol.* **74**, 2847–2854 (2000).
23. J. W. Kim, J. M. Cunningham, *J. Biol. Chem.* **268**, 16316–16320 (1993).
24. J. Sugimoto, D. J. Schust, T. Yamazaki, Y. Kudo, *Sci. Rep.* **12**, 10552 (2022).
25. P. Perelman *et al.*, *PLOS Genet.* **7**, e1001342 (2011).
26. Z. Yang, *Mol. Biol. Evol.* **24**, 1586–1591 (2007).

27. D. Blanco-Melo, R. J. Gifford, P. D. Bieniasz, *eLife* **6**, e22519 (2017).
28. G. Magiorkinis, R. J. Gifford, A. Katzourakis, J. De Ranter, R. Belshaw, *Proc. Natl. Acad. Sci. U.S.A.* **109**, 7385–7390 (2012).
29. Y. Tang *et al*., *Cell Rep.* **30**, 4528–4539.e4 (2020).
30. M. Singh, Manu-1512/Envelopes_Suppressyn: Evolution and antiviral activity of a human protein of retroviral origin. Zenodo (2022).

ACKNOWLEDGMENTS

We thank V. Planelles for sharing reporter virus plasmids and training; W. Johnson for sharing his SMRVenv expression plasmid; L. Aagaard for sharing shRNA transduction constructs; J. Lis for providing the lentiviral packaging construct; A. Koren and R. Rebello for providing embryonic stem cell cultures and technical support, respectively; and L. Carbone and M. Okhovat for sharing gibbon genome sequences. We thank R. Malfavon-Borja for producing an initial list of envORFs in the human genome. We thank M. Clare for her contribution to evolutionary sequence analyses. We thank A. Iwasaki for her critical reading of this manuscript. We thank members of the Feschotte lab for helpful advice and discussion throughout the project. **Funding:** This work was funded by National Institutes of Health (NIH) grant R01 GM112972 (C.F.), NIH grant R35 GM122550 (C.F.), Champalimaud Foundation CICE-FEDER-P12-CTS-2256 (J.G.-P.), The Wellcome Trust-University of Edinburgh Institutional Strategic Support Fund ISFF2 (J.G.-P.), European Research Council ERC-Consolidator grant ERC-STG-2012-309433 (J.G.-P.), Howard Hughes Medical Institute International Early Career Scientist grant IECS-55007420 (J.G.-P.), and a private donation from F. Serrano, *Trading y Bolsa para Torpes* (J.G.-P.). **Author contributions:** C.F. conceived of this project. J.A.F. and C.F. designed and developed this project. J.A.F. designed and conducted all experiments and evolutionary sequence analyses and analyzed all experimental data. M.S. performed all gene expression and regulation analyses. H.B.C. and R.A.K. helped perform infection assays and evolutionary sequence analyses. C.B.C. obtained placental tissues and performed stains. J.L.C. and J.G.-P. obtained, cultured, and prepared human embryos for microscopy. M.B.-B. performed embryo stains and imaging. J.A.F., C.F., and M.S. wrote the manuscript. **Competing interests:** The authors declare that they have no competing interests. **Data and materials availability:** Materials generated for this study (cell lines, plasmids, and primers) are available upon request from C.F. envORF annotations are included among the supplementary data files. Accessibility information for the publicly available high-throughput datasets used in this study are presented in table S1. The codes used to process and plot the high-throughput datasets have been deposited on Zenodo (*30*).

SUPPLEMENTARY MATERIALS

science.org/doi/10.1126/science.abq7871
Materials and Methods
Figs. S1 to S16
Tables S1 and S2
References (*31–81*)
MDAR Reproducibility Checklist
Data S1 to S4

Submitted 9 May 2022; accepted 12 September 2022
10.1126/science.abq7871

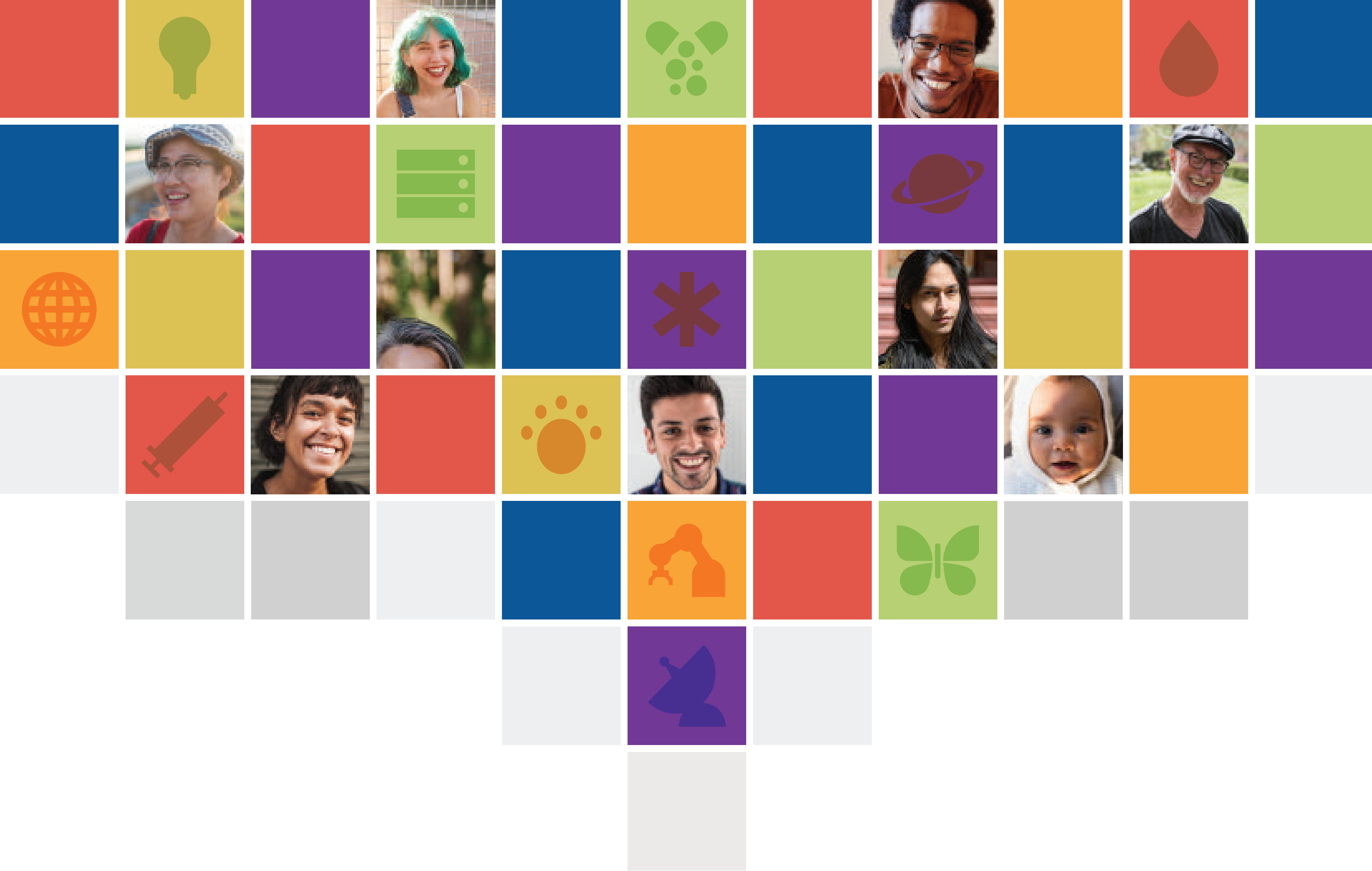

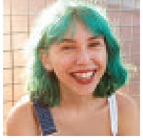

Join us in Washington, DC or Online for the 2023 AAAS Annual Meeting

Learn about groundbreaking multi-disciplinary research that advances knowledge and responds equitably to the needs of humanity:

- Plenary and Topical Sessions by accomplished speakers
- Scientific Sessions covering exciting advances in research and policy
- Lightning Talks on current scientific projects and initiatives
- E-poster presentations highlighting student STEM research
- Online and in-person networking opportunities and much more!

AAAS requires that all participants in its in-person meetings be fully vaccinated. For more information, **visit aaas.org/meetings**

CONNECT WITH US!
#AAASmtg

🌐 aaas.org/meetings

@AAASmeetings

/AAAS.Science

Science for Humanity

The scientific endeavor aims to provide findings, models, tools, and advances to better understand and address the myriad complex challenges facing society. Meeting this goal requires collective objectivity determined by a wealth of individual and diverse perspectives and experiences—a sample as broad as the diversity of disciplines in the scientific endeavor itself.

Highlighting the importance and just integration of our multiplicity, the 2023 AAAS Annual Meeting will feature groundbreaking multi-disciplinary research—research that advances knowledge and responds to the needs of humanity.

We thank the sponsors of the AAAS Annual Meeting!

Drexel UNIVERSITY

ASU Arizona State University

Get in touch with us about sponsorship and exhibit opportunities in Washington, DC and on the meeting virtual platform:
meetings.aaas.org/sponsors-exhibitors

AAAS S&T Policy Fellowships has turned 50—Forward!

For the last half century, the AAAS Science & Technology Policy Fellowships (STPF) has been bringing science to the US Government and helping enable the formation and execution of science-based policy. This Annual Meeting, STPF's past will be applauded and its future feted with special programming and activities. Celebrate with us the many hands and minds that have dedicated themselves to science in service of society.

A special thank you to our founding associations:

The American Society of Mechanical Engineers

American Physical Society

Institute of Electrical and Electronics Engineers

AAAS | Science & Technology Policy Fellowships | 50 YEARS

For full details see the online agenda or contact stpf-alumni@aaas.org to be added to the mailing list.

Invited Lecturers

AAAS President's Address

Gilda A. Barabino
President, AAAS
Chair, 2023 Annual Meeting

Doomed to Repeat: Why the History of Science is Indispensable

A debate moderated by Holden Thorp
Editor-in-Chief of *Science* family of Journals

Two Decades after the Day After Tomorrow: The Quest for How the Ocean Overturns

Susan Lozier
Georgia Institute of Technology

Sign Languages of The World

Carol Padden
University of California, San Diego

Homo Narrans Through the Looking Glass of Dark Matter

Chandra Prescod-Weinstein
University of New Hampshire

Communicating for Action to Address Latino Health Inequities

Amelie Ramirez
University of Texas Health Science Center at San Antonio

Policy and Technological Innovations Shaping the Energy Transition

Geri Richmond
U.S. Department of Energy

New Approach for Reducing Viral Respiratory Infections

Richard N. Zare
Stanford University

Conversation on the Use of Continental Ancestry

Moderator:

Agustín Fuentes
Princeton University

Speakers:

Joseph Graves
North Carolina Agricultural and Technical State University

Pilar Ossario
University of Wisconsin Law School

Anna Lewis
Edmond J. Safra Center for Ethics, Harvard University

BE A PART OF THE CONVERSATION

Diversity, Equity and Inclusion
Research Funding and Infrastructure
Climate Change
STEM Education
Science Communication
Artificial Intelligence
Information Technology and Security
International S&T Collaboration
Science and Values
Science Policy
Social and Behavioral Sciences
Global and Public Health

and more...

The 2023 AAAS Annual Meeting will convene in-person in Washington, D.C. for the first time in two years. Virtual access to the meeting will be available as well. Join us March 2-5, 2023!

Sign up for **Basic Access Registration** at no cost to to explore the Exhibit Hall, attend the live workshops, the e-poster competition, and the plenary sessions.

Purchase a **Deluxe Access Registration** (see below for fees) to attend the topical lectures, scientific sessions, lightning talks, special sessions, and all that is included in the Basic Access Registration. As a bonus, you will have access to all the on-demand videos captured at the conference.

ADVANCE DELUXE REGISTRATION RATES	AAAS Member Deluxe Access In-person & Virtual	Non-Member Deluxe Access In-person & Virtual	Deluxe Access: Virtual Only
General Attendee	$355	$500	$240
Postdoc	$155	$300	$155
Retired Professional	$285	$415	$240
Student	$75	$110	$75

Advance registration is available now through **February 7, 2023**. On-site registration rates will apply thereafter.

CONNECT WITH US!
#AAASmtg

aaas.org/meetings
@AAASmeetings
/AAAS.Science

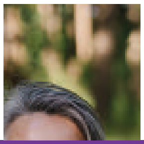

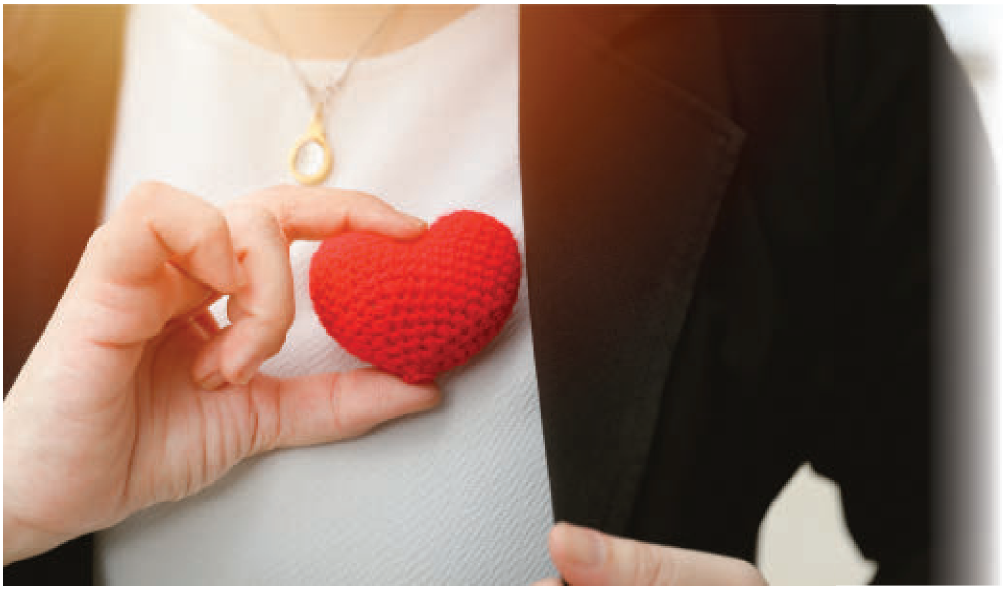

Science 2022
TOP EMPLOYERS

2022's Top Employers provide safety, support, and success for scientists

When it comes to selecting an employer that will value their expertise, voice, and career goals, scientists use a specific metric: safety. **By Alaina G. Levine**

On the day of a critically important meeting that had been in the works for months, Gene Sullivan had a funeral to attend. When the chief product strategy officer at **Insmed** (No. 1), a global biotech company based in Bridgewater, New Jersey, learned of a death in his family that would compel him to miss the conversation, he emailed his boss, the CEO. Within minutes he received a response that elicited a sigh of relief: Don't worry about the meeting at all, the email stated, we've got your back. His boss's simple and caring response meant the world to Sullivan and is an emblem of Insmed's dedication to its employees. "It's reflective of the CEO, and a lot of our culture comes from him," says Sullivan, noting that this wasn't the only time he had observed this kindness. "When an esteemed researcher in our group was ill, the entire organization was bending over backwards to allow him to work when he could and give him the time he needed for medical treatments. I feel proud of this organization."

Workplace pride is just one parameter scientists use to measure how much they appreciate their employer. In a world where companies have the capacity to behave unethically and uncompassionately and toss their best resource, human staff, to the side, it is gratifying to know there are companies that care, and that purposefully nurture an ecosystem that puts the needs of their team members first. For *Science's* top employers—20 of the best worldwide companies as chosen by our readers—the culture of concern they create is one that stands by safety in every sense of the word. Scientists who invest their careers with an organization want to know that they will receive all manner of protection, be it mental, emotional, physical, and even familial, in good times and bad. And when they do, it becomes a point of pride and long-term devotion.

Since 2002, *Science* has been studying the best organizations in biotech, pharma, and biopharma as part of its Top Employers Survey, conducted by Cell Associates, LLC. In the spring of this year, the global survey was completed by over 6,200 respondents, just under one third of whom have a doctorate. 37% said they have been in the workforce for more than two decades, and over half work in some aspect of research and development. Additionally, while 64% of respondents reported that although they are established in their career, they are still moving upwards, only 19% stated they are likely to change jobs in the next year.

The top 20 companies were selected using a statistical process that calculates a unique ranking score for each company rated, notes the team at Cell Associates. Only organizations that were rated by 35 or more respondents were eligible to become part of the top 20 best employers. And looking at the survey results, it is clear that scientists demand and receive workplaces that respect and value them. As Cell Associates notes, "Organizations that are seen as innovative leaders in the industry, that respect their employees, that have loyal employees who are provided the autonomy of decision making they need to do their best, and that are socially responsible are selected as best in class."

Safety = success

For scientists seeking professional advancement, safety encompasses many variables they use to select the right

cont.>

PHOTO: © QUALITY STOCK ARTS/SHUTTERSTOCK.COM

Top Twenty Employers

IMAGE: © WINDAWAKE/SHUTTERSTOCK.COM

2022 Rank	2021 Rank	Employer (global headquarters)	Innovative leader in the industry	Treats employees with respect	Is socially responsible	Provides employees with autonomy	Has loyal employees
1	1	Insmed (Bridgewater, NJ)	•	•	•		
2	3	Alnylam Pharmaceuticals (Cambridge, MA)	•	•	•		
3	4	Regeneron (Tarrytown, NY)	•		•		•
4	2	Incyte (Wilmington, DE))	•	•	•		
5	6	Syngenta Group (Basel, Switzerland)	•		•		•
6	5	Spark Therapeutics (Philadelphia, PA)	•	•	•		
7	7	Moderna (Cambridge, MA)	•	•	•		
8	12	Biocon Limited (Bangalore, India)	•		•		•
9	8	Vertex Pharmaceuticals (Boston, MA)	•	•	•		
10	9	Merck KGaA (Darmstadt, Germany)	•		•		•
11	10	Genentech (South San Francisco, CA)	•	•	•		
12	17	GSK (London, United Kingdom)		•	•		•
13	11	Abbott (Abbott Park, IL)	•	•			•
14	20	Roche – excluding Genentech (Basel, Switzerland)	•	•			•
15	14	Takeda Pharmaceutical Company Limited (Tokyo, Japan)		•	•		•
16	15	Novo Nordisk (Bagsvaerd, Denmark)		•	•	•	
17	19	Novartis (Basel, Switzerland)	•	•	•		
18	–	Dr. Reddy's Laboratories Limited (Hyderabad, India)		•	•	•	
19	18	Eli Lilly and Company (Indianapolis, IN)		•	•		•
20	–	Boehringer Ingelheim (Ingelheim, Germany)		•	•		•

The 20 companies with the best reputations as employers and the top three driving characteristics for each company, according to respondents in the 2022 survey undertaken for the *Science*/AAAS Custom Publishing Office.
The companies without a 2021 rank did not receive enough mentions to qualify or did not receive a high enough ranking from the 2021 survey.

workplace, and top employers recognize this. For these employees, safety relates not only to protecting people, but also ideas and creativity. They want to know that if they suggest bold solutions to company problems, they will be well received and valued.

Before Hans Clevers, head of pharma research and early development at **Roche** (No. 14), based in Basel, Switzerland, transitioned into this role from that of board member, he spent 3 years visiting multiple company sites to ascertain what makes it tick. “It struck me that there are people who work for us for a long time,” the M.D./Ph.D. says. “There is enormous competence but there is a safe environment where they feel comfortable. I decided to take this job because of this experience. At Roche, we have a safe environment where everyone can express their ideas and opinions in their own way, without fear of negative consequences.” Indeed, “protecting people and the environment isn’t just a legal or social obligation, it’s integral to our operations,” Roche proudly declares on its website.

At Insmed, safety means comfort to employees, who know they can change direction and follow the science wherever it may go without fear of reprimand or repercussion. Lisa Nair, vice president of global quality assurance, recalls a project that her colleagues were tackling in the development pipeline. When a setback occurred, the leadership team welcomed it with open arms and a belief that this “failure” was fuel. “One of our C-suite executives asked, ‘How do we turn this into an advantage for our patients?’” she recalls. “This was a powerful message for the team of scientists and engineers working on the project. It changed their mindset. That [kind of] message from the top empowers the organization to think creatively and to put the patient at the forefront of our minds.”

Science as the North Star

Not surprisingly, science is a priority for science-educated talent when they consider their employment options. They want to know that there are robust investments in R&D infrastructure within their chosen companies. Top employers go above and beyond in this respect because they recognize the value of support for discovery: It leads to extremely positive outcomes for patients as well as recruitment and retention of talented scientists. John Lepore, senior vice president and head of research at the Brentford, UK location of global biopharma giant for **GSK** (No. 12), has been with the company for 16 years and loves being a member of a team that is so devoted to finding transformational medicines by unlocking the secrets of nature. “It’s a personally fulfilling career for me, and I have seen my own opportunities grow,” he says. “We’ve become a world leader in using genetics, genomics and the science of the immune system for identifying novel drug targets, enabled by technologies like artificial intelligence and machine learning. We explore the science of immunology across all our different therapeutic areas. Because of the strength of the science and its potential in those areas, we have become a magnet for people.”

For Hanne Bak, senior vice president of preclinical manufacturing and process development at **Regeneron** (No. 3), the American biotech headquartered in Tarrytown, New York, science is prioritized because of its mission and familial ties—M.D./Ph.D. scientists launched and continue to lead this global force, which like many of the top employers, contributed to COVID-19 therapies or vaccines. “It may sound like something you put on a wall, but Regeneron is a science-first culture, founded by scientists who know the value of investing in science to solve problems,” she explains. Strategic business decision making are made by following the science, not the other way around.

Nimbleness of scientific and business systems is closely tied to innovation, and often leads to organizational success and better patient outcomes. A few years ago, Roche

cont.>

DRIVING CHARACTERISTICS OF TOP EMPLOYERS

2022	2021
1. Is an innovative leader in the industry	1. Is an innovative leader in the industry
2. Treats its employees with respect	2. Treats its employees with respect
3. Is socially responsible	3. Is socially responsible
4. Provides people in the organization with the autonomy of decision making they need to do their best	4. Has loyal employees
5. Has loyal employees	5. Easily adapts to change

* Driving characteristics are listed in descending order of impact on overall employer rankings.
** Shaded background indicates the characteristics in common for the 2 years.

leaders decided that the traditional company structure with hierarchies was no longer appropriate for fostering innovation and initiated a transformation into a team-focused organization. "We removed layers, making things easier for our employees," says Clevers. The teams are self-assembled, based on a need, gap, or problem that requires solving, and are naturally multidisciplinary. "People can assign roles to themselves on these teams. You don't report to a boss. The team leader is like a coach and the team makes decisions collectively—it's not in the hands of one person." The results so far have been fabulous: "There is a sense that you have your fate in your own hands; there is much more emphasis on the individual career plan and the freedom that comes with teams," he adds.

Other top employers have also ditched the standard corporate architecture of yesteryear, acknowledging that a more amorphous or flexible system more proactively engages and supports the birth of brilliant ideas, thereby encouraging creativity. Regeneron, for example, uses a matrix structure. Teaming arrangements at GSK are determined not by product line but by promising areas of scientific concentration and expertise. "We have a follow-the-science strategy for early discovery," says Lepore. "We don't only set out to say, 'Let's see if we can find targets in disease A, B, and C.' We say, 'Let's look at the science and see what other diseases it could lead to.' I am in a group that looks at particular immunological mechanisms, and the world is my oyster to determine where to apply this." Given the preponderance of survey respondents referencing innovation, culture, flexibility, and empowerment, it seems likely that scientists will continue to crave a workplace that is as agile as they are.

Concentrating on culture

Top employers recognize that to attract top scientific talent, they need to create a space for creativity, exploration, and innovation, aspects that often mirror academic culture. After all, Ph.D. scientists are used to certain expectations of scholarly liberty and intellectual adventure from their time in higher education. For example, Roche's scientists work on multiple projects that can extend beyond their normal job responsibilities. "We want to cultivate the freedom you see in academia," says Clevers, who spent 35 years in academia and founded several startups. "This is baked into the organization. They have the freedom to try things out … We know innovation can come from anywhere." Indeed, with half of Roche's successful pipelines coming from collaborations with academia, startups, and mergers and acquisitions, there is an emphasis on novel partnerships, according to Clevers.

A laser-sharp focus on developing stronger patient interventions is a key characteristic of top employers, one that aids these organizations in their recruitment. "It gives us so much energy to apply our research to make medicines where we can help patients the most," says Lepore. "A lot of our talent comes to us because they see a cultural element of being ambitious for patients. It's in our DNA literally and figuratively to help patients with that drive and focus." He shares the story of a colleague who was behind a key insight related to GSK's contribution to a potential new treatment for hepatitis B. "She is one of the only people in the world who can figure out the mechanisms of this molecule [related to hepatitis B]," says Lepore. "She recently talked about losing her brother to complications of hep B and said she determined that GSK was the best place to focus her career to do this."

An ecosystem that is punctuated by collegiality, collaboration, and community is one of the many reasons scientific staff stay with **Novartis** (No. 17), a pharmaceutical firm based in Basel, Switzerland, with early-stage research headquarters in Cambridge, Massachusetts. "It's awesome to come to work for the comradery and people and team approach to tackling science," says Nicole Renaud, U.S. head of data science in chemical biology and therapeutics at the Novartis Institutes for BioMedical Research, whose Ph.D. is in human and statistical genetics. "People are so willing to share their craft and work together as a team. The culture is really curiosity driven, taking that 'challenge accepted' approach to drug discovery."

Pharma and biotech firms spend a lot of energy, money, and time carefully considering how to actualize innovation. Strategic planning and board of directors meetings are often interspersed with questions about initiating official mechanisms that will spur teams to success. Innovation contests, formal discovery processes, and development devices that systemize the identification, cultivation, and funding of creative sparks and novel solutions, while in vogue, are not the only path

cont.>

IMAGE: © MAII YOSSAKORN/SHUTTERSTOCK.COM

COMPARISON OF TOP TEN COMPANIES BY TOP THREE CHARACTERISTICS

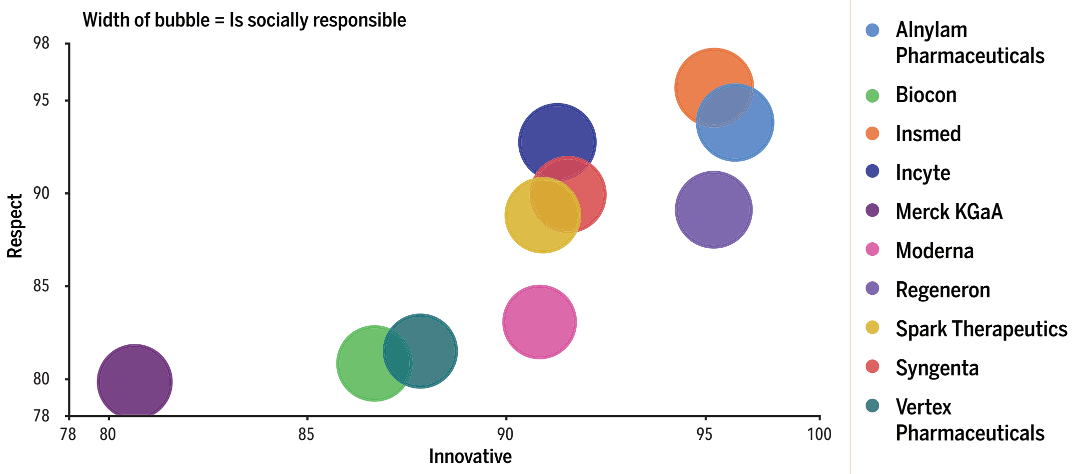

Comparison of the top 10 companies on the basis of 3 of the top drivers (scored out of 100): Is an innovative leader in the industry (x-axis), Treats employees with respect (y-axis), and Is socially responsible (bubble width).

to productivity. Some top employers rely more on the organic nature of internal collaboration and conversation, which often sparks creativity. "Those types of discussions are happening all the time every day," says Bak. "So when you have those deep conversations, you don't need innovation competitions. We don't need something that is special to pull it out—it's how we operate. It is woven into our DNA." When her team was trying to exploit a mechanistic understanding of a certain attribute of a molecule and its impact on the manufacturing process, she didn't have to wait for a team conclave or file a certain form to access the resources she needed—she simply reached out to colleagues in another corner of Regeneron. "I always marvel that when you ask people to help you or generate data for you, you get a yes," she says. "You don't have to seek approval or be within a budget. That's part of why we can unlock [creativity]." Perhaps this flexibility in fostering innovation, untethered to a specific corporate apparatus, is partly why the company experienced a 14% increase in its workforce last year, according to Christina Chan, senior vice president of corporate communications and citizenship at Regeneron.

GSK is also organic, but it leverages an ingenious rewards system for its coolest ideas. The Transformational Medicine and Vaccines Awards Program doesn't just honor "the person who last touched the medicine, but we go back in time to find the people who came up with the ideas and contributed to the key inflection points," says Lepore. "We celebrate good thinking and good science."

At Insmed, innovation is driven by a focus on unmet needs for treatments for rare diseases, something that requires a novel approach to problem solving. "There isn't a well-trodden path, so innovation is a necessity," says Sullivan. "We are forging new ground. The research group has a particular playground to explore, and they are given the freedom to try new things." This freedom has enabled Insmed to cultivate bold improvements in everything from basic R&D systems and outcomes to preclinical analysis of compounds, and from designing effective trials to the interventions themselves. Innovation is "part of our core ethos," adds Nair. "If you see a problem, you're empowered to research that and socialize it and gain support for it. And [the solution] is supported as well."

Devotion to diversity, equity, and inclusion

Lepore is very direct about what makes GSK attractive to talent: "Championing diversity is helping us tap into the best ideas," he says. "All of us in senior leadership take it very seriously and have a profound recognition that people with diverse backgrounds enable the best ideas and contribute to the diversity of thought." The biopharma powerhouse supports numerous diversity, equity, and inclusion initiatives. On the hiring front, they purposefully pursue diverse pools of candidates with established aspirations and progress incentives. GSK has a fellowship training program with historically Black colleges and universities (HBCUs) like Howard University in Washington, D.C. The company also prioritizes clinical trial diversity.

Diversity also means implementing a different model of employee support, one in which the company molds to the staff's unique needs, concerns, and challenges and not the other way around. In fact, top employers act proactively to protect and help their most precious resource: people. Nair recalls that the spouse of one of Insmed's team members is a health worker who was deemed essential during the pandemic, obligating this person to work extra shifts. The family had a small child, and suddenly the situation at home became untenable. While the employee never mentioned their challenges, "we noticed them and said, 'If this isn't working for you, that's no problem,'" she recounts. Her team offered multiple options, including working different hours and days and cutting back the schedule to unburden that employee. "It was very empowering, and you felt you were supporting a colleague and a friend in their personal journey." It's a standard scenario for pharma, which embraces a flexible work environment, knowing that when employees feel safe in

cont.>

IMAGE: © EAMESBOT/SHUTTERSTOCK.COM

POSTDOCTORAL TRAINING PROGRAM

PURSUE YOUR PASSION FOR SCIENCE IN A DYNAMIC AND INNOVATIVE ENVIRONMENT

Applications Accepted October 1 to December 1, 2022
Start dates flexible, but if possible, Summer 2023

LEARN MORE AT
https://www.regeneron.com/postdoctoral-training-program

REGENERON
SCIENCE TO MEDICINE®

Who's the top employer for 2022?

Science Careers' annual survey reveals the top companies in biotech & pharma voted on by *Science* readers.

Read the article at sciencecareers.org/topemployers

Science 2022 TOP EMPLOYER

POSITIONS OPEN

HEALTH
UNIVERSITY OF UTAH

TENURE-TRACK ASSISTANT OR ASSOCIATE PROFESSOR

In anticipation of substantial growth over the next five years, the Department of Human Genetics at the University of Utah School of Medicine (**www.genetics.utah.edu**) seeks outstanding applicants for one or more tenure-track positions at the level of **Assistant** or **Associate Professor**.

We seek highly creative scientists who use genetics to investigate fundamental biological problems. We encourage applicants whose research focuses on evolutionary and functional genetics and genomics; human and medical genetics; and research programs using established model or unconventional organisms. In addition to this search, we are hiring new faculty who specialize in computational genomics.

As part of a vibrant community of faculty with a strong track record of collaborative mentorship, research, and funding, the Department of Human Genetics lies at the interface between basic and clinical sciences. This creates ample opportunities for interdisciplinary research (e.g., our Center for Genetic Discovery, Transformative Excellence Program in Evolutionary Genetics and Genomics, and Center for Genomic Medicine). As a department, we value diversity and equity, and believe that the best science is done when researchers of diverse backgrounds are integrated and supported in an inclusive manner. We seek faculty who share these values. Our institution is set in a unique geographical landscape that attracts a heterogeneous and productive scientific community.

Successful candidates will receive a generous startup package and enjoy a stimulating research environment that places a strong emphasis on innovation and interaction.

Application deadline:
Nov. 1, 2022 (https://utah.peopleadmin.com/postings/138515)

For questions, please contact Kandace Leavitt:
kandace.leavitt@genetics.utah.edu

Featured participants

GSK
www.gsk.com
Insmed
www.insmed.com
Novartis
www.novartis.com
Regeneron
www.regeneron.com
Roche
www.roche.com

that respect, they can provide better solutions. Some of Insmed's employee work schedule improvements stem from its response to the pandemic, but most of the improvements are just a symbol of its makeup. "My team is a global team, and in order to support patients all over the world, we create an environment where people can have flexible work schedules to support themselves and their families," says Nair.

Passion beyond profits

One of the most interesting data points of the survey is not directly related to science, patients, or profits, but to passion. It is not surprising that scientists position passion as a top metric for their choice of employers—after all, it is their passion to unveil the hidden corners of the universe that drives some toward science in the first place. At Roche, passion is explicitly part of their vision: "We foster a culture of respect, trust, and openness that helps us to bring our authentic selves into our work, develop genuine relationships, and pursue our passions," says Clevers.

And these passions take many forms. For scientists, it always starts with the science. "[Doing] the science is like being a kid in the candy store," says Susan Moody of her experience as executive director and clinical program leader, translational clinical oncology, Novartis Institutes for BioMedical Research. "There's always so much cool, innovative work going on." Also high on the list is the passion to help people. "There is a trust that we are working toward the common goal of helping patients who are suffering," she adds.

That's not all. From encouraging more kids to go into science, technology, engineering, and mathematics (STEM) careers to sponsoring community enterprises where companies give back and encourage their staff to do so as well, top employers fuel the passion that creates a loyal workforce. Regeneron's employees are very engaged in the many causes the company supports, from the Regeneron International Science and Engineering Fair to volunteering for philanthropic endeavors. What originated as the firm's Day for Doing Good has morphed from a one-day event to several week-long events, an annual concentration of activities that advance community nonprofits. "We look for people who have a deep purpose. It should be no surprise that we support equity and STEM education," says Chan. "We take their engagement and continue to grow it. [Regeneron's mantra,] 'Doing Well by Doing Good,' helps feed their souls beyond themselves, knowing that the company is willing to invest in them and their communities as well."

Indeed, an investment in human resources development is often the one that produces the biggest return on investment.

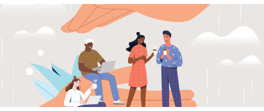

DEMOGRAPHICS

GENDER:

55% Male, 40% Female, 5% No response

EXPERIENCE:

76% report having not yet reached a career peak.
70% report having 10 years or more of work experience.

HIGHEST DEGREE EARNED:

30% Doctorate, 33% Masters, 32% Bachelors, 5% Other

COMPANY TYPE:

32% Biotech, 38% Biopharma, 22% Pharma, 8% Other

NATURE OF WORK (TOP RESPONSES):

Respondents were allowed to select more than one function to describe jobs: 12% Basic Research, 16% Applied Research, 24% Development, 9% Production, 11% QA/QC/Regulatory Affairs, 3% Human Resources/Public Affairs, 9% Administrative/Executive, 15% Other

GEOGRAPHY:

63% North America, 15% Europe, 17% Asia/Pacific Rim, 5% rest of world

Top employees pursue a systematic approach to professional development and advancement. "We have always taken employee growth very seriously and our retention rates are very good," says Nair. "It's not just words on a paper—they are lived, breathed, and experienced every day, and it's because of this that people stay at Insmed." At GSK, scientists "come here because it's an important place to build their career while making important medicines for patients, so it's exciting and fun," says Lepore. "But then we have to keep them here. We spend a lot of time in planning career paths. It's a longitudinal discussion between managers and staff."

Scientists looking for a job and a place to establish and grow their careers have a choice of employers. What ultimately drives that choice is not data, but rather a belief that the 40-plus hours per week they sacrifice is for the greater good, for both themselves and for patients, and that their employer is a sanctuary of science, clarity, and light, not an inferno of disrespect and dissonance. *Science*'s top employers are those that not only recognize the opportunity to shine brightly from a corporate citizenship perspective, but also embrace the chance to offer a secure and supportive environment to talented scientists who want to help their fellow humans.

To read this article online, visit ScienceCareers.org/TopEmployers.

Alaina G. Levine is a professional speaker, STEM career coach, and author of the books Networking for Nerds *(Wiley, 2015) and* Create Your Unicorn Career *(forthcoming).*

IMAGE: © MENTALMIND/SHUTTERSTOCK.COM

MIT Institute for Medical Engineering and Science
Ragon Institute Tenured Faculty Position

The Ragon Institute, together with the Institute for Medical Engineering and Science (IMES) at The Massachusetts Institute of Technology (MIT), in Cambridge, MA is seeking outstanding scientists for a **tenured faculty position** to start on **July 1, 2023** or on a mutually agreed date thereafter. The Ragon Institute has its own recently renovated building located in Cambridge, MA. The Ragon Institute was officially established in February 2009 as a joint institute involving faculty from Massachusetts General Hospital (MGH), MIT, and Harvard University. IMES was established in 2012 as the center for Human Science on the MIT campus, and integrates engineering, science, and medicine to advance and accelerate innovation in health through research and education.

This search is for a candidate to be hired into an **Associate Professor with Tenure or Full Professor faculty position at MIT**. Applicants must have a Ph.D. and/or M.D. (or equivalent degree) in medical engineering, medical science, or a closely related field, have a track record of exceptional achievement in basic or translational research, and an outstanding independent research program that supports the two institutes' shared goal of harnessing the immune system to prevent and cure human diseases.

Several opportunities exist at the interface of IMES and the Ragon Institute, such as addressing challenges pertinent to infectious diseases and auto-immune disorders. Broad areas of mutual interest include understanding the physical and biological mechanisms underlying how the immune system functions, applied microbiology and virology, and efforts that leverage this knowledge and engineering design to develop therapies, diagnostics, and vaccines that can be translated to the clinic. Of particular mutual interest include use of computational approaches, including systems biology, artificial intelligence, machine learning, physics-based modeling, and approaches directed toward understanding innate and adaptive immunity with the goal of preventing and curing disease. Additional specific topics include the development of new vaccination concepts and adjuvants; the design of new delivery approaches for vaccines and therapies; and diagnostic approaches that enable rapid and reliable detection of pathogens and monitoring of biomarkers of immunity. The applicant should present a strong research plan which can synergize with ongoing basic, applied and translational research efforts at the Ragon Institute and in IMES.

Faculty duties include teaching at the undergraduate and graduate levels, advising students, conducting original scholarly research, and developing course materials at the undergraduate and graduate levels. The successful candidate will be provided with a generous start-up package to complement outstanding laboratory and office space at the Ragon Institute, as well as access to state-of-the-art core facilities including advanced flow cytometry, microscopy, BSL-3 facilities, and an extensive clinical specimen repository. The successful candidate will be expected to build and maintain an internationally recognized, extramurally funded research program complemented by substantial support from Institute funds. The candidate should possess the ability to work collaboratively with other scientists and engineers, in addition to the scholarly qualities required to mentor doctoral students from graduate programs at MIT.

Interested candidates should submit application materials electronically **https://faculty-searches.mit.edu/mit-ragon**. Each application must include: a curriculum vitae; the names and addresses of three or more references; a strategic statement of research interests; and a statement of teaching interests. In addition, candidates should provide a statement regarding their views on diversity, inclusion, and belonging, including past and current contributions as well as their vision and plans for the future in these areas. It is the responsibility of the candidate to arrange for reference letters to be uploaded at **https://faculty-searches.mit.edu/letters/**.

Please address questions to **imes-search@mit.edu**.
Responses received by **December 1, 2022** will be given priority.

With MIT's strong commitment to diversity in engineering and science education and research, we especially encourage those who will contribute to our diversity and outreach efforts to apply.

MIT is an equal employment opportunity employer. All qualified applicants will receive consideration for employment and will not be discriminated against on the basis of race, skin color, gender identity, sexual orientation, religion, disability, age, genetic information, veteran status, ancestry, or national or ethnic origin.

WORKING LIFE

By **Kathleen Martin** *and* **John Hwa**

Better together

Our postdoctoral fellow came by our offices distraught, seeking advice. His wife's adviser was moving to another institution, leaving her in urgent need of a new postdoctoral position. To make matters more complicated, she would soon give birth and needed a position that offered some paid maternity leave. We listened sympathetically and suggested some options, most of which the couple had already considered and discarded. That evening, chatting at home about the day's events, we shared our concerns that we might end up losing our trainee. But we had an idea for an unconventional solution—one that grew out of our own experiences as a dual scientist couple.

Like many scientist couples, we met in graduate school and navigated our careers together. Thanks to the creative efforts of a department chair, we secured faculty positions at the same institution. But we had been cautioned that establishing ourselves as independent scientists might be challenging, as all too often one member of a scientist couple ends up being reduced to "so-and-so's spouse." Our offers included labs on separate but nearby campuses, with primary appointments in different departments and research programs in distinct areas of cardiovascular biology. That approach allowed us to forge separate identities—so successfully that some colleagues, even after years of interactions, were surprised to learn we were married.

ILLUSTRATION: ROBERT NEUBECKER

> **"In each couple, the spouses ... are independent yet interlinked."**

Then, at midcareer, we unexpectedly received offers from a new institution that offered a rare opportunity: two positions that included startup packages, an exciting scientific environment, and adjacent lab and office space in a new, open-floor-plan research center. We had already begun to collaborate, but had some reservations about spending all our working hours in neighboring labs and offices. Would being together 24 hours a day strain or strengthen our relationship?

In the end we figured that if we can survive cooking together—one of us is a recipe stickler, the other improvises wildly—we could handle adjoining labs. And we soon found the advantages of working together outweighed any negatives. Having your strongest supporter and collaborator nearby is a major asset when navigating stressful deadlines, tough critiques, and logistical challenges. Our differences are often complementary: When one spouse's rigor and pragmatism pair with the other's adventurous creativity, we both do our best work. We disagree from time to time, but communication and compromise propel both our science and our relationship forward. The physical proximity also allows us to share equipment and reagents and to serve as an additional mentor to each other's trainees, who benefit from our different perspectives and expertise.

So, 3 years after beginning our experiment of working more closely together, we realized this could be the solution to our trainee's problem. We decided to offer his spouse a position.

The couple was surprised, not having considered this possibility. We discussed the pros and cons with them, recounting our own journey. We assured them they would each report to a separate primary adviser, pursue distinct projects in different fields, and, most important, that if too much togetherness ever became a strain on their relationship, we would help one of them find a new position at our institution. With some trepidation but immense relief, they agreed.

That was 10 years ago. They fared so well that when other opportunities arose over the years we extended offers to additional couples. We now have five pairs of spouses in our labs, a fact that inevitably prompts shock, laughter, and curiosity from our colleagues. In each couple, the spouses bring different strengths, temperaments, and approaches to science. Acknowledging these differences and any mismatches in their career stages, we customize our mentoring approach, recognizing that they are independent yet interlinked. The multiple spousal teams have also created camaraderie and a supportive network within our labs, and we are pleased that we have not yet had to make good on our promise to find separate opportunities for any of them. For us, and the couples in our labs, science is better when we can do it together. ■

Kathleen Martin and John Hwa are professors at the Yale School of Medicine. Send your career story to SciCareerEditor@aaas.org.


Share

mRNA-LNP Products & Services

For Vaccine and Immunotherapy Development

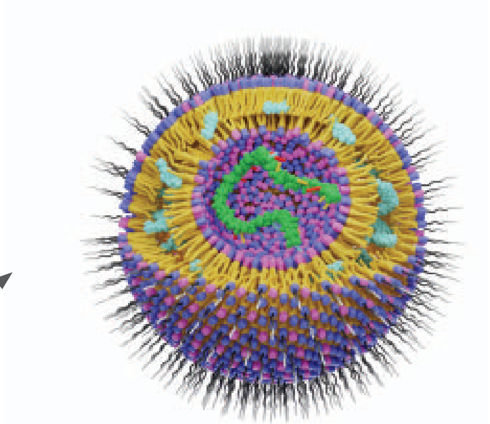

mRNA-LNP Formulation

Antibody Engineering

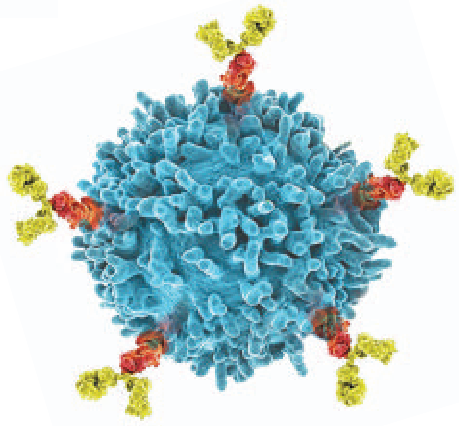

CAR-T/NK Development

mRNA-LNP Products

- eGFP
- eGFP (DNA/LNP)
- mCherry
- mCherry-LUC
- Luciferase
- IL-15
- Anti-CD19
- Anti-BCMA
- Anti-HER2
- Anti-EpCam/CD3
- Cas9
- EGFP DNA/LNP
- COVID-19 Spike protein (Alpha variant)
- COVID-19 Spike protein (Omicron variant)
- COVID-19 Spike protein (Delta variant)
- COVID-19 Nucleocapsid
- COVID-19 RBD protein
- MAGE3/MHC

Discover more | www.promab.com

ProMab
Biotechnologies, Inc.

2600 Hilltop Dr, Building B, Richmond, CA 94806
1.866.339.0871 | info@promab.com

SCAN ME